UNIVERSITAT DE BARCELONA

Computational Study on the Application of Two-Dimensional Materials in Heterogeneous Catalysis

Ling Meng

Computational Study on the Application of Two-Dimensional Materials in Heterogeneous Catalysis

Ling Meng

UNIVERSITAT DE BARCELONA

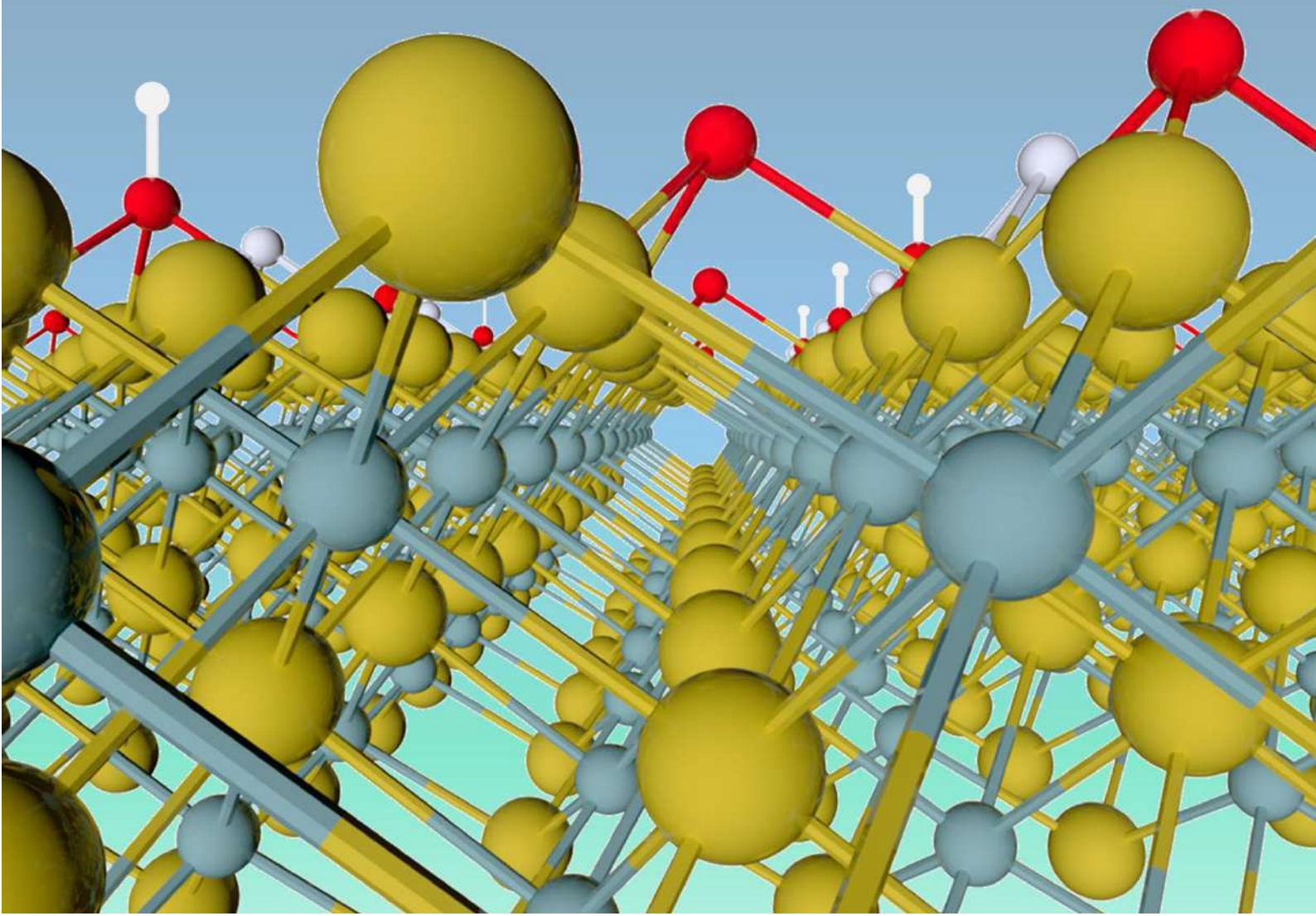

Memòria presentada per

Ling Meng

Per a optar al grau de Doctor per la

Universitat de Barcelona

Programa de doctorat en Química Teòrica i Modelització Computacional

Computational Study on the Application of Two-Dimensional Materials in Heterogeneous Catalysis

Dirigida per:

Dr. Francesc Viñes Solana
Universitat de Barcelona

Prof. Francesc Illas Riera
Universitat de Barcelona

Tutor:

Dr. Pablo Gamallo Belmonte
Universitat de Barcelona

UNIVERSITAT DE BARCELONA

Barcelona, September, 2024

Abstract

Currently, global fossil fuel consumption is increasing, environmental problems are becoming serious, new clean energy technologies are being actively explored. High-performance catalytic materials play a crucial role in the field of energy storage and conversion, here, two-dimensional (2D) catalytic materials have emerged as ideal choices for a wide range of catalytic processes due to their low cost, superior physical/chemical properties, and unique geometric and electronic characteristics. In this Thesis, two related 2D materials are explored: (*i*) MXenes, for hydrogenation reactions in heterogeneous catalysis, as well as the effect of surface terminations in electrocatalysis; (*ii*) the symmetric and asymmetric structures of N-doped graphene supported single metal atom catalysts (NG-SAC) electrocatalytic applications.

In the first part, density functional theory (DFT) is employed to construct Pourbaix diagrams for around 450 surface terminations of $Ti_3C_2T_x$ (0001) MXene, focusing on identifying stable surface structures under working conditions and examining the impact of different surface terminations on the electrocatalytic performance of hydrogen evolution reaction (HER), carbon dioxide reduction reaction (CO_2RR), and nitrogen reduction reaction (NRR). Our findings reveal that surface functional groups significantly reduce the limiting potential and cost. For HER, higher proportions of –O groups enhance catalysis by modulating hydrogen bonding. For CO_2RR and NRR, –OH groups act as proton donors, improving catalytic activity, and –F groups also contribute to CO_2RR catalysis. Moreover, the hydrogenation of olefins on Mo_2C (0001) MXene was also investigated in collaboration with Prof. Alexey Fedorov (ETH Zurich, Switzerland) and Prof. Dr. Igor V. Koptyug (International Chromatography Center, SB RAS, Russia) to better understand the mechanisms behind paired and unpaired H_2 additions.

In the second part, the key role of NG-SAC catalysts with broken geometrically symmetric structures in improving the electrocatalytic efficiency of CER was explored. Through an extensive and detailed comparative study, low-coordination NG-SAC is found to be the key active sites, which contrasts with the traditionally considered high-coordination geometries. In addition, NG-SAC catalysts for oxygen reduction reaction (ORR) in alkaline media also were screened, and by analyzing the different transition metals anchored, catalysts with high activity and stability were identified, demonstrating their potential as alternatives for expensive platinum-based catalysts.

Acknowledgements

The gears of fate quietly turned in 2020, and I was incredibly fortunate to read an article by Prof. Francesc Viñes and Prof. Francesc Illas on a particular day of that year. I emailed you with much expectation, asking if you would be willing to consider me as your PhD student. The moment you replied 'yes', I was happy for a long time. As I am a non-EU resident, you helped me consult various documents that I was asked to submit, and solved a lot of problems for me before I even arrived, and after I arrived, you also helped me with my expired visa. During my PhD period, from academics to life, your unconditional help has warmed my heart to today.

Next, I'm deeply grateful to Prof. Francesc Viñes and Prof. Francesc Illas for your invaluable guidance and support throughout the research process, as well for the comfortable research environment. Your encouragement and advice have been crucial to my growth, and your patient when I made mistakes, and I have to say that you are the best teachers in my life. The years I spent here are the happiest and most fulfilling of my life, I am very honoured to be your student. Also special thanks to Prof. Pablo Gamallo Belmonte, for recommending me to company when I looked for a job, as well to Prof. Angel Morales-García, my ex-office colleague in the same group, for the help and encounter I had with all of you, and finally, a special thanks to Prof. Kai S. Exner for his patient advice and guidance during my stay in Germany.

Also, Many thanks to Dr. Martí López, and my office colleagues Dr. Pablo Lozano Reis, Manuel Antonio Cánovas Montes, Néstor García, David Carvalho, Manel Serrano, as well David Vázquez, Dr. María Voccia and Dr. Moses Abraham, for your great help at all stages of my research and life, thank you for your patience and always providing me with support and advice when I encountered difficulties, as well for your selfless help and sincere friendship, moreover, also thanks to all colleges in my group: Adrià Calzada, Daniel Dolz, Diego Ontiveros, Miquel Allès, Raul Morales and Eleonora Romeo, the time I worked with you is an invaluable treasure.

Still, I would like to thank my Master supervisors, Prof. Yan Likai and Prof. Su Zhongmin, for always contacting and caring about me even after I graduated and giving me help as much as they could. In addition, I would like to thank all my good friends, Fengxia Deng, Cao Wei, Yongpeng Yang, Jianhua Hou, Lele Zhao, Ruoshi Wang, and Zhang Chi, for being like family members. Most importantly, thank you for your friendship and for being important part of my life.

Finally, I am very grateful to my beloved family, especially my parents and my boyfriend Sun Changzhe, for your unconditional love and all that you give to me, for tolerating my bad emotions over the years, for your support and understanding when I am down, your support is the strong that enables me to do work well, thank you for all that you have done for me. Also, thanks to my cousins for always sharing with me when I am happy and comforting me when I am sad.

At this moment, as I write these words, it means that my PhD period is coming to end, and the countdown to say goodbye with all of you whom I met during my PhD also begins. But as someone once said, parting is the second most romantic thing in the world, because from then on, every meet will turn into a reunion, and reunion is the most romantic thing in the world. Therefore, besides sincerely thanking all the people who have helped and supported me—whether in the past or present, looking forward to each future reunion with all of you.:)

致谢

命运的齿轮在 2020 年悄然转动，我非常幸运地在那年的某一天读到了 Francesc Viñes 教授和 Francesc Illas 教授的文章。我满怀期待地给你们发了一封邮件，询问是否愿意考虑接收我为博士生。当你们回复“是”的那一刻，我开心了很久。由于我是非欧盟居民，你们帮我查询了所需提交的各种文件，并在我到达之前为我解决了很多问题。而在我到达后，也帮助我处理即将到期的签证问题。在我整个博士阶段，从学术到生活，你们无条件的帮助让我至今心怀感激。

接下来，我要由衷感谢 Francesc Viñes 教授和 Francesc Illas 教授，感谢你们在整个研究过程中提供的宝贵指导和支持，以及为我创造了舒适的科研环境。你们的鼓励和建议对我的成长至关重要，在我犯错误时也总是耐心包容。我必须说，你们是我生命中遇到的最好的老师之一。在这里度过的几年是我人生中最快乐、最充实的几年，能够成为你们的学生我深感荣幸。同时，我也要特别感谢 Pablo Gamallo Belmonte 教授，感谢您在我找工作时帮我推荐工作。还要感谢同组的 Angel Morales-García 教授，我的前办公室同事，感谢你们给予我的帮助以及我们的相遇。最后，特别感谢在我德国期间耐心给予我建议和指导的 Kai S. Exner 教授，万分感谢。

同时，我要感谢 Martí López 博士, 我的办公室的同事 Pablo Loza-no Reis 博士、Manuel Antonio Cánovas Montes、Néstor García、David Carvalho、Manel Serrano，以及 David Vázquez、María Voccia 博士，Moses Abraham 博士，感谢你们在我研究和生活的各个阶段给予了我极大的帮助。感谢你们的耐心，在我遇到困难时给予我的支持和建议，以及无私的帮助和真诚的友谊，此外，还要感谢我组内的所有成员： Adrià Calzada、Daniel Dolz、Diego Ontiveros、Miquel Allès、Raul Morales 和 Eleonora Romeo，与你们共事的时光是我宝贵的财富。

此外，我还要感谢我的硕士导师颜立楷教授和苏忠民教授，即使我已经毕业，依然与我保持联系，关心我的发展，并在力所能及的范围内给予我帮助。另外，我还要感谢我的所有好朋友，邓凤霞，曹伟，杨永鹏，侯建华，赵乐乐，王若诗，张翅等人，感谢你们像家人一样陪伴在我身边，最重要的是感谢你们的友谊，感谢你们成为我生活中重要的一部分。

最后，我非常感激我挚爱的家人们，特别是我的父母和我的男朋友孙长哲，感谢你们无条件的爱和对我的付出，感谢你们多年来包容我的坏情绪，在我情绪低落时给予的支持和理解。你们的支持是我能够顺利完成这项工作的坚强后盾，感谢你们为我所做的一切。还有我的表兄弟姐妹们，感谢你们总是在我开心时与我分享快乐，在我难过时给予安慰。

此时此刻，当我写下这些文字时，意味着我的博士生涯即将画上句号，与博士阶段相遇的各位的分别也已进入倒计时。但有人曾说过，分别是世界上第二浪漫的事，因为从此之后，每一次相遇都将变成重逢，而重逢，是世界上第一浪漫的事。因此，除了衷心感谢所有曾经帮助和支持过我的人——无论是过去还是现在，我更期待未来与各位的每一次重逢。

Abbreviations

AIT	*Ab Initio* Thermodynamics
bcc	Body Centered Cubic
BEP	Brønsted-Evans-Polanyi Relationship
BO	Born-Oppenheimer
CO_2RR	Carbon Dioxide Reduction Reaction
CER	Chlorine Evolution Reaction
CFE	Computational Fluorine Electrode
CHE	Computational Hydrogen Electrode
CI-NEB	Climbing Image Nudged Elastic Band
CN	Coordination Number
CPET	Concerted Proton Electron Transfer
DFT	Density Functional Theory
DOS	Density of States
ESM	Energy Span Model
ESSI	Electrochemical-Step Symmetry Index
EXAFS	Extended X-Ray Absorption Fine Structure
FE	Faradaic Efficiency
fcc	Face Centered Cubic
GGA	Generalized Gradient Approximation
hcp	Hexagonal Closed Packed
HER	Hydrogen Evolution Reaction
IPCC	Intergovernmental Panel on Climate Change
IS	Initial State
IUPAC	International Union of Pure and Applied Chemistry
KPD	Kinetic Phase Diagram
LDA	Local Density Approximation
NG-SAC	N-Doped Graphene Supported Single Atom Catalyst
NMV	Normal Modes of Vibration
NRR	Nitrogen Reduction Reaction
ODC	Oxygen Depolarized Cathodes
OER	Oxygen Evolution Reaction

ORR	Oxygen Reduction Reaction
PBE	Perdew-Burke-Ernzerhof
PES	Potential Energy Surface
PCET	Proton-Coupled Electron Transfer
PDOS	Projected Density of States
PDS	Potential-Determining Step
p-H_2	Para-Hydrogen
PHIP	Para-Hydrogen Induced Polarization
PW	Plane Waves
RHE	Reversible Hydrogen Electrode
RDI	Rate-Determining Intermediate
RDTS	Rate-Determining Transition State
SAC	Single Atom Catalyst
SHE	Standard Hydrogen Electrode
2D	Two-Dimensional
TOF	Turnover Frequency
TF	Thomas−Fermi
TM	Transition Metal
TMD	Transition Metal Dichalcogenides
TS	Transition State
TST	Transition State Theory
VH	Volmer-Heyrovsky
VT	Volmer-Tafel
ZPE	Zero Point Energy

Table of Contents

Chapter 1

Introduction

1.1. Motivation and Catalysis

In recent decades, increasing global dependence on fossil fuels has led to growing severe environmental pollution and energy crises.[1] Reports from the Intergovernmental Panel on Climate Change (IPCC)[2] emphasize the detrimental consequences of rising global greenhouse gas emissions and the urgency of getting rid of our dependence on fossil fuels. Thus, the concept of clean energy has emerged,[3] aiming to suppress emissions, improve energy efficiency and promote sustainable development through the utilization of renewable energy sources such as solar,[4] wind,[5] and water,[6] which is a foreseeable trend in future global energy development. Despite the inevitable transition towards renewable energy sources, the production and utilization remain insufficient.[7] Therefore, the main challenge is to better develop and utilize sustainable and clean energy sources.

The term "catalysis" was first introduced by the Swedish chemist Berzelius in 1835 and first defined by Ostwald in 1894 as "*Catalysis is the acceleration of a slow chemical process by the presence of a foreign material"*.[8,9] In 1996, the International Union of Pure and Applied Chemistry (IUPAC) stated that "*A substance that increases the rate of a reaction without modifying the overall standard Gibbs energy change in the reaction; the process is called catalysis*".[10] It is estimated that around 90% of the chemical industry involves catalysis at some stage of production.[11] Obviously, catalysis cannot be achieved without a substance called catalyst, a chemical compound or material that allows the reaction to take place by an alternative mechanism that is much faster than the non-catalyzed mechanism,[12] usually reacting with one or more reactants to form an intermediate, which subsequently produces the final reaction product. However, ideally, the catalyst is not consumed by the reaction and remains unchanged after the reaction.[13] It is important to note that catalysts do not alter the thermodynamics or equilibrium position of the reaction, as they serve only to facilitate forward and reverse reactions,[14] increasing the reaction rate constants, but lowering the activation energy required for the reaction to take place, as shown in Figure 1.1.

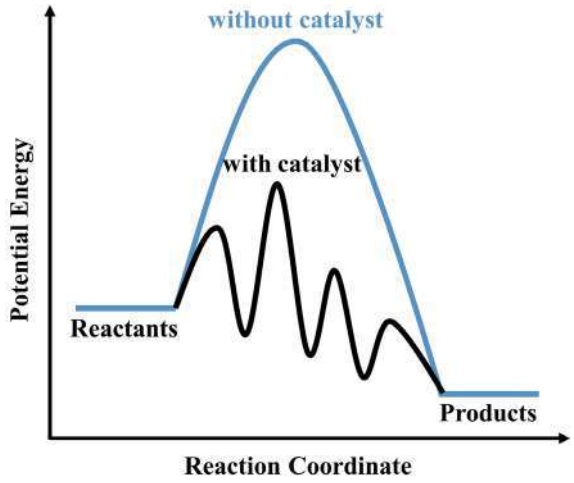

Figure 1.1. Schematic representation of a generic energy profile for a complex reaction. The blue line represents the energy barrier needed without the catalyst and the black line represents the different energy barriers to surmount the possible elementary steps when the reaction is catalyzed.

Catalysis has significantly impacted the chemical industry and academic field over the past century, playing a crucial role in addressing environmental pollution and energy crises.[15,16] It is primarily manifested in four aspects: *i*) Enhancing reaction efficiency and reducing industrial energy consumption;[17] *ii*) accelerating the decomposition of vehicle exhaust and industrial waste to mitigate pollution;[18] *iii*) converting harmful chemicals into high-value products such as ethanol through catalytic reduction of CO_2;[19] *iv*) playing a critical role in clean energy production by efficiently utilizing resources, such as hydrogen production via water electrolysis.[20]

Catalysis can be divided into homogeneous and heterogeneous. In homogeneous catalysis, the catalyst and reactants are in the same phase, whereas in heterogeneous, in different phases, with the reaction occurring at or near the interface between the phases.[21] Here one should add enzymatic catalysis, although this is not at all considered in the present work. On the other hand, even if homogeneous catalysts can play a crucial role in the industrial production of chemicals (such as converting cellulose into high-value jet fuel)[22] and offer advantages like high activity and selectivity, their separation process is expensive, time-consuming, and often requires significant energy.[23] In contrast, in heterogeneous catalysis,[24] products easily detach from the catalyst surface and are easy to separate, resulting in higher efficiency and lower costs, not only that, heterogeneous catalysts also can continuously generate active sites with reactants under reaction conditions, thus are heavily relied upon by the chemical and energy industries, such as the Haber-Bosch process for ammonia synthesis.[25] Generally, heterogeneous catalytic reactions begin with

the adsorption of gas- or liquid-phase reactants on the catalyst surface, specifically on active sites of surface to activate for the subsequent chemical transformation reaction, finally, the product desorbs and is released into the surrounding medium with catalyst regeneration.[26] Ideally, a catalyst can be used thousands of times, which leads to the concept of catalytic cycle.[27] Note also that, according to the *Sabatier* principle,[28] the initial adsorption step mentioned above should strike a balance —not too weak to limit catalytic activity, nor too strong to prevent desorption, avoiding catalyst poisoning by surface blockage, and the same for product desorption.

Electrocatalysis[29] and thermocatalysis[30] are two primary categories of heterogeneous catalysis, the former involves a catalytic process that utilize electrical currents to drive electrochemical reactions on electrodes surface, wherein electrocatalyst facilitates the electron transfer between the reactants and the electrode to promote the desired electrochemical reactions; the latter refers to the use of heat to accelerate a chemical reaction, wherein thermocatalyst facilitates the reaction by providing an alternative reaction pathway with reduced activation energy, thus enabling faster reaction at a specific temperature. Therefore, the development of highly efficient and cost-effective electro/thermocatalysts is essential to translate cutting-edge technology from fundamental research to practical applications, despite having made some advancements previously,[31,32] challenges such as insufficient catalytic efficiency, low selectivity or high cost still remain.[33] Presently, scientists are delving into the mechanisms of catalytic reactions and the features influencing catalytic performance, so that composition, size, and morphology of the catalyst can be precisely controlled to further improve performance.[34,35]

1.2. Two-Dimensional (2D) Materials

Since the successful exfoliation of graphene,[36] two-dimensional (2D) materials, such as Transition Metal Dichalcogenides (TMDs),[37] black phosphorus,[38] and MXenes,[39] have been rapidly developed, with unique geometric and electronic properties,[40] such as high surface area, good electrical conductivity, and tunable band gaps, etc. The thickness of 2D materials is of a few atoms only,[41] allowing precise control of this thickness to fine-tune their electronic properties,[42] which is not achievable with 0D (*e.g.* nanoparticles), 1D (*e.g.* nanowires)[43] and 3D materials (*e.g.* bulk or extended surfaces).[44] 2D materials also are highly sensitive to external stimuli, such as chemical modifications, chemical doping, and molecular adsorption,[45] as well can be used as catalyst supports or electron donors,[46] these advantages indicate the outstanding performance of 2D materials in the

fields of catalysis,[47] electrochemical reactions,[48] energy storage and conversion,[49] and thus serving as frontier in heterogeneous catalysis research.

MXenes are a new family of 2D materials composed of transition metal carbides, nitrides, and carbonitrides, with the general formula $M_{n+1}X_nT_x$ (n = 1, 2, 3), where *M* represents early transition metals (TMs) from the *d* block, including Sc, Ti, Zr, Hf, V, Nb, Ta, Cr, Mo, W, Mn, etc., X generally represents C and/or N, while T_x refers to surface functional groups.[50,51] Higher *n* values in MXenes generally correspond to greater stability and determine the thickness of the MXene layers.[52] Their unique 2D structure and open *d* orbitals have attracted significant attention in catalytic community.[53] MXenes are typically obtained by selective etching from precursor MAX phases, where *A* is usually a *p*-block element like Al or Si, usually removed using a hydrofluoric acid (HF) solution,[54] although *in situ* HF, *i.e.*, admixing lithium fluoride (LiF) and hydrochloric acid (HCl), can also be used.[55] By these methods, mixtures of –O, –H, –OH, and –F functional groups T_x can be obtained.[56,57] However, the type and quantity of these terminations are very sensitive to the synthesis conditions (*e.g.* etching time, temperature or HF concentration).[58,59] For example, high concentrations of HF lead to more –F terminations, whereas more –O species are found when lower concentrations of HF are used.[57,60] In addition, successful F-free synthesis protocols[61] have been reported, and even cleaning protocols[62] or new synthetic routes[63] for obtaining T_x-free MXenes, or even tuning of the T_x with various other terminations. In recent years, computational and experimental evidence have shown outstanding performance in various catalytic processes such as hydrogen evolution,[64] hydrogenation reactions,[65] CO oxidation,[66] CO_2 activation and conversion,[67] and N_2 fixation.[68] In summary, it is feasible to design MXenes tailored for specific applications by adjusting their composition, size, and surface terminations.

Graphene, composed of monolayer of carbon atoms arranged in a hexagonal pattern, is the most widely studied 2D material,[69] and possesses strong chemical resistance, high thermal stability, easy recyclability, and good dispersibility, which makes it highly suitable for catalytic applications.[70] Moreover, due to its large surface area, excellent adsorption properties, and high compatibility with various functional groups, offer new possibilities and flexibility in designing and synthesizing graphene-based catalysts tailored for specific applications.[71] Extensive research has been conducted on graphene to enhance their applications in heterogeneous catalysis,[72] for instance, utilizing edges, defects, or dopants of graphene can enable metal-free catalysis, enhancing catalytic performance

by fine-tuning its electronic structure, while the size-tunable monoatomic layer structure enhances the density of active sites.[73,74] Furthermore, the unique electron structure of graphene can anchor metals and modulate the catalytic behavior on its surface.[75,76] Doped graphene, especially nitrogen (N)-doped graphene,[77] has received widespread attention due to its simple, efficient, stable and readily available chemical doping method, and has been playing an important role in catalysis, moreover, N-doped graphene anchoring single-atom structures can achieves 100% dispersion on it, maximizing the exposure of catalytic active sites,[78] and exhibits excellent activity and high selectivity as homogeneous catalysts, along with the stability and ease of separation typical of heterogeneous catalysts, serving as a bridge between homogeneous and heterogeneous catalysis,[79] overall, until now, researchers are still exploring constantly around how to improve the activity of graphene.

1.3. Overview

This PhD thesis conducts fundamental research on heterogeneous catalysis of two different 2D materials by means of theoretical and computational methods. The manuscript is divided into four sections. Chapter 1 provides a brief introduction to the necessity of clean energy development and the evolution of catalysis. Chapter 2 describes the theoretical methods used for analyzing studied systems. Chapters 3 and 4 present the main research results in the form of peer-reviewed journal articles. First, Chapter 3 discusses the application of 2D MXene materials in heterogeneous catalysis, divided into three sections. The first section deals with the investigation at Ti_3C_2 (0001) MXene material, focusing on addressing the issues that overlooked in previous theoretical calculations on surface functional groups, selecting potential surface terminations under electrochemical working conditions, and their effects on the Hydrogen Evolution Reaction (HER) and CO_2 Reduction Reaction (CO_2RR) mechanisms. The second section focuses on boron-based Ti_3C_2 (0001) MXene materials, analyzing the effects of different configurations of boron and various mixed surface terminations on the electrocatalytic performance of the Nitrogen Reduction Reaction (NRR). The third section explores the detailed mechanism of olefin hydrogenation thermochemical reaction on Mo_2C (0001) MXene, and compares with Rh(111) to explain the observed paired H_2 additions in experiments. Chapter 4 mainly treats the application of N-doped graphene supported single metal atom (NG-SAC) 2D materials in electrocatalysis, divided into two sections. The first section explores the ef-

fect of geometry symmetry on the catalytic activity of NG-Pt in the electrochemical Chlorine Evolution Reaction (CER) and water splitting reactions. The second part studies the catalytic performance of non-precious metal NG-SAC in the electrochemical Oxygen Reduction Reaction (ORR) in alkaline media.

1.4. References

1. Ma, R.; Abid, N.; Yang, S.; Ahmad, F., From Crisis to Resilience: Strengthening Climate Action in OECD Countries through Environmental Policy and Energy Transition. *Environ. Sci. Pollut. Res.* **2023,** *30*, 115480–115495.
2. IPCC, 2023: Climate Change 2023: Synthesis Report. Contribution of Working Groups I, II and III to the Sixth Assessment Report of the Intergovernmental Panel on Climate Change [Core Writing Team, H. Lee and J. Romero (eds.)]. IPCC, Geneva, Switzerland, pp. 35–115, doi: 10.59327/IPCC/AR6-9789291691647.
3. Soergel, B.; Kriegler, E.; Weindl, I.; Rauner, S.; Dirnaichner, A.; Ruhe, C.; Hofmann, M.; Bauer, N.; Bertram, C.; Bodirsky, B. L.; Leimbach, M.; Leininger, J.; Levesque, A.; Luderer, G.; Pehl, M.; Wingens, C.; Baumstark, L.; Beier, F.; Dietrich, J. P.; Humpenöder, F.; von Jeetze, P.; Klein, D.; Koch, J.; Pietzcker, R.; Strefler, J.; Lotze-Campen, H.; Popp, A., A Sustainable Development Pathway for Climate Action within the UN 2030 Agenda. *Nat. Clim. Change.* **2021,** *11*, 656–664.
4. Sun, J.; Xie, Y.; Zhou, S.; Dan, J., The Role of Solar Energy in Achieving Net-Zero Emission and Green Growth: A Global Analysis. *Econ. Chang. Restruct.* **2024**, *57*, 46.
5. Hannan, M. A.; Al-Shetwi, A. Q.; Mollik, M. S.; Ker, P. J.; Mannan, M.; Mansor, M.; Al-Masri, H. M. K.; Mahlia, T. M. I., Wind Energy Conversions, Controls, and Applications: A Review for Sustainable Technologies and Directions. *Sustainability* **2023,** *15*, 3986.
6. Shiva Kumar, S.; Lim, H., An Overview of Water Electrolysis Technologies for Green Hydrogen Production. *Energy Rep.* **2022,** *8*, 13793–13813.
7. He, X.; Li, Y.; Li, H., Catalysis in Energy and the Environment: Opportunities and Challenges. *Molecules* **2024,** *29*, 1932.
8. Roduner, E., Understanding Catalysis. *Chem. Soc. Rev.* **2014**, *43*, 8226–8239.
9. Ertl, G., Wilhelm Ostwald: Founder of Physical Chemistry and Nobel Laureate 1909. *Angew. Chem., Int. Ed. Engl.* **2009**, *48*, 6600–6606.
10. Laidler, K. J., A Glossary of Terms Used in Chemical Kinetics, including Reaction Dynamics (IUPAC Recommendations 1996). **1996,** *68*, 149–192.

11. Carroll, G. T.; Kirschman, D. L., Catalytic Surgical Smoke Filtration Unit Reduces Formaldehyde Levels in a Simulated Operating Room Environment. *ACS Chem. Health Saf.* **2023,** *30*, 21–28.
12. Laidler, K. J.; Meiser, J. H. Physical Chemistry. Benjamin/Cummings. p. 425. ISBN 0-8053-5682-7, **1982**. "Inhibitors do not work by introducing a higher reaction path; this would not reduce the rate, since the reaction would continue to occur by the alternative mechanism".
13. Bond, G. C., *Heterogeneous Catalysis: Principles and Applications*. 2nd ed, **1987**.
14. Bowker M., The Basis and Applications of Heterogeneous Catalysis, Oxford University Press, **1998**.
15. Zybert, M., Applied Catalysis in Chemical Industry: Synthesis, Catalyst Design, and Evaluation. **2023,** *13*, 607.
16. Domínguez de María, P., Grand Challenges in Industrial Catalysis: Let´s Put Academia and Industry on the Same Page! *Front. Catal.* **2024,** *3*.
17. Isahak, W. N. R. W.; Al-Amiery, A., Catalysts Driving Efficiency and Innovation in Thermal Reactions: A Comprehensive Review. *Green Tech. Sustain.* **2024,** *2*, 100078.
18. Sassykova L. R, Aubakirov Y. A, Sendilvelan S, Tashmukhambetova Z. K, Fai zullaeva M. F, Bhaskar K, Batyrbayeva A. A, Ryskaliyeva R. G, Tyussyupova B. B, Zhakupova A. A. Sarybayev M. A. The Main Components of Vehicle Exhaust Gases and Their Effective Catalytic Neutralization. *Orient. J. Chem.* **2019,** *1*, 35.
19. Ali, S. S.; Ali, S. S.; Tabassum, N., A Review on CO_2 Hydrogenation to Ethanol: Reaction Mechanism and Experimental Studies. *J. Environ. Chem. Eng.* **2022,** *10*, 106962.
20. Cheng, Y.; Jiang, S. P., Advances in Electrocatalysts for Oxygen Evolution Reaction of Water Electrolysis from Metal Oxides to Carbon Nanotubes. *Prog. in Nat. Sci-Mater.* **2015,** *25*, 545–553.
21. IUPAC, *Compendium of Chemical Terminology*, 2nd ed. (the "Gold Book") (1997). Online corrected version: (2006–) "catalyst".
22. Bender, T. A.; Dabrowski, J. A.; Gagné, M. R., Homogeneous Catalysis for the Production of Low-Volume, High-Value Chemicals from Biomass. *Nat. Rev. Chem.* **2018,** *2*, 35–46.

23. Cole-Hamilton, D. J., Homogeneous Catalysis--New Approaches to Catalyst Separation, Recovery, and Recycling. *Science (New York, N.Y.)* **2003,** *299*, 1702–1706.
24. Schlögl, R., Heterogeneous Catalysis. *Angew. Chem. Int. Ed.* **2015,** *54*, 3465–3520.
25. Modak, J. M., Haber Process for Ammonia Synthesis. *Resonance* **2002,** *7*, 69–77.
26. Lott, P.; Deutschmann, O., Heterogeneous Chemical Reactions—A Cornerstone in Emission Reduction of Local Pollutants and Greenhouse Gases. *Proc. Combust. Inst.* **2023,** *39*, 3183–3215.
27. Keil, F. J., Complexities in Modeling of Heterogeneous Catalytic Reactions. *Comput. Math. Appl.* **2013,** *65*, 1674–1697.
28. Kari, J.; Olsen, J. P.; Jensen, K.; Badino, S. F.; Krogh, K. B. R. M.; Borch, K.; Westh, P., Sabatier Principle for Interfacial (Heterogeneous) Enzyme Catalysis. *ACS Catal.* **2018,** *8*, 11966–11972.
29. Trogadas, P.; Coppens, M.-O., Nature-Inspired Electrocatalysts and Devices for Energy Conversion. *Chem. Soc. Rev.* **2020,** *49*, 3107–3141.
30. Fang, S.; Hu, Y. H., Thermo-Photo Catalysis: A Whole Greater than the Sum of its Parts. *Chem. Soc. Rev.* **2022,** *51*, 3609–3647.
31. Guo, W.; Yu, L.; Tang, L.; Wan, Y.; Lin, Y., Recent Advances in Mechanistic Understanding of Metal-Free Carbon Thermocatalysis and Electrocatalysis with Model Molecules. *Nanomicro Lett.* **2024,** *16*, 125.
32. Jadhav, H. S.; Roy, A.; Thorat, G. M.; Seo, J. G., Facile and Cost-Effective Growth of a Highly Efficient $MgCo_2O_4$ Electrocatalyst for Methanol Oxidation. *Inorg. Chem. Front.* **2018,** *5*, 1115–1120.
33. Debe, M. K., Electrocatalyst Approaches and Challenges for Automotive Fuel Cells. *Nature* **2012,** *486*, 43–51.
34. Stamenkovic, V. R.; Strmcnik, D.; Lopes, P. P.; Markovic, N. M., Energy and fuels from electrochemical interfaces. *Nat. Mater.* **2017,** *16*, 57–69.
35. Luo, M.; Guo, S., Strain-Controlled Electrocatalysis on Multimetallic Nanomaterals. *Nat. Rev. Mater.* **2017,** *2*, 17059.
36. Novoselov, K. S.; Geim, A. K.; Morozov, S. V.; Jiang, D. E.; Zhang, Y.; Dubonos, S. V.; Grigorieva, I. V.; Firsov, A., Electric Field Effect in Atomically Thin Carbon Films. *Science* **2004,** *306*, 666–669.

37. Choi, W.; Choudhary, N.; Han, G. H.; Park, J.; Akinwande, D.; Lee, Y. H., Recent Development of Two-Dimensional Transition Metal Dichalcogenides and Their Applications. *Mater. Today* **2017,** *20*, 116–130.
38. Cheng, J.; Gao, L.; Li, T.; Mei, S.; Wang, C.; Wen, B.; Huang, W.; Li, C.; Zheng, G.; Wang, H.; Zhang, H., Two-Dimensional Black Phosphorus Nanomaterials: Emerging Advances in Electrochemical Energy Storage Science. *Nanomicro Lett.* **2020,** *12*, 179.
39. Gogotsi, Y.; Huang, Q., MXenes: Two-Dimensional Building Blocks for Future Materials and Devices. *ACS Nano* **2021,** *15*, 5775–5780.
40. Deng, D.; Novoselov, K. S.; Fu, Q.; Zheng, N.; Tian, Z.; Bao, X., Catalysis with Two-Dimensional Materials and Their Heterostructures. *Nat. Nanotechnol.* **2016,** *11*, 218–230.
41. Shanmugam, V.; Mensah, R. A.; Babu, K.; Gawusu, S.; Chanda, A.; Tu, Y.; Neisiany, R. E.; Försth, M.; Sas, G.; Das, O., A Review of the Synthesis, Properties, and Applications of 2D Materials. Part. Part. Syst. Charact. 2022, 39, 2200031.
42. Chen, W.; Gui, X.; Yang, L.; Zhu, H.; Tang, Z., Wrinkling of Two-Dimensional Materials: Methods, Properties and Applications. *Nanoscale Horiz.* **2019,** *4*, 291–320.
43. Paras; Yadav, K.; Kumar, P.; Teja, D. R.; Chakraborty, S.; Chakraborty, M.; Mohapatra, S. S.; Sahoo, A.; Chou, M. M. C.; Liang, C.T.; Hang, D.R., A Review on Low-Dimensional Nanomaterials: Nanofabrication, Characterization and Applications. *Nanomaterials* **2023,** *13*, 160.
44. Kolobov, A.V., Tominaga, J. (2016). Bulk TMDCs: Review of Structure and Properties. In: *Two-Dimensional Transition-Metal Dichalcogenides*. Springer Series in Materials Science, vol 239. Springer, Cham. https://doi.org/10.1007/978-3-319-31450-1_3.
45. Guo, Y.; Xu, K.; Wu, C.; Zhao, J.; Xie, Y., Surface Chemical Modification for Engineering the Intrinsic Physical Properties of Inorganic Two-Dimensional Nanomaterials. *Chem. Soc. Rev.* **2015,** *44*, 637–646.
46. Zhao, L.; Wang, B.; Wang, R., A Critical Review on New and Efficient 2D Materials for Catalysis. *Adv. Mater. Interfaces* **2022,** *9*, 2200771.

47. Shifa, T. A.; Wang, F.; Liu, Y.; He, J., Heterostructures Based on 2D Materials: A Versatile Platform for Efficient Catalysis. *Adv. Mater.* **2019,** *31*, 1804828.
48. Zagal, J. H., Metallophthalocyanines as Catalysts in Electrochemical Reactions. *Coord. Chem. Rev.* **1992,** *119*, 89–136
49. Xiong, P.; Sun, B.; Sakai, N.; Ma, R.; Sasaki, T.; Wang, S.; Zhang, J.; Wang, G., 2D Superlattices for Efficient Energy Storage and Conversion. *Adv. Mater.* **2020,** *32*, 1902654.
50. Morales-García, Á.; Calle-Vallejo, F.; Illas, F., MXenes: New Horizons in Catalysis. *ACS Catal.* **2020,** *10*, 13487–13503
51. VahidMohammadi, A.; Rosen, J.; Gogotsi, Y., The World of Two-Dimensional Carbides and Nitrides (MXenes). *Science* **2021,** *372*, eabf1581.
52. Naguib, M.; Kurtoglu, M.; Presser, V.; Lu, J.; Niu, J.; Heon, M.; Hultman, L.; Gogotsi, Y.; Barsoum, M. W., Two-Dimensional Nanocrystals Produced by Exfoliation of Ti_3AlC_2. *Adv. Mater.* **2011,** *23*, 4248–4253.
53. Oschinski, H.; Morales-García, Á.; Illas, F., Interaction of First Row Transition Metals with M2C (M = Ti, Zr, Hf, V, Nb, Ta, Cr, Mo, and W) MXenes: A Quest for Single-Atom Catalysts. *J. Phys. Chem. C* **2021,** *125*, 2477–2484.
54. Naguib, M.; Mashtalir, O.; Carle, J.; Presser, V.; Lu, J.; Hultman, L.; Gogotsi, Y.; Barsoum, M. W. Two-Dimensional Transition Metal Carbides. *ACS Nano* **2012,** *6*, 1322–1331.
55. Ghidiu, M.; Lukatskaya, M. R.; Zhao, M.Q.; Gogotsi, Y.; Barsoum, M. W. Conductive Two-Dimensional Titanium Carbide 'Clay' with High Volumetric Capacitance. *Nature* **2014**, *516*, 78–81.
56. Tan, X. Q.; Mo, W.; Lin, X.; Loh, J. Y.; Mohamed, A. R.; Ong, W. J. Retrospective Insights into Recent MXene-Based Catalysts for CO_2 Electro/Photoreduction: How Far Have We Gone? *Nanoscale* **2023**, *15*, 6536–6562.
57. Hope, M. A.; Forse, A. C.; Griffith, K. J.; Lukatskaya, M. R.; Ghidiu, M.; Gogotsi, Y.; Grey, C. P. NMR Reveals the Surface Functionalisation of Ti_3C_2 MXene. *Phys. Chem. Chem. Phys.* **2016,** *18*, 5099–5102.
58. Wyatt, B. C.; Rosenkranz, A.; Anasori, B. 2D MXenes: Tunable Mechanical and Tribological Properties. *Adv. Mater.* **2021**, *33*, 2007973.

59. Benchakar, M.; Loupias, L.; Garnero, C.; Bilyk, T.; Morais, C.; Canaff, C.; Guignard, N.; Morisset, S.; Pazniak, H.; Hurand, S.; Chartier, P.; Pacaud, J.; Mauchamp, V.; Barsoum, M. W.; Habrioux, A.; Célérier, S., One MAX phase, Different MXenes: A Guideline to Understand the Crucial Role of Etching Conditions on $Ti_3C_2T_x$ Surface Chemistry. *Appl. Surf. Sci.* **2020,** *530*, 147209.
60. Sun, J.; Liu, B.; Zhao, Q.; Kirk, C. H.; Wang, J. MAX, MXene, or MX: What Are They and Which One Is Better? *Adv. Mater.* **2023**, 2306072.
61. Pang, S. Y.; Wong, Y. T.; Yuan, S.; Liu, Y.; Tsang, M. K.; Yang, Z.; Huang, H.; Wong, W. T.; Hao, J. Universal Strategy for HF-Free Facile and Rapid Synthesis of Two-Dimensional MXenes as Multifunctional Energy Materials. *J. Am. Chem. Soc.* **2019**, *141*, 9610–9616.
62. Meshkian, R.; Lind, H.; Halim, J.; El Ghazaly, A.; Thörnberg, J.; Tao, -Q.; Dahlqvist, M.; Palisaitis, J.; Persson, P. O. Å.; Rosen, J. Theoretical Analysis, Synthesis, and Characterization of 2D $W_{1.33}C$ (MXene) with Ordered Vacancies. *ACS Appl. Na no Mater.* **2019**, *2*, 6209–6219.
63. Kamysbayev, V.; Filatov, A. S.; Hu, H.; Rui, X.; Lagunas, F.; Wang, D.; Klie, R. F.; Talapin, D. V. Covalent Surface Modifications and Superconductivity of Two-Dimensional Metal Carbide MXenes. *Science* **2020,** *369*, 979–983.
64. Seh, Z. W.; Fredrickson, K. D.; Anasori, B.; Kibsgaard, J.; Strickler, A. L.; Lukatskaya, M. R.; Gogotsi, Y.; Jaramillo, T. F.; Vojvodic, A., Two-Dimensional Molybdenum Carbide (MXene) as an Efficient Electrocatalyst for Hydrogen Evolution. *ACS Energy Lett.* **2016,** *1*, 589–594.
65. López, M.; Morales-García, Á.; Viñes, F.; Illas, F., Thermodynamics and Kinetics of Molecular Hydrogen Adsorption and Dissociation on MXenes: Relevance to Heterogeneously Catalyzed Hydrogenation Reactions. *ACS Catal.* **2021,** *11*, 12850–12857.
66. Zhang, X.; Lei, J.; Wu, D.; Zhao, X.; Jing, Y.; Zhou, Z., A Ti-Anchored Ti_2CO_2 Monolayer (MXene) as a Single-Atom Catalyst for CO Oxidation. *J. Mater. Chem. A* **2016,** *4*, 4871–4876.
67. Wang, B.; Zhou, A.; Liu, F.; Cao, J.; Wang, L.; Hu, Q., Carbon Dioxide Adsorption of Two-Dimensional Carbide MXenes. *J. Adv. Ceram.* **2018,** *7*, 237–245.

68. Gouveia, J. D.; Morales-García, Á.; Viñes, F.; Gomes, J. R. B.; Illas, F., Facile Heterogeneously Catalyzed Nitrogen Fixation by MXenes. *ACS Catal.* **2020,** *10*, 5049–5056.
69. Zhu, Y.; Murali, S.; Cai, W.; Li, X.; Suk, J. W.; Potts, J. R.; Ruoff, R. S., Graphene and Graphene Oxide: Synthesis, Properties, and Applications. *Adv. Mater.* **2010,** *22*, 3906–3924.
70. Marinkas, A.; Arena, F.; Mitzel, J.; Prinz, G. M.; Heinzel, A.; Peinecke, V.; Natter, H., Graphene as Catalyst Support: The Influences of Carbon Additives and Catalyst Preparation Methods on the Performance of PEM Fuel Cells. *Carbon* **2013,** *58*, 139–150.
71. Yan, Y.; Shin, W. I.; Chen, H.; Lee, S.-M.; Manickam, S.; Hanson, S.; Zhao, H.; Lester, E.; Wu, T.; Pang, C. H., A Recent Trend: Application of Graphene in Catalysis. *Carbon Lett.* **2021,** *31*, 177–199.
72. Wang, Y.; Mao, J.; Meng, X.; Yu, L.; Deng, D.; Bao, X., Catalysis with Two-Dimensional Materials Confining Single Atoms: Concept, Design, and Applications. *Chem. Rev.* **2019,** *119*, 1806–1854.
73. Deng, D.; Yu, L.; Pan, X.; Wang, S.; Chen, X.; Hu, P.; Sun, L.; Bao, X. Size Effect of Graphene on Electrocatalytic Activation of Oxygen. *Chem. Commun.* **2011**, *47*, 10016−10018.
74. Deng, D.; Pan, X.; Yu, L.; Cui, Y.; Jiang, Y.; Qi, J.; Li, W.-X.; Fu, Q.; Ma, X.; Xue, Q.; Sun, G.; Bao, X., Toward N-Doped Graphene via Solvothermal Synthesis. *Chem. Mater.* **2011,** *23*, 1188–1193.
75. Wang, Y.; Rong, Z.; Wang, Y.; Qu, J., Ruthenium Nanoparticles Loaded on Functionalized Graphene for Liquid-Phase Hydrogenation of Fine Chemicals: Comparison with Carbon Nanotube. *J. Catal.* **2016**, *333*, 8−16.
76. Wang, Y.; Rong, Z.; Wang, Y.; Wang, T.; Du, Q.; Wang, Y.; Qu, J., Graphene-Based Metal/Acid Bifunctional Catalyst for the Conversion of Levulinic Acid to γ-Valerolactone. *ACS Sustain. Chem. Eng.* **2017**, *5*, 1538−1548.
77. Wei, D.; Liu, Y.; Wang, Y.; Zhang, H.; Huang, L.; Yu, G., Synthesis of N-Doped Graphene by Chemical Vapor Deposition and Its Electrical Properties. *Nano Lett.* **2009,** *9*, 1752–1758.

78. Datye, A. K.; Guo, H., Single Atom Catalysis Poised to Transition from an Academic Curiosity to an Industrially Relevant Technology. *Nat. Commun.* **2021,** *12*, 895.

79. Fei, H.; Dong, J.; Chen, D.; Hu, T.; Duan, X.; Shakir, I.; Huang, Y.; Duan, X., Single Atom Electrocatalysts Supported on Graphene or Graphene-Like Carbons. *Chem. Soc. Rev.* **2019,** *48*, 5207–5241.

Chapter 2

Theoretical Methods

2.1. The Schrödinger Equation

The time-dependent Schrödinger equation is key in quantum mechanics as it describes the time evolution of the wavefunction of any system of elementary particles. In many practical applications, especially in chemistry and material science, it is often sufficient to consider the non-relativistic, time-independent form of the Schrödinger equation, that is, the atomic units are adopted with no charge of the electron, as well the mass of 1, which describes the static electronic structure of a system, as Eq. 2.1:

$$\hat{H}\psi\left(\vec{R},\vec{r}\right) = E\psi\left(\vec{R},\vec{r}\right) \tag{2.1},$$

$$\hat{H} = \hat{T}_e + \hat{T}_N + \hat{V}_{eN} + \hat{V}_{ee} + \hat{V}_{NN} \tag{2.2},$$

$$= -\sum_{i=1}^{N}\frac{1}{2}\nabla_i^2 - \sum_{A=1}^{M}\frac{1}{2m_A}\nabla_A^2 - \sum_{i=1}^{N}\sum_{A=1}^{M}\frac{Z_A}{r_{iA}} + \sum_{i=1}^{N}\sum_{j>i}^{N}\frac{1}{r_{ij}} + \sum_{A=1}^{M}\sum_{B>A}^{M}\frac{Z_A Z_B}{R_{AB}} \tag{2.3},$$

where the wavefunction $\psi\left(\vec{R},\vec{r}\right)$ depends on the positions of the nuclei $\vec{R}$ and the electrons $\vec{r}$, $\hat{H}$ is the Hamiltonian operator, and E represents the total energy of the system. The $\hat{H}$ includes all energy related operators of the system and is composed of kinetic energy of the electrons ($\hat{T}_e$) and the nuclei ($\hat{T}_N$), and potential energy terms of electron-nuclei interaction potential ($\hat{V}_{eN}$), electron-electron repulsion ($\hat{V}_{ee}$) and nuclei-nuclei repulsion ($\hat{V}_{NN}$), as shown in Eq. 2.2. For a system with M nuclei and N electrons, the kinetic energy and potential energy terms are as in Eq. 2.3, where m_A and Z_A represent the mass and charge of nucleus A respectively, while ∇_i^2 and ∇_A^2 are the Laplacian operators corresponding to the coordinates of the i^{th} electron and the A^{th} nucleus, respectively.

To simplify solving the Schrödinger equation, the Born-Oppenheimer (BO) approximation is often used.[1] This approximation relies on the fact that nuclei are much more massive than electrons and thus move much more slowly and allows one to solve the equation in two steps. In the first step, the moving electrons can be assumed to instantaneously adapt to the field created by fixed nuclei at certain positions. Under this approximation, the nuclear kinetic energy term $\hat{T}_N$ can be neglected, and the nucleus-nucleus

repulsion term $\hat{V}_{NN}$ can be treated as a constant by fixing the nuclei positions. However, the remaining terms, $\hat{T}_e$, $\hat{V}_{eN}$, and $\hat{V}_{ee}$, comprise the electronic Hamiltonian, denoted as $\hat{H}_{el}$, which is utilized to determine the electronic energy E_{el} of the system, as Eq. 2.4-5,

$$\hat{H}_{el} = -\sum_{i=1}^{N}\frac{1}{2}\nabla_i^2 - \sum_{i=1}^{N}\sum_{A=1}^{M}\frac{Z_A}{r_{iA}} + \sum_{i=1}^{N}\sum_{j>i}^{N}\frac{1}{r_{ij}} \quad (2.4),$$

$$\hat{H}_{el}\psi_{el} = E_{el}\psi_{el} \quad (2.5),$$

where the electronic wavefunction ψ_{el} depends on the coordinates of the electrons, with the coordinates of the nuclei as parameters.

However, once the term $\hat{V}_{NN}$ is added, the quantity obtained corresponds to the potential felt by the nucleus, leading to the concept of the potential energy surface (PES), which is the key to the microscopic mechanisms that govern all of the chemistry in the ground state or in any excited state. In the second step, the motion of the nuclei on the potential energy surface is considered. This, however, becomes too complicated except for systems containing a few atoms only. The resulting field is usually referred to as quantum dynamic. Fortunately, a considerable amount of useful information can be extracted from the analysis of the PES and this is where most applications, including those in the present thesis, rely on.

Even with the BO approximation, the high-dimensionality of ψ_{el} makes numerical solution of the electronic Scrödinger equation extremely challenging. Therefore, various approximation methods have been developed over the years to address this issue, primarily categorized into wavefunction methods and Density Functional Theory (DFT).

Generally, wavefunction methods involve directly constructing and manipulating the electronic wavefunction of the system, often yielding highly accurate results but at a high computational cost. Hartree-Fock (HF),[2] Møller-Plesset perturbation theory,[3] or various multiconfigurational self-consistent field and configuration interaction approaches[4-6] are available. In particular, those based on the coupled cluster expansion are able to provide results within chemical accuracy defines as 1 kcal/mol.[7] These methods, while highly accurate, cannot be applied to large systems, as those of interest in the present thesis. On the other hand, DFT based methods, provide a good balance between computational cost and accuracy for most systems and is currently the most widely used electronic structure method in computational chemistry and computational materials science.

In summary, the Schrödinger equation and its approximate solutions provide powerful tools for understanding and predicting the behaviour of microscopic systems. These methods are extensively applied in chemistry, physics, and materials science to explore molecular structures, reaction pathways, and material properties.[8]

2.2. Density Functional Theory

DFT[9] is a quantum mechanical method that uses electron density $\rho(\vec{r})$ instead of the wavefunction as the fundamental quantity to describe and determine the properties of a system. In a system containing *N* electrons, the electronic wavefunction $\psi_{el,R}(\vec{r})$ involves 4*N* variables (*i.e.*, three spatial and one spin coordinates per electron), while the electron density, $\rho(\vec{r})$, depends on three spatial coordinates only, simplifying this complex wavefunction problem into a more straightforward and intuitive three-dimensional particle density problem, and corresponding to the probability of finding any of the *N* electrons within the volume element $d\vec{r}$. The electron density is defined as the integral over the spin coordinates of all electrons and over all but one of the spatial variables:

$$\rho(\vec{r}) = N \int \cdots \int |\psi(s_2\overrightarrow{r_2}, \ldots, s_N\overrightarrow{r_N})|^2 \, ds_2 d\vec{r}_2 \cdots ds_N d\overrightarrow{r_N} = \sum_{i=1}^{N} |\phi_i(\vec{r})|^2 \quad (2.6),$$

where s_i, $\vec{r}_i$ and $\Phi_i(\vec{r})$ represent the projection of the spin, the spatial coordinates, and the orbital of i^{th} electron, respectively. From Eq 2.6 it is clear that $\rho(\vec{r})$ can be directly obtained from the wavefunction which in turn determines the electronic energy. DFT started from the Thomas-Fermi (TF) model described below and provides a shortcut, so that the electronic energy can be obtained from $\rho(\vec{r})$ only.

DFT is used to study the properties of molecules and condensed matter, making it suitable for calculating larger molecular systems. It shows sufficient accuracy, especially for systems containing transition metal atoms or ions, and is widely used in condensed matter physics and computational chemistry.

2.2.1. Thomas-Fermi Model

Shortly after the Schrödinger equation was proposed, Thomas[10] and Fermi[11] introduced a model, which is based on the concept of a uniform electron gas, where electrons are not affected by any external forces, thus there are no interactions between the electrons. The model uses electron density to represent the kinetic energy of the system, simplifying the Schrödinger equation into a wave equation. According to the Thomas-Fermi model, the

expression for the kinetic energy (T_{TF}) of the uniform electron gas, as a functional of the electron density $\rho(\vec{r})$, can be written as:

$$T_{TF}[\rho] = C_F \int \rho^{5/3}(\vec{r}) d\vec{r} \quad (2.7),$$

where $C_F = \frac{3}{10}(3\pi^2)^{2/3} = 2.817$ is known as the Fermi constant in atomic units.

Then, the total energy of the electron gas (E_{TF}) as a density functional is expressed as:

$$E_{TF}[\rho](\vec{r}) = C_F \int \rho^{5/3}(\vec{r}) d\vec{r} - Z \int \frac{\rho(\vec{r})}{r} d\vec{r} + \frac{1}{2} \iint \frac{\rho(\vec{r_1})\rho(\vec{r_2})}{|\vec{r_1} - \vec{r_2}|} d\vec{r_1} d\vec{r_2} \quad (2.8),$$

where the first term represents the kinetic energy, the second term indicates the external potential energy, and the third term is the average classical electrostatic interaction potential energy between electron densities, and *Z* denotes the nuclear charge number.

The key feature of TF model is using the electron density as the variable for the total energy functional, which subsequently led to the development of DFT. However, the TF model only expresses the kinetic energy based on the density of a uniform electron gas, without considering the exchange-correlation effects between electrons, therefore, it is limited use. Subsequent improvements to this model were proposed by Hohenberg and Kohn, which eventually broke the constraints imposed by the energy functional form based on the TF model, establishing the foundation of modern density functional theory.

2.2.2. The Hohenberg and Kohn Theorems

In 1964, building upon the Thomas-Fermi model, Hohenberg and Kohn proved[12] two fundamental theorems:

> 1st theorem: "*The external potential $V_{ext}(\vec{r})$ of a non-degenerate electronic state, and hence the total energy, is a unique functional of $\rho(\vec{r})$*"
>
> 2nd theorem: "*The ground state energy can be obtained variationally and the density that minimizes the energy is the exact ground state energy*"

Regarding the 1st theorem, the electron density from a unique external potential is uniquely identified, thereby uniquely determining the energy ($E[\rho(\vec{r})]$) of system, expressed as:

$$E[\rho(\vec{r})] = F[\rho(\vec{r})] + E_{ext}(\rho) \quad (2.9),$$

where $F[\rho(\vec{r})]$ represents the functional independent of the external field, including the electronic kinetic energy, Coulomb interaction between electrons, and exchange-correlation energy. $E_{ext}(\rho)$ denotes the effect of the external field and, since it is a one-electron operator, it can be expressed as:

$$E_{ext}(\rho) = \int d\vec{r}\, V_{ext}(\vec{r})\rho(\vec{r}) \tag{2.10}.$$

Regarding the 2nd theorem, showing that it is sufficient to determine the accurate ground-state energy by minimizing the energy alone. Assuming $F[\rho(\vec{r})]$ is known, through variation of the density function, one can obtain the minimum total energy of the system, thereby determining the accurate ground-state density and energy. However, $F[\rho(\vec{r})]$ only determines the properties of the ground state and does not provide any information about excited states. Although the significance of the Hohenberg-Kohn theorem is profound, it cannot resolve the following issues: how to determine electron density functional and the kinetic energy functional.

2.2.3. The Kohn-Sham Equations

In 1965, Kohn and Sham developed the well-known Kohn-Sham equations,[13] suggesting that there is an ideal system of non-interacting electron, with density equal to that of the real system. For non-interacting system, the wavefunction can be written as a Slater determinant with orbitals $\phi_i(\vec{r})$. The electron density and the kinetic energy can be easily obtained and the same for the classical Coulomb repulsion. This leave out exchange-correlation effects that need to be accounted by a proper functional termed $E_{xc}[\rho(\vec{r})]$,which plays a pivotal role in practical DFT. Therefore, the Kohn-Sham approach gives a form to $F[\rho(\vec{r})]$ and the total energy can be expressed:

$$E[\rho(\vec{r})] = F[\rho(\vec{r})] + E_{ext}[\rho(\vec{r})] = T_s[\rho(\vec{r})] + J[\rho(\vec{r})] + E_{xc}[\rho(\vec{r})] + E_{ext}[\rho(\vec{r})] \tag{2.11},$$

here, $T_s[\rho(\vec{r})]$ represents the kinetic energy of the system in the absence of electron-electron interactions, $J[\rho(\vec{r})]$ denotes the classical Coulomb energy, and $E_{xc}[\rho(\vec{r})]$ represents the exchange-correlation energy. The terms in Eq. 2.11 can be respectively defined as:

$$T_s[\rho(\vec{r})] = \sum_{i=1}^{N} \int d\vec{r}\phi_r^*(\vec{r})(-\frac{\hbar^2}{2m}\nabla^2) + \phi_i(\vec{r}) \tag{2.12},$$

$$E_{ext}[\rho(\vec{r})] = \int d\vec{r}\, V_{ext}\, \rho(\vec{r})(\vec{r}) \tag{2.13},$$

$$J[\rho(\vec{r})] = -\frac{1}{2}\int d\vec{r}\int d\vec{r}'\,\frac{\rho(\vec{r})\rho(\vec{r}')}{|\vec{r}-\vec{r}'|} \quad (2.14),$$

$$E_{xc}[\rho(\vec{r})] = T[\rho(\vec{r})] - T_s[\rho(\vec{r})] + V_{ee}[\rho(\vec{r})] - J[\rho(\vec{r})] \quad (2.15).$$

Note that, Eq. 2.10 and 2.13 are actually the same and added here just for convenience. Now, by varying the functional form of the energy with respect to the density function $\rho(\vec{r})$, which in turn implies varying the $\phi_i(\vec{r})$ orbitals, usually expanded in a convenitent basis set, the Kohn-Sham equations are derived:

$$(\hat{T}_s + \hat{V}_{eef})\phi_i(\vec{r}) = \varepsilon_i\phi_i(\vec{r}) \quad (2.16),$$

in which,

$$V_{eef}(\vec{r}) = V_{ext}(\vec{r}) + e^2\int\frac{\rho(\vec{r}')}{|\vec{r}-\vec{r}'|}d\vec{r}' + \frac{\delta E_{XC}}{\delta\rho(\vec{r})} \quad (2.17),$$

where $V_{eef}(\vec{r})$ is the local effective potential, $V_{ext}(\vec{r})$ is the potential energy of attraction of the nucleus to the electron, and the last two terms represent the electron-electron Coulomb interaction and the exchange-correlation energy.

The Kohn-Sham equations are solved iteratively using a self-consistent field method, where initial guessed $\phi_i(\vec{r})$ are refined until the energy difference between iterations meets a specified accuracy threshold, demonstrating calculation convergence. In principle, the Kohn-Sham method is accurate, with the primary challenge being the accurate determination of the exchange-correlation energy.

2.2.4. Exchange-Correlation Functionals

In the Kohn-Sham equations, only the exchange-correlation energy E_{xc} is approximated, while the other terms are determined exactly. Therefore, accurately determining E_{xc} is crucial for improving the precision of DFT. The main approximations for E_{xc} include the Local Density Approximation (LDA)[14] and the Generalized Gradient Approximation (GGA).[15] The family of density functional is growing with meta-GGA, hybrid, double hybrid and range separated approaches reported in the literature.[16] These, however, as they are not best suited for the system under studies in this PhD thesis, yet they are suitable for other materials, *e.g.* in spin cross-over materials[17] and semiconductors,[18] will not be further commented here.

The LDA was proposed by Kohn and Sham based on the homogeneous electron gas model.[19] When the number of electrons *N* and the volume *V* of the electron gas approach infinity, the electron density ρ becomes a finite value, and remains constant at all

points in space, which is known as the LDA model. In LDA, the exchange-correlation energy can be expressed as:

$$E_{xc}^{LDA}[\rho(\vec{r})] = \int \rho(\vec{r})\varepsilon_{xc}[\rho(\vec{r})]d\vec{r} \quad (2.18),$$

where, $\varepsilon_{xc}[\rho(\vec{r})]d\vec{r}$ describes the exchange-correlation potential of a uniform non-interacting electron gas with density ρ.

The LDA can provide fairly accurate results, particularly when spatial variation of electron density in the system is small, as in metals, and this approximation is quite suitable. However, when the electrons in the system are highly localized, as in molecules, and the charge density distribution is uneven, the local density approximation becomes inappropriate.

In dealing with real systems, the exchange-correlation energy can be expanded in terms of gradients, and the non-uniformity of the electron density in real systems can be accounted for. In this scenario, the introduction of a new variable, the density gradient $\nabla\rho(\vec{r})$, giving rise to GGA, where the exchange-correlation energy becomes a functional of both the electron density and the gradient of the electron density. The specific expression is given by:

$$E_{xc}^{GGA} = \int \rho(\vec{r})\varepsilon_{xc}[\rho(\vec{r}), |\nabla\rho(\vec{r})]d\vec{r} \quad (2.19).$$

Comparing to LDA, GGA has significantly improved accuracy and provides more precise computational results, leading to widespread applications of GGA functionals across various fields. With ongoing developments in theoretical computational methods, GGA functionals have evolved into multiple forms, among which Perdew-Wang (PW91),[20] Perdew-Burke-Ernzerhof (PBE),[21] and others[22-24] are widely used functionals.

2.2.5. Including Dispersive Forces

Dispersive Forces are essential weak intermolecular interactions that describe the attraction between neutral molecules or groups, play a critical role in various processes such as polymer formation, the structure of biomolecules, and the adsorption of molecules on solid surfaces, arising from the formation of instantaneous dipoles that, which cannot be accurately described by conventional DFT. Therefore, to ensure computational accuracy,

dispersion terms (E_{disp}) are added to the energies obtained from standard density functional calculations E_{DFT}. There are many methods aimed to account for these interactions.[25] In the simplest one, the energy is expressed as:

$$E_{tot} = E_{DFT} + E_{disp} \tag{2.20},$$

$$E_{disp} = -\sum_{A,B} f(r_{AB}, A, B)\frac{C_6^{AB}}{r_{AB}^6} \tag{2.21}.$$

Here, C_6^{AB} is dispersion coefficient of element pairs *A* and *B*, r_{AB}^6 is the intermolecular distance between element pairs *A* and *B*, and $f(r_{AB}, A, B)$ is a damping function that is equal to one for large r and decreases E_{disp} to zero, or to a constant for small r. Grimme and coworkers,[26-28] in accordance with the described framework, pioneered the development of the semi-empirical correction DFT-D approach, which, once parameterized, yields highly reliable results with negligible computational cost. DFT-D encompasses both DFT-D2 and DFT-D3, two widely employed known for their broad applicability and high accuracy. This PhD thesis employs the GGA-PBE functional, supplemented by the DFT-D3 correction.

2.3. Handling Periodic Systems

This PhD thesis focuses primarily on crystalline solids, defined by their periodically ordered atomic structure. This periodicity allows to focus on a portion of the system, known as the unit cell, which, when translated in three-dimensional space, reproduces the entire solid. The unit cell contains a certain number of atoms, known as the atomic basis. The Schrödinger equation only needs to be solved for the atoms within the unit cell, provided that the wave function or electron density remains invariant when a translation operator is applied. The lattice is defined by the three vectors of the unit cell (a_i), from which the translation operator ($\hat{T}$) is constructed:

$$\hat{T} = n_1\hat{a}_1 + n_2\hat{a}_2 + n_3\hat{a}_3 \tag{2.22},$$

where $n_1, n_2,$ and n_3 are integers. The infinite array of discrete points obtained from Eq. 2.22 is called the Bravais lattice. While there are infinite ways to construct a unit cell that describes a periodic solid, the smallest and irreducible unit cell is unique and is called the primitive cell. Common types of unit cells include cubic, body-centered cubic (*bcc*), face-centered cubic (*fcc*), and hexagonal close packed (*hcp*), as shown in Figure 2.1.

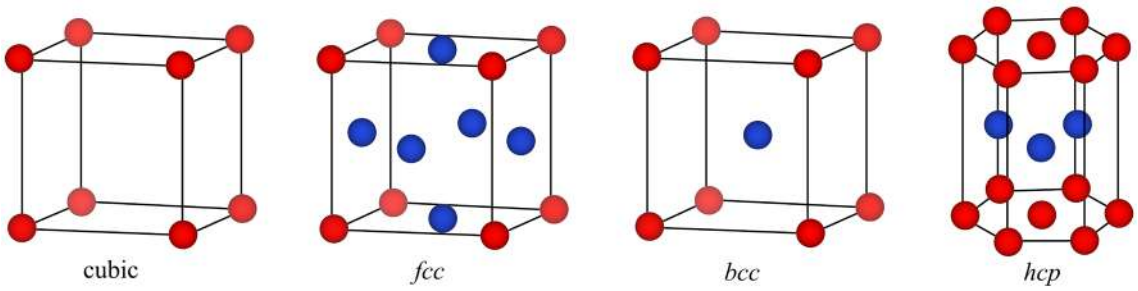

Figure 2.1. From left to right, a schematic representation of cubic, face-centered cubic (*fcc*), body-centered cubic (*bcc*), and hexagonal closed packed (*hcp*) unit cells. The red atoms form the primary framework, positioned at the edges and corners of the unit cells, while the blue atoms represent the internal positions of the corresponding atoms within the unit cells.

The use of reciprocal space (**k**-space) is very convenient for analyzing periodic systems. The reciprocal lattice, a subset of points in the reciprocal space, is a mathematical construction used to study the properties of periodic crystalline lattices. Each lattice $A = \{a_1, a_2, a_3\}$ has a corresponding reciprocal lattice $B = \{b_1, b_2, b_3\}$, which satisfies the following relations:

$$b_i = 2\pi \frac{a_j \times a_k}{a_i \cdot (a_j \times a_k)} \forall_{i,j,k} \in \{1,2,3\} \quad (2.23),$$

$$a_i \cdot b_i = (2\pi)\delta_{i,j} \quad (2.24).$$

Note the volume of the unit cell of the reciprocal lattice $(2\pi)^3/V_C$ is inversely proportional to the volume of the real space unit cell V_C. In addition, Bloch's theorem[29] provides the theoretical framework to analyze the expansion of the wavefunction in reciprocal space, where the values of all observables at a certain position within the unit cell are the same for equivalent positions throughout the entire Bravais lattice. In a perfectly periodic crystal, the potential $V(\vec{r})$ satisfies the condition:

$$\hat{T}V(\vec{r}) = V(\vec{r} + \vec{R}) = V(\vec{r}) \quad (2.25).$$

This equation indicates that the potential at a point $(\vec{r})$ is identical to the potential at a point $(\vec{r} + \vec{R})$, where $\vec{R}$ is a vector that translates $\vec{r}$ to an equivalent point in a replicated unit cell using the translation operator $\hat{T}$.

Planes inside a Bravais lattice are defined by the positions of three non-collinear points. These planes are commonly denoted using Miller indices, which indices (*hkl*) are determined by taking the inverses of the intercepts (or using 0 if there is no intercept) of the planes with the reference axes in the coordinate system, and then multiplying by the least common multiple to obtain integers *h*, *k*, and *l*. This notation is used to identify

different crystallographic planes inside a cubic unit cell, as shown for the (100), (110), and (111) planes, as shown in Figure 2.2. The (100) plane indicates movement along the *x*-axis only, the (110) plane along the *x*-*y* diagonal, and the (111) plane along the *x*-*y*-*z* diagonal.

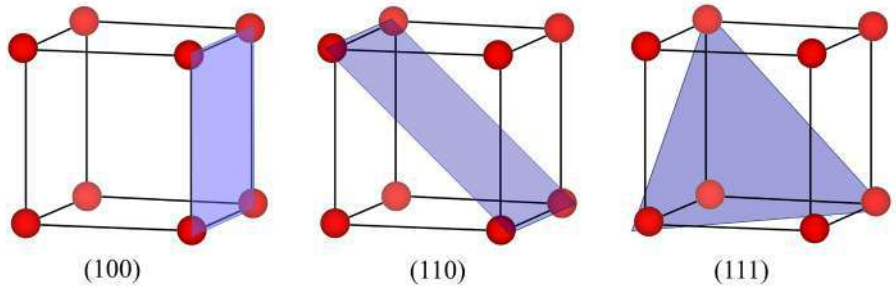

Figure 2.2. From left to right, the (100), (110), and (111) crystallographic planes inside a cubic unit cell in the Miller indices notation.

To describe electron density in periodic systems, an appropriate basis set is essential, a common choice is to use basis set of Plane Waves (PW):

$$\eta^{PW} = e^{i\vec{k}\vec{T}} \tag{2.26},$$

where the vector $\vec{k}$ is related to the momentum $\vec{p}$ of the plane wave by $\vec{p} = \hbar\vec{k}$, and $\vec{T}$ is any translational vector that keeps the Hamiltonian unchanged. The PW extend throughout space, inherently including periodic boundary conditions. However, many PWs are needed to describe the atomic core region, where large oscillations of the electron density occur which makes the methods of little use. Fortunately, since valence electrons primarily determine chemical and physical properties,[30] while core are electrons almost fixed at their atomic shape, a good approximation is to treat the core electrons as *frozen*. Therefore, the all-electron potential experienced by a valence electron is replaced by a pseudopotential, which mimics the effect of core electrons on the valence electron density, and the valence electrons are then described by pseudo wavefunctions with fewer nodes, reducing the PW basis set size and making the overall approach useful for practical applications. Besides, using pseudopotentials allows for the inclusion of relativistic effects, especially for heavy atoms, without raising computational expenses, as these essentially involve the core electrons.

Finally, most studies involving solid surfaces, including the studies in this thesis, are typically conducted using the periodic slab model by constructing the extending unit

cell along the lattice vector perpendicular to the desired surface plane. Introducing a vacuum between the cell prevents interactions between them. The slab includes multiple atomic layers to accurately capture both the bulk and surface electronic properties.

2.4. Computational Hydrogen Electrode Model

The Computational Hydrogen Electrode (CHE) model, proposed by Nørskov *et al.*,[31] is one of the basis of this PhD thesis in the study of all fundamental electrocatalytic reactions. This model simplifies the coupling protons and electrons, at 1 atm, 0 V, and all *pH* values, to gas-phase molecular hydrogen at equilibrium states.

$$H^{+}_{(aq)} + e^{-} \leftrightarrow \tfrac{1}{2}\cdot H_{2(g)} \qquad (2.27).$$

Therefore, under these conditions, the electrochemical potential of an aqueous proton-electron pair is that of $\frac{1}{2}\cdot H_{2(g)}$, instead of referencing to that of the $H^{+} + e^{-}$ pair which otherwise is difficult to compute. The effect of the electrode potential can also be incorporated into the equation with the term eU, where e is the charge of an electron and U is the electrode potential in V relative to the reversible hydrogen electrode (RHE), as measured potentials do not change with pH.

$$\frac{1}{2}\mu(H_2) - eU = \mu(H^{+} + e^{-}) \qquad (2.28).$$

The CHE model facilitates the calculation of the Gibbs free energies for reactions involving proton-electron transfers, simplifying the study of electrocatalytic processes, thus built energy profiles for reactions involving several proton-electron transfer steps.

2.5. Thermodynamic Approach

To outline the reaction mechanisms, the thermodynamic approach, as extendedly employed in previous studies, has been used.[32,33] The first step in outlining the reaction free energy profiles is to estimate the total adsorption energies of the intermediate species, denoted as $\Delta E^{i}_{\mathrm{ads}}$,

$$\Delta E^{i}_{\mathrm{ads}} = E_{i/\mathrm{sub}} - (E_{\mathrm{sub}} + E_i) \qquad (2.29).$$

where, E_{sub} represents the substrate energy, specifically for the studied Ti_3C_2 MXene with the surface termination in thesis. E_i is the energy of the adsorbed species i in vacuum at the optimized geometry. In practice, this is calculated at the **Γ**-point within a 9×10×11 $Å^3$ broken-symmetry box for appropriate orbital occupation. $E_{i/\mathrm{sub}}$ indicates the energy of the i moiety adsorbed on the specific substrate model also at minimum energy structure. The more negative $\Delta E^{i}_{\mathrm{ads}}$ implies stronger adsorption.

Next, the estimate of ΔG values is based on the aforementioned CHE reference, where the Gibbs free energies of $H^+_{(aq)} + e^-$, and the final state $½\cdot H_{2(g)}$ are identical. Furthermore, for any elementary reaction step, ΔG can be obtained as:

$$\Delta G = \Delta E + \Delta E_{ZPE} - T\cdot\Delta S \quad (2.30),$$

where ΔE accounts for the energy difference of the reaction step, ΔE_{ZPE} accounts for the change in Zero-Point Energy (ZPE), and ΔS is the entropy change. The ΔE term can be directly obtained from the optimization calculations:

$$\Delta E = E_{AH^*} - E_{A^*} - ½\cdot E_{H_2} \quad (2.31).$$

Similarly, ΔE_{ZPE} term can be obtained as follows:

$$\Delta E_{ZPE} = E^{ZPE}_{AH^*} - E^{ZPE}_{A^*} - ½\cdot E^{ZPE}_{H_2} \quad (2.32),$$

where the ZPE term is derived from the computed vibrational frequencies:

$$E^{ZPE} = \frac{1}{2}\sum_{i=1}^{NMV} h\nu_i \quad (2.33),$$

where ν_i represents the vibrational frequencies of Normal Modes of Vibration (NMV), and h is Planck's constant. For linear molecules in vacuum, the number of NMV is $3N$-5 for a system with N atoms, whereas for other types of molecules, NMV is $3N$-6. Upon adsorption, any molecule or atom has $3N$ NMV because free translations and rotations become restricted vibrational modes upon adsorption. Similarly, the entropy change ΔS can be calculated as:

$$\Delta S = S_{AH^*} - S_{A^*} - ½\cdot S_{H_2} \quad (2.34).$$

The entropy of gas-phase molecules is obtained from the National Institute of Standards and Technology (NIST) webbook,[34] while for adsorbed species, only vibrational entropy (S_{vib}) is considered due to the ground state character and the restriction of translations and rotations upon adsorption.[35] Therefore, for adsorbed species:

$$S = S_{vib} = k_B \sum_{i=1}^{NMV} \ln(1 - e^{-\frac{h\nu_i}{k_B T}}) - \sum_{i=1}^{NMV} h\nu_i \left(\frac{1}{e^{\frac{h\nu_i}{k_B T}} - 1}\right) \quad (2.35),$$

where k_B is Boltzmann's constant, T is the temperature. Note, however, that the estimate of the adsorption free energy (ΔG^{ad}) in applications in thermocatalysis such as the ethene hydrogenation reaction discussed in Section 3.4, ΔG^{ad} is approximately given as in Eq. 2.36 which is a function of the operating temperature, T, and species partial pressure, p,

$$\Delta G^{ad}(T,\ p) \approx\ [E^{total}(N_i, N_M) +\ E^{ZPE}_{(N_i,N_M)}] - E^{total}(0, N_M) - N_i[E_i^{total}\ +\ E_i^{ZPE}]\ - N_i\Delta\mu_i(T,p) \quad (2.36),$$

where N_i denotes the count of the adsorbed species, typically 1 in the studied system of Section 3.4, while E_i^{total}, $E^{ZPE}_{(N_i,N_M)}$ and E_i^{ZPE} respectively represent the total energy, ZPE contributions of the adsorbed species, and the species in vacuum. In the context of the study in Section 3.4, $E^{total}(N_i, N_M)$ and $E^{total}(0, N_M)$ correspond to $E_{i/sub}$ and E_{sub}, the total energies of the surface model with and without the adsorbed species *i*, respectively. Furthermore, $\Delta\mu_i(T,p)$ represents the change in chemical potential of the adsorbed species relative to the gas phase, which can be expressed using *Ab Initio* Thermodynamics (AIT), incorporating contributions from kinetics, rotation, vibration, and electronic states:

$$\Delta\mu_i(T,p) = k_BT\left\{ln\left[\left(\frac{2\pi m_i}{h^2}\right)^{3/2}\frac{(k_BT)^{5/2}}{p_i}\right] +\ ln\left(\frac{k_BT}{\sigma_i^{sym}B_{0,i}}\right) -\ \sum_{n=1}^{NMV} ln\left[1 - exp\left(\frac{-h\nu_{n,i}}{k_BT}\right)\right] + ln\left(I_i^{spin}\right)\right\} \quad (2.37).$$

where k_B is the Boltzmann constant, m_i is the mass of the *i*th molecule, p_i is the partial pressure of the *i*th species, σ_i^{sym} is the symmetry number of *i*th molecule —2 for H_2, 4 for C_2H_4, 6 for C_2H_6. $B_{0,i}$ is the rotational constant given by $B_{0,i} = \frac{\hbar^2}{2I_i}$, where I_i is the moment of inertia of the molecule defined as $I_i = \sum_a m_a {r_a}^2$, with m_a being the mass of *a* atoms comprising the *i*th molecule and r_a refers to the distance to the center of mass to the *a* atom. Each vibrational normal mode of the *i*th molecule is assigned by $\nu_{n,i}$, while I_i^{spin} denotes the electronic spin degeneracy of the ground state.

For molecules C_2H_4, C_2H_6, and H_2 involved in catalysis as discussed in Section 3.4, the gas-phase references are well-defined. For radical species like C_2H_5 and single H atoms, it is convenient to express their chemical potentials as a combination of gas-phase species, *i.e.*, $\mu_H(T,p) = \frac{1}{2}\mu_{H_2}(T,p)$, so that $\mu_{C_2H_5}(T,p) = \mu_{C_2H_4}(T,p) + 1/2\ \mu_{H_2}(T,p)$.

Finally, in order to evaluate the experimental feasibility of synthesizing B-based MXene models in Section 3.3, their thermodynamic stability was investigated. Here, a key parameter to assess the structural stability of these conceptual electrocatalysts is the mean adsorption, E_{ads}, defined as:

$$E_{ads} = \frac{E_{n\mathrm{B/MXene}} - E_{\mathrm{MXene}} - n * E_{\mathrm{B}}}{n} \quad (2.38).$$

Here, $E_{n\mathrm{B/MXene}}$, E_{MXene}, and E_{B} represent the total energies of MXene with and without *n* B atoms, and the energy of isolated B atoms, respectively. To assess the thermodynamic stability, E_{ads} should be compared to the computed bulk cohesive energy of boron, E_{coh}.[36,37] Defining $E_{\mathrm{diff}} = E_{\mathrm{ads}} - E_{\mathrm{coh}}$, it is clear that an adsorption energy stronger than the cohesive energy would energetically favor the presence of isolated B atoms. The B bulk cohesive energy was computed by optimizing the atomic structure of bulk boron using a 5×5×1 **k**-point mesh, yielding a value of -6.45 eV/atom, slightly higher than the experimental value of -5.81 eV/atom.[38] Additionally, the stability of the catalysts was assessed by calculating the formation energy, E_{f}, considering bulk Ti, graphite, O_2, and H_2 as reactants in their standard states, the calculations for Ti and graphite followed similar methodologies as those used for bulk boron.

2.6. Surface Pourbaix Diagram

The Pourbaix diagrams are crucial to determine the state of a surface under external potential (U) and pH conditions.[39] In MXenes, the diversity of surface terminations and compositions leads to combinatorial and structural complexity. Therefore, constructing Pourbaix diagrams aims to identify the thermodynamically most stable surface termination of studied Ti_3C_2 MXenes in Chapter 3.2 under the realistic working conditions of HER and CO_2RR.

In this thesis, $H_{2(g)}$ and $F_{2(g)}$ are used as reference substances for calculating –H and –F terminations at 1 bar and 298.15 K, which are based on CHE as Eq. 2.27, and Computational Fluorine Electrode (CFE) as Eq. 2.39 under equilibrium conditions:

$$\tfrac{1}{2}\cdot \mathrm{F}_{2(g)} + \mathrm{e}^- \leftrightarrow \mathrm{F}^-_{(aq)} \qquad (2.39).$$

The reduction potentials used are 0 and -2.87 eV for hydrogen, U, and fluorine, U_{F}, respectively.[40] For –OH and –O terminations, water vapor is used as a reference at 0.035 bar and 298.15 K, where in equilibrium with liquid water.[31] Using the CHE and CFE, the computational Pourbaix diagram can be constructed based on the aforementioned equilibrium conditions:

$$\mu\left(\mathrm{H}^+_{(aq)}\right) + \mu(e^-) = G\left(\mathrm{H}^+_{(aq)}\right) + G(e^-) = \frac{1}{2}G(\mathrm{H}_2^{(g)}) \qquad (2.40),$$

$$\mu\left(\mathrm{F}^-_{(aq)}\right) - \mu(e^-) = G\left(\mathrm{F}^-_{(aq)}\right) - G(e^-) = \frac{1}{2}G(\mathrm{F}_2^{(g)}) \qquad (2.41),$$

where μ and G are the chemical potentials and Gibbs free energies of the specified species. Using these references, the formation Gibbs free energy of a given surface termination at zero pH and U, denoted as $\Delta G(0,0)$, is calculated as:

$$\Delta G(0,0) = \Delta G = \Delta E + \Delta E_{ZPE} - T\cdot\Delta S \quad (2.42).$$

Once $\Delta G(0,0)$ is obtained, the pH and U dependent ΔG, $\Delta G(\mathrm{pH},U)$ can be calculated using:[41,42]

$$\Delta G(\mathrm{pH},U) = \Delta G(0,0) - \upsilon(\mathrm{H^+})k_B T\cdot\ln 10\cdot pH - \upsilon(e^-)eU - \upsilon(\mathrm{F^-})eU_F \quad (2.43),$$

where $\upsilon(\mathrm{H^+})$, $\upsilon(\mathrm{F^-})$, and $\upsilon(e^-)$ are the stoichiometric coefficients of the formation chemical equation. For example, for a $p(3\times3)$ slab with 9 free surface sites, the formation of a surface with 3 O* and 6 F* can be represented as:

$$3\cdot H_2O + 3\cdot F_2 + 9\cdot * \rightarrow 3\cdot O^* + 6\cdot F^* + 3\cdot H_2 \quad (2.44).$$

When considering pH and U, and the presence of H^+ and F^- species in solution, the equation should be rewritten as:

$$3\cdot H_2O + 6\cdot F^- + 9\cdot * \rightarrow 3\cdot O^* + 6\cdot F^* + 6\cdot H^+ + 12\cdot e^- \quad (2.45),$$

where $\upsilon(\mathrm{H^+})$, $\upsilon(\mathrm{F^-})$, and $\upsilon(e^-)$ would be 6, –6, and 12, respectively. Using the above method, ΔG as a function of pH and U for any surface termination can be obtained. Thus, the relative stability of different terminations of MXenes under realistic conditions can be determined, with the most stable termination being the one with the lowest ΔG at given pH and U conditions.

2.7. Transition State Theory

Chemical kinetics deals with the rates of chemical reactions and how these rates are affected by several factors, such as concentration and temperature among others. Knowledge of these rates is crucial for providing evidence on how reactions evolve and the mechanisms of chemical processes under different conditions. Initially, the empirical Arrhenius rate law[43] was widely used to determine the energy barriers of reactions, but due to its empirical derivation, did not consider the molecular mechanisms involved. Later, in 1935, Eyring *et al.*[44] formulated the Transition State Theory (TST) to explain the reaction rates involving elementary chemical reactions. TST assumes a special chemical equilibrium between the reactants and the activated Transition State (TS) complex, which then decomposes to form the reaction products. This TS represents a stationary (null gradient) saddle point (one and only one negative eigenvalue of the Hessian matrix)

on the potential energy surface connecting the reactants and products.[45] The energy difference between the TS and the reactants is named the activation energy, E_a, which is the main factor affecting the reaction rate and provides a rigorous derivation of the Arrhenius interpretation.

Many algorithms have been proposed to locate TS.[46,47] Here, we used the Climbing Image Nudged Elastic Band (CI-NEB) method.[48] The NEB method is a methodology for finding the saddle point and minimum energy path between known reactants and products. This CI-NEB method works by optimizing several connected intermediate images along the reaction path. Each image finds the lowest possible energy while connected to the neighboring images by a harmonic potential. Briefly, this constrained optimization is achieved by adding spring forces along the band connecting the images, so the structures of the images do not evolve toward a minimum, as the optimization is constrained by the chain of springs connecting them. At the same time, the highest-energy image moves upward along the reaction path until the assumed transition state is found. Nevertheless, the structure needs to be properly characterized by explicit calculation of the vibrational frequencies.

In this thesis, we calculated the transition state barriers for the thermocatalysis of hydrogenation reactions in Chapter 3.4. We did not calculate Proton-Coupled Electron Transfer (PCET) barriers in other electrochemical studies due to the lack of a dependable method for obtaining electrochemical barriers.[49] However, when the studied systems follow the Brønsted-Evans-Polanyi (BEP) relationship,[50,51] one can write $E = E_a + \alpha\Delta H$, where the difference in activation energy, E_a, between two reactions is proportional to the difference in their reaction enthalpies, E, implying that any PCET step features a latest transition state when endergonic, and an earliest transition state when exergonic.

2.8. Rates Estimation

In general, according to the *Sabatier* principle,[52] the best catalyst should bind atoms and molecules with an optimum bonding strength: not too weak to activate the reactants, and not too strong to desorb the products. Adsorption and desorption of reactants and products are critical factors in catalytic processes, directly impacting reaction efficiency and selectivity. Thus, apart from examining the energy changes thermodynamically, the rates of adsorption and desorption were also explored under various temperature and pressure conditions from a kinetic viewpoint through collision theory[53] and TST.[54]

The non-activated adsorption rate of a species (r_{ads}) can be calculated using collision theory[53] as follows:

$$r_{ads} = \frac{S_0 \cdot p_i \cdot A}{\sqrt{2\pi \cdot m_i \cdot k_B \cdot T}} \quad (2.46),$$

where S_0 represents the initial sticking coefficient, p_i denotes the partial pressure of reactants in the gas phase, and A signifies the surface area of an adsorption site, estimated by dividing the surface supercell area.

The desorption rate r_{des} is estimated using TST,[54] assuming the desorbed transition state is a late two-dimensional transition state, where the desorption energy ΔE^i_{des} is the negative of the adsorption energy ΔE^i_{ads}:

$$r_{des} = v_{des} \cdot exp\left(\frac{\Delta E^i_{\text{ads}}}{k_B \cdot T}\right);\ v_{des} = \frac{k_B \cdot T}{h} \frac{q^{gas}_{trans,2D} \cdot q^{gas}_{rot} \cdot q^{gas}_{vib}}{q^{ads}_{vib}} \quad (2.47),$$

where, ΔE^i_{ads} is the non-ZPE corrected adsorption energy. In these rate definitions, ZPE is accounted for in the vibrational partition function. The pre-factor v_{des} is given by various partition functions, q, which include:

$$q^{gas}_{trans,2D} = A \cdot \frac{2\pi \cdot m \cdot k_B \cdot T}{h^2} \quad (2.48),$$

$$q^{ads/gas}_{vib} = \prod_n \frac{exp\left(-\frac{h \cdot v_n}{2 \cdot k_B \cdot T}\right)}{1 - exp\left(-\frac{h \cdot v_n}{k_B \cdot T}\right)} \quad (2.49),$$

$$q^{gas}_{rot} = \frac{T}{\sigma^{sym} \cdot T_{rot}} \quad (2.50).$$

The partition functions, $q^{gas}_{trans,2D}$, q^{gas}_{rot}, and q^{gas}_{vib} refer to the gas phase translational partition function including only 2D degrees of freedom (as the third dimension is the reaction coordinate for desorption), the rotational partition function, and the vibrational partition function, respectively, computed in a large box. The q^{ads}_{vib} is the vibrational partition function of the adsorbed molecule, where six degrees of freedom correspond to frustrated rotations and translations. Finally, in the rotational partition functions (Eq. 2.50), T_{rot} is the rotational temperature of the adsorbed species.

Furthermore, for the reaction and diffusion steps with transition state calculation, particularly as discussed in Section 3.4 regarding the calculation of reaction rates, r_j, the methodology follows a similar approach as outlined for the desorption rate using TST,[55] defined as:

$$r_j = v \cdot exp\left(-\frac{\Delta E_{TS}}{k_B \cdot T}\right);\ v = \frac{k_B \cdot T}{h}\frac{q_{vib}^{TS}}{q_{vib}^{IS}} \quad (2.51),$$

where ΔE_{TS} represents the energy barrier without zero-point energy corrections, the prefactor v is determined by the partition function, which involves the vibrational partition functions of the Initial State (IS) and TS on the surface. The $q_{vib}^{TS/IS}$ denotes the vibrational partition given by:

$$q_{vib}^{TS/IS} = \prod_n \frac{exp\left(-\frac{h \cdot v_n}{2 \cdot k_B \cdot T}\right)}{1 - exp\left(-\frac{h \cdot v_n}{k_B \cdot T}\right)} \quad (2.52).$$

Finally, for the studies in this thesis, these equations and definitions provide a comprehensive framework for obtaining adsorption, desorption, and reaction rates in terms of transition state theory and collision theory.

2.9. Reaction Activity Descriptors

In catalysis, descriptors of reaction activity are crucial concepts that help quantify and understand the performance and energy requirements of reactions under specific conditions, such as ΔG_{max}, overpotential (η), and limiting potential (U_L), providing essential perspectives for a thorough analysis of reaction activity. By utilizing these descriptors, we can effectively assess and compare the efficiency and feasibility of various catalytic reactions.

The descriptor ΔG_{max} refers to the maximum free energy difference between intermediate states of elementary steps, *i.e.*, the minimum energy required for the reaction to reach spontaneity, which can be obtained from the Gibbs free energy profile of the reaction, and serves as a primary metric for quantitatively assessing reaction activity. Typically, elementary steps with ΔG_{max} are Potential Determining Steps (PDS).[56]

Next, the reaction limiting potential U_L can be further evaluated, which is defined as the minimum potential required under specific reaction conditions for a particular electrochemical reaction to occur spontaneously. For instance, in the context of the CO_2 reduction reaction (CO_2RR) discussed in Section 3.2, U_L represents the potential at which each elementary electrochemical hydrogenation step becomes exergonic, indicating the minimum energy input necessary for the reaction to proceed. The expression is given as follows:

$$U_L = -\frac{\Delta G_{max}}{e} \quad (2.53).$$

where, generally, the smaller the limiting potential, the higher the reaction activity.

In electrochemical processes, certain resistances, such as the internal resistance of the electrocatalyst and the resistance of the solvent, are unavoidable. These resistances, especially kinetic barriers, require the application of a greater potential. In this context, the concept of overpotential is introduced,[57] which is the difference between the standard equilibrium electrode potential (U_E) of a reaction (such as 0 V for hydrogen evolution reaction (HER); -0.24 V[58] for the reduction of CO_2 to CH_4) and the actual potential required to drive the reaction, and can be expressed as:

$$\eta = U_E - U_L \tag{2.54},$$

generally, the closer η is to zero, the better the catalytic performance.

2.10. The Span Model

The Energy Span Model (ESM)[59] offers a method to quantify catalytic performance that surpasses traditional approaches by focusing on the free energy of reaction intermediates and transition states in the catalytic cycle. Compared to traditional methods, it provides a more intuitive and comprehensive way to understand and predict catalyst activity.[60]

In the span model, the ΔG_{max} corresponds to the potential determining step that is defined as the maximum free energy difference between intermediate states i with the highest energy, PDI_i, and j with the lowest energy, PDI_j, expanding beyond the elementary reaction framework:

$$\Delta G_{max}^{span} = E_{highest}^{PDI_i} - E_{lowest}^{PDI_j} \tag{2.55},$$

when considering the Rate-Determining Transition State (RDTS), referring to the transition state with the highest energy, it significantly influences the reaction rate. Correspondingly, the Rate-Determining Intermediate (RDI) is the intermediate with the lowest energy, used to determine the energy span, defined as:

$$E_b^{span} = E_{highest}^{RDTS} - E_{lowest}^{RDI} \tag{2.56}.$$

These metric captures the crucial energy difference that influences the overall reaction thermodynamics and kinetics. For more comprehensive insights into the application and validity of the energy span model, additional details can be found in the existing literature.[61-63]

2.11. Computational Details

In this thesis, the widely tested and popular GGA-PBE exchange-correlation functional was employed, as it offers an excellent balance between computational cost and accuracy,[64] while providing sufficient precision in describing the electronic structure and related properties of two-dimensional materials.[65,66] Additionally, the aforementioned D3 approach proposed by Grimme *et al.*[28] was used to account for interactions involving dispersion. The valence electron density was expanded using a plane wave basis set with a cutoff kinetic energy of 415 eV to ensure that the total energies converged within chemical accuracy below 1 kcal·mol^{-1} —*ca.* 0.04 eV.[67]

During structural optimizations, the convergence of the electronic self-consistent field steps was controlled using a criterion of 10^{-5} eV, and atomic positions were relaxed until the forces on the atoms were below 0.01 eV·Å^{-1}. It is important to note that, unless specified otherwise, all calculations were conducted taking spin polarization into account. The vibrational frequencies were determined by constructing and diagonalizing the corresponding block of the Hessian matrix, using finite differences of analytical gradients with step sizes of 0.03 Å as done in previous works.[68,69]

2.12. References

1. Born, M.; Oppenheimer, R., *Zur Quantentheorie der Molekeln*. *Ann. Phys.* **1927,** *389*, 457–484.
2. Hartree, D. R., The Wave Mechanics of an Atom with a Non-Coulomb Central Field. Part II. Some Results and Discussion. *Math. Proc. Camb. Philos. Soc.* **1928,** *24*, 111–132.
3. Møller, C.; Plesset, M. S., Note on an Approximation Treatment for Many-Electron Systems. *Phys. Rev.* **1934,** *46*, 618–622.
4. Shepard, R., The Multiconfiguration Self-Consistent Field Method. In Advances in Chemical Physics, K.P. Lawley (Ed.), **1987**.
5. Sherrill, C. D.; Schaefer III, H. F., The Configuration Interaction Method: Advances in Highly Correlated Approaches. In *Advances in quantum chemistry*, Elsevier: 1999; Vol. 34, pp 143–269.
6. Szalay, P. G.; Müller, T.; Gidofalvi, G.; Lischka, H.; Shepard, R., Multiconfiguration Self-Consistent Field and Multireference Configuration Interaction Methods and Applications. *Chem. Rev.* **2012,** *112*, 108–181.
7. Schmitz, G.; Hättig, C., Accuracy of Explicitly Correlated Local PNO-CCSD(T). *J. Chem. Theory Comput.* **2017,** *13*, 2623–2633.
8. Laloe, F., Do We Really Understand Quantum Mechanics, Cambridge University Press, **2012**, ISBN 978-1-107-02501-1.
9. Baseden, K. A.; Tye, J. W., Introduction to Density Functional Theory: Calculations by Hand on the Helium Atom. *J. Chem. Educ.* **2014,** *91*, 2116–2123.
10. Thomas, L. H., The calculation of atomic fields. *Math. Proc. Camb. Philos. Soc.* **1927,** *23*, 542–548.
11. Fermi, E., A Statistical Method for the Determination of Some Priorities of the Atom. Rend. Accad. Naz. Lincei, **1927**, *6*, 602–607.
12. Hohenberg, P.; Kohn, W., Inhomogeneous Electron Gas. *Phys. Rev.* **1964,** *136*, B864–B871.
13. Kohn W.; Sham L. J., Self-Consistent Equations Including Exchange and Correlation Effects. *Phys. Rev.* **1965,** *140*, A1133–A1138.
14. Perdew, J. P.; Zunger, A., Self-Interaction Correction to Density-Functional Approximations for Many-Electron Systems. *Phys. Rev. B* **1981,** *23*, 5048–5079.

15 . Hua, X.; Chen, X.; Goddard, W. A., Generalized Generalized Gradient Approximation: An Improved Density-Functional Theory for Accurate Orbital Eigenvalues. *Physical Review B* **1997,** *55*, 16103–16109.

16. Goerigk, L.; Hansen, A.; Bauer, C.; Ehrlich, S.; Najibi, A.; Grimme, S., A Look at the Density Functional Theory Zoo with the Advanced GMTKN55 Database for General Main Group Thermochemistry, Kinetics and Noncovalent Interactions. *Phys. Chem. Chem. Phys.* **2017,** *19*, 32184–32215.

17. Mejía-Rodríguez, D.; Trickey, S. B., Spin-Crossover from a Well-Behaved, Low-Cost meta-GGA Density Functional. *J. Phys. Chem. A* **2020,** *124*, 9889–9894.

18. Cui, H.; Yang, S.; Yuan, J.H.; Li, L.-H.; Ye, F.; Huang, J.; Xue, K.H.; Miao, X., Shell DFT-1/2 method towards engineering accuracy for semiconductors: GGA versus LDA. *Comput. Mater. Sci.* **2022,** *213*, 111669.

19. Bagayoko, D., Understanding Density Functional Theory (DFT) and Completing It in Practice. *AIP Adv.* **2014,** *4*, 127104.

20. Perdew J. P., Electronic structure of solids'91, edited by P. Ziesche and H. Eschrig (Akademie Verlag, Berlin, 1991), p. 11

21. Perdew, J. P.; Burke, K.; Ernzerhof, M. Generalized Gradient Approximation Made Simple. *Phys. Rev. Lett.*, **1996**, *77*, 3865–3868.

22. Wellendorff, J.; Lundgaard, K. T.; Møgelhøj, A.; Petzold, V.; Landis, D. D.; Nørskov, J. K.; Bligaard, T.; Jacobsen, K. W., Density Functionals for Surface Science: Exchange Correlation Model Development with Bayesian Error Estimation. *Phys. Rev. B* **2012**, *85*, 235149–235172.

23. Tao, J.; Perdew, J. P.; Staroverov, V. N.; Scuseria, G. E., Climbing the Density Functional Ladder: Nonempirical Meta-Generalized Gradient Approximation Designed for Molecules and Solids. *Phy. Rev. Lett.* **2003,** *91*, 146401.

24. Perdew, J. P.; Ernzerhof, M.; Burke, K., Rationale for Mixing Exact Exchange with Density Functional Approximations. *J. Chem. Phys.* **1996,** *105*, 9982–9985.

25 Ramalho, J. P. P.; Gomes, J. R. B.; Illas, F., Accounting for van der Waals Interactions Between Adsorbates and Surfaces in Density Functional Theory Based Calculations: Selected Examples. *RSC Adv.* **2013,** *3*, 13085–13100.

26. Grimme, S., Accurate Description of van der Waals Complexes by Density Functional Theory Including Empirical Corrections. *J. Comput. Chem.* **2004,** *25*, 1463–1473.
27. Grimme, S., Semiempirical GGA-Type Density Functional Constructed with a Long-Range Dispersion Correction. *J. Comput. Chem.* **2006,** *27*, 1787–1799.
28. Grimme, S.; Antony, J.; Ehrlich, S.; Krieg, H., A Consistent and Accurate ab initio Parametrization of Density Functional Dispersion Correction (DFT-D) for the 94 Elements H-Pu. *J. Chem. Phys.* **2010,** *132*, 154104.
29. Bloch, F., Measurement of the Electrical Theory of Ferromagneticism and Electrical Flexibility. *Z. Physik* **1929,** *57*, 545–555.
30. Schwerdtfeger, P., The Pseudopotential Approximation in Electronic Structure Theory. *Chem. Phys. Chem.* **2011,** *12*, 3143–3155.
31. J. K. Nørskov, J. Rossmeisl, A. Logadottir, L. Lindqvist, J. R. Kitchin, T. Bligaard and H. Jónsson, Origin of the Overpotential for Oxygen Reduction at a Fuel-Cell Cathode. *J. Phys. Chem. B* **2004,** *108*, 17886−17892.
32. Fishtik, I.; Datta, R., A Thermodynamic Approach to the Systematic Elucidation of Unique Reaction Routes in Catalytic Reactions. *Chem. Eng. Sci.* **2000,** *55*, 4029–4043.
33. Xiao, Y.; Zhang, W., High Throughput Screening of M_3C_2 MXenes for Efficient CO_2 Reduction Conversion into Hydrocarbon Fuels. *Nanoscale* **2020,** *12*, 7660–7673.
34. NIST Standard Reference Database SRD Number 69, DOI: 10.18434/T4D303.
35. Li, Q.; Ouyang, Y.; Lu, S.; Bai, X.; Zhang, Y.; Shi, L.; Ling, C.; Wang, J. J. C. C., Perspective on Theoretical Methods and Modeling Relating to Electrocatalysis Processes. **2020,** *56*, 9937–9949.
36. Kim, S.; Ruiz-Puigdollers, A.; Gamallo, P.; Viñes, F.; Lee, J. Y., Functionalization of γ-Graphyne by Transition Metal Adatoms. *Carbon* **2017,** *120*, 63−70.
37. Oschinski, H.; Morales-García, Á.; Illas, F., Interaction of First Row Transition Metals with M_2C (M = Ti, Zr, Hf, V, Nb, Ta, Cr, Mo, and W) MXenes: A Quest for Single-Atom Catalysts. *J. Phys. Chem. C* **2021,** *125*, 2477−2484.

38. Kim, S.; Gamallo, P.; Viñes, F.; Lee, J. Y.; Illas, F., Substrate-Mediated Single-Atom Isolation: Dispersion of Ni and La on γ-Graphyne. *Theor. Chem. Acc.* **2017,** *136*, 80.
39. M. Pourbaix, *Atlas of Electrochemical Equilibria in Aqueous Solutions*. National Association of Corrosion Engineers (NACE), Houston, Texas, USA, 1974.
40. D. F. Sriver and P. W. Atkins, *Inorganic Chemistry*, 5th ed., Freeman, W.H. and Company, New York, 2009.
41. López, M.; Exner, K. S.; Viñes, F.; Illas, F., Computational Pourbaix Diagrams for MXenes: A Key Ingredient toward Proper Theoretical Electrocatalytic Studies. *Adv. Theory Simul.* **2023,** *6*, 2200217.
42. Hansen, H. A.; Man, I. C.; Studt, F.; Abild-Pedersen, F.; Bligaard, T.; Rossmeisl, J., Electrochemical Chlorine Evolution at Rutile Oxide (110) Surfaces. *Phys. Chem. Chem. Phys.* **2010,** *12*, 283–290.
43. Anslyn, E. V.; Dougherty, D. A., Transition State Theory and Related Topics. *Modern Physical Organic Chemistry*. University Science Books. **2006,** pp. 365–373. ISBN 1891389319.
44. Eyring, H., The Activated Complex in Chemical Reactions. *J. Chem. Phys.* **1935,** *3*, 107–115.
45. McIver Jr, J. W.; Komornicki, A., Structure of Transition States in Organic Reactions. General Theory and an Application to the Cyclobutene-Butadiene Isomerization using a Semiempirical Molecular Orbital Method. **1972,** *94*, 2625–2633.
46. Komornicki, A.; Ishida, K.; Morokuma, K.; Ditchfield, R.; Conrad, M., Efficient Determination and Characterization of Transition States Using Ab-Initio Methods. *Chem. Phys. Lett.* **1977,** *45*, 595–602.
47. Schlegel, H. B., Exploring Potential Energy Surfaces for Chemical Reactions: an Overview of Some Practical Methods. *J. Comput. Chem.* **2003,** *24*, 1514–1527.
48. Henkelman, G.; Uberuaga, B. P.; Jónsson, H., A Climbing Image Nudged Elastic Band Method for Finding Saddle Points and Minimum Energy Paths. *J. Chem. Phys.* **2000,** *113*, 9901–9904.

49. Bagger, A.; Arnarson, L.; Hansen, M. H.; Spohr, E.; Rossmeisl, J., Electrochemical CO Reduction: A Property of the Electrochemical Interface. *J. Am. Chem. Soc.* **2019,** *141*, 1506–1514.
50. Bronsted, J. N., Acid and Basic Catalysis. *Chem. Rev.* **1928,** *5*, 231–338.
51. K.; Chi, L.; Rosen, J.; Bjork, J., Termination-Accelerated Electrochemical Nitrogen Fixation on Single-Atom Catalysts Supported by MXenes. *J. Phys. Chem. Lett.* **2022,** *13*, 2800–2807.
52. Rothenberg, G., Catalysis: Concepts and Green Applications. Wiley-VCH. p. 65. ISBN 978-3-527-31824-7.
53. "Collision Theory." Chemistry LibreTexts, Libretexts, 22 May 2017.
54. Kunkel, C.; Viñes, F.; Illas, F., Transition Metal Carbides as Novel Materials for CO_2 Capture, Storage, and Activation. *Energy Environ. Sci.* **2016**, *9*, 141–144.
55. Truhlar, D. G.; Garrett, B. C.; Klippenstein, S. J., Current Status of Transition-State Theory. *J. Phys. Chem.* **1996**, *100*, 12771–12800.
56. Koper, M. T. M., Analysis of Electrocatalytic Reaction Schemes: Distinction Between Rate-Determining and Potential-Determining Steps. *J. Solid State Electrochem.* **2013,** *17*, 339–344.
57. Bard, A. J.; Faulkner, L. R., Electrochemical Methods: Fundamentals and Applications. **2001,** Wiley. ISBN 978-0-471-04372-0.
58. Lu, S.; Lou, F.; Yu, Z., Recent Progress in Two-Dimensional Materials for Electrocatalytic CO_2 Reduction. *Catalysts* **2022**, *12*, 228.
59. Kozuch, S.; Shaik, S., How to Conceptualize Catalytic Cycles? The Energetic Span Model. *Acc. Chem. Res.* **2011,** *44*, 101–110.
60. Exner, K. S., A Universal Descriptor for the Screening of Electrode Materials for Multiple-Electron Processes: Beyond the Thermodynamic Overpotential. *ACS Catal.* **2020,** *10*, 12607–12617.
61. Exner, K. S., Why Approximating Electrocatalytic Activity by A Single Free-Energy Change is Insufficient. *Electrochim. Acta* **2021,** *375*, 137975.
62. Razzaq, S.; Exner, K. S., Method to Determine the Bifunctional Index for the Oxygen Electrocatalysis from Theory. *ChemElectroChem* **2022,** *9*, e202101603.

63. Exner, K. S., Beyond the Thermodynamic Volcano Picture in the Nitrogen Reduction Reaction Over Transition-Metal Oxides: Implications for Materials Screening. *Chin. J. Catal.* **2022,** *43*, 2871–2880.
64. Fischer, M.; Evers, F. O.; Formalik, F.; Olejniczak, A., Benchmarking DFT-GGA Calculations for the Structure Optimisation of Neutral-Framework Zeotypes. *Theor. Chem. Acc.* **2016,** *135*, 257.
65. Parey, V.; Abraham, B. M.; Mir, S. H.; Singh, J. K., High-Throughput Screening of Atomic Defects in MXenes for CO_2 Capture, Activation, and Dissociation. *ACS Appl. Mater. Interfaces* **2021,** *13*, 35585−35594.
66. Ontiveros, D.; Viñes, F.; Sousa, F. Bandgap Engineering of MXene Compounds for Water Splitting. *J. Mater. Chem. A* **2023,** *11*, 13754–13764.
67. Morales-Salvador, R.; Gouveia, J. D.; Morales-García, Á.; Viñes, F.; Gomes, J. R. B.; Illas, F. Carbon Capture and Usage by MXenes. *ACS Catal.* **2021,** *11*, 11248–11255.
68. López, M.; Morales-García, Á.; Viñes, F.; Illas, F. Thermodynamics and Kinetics of Molecular Hydrogen Adsorption and Dissociation on MXenes: Relevance to Heterogeneously Catalyzed Hydrogenation Reactions. *ACS Catal.* **2021**, *11*, 12850–12857.
69. Gouveia, J. D.; Morales-García, Á.; Viñes, F.; Illas, F.; Gomes, J. R. B. MXenes as Promising Catalysts for Water Dissociation. *Appl. Catal. B: Environ* **2020**, *260*, 118191.

Chapter 3

2D-MXenes in Advancing Electrochemical and Thermal Catalysis

3.1. Introduction

The escalating challenges of climate change and resource depletion driven by the growing energy demand have underscored the urgent need to transition towards renewable and cleaner energy sources.[1,2] Among various potential solutions, hydrogen (H_2) has gained significant attention due to its high energy density and environmentally friendly characteristics.[3,4] Particularly, the production of green hydrogen through the electrocatalytic HER using renewable sources like wind and solar energy,[5] paves the way for sustainable energy future. Similarly, carbon dioxide (CO_2) emissions are a major contribution to global greenhouse gas,[6] but carbon reduction technologies such as electrocatalytic CO_2RR[7] offer the possibility to convert CO_2 into useful chemicals and fuels, achieving carbon cycle.

Two-dimensional MXene materials have been identified as efficient electrocatalysts due to their high surface area, active sites, conductivity, stability, corrosion resistance, and hydrophilicity.[8] However, existing research has predominantly focused on pristine MXenes or surfaces with full –O or –OH terminations,[9-11] overlooking the fact that synthesized MXenes typically are likely to exhibit mixed surface terminations. Therefore, we propose a comprehensive DFT study using Ti_3C_2 MXene, first synthesised in 2011,[12] as MXene prototype, which is currently the most well-studied and mature MXene material, to investigate the influence of different surface terminations on the stability and catalytic activity of HER and CO_2RR, determining the most effective surface composition for these crucial catalytic processes.

The pursuit of sustainability goals also drives improvements in ammonia (NH_3) synthesis technologies,[13] as the high temperature and pressure conditions result in significant energy consumption and CO_2 emissions in traditional Haber-Bosch process.[14] Hence, alternative NH_3 synthesis technologies under milder conditions, such as electrocatalytic NRR, have emerged.[15] Notably, the unique electronic structure and chemical

properties of boron (B) atom,[16,17] which contain both occupied and vacant orbitals simultaneously, show promising potential for strong N_2 fixation. Thus, introducing different B-doped configurations in the Ti_3C_2 MXene, and exploring previously unconsidered surface terminations provide new insights into NRR catalytic performance.

Lastly, hydrogenation reactions also play a vital role in numerous technological applications spanning from environmental treatment to petrochemical and fine chemical industries.[18] The fundamental understanding at the atomic level of these reactions, is crucial for further improvements, here taking ethene hydrogenation as an example, revealing the reaction mechanisms of olefin hydrogenation on Rh (111) and 2D-Mo_2C pristine MXene (0001) surface by DFT, discussing the paired/non-paired hydrogenation mechanisms behind them.

Overall, this chapter primarily discuss MXene-based electrocatalytic reduction reactions (HER, CO_2RR, NRR) and thermal catalytic olefin hydrogenation, providing a crucial scientific foundation for future energy transition and chemical engineering processes.

3.2. Effect of Terminations of Hydrogen Evolution Reaction and Carbon Dioxide Reduction Reaction on MXenes

3.2.1. Introduction

Previous both theoretical and experimental studies have shown that some members of the MXene family have the potential to serve as catalysts for the HER[19-21] and CO_2RR.[22,23] As synthesised MXenes exhibit a variety of surface functional groups T_x on the substrate surface, typically including pristine (no termination),[24,25] a mixture of surface terminations such as –O, –OH, –H and –F, or without –F,[26-28] in addition, theoretical assessments also point out that the mixture of T_x are more energetically stable.[9,29] However, computational studies almost always assumed T_x to be composed fully of –O or –OH only. For instance, Pandey *et al.*[30] investigated HER performance on fully O-terminated M_2X, M_3X_2, and M_4X_3 using the free Gibbs energy of hydrogen adsorption at equilibrium coverage as an activity descriptor. Handoko *et al.*[10] and Chen et al.[11] explored the surface termination of full –O and –OH moiety, respectively, and found that O-terminated MXenes improve the stability of reaction intermediates with coordinating hydrogen atoms, whereas OH-terminated MXenes show high reactivity due to the already presence of hydrogen atoms of –OH. These works demonstrate that to some extent, catalytic performance can be affected by T_x group. Therefore, it is critical to realistically simulate the MXene surface terminations under HER/CO_2RR working conditions of *pH* and applied potential U, and explore the roles and influence of different functional group types in the potential-determining steps (PDS) and reaction mechanisms. We delve into exploring the surface stability of the Ti_3C_2 MXene and the corresponding HER and CO_2RR mechanism under working conditions in acidic solutions, where the kinetic reaction rate is higher and provides an abundant source of protons (H^+), while also evaluating various key thermodynamic and kinetic electronic property descriptors related to the intrinsic activity of electrochemical HER reaction by summarizing other relevant works, as well a comprehensive review of the most significant advances of MXenes in CO_2RR electrocatalysis, critically discussing the evolution and implications of the MXene models, with attention to unresolved research issues and future perspectives.

This part of the thesis lead to two research articles publishing in *Journal of Materials Chemistry A*, titled "*Effect of Terminations on the Hydrogen Evolution Reaction Mechanism on Ti_3C_2 MXene*",[31] and "*Surface Termination Dependent Car-*

bon Dioxide Reduction Reaction on Ti_3C_2 MXene",[32] and two review articles, titled "*Theoretical Modelling of the Hydrogen Evolution Reaction on MXenes: A Critical Review*" in *Current Opinion in Electrochemistry*,[33] and "*MXenes as Electrocatalysts for the CO_2 Reduction Reaction: Recent Advances and Future Challenges*", published in *ChemElectroChem*.[34] The supporting information of research articles can be found in Appendies A and B, respectively, which are provided at the end of this thesis. Subsequent pages contain a summary of these articles. My contributions to the research articles comprise: (a) carrying out the DFT calculations and data treatment, (b) analysis of the calculations results, (c) surveying and summarizing the relevant publications, and (d) writing the initial manuscripts of papers and making the corresponding figures.

3.2.2. Reaction System

3.2.2.1. Hydrogen Evolution Reaction (HER)

The HER at a specific electrode can be expressed[35] as Eq. 3.1,

$$2H^+_{(aq)} + 2e^- \leftrightarrow H_{2(g)} \quad (3.1),$$

according to the CHE,[36] the equilibrium can be assumed as Eq. 3.2, which is also used to evaluate the HER activity,

$$H^+_{(aq)} + e^- \leftrightarrow \tfrac{1}{2}\cdot H_{2(g)} \quad (3.2).$$

In the context of Eq. 3.2, two well-recognized general mechanisms for HER have been identified, namely Volmer-Heyrovsky (VH) and Volmer-Tafel (VT),[37,38] as shown in Figure 3.1. Both involve a first electrochemical Volmer step as Eq. 3.3,

$$\text{Volmer step: } H^+ + e^- + * \rightarrow H^* \quad (3.3);$$

here, * represents an active site, H* represents adsorbed hydrogen atom on surface, and proton is available from aqueous medium, *i.e.* not from the catalyst itself. The differences between the two mechanisms lie in the second step, illustrated in Eqs. 3.4 and 3.5,

$$\text{Heyrovsky step: } H^+ + e^- + H^* \rightarrow * + H_2 \quad (3.4),$$

$$\text{Tafel step: } 2H^* \rightarrow * + H_2 \quad (3.5),$$

where the Heyrovsky step is electrochemical, while the Tafel step is the recombination of two previously reduced protons.

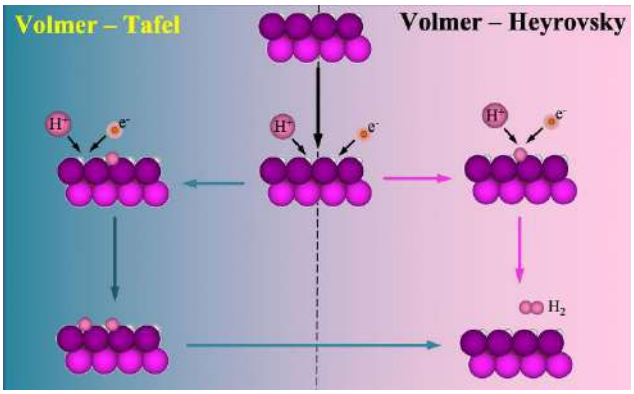

Figure 3.1. Schematic view of the two main HER mechanisms. The cycle with green arrows corresponds to the VT mechanism whereas orange arrows refer to the description of VH. Note that the first step, starting on the top of each cycle is the same for both VT and VH, but the formation of H_2 in the VT mechanism is of chemical nature whereas it is an electrochemical step in the VH pathway. Picture adapted from the original picture in Ref. 38.

However, it should be noted that the above VH and VT mechanisms are easily applicable to common O-terminated or rare studied F-terminated MXenes, but they may not be suitable for OH-terminated and H-terminated MXenes, in which the adsorbed H moieties is present before any above electrochemical step, and the reduction reaction may begin by utilizing one or two H atoms from –OH and/or –H terminations instead of starting with the reduction of H^+ from the aqueous medium in the VH or VT mechanisms. For instance, on a –OH terminated Ti_3C_2, the VH reaction sequence would be altered as Eqs. 3.6-8,

$$H^+ + e^- + –OH^* \rightarrow –O^* + H_2^* \quad (3.6),$$

$$H_2^* \rightarrow H_2 + * \quad (3.7),$$

$$H^+ + e^- + –O^* \rightarrow –OH^* \quad (3.8),$$

where –OH* and –O* indicate the termination of –OH and –O on MXene surface, respectively. Similarly, in the VT mechanism, the H_2 generation can occur through the participation of two H atoms from –OH surface groups, subsequently leading to the restoration of –OH moieties as Eqs. 3.9-11,

$$2 \cdot –OH^* \rightarrow 2 \cdot –O^* + H_2^* \quad (3.9),$$

$$H_2^* \rightarrow H_2 + * \quad (3.10),$$

$$(2\times)\ H^+ + e^- + {-O^*} \rightarrow {-OH^*} \qquad (3.11).$$

where the (2×) symbol denoted that the step happens twice.

3.2.2.1. CO_2 Reduction Reaction (CO_2RR)

Several CO_2RRs involving varying electrons are present in Eqs. 3.12-15 along with their respective standard equilibrium potentials[39] (E^0), with comparison to the Reversible Hydrogen Electrode (RHE).

$$CO_2 + 2H^+ + 2e^- \rightarrow CO + H_2O \qquad E^0 = -0.11\ V \qquad (3.12),$$

$$CO_2 + 2H^+ + 2e^- \rightarrow HCOOH \qquad E^0 = -0.22\ V \qquad (3.13),$$

$$CO_2 + 6H^+ + 6e^- \rightarrow CH_3OH + 2H_2O \qquad E^0 = 0.02\ V \qquad (3.14),$$

$$CO_2 + 8H^+ + 8e^- \rightarrow CH_4 + 2H_2O \qquad E^0 = 0.17\ V \qquad (3.15).$$

In this Chapter, we focus on methane production through eight-electron reduction process in CO_2RR. The reaction network is extensive, involving various intermediate species and C_1 products like CH_2O and CH_3OH,[40] as depicted in Figure 3.2.

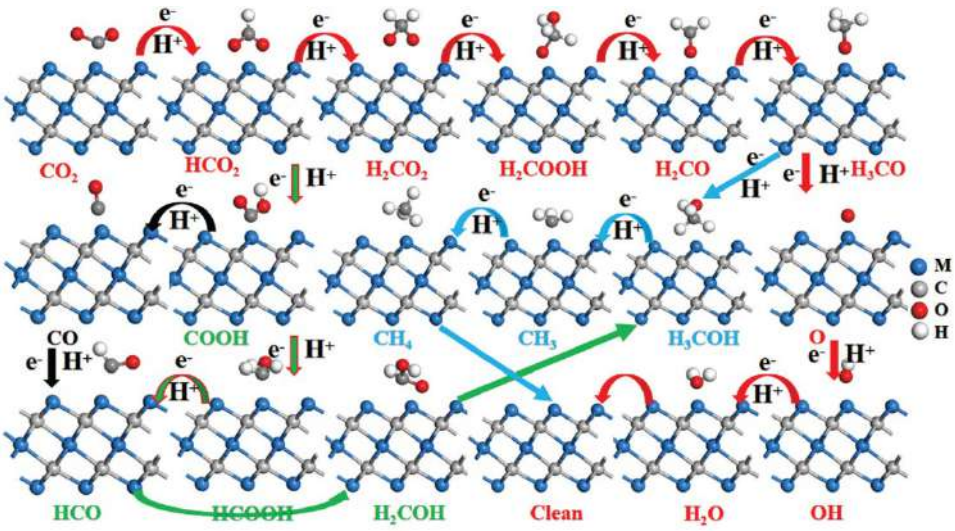

Figure 3.2. Proposed CO_2RR possible mechanism pathways to CH_4 involving different products on MXenes. Picture adapted from the original picture in Ref. 40.

Early studies often assumed that the reduction of any precursor adsorbate species A* occurs in a single elementary step, where an H^+ and an electron e^- combine to form AH*, as Eq. 3.16,

$$A^* + H^+ + e^- \rightarrow AH^* \qquad (3.16).$$

However, similar to HER, the presence of –OH groups as hydrogen sources can alter the scenario. For instance, A* can be hydrogenated by the H atom of –OH group,

$$A^* + –OH \rightarrow AH^* + –O \quad (3.17),$$

leaving a –O moiety in this chemical process. Subsequently, an electrochemical step can reduce a proton on the formed –O group, regenerating the –OH group as Eq. 3.18,

$$–O + H^+ + e^- \rightarrow –OH \quad (3.18).$$

It is also worth noting that not only precursor adsorbate species A*, but also –O groups can serve as reduction sites for proton storage, as in Eq. 3.18, and subsequently, the as-formed –OH could participate in later hydrogenation reaction. Considering these various pathways provides a more comprehensive understanding of the involvement of surface terminations and subsequent mechanisms in the CO_2RR process.

3.2.3. Results

3.2.3.1. Surface Terminations Stability Analysis

The Pourbaix diagram is essential for determining surface composition information to identify the most thermodynamically stable surface terminations of Ti_3C_2(0001) MXene under practical working conditions of *pH* and *U*.[41] Here, four different surface termination groups, –O, –OH, –H, and –F, were firstly considered in the highly symmetric top metal (T), bridge (B), three-fold hollow C (H_C), and three-fold hollow Ti (H_{Ti}) on the Ti_3C_2 *p*(3×3) supercell, as shown in Figure 3.3. The results indicated that the H_{Ti} site is preferred for surface termination samplings. In this way, two versions of the Pourbaix diagram were obtained considering only full coverage of –O, –OH, –H, or –F, as shown in Figure 3.4. One version is for F-free synthesis, *i.e.*, in absence of fluorine anions,[42-44] and the other regarding fluorine, for MXenes synthesized using HF or *in situ* HF.[26,27,45] The Pourbaix diagrams in Figure 3.4 agree with previous assessments,[19,46] that the Ti_3C_2 (0001) surface is generally O-terminated at positive *U* (with respect to the RHE reference), *i.e.* above the equilibrium line, conversely, below this line, the –OH termination is preferred, which aligns with favourable H^+ reduction, in addition, –H termination becomes preferable only at very negative potentials. Furthermore, the –O and –OH terminations are very close to the equilibrium line, suggesting the possibility of existence of binary systems between them. Finally, it is noted that –F has a small but critical influence region near the equilibrium line, especially in the low *pH* range (up to *pH* = 2). Therefore, in

principle, binary or even ternary surface terminations should be considered to properly simulate the Ti_3C_2 (0001) surface for reduction reactions of HER and CO_2RR.

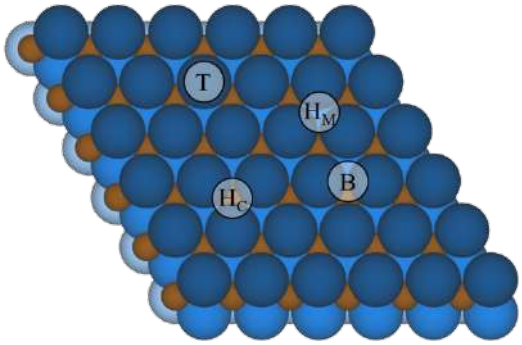

Figure 3.3. Top view of the Ti_3C_2 (0001) surface model, where brown spheres denote C atoms, and three different Ti layers are shown with different shades of blue, being the topmost one the darkest. High-symmetry sites are tagged, including top (T) and bridge (B) sites, and three-fold hollow carbon (H_C) and hollow metal (H_M) sites.[31]

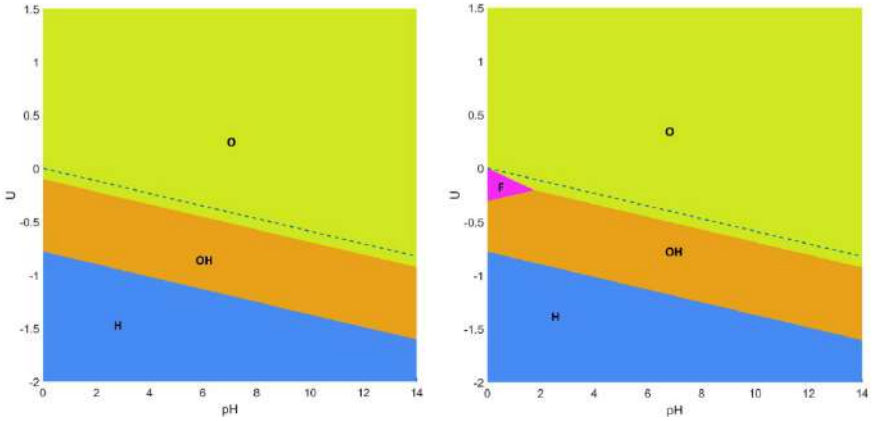

Figure 3.4. Pourbaix diagrams for Ti_3C_2 MXene (0001) surface regarding fully –O, –OH, and –H terminated surfaces (left), or including as well fully –F terminated surfaces (right). Regions of preferred stability are coloured and tagged. The blue, dashed line indicates the HER equilibrium potential using the RHE.[31]

To explicitly address this issue, mixed terminations were considered, resulting in Pourbaix diagrams for both F-free and F-containing situations, as shown in Figure 3.5, confirming that in order to represent a realistic situation near the equilibrium line, mixed terminations have to be considered. Moreover, the –O termination above the equilibrium line in Figure 3.4 is actually an O-rich situation but still includes other surface groups, for instance, above the equilibrium line, the $–O_{2/3}OH_{1/3}$ model appears first, followed by the $–O_{3/4}OH_{1/4}$, and fully –O termination is found approximately 0.4 V above the equilibrium line. Overall, single, binary, and ternary combinations were considered, as well as different surface compositions, for each composition, different topological structures also were

studied, around 450 different surface terminations, as shown in Figures S2-S7 in Appendix A, making this study the most comprehensive assessment of the Ti_3C_2 (0001) MXene surface Pourbaix diagram to date.[47]

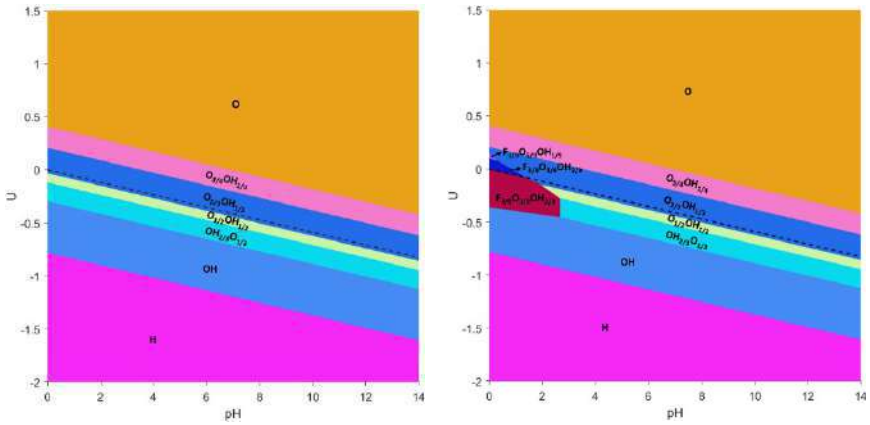

Figure 3.5. Pourbaix diagrams for Ti_3C_2 MXene (0001) surface regarding all single, binary, and ternary surface compositions including –O, –OH, –H, and –F terminations, as well as free sites. Left image corresponds to situations without any –F termination, while right image corresponds to situations when regarding–F termination. The black, dashed line indicates the HER equilibrium potential with respect RHE reference.[31]

Ideally, for HER, one would seek a situation close to the standard HER equilibrium potential of 0 V and a low *pH* to facilitate the reaction kinetics, and thus, the F-free models, $–O_{1/3}OH_{2/3}$, $–O_{1/2}OH_{1/2}$, $–O_{2/3}OH_{1/3}$, the F-containing–$F_{1/3}O_{1/3}OH_{1/3}$ and $–F_{3/9}O_{4/9}OH_{2/9}$ models, are considered the most suitable and realistic. Besides these models, pristine and fully terminated Ti_3C_2 with –O, –OH, –F, and –H terminations are also included for comparison. Whereas for CO_2RR, one would aim for the negative potential and low *pH* values, considering the typical applications of MXene-based electrocatalysts for CO_2RR generating CH_4 in the $pH < 4$ and $-0.75\ V < U < 0\ V$ potential range,[10,11,22,23,48] the most suitable and realistic $Ti_3C_2T_x$ models are F-free of $–OH_{2/3}O_{1/3}$, $–OH_{1/2}O_{1/2}$, $–OH_{1/3}O_{2/3}$, and fully OH-terminated, as well the F-containing $–F_{1/3}OH_{1/3}O_{1/3}$ model.

3.2.3.2. Electrocatalytic Mechanism of HER

Now we focus on HER performance for the selected, representative cases (Figures 3.6-3.7). As mentioned above, both VH and VT mechanisms take into account the possible involvement of hydrogen atom on H- and OH-terminated Ti_3C_2(0001) MXenes. Therefore, here three possible reaction mechanisms were considered: *i*) H^+ reduction occurring at –O sites followed by Heyrovsky step directly generating $H_{2(g)}$, named O-TER; *ii*) H^+ reduction at –OH sites followed by Heyrovsky step at the as-generated –O site, named

OH-TER; *iii*) Tafel step occurring between two surface –OH groups followed by two consecutive Volmer steps regenerating –OH sites, denoted TER-TER.

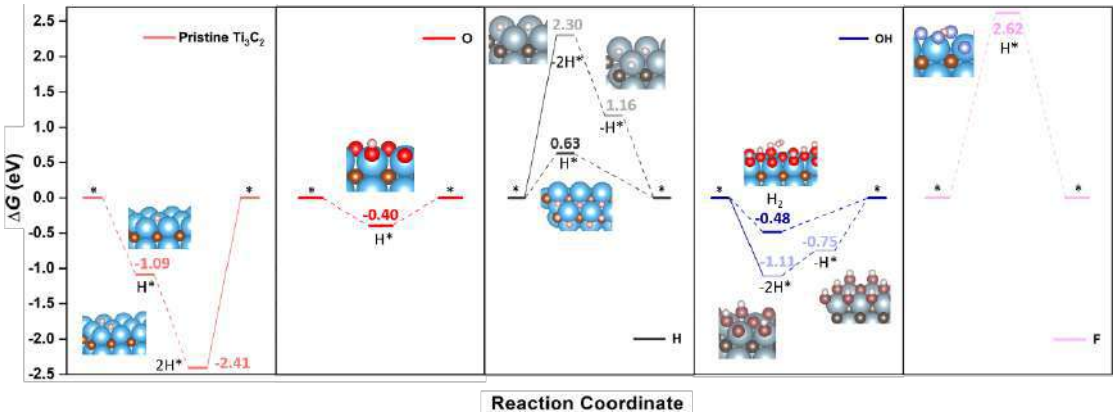

Figure 3.6. Gibbs free energy, Δ*G*, diagram of HER on pristine or fully –O, –OH, –F, or –H terminated Ti_3C_2 (0001) surface under standard working conditions. Solid lines represent the chemical step of the as-generated H_2 desorption, while dashed lines represent the electrochemical steps of Proton Coupled Electron Transfer (PCET). Inset images are side or eagle-eye views of the reaction intermediates, except of H* state on –H termination, which depicts a top view to better observe the H* allocation on a surface empty H_C site. Color coding as in Fig. 1, plus H, O, and F atoms are shown as white, red, and violet spheres.[31]

Firstly, pristine Ti_3C_2 and fully terminated samples, *i.e.*, –O, –OH, –F and –H terminated samples were studied. Figure 3.6 shows the Gibbs free energy reaction profiles for these five cases under standard working conditions —T = 298.15 K, p_{H_2} = 1 bar, pH = 0, U = 0 V—, where the pristine Ti_3C_2 exhibits excessively high reactivity, with Δ*G* for two protons under the VT mechanism being -1.09 and -1.32 eV, hence unsuitable for practical HER applications. On the other hand, the fully F-terminated surface significantly diminishes the HER activity, with Δ*G* of 2.62 eV in the VH mechanism, highlighting the detrimental effect of –F termination on electrocatalytic performance, coinciding with the earlier statement that the large number of –F groups imply poor electrocatalytic activity and selectivity.[49]

However, when considering –O and –OH surface terminations, HER activity becomes more favourable. The overpotential for –O termination is -0.40 V in the VH mechanism, but at such overpotential, Ti_3C_2 surface is predominantly terminated by –OH groups, as shown in Figure 3.4. In fact, the presence of –OH termination introduces complexity to the reaction mechanism, *i.e.*, the aforementioned *ii*) OH-TER and *iii*) TER-TER mechanisms. The PDS and overpotential vary accordingly, but still in line with the overpotential of the OH-terminated phase as seen in the Pourbaix diagrams of Figure 3.4. Similarly, in the case of H-terminated Ti_3C_2 model, the first proton reduction occupies

the H_C site, with the overpotential of -0.63 V, also close to the region of H terminations in the Pourbaix diagram (*cf.* Figure 3.4).

In addition, it was found that the influence of mixed terminations further modulates HER activity, with certain combinations leading to more favourable reaction pathways (*cf.* Figure 3.7). Firstly, the F-free models were considered, especially on the $–O_{1/2}OH_{1/2}$ model with an equal amount of –OH and –O groups, favours the OH-TER mechanism, making the entire process exothermic with the application of -0.23 V potential. Obviously, increasing the amount of –O groups favour the O-TER mechanism, while it is detrimental to other mechanisms involving –OH groups (*i.e.*, OH-TER and TER-TER). In addition, when the –O/–OH ratio is out of balance, *i.e.*, more –OH groups than –O groups, as the model of $–O_{1/3}OH_{2/3}$, the OH-TER pathway is preferred with a PDS of -0.08 V only. The overpotentials of these models are also well within the stability region of Pourbaix diagram, see Figure 3.5.

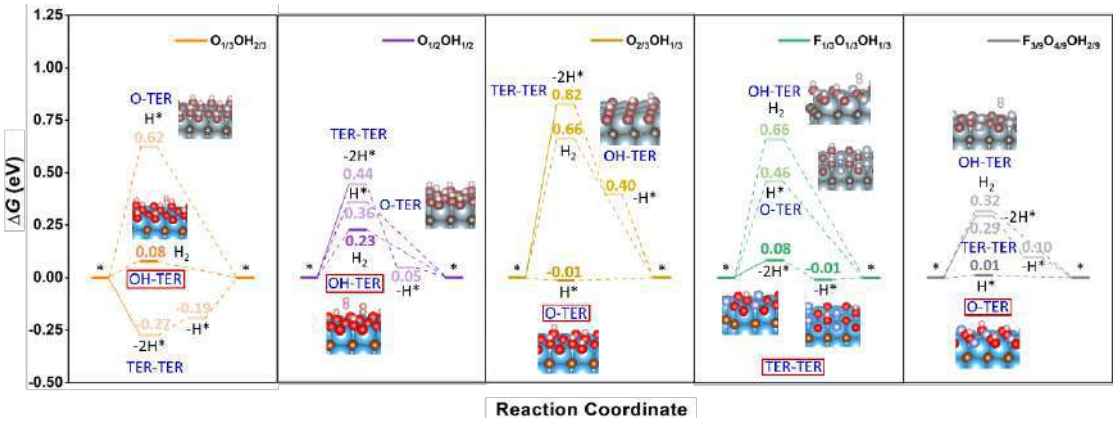

Figure 3.7. Gibbs free energy, Δ*G*, diagram of HER on selected binary and ternary terminations of Ti_3C_2 (0001) surface combining –O, –OH, and –F moieties, at standard working conditions. Solid lines represent the chemical step of the as-generated H_2 desorption, while dashed lines represent the electrochemical CPET steps. Color coding as in Figure 3.6.[31]

For the F-containing models, starting from the model $–F_{1/3}O_{1/3}OH_{1/3}$, which corresponds to the most stable situation at low *pH* and low *U*, can be compared with the reference models of $–O_{2/3}OH_{1/3}$ and $–O_{1/3}OH_{2/3}$, where half of the –O groups and –OH groups are replaced by –F groups. It can be observed that the stability of the O-TER observed in the O-rich $–O_{2/3}OH_{1/3}$ decreases, and the same occurs for OH-TER of the OH-rich model $–O_{1/3}OH_{2/3}$. However, for the TER-TER, the situation is not so unfavourable, with a chemical H recombination step involving a Δ*G* of 0.08 eV only, and second recovered Volmer step is PDS with overpotential only -0.01 V. Similarly, in the $–F_{3/9}O_{4/9}OH_{2/9}$ model, the Δ*G* of the Volmer step of the O-TER mechanism is 0.01 eV. Both of these F-

containing models essentially consistent with the equilibrium potential of the HER as shown in the Pourbaix diagram (*cf.* Figure 3.5).

After analysing the effect of mixed termination on several HER mechanisms, the competitiveness of the VT mechanism on these models were conducted, as shown in Figure 3.8. In the case of full –O termination, the two reduction steps are exothermic, but this termination is only stable at high *U* (*cf.* Figure 3.4). As for the binary and ternary cases, the VT for $–O_{1/3}OH_{2/3}$, $–O_{1/2}OH_{1/2}$ and $–F_{1/3}O_{1/3}OH_{1/3}$ all require high overpotentials, the only viable model is $–O_{2/3}OH_{1/3}$, with the *U* of only -0.09 V, but still not superior to the above VH mechanism. Thus, the VT mechanism is not preferred in any of the models that have been explored. Overall, $–O_{2/3}OH_{1/3}$, $–F_{1/3}O_{1/3}OH_{1/3}$, as well as $–F_{3/9}O_{4/9}OH_{2/9}$ models require an almost negligible overpotential of 0.01 V, that is close to HER equilibrium line, highlighting the intricate relationship between surface chemistry and hydrogen reactivity in Ti_3C_2 MXene, providing valuable insights into the rational design of efficient electrocatalysts for HER.

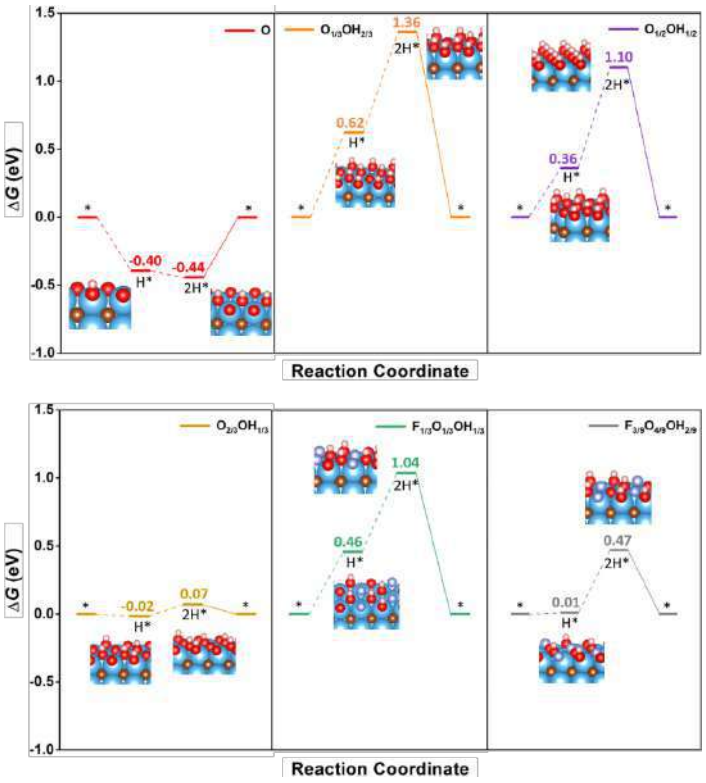

Figure 3.8. Gibbs free energy, Δ*G*, diagram of HER on selected binary and ternary terminations of Ti_3C_2 (0001) surface combining –O, –OH, and –F moieties, at standard working conditions, following the standard Volmer-Tafel mechanism sequence. Solid lines represent the chemical step of the as-generated H_2 desorption, while dashed lines represent the electrochemical PCET steps. Color coding as in Figure 3.6.[31]

3.2.3.3. Electrocatalysis Mechanism of CO_2RR

Based on the above Pourbaix diagram analysis, the CO_2RR were explored on five surface-terminated $Ti_3C_2T_x$ models, including F-free $–OH_{2/3}O_{1/3}$, $–OH_{1/2}O_{1/2}$, $–OH_{1/3}O_{2/3}$, fully OH-terminated, and F-containing $–F_{1/3}OH_{1/3}O_{1/3}$ (*cf.* Figure 3.9). The initial challenge is to determine whether CO_2 is adsorbed and activated on these terminated surfaces. According to *Le Sabatier* principle,[50] CO_2 should be moderately adsorbed—weak enough to avoid catalyst poisoning but strong enough to facilitate bond breaking.[51] Conversely, products like CH_4 should also be moderately adsorbed to facilitate their release and, more importantly, to avoid self-poisoning of the electrocatalyst by the methane product. The adsorption configurations and energies of CO_2 are shown in Figures 3.10 and 3.11, indicating that the presence of a high number of –O groups is detrimental to CO_2 activation, maintaining its linear geometry, however in fully –OH terminated surface, aligning with the activation of CO_2.[52,53] This behaviour contrasts with the adsorption energies of CH_4, which is physisorbed on any surface model, with E_{ads} ranging from -0.21 to -0.27 eV. Notably, CO_2 and CH_4 adsorption energies for the $–OH_{1/3}O_{2/3}$ and $–F_{1/3}OH_{1/3}O_{1/3}$ models are almost identical, as they involve very similar local environment for stabilising molecules. Similarly, the adsorption/desorption rates and generated kinetic phase diagrams was estimated and shown in Figure 3.12, all surface models favour the CO_2 reactant adsorption and CH_4 product release based on the working conditions of temperature (T) and gas pressure (p), meeting the prerequisite for reaction. Among all models, the fully –OH terminated model exhibits the strongest CO_2 adsorption and CH_4 desorption capabilities, as the surface concentration of the –OH moiety decreases, these differences gradually diminish. Additionally, in the presence of –F, such as in the $–F_{1/3}OH_{1/3}O_{1/3}$ model, similar kinetic phase diagrams are obtained compared to the $–OH_{2/3}O_{1/3}$ model. This implies that, to some extent, the –OH and –F groups play similar roles, with charges of approximately -1 *e* and comparable electric fields.

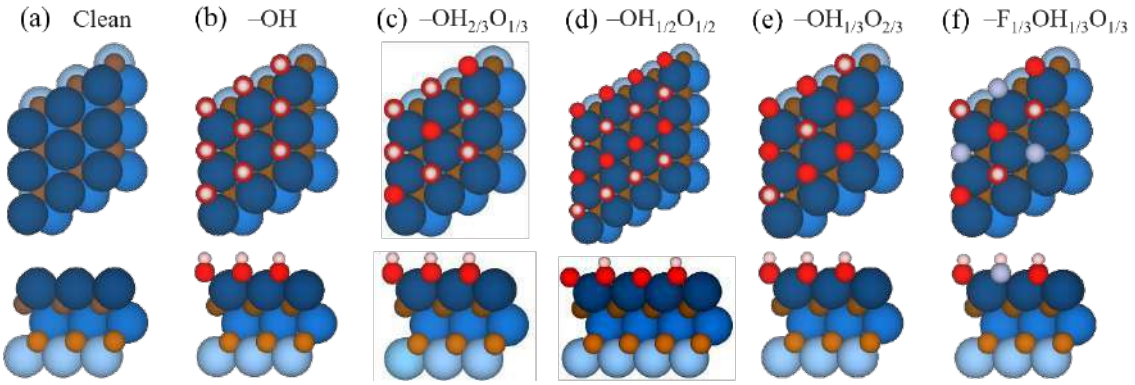

Figure 3.9. Top (upper images) and side (lower images) views of *p*(3×3) Ti_3C_2 MXene (0001) surface with (a) clean surface, (b) full –OH, (c) $–OH_{2/3}O_{1/3}$, (d) $–OH_{1/2}O_{1/2}$ —here of *p*(4×4) supercell—, (e) $–OH_{1/3}O_{2/3}$, (f) $–F_{1/3}OH_{1/3}O_{1/3}$ terminations. Termination H, O, and F atoms are represented by white, red, and light lilac spheres, respectively, while Ti and C atoms are shown as blue and brown spheres, with different levels of shading depending on their stacking position, with darker versions being closer to the shown surface.[32]

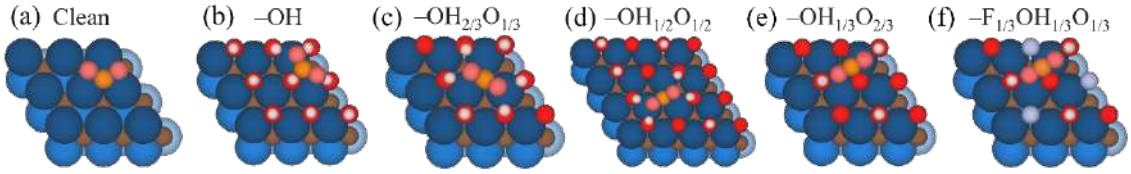

Figure 3.10. Top views of optimal CO_2 adsorption sites on Ti_3C_2 MXene model (0001) surface with (a) clean surface, (b) full –OH, (c) $–OH_{2/3}O_{1/3}$, (d) $–OH_{1/2}O_{1/2}$, (e) $–OH_{1/3}O_{2/3}$, (f) $–F_{1/3}OH_{1/3}O_{1/3}$ terminations. Colour coding as in Fig. 1, with CO_2 C and O atoms shown as orange and pink spheres, respectively.[32]

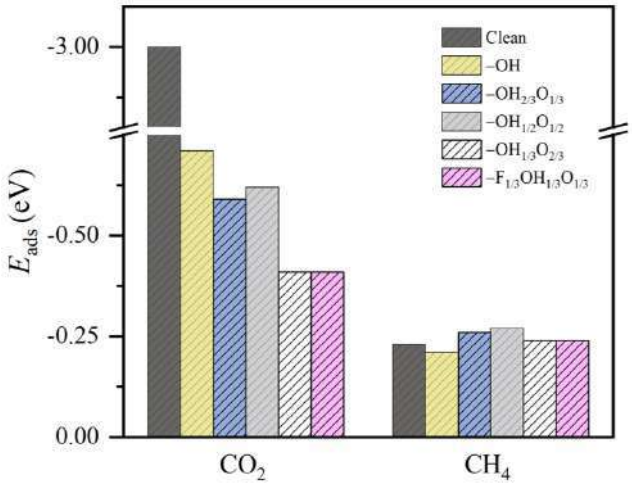

Figure 3.11. Adsorption energies of CO_2 and CH_4, E_{ads}, on the studied $Ti_3C_2T_x$ MXene (0001) surface models with (a) clean surface, (b) full –OH, (c) $–OH_{2/3}O_{1/3}$, (d) $–OH_{1/2}O_{1/2}$, (e) $–OH_{1/3}O_{2/3}$, (f) $–F_{1/3}OH_{1/3}O_{1/3}$ terminations. All values are given in eV.[32]

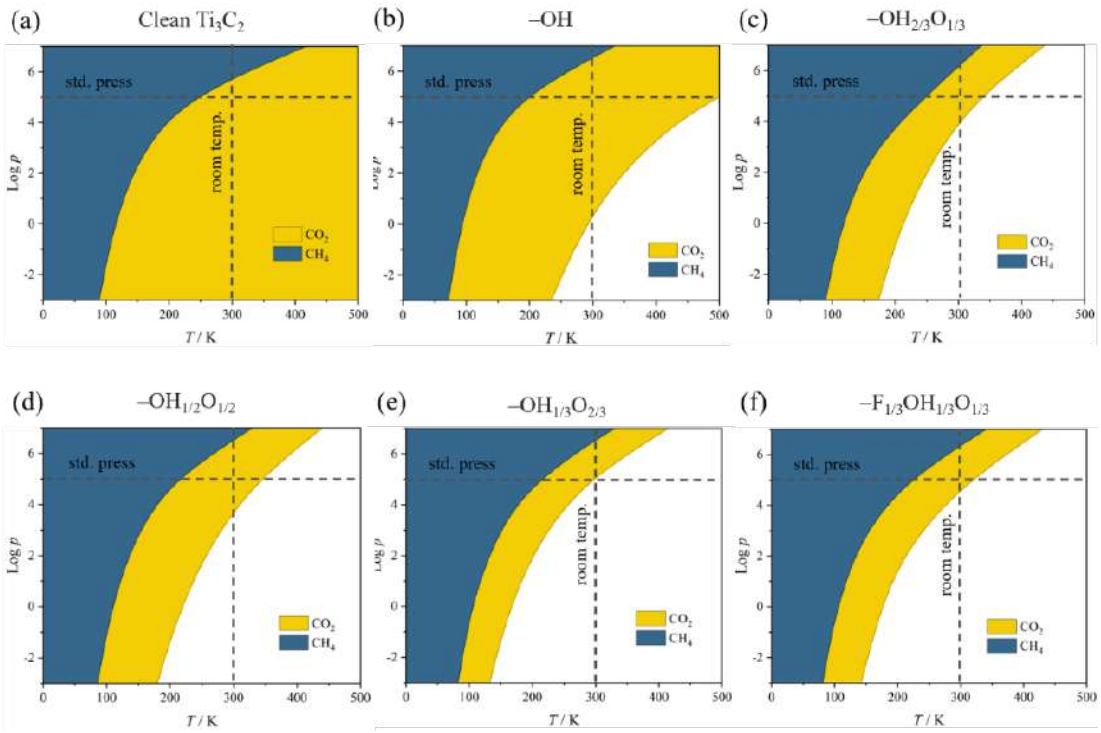

Figure 3.12. Calculated adsorption/desorption kinetic phase diagrams for CO_2 and CH_4 on (a) clean surface, (b) full –OH, (c) $–OH_{2/3}O_{1/3}$, (d) $–OH_{1/2}O_{1/2}$, (e) $–OH_{1/3}O_{2/3}$, (f) $–F_{1/3}OH_{1/3}O_{1/3}$ terminations as a function of the logarithm of gases pressures, p, in Pa. Coloured regions imply preference towards adsorption, while colourless areas represent regions where one would expect surfaces to be free of such molecules.[32]

The exploration of the CO_2RR electrocatalytic performance continues by extracting the limiting potential (U_L), as it is usually considered the main indicator of electrocatalytic performance. This is easily determined from the Gibbs free energy reaction profiles. Additionally, the energy cost of capturing H atom by surface –OH groups, defined as $E_{H_{vac}}$, is utilized to discuss the ease of H transfer from surface –OH groups.

$$E_{H_{vac}} = E_{T_x-H} + ½\cdot E_{H_2} - E_{T_x} \quad (3.19),$$

where E_{T_x-H} describes the energy of T_x-terminated MXene with H atoms but lacking one H atom, $½\cdot E_{H_2}$ represents the formation energy of a single H atom released as half of an H_2 molecule, and E_{T_x} is the energy of T_x-terminated MXene with H atoms. A more negative $E_{H_{vac}}$ indicates weaker binding of H to the MXene surface, hence easier transfer.

Starting with highly active –OH terminations, which, due to its high affinity for CO_2 adsorption, leads to stable adsorbed formate (HCO_2*) formation involving the transfer of a H atom from a –OH group with an energy of 2.22 eV, as shown in Figure 3.13. It is important to note here that the hydrogen transfer from –OH groups is spontaneous and not designed on all models. The subsequent steps involve Proton Coupled Electron Transfer (PCET) steps— often also described as Concerted Proton Electron Transfer (CPET)—,

where the hydrogenation of the C atom is favoured, attracting additional surface H atoms from vicinal –OH groups to form methylene glycol $H_2C(OH)_2$*. After $H_2C(OH)_2$* formation, the second PCET regenerates the –OH group, with ΔG at 0.73 eV, which can participate again in the third PCET to form rather favourable methanol CH_3OH* with ΔG of -1.07 eV, thermodynamically superior to CH_3OH* desorption. Finally, in the fourth PCET, a similar scenario occurs, where the reduced proton combines with a H transfer from a –OH group to form methane CH_4* and water. These four PCET steps consume four surface –OH groups, with subsequent steps involving the regeneration, with ΔG values of 0.45, 0.51, 0.63, and 0.85 eV, respectively.

The synergy between solution protons and surface –OH groups significantly influence energy, reducing the formation steps of methylene glycol, methanol, and methane. This mechanism benefits from the low $E_{H_{vac}}$ value of the –OH group, -0.56 eV, indicating the relative ease of capturing these surface H atoms, emphasizing the high involvement of H atoms of –OH groups, and suggesting that specific intermediate/molecular synthesis is not the PDS but rather surface regeneration, with limiting potential (U_L) of -0.85 eV, falling within the stability region of –OH-terminated Ti_3C_2 electrocatalyst according to Pourbaix diagrams (*cf.* Figure 3.5).

When the –OH groups are partially replaced by –O, as in the $–OH_{2/3}O_{1/3}$ model, the involvement of surface H atoms decreases, hindering the capture of surface H atoms before PCET start and the upcoming steps, as shown in Figure 3.14, consistent with the positive $E_{H_{vac}}$ value of 0.12 eV. As a result, CO_2 adsorption weakens, and the initial formation of HCO_2* occurs via first PCET with a ΔG of -0.35 eV. Then $H_2C(OH)_2$* formation is promoted through subsequent PCET steps, with two H transfers from –OH and a PDS ΔG of 0.71 eV, and followed by the regeneration of consumed –OH groups with ΔG at 0.3 eV and 0.24 eV, respectively. However, proton reduction tends to occur at –O groups rather than at the corresponding intermediates, resulting in a ΔG of 0.61 eV, followed by CH_3OH* formation with ΔG of -1.18 eV. Then CH_3OH* + H* adduct formation becomes the PDS with a U_L of -0.84 V *vs.* standard hydrogen electrode (SHE), and so, similar to fully –OH termination. However, U_L falls within the stability region only at neutral *pH* (Figure 3.5), although the activity is generally lower compared to acidic conditions. Moreover, even if here the U_L is similar to that of the full –OH model, the PDS also corresponds to a late electrochemical stage —the CH_3OH* + H* adduct formation, instead of –OH regeneration—, and the mechanisms present similarities, including

$H_2C(OH)_2$* formation and decomposition, and CH_3OH* decomposition. The main difference between both models is the involvement of both –OH and –O groups, as H donors and acceptors, respectively. The –OH may be regarded as a H reservoir, and also as a donor, thus having a dual functionality.

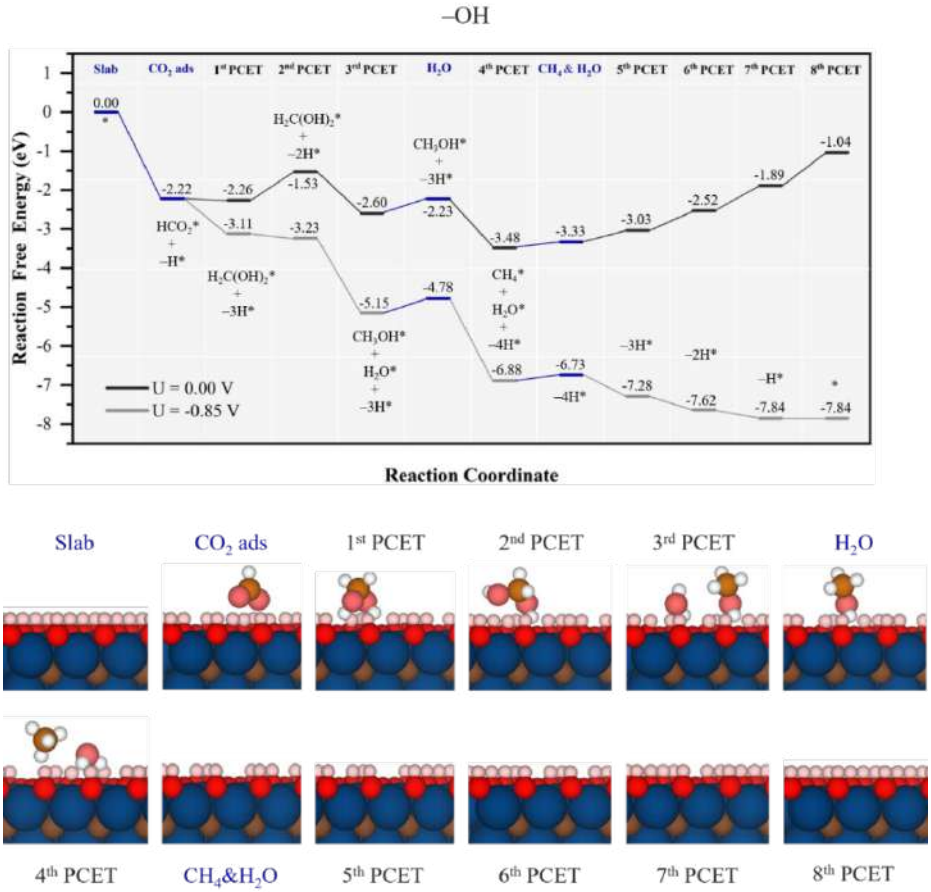

Figure 3.13. Gibbs free energy, ΔG, diagram of CO_2RR on fully –OH terminated Ti_3C_2 MXene, under standard working conditions. Blue lines represent chemical steps of as-generated H_2O or CH_4 desorption, or CO_2 adsorption, while black and grey lines represent the electrochemical PCET steps under zero and applied $U = U_L$ calculated potential of -0.85 V *vs.* SHE, respectively. The –nH* symbols refer to how many H atoms have been transferred from surface –OH groups at the reaction stage. Bottom panels show side views of atomic structures of different reaction stages. Colour code is as in Figure 3.9.[32]

Further increasing the –O/–OH ratio, for instance as in the $–OH_{1/2}O_{1/2}$ model, maintains some similarities with the $–OH_{2/3}O_{1/3}$ model, as seen in Figures 3.14 and 3.15, with the $E_{H_{vac}}$ value of 0.26 eV. The first CPET, coupled with H transfer from one –OH group, leads to the formation of formic acid HCOOH*, with ΔG of -0.3 eV, the second CPET lead to formate with ΔG = -0.11 eV, returning an H to –O group and reducing nearby –O groups, thus the formate stability is closely related to the presence of vicinal –O groups. After formate synthesis, the third CPET once again involves H transfer from two adjacent

–OH groups and a proton reduction, resulting in $H_2C(OH)_2$*, with an energy cost of 0.41 eV, followed again by another reduction of –O group with a cost of only 0.15 eV. The remaining reaction steps follow a similar way to the $–OH_{2/3}O_{1/3}$ model, where the PDS is the electrochemical recovery of –OH with a U_L of -0.7 V *vs.* SHE. Here, –OH groups act as H-donors and –O groups as reservoir in proton reduction.

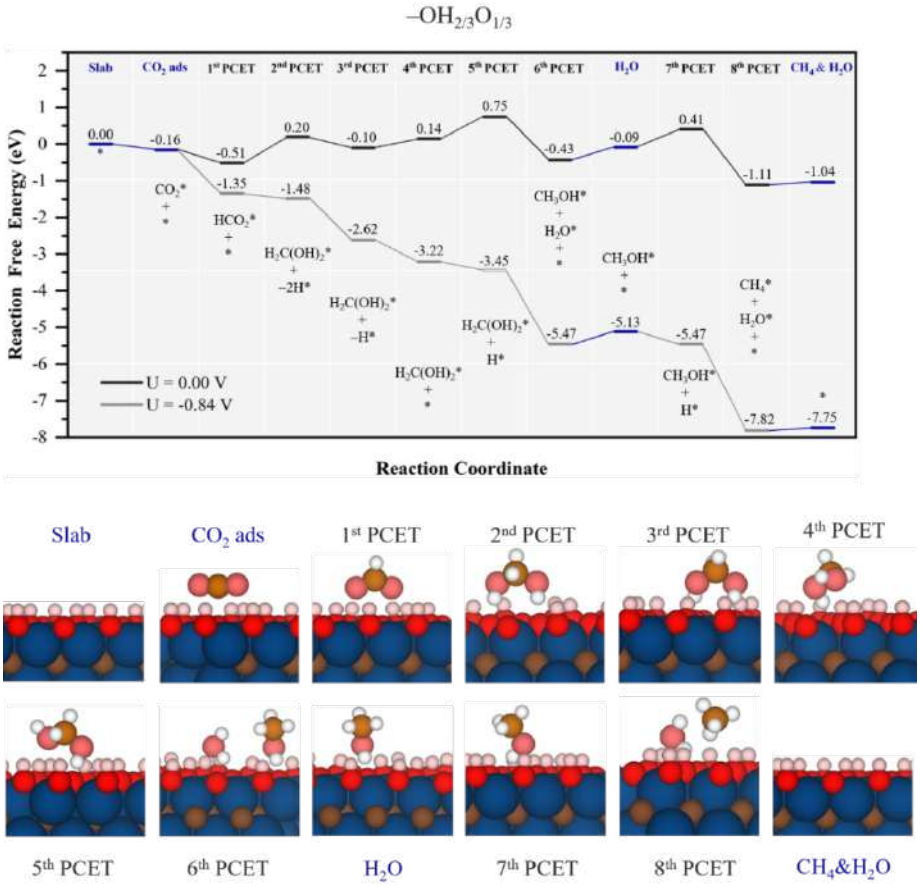

Figure 3.14. Gibbs free energy, Δ*G*, diagram of CO_2RR on $–OH_{2/3}O_{1/3}$ Ti_3C_2 MXene model, under standard working conditions and at a $U = U_L$ calculated potential of -0.84 V *vs.* SHE. The nH* symbols refer to how many H atoms have been reduced over surface –O groups at the given reaction stage. Bottom panels show side views of atomic structures of different reaction stages. Colour code is as in Figure 3.9.[32]

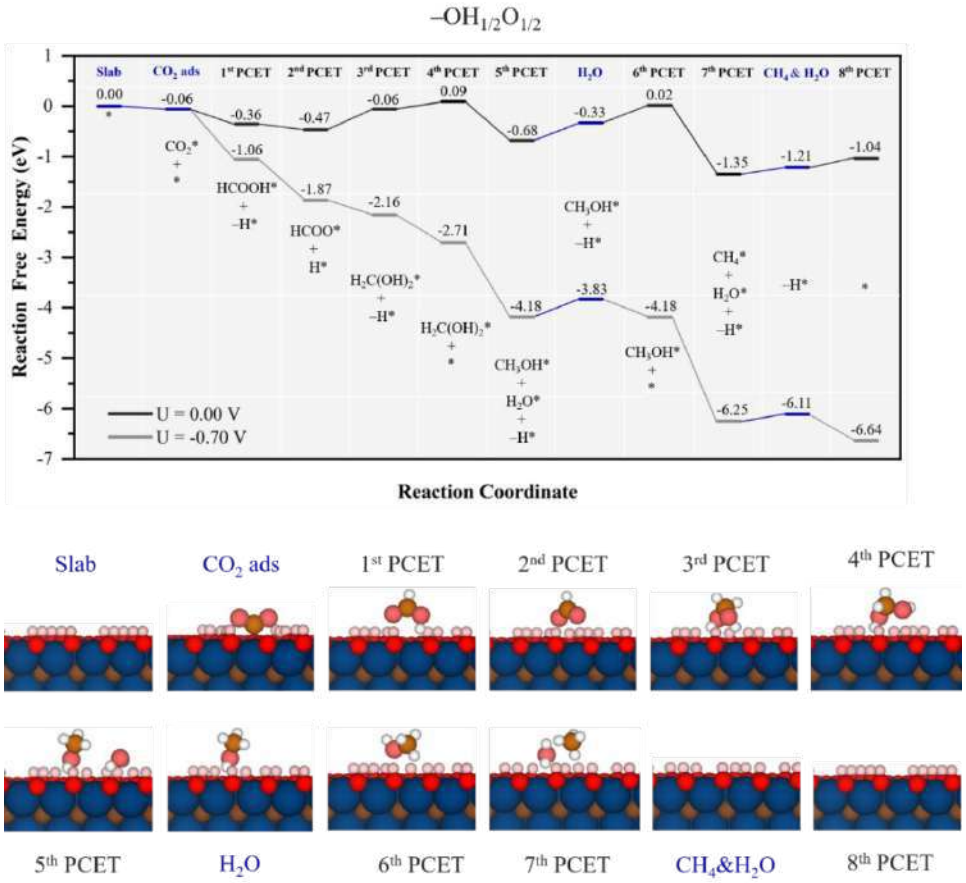

Figure 3.15. Gibbs free energy, Δ*G*, diagram of CO_2RR on –$OH_{1/2}O_{1/2}$ Ti_3C_2 MXene model, under standard working conditions and at a $U = U_L$ calculated potential of -0.70 V *vs.* SHE. Colour code and notation as in Figure 3.13 and 3.14. Bottom panels show side views of atomic structures of different reaction stages. Colour code is as in Figure 3.9.[32]

Increasing –O content further, as in the –$OH_{1/3}O_{2/3}$ model in Figure 3.16, the first CPET involves proton reduction coupled with –OH H transfer, forming HCOOH* with ΔG = 0.37 eV as PDS. The second and third PCETs involve almost isoenergetic proton reductions on surface –O groups, and no more involvement of –OH groups, which may be related to the increase of $E_{H_{vac}}$ up to 0.73 eV. The fourth PCET, forming $H_2C(OH)_2$* with only 0.03 eV. Following this, the reaction becomes exothermic, with proton reduction on an –O group and the decomposition of $H_2C(OH)_2$* to CH_3OH* with ΔG of -0.5 eV, and then the –O group and proton reduction proceed successively to form the final product CH_4*. Overall, the reaction profile is closer to ΔG = 0 eV, with smaller energy fluctuations and a U_L of -0.37 V vs. SHE for the first PCET forming HCOOH*. This model is more effective under less acidic conditions (*cf.* Figure 3.5), in addition, despite the low U_L of -0.37 V, the HER U_L is just -0.01 V, reducing $CH_{4(g)}$ selectivity.

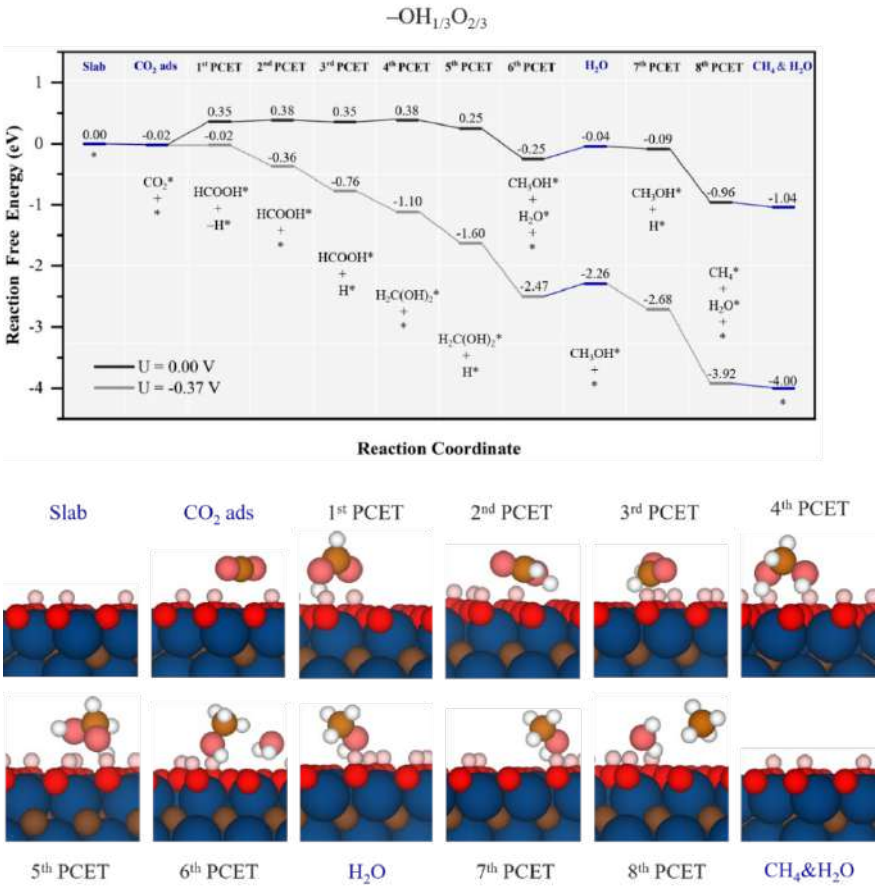

Figure 3.16. Gibbs free energy, ΔG, diagram of CO_2RR on $–OH_{1/3}O_{2/3}$ Ti_3C_2 MXene model, under standard working conditions and at a $U = U_L$ calculated potential of -037 V *vs.* SHE. Colour code and notation as in Figure 3.13 and 3.14. Bottom panels show side views of atomic structures of different reaction stages. Colour code is as in Figure 3.9.[32]

Generally, U_L decreases with decreasing –OH ratio, but it does not reach its minimum with full –O termination. Studies by Handoko *et al.*[10] on Ti_2CO_2 found a higher U_L of 0.52 V *vs.* RHE, similar to Morales *et al.*[54] for Ti_3C_2 and Ti_2C MXenes, and according to the Pourbaix diagram (*cf.* Figure 3.5), full –O termination at zero potential requires pH > 7, but alkaline conditions are not ideal for CO_2RR activity.[55]

Regarding the influence of –F surface groups on CO_2RR performance, analysis in the $–F_{1/3}OH_{1/3}O_{1/3}$ model (*cf.* Figure 3.17) shows similar performance to the $–OH_{1/2}O_{1/2}$ model, as well $E_{H_{vac}}$ value of 0.31 eV. The first PCET and nearby –OH H transfer form HCOOH* with ΔG of -0.13 eV, aligning with $–OH_{1/2}O_{1/2}$ model. The second PCET regenerates –OH and is the PDS with U_L at -0.51 V vs. SHE. Subsequently, in contrast to the $–OH_{1/2}O_{1/2}$ model, it favours forming formaldehyde CH_2O*and water rather than $H_2C(OH)_2$*, with ΔG of 0.22 eV. The fourth PCET forms CH_3OH* with a combined

PCET and –OH H transfer with Δ*G* of -0.78 eV, followed by –OH regeneration and consumption to form methane forming CH_4*. The $–F_{1/3}OH_{1/3}O_{1/3}$ model is close to its stability region (*cf.* Figure 3.5). The ease of reducing –O groups near CH_3OH* alters the free energy reaction profile of $–F_{1/3}OH_{1/3}O_{1/3}$ model, lowering the PDS cost relative to the $–OH_{1/2}O_{1/2}$ case, and maintaining the PDS at HCOOH* formation, essentially unaffected by the presence of the –F groups. However, as with the $–OH_{2/3}O_{1/3}$ model, HER remains a major competitor with U_L of -0.01 V.[31]

Overall, a high concentration of surface –OH groups and surface H atoms enhances adsorption, stabilizes intermediates, and promotes reduction steps, thereby improving the activity and selectivity for electrocatalytic CO_2 reduction to methane. On the other hand, surfaces with partial –OH and –O termination, while still active, show different reaction pathways and limiting potentials due to the decreased involvement of surface H atoms. Therefore, surface termination and the concentration of surface H atoms play a crucial role in the MXene electrocatalytic CO_2 reduction to CH_4.

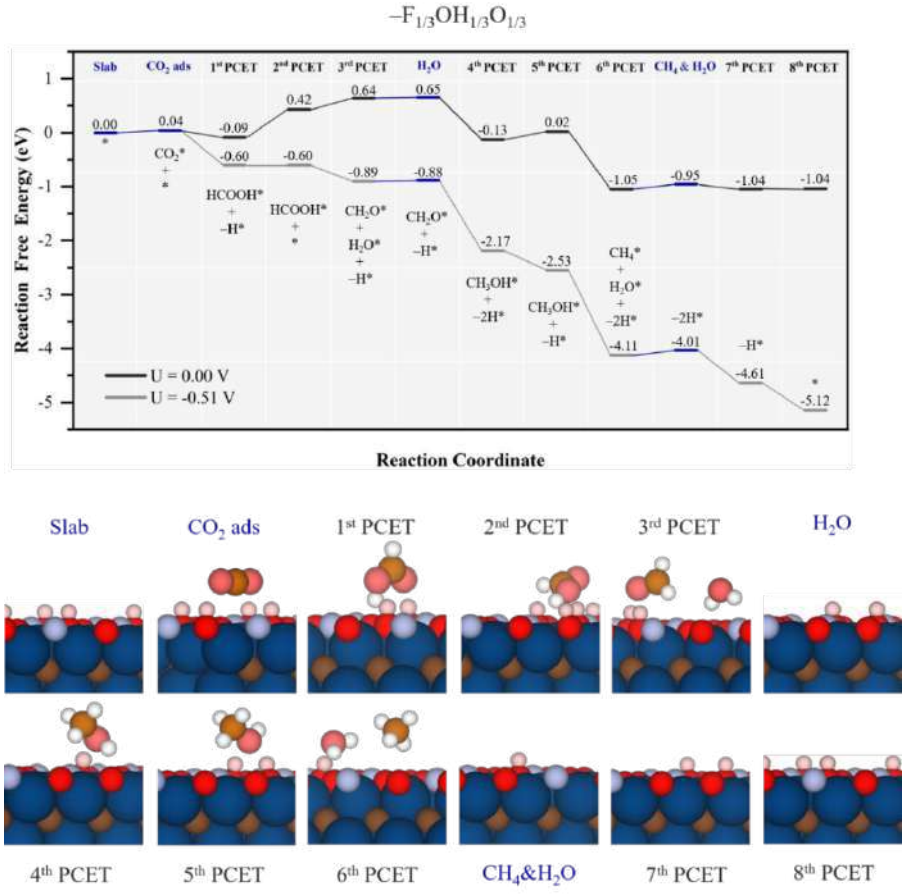

Figure 3.17. Gibbs free energy, Δ*G*, diagram of CO_2RR on $–F_{1/3}OH_{1/3}O_{1/3}$ Ti_3C_2 MXene model, under standard working conditions and at a $U = U_L$ calculated potential of -0.51 V *vs.* SHE. Notation is as in Figures 3.13 and 3.14. Bottom panels show side views of atomic structures of different reaction stages. Colour code is as in Figure 3.9.[32]

3.2.3.4 Catalytic Performance of HER/CO_2RR

The standard for a good HER activity is typically defined by $|\Delta G_H| < 0.2$ eV.[19,56] The theoretical overpotential η can be estimated based on previous reaction profiles, which are included in Table 3.1 and the typical volcano plot in Figure 3.18. It is evident that Ti_3C_2 MXene with mixed termination groups exhibits better HER activity compared to fully terminated ones, especially in cases like O-enriched $–O_{2/3}OH_{1/3}$ and the F-terminated $–F_{1/3}O_{1/3}OH_{1/3}$. The –F groups on the surface do not hinder the process, in fact, low –F coverage like $–F_{1/3}$ can further enhance the HER process due to subtle lateral interactions that help preventing surface passivation caused by excessive reactivity towards H*. Increasing the concentration of –O groups is beneficial for HER up to a certain extent,[49] like in the case of $–O_{2/3}OH_{1/3}$, as fully O-terminated surfaces exhibit excessive reactivity towards H*. Additionally, compared to other materials reported in literatures, Ti_3C_2 MXene with appropriate surface terminations shows promising HER catalytic performance, potentially outperforming materials like Pt,[57] MoS_2,[58] WS_2,[59] N-doped graphitic carbon nitride (C_3N_4@NG),[60] and C_3N.[61] The optimal scenarios observed, such as models of $–O_{2/3}OH_{1/3}$, $–F_{1/3}O_{1/3}OH_{1/3}$, and $–F_{3/9}O_{4/9}OH_{2/9}$, indicate the potential of Ti_3C_2 MXene as a prospective HER material, however, considering the presence of other stoichiometries and arrangements not accounted for in this study, these findings should be viewed as indicative, not definitive.

Table 3.1. Summary of the potential determining steps, based on the calculated ΔG_H as a descriptor, on the explored Ti_3C_2 models, either pristine, or covered according to the specified terminations. The required overpotential, η, is specified, as well as the preferred VH or VT mechanism, specifying the subtype of path, either O-TER, OH-TER, or TER-TER. In the case of pristine Ti_3C_2, note that the strong H-affinity prevents any H_2 formation, regardless of η.[32]

Model	PCET	PDS	$E_{H_{vac}}$	U_L
–OH	8th	–H* → *	-0.56	-0.85
$–OH_{2/3}O_{1/3}$	7th	$CH_3OH^* + * \rightarrow CH_3OH^* + H^*$	0.12	-0.84
$–OH_{1/2}O_{1/2}$	6th	$CH_3OH^* + –H^* \rightarrow CH_3OH^* + *$	0.26	-0.70
$–OH_{1/3}O_{2/3}$	1st	$CO_2^* \rightarrow HCOOH^* + –H^*$	0.73	-0.37
$–F_{1/3}OH_{1/3}O_{1/3}$	2nd	$HCOOH^* + –H^* \rightarrow HCOOH^* + *$	0.31	-0.51

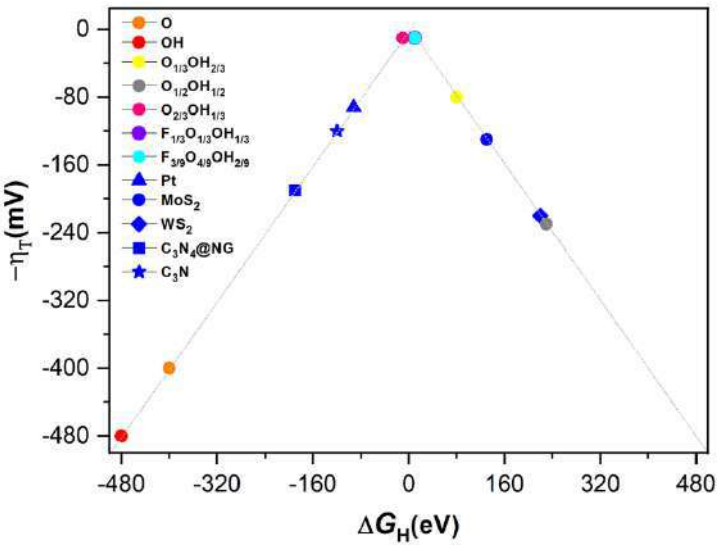

Figure 3.18. Volcano plot of -η *vs.* ΔG_H on the different terminated Ti_3C_2 surface models, including fully O- and OH-terminated cases, as well as binary situations represented by the $O_{1/3}OH_{2/3}$, $O_{1/2}OH_{1/2}$, and $O_{2/3}OH_{1/3}$ models, and ternary ones as in the $F_{1/3}O_{1/3}OH_{1/3}$ and $F_{3/9}O_{4/9}OH_{2/9}$ models. In addition, references values for Pt, MoS_2, WS_2, C_3N_4@NG, and C_3N are included for comparison.[32]

Now, shifting to the performance of the studied models for CO_2RR, Table 3.2 summarizes the results for five studied models, where the ideal catalyst should have as small U_L as possible for higher activity and faster CO_2RR kinetics. Additionally, it is visible in the captured trends in Figure 3.19 that a linear relationship exists between $E_{H_{vac}}$ and the –OH/–O ratio, with similar values for the $–OH_{1/2}O_{1/2}$ and $–F_{1/3}OH_{1/3}O_{1/3}$ models. As the presence of surface –O groups increase, $E_{H_{vac}}$ increases while U_L values decrease. This can be distinguished into two regions: *i*) one with –OH as the primary surface termination having a quiet low U_L value, and another *ii*) where protons are reduced on –O groups, and later transferring these H atoms, resulting in smaller U_L values. The higher involvement of –O surface groups typically promote the latest PCET steps and moves the PDS to earlier stages of the reaction, and the presence of –F groups is not inherently harmful and can lead to deviations in trends, lowering U_L costs.[62,63] Moreover, the reaction profile contests the traditional mechanism of solely H^+ reduction upon reaction molecules, revealing *i*) a Volmer step sequence on near –O groups, followed by H transfer from these formed –OH to the moiety, *ii*) H transfer from already existing –OH groups, followed by proton reduction on the generated –O groups, and *iii*) simultaneous hydrogenation of a moiety, coupling the electrochemical step of H^+ reduction with H chemical transfers from surface –OH groups. In fact, the simultaneous presence of –OH and –O groups offer flexibility in multiple reaction pathways, ultimately reducing reaction costs, a feature missing in previous work with only –O groups.

Table 3.2. Summary of the CPET PDS as well as specific electrochemical reaction step, on the explored surface-terminated Ti_3C_2 models, under CO_2RR working conditions. The required U_L —in V— and surface $E_{H_{vac}}$ —in eV— values are specified.[32]

Model	PCET	PDS	$E_{H_{vac}}$	U_L
–OH	8th	–H* → *	-0.56	-0.85
–$OH_{2/3}O_{1/3}$	7th	CH_3OH* + * → CH_3OH* + H*	0.12	-0.84
–$OH_{1/2}O_{1/2}$	6th	CH_3OH* + –H* → CH_3OH* + *	0.26	-0.70
–$OH_{1/3}O_{2/3}$	1st	CO_2* → HCOOH* + –H*	0.73	-0.37
–$F_{1/3}OH_{1/3}O_{1/3}$	2nd	HCOOH* + –H* → HCOOH* + *	0.31	-0.51

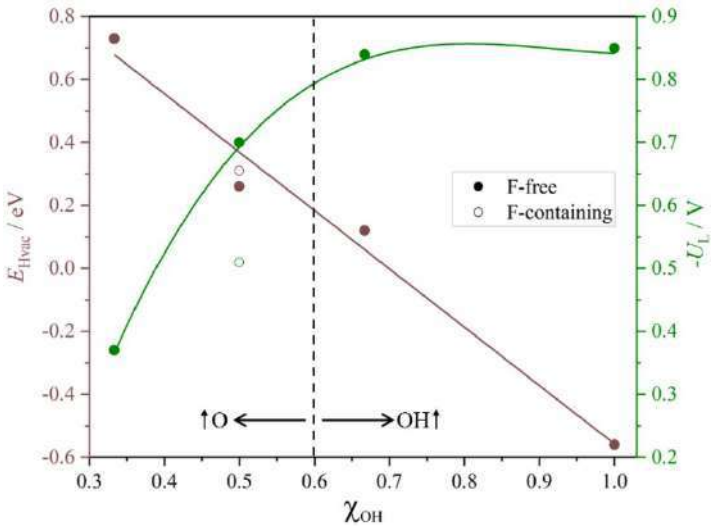

Figure 3.19. Plots of H-vacancy energies, $E_{H_{vac}}$, given in eV, and minus the limiting potential, -U_L, given in V, as a function of –OH group partition coefficients (χ_{OH}) with respect –O groups.[32]

However, considering the surface stability of electrocatalysts predicted by the Pourbaix diagram in Figure 3.5, despite some models exhibit low U_L values, such as -0.37 V for –$OH_{1/3}O_{2/3}$ or -0.51 V for –$F_{1/3}OH_{1/3}O_{1/3}$, their stability ranges imply that the surface will eventually transition to a fully –OH model at low pH values or react slowly under high pH conditions. Additionally, low –F concentration like –$F_{1/3}OH_{1/3}O_{1/3}$ are not inherently detrimental, as these groups can help move the PDS to earlier stages, thus reducing U_L and reaction costs. These open the door to modulate the electrocatalyst performance by controlling surface –F content, an aspect overlooked by F-free synthesis methods.[64]

Another key point implies comparing the CO_2RR activity reported with other MXenes reported in the literatures,[10,11,22,36,65-68] as shown in Figure 3.20, clearly showing that despite deviations from different calculation methods, U_L values of MXene-based

electrocatalysts are generally lower than those of Cu based electrodes, typically around -0.93 V,[11,69] highlighting the potential of these materials in CO_2 conversion. Lastly, it is noteworthy that the competition between CO_2RR and HER, as shown in Figure 3.21, indicates a general trend, that the smaller the U_L, the lower the selectivity for CO_2RR.[70] In fact, an increase in the –OH/–O ratio appears to enhance the selectivity of CO_2RR, reaching a maximum with the fully –OH model. While these models are selective for HER, strategies such as limiting H^+ transfer rates,[71-73] using non-aqueous proton donors,[74,75] restricting electron transfer rates,[76,77] or modulating the magnetic moments of active sites can suppress HER for the $–OH_{1/3}O_{2/3}$ and $–F_{1/3}OH_{1/3}O_{1/3}$ models.[78]

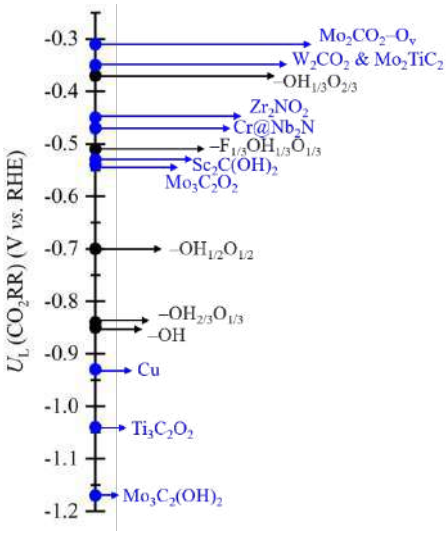

Figure 3.20. Comparison of the methane U_L from the presently studied terminated models on $Ti_3C_2T_x$ (black dots) alongside with other values reported in the literature for MXene-based systems, and Cu as a reference (blue dots). All values are given in V.[32]

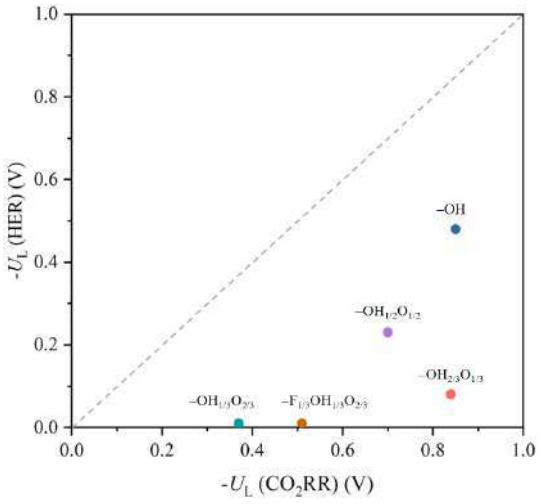

Figure 3.21. Comparison of $-U_L$ for CO_2RR *vs.* $-U_L$ for HER on the explored terminated $Ti_3C_2T_x$ models. Values for HER are taken from literature.[32]

3.2.3.5. Future Developments

In addition, a review of the progress of MXene as electrocatalysts for HER and CO_2RR was conducted. MXenes have gained attention for their potential to substitute traditional Pt-based catalysts in HER,[79,80] however, assessing and designing MXenes have been simplified through experimental or theoretical descriptors.[81,82] Therefore, we analysed the latest methods for establishing theoretical models of HER in MXenes, aiming to evaluate the intrinsic activity of this electrocatalytic reaction. Firstly, we propose further research to explore the role of mixed surface terminations under realistic conditions, as most studies have focused on specific terminations.[31,32] Additionally, advanced methods such as explicitly incorporating solvation effects[83] and using grand canonical DFT[84] can reshape the understanding of electron transfer reactions and catalytic activity of MXene materials. Furthermore, the summaries of various thermodynamic, kinetic, and electronic property-related descriptors, as well as linear scaling relationships, were discussed.[19,30,46,85-87] Finally, it was indicated that machine learning[88] is widely used to accelerate the discovery and design of catalytic materials, but its development is still ongoing.

MXenes have attracted attention due to their higher chemical activity and selectivity, overcoming limitations of traditional metal electrocatalysts, such as copper, and potentially breaking the scaling relationship between traditional reaction intermediates and expected products. We reviewed three generations of progress in computational descriptions of CO_2RR on MXenes, indicating the importance of improvements from the initial model of CO_2 activation to different surface termination models for small U_L and tunable selectivity. In recent years, possible methods for modulating catalytic activity and selectivity were discussed, including doping, defects, supported single metal atoms, solvent effects, and electric field effects. However, challenges such as the realism of the model, accuracy of the analysis, and feasibility of synthesis still exist. A full description of the work done can be found in Refs. 31–34.

3.2.4. Conclusions

These findings, coupled with additional data and analyses presented in the research articles below, lead to the following conclusions:

- Pourbaix diagrams were constructed to identify the stability of approximately 450 surface terminations of MXene with variations in composition and species ratios, and further considering more realistic termination models under specified reduction conditions.

- Fully –O, –OH, –H, and –F terminations are only optimal at extreme potentials *vs.* SHE. Binary and ternary models mixing –O, –OH, and –F moieties are remarkable under several conditions.
- Studies showed that the Volmer-Heyrovsky mechanism is most effective under various termination conditions, whereas MXene models with mixed terminations, as $–O_{2/3}OH_{1/3}$, $–F_{1/3}O_{1/3}OH_{1/3}$, and $–F_{3/9}O_{4/9}OH_{2/9}$, near the HER equilibrium line, exhibit minimal overpotential of 0.01 V, making them superior to fully terminated MXenes in HER performance.
- Higher concentrations of –O moieties on the Ti_3C_2 surface result in stronger ability for H^+ reduction in HER, with moderate bond strengths observed when –O coverage is at 2/3.
- The presence of –F groups is not detrimental, and actually contributed to favouring H^+ reduction, particularly when combined with higher concentrations of –O moieties.
- In the CO_2RR, the involvement of –OH groups on the surface of MXene as hydrogen donors, along with simultaneous proton reduction and –OH H transfer, can reduce limiting potential, U_L, and energy costs, maximizing the activity for CO_2RR.
- A linear relationship between $E_{H_{vac}}$ and –OH/–O ratio is observed, with $E_{H_{vac}}$ increasing as the presence of surface –O group increases, leading to a decrease in U_L value.
- In the $–F_{1/3}OH_{1/3}O_{1/3}$ model, the presence of –F is harmless and can advance the limiting step while reducing U_L. Overall, the results indicate that MXenes are competitive in the CO_2RR compared to copper electrocatalysts.

3.3. Unveiling the Synergy between Surface Terminations and Boron Configuration in Boron-Based Ti_3C_2 MXenes Electrocatalysts for Nitrogen Reduction Reaction

3.3.1. Introduction

Gaseous nitrogen (N_2) possesses strong triple bonds and is one of the most abundant nitrogen-containing compounds on Earth. It is extensively utilized in the chemical industry for the traditional Haber-Bosch process to synthesize ammonia (NH_3).[89,90] However, this process requires not only the presence of a catalyst but also high temperature (above 350°C) and high pressure (above 150 bar), leading to significant energy consumption and substantial CO_2 emissions.[91,92] Therefore, in order to pursue long-term sustainability, there is active exploration of alternative ammonia synthesis technologies that operate under milder conditions.[93,94]

Inspired by natural biological nitrogen fixation,[95] there is a strong interest in ammonia synthesis methods that operate under moderate conditions, that is room temperature and atmospheric pressure,[96,97] particularly, electrocatalytic Nitrogen Reduction Reaction (NRR).[98,99] Developing efficient and highly selective NRR electrocatalysts is of significant economic importance and urgency, such as utilizing MXenes as NRR catalysts, specifically $M_2C(0001)$ surfaces,[100] can easily adsorb and dissociate N_2, moreover, M_3C_2 MXenes can capture, activate, and electrochemically convert N_2 to NH_3 with the overpotentials lower 0.90 V.[101]

However, these predictions are based on models involving clean, bare surfaces,[31,102] realistic scenarios require consideration of mixed terminations,[34,103,104,] and there is experimental evidence[105] indicating that surface engineering of MXenes, especially the type and concentration of surface terminations, is crucial for facilitating electron transfer, surface adsorption, and N_2 activation. For instance, research[106] has shown that an increase in –OH groups on the Ti_3C_2 MXene surface enhances NH_3 production, and $Ti_3C_2T_x$ MXene functionalized with medium- concentration –F terminations can enhance N_2 adsorption and activation.[107]

The focus of this study remains on the earliest synthesized Ti_3C_2.[26] The case of boron atom is particularly attractive,[108,109] which is significant potential in N_2 fixation, including catalysts based on g-C_3N_4, graphene, and two-dimensional boron sheets, and can also occupy the oxygen vacancies on the MXene surface to form B-doped MXene materials.[110,111] However, previous studies[112-114] have used oversimplified models, con-

sidering B only substituting –O surface groups, without thoroughly investigating, therefore more detailed research proximity to terminations, configuration and quantity is necessary to explore. Following earlier research on single boron MXene NRR catalysts, this study employs ten unique models based on $Ti_3C_2T_x$, as shown in Figure 3.22, to gain detailed insights into the NRR process under realistic working conditions.

This work produced one article under review in *ACS Catalysis* entitled "*Unveiling the Synergy between Surface Terminations and Boron Configuration in Boron-Based Ti_3C_2 MXenes Electrocatalysts for Nitrogen Reduction Reaction*",[115] with the supporting information, included in Appendix C, provided at the end of this thesis. Subsequent pages contain a summary of this article. My contributions to this research article comprise: (a) Carrying out the DFT calculations and data treatment, (b) analysis of the calculations results, (c) surveying and summarizing the relevant publications, and (d) writing the initial manuscript of paper and making the corresponding figures. A full description of the work done can be found in Ref. 115.

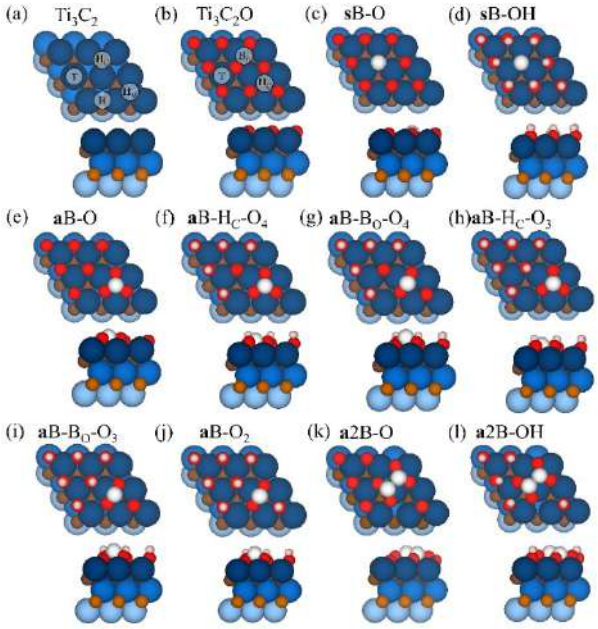

Figure 3.22. Top (upper images) and side (lower images) views of the ten models derived from the employed *p*(3×3) MXene supercells, including; (a) pristine Ti_3C_2 (0001) with the top (T), bridge (B), hollow carbon (H_C), and hollow metal (H_M) four high-symmetry sites tagged; (b) Ti_3C_2O (0001) with T, H_C, and O-bridge (B_O) three high-symmetry sites tagged; (c) **s**B@$Ti_3C_2O_{8/9}$ (**s**B-O); (d) **s**B@$Ti_3C_2OH_{8/9}$ (**s**B-OH); (e) **a**B@Ti_3C_2O with B on H_C (**a**B-O); (f) **a**B@$Ti_3C_2O_{4/9}OH_{5/9}$ with B on H_C (**a**B-H_C-O_4); (g) **a**B@$Ti_3C_2O_{4/9}OH_{5/9}$ with B on B_O (**a**B-B_O-O_4); (h) **a**B@$Ti_3C_2O_{1/3}OH_{2/3}$ with B on H_C (**a**B-H_C-O_3); (i) **a**B@$Ti_3C_2O_{1/3}OH_{2/3}$ with B on B_O (**a**B-B_O-O_3); (j) **a**B@$Ti_3C_2O_{2/9}OH_{7/9}$ (**a**B-O_2); (k) **a**2B@Ti_3C_2O (**a**2B-O), and (l) **a**2B@$Ti_3C_2O_{4/9}OH_{5/9}$ (**a**2B-OH). H and O atoms in the termination groups are represented by light pink and red spheres, respectively, while the B atoms are represented by white spheres. Ti and C atoms

are shown as blue and brown spheres, with different levels of shading depending on their stacking position, with darker versions being closer to the shown surface.[115]

3.3.2. The NRR Mechanisms

In this study, a reaction network for NRR on MXene was investigated, beyond *distal* and *alternating* mechanisms, thus including in *end-on* adsorption modes, or *enzymatic* mechanism, in *side-on* adsorption modes.[116,117] Moreover, physical adsorption is also considered as a potential step in this study, as shown in Figure 3.23. The *distal* mechanism involves Concerted Proton-Electron Transfer (CPET)[36] attacking the farthest N atom from the catalyst surface, proceeding through subsequent CPET steps to synthesize and release the first $NH_{3(g)}$, leaving a N* adatom on the catalyst surface, which is then fully reduced to obtain the second $NH_{3(g)}$. In contrast, in the *alternating* mechanism, CPET alternates in between the two N atoms of the *end-on* situation. Lastly, the *enzymatic* mechanism mimics the biological mechanism of fixing N_2, starting from an activated *side-on* adsorption mode, favouring an alternating pattern of CPET between two N atoms. Before delving into the reaction free energy, it is worth noting that in the **a**2B model (see Figure 3.24) with dual active sites, NH_2NH_2* does not appear in the *enzymatic* mechanism due to the N–N bond cleavage during the hydrogenation of NH_2NH_2* to two NH_2*. Additionally, a hybrid scenario may occur where $NHNH_2$* is formed during the reduction of NNH_2*, instead of obtaining $NH_{3(g)}$ and N* atoms through the *distal* pathway, or in *enzymatic* pathway, $NHNH_2$* is hydrogenated to NH* and $NH_{3(g)}$ instead of forming NH_2NH_2*. Therefore, the following will also discuss these *mixed* pathways that connect the *distal*, *alternating*, or *alternating* pathways.

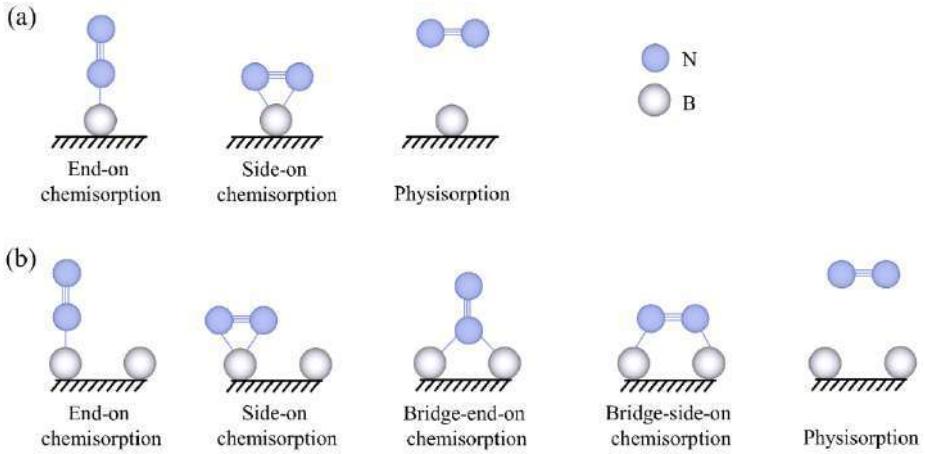

Figure 3.23. Various adsorption configurations for N_2 adsorption, including chemisorption and physisorption for (a) single boron and (b) B_2 dimer models shown in Figure 3.22.[115]

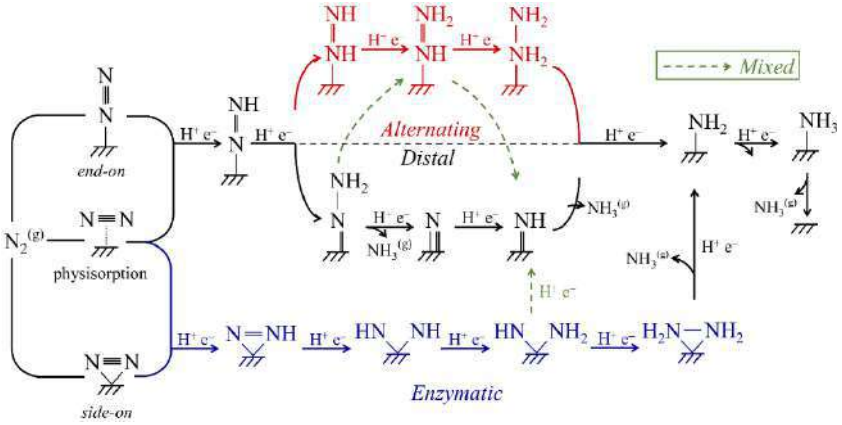

Figure 3.24. Schematic diagram of possible reaction pathways for NRR on B-based Ti_3C_2 MXene. The black, grey, and blue solid arrows represent the *distal*, *alternating*, and *enzymatic* pathways, respectively. The black dashed arrows represent the *mixed* pathway.[115]

3.3.3. Results

3.3.3.1. Stability of B-based MXenes

In the case of Ti_3C_2O, sampling was conducted on four potential high symmetry adsorption sites[118,119] (see Figure 3.22), with the H_C site being the most favourable on **a**B-O_2, **a**B-O_3, and **a**B-O_4 models, followed by the B_O site. In the presence of B_2 dimers (see Figures 3.22k and 3.22l), a semi-bridge configuration, resembling ethene, was discovered. The stability of each model, estimated from adsorption energy (E_{ads}), difference between adsorption energy and cohesive energy (E_{diff}), and formation energies per atom values (E_f) of B, is listed in Table S1 of Appendix C, showing negative formation energies for all models, ranging from -0.37 eV/atom for **s**B-OH to -0.54 eV/atom for **a**B-O, indicating stability relative to their elemental composition. Furthermore, the E_{ads} of B can vary significantly, from -2.53 eV for **s**B-O to -7.66 eV for **a**B-O, where more negative E_f values correspond to more negative E_{ads} values. The structural stability appears to be related to the arrangement of boron and variations in termination groups. For the B substitution (**s**B) model, stability increases gradually with a decrease in the number of –O groups and an increase in –OH groups, while for the B adsorption (**a**B) situation, stability decreases gradually. Additionally, the B adsorption site and atomic coordination have some influence on stability, with B being generally more stable in the H_C site than in the B_O site. Increasing the amount of boron (B), as in the dimer cases discussed, reduces the system stability. Importantly, a few cases show E_{ads} values larger than B-bulk cohesive energy,

with negative E_{diff} values observed, particularly for **a**B-O, **a**B-H_C-O_4, and **a**2B-O, while the E_{diff} value for **a**B-H_C-O_3 is close to zero. It is evident that B adsorption favours complete or large coverage by –O atoms. Additionally, the Density of States (DOS) and Projected DOS (PDOS) from Figure S2 in Appendix C indicate metallic behaviour in all systems, where Ti *d* orbitals, C, B, T_x = O, OH *p* orbitals, and H *s* orbitals are active near the Fermi level. However, **s**B and **a**B exhibit significant differences, with the former having limited interaction with atomic orbitals of other elements, while the latter shows strong covalent mixing with –O group *p* orbitals in the -6 to -10 eV region.

3.3.3.2. N_2 Adsorption

N_2 adsorption is a necessary condition for NRR and can be categorized into physisorbed and chemisorbed scenarios. In the first case, interactions between doped B and N_2 are negligible with little charge transfer, while chemisorption can involve *end-on* and *side-on* structures,[120] as well *bridge* configurations,[121] as shown in Figure 3.23, along with adsorption energy, Bader charge, and molecular bond lengths of N_2, provided in Table S2 of Appendix C. The physisorbed (-*p* states) are easily identified by small E_{ads} values ranging from -0.09 eV (**a**B-O-*p*) to -0.30 eV (**a**2B-OH-*p*) with concomitant large *d*(BN) distances ranging from 3.26 Å (**a**B-O-*p*) to 3.51 Å (**a**2B-OH-*p*), while the *d*(NN) distance remains essentially constant at 1.12 Å, consistent with gas-phase molecular values calculated in vacuum. For chemisorbed states, interactions between N_2 and active B centres may involve σ-donation from N_2 or B back-donation to the empty 2π* molecular orbital of N_2.[122,123] Compared to **a**B, **s**B exhibits significantly stronger N_2 adsorption capabilities, with adsorption energies ranging from -1.43 eV (**s**B-O-*s*) to -2.79 eV (**s**B-OH-*e*), consistent with reported inherent N_2 affinity of pristine MXenes.[124] However, **a**B cases show weaker chemisorption, with adsorption energy values ranging from -0.37 eV (**a**B-B_O-O_4-*s*) to -1.19 eV (**a**B-O_2-*s*).

Additionally, the structural and bonding analysis indicates that –OH environments and *side-on* adsorption modes enhance N_2 interactions on the **s**B model, while for **a**B, when B is adsorbed at the H_C site, its three sp^3 hybridized orbitals and three electrons are utilized for –O coordination, leaving an empty sp^3 orbital as a potential acceptor, making electron feedback less likely, thus explaining why these sites lead to physisorption. For **a**2B dimers, *bridge-side-on* adsorption maximizes interaction with N_2, where each B has a free electron bonding with each N atom in the N_2 molecule, ultimately weakening the molecular bond. Therefore, the donation and back-donation mechanism, B electron

charges, and coordination modes freeing sp^3 electrons play a crucial role in N_2 adsorption and activation.

Lastly, we compared the adsorption and desorption rates of all models and adsorption modes by kinetic phase diagrams acquired in the past,[125,126] denoted as r_{ads} and r_{des}, respectively, as Figure 3.25. It can be observed that under reaction conditions at T=300 K and 1 bar $N_{2(g)}$ partial pressure, many models and sites exhibit higher r_{ads} than r_{des}, especially **a**2B-O-*bs*, **a**B-B$_O$-O$_4$-*e*, **a**B-B$_O$-O$_3$-*e*, **a**B-O$_2$-*e*, **a**B-O$_2$-*s*, **s**B-O-*s*, **s**B-OH-*s*, **s**B-O-*e*, and **s**B-OH-*e*; thus, in all cases, chemically bonded N_2 is activated with E_{ads} stronger than -0.67 eV, consistent with values in Table S2 of Appendix C, emphasizing the feasibility of the **s**B mode over the **a**B mode. By correlating N_2 adsorption capabilities with doping model stability, **a**2B-O is the only model with a prior kinetic stability and the ability to adsorb and activate $N_{2(g)}$. However, other related models will also be investigated in the NRR Gibbs energy profiles, as these systems may be kinetically metastable and can capture trends and mechanism changes in the model composition.

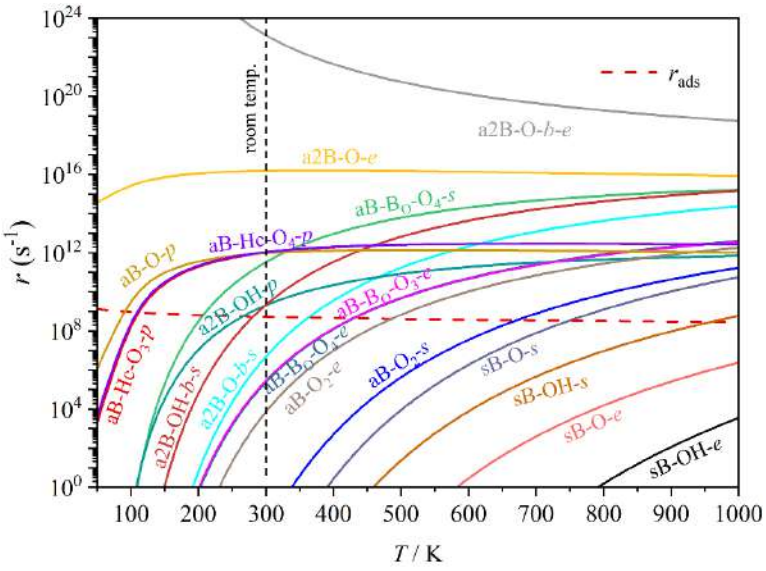

Figure 3.25. Calculated adsorption, r_{ads}, and desorption, r_{des}, N_2 rates on studied models shown in Fig. S5 of the SI, as a function of temperature, T, and the gas partial pressure, p, here shown for 1 bar. Black dashes line represents r_{ads} for *end-on* (*e*) and *side-on* (*s*), as well as *bridge-end-on* (*b*-*e*) and *bridge-side-on* (*b*-*s*) chemisorption, and red dashed line represents r_{ads} for physisorption.[115]

3.3.3.3. NRR Reaction Free Energy Profiles

The above possible mechanisms for NRR were analyzed to determine the most favourable pathway, while investigating the influence of B-doped sites (**a**B *vs.* **s**B), individual B atoms or dimers (**a**B *vs.* **a**2B), and the impact of nearby functional groups. The analysis

begins with the substitution of B scenario (**s**B), with –O or –OH surface groups, as depicted in Figure 3.26. Notably, these models exhibit an unusually strong N_2 adsorption capability in Figure 3.25. In the **s**B-O model, except for the $NHNH_2$* and final NH_3* generation steps, all other CPET steps are exothermic, ΔG_{max} corresponding to the final last one, valued at 1.40 eV and defining the PDS, indicating the thermodynamically most favourable path that follows a *mixed* route, mainly following *distal* mechanism, except for the $NHNH_2$* formation which correspond to *alternating* one. In the **s**B-OH model, NH_2*→NH_3* is also the PDS, with ΔG_{max} of 1.47 eV, following the *distal* mechanism except for the hydrogenation of the $NHNH_2$* species, which proceeds directly to NH* and NH_3* via a *mixed* pathway. Unlike the **s**B-O model, all steps in the **s**B-OH model, except for the $NHNH_2$* hydrogenation step, are either endothermic or balanced. It is important to note that, as discussed for the CO_2RR on the $Ti_3C_2T_x$ model in above Chapter 3.2, surface –OH groups can transfer H atoms, a feature also found in the *alternating* pathway during N_2H* reduction, where an adjacent –OH group transfers its H, as shown in Figure 3.26, establishing a more stable intermediate $NHNH_2$*.

Under adsorbed B (**a**B) scenarios, B can be located at bridge (B_O) or hollow centre (H_C) sites, leading to potential variations in reaction pathways. In **a**B-O, the B atom is located at the H_C site, as shown in Figure 3.27, the reaction sequence following N_2 physisorption leads to N_2H*, with a ΔG of 1.37 eV for the PDS, where B positioned at H_C or B_O almost equally. The reaction primarily proceeds via an *alternating* mechanism involving NHNH*, alternating between H_C and B_O. This is due to the addition of H leads to the cleavage of the N-N bond, which results in the formation of lone pairs of electrons, that can be used to form new covalent bonds with B, while also breaking a B-O bond and adopting a B_O configuration. By adding new H bonds, the additional B-N bond formed is broken, with lone pairs of electrons of N used for new N-H bonds, followed by B returning to the H_C configuration to maximize bonding with surface O atoms.

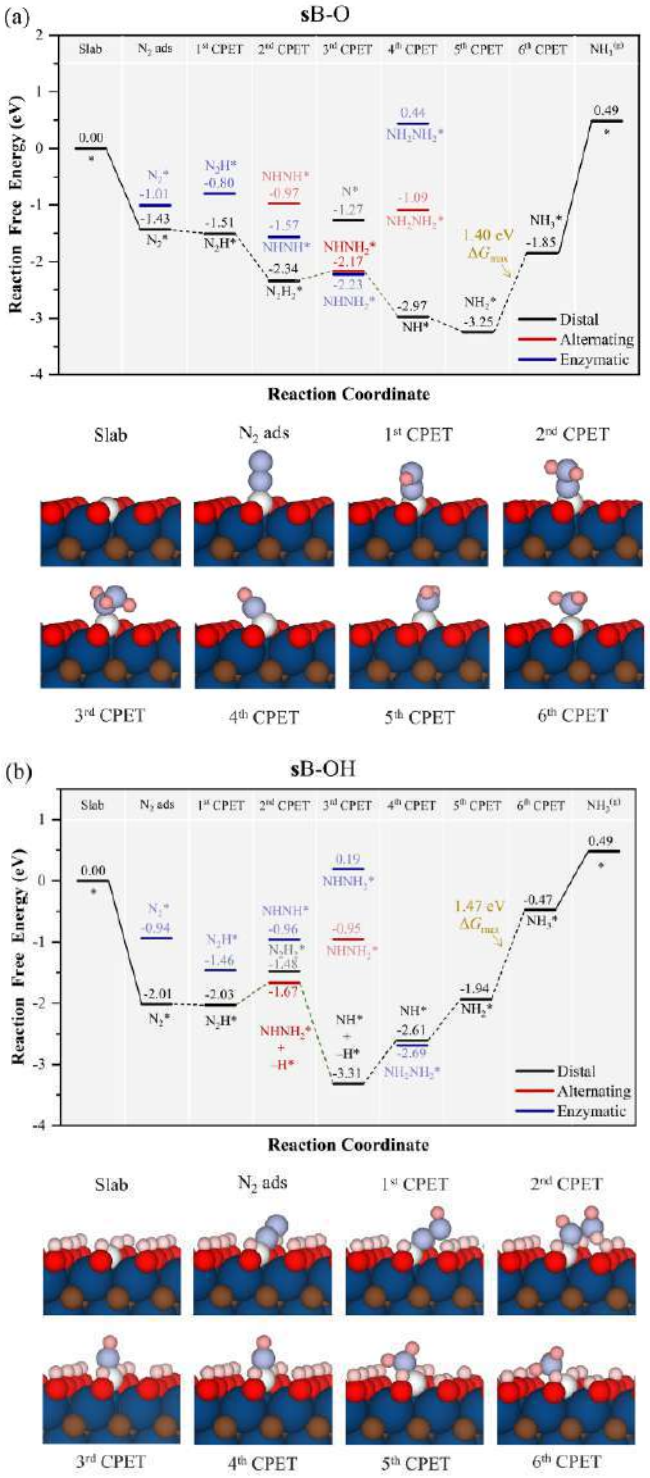

Figure 3.26. Gibbs free energy, Δ*G*, diagrams of NRR on (a) **s**B-O (top), and (b) **s**B-OH (bottom), under standard working conditions of $T = 300$ K, partial gases pressures of 1 bar, $pH = 0$, and $U = 0$ V. Solid lines represent chemical steps such as $N_{2(g)}$ adsorption or as-generated $NH_{3(g)}$ desorption, while dashed lines represent CPET steps. The –H* notation implies the H transfer from surface –OH group. Below the reaction paths, side views of the atomic models for the different reaction steps are shown. N and B atoms are shown in light blue and white colour respectively, the H atoms of –OH group and the proton of CPET are represented by light pink and dark pink respectively, while the rest of the colour coding is as in Figure 3.22. Black numbers and symbols indicate the optimal path, while gray ones indicate non-optimal.[115]

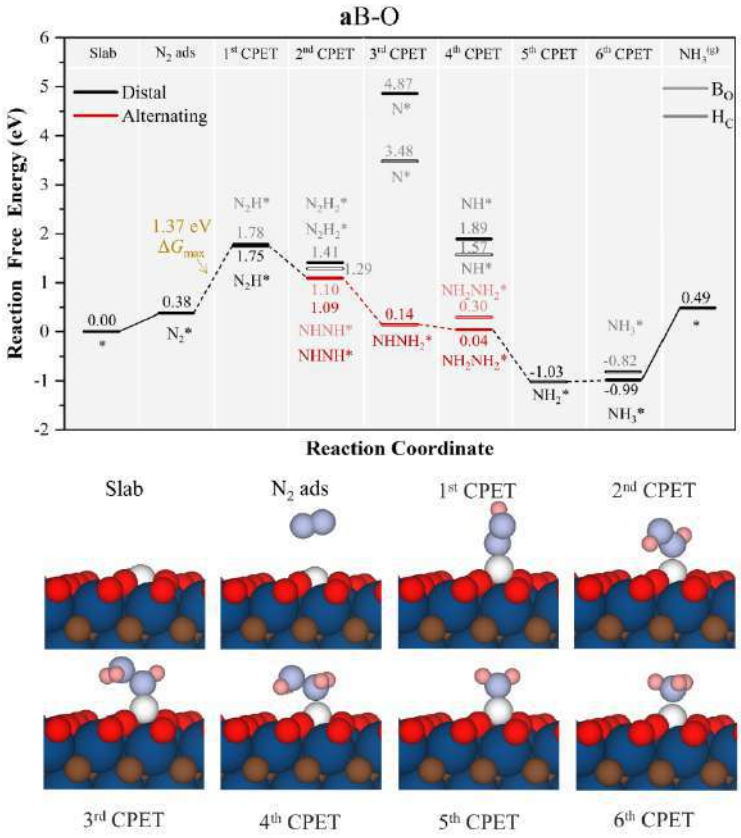

Figure 3.27. Gibbs free energy, Δ*G*, diagrams of NRR on **a**B-O under standard working conditions of T = 300 K, partial gases pressures of 1 bar, pH = 0, and U = 0 V. Solid lines represent chemical steps such as $N_{2(g)}$ adsorption or as-generated $NH_{3(g)}$ desorption, while dashed lines represent CPET steps. Below the reaction paths, side views of the atomic models for the different reaction steps are shown, colour-coded as in Figure 3.26.[115]

The next model **a**B-O$_4$, with $^4/_9$ of the surface consisting of –O groups, the rest being –OH groups. The NRR free energy reaction profile is depicted in Figure 3.28, starting from B at the more stable H$_C$ site. Here, the first costly step is the initial CPET forming N$_2$H* in the B$_O$ mode, with a Δ*G* of 0.93 eV. However, by maintaining B in the B$_O$ position and following a *mixed* pathway, the PDS is the final NH$_3$* formation, similar to the **s**B model, with a Δ*G* of 1.19 eV.

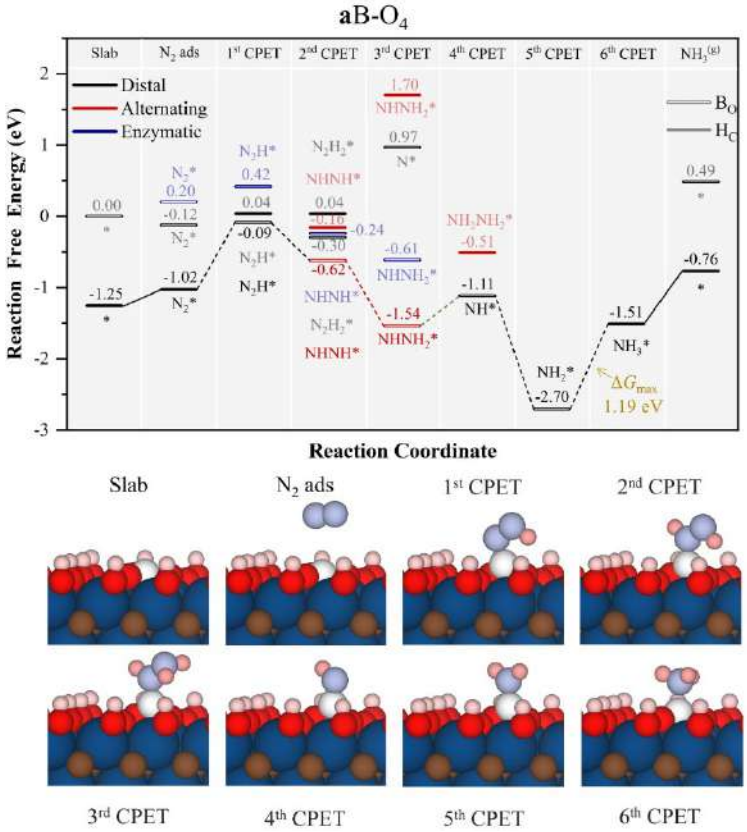

Figure 3.28. Gibbs free energy, ΔG, diagrams of NRR on **a**B-O_4 under standard working conditions of T = 300 K, partial gases pressures of 1 bar, pH = 0, and U = 0 V. Solid lines represent chemical steps such as $N_{2(g)}$ adsorption or as-generated $NH_{3(g)}$ desorption, while dashed lines represent CPET steps. Below the reaction paths, side views of the atomic models for the different reaction steps are shown, color-coded is as in Figure 3.26.[115]

As the number of nearby participating –OH groups increase as in the **a**B-O_3 model, a change in the scenario is clearly seen, as depicted in Figure 3.29. Here, the initial free energy profile is analogous to **a**B-O_4, starting from H_C site until the formation of N_2H*, with a ΔG of 0.52 eV. From this point on, further hydrogenation via a *distal-alternating mixed* pathway implies an adjacent –OH group simultaneously transferring a H to form $NHNH_2$*, which is quite exothermic at -1.66 eV. Then the next CPET involves forming the first $NH_{3(g)}$ after NH* is left, with a ΔG of 0.37 eV, followed by formation of NH_2*, once again highly exothermic at -1.6 eV. Then, the as-generated –O can be hydrogenated to recover the former –OH group, with a ΔG of 0.60 eV, and the formation of –OH groups from pre-existing –O groups is the costliest CPET, thereby constituting the PDS, with a ΔG of 0.83 eV, followed by the formation of a second NH_3 molecule.

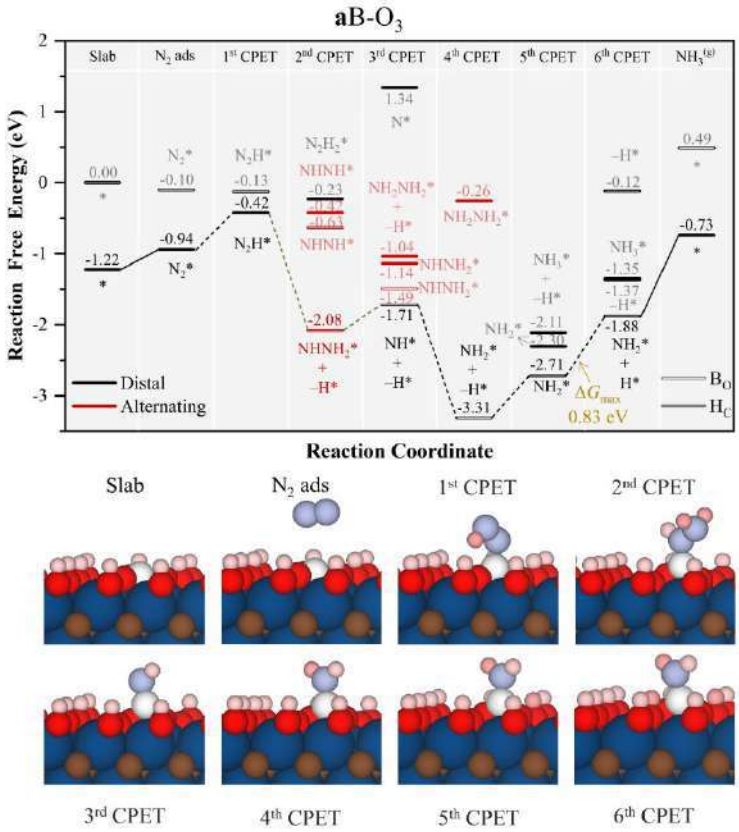

Figure 3.29. Gibbs free energy, ΔG, diagrams of NRR on **a**B-O_3 under standard working conditions of T = 300 K, partial gases pressures of 1 bar, pH = 0, and U = 0 V. Solid lines represent chemical steps such as $N_{2(g)}$ adsorption or as-generated $NH_{3(g)}$ desorption, while dashed lines represent CPET steps. Below the reaction paths, side views of the atomic models for the different reaction steps are shown, colour-coded and notation as in Figure 3.26.[115]

Finally in the **a**B-O_2 model, the reaction primarily occurs at the B_O site, as shown in Figure 3.30. Initially, N_2 follows an *enzymatic* mechanism, with further hydrogenation from $NHNH_2$* resulting in a stable transition to NH_2*. This initiates the *distal* pathway involving a H transfer from a neighbouring surface –OH group, with a ΔG of -2.11 eV. Subsequently, the as-generated –O group is compensated, and next the second NH_3 molecule is formed with a ΔG of 1.14 eV. After NH_3 desorption, the final CPET recovers the second surface –OH, which constitutes the PDS with a ΔG of 2.01 eV. Thus, for high –OH coverage like **a**B-O_2 and **a**B-O_3, the involvement of surface –OH groups should be emphasized to modulate the reaction profile since both models involve –OH participation in the PDS formation. However, the results from **a**B-O_2 suggest that an excessive amount of surface –OH groups is not necessary, as a moderate amount can enhance the reaction, as observed in **a**B-O_3 with a ΔG_{max} of 0.83 eV, currently the lowest.

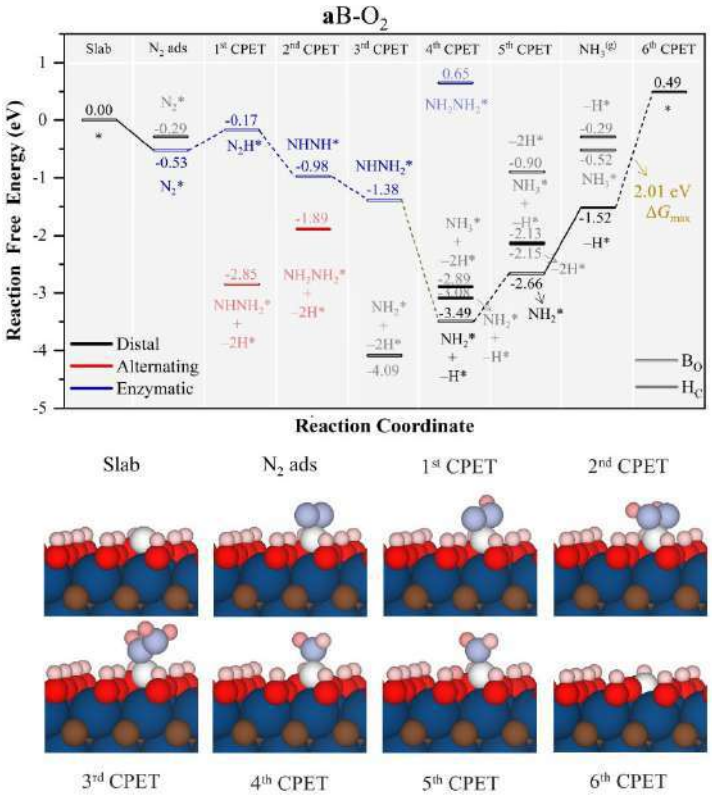

Figure 3.30. Gibbs free energy, Δ*G*, diagrams of NRR on **a**B-O_2 under standard working conditions of T = 300 K, partial gases pressures of 1 bar, pH = 0, and U = 0 V. Solid lines represent chemical steps such as $N_{2(g)}$ adsorption or as-generated $NH_{3(g)}$ desorption, while dashed lines represent CPET steps. Below the reaction paths, side views of the atomic models for the different reaction steps are shown, colour-code and notation are as in Figure 3.26.[115]

Comparatively, at the dual adsorption B site (*cf.* **a**2B in Figure 3.31), two additional $N_{2(g)}$ adsorption modes, *be* and *bs*, are possible, as illustrated in Figure 3.23. Nonetheless, due to the faster N_2 adsorption on **a**2B-O *bs*, as shown in Figure 3.25, the reaction free energy profiles were generated starting from this mode, as depicted in Figure 3.31, with T_N representing top adsorption on a nitrogen atom and B_N representing bridging adsorption between two nitrogen atoms. Here, the B_2 surface dimer facilitates the *enzymatic* mechanism downhill up to $NHNH_2$*, then the *mixed* shortcut reaches the *distal* to form NH* and NH_2*, binding two B atoms, finalizing in the final NH_3* formation with PDS at Δ*G* of 1.51 eV. Interestingly, in the **a**2B-OH model, the reaction pathway is more intricate. Despite the slight advantage of N_2 *bs*, the high stability of the intermediate in the *mixed* path reaction along the *enzymatic* leads to the final NH_3* formation as PDS, with Δ*G* of 2.1 eV. However, it can be argued that by enabling the reaction path through *alternating* pathways on the dimer of bridge and top sites, as shown in Figure S8 of Appendix C, the PDS results in the NH_2NH_2* formation with a Δ*G* of 0.99 eV. Nevertheless, when all sites are occupied by the most favorable mechanism, thermodynamics will be larger.

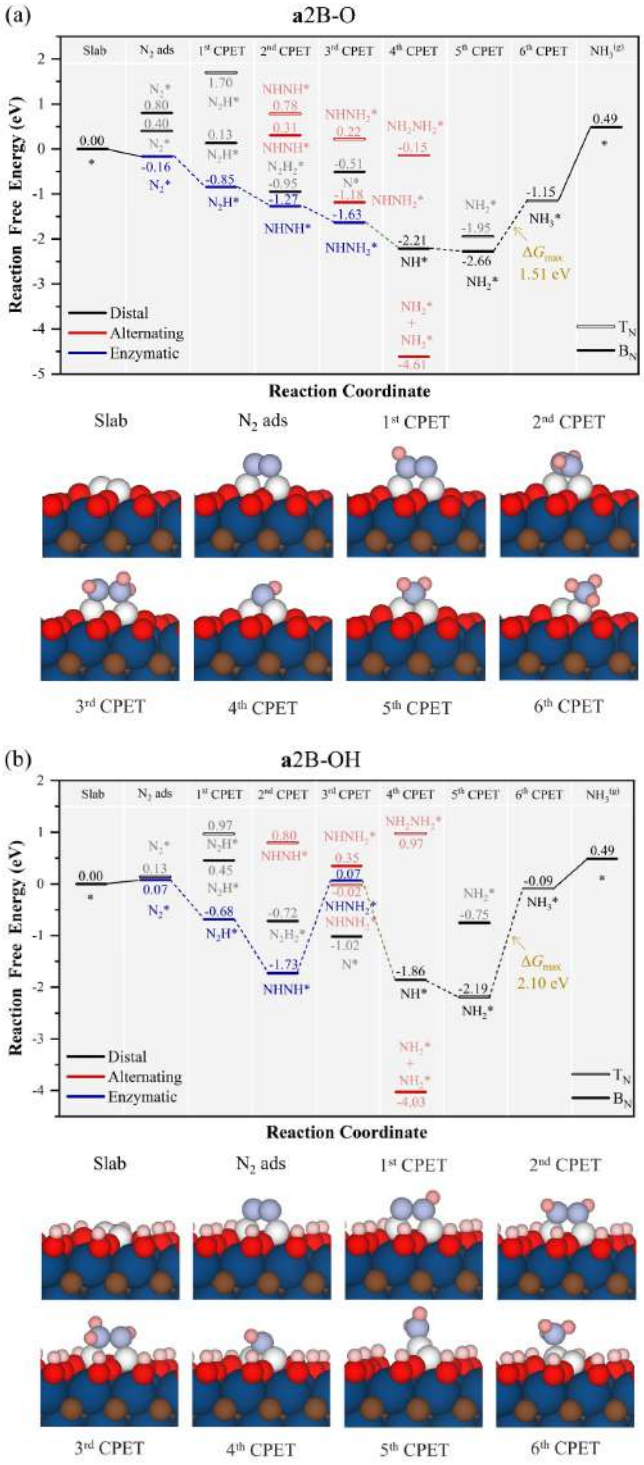

Figure 3.31. Gibbs free energy, Δ*G*, diagrams of NRR on (a) **a**2B-O (top), and (b) **a**2B-OH (bottom), under standard working conditions of $T = 300$ K, partial gases pressures of 1 bar, $pH = 0$, and $U = 0$ V. Solid lines represent chemical steps such as $N_{2(g)}$ adsorption or as-generated $NH_{3(g)}$ desorption, while dashed lines represent CPET steps. T_N represents adsorption on top of a nitrogen atom and T_B represents adsorption on a bridge between two nitrogen atoms. Below the reaction paths, side views of the atomic models for the different reaction steps are shown. Colour code is as in Figure 3.26.[115]

3.3.3.4. Performance and NRR *vs.* HER

The assessment of overall performance currently relies on the calculated ΔG_{max} value and its corresponding U_L value. Figure 3.32a compares the B-doped $Ti_3C_2T_x$ models as NRR electrocatalyst with the reference Ru (0001), which has a ΔG of -1.08 V,[71] yet gained using the RPBE functional with no dispersion correction interactions, so one should avoid making clear differences for ΔG differences within the DFT standard accuracy of *ca.* 0.2 eV. Nonetheless, Figure 3.32a demonstrates this clear benefit and may be extended to other MXene components. Additionally, HER[116] is the primary competing side reaction for NRR, potentially reducing the Faradaic Efficiency (FE) in experiment. As shown in Figure 3.32b. the studied models exhibit notable differences and allow for a comparison between the U_L of NRR, U_L(NRR), and HER, U_L(HER) in Figure 3.32c. The competition in NRR is evident, as in some cases, HER is easier to achieve than NRR on fully O-terminated models like **a**B-O and **a**2B-O. However, for surface with mixtures of –O and –OH groups, such as **a**B-O_3 and **a**B-O_4, NRR is more favourable than HER. Lastly, the competition between NRR and HER is more intense on substituted **s**B-O and **s**B-OH, as well on adsorbed **a**B-O_2 covered by high –OH groups. In cases where lower U_L in NRR relative to HER is required, and the **a**B-O_3 scenario is optimal. Strategies to inhibit HER include limiting proton concentration or transfer rates,[72,73] using nonaqueous proton donors to inhibit hydrogen adsorption on catalysts, and providing protective layers to prevent proton transfer to the surface.[74,75]

Furthermore, it is worth discussing the experimental synthesis feasibility of the aforementioned NRR electrocatalyst candidates. The preparation of B-doped $Ti_3C_2T_x$ involves placing the solution in a Teflon-lined autoclave and conducting a 24-hour hydrothermal treatment at 180°C.[127] However, previous studies[122,110] have indicated that high-temperature treatments can lead to the removal of surface –OH groups, posing a challenge when aiming for the high selective **a**B-O_4 and best performance of **a**B-O_3. Nevertheless, previous research[33,47] on calculating Pourbaix diagrams has shown that the stability of surface terminations is a function of *pH* and *U*, where pure –O, –OH, and mixed –O/–OH scenarios can be achieved at low *pH* and slightly positive, negative, and near-zero overpotentials, thus addressing stability concerns under low *pH* and potential working conditions.

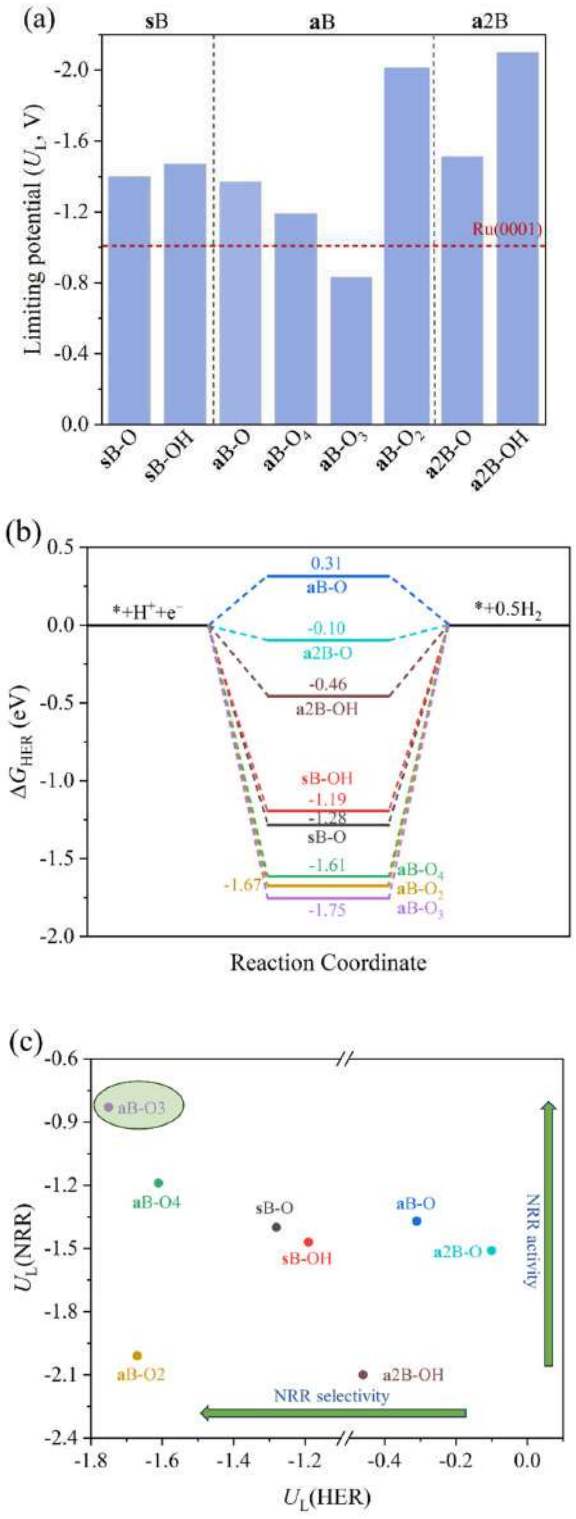

Figure 3.32. (a) Comparison of U_L(NRR) of the different models with respect to Ru (0001) reference, (b) free energy change for HER on the studied catalysts, and (c) U_L(NRR) *vs.* U_L(HER).[115]

3.3.4. Conclusions

These findings, coupled with additional data and analyses presented in the research articles below, lead to the following conclusions:

- The **s**B models have the strongest N_2 adsorption capacity, followed by low-coordinated **a**B, however, **a**B generally has smaller U_L values compared to **s**B.
- The free energy reaction profile is influenced by the simultaneous transfer of H atoms from adjacent surface –OH groups, which can stabilize reaction intermediates, thereby reducing the energy cost of the reaction.
- A moderate amount of –OH groups on the catalyst surface, neither excessive nor too low, is beneficial for NRR performance, especially when B is in the H_C site surrounding by –OH groups, *i.e.* **a**B-O_3, which shows significantly higher NRR performance compared to cases with fully O-terminated surfaces, such as **s**B-O, **a**B-O, and **a**2B-O, as well cases with high and relatively low –OH coverage like **a**B-O_2 and **a**B-O_4.
- Moreover, **a**B-O_3 also shows competitive performance in the HER reaction.
- According to computationally derived Pourbaix diagrams, these models are considered stable under working conditions.

3.4. Contrasting Metallic (Rh^0) and Carbidic (2D-Mo_2C MXene) Surfaces in Olefin Hydrogenation Provides Insights on the Origin of the Pairwise Hydrogen Addition

3.4.1. Introduction

Hydrogenation reactions are pivotal in heterogeneous catalysis, involving environmental treatment, petrochemicals, and fine chemical synthesis.[128] The active sites provided by heterogeneous catalyst surfaces can weaken H_2 bonds, leading to dissociative chemisorption and the generation of active surface H adatoms (H*).[129] The catalytic hydrogenation of olefins, such as the widely studied example of ethene hydrogenation ($C_2H_{4(g)} + H_{2(g)} \rightarrow C_2H_{6(g)}$), is well represented.[130,131] The mechanism proposed by Horiuti and Polanyi is widely accepted as the main pathway for olefin hydrogenation, where H atoms added typically originate from different H_2 molecule, hence being non-pairwise.[132] However, various types of heterogeneous catalysts have been proven to facilitate pairwise hydrogen addition, where two H atoms in the hydrogenation product molecule come from the same H_2 molecule.[133]

Para-hydrogen (*p*-H_2) is the nuclear spin isomer of H_2, with the opposite spin orientation of its two H atoms. When *p*-H_2 is added in pairwise manner, to various alkenes or alkynes, a non-equilibrium distribution of nuclear spin states in the products leads to significantly enhanced NMR signals. Para-Hydrogen Induced Polarization (PHIP) is a method to evaluate catalyst selectivity for pairwise addition of H_2, as the detected NMR signal enhancement is directly proportional to the pairwise selectivity.[134,135] Various metal-based catalysts have been demonstrated to achieve the pairwise selectivity of several percent by PHIP.[133] These experiments involving *p*-H_2 are generally inconsistent with the widely accepted Horiuti-Polanyi mechanism hypothesis implying rapid H* species diffusion;[136] however, an alternative reaction pathway proposed by Farkas involves slow diffusion of H*, allowing for a pairwise addition pathway (see Figure 3.33),[137] where both pairwise and non-pairwise hydrogen additions can theoretically follow concerted and stepwise mechanisms.[138]

Despite these arguments, predicting (or even explaining) selectivity preference to the pairwise hydrogen addition pathway for a given catalytic surface remains challenging. To understand the relationship between the diffusion rate of H* species, energy barriers along the hydrogenation pathway, and the contribution of pairwise addition to the overall hydrogenation rate, DFT calculations were performed for the hydrogenation of ethene (C_2H_4) to ethane (C_2H_6) on two systems where experiments show a different pairwise

contribution. The first system involves a well-defined $Mo_2C(0001)$[45] MXene whereas the second one is the Rh(111) surface,[139] both of them showing pairwise hydrogen addition, but in Rh (111) contributing up to 8%.

In order to investigate the origin of the PHIP effect and ease the on-coming discussion, only the stepwise mechanism was considered due to the energetics associated with these two mechanisms are almost identical, using a pool of diffusing H* adatoms on the 2D-Mo_2C (0001) and the Rh (111) surfaces. DFT predictions were evaluated through pairwise hydrogen addition experiment on propene using two-dimensional Mo_2C_{1-x} and Rh/TiO_2 catalysts.[140] The reason of selecting simpler ethene model over propene was that the observed H_2 activation primarily originating from the electrostatic potential and metal charges of catalytic surface, with tiny impact on the substrate.[141] Nonetheless, both ethene and propene are homologous olefins with a single double bond and similar reactive site,[140] and the hydrogenation rate of ethene is one order of magnitude higher than that of propene,[142,143] indicating a minimal difference in activation energy barriers of only 0.06-0.1 eV according to the Arrhenius equation. Therefore, using the simpler ethylene structure reduces computational complexity and time while providing results comparable to propene. Finally, the effect of surface coverage (including hydrides and alkene adsorbates) on the ethene hydrogenation rate was also studied.

This work produced the publication of one research article in *ACS Catalysis*, titled "*Contrasting Metallic (Rh^0) and Carbidic (2D-Mo_2C MXene) Surfaces in Olefin Hydrogenation Provides Insights on the Origin of the Pairwise Hydrogen Addition*"[144] with the supporting information for can be found in Appendix D provided at the end of this thesis. Subsequent pages contain a summary of this article. My contributions to the research articles comprise: (a) Carrying out the DFT calculations and data treatment, (b) analysis of the calculations results, (c) surveying and summarizing the relevant publications, and (d) comparing computational results with experimental results. A full description of the work done can be found in Ref. 144.

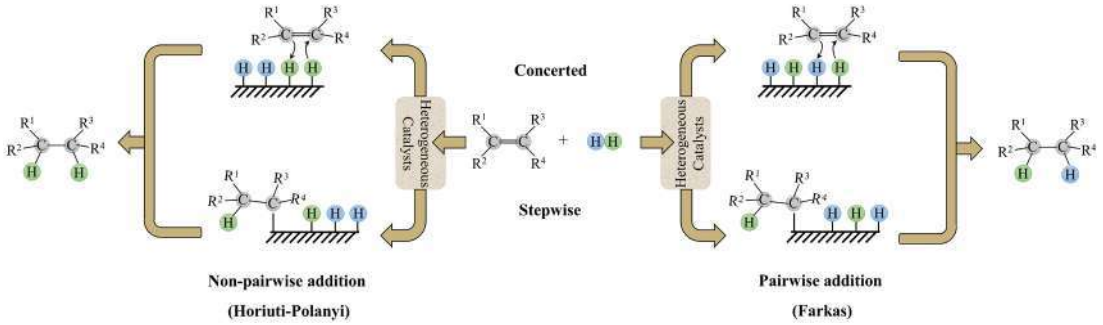

Figure 3.33. The Horiuti-Polanyi (non-pairwise) and Farkas (pairwise) hydrogen addition mechanisms.[144]

3.4.2. Hydrogenation Mechanism

Once the reactants are adsorbed, as far as the ethylene hydrogenation mechanism is concerned, we consider the reaction steps as follows:

(i) H_2 dissociation, ΔE_{diss}: $H_2^* + * \rightleftharpoons 2 \cdot H^*$ (3.20),

(ii) First hydrogen transfer, ΔE_H^{1st}: $C_2H_4^* + H^* \rightleftharpoons C_2H_5^* + *$ (3.21),

(iii) Second hydrogen transfer, ΔE_H^{2nd}: $C_2H_5^* + H^* \rightleftharpoons C_2H_6^* + *$ (3.22).

including also adsorption and desorption steps of H_2, C_2H_4, and C_2H_6.

3.4.3. Results

3.4.3.1. Adsorption Energy and Rate

Adsorption of reactants (C_2H_4* and H_2*), products (C_2H_6*) and intermediates (H* and C_2H_5*) on high-symmetry sites of the ABC- or ABA-stacked 2D Mo_2C(0001) and Rh(111) surface were evaluated, as shown in Figure S1 in Appendix D, with the optimal adsorption sites illustrated in Figure S2 in Appendix D. The observed H_2 lowest adsorption energy on the 2D Mo_2C MXene model aligns with previous reports,[119] while the adsorption free energies of reactants and products, ΔG_{ads}, displayed in Figure 3.34, demonstrating that, regardless of stacking mode, except for C_2H_6, the ΔG_{ads} of the 2D-Mo_2C model is larger than on Rh (111). In the 2D-Mo_2C model, the adsorption free energy of ABC-Mo_2C is larger than ABA-Mo_2C, consistent with the lower stability of ABC stacking compared to ABA stacking.[145]

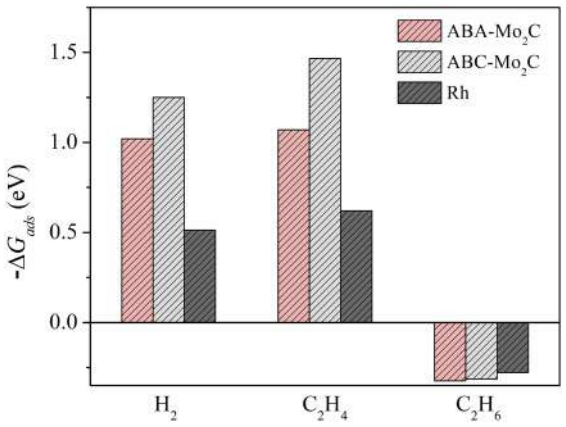

Figure 3.34. Adsorption free energies of H_2 (assuming spontaneous dissociation into 2H*), C_2H_4, and C_2H_6 on the ABA-Mo_2C, ABC-Mo_2C and Rh (111) surfaces under 1 bar of gas pressure and 250 °C or 60 °C for the 2D-Mo_2C and Rh (111) models, respectively.[144]

The calculated adsorption energies are utilized to estimate adsorption and desorption rates, further used to derive a Kinetic Phase Diagram (KPD),[146] as shown in Figure

3.35. Considering the ease of H_2* dissociation, where H_2* forms 2 H* and subsequently desorbs, used in the KPD, the surface exhibits slightly higher affinity for C_2H_4 relative to H_2. Clearly, under working conditions, reactants C_2H_4 and H_2 (undergoing dissociation into 2 H*) can adsorb on all three surfaces, while C_2H_6 will desorb easily, which is a favourable characteristic for catalyst performance. The process of H_2* dissociating into 2 H* was also evaluated on the studied surfaces, with H* preferentially adsorbing on the H_B and H_M sites of ABA-Mo_2C and ABC-Mo_2C models, while on Rh(111), although H_{fcc} is the most stable adsorption site for H*, the adsorption energy on H_{hcp} is only 0.03 eV lower than on H_{fcc} (see Figure S1 in Appendix D), indicating competition between these two sites for H* species, with estimated dissociation barriers of 0.28 eV and 0.11 eV for ABA- and ABC-Mo_2C models, respectively, and 0.06 eV towards neighbouring H_{fcc} and H_{hcp} sites, and 0.08 eV towards two neighbouring H_{fcc} sites on Rh (111). Therefore, H_2* dissociation is a low-barrier step on all three surfaces, with dissociation on 2D-Mo_2C (0001) slightly more challenging than on Rh (111). Considering the significantly stronger interaction of C_2H_4 molecule compared to H_2 molecule on all three surfaces, it is foreseeable that H_2* dissociation can also occur in the presence of C_2H_4*, with dissociation barriers of 0.19, 0.09, and 0.01 eV for ABA-, ABC-Mo_2C, and Rh models, respectively. See Appendix D for more details.

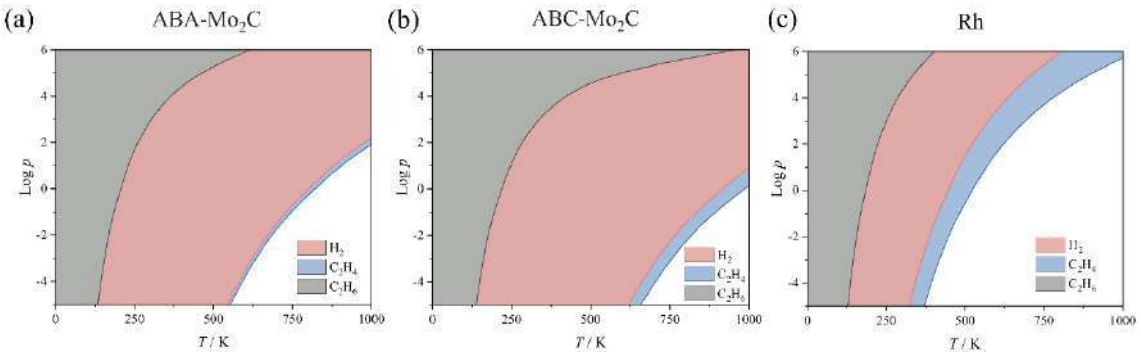

Figure 3.35. Calculated kinetic phase diagrams for H_2, C_2H_4, and C_2H_6 on the (a) ABA-Mo_2C, (b) ABC-Mo_2C, and (c) Rh(111) models as a function of temperature T, in K, and standard logarithmic function of the gas pressures, p, in Pa. Colored regions imply a preference toward adsorption, while white areas represent regions where clean surfaces are preferred.[144]

3.4.3.2. Hydrogenation Mechanism Analysis

As previously mentioned, the mechanism for the hydrogenation of olefins on heterogeneous catalysts involves the dissociative chemisorption of H_2,[147] followed by H* adatom diffusion[148] before transferring to the unsaturated hydrocarbon. Calculations explored H* adatom diffusion considering the absence of C_2H_4*, revealing diffusion barriers E_b on the

ABA and ABC-Mo_2C models of 0.35 eV and 0.27 eV, respectively, and on Rh (111) surface as 0.16 eV. These values slightly vary in the presence of C_2H_4*, with E_b values on the ABA- and ABC-Mo_2C models being 0.37 eV and 0.28 eV, respectively, and on Rh (111) as 0.10 eV. In summary, the results indicate that the E_b for H_2 dissociation is lower than that for H* diffusion, regardless of the presence of C_2H_4*.

The energetics of the ethene hydrogenation steps were then evaluated, with the first step of H* transfer reaction pathway shown in Figure 3.36. On the ABC-2D-Mo_2C model, the range of ΔE for forming C_2H_5* from C_2H_4* and H* is between 0.28 eV and 0.57 eV, comparable to the ΔE on Rh (111) of 0.39 eV. Similarly, the E_b range on the ABA-2D-Mo_2C model is between 0.64 eV and 0.84 eV, slightly lower than the 0.91 eV on Rh (111). Thus, regardless of the stacking, the first step of H* transfer from C_2H_4* to C_2H_5* is more favourable on 2D-Mo_2C compared to Rh (111), as shown in Figure 3.37.

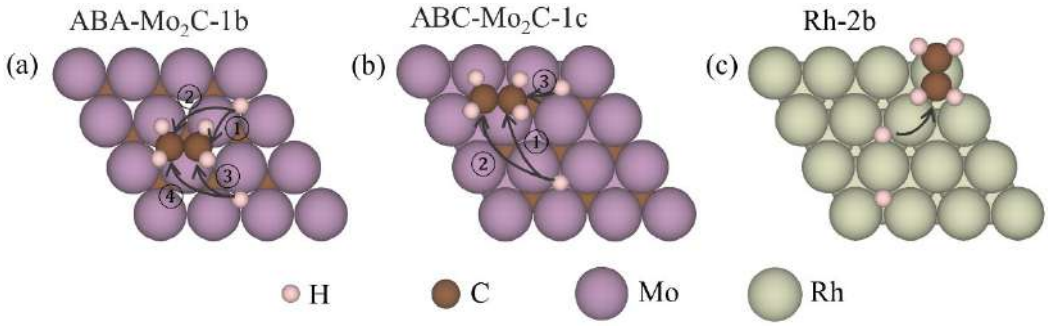

Figure 3.36. The potential routes of the first step of the C_2H_4 hydrogenation reaction on (a) ABA-Mo_2C-1b, (b) ABC-Mo_2C-1c, and (c) Rh-2b. See Figure S7 in Appendix D for definition of notations.[144]

The second hydrogenation step converts C_2H_5* and H* to C_2H_6*, where it is slightly exothermic on Rh(111) by -0.10 eV with a moderate E_b of 0.55 eV. However, on the 2D-Mo_2C model, this step is endothermic, ranging from 0.86 eV to 1.32 eV, leading to higher E_b values ranging from 1.77 eV to 2.11 eV. The binding of C_2H_4* and C_2H_5* species is stronger on 2D-Mo_2C, resulting in a minor change in the barrier for the first step of hydrogenation but making the second step considerably more challenging, leading to higher barriers as per the BEP relation.[149] Due to the stronger adsorption of C_2H_4* and the lower energy barrier for H_2 dissociation, high coverage of C_2H_4* and H* adatoms under reaction conditions can be promoted, potentially altering the energy barriers. To investigate this effect, we considered surface models with ¾ monolayer (ML) coverage of C_2H_4* or H*. The results indicate that a ¾ ML coverage of either C_2H_4* or H* has only a slight impact on certain steps, thus the overall reaction profile remains qualitatively unchanged, as shown in Figure 3.37. On Rh(111), the impact is negligible, with a decrease of 0.14 eV

observed under ¾ ML H* coverage. Similar effects are seen on the 2D-Mo_2C model, but with more pronounced variations, under ¾ ML H coverage, the E_b decreases by 0.49 eV for ABA-Mo_2C and 0.35 eV for ABC-Mo_2C. However, under ¾ ML C_2H_4* coverage, the E_b increases by 0.1 eV for ABA-Mo_2C but decreases by 0.53 eV for ABC-Mo_2C, attributed to the differences in stacking arrangements of C_2H_4* as Figures S11 and S12 shown in Appendix D. Overall, ethene hydrogenation on 2D-Mo_2C is more endothermic and has a higher reaction barrier compared to Rh (111), regardless of stacking or coverage of H* and C_2H_4*. The H* adatom diffusion barrier in the ¾ ML C_2H_4* model is comparable to that on the uncovered surface, with the E_b variations in the 0.01 eV range, however, under ¾ ML H* coverage, the diffusion barrier values on ABA- and ABC-Mo_2C are 0.42 eV, compared to 0.35 eV and 0.27 eV on the uncovered surface, respectively, more details in Table S11 in Appendix D.

Based on the present DFT results, the relative ratio of pairwise and non-pairwise hydrogenation pathways can be assessed, with the latter controlled by the H* diffusion barrier. The ratio of diffusion rate (r_{diff}) to the reaction rate obtained using the span model (r_{span}), as shown in Figure 3.38, indicating that a value greater than 1 suggests H* diffusion is faster than hydrogenation. The results suggest that the non-pairwise mechanism is expected to dominate on any model catalyst surface studied, with the possibility of the pairwise mechanism being more significant on the Rh (111) surface compared to the 2D-Mo_2C(0001) surface, regardless of the H* and C_2H_4* coverage. The precision limitation of ±0.2 eV for DFT is also considered, but the aforementioned trends remain unchanged.

Furthermore, Eley-Rideal mechanism based on the concerted addition of H_2, enables the direct reaction of H_2 molecules in gas phase with C_2H_4*, thus avoiding the formation of H* adatoms, that could lead to highly selective pairwise H_2 addition. However, all computational led to high DFT energy barriers of at least 4.84, 5.12, and 2.28 eV for ABA- and ABC-2D-Mo_2C (0001) and Rh (111) surfaces, respectively. Therefore, a competitive pairwise hydrogenation mechanism following Eley-Rideal dynamics can be ruled out.

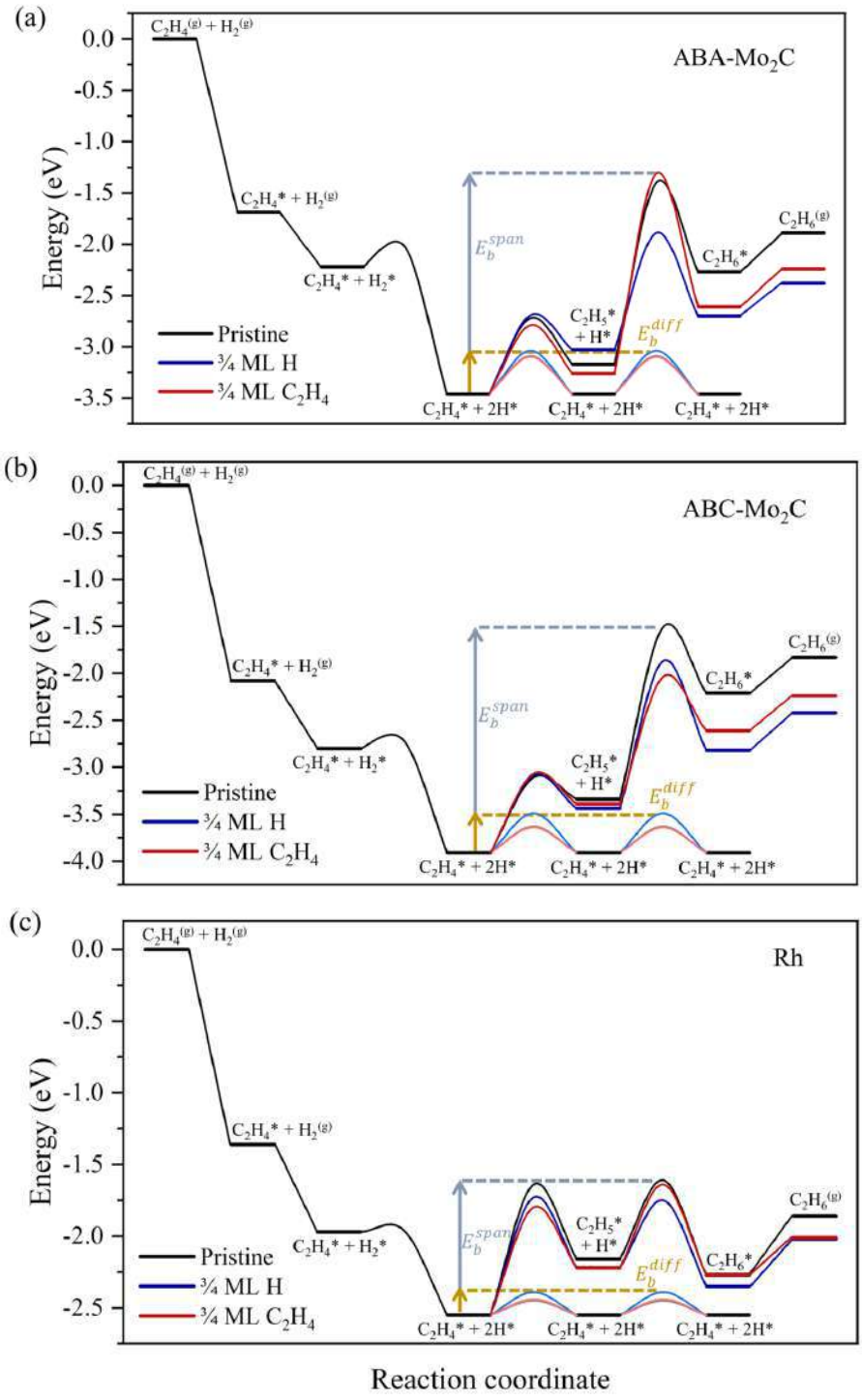

Figure 3.37. Total reaction energy profiles on the pristine (black) (0001) surfaces of (a) ABA-Mo_2C and (b) ABC-Mo_2C, and (c) Rh (111). From C_2H_4* + 2H* state, there are superimposed the forward paths when having ¾ ML H* (blue), and ¾ ML C_2H_4* (red). The diffusive paths of H* adatoms are shown in lighter shades of the respective colored traces. Note that pristine diffusive path (grey) and that of the ¾ ML C_2H_4* model (pink) essentially superimpose.[144]

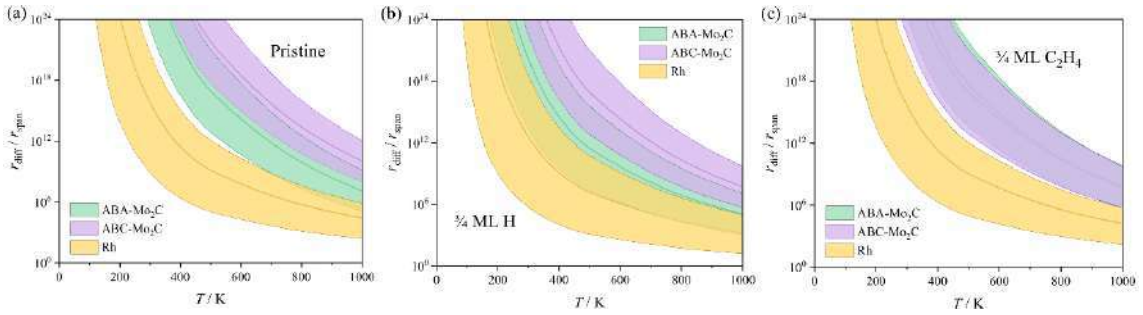

Figure 3.38. Calculated ratio between the rates of H* diffusion, r_{diff}, and the reaction rate obtained using the span model energy barrier, r_{span}, on ABA- and ABC 2D-Mo_2C (0001) surfaces, and Rh (111) surface, using (a) pristine surfaces, (b) a surface with coverage of ¾ ML of H* or (c) ¾ ML of C_2H_4. Shaded regions reflect the DFT uncertainty of ±0.2 eV on the estimated energy barriers.[144]

3.4.3.3. Discussion

The selectivity of pairwise hydrogen addition evaluated through experimental NMR signal enhancement is significantly higher on Rh/TiO_2 than on Mo_2CT_x−500, consistent with DFT calculations. However, quantitatively, DFT calculations predict diffusion rates to be 4-12 orders of magnitude faster than hydrogenation reactions under typical experimental conditions. The significant disparity makes it challenging for any reasonable computational model refinement or associated errors to have a significant impact. Further calculations indicate that even if H_2 molecules dissociate at the presence of C_2H_4*, the diffusion of H* adatoms is notably faster than their transfer to ethene, indicating no significant increase in the likelihood of pairwise hydrogen addition, with the observed PHIP effect on the metal surface attributed to adsorbates significantly decreasing H* adatom diffusion, thereby favouring pairwise hydrogen addition.[150] However, in this scenario, DFT calculations suggest that due to the presence of high surface coverage of co-adsorbates (¾ ML of H* or C_2H_4*), diffusion and reaction rates remain unchanged, making the presence of adsorbates less likely to be the determining factor for the appearance of the PHIP effect. Although other adsorbates (such as $CH_3CH{=}CH_2$*) may have a more pronounced impact on the r_{diff}/r_{span} ratio, the observed several orders of magnitude difference in the r_{diff}/r_{span} ratio during the ethene hydrogenation process in this study strongly indicates that the adsorbates present on the catalyst surface cannot account for the contribution to the pairwise hydrogenation mechanism, at least within the surface coverage range considered in this study.

Therefore, alternative explanations for pairwise H_2 addition need to be considered. Specifically, the Eley-Rideal mechanism in high pairwise selectivity, however, it was ruled out due to high energy barrier. Some other hydrogenation mechanisms occasionally

proposed here also fail to explain, as mechanisms like the Horiuti-Polanyi, would involve random H* adatoms.[151,152] Our DFT results suggest that for a similar C_2H_5* + H* configuration, the second H* adatom is more likely to diffuse away rather than complete the hydrogenation cycle, implying that the substrate-assisted hydrogenation mechanism is non-pairwise.

Furthermore, other experimental studies on the PHIP effect indicate that pairwise hydrogen addition is essentially prevalent in hydrogenations catalyzed by various heterogeneous catalysts.[133] Therefore, a reasonable conclusion is that these results point towards the existence of additional reaction pathways inherently favor pairwise pathway, operating concurrently with the dominant Horiuti-Polanyi mechanism and significantly contributing to the overall reaction yield. When this concurrent mechanism involves the dissociation of H_2, the migration of the generated H* species should be strongly inhibited, for instance in the case of molecular transition metal catalysts operating through oxidative addition of H_2, olefin insertion, and reductive elimination steps. For Rh/TiO_2, the presence of these H_2 pairwise sites may be a result of the SMSI effect. When the SMSI effect is not available, a plausible mechanism may rely on the blocked H* adatoms diffusion caused by occupied sites and the simultaneous competing diffusion of many H* adatoms, dynamically preventing diffusion until a neighbouring site is available, a factor not considered in diffusion rate calculations. In such a scenario, there are fewer opportunities for H* diffusion, making it more likely for the two generated H* adatoms to be added in pairs to C_2H_4*.[153] Another mechanism based on the concerted addition of H_2 with the substrate completely avoids the formation of H* adatoms and presents reaction barriers competing with the Horiuti-Polanyi pathway, leading to high selectivity for pairwise H_2 addition. Future research should explore these possibilities.

3.4.4. Conclusions

These findings, coupled with additional data and analyses presented in the research articles below, lead to the following conclusions:

- DFT calculations were carried to elucidate the reaction mechanisms of ethene hydrogenation on well-defined model Rh (111) surface and 2D-Mo_2C (0001) surfaces with ABC and ABA stacking. These were combined to experimental PHIP measurements for propene hydrogenation on 2D-Mo_2C_{1-x} and Rh/TiO_2 catalysts to evaluate pairwise *vs.* non-pairwise hydrogenation mechanisms.

- DFT calculations and experimental observations consistently show that 2D-Mo_2C(0001) and Rh(111) can effectively catalyse the hydrogenation of ethene, additionally, the first H* transfer from C_2H_4* to form C_2H_5* proceeds with similar barriers on both systems. However, the hydrogenation of the C_2H_5* to C_2H_6* is more endothermic on the 2D-Mo_2C(0001), and features significantly higher energy barriers than on Rh (111), regardless of the surface coverage of H* and C_2H_4*, leading to a lower rate of ethene hydrogenation on 2D-Mo_2C(0001), consistent with experimental results.
- Experimental evidence clearly indicates a significant contribution of the pairwise H_2 addition, however, the widely accepted Horiuti-Polanyi mechanism in DFT suggests that this is less likely to occur due to the rapid diffusion of H*, as well the Eley-Rideal mechanism, and therefore we propose that dynamic site blocking could occur at higher adsorbates coverage, or that another general mechanism would greatly limit the H* diffusion.

3.5. Publications

Journal of Materials Chemistry A

ROYAL SOCIETY OF CHEMISTRY

PAPER

View Article Online
View Journal | View Issue

Check for updates

Cite this: J. Mater. Chem. A, 2023, 11, 6886

Effect of terminations on the hydrogen evolution reaction mechanism on Ti_3C_2 MXene†

Ling Meng, [ab] Li-Kai Yan, [*b] Francesc Viñes [*a] and Francesc Illas [a]

Two-dimensional (2D) MXene materials are proposed as high-efficiency hydrogen evolution reaction (HER) electrocatalysts. Most computational studies addressed the HER assuming a fully O-termination, even if as-synthesized MXenes feature a mixture of –O, –OH, –F, or even –H surface groups. To better understand the electrocatalytic surface composition and mechanism under HER equilibrium conditions in the Ti_3C_2 MXene model material, we composed Pourbaix diagrams considering *ca.* 450 topologically different surface terminations, including pristine Ti_3C_2, full –O, –OH, –F, and –H terminations, and binary and ternary situations with different group ratios. Realistic models built from Pourbaix diagrams near HER equilibrium conditions of low pH and *U* were used to investigate the Volmer–Heyrovsky and Volmer–Tafel mechanisms, with the particularity of considering, or not, the participation of H atoms from –OH or –H termination groups at different reaction stages. Results pointed out that the models close to the HER equilibrium line, $O_{2/3}OH_{1/3}$, $F_{1/3}O_{1/3}OH_{1/3}$, and $F_{3/9}O_{4/9}OH_{2/9}$, require an almost negligible overpotential of 0.01 V, while surface charges explain the impact of higher ratios of –O groups on modulating the H bond, and the positive influence of having surface –F groups.

Received 14th January 2023
Accepted 26th February 2023

DOI: 10.1039/d3ta00261f

rsc.li/materials-a

1. Introduction

The long-term problem of reaching a sustainable future by using clean and renewable energy sources has remained unsolved. A prospective candidate, hydrogen (H_2), has attracted great attraction as a possible clean and renewable energy source thanks to its high energy density and non-polluting properties when used as fuel,[1,2] especially when it is obtained from a renewable source such as wind and solar energy. The hydrogen thus obtained is usually referred to as *green* hydrogen to differentiate from that obtained from methane steam reforming, so far the most used source. When electricity can be obtained from these renewable sources, the electrocatalytic water reduction becomes a highly appealing way of producing H_2,[3,4] and here high-performing electrocatalysts are key to maximize the efficiency of the hydrogen evolution reaction (HER) process. Hitherto, Pt has been the most efficient electrocatalyst for the HER,[5,6] although its intrinsic HER activity is limited by mass-transport.[7] Moreover, the scarcity and high cost of Pt hinder its applications for large-scale electrocatalytic hydrogen production, and, therefore, the development of non-precious, Earth-abundant HER electrocatalysts, with high activities is essential to make the field move forward.

Recently, great research endeavors have been placed at meeting this goal by exploring non-precious metal substitutes such as Ni or Ni-based alloys.[8,9] However, while Ni is widely commercially used as a HER electrocatalyst, it is naturally unstable in acidic solutions, similar to other electrocatalysts used for the HER. Beyond Ni, various promising noble metal free two-dimensional (2D) materials with high activity towards the HER were proposed, including molybdenum dichalcogenides (MoS_2),[10–12] metal phosphides,[13] g-C_3N_4,[14–16] and graphene-based compounds.[17] However, one crucial weakness of these 2D catalysts is that they often exhibit a semiconducting nature, and have poor charge transfer properties.[10] Even if 1T-MoS_2 overcomes this handicap by being a relatively good conductor, it has been found to be unstable under ambient conditions.[12] Another drawback is that the catalytically active sites are normally restricted to edge or defective atoms, whilst most in-plane atoms are catalytically inert,[18] reducing the overall atomic efficiency and performance of the electrocatalyst. Therefore, a constant search for new stable 2D HER electrocatalysts with good charge transfer kinetics while displaying multiple, regular catalytic active sites is of utmost importance.

It is just in this aspect that MXenes have attracted great attention as electrocatalysts for the HER. MXenes are 2D transition metal carbide, nitride, or carbonitride materials with the general chemical formula of $M_{n+1}X_nT_x$, where normally $n = 1$–3, M is an early transition metal, and X = C and/or N.[19] The most-extended MXene synthesis involves the selective etching

[a]Departament de Ciència de Materials i Química Física & Institut de Química Teòrica i Computacional (IQTCUB), Universitat de Barcelona, c/Martí i Franquès 1, 08028 Barcelona, Spain. E-mail: francesc.vines@ub.edu

[b]Institute of Functional Material Chemistry, Key Laboratory of Polyoxometalate Science of Ministry of Education, Faculty of Chemistry, Northeast Normal University, Changchun 130024, P. R. China. E-mail: yanlk924@nenu.edu.cn

† Electronic supplementary information (ESI) available. See DOI: https://doi.org/10.1039/d3ta00261f

of the A element from a MAX phase precursor material, using F-containing etchants such as hydrofluoric acid (HF), or with HF produced *in situ* by mixing lithium fluoride (LiF) with hydrochloric acid (HCl). As a result, the as-synthesized MXenes display diverse surface functional groups on their basal planes, usually denoted as T_x, normally being –O, –OH, –H, or –F.[20,21] Aside from the above methods, F-free synthesis procedures have been reported,[22] with recent advances in controlling the surface termination with a variety of functionalities,[23] and even procedures and treatments to obtain MXenes with no surface termination.[23,24]

Note that these procedures may lead to the appearance of internal or external defects,[25] which, actually, can also be inherited from the precursor MAX phase. The presence of such defects can be affected by the synthesis methodologies and other factors, *e.g.* acid concentration, etching time, *etc.*,[26] and their existence may be influenced by the surface termination; *e.g.*, metal vacancy formation has been found to be more difficult on –O terminations than on –OH ones.[27] Still, given, normally, a low concentration of defects, the surface chemical activity of MXenes is mostly determined by regular, defect-free sites, and the surface terminations they display. Such MXenes have attracted considerable attention in heterogeneous catalysis given their high surface area, high electronic conductivity, and high chemical and catalytic activities, with abundant active sites, while their composition, width, and surface terminations are the sandbox based on which tailor-made MXenes can be set up for specific applications.[28]

In the particular context of the HER, previous theoretical and experimental studies have shown that some members of the MXene family are promising candidates for the HER.[18,29–34] However, these earlier computational studies assumed that the MXene basal plane functional group T_x consisted exclusively of either only –O or only –OH moieties, even though experimentally a diversity of –O, –OH, and –F moieties is detected.[35] Also, theoretical assessments point to mixtures of moieties as being energetically more stable.[36] In addition, MXenes have affinity towards H adatoms,[37] and water is an easy supplier of –H terminations,[38] even if it is difficult to unequivocally experimentally detect them. Actually, it is critical to realistically represent the MXene surface termination under HER working conditions of pH and applied potential, U. This aspect is crucial to understand the influence of the different types of functionalization in the HER potential determining step and the reaction mechanism. Here we focus on acidic environments, where proton (H^+) activity is larger, avoiding alkaline conditions where HER performance is found to be more sluggish.[39,40]

This is indeed tackled here on the prototypical Ti_3C_2 MXene, extensively experimentally synthesized with various functionalizations,[41–43] considering first the computed stability of hundreds of topologically different surface models with different ratios of –O, –OH, –H, and –F groups, used to build Pourbaix diagrams of surface termination stability dependent on pH and the applied potential, U. The obtained surface models suitable for HER conditions, considering both F-containing and F-free situations, allowed for a proper and detailed description of the reaction mechanism, highlighting (i) the presence of fluorine on the Ti_3C_2 surface unless obtained in F-absent situations, (ii) that, at variance with previous studies,[18,44–46] not only –O termination is regarded as a possible HER active site, but it may involve surface –OH groups, implying two different hydrogen sources, either protons (H^+) present in the medium, or surface H atoms, which make the reaction mechanism more complex, (iii) that –F groups can be beneficial at modulating the H bond strength, and not *per se* detrimental, and, finally, (iv) that the HER performance of the realistic models reveal that O-rich/OH-poor models, and stable ternary mixtures containing –F, –O, and –OH groups may lead to almost negligible estimated overpotentials, making such Ti_3C_2 terminated models excellent materials for the HER electrocatalysis.

2. Theoretical aspects

2.1. Computational details

The results reported in the present work were obtained from periodic density functional theory (DFT) calculations carried out using the Vienna *ab initio* simulation package (VASP).[47] The core electrons and their effect on the valence electron density were described by the projector augmented wave (PAW) method.[48] The exchange–correlation interaction was approximated by the Perdew–Burke–Ernzerhof (PBE) generalized gradient approximation functional.[49] A basis set of plane waves was used, employing a kinetic energy cutoff of 415 eV. An energetic electronic optimization convergence criterion of 10^{-5} eV was used, while atomic optimizations were finalized once all forces acting on atoms were below 0.01 eV $Å^{-1}$. The necessary numerical integrations in the reciprocal space were carried out using k-points Γ-centred Monkhorst–Pack meshes of 5 × 5 × 1 dimensions.[50] The effect of dispersion was accounted for using Grimme's D3 approach (PBE-D3).[51] Note that present and past test calculations varying the optimization thresholds, k-point density, and the size of the basis set led to variations in the total energy well below chemical accuracy, *i.e.*, below ~0.04 eV —1 kcal mol^{-1}.[52] Vibrational frequencies of H_2 molecule in vacuum (see below) and the corresponding ones in the terminated Ti_3C_2 models were obtained by construction and diagonalization of the Hessian matrix, whose elements were computed by finite differences of analytical gradients with finite displacements of 0.03 Å in length. Note that such frequencies were obtained only for the terminations and adsorbed species, while atoms in the Ti_3C_2 MXene substrate were kept fixed in the optimized geometry. In this way, vibrational degrees of freedom on the surface terminations and adsorbed moieties are decoupled from Ti_3C_2 phonons, an approximation with negligible impact in the computed frequencies.[37,38,52]

Pristine and fully –O, –OH, –H, and –F covered Ti_3C_2 were firstly evaluated using a $p(2 \times 2)$ supercell. The cases mixing different moieties were evaluated using either a $p(2\times2)$ or a $p(3 \times 3)$ supercell. A maximum monolayer (ML) coverage is defined when having one surface moiety per each surface metal atom, four or nine for the $p(2 \times 2)$ or a $p(3 \times 3)$ supercell, respectively. In the case of the $p(2 \times 2)$ supercell, $\frac{1}{2}$ ML *vs.* $\frac{1}{2}$ ML binary coverages were evaluated, as well as $\frac{1}{4}$ *vs.* $\frac{3}{4}$ of a ML. Ternary situations were explored as well, considering $\frac{1}{4}$, $\frac{1}{4}$, and $\frac{1}{2}$ of a ML. For the $p(3 \times 3)$ supercell $\frac{1}{3}$ *vs.* $\frac{2}{3}$ binary situations were

View Article Online
Journal of Materials Chemistry A Paper

examined, as well as ternary situations with $\frac{1}{3}$ of each component. The slab models contained 20 Å of vacuum to properly isolate the models explored.

2.2. HER reaction mechanisms

In general, there are two possible well-agreed mechanisms for the HER reaction, namely the Volmer–Tafel and Volmer–Heyrovsky mechanisms.[53] In both cases, the first step is the same, the Volmer step, where a proton, H^+, is reduced on the electrocatalytic surface by an electron, e^-;

$$H^+ + e^- + * \rightarrow H^*, \quad (1)$$

where * represents a surface electrocatalytic active site. However, the two mechanisms differ in the second step: in the Volmer–Tafel mechanism, the Tafel step implies that two previous Volmer steps have occurred, and, so, two reduced H* entities exist. These can then combine in a chemical step —with no further electron transfer—to create a H_2 molecule which is directly desorbed from the electrocatalyst surface;

$$2H^* \rightarrow H_2 + 2^*. \quad (2)$$

Notice that this mechanism is somehow similar to the Langmuir–Hinshelwood one in gas-phase heterogeneous catalysis, *i.e.*, all reactants must first adsorb, prior to the reaction among them. Furthermore, one should be aware that generally the Volmer–Tafel mechanism does not consider the H_2* moiety, *i.e.*, it assumes that whenever H_2 is formed, it automatically desorbs. Still, in case the H_2 molecule is moderately adsorbed, one could rephrase the full Volmer–Tafel mechanism as

$$(2\times)\ H^+ + e^- + * \rightarrow H^*, \quad (3)$$

$$2H^* \rightarrow H_2^* + *, \quad (4)$$

$$H_2^* \rightarrow H_2 + *. \quad (5)$$

In the Volmer–Heyrovsky mechanism, the second proton is reduced directly over the previously reduced proton of the previous Volmer step, directly generating, again, the H_2 molecule. Thus

$$H^* + H^+ + e^- \rightarrow H_2 + *. \quad (6)$$

Indeed, this mechanism is reminiscent of the Eley–Rideal mechanism in gas-phase heterogeneous catalysis; *i.e.*, only one reactant is adsorbed, and the other one directly attacks the adsorbed one from the gas phase. Still, the H_2* moiety is generally ignored, but the Volmer–Heyrovsky mechanism could be rewritten as

$$H^+ + e^- + * \rightarrow H^*, \quad (7)$$

$$H^+ + e^- + H^* \rightarrow H_2^*, \quad (8)$$

$$H_2^* \rightarrow H_2 + *. \quad (9)$$

In the present study we regarded all the possible reaction mechanisms and elementary reaction steps, although in most examples in the literature,[38,44–46] the Volmer–Heyrovsky was the only mechanism considered, and, moreover, regarding only the H reduction on fully O-terminated MXenes, like $Ti_3C_2O_2$, even when high H coverage situations were involved. Thus, in addition to O-termination, we regarded –H, –OH, and –F full terminations, and binary and ternary combinations of them, as explained above. Notice that the inclusion of –OH and –H terminations implies that the reaction sequence can involve hydrogen atoms from surface terminations. Thus, instead of starting through the reduction of one or two H^+ from the aqueous medium, for either Volmer–Heyrovsky or Volmer–Tafel mechanisms, the reaction may start through one or two H atoms of –OH and/or –H terminations. For example, on a –OH terminated Ti_3C_2, the Volmer–Heyrovsky reaction sequence could well be

$$H^+ + e^- + \text{–OH} \rightarrow \text{–O} + H_2^*, \quad (10)$$

$$H_2^* \rightarrow H_2 + *, \quad (11)$$

$$H^+ + e^- + \text{–O} \rightarrow \text{–OH}. \quad (12)$$

Notice that the direct formation of water upon a Volmer step on a surface –OH moiety has been disregarded as competitive since water removal requires the energetic cost of a surface O removal, plus free MXene surface sites are known to very easily adsorb H_2O and dissociate it.[38,54] While for the Volmer–Tafel mechanism, the formation of H_2 from two H atoms from –OH surface groups could occur first, and then followed by the regeneration of the –OH moieties. Thus

$$2\text{–OH} \rightarrow 2\text{–O} + H_2^*, \quad (13)$$

$$H_2^* \rightarrow H_2 + *, \quad (14)$$

$$(2\times)\ H^+ + e^- + \text{–O} \rightarrow \text{–OH}. \quad (15)$$

In the present work, all these alternative reaction step sequences have been thoroughly investigated in all the surface models, to have a clear, holistic picture of the reaction mechanism.

2.3. Thermodynamic approach

For any of the above-mentioned mechanisms, we first consider the reaction thermodynamic profile by calculating the Gibbs free energy of hydrogen adsorption, obviously considering only minima in the potential energy surface. Note that the deliberate use of this approach neglects further kinetic aspects, succinctly assuming that energy barriers are simply differences in Gibbs free energies between minima. This approach has to be taken with a grain of salt, since, on one hand, one neglects that electrochemical steps involve a transition state, and the involved energy barriers will be larger than Gibbs free energy differences. The thermodynamic approach can be justified from the Brønsted–Evans–Polanyi (BEP) relationship that usually holds true,[55,56] and so energy barriers would be linearly

View Article Online
Paper Journal of Materials Chemistry A

proportional to the Gibbs free energy difference, although bearing in mind the kinetics on the coupled proton–electron transfer steps may imply breaking these relationships. In any case, the kinetic aspects could be important, as shown, *e.g.*, in the chlorine evolution reaction (CER), oxygen evolution reaction (OER), and oxygen reduction reaction (ORR).[57,58] Further than that, other aspects could be critical in the proper HER performance, such as mass transport limitations.[7] In any case, such detailed analyses are out of the scope of the present study, which aims at determining how surface terminations affect the HER reaction landscape, and for that we rely on the thermodynamic approach as a first educated guess, as extendedly used in the past.[5,6,11–13,18,24–29]

Following the seminal work of Nørskov *et al.* introducing the computational hydrogen electrode (CHE),[59] one can consider standard equilibrium conditions of pH = 0, $U = 0$ V, temperature, T, of 298.15 K, and a partial pressure of H_2, p_{H_2}, of 1 bar. Under these standard working conditions, the complete HER pathway can be described as

$$H_{(aq)}^{+} + e^{-} \rightarrow \tfrac{1}{2}H_2^{(g)}, \Delta G^{\circ} = 0 \text{ eV}, \quad (16)$$

where the chemical potentials or Gibbs free energies of the initial state, that is $H_{(aq)}^{+} + e^{-}$, and that of the product, $\frac{1}{2}H_2^{(g)}$, are identical. Also, for any reaction intermediate, one can get the ΔG, *e.g.*, for adsorbed H*, one obtains ΔG_H as

$$\Delta G_H = \Delta E_H + \Delta E_{ZPE} - T\Delta S_H, \quad (17)$$

where ΔE_H is the reaction step energy difference, ΔE_{ZPE} the change in zero point energy (ZPE), and ΔS_H the change in entropy upon adsorption. The ΔE_H term can be easily obtained from the total energies obtained during the computational optimizations, so that

$$\Delta E_H = E_{nH/MXene} - E_{(n-1)H/MXene} - \tfrac{1}{2}E_{H_2}, \quad (18)$$

where $E_{nH/MXene}$ is the total energy of n H adatoms adsorbed on the MXene model, $E_{(n-1)H/MXene}$ the corresponding energy on a model having $n - 1$ H adatoms, and E_{H_2} the energy of a H_2 molecule in vacuum. Likewise, the ΔE_{ZPE} term is obtained as

$$\Delta E_{ZPE} = E_{nH/MXene}^{ZPE} - E_{(n-1)H/MXene}^{ZPE} - 1/2E_{H_2}^{ZPE}, \quad (19)$$

where $E_{nH/MXene}^{ZPE}$, $E_{(n-1)H/MXene}^{ZPE}$, and $E_{H_2}^{ZPE}$ are the ZPE energies of the MXene having n adsorbed H adatoms, $n - 1$ adsorbed H adatoms, or the H_2 molecule in vacuum, respectively. The ZPE energy term, E^{ZPE}, is obtained from the computed vibrational frequencies, so that

$$E_{ZPE} = \frac{1}{2}\sum_{i=1}^{NMV} h\nu_i, \quad (20)$$

where h is the Planck's constant, and ν_i the vibrational frequency of each of the normal modes of vibration (NMVs), taken, for a system having N atoms, as $3N - 5$ for the linear H_2 molecule in vacuum, and $3N$ for adsorbed atoms/molecules, since free translations and rotations become frustrated vibrational modes upon adsorption. Similar to ΔE_H, the ΔS_H term is calculated as

$$\Delta S_H = S_{nH/MXene} - S_{(n-1)H/MXene} - \tfrac{1}{2}S_{H_2}, \quad (21)$$

where $S_{nH/MXene}$, $S_{(n-1)H/MXene}$, and S_{H_2} are the entropies of the MXene model having n H adatoms, the MXene model having $n - 1$ H adatoms, and the H_2 molecule in vacuum, respectively. The gas phase entropy of H_2, 130.68 J mol^{-1} K^{-1} has been taken as tabulated in the National Institute of Standards and Technology (NIST) webbook,[60] while for the adsorbed moieties only the vibrational entropy, S_{vib}, is accounted for, given the ground state character and the aforementioned frustration of translations and rotations upon adsorption.[61] Thus

$$S = S_{vib} = k_B\sum_{i=1}^{NMV}\ln\left(1 - e^{-\frac{h\nu_i}{k_B T}}\right) - \sum_{i=1}^{NMV} h\nu_i\left(\frac{1}{e^{\frac{h\nu_i}{k_B T}} - 1}\right), \quad (22)$$

where k_B is the Boltzmann's constant.

2.4. Surface Pourbaix diagrams

The Pourbaix diagram analysis is a key aspect to be regarded since the diagrams provide information about the surface composition under electrocatalytic conditions. In the case of the studied MXenes they allow determining which is the thermodynamically most stable surface termination under working conditions of pH and U.[62] Details of the computational estimate of these diagrams can be found elsewhere,[63] but let us here briefly explain the procedure. For any surface composition, the ΔG of formation is obtained, using certain molecular references. In the present case, one uses $H_2^{(g)}$ and $F_2^{(g)}$ references at 1 bar and 298.15 K for –H and –F terminations, using the standard hydrogen electrode (SHE) and standard fluorine electrode (SFE) under equilibrium conditions, so that

$$H_{(aq)}^{+} + e^{-} \leftrightarrow \tfrac{1}{2}H_2^{(g)}, \quad (23)$$

$$\tfrac{1}{2}F_2^{(g)} + e^{-} \leftrightarrow F_{(aq)}^{-}. \quad (24)$$

Here, values of 0 and −2.87 eV are used for the reduction potentials of hydrogen, U, and of fluorine, U_F, respectively.[64] In the case of –OH and –O terminations, water vapor is used as a reference, taken at 0.035 bar and 298.15 K, conditions under which water vapor is in equilibrium with liquid water, that is, their chemical potentials or Gibbs free energies are equal.[59] The computational Pourbaix diagram construction makes use of the CHE[63] and the computational fluorine electrode (CFE), so that, under the aforementioned equilibrium conditions

$$\mu\left(H_{(aq)}^{+}\right) + \mu(e^{-}) = G\left(H_{(aq)}^{+}\right) + G(e^{-}) = \frac{1}{2}G\left(H_2^{(g)}\right), \quad (25)$$

$$\mu\left(F_{(aq)}^{-}\right) - \mu(e^{-}) = G\left(F_{(aq)}^{-}\right) - G(e^{-}) = 1/2G\left(F_2^{(g)}\right), \quad (26)$$

where μ and G are simply the chemical potentials or Gibbs free energies of the specified species.

Making use of these references and of the gas phase ones, one can calculate the formation energy of a given surface termination at zero pH and U, $\Delta G(0,0)$, as

$$\Delta G(0,0) = \Delta G = \Delta E + \Delta E_{ZPE} - T\Delta S, \quad (27)$$

with the different contributions obtained in a similar fashion as detailed above for ΔG_H, and gas phase molecule entropy taken from thermodynamic tables.[65] Once $\Delta G(0,0)$ is obtained, the pH and U dependent ΔG, $\Delta G(\mathrm{pH},U)$, can be obtained, as derived,[63,66] from the following equation:

$$\Delta G(\mathrm{pH},U) = \Delta G(0,0) - \upsilon(\mathrm{H}^+)k_B T \ln 10\ \mathrm{pH} - \upsilon(\mathrm{e}^-)eU - \upsilon(\mathrm{F}^-)eU_F, \quad (28)$$

where $\upsilon(\mathrm{H}^+)$, $\upsilon(\mathrm{F}^-)$, and $\upsilon(\mathrm{e}^-)$ are the stoichiometric coefficients of the formation chemical equation. As an example, let us take a $p(3 \times 3)$ slab with 9 free surface sites, *. Thus, the formation of a surface having 3 O* and 6 F* would read as

$$3H_2O + 3F_2 + 9^* \rightarrow 3O^* + 6F^* + 3H_2, \quad (29)$$

for the $\Delta G(0,0)$ term considering gas phase species, but when considering pH and U, and the presence of H^+ and F^- species in solution, the equation can be rewritten as

$$3H_2O + 6F^- + 9^* \rightarrow 3O^* + 6F^* + 6H^+ + 12e^-, \quad (30)$$

where $\upsilon(\mathrm{H}^+)$, $\upsilon(\mathrm{F}^-)$, and $\upsilon(\mathrm{e}^-)$ would be 6, −6, and 12, respectively.

Following the above recipe, one can get the ΔG for any surface termination as a function of pH and U. Thus, the relative stability of different terminations under realistic conditions can be determined, the most stable at a given pH and U being the one with the lowest ΔG. Such info can be used to draw the Pourbaix diagrams by either making a fine grid of points and evaluating ΔG values of all the explored situations while taking the minima, or finding equilibrium lines in between competing surface terminations, for conditions in between phases A and B where $\Delta G(\mathrm{A}) = \Delta G(\mathrm{B})$. Note that, computationally, one can directly relate the computed ΔG_s when using the same supercell; however, it is worth pointing out that, when using different supercells, ΔG_s must be normalized and compared as given per surface area.

3. Results and discussion

3.1. Surface termination analysis

Prior to finding suitable models for evaluating the HER on Ti_3C_2 MXene, the four different surface termination moieties, namely –O, –OH, –H, and –F were considered on the Ti_3C_2 $p(3 \times 3)$ supercell at high-symmetry top metal (T), bridge (B), three-fold hollow C (H_C), and three-fold hollow Ti (H_{Ti}) positions, see Fig. 1, thus sampling at low-coverage regimes. Along with previous records with the same computational setup,[37,38,52] the H_{Ti} site is regularly preferred. To further confirm the preference of surface termination moieties towards H_{Ti} sites, the full –OH terminated and a mixture of $\frac{2}{3}$ of –O and $\frac{1}{3}$ of –OH were examined here, both occupying H_C or H_{Ti}, finding a clear preference for the latter by −0.23 to −0.64 eV per moiety unit, respectively, see Fig. S1 in the ESI.† Accordingly, the posterior surface termination samplings were examined only on H_{Ti} sites.

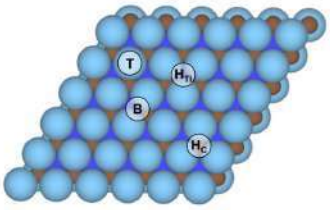

Fig. 1 Top view of the Ti_3C_2 MXene model (0001) surface, where brown spheres denote C atoms, and light and dark blue spheres surface and subsurface Ti atoms, respectively. High-symmetry sites are tagged.

In this way, 95 different surface terminations were explored considering mono, binary, and ternary situations combining –OH, –O, –H, –F, and free sites. For binary and ternary cases, different surface compositions were also considered, and for each one, different topologically distinct arrangements were studied, see Fig. S2–S7 in the ESI,† leading to a final number of 385 distinct surface terminations, making the present study the most complete so far regarding Pourbaix diagram evaluation of the Ti_3C_2 MXene model (0001) surface.[63]

Let us start the discussion with the simplest Pourbaix diagrams, regarding only full coverage situations of –O, –OH, –H, or –F. Fig. 2 shows two versions either considering F-free synthesis, thus in the absence of fluorine anions,[67–69] or regarding fluorine explicitly useful, *e.g.*, for MXenes synthesized using HF or *in situ* HF.[19–21] The Pourbaix diagrams in Fig. 2 agree with previous assessments,[18,70] particularly in the sense that generally the Ti_3C_2 (0001) surface is O-terminated at positive U with respect to the reversible hydrogen electrode (RHE) reference, or, in other words, above the HER equilibrium potential line, noting that, just below it, the –OH termination is preferred, in accordance with a favorable H^+ reduction. Only at very negative potentials the H-termination becomes preferable, while free surface metal sites without termination are never found to be preferred. The equilibrium line in between –O and –OH terminations is actually very close to the HER equilibrium line, which suggests the existence of binary systems in between. Finally, note that –F has a small, yet key region of influence around the HER equilibrium line, particularly for very low pH values, up to pH = 2, exactly the region where HER conditions are sought, *i.e.*, U values close to the HER equilibrium line, and a strong acidic medium, with a high concentration of H^+ reactant. Thus, binary and even ternary surface terminations are in principle to be considered in duly modeling the HER on the Ti_3C_2 (0001) surface, and at this stage only free sites and –H terminations could be, in principle, ruled out, unless working at very low U.

In order to explicitly address this issue, the aforementioned mixed terminations were considered, and the resulting

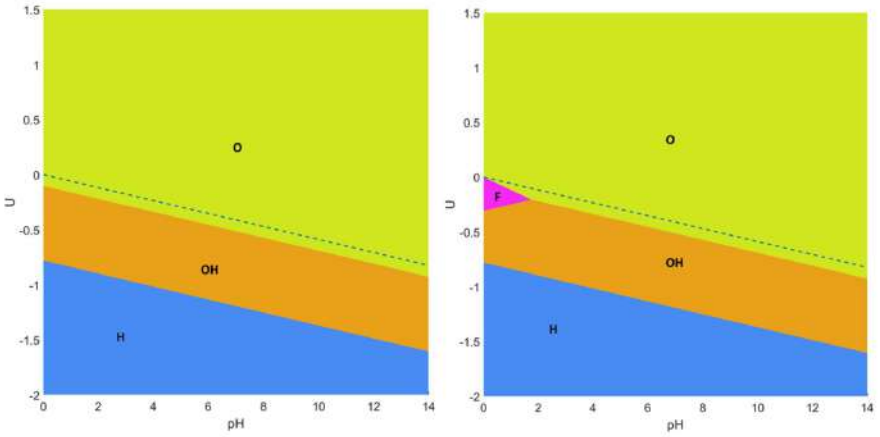

Fig. 2 Pourbaix diagrams for the Ti_3C_2 MXene (0001) surface regarding fully –O, –OH, and –H terminated surfaces (left), or including as well fully –F terminated surfaces (right). Regions of preferred stability are colored and tagged. The blue, dashed line indicates the HER equilibrium potential using the RHE.

Pourbaix diagrams, either for F-containing or F-free situations, are shown in Fig. 3. From these diagrams, several aspects need to be pointed out. On one hand, the large regions of fully –O, –OH, or –H terminations as observed in the simplified Pourbaix diagrams of Fig. 2 are not realistic, and mixed situations constitute actually the preferred situation in the vicinity of the HER equilibrium line. Thus, the O-termination just above the HER equilibrium line, commented when discussing Fig. 2, is indeed an O-rich case, but containing a fraction of OH moieties, as observed by the sequential preference of the $O_{2/3}OH_{1/3}$ model, followed by the $O_{3/4}OH_{1/4}$ model, and only fully –O terminations are found *ca.* 0.4 V above the HER equilibrium line. Likewise, the –OH region under the HER equilibrium line in Fig. 2 is, in fact, an OH-rich mixture as denoted firstly by the

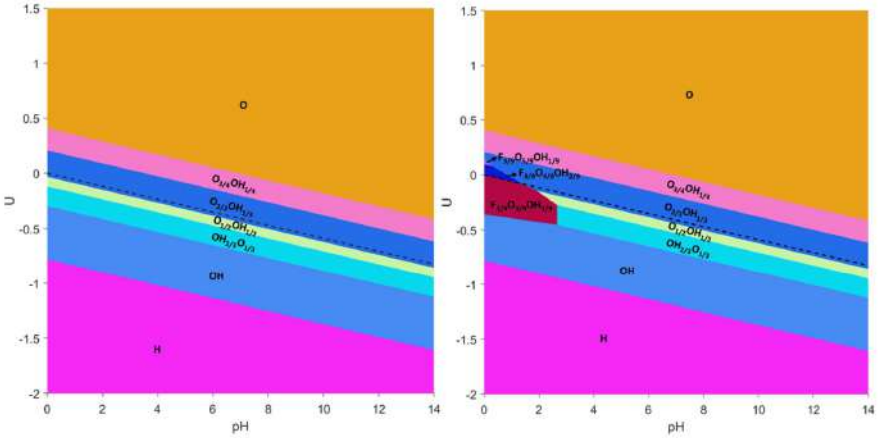

Fig. 3 Pourbaix diagrams for the Ti_3C_2 MXene (0001) surface regarding all single, binary, and ternary surface compositions including –O, –OH, –H, and –F terminations, as well as free sites. The left image corresponds to situations without any –F termination, while the right image corresponds to situations when considering –F termination. The black, dashed line indicates the HER equilibrium potential with respect to the RHE reference.

View Article Online
Journal of Materials Chemistry A Paper

$OH_{1/2}O_{1/2}$ model, followed by the $OH_{2/3}O_{1/3}$ model, and only the fully –OH model is found *ca.* −0.3 V below the HER equilibrium line. Only by going to more negative potentials, more than −0.8 V below the HER equilibrium line, would one reach the fully –H terminated model.

Moreover, the present F-free Pourbaix diagram, see Fig. 3, reinforces previous assessments[18,63] in which in the vicinity of HER equilibrium conditions the Ti_3C_2 (0001) surface involves a mixture of –O and –OH terminations, –OH rich at *U* values more negative than HER equilibrium line and –O rich at U values more positive than HER equilibrium line, but essentially ruling out having fully –O terminated Ti_3C_2 as a viable model for the HER.[71,72] Furthermore, the –OH termination is just preferred over a certain potential margin, and not stable at very low potentials as sometimes claimed in the literature,[18] neither essentially non-existing as pointed out in others,[63] plus the fully –H termination is viable at very low potentials, rather than the ideal, non-terminated surface.[18]

Still, the obtained Pourbaix diagram underscores the O-affinity of the Ti_3C_2 (0001) surface, plus the H-affinity of $Ti_3C_2O_2$, given the appearance of a certain ratio of –OH moieties above the HER equilibrium line. As forecasted from fully single-terminated situations in Fig. 2, the Pourbaix diagram becomes disrupted when regarding –F moieties, see Fig. 3. There, one has to first highlight the stability of the $F_{1/3}O_{1/3}OH_{1/3}$ model up to a pH of 2.87 and particularly close but below the HER equilibrium line, shown as a black dashed line in Fig. 3, with the region of prevalence of $F_{1/3}O_{1/3}OH_{1/3}$ being exactly the ideal conditions to carry out the HER. Actually, a previous study[73] claimed that the HER catalytic activity of Ti-based MXenes is experimentally and computationally correlated with the ratio of –F and –O functional groups, where large amounts of –F show poor catalytic activity and selectivity compared to low amounts of –F, plus the observation that a monotonous increase of –O termination increases the electrochemical potential.

In any case, the above commented Pourbaix diagram already underscores the need to account for such –F moieties, at least on $Ti_3C_2T_x$, when obtained through F-containing synthetic procedures. To further inspect this, additional ternary models containing –F, –O, and –OH moieties were calculated by increasing or decreasing the –O/–OH ratio, that is, through $F_{3/9}O_{5/9}OH_{1/9}$, $F_{3/9}O_{4/9}OH_{2/9}$, $F_{3/9}O_{2/9}OH_{4/9}$, and $F_{3/9}O_{1/9}OH_{5/9}$ models. These four models involved the systematic exploration of the topologically different arrangements, see Fig. S8 and S9 in the ESI,† accounting for 64 extra surface terminations. The impact of these terminations is only observed at very low pH and just above the HER equilibrium line, where small regions are observed for the $F_{3/9}O_{4/9}OH_{2/9}$ and $F_{3/9}O_{5/9}OH_{1/9}$ models, in which the presence of –F is maintained, while the surface becomes –O richer at the expense of the –OH groups. In any case, Fig. 3 reveals a number of surface terminations that could be relevant in the HER, either for F-containing or F-free $Ti_3C_2T_x$.

One still has to keep in mind that the present Pourbaix diagrams are the result of a series of terminations and topological arrangements that are anyway constrained by the employed supercells, and so, other arrangements could and would be possible. Besides, situations shown in Fig. 3 correspond to the most stable cases, but there are other arrangements which are close in energy that could well be appearing on the surface, especially when having in mind the inherent energy accuracy limitation of DFT-based calculations. Thus, a number of close possibilities should be regarded when inspecting the HER on $Ti_3C_2T_x$, as shown in detail below.

Last but not least, when considering the terminations in Fig. 2 and 3 for electrocatalytic HER applications, one should first regard whether the material remains conductive, or becomes a semiconductor, since the latter would handicap the electronic transference. To tackle this issue, the density of states (DOS) and projected DOS (PDOS) were obtained and are shown in Fig. S10 of the ESI,† revealing, briefly, that pristine Ti_3C_2, any fully terminated $Ti_3C_2T_x$, and any binary or ternary combinations of surface terminations lead to a metallic system, with the characteristic bonding, non-bonding, and anti-bonding regions of parent three-dimensional transition metal carbide (TMC) bulk structures,[74] with the participation of Ti d orbitals, C and T_x = O, OH, F p orbitals, and H s orbitals. Notice that by mixing Ti d states with O, OH, F p or H s orbitals, new states appear close to the Fermi level, E_F, arising from terminations, which may have a key impact in the H^+ adsorption, and, consequently, on the HER electrocatalysis.

Aside from the above, charge density difference (CDD) plots, shown in Fig. S11 of the ESI,† reveal that, while Ti atoms become positively charged at the expense of giving their electron density to C atoms,[75] any –O, –OH, –H and –F groups also become negatively charged, again at the expense of the electron density of surface Ti atoms. This leads to charge accumulations which are more prominent for –O terminations, compared to –F and –OH groups, in line with a formal $-2e$ charge of O adatoms, while –F and –OH would have a charge close to $-1e$. In the case of –H, there is some electron accumulation, but more attenuated. Finally, on the binary and ternary systems, one clearly observes charge distributions, which can be easily interpreted as compatible with local rearrangements similar to the just mentioned full-terminated cases.

3.2. HER electrocatalysis mechanisms

Having established the surface stabilities through the computationally derived Pourbaix diagrams, and the overall electronic picture, it is now the turn of inspecting the HER performance on selected, representative cases. Let us begin with pristine Ti_3C_2 and fully terminated cases, that is, with –O, –OH, –F, and –H terminations. As aforementioned, both Volmer–Heyrovsky and Volmer–Tafel mechanisms are studied, and also considering the possible involvement of H atoms from –H and –OH terminations. Fig. 4 shows the Gibbs free energy reaction profiles for these five cases under standard working conditions —T = 298.15 K, p_{H_2} = 1 bar, pH = 0, U = 0 V— regarding different reaction mechanisms and sequences, depending on whether surface termination coming from –H or –OH groups is involved or not.

Let us first inspect the most extreme surface termination, which would be pristine Ti_3C_2. Pristine Ti_3C_2 is excessively chemically active, binding too strongly to the H adatom, with

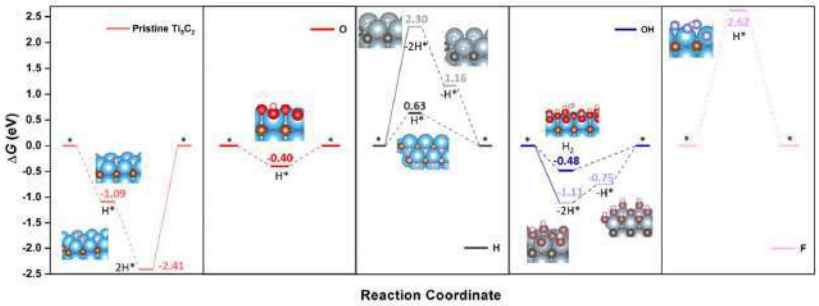

Fig. 4 Gibbs free energy, ΔG, diagram of the HER on pristine or fully –O, –OH, –F, or –H terminated Ti_3C_2 (0001) surface under standard working conditions. Solid lines represent the chemical step of the as-generated H_2 desorption, while dashed lines represent the electrochemical steps of proton coupled electron transfer (PCET). Inset images are side or eagle-eye views of the reaction intermediates, except for the H* state on –H termination, which depicts a top view to better observe the H* allocation on a surface empty H_C site. Color coding as in Fig. 1, plus H, O, and F atoms are shown as white, red, and violet spheres. Preferred reaction mechanism and associated images are shown with bright coloring, while shadowed colors and images refer to other, non-preferred mechanisms.

sequential computed ΔG_s of −1.09 and −1.32 eV for the reduction of two protons following a Volmer–Tafel mechanism. Even though the two proton coupled electron transfers (PCETs) are energetically downhill, the formation of $H_2^{(g)}$ through the H* recombination in a chemical step is uphill by 2.41 eV, which implies a prohibitive annealing while trying to maintain the electrochemical conditions. Here basically the pristine Ti_3C_2 (0001) surface would be too reactive, and would successively reduce protons or hydroxyl groups coming from water so as to achieve a suitable surface termination according to the Pourbaix diagram (*cf.* Fig. 3). On the other extreme, one would have the –F terminated Ti_3C_2 surface with a severely decimated H-affinity, and a greatly unfavored first H^+ reduction, with a ΔG = 2.62 eV, which could only work by applying a negative U of −2.62 V to lower the first electron transfer. The second PCET would rather follow here the Volmer–Heyrovsky mechanism. This result goes along with the aforementioned statement that large amounts of –F surface moieties imply poorer electrocatalytic activities and selectivities.[73]

Focusing on more suited surface terminations, the –O termination chemical activity gets attenuated in a large proportion, featuring a ΔG of −0.40 eV for first H^+ reduction following the Volmer–Heyrovsky mechanism, thus requiring a U of −0.40 V to reduce the energetic costs of the second PCET, although at such overpotentials, the Ti_3C_2 surface would be mostly terminated by –OH groups, see Fig. 2 and 3. Actually, when inspecting –OH termination, the reaction energetics and mechanism already become more complicated. On one hand, one could consider a situation where two neighboring –OH termination moieties react to create two –O moieties plus a $H_2^{(g)}$ molecule. This chemical step has a ΔG of −1.11 eV, and would be followed by two consecutive H^+ reductions on the as-generated –O termination sites to regenerate the electrocatalyst surface. In the literature, the corresponding overpotential is calculated, whenever considered, assuming that both H^+ reduction steps are equally costly, and so the applied overpotential would be *ca.* −0.56 V, while the direct H^+ reduction on an –OH surface moiety, following a Volmer–Heyrovsky mechanism, to directly generate $H_2^{(g)}$ has a ΔG of −0.48 eV, to be followed by the reduction of a H^+ on the as-generated –O moiety to regenerate the electrocatalyst surface.

By this simpler view, one would consider that both mechanisms, considering one or two –OH terminations, could be somewhat competitive, differing by only 0.08 eV in the potential determining step, with a preference though on the Volmer–Heyrovsky mechanism. However, a closer inspection of the mechanism involving two surface –OH terminations leads to an easier first H^+ reduction, with a ΔG of 0.36 eV, while the second H^+ reduction is more costly, with a ΔG of 0.75 eV, acting as a rate and potential determining step. Thus, a Volmer–Heyrovsky reaction sequence as depicted in eqn (10)–(12) seems to be the most preferred one in –OH terminated Ti_3C_2, with a U of 0.48 V, in line with the overpotential of the OH-terminated phase as seen in the Pourbaix diagrams of Fig. 3.

Finally, in the H-terminated model, the Volmer–Tafel mechanism involving first the –H moiety recombination is found to be energetically quite costly, by 2.30 eV, making it prohibitive, even though the posterior electrocatalyst regeneration is quite downhill, with first and second H^+ reduction steps involving ΔG_s of −1.14 and −1.16 eV, respectively. Actually, on a fully H-terminated Ti_3C_2 (0001) model, the first H^+ reduction is a Volmer step, occupying a H_C site, with no direct formation of $H_2^{(g)}$, and with a ΔG of 0.63 eV, while the second H^+ reduction would follow a Heyrovsky step. Note here as well that the potential determining step implies a U of −0.63 V, which is close to the region of prevalence of –H termination on the Pourbaix diagrams, see Fig. 3.

However, as seen in Fig. 3, at low pH and seeking low U working values, one should not use the fully terminated models, and consider models with binary and/or ternary situations, depending on whether one would have fluorine or not. This is evaluated in Fig. 5 for a list of suitable terminations derived

View Article Online
Journal of Materials Chemistry A
Paper

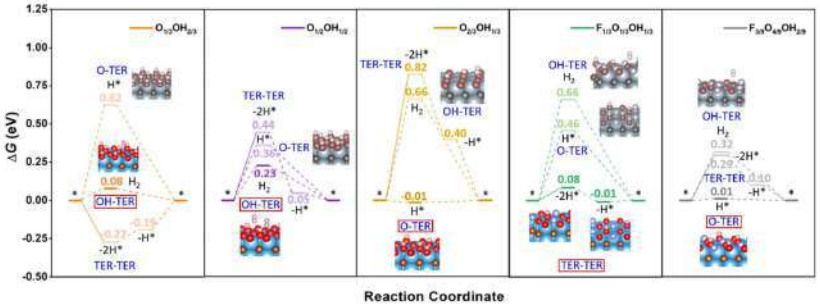

Fig. 5 Gibbs free energy, ΔG, diagram of the HER on selected binary and ternary terminations of the Ti_3C_2 (0001) surface combining –O, –OH, and –F moieties, under standard working conditions. Solid lines represent the chemical step of the as-generated H_2 desorption, while dashed lines represent the electrochemical PCET steps. Color coding as in Fig. 4.

from the realistic Pourbaix diagrams including F-free $O_{1/3}OH_{2/3}$, $O_{1/2}OH_{1/2}$, and $O_{2/3}OH_{1/3}$, but also the F-containing $F_{1/3}O_{1/3}OH_{1/3}$ and $F_{3/9}O_{4/9}OH_{2/9}$ models. Focusing on F-free models, one has different proportions of –O and –OH moieties, but their mutual existence opens three possible reaction mechanisms; (i) the H^+ reduction occurs on an –O site, followed by a Heyrovsky step on top to directly generate $H_2^{(g)}$, hereafter denoted as O-TER, (ii) the H^+ reduction occurs on a –OH site, following a Heyrovsky step, and a subsequent H^+ reduction on the as-generated free –O site, hereafter denoted as OH-TER, and (iii) a Tafel step between two surface –OH moieties, followed by two subsequent Volmer steps to regenerate the –OH sites, by reducing the as-freed –O sites, named TER–TER.

Keeping this in mind, the $O_{1/2}OH_{1/2}$ model shows a TER–TER profile where $H_2^{(g)}$ formation is moderately costly, by ΔG = 0.44 eV, followed by two consecutive H^+ reductions with ΔG values of −0.39 and −0.05 eV, respectively. Actually, the first chemical step in this mechanism is unavoidably endergonic, and cannot be reduced by a potential application, which could otherwise lower the electrochemical steps just by applying a U of −0.05 V. This does not happen in either the OH- or the O-TER mechanism. In the latter, the first Volmer step has a positive ΔG of 0.36 eV, higher than that of the Heyrovsky step of OH-TER of ΔG 0.23 eV. Thus, the OH-TER path could make the full process exergonic by applying a U of −0.23 V, close to the $O_{1/2}OH_{1/2}$ stability region on the F-free Pourbaix diagram in Fig. 3.

The results discussed just above involve a model with equal number of –OH and –O groups; by unbalancing this ratio by having more –O groups, like in the $O_{2/3}OH_{1/3}$ model, see Fig. 5, the TER–TER mechanism gets more endergonic in the first Tafel step, with a ΔG of 0.82 eV, and even the first replenishment H^+ reduction Volmer step, with ΔG of −0.42 eV, is located 0.40 eV above the equilibrium ΔG = 0 eV line, and so a U of −0.42 V would be needed to make the full process exergonic. The same situation is found in the OH-TER mechanism, where the first Heyrovsky step involves a ΔG up to 0.66 eV. Thus, compared to the $O_{1/2}OH_{1/2}$ model, the Tafel step increases in free energy by 0.38 eV and the OH-TER Heyrovsky step by a similar 0.43 eV. On the other hand, compared to the U of −0.23 V in the $O_{1/2}OH_{1/2}$ model, the O-TER step has a first Volmer step of solely −0.01 eV, implying the need of a U only slightly more negative than −0.01 V to make the full process exergonic. Clearly, the imbalance towards increasing the number of –O moieties favours the O-TER mechanism, while it is a handicap to the other mechanisms involving –OH moieties, namely, the OH-TER and TER–TER, plus the resulting overpotential falls well within the stability region of the $O_{2/3}OH_{1/3}$ model, quite in the HER equilibrium line, see Fig. 3.

Compared to the $O_{1/2}OH_{1/2}$ model, when the –O/–OH ratio imbalance is applied in the other direction, that is, when having more –OH moieties than –the O ones, as in the $O_{1/3}OH_{2/3}$ model, the O-TER is destabilized, with a first Volmer step rising up 0.26 eV up to a value of 0.62 eV. On the other hand, the OH-TER path gets its Heyrovsky step stabilized by 0.15 eV to a final value of ΔG = 0.08 eV. Finally, the TER–TER path changes from being quite endergonic in the recombination chemical step of 0.44 eV in the $O_{1/2}OH_{1/2}$ model, to sensibly exergonic by −0.27 eV in the OH-rich $O_{1/3}OH_{2/3}$ model. In the last situation, the OH-TER path is preferred, with a potential determining step of U = −0.08 V, while on the TER–TER path, a U of −0.19 V for the second PCET is required to make the full process exergonic. Particularly, the overpotential of the last mechanism falls within the $O_{1/3}OH_{2/3}$ stability line as shown in the Pourbaix diagram of Fig. 3.

Up to this point, we tackled F-free models only, but the question regarding the effect of –F moieties on the HER performance remains open. Let us first address the $F_{1/3}O_{1/3}OH_{1/3}$ model which is the most stable one at low pH and low U with respect to the RHE (*cf.* Fig. 3). Here one can compare with the $O_{2/3}OH_{1/3}$ reference, where half of the –O moieties are replaced by –F groups. Consequently, the observed stabilization of the O-TER path under the O-rich conditions in the $O_{2/3}OH_{1/3}$ model is decimated and, consequently, the H* intermediate after a Volmer step involves a ΔG increase of 0.47 eV up to a final value of 0.46 eV. A similar effect is observed on the OH-TER and

TER–TER paths when compared to the OH-rich $O_{1/3}OH_{2/3}$ reference. The stabilization of such paths involving –OH groups is now hampered, making it rise the Heyrovsky step of OH-TER by 0.58 eV up to a final value of 0.66 eV. However, this is not so adverse for the TER–TER path, which was slightly exergonic. In the $F_{1/3}O_{1/3}OH_{1/3}$ model, the chemical H* recombination step is barely endergonic by 0.08 eV, and the potential determining step is the second recovering Volmer step requiring only a U of −0.01 V, ideally fitting in the model stability region shown by the Pourbaix diagram (*cf.* Fig. 3), and essentially matching the HER equilibrium potential *vs.* RHE. Here the –F surface moiety has no longer been considered as the active site given the very high overpotential found in the fully –F terminated model of 2.62 V compared to the values of 0.40 and 0.48 V for fully –O and –OH models. Besides, charge density difference (CDD) plots in Fig. S11 of the ESI† reveal a lower electron accumulation on –F moieties compared to –O and –OH groups, implying that the former is less attractive towards H^+ reactants.

Further support to the –O termination role favouring the O-TER path is provided by the $F_{3/9}O_{4/9}OH_{2/9}$ model, where a –OH moiety is substituted by an –O one. From the previous reasoning, it should stabilize O-TER, and that is indeed what happens. In going from the $F_{1/3}O_{1/3}OH_{1/3}$ to the $F_{3/9}O_{4/9}OH_{2/9}$ model, O-TER gets stabilized by 0.45 eV to a final ΔG value of the Volmer step of solely 0.01 eV. On the other hand, the TER–TER path is no longer the preferred patch, since the Tafel step is more endergonic, by 0.21 eV up to a value of 0.29 eV, and the subsequent first Volmer step is 0.10 eV above the HER equilibrium, requiring a U of −0.10 V to make the full electrochemical steps exergonic. With respect to the OH-TER path, it still gets disfavoured, with an initial Heyrovsky step of 0.32 eV. In any case, the F-containing models are those that adjust best their U with the HER working conditions.

Having analysed the influence of mixed terminations on several HER mechanisms, one may wonder whether the standard Volmer–Tafel path could be competitive on such models. Fig. 6 shows that, for the fully O-terminated case, the binary and ternary models would require working at excessively low U overpotentials. The standard Volmer–Tafel path has not been considered for pristine Ti_3C_2 since it is excessively active, *vide supra*, whereas the fully F-terminated case has also been disregarded since it is excessively inactive (*cf.* Fig. 4). Also, the fully OH-terminated case has not been investigated because there is simply no room for Volmer steps and this is also the situation for the fully H-terminated case. Inspecting the profiles in Fig. 6, one realizes that PCET steps are exergonic in the fully O-terminated case, because of the strong affinity towards H. Note that this termination would be only stable at high U values, see Fig. 3. As per the binary and ternary cases, the Volmer steps are quite endergonic for $O_{1/3}OH_{2/3}$, $O_{1/2}OH_{1/2}$, and $F_{1/3}O_{1/3}OH_{1/3}$, with potential determining steps with U values of −0.74, −0.74, and −0.58 V, respectively. The $F_{3/9}O_{4/9}OH_{2/9}$ model is not so endergonic, but with a sensible U value of −0.46 V. Indeed, the only viable Volmer–Tafel mechanism is found in the case of $O_{2/3}OH_{1/3}$, with very low ΔG_H values for the two consecutive Volmer steps, and a U value of solely −0.09 V, competitive to the value of −0.01 V for the same model following the O-TER Volmer–Heyrovsky mechanism, but not preferred to this last one, though. Thus, except perhaps for the last commented possible competitive pathway, the standard Volmer–Tafel mechanism is not preferred in any of the explored models, but other sequencing of the mechanisms, like the TER–TER, are actually favourable in some models as already commented.

3.3. HER electrocatalysis performance

All in all, an optimal HER catalyst should have a very small ΔG_H, ideally going to 0, implying no overpotential. This is because an excessively low ΔG_H makes it difficult for H* adatoms to combine and form H_2, while excessively positive ΔG_H leads to slow HER kinetics.[76] In general, it is well accepted that a good HER activity would follow the classical rule of $|\Delta G_H| < 0.2$ eV,[77] adopted as well in discussing the present calculations. On the other hand, F-free models can also display very low U values, ranging from −0.01 to −0.23 V, while these overpotentials are either within or close to those where the stability regions of the considered models lie, meaning that these can be regarded as valid, in particular when accounting for the DFT inherent accuracy, *vide supra*.

Thus, having –F groups on the surface is not necessarily detrimental, and indeed helps understanding previous experimental observations,[73] in the sense that large –F coverages, approaching the full –F situation, make HER unpracticable. However, according to the present study, low coverages of –F moieties, like $F_{1/3}$, can further improve the HER process by reducing the $|\Delta G_H|$ constraint beyond that encountered in the F-free situations. This is probably due to subtle lateral interactions, and also helping to avoid having patches of only –O termination, which became excessively active towards H leading to a passivated surface. Aside from this, the observed increase of concentration of –O moieties is beneficial for the HER,[73] but up to a certain degree, *e.g.* $O_{2/3}$, since a fully O-terminated situation is too active towards hydrogen, plus actually not stable under working conditions according to the Pourbaix diagrams in Fig. 3.

With the previous reaction profiles, one can get estimates of the theoretical overpotential, $\eta = U_{RHE} - U$, at which the HER could be carried out. These are encompassed in Tables 1 and S1 of the ESI† for the most likely reaction mechanism, and the values represented in Fig. 7 on a typical volcano plot,[78] where the abscissa represents the ΔG_H descriptor while the ordinate represents the overpotential. Notice that values on the left and right branches of the volcano plot represent strong and weak H* adsorptions, respectively. In any case, one can readily observe that any Ti_3C_2 MXene with mixed termination groups feature better HER activity than those fully terminated, and that, in particular, F-free O-rich situations such as the one in the $O_{2/3}OH_{1/3}$ model, and F-containing situations as in the $F_{1/3}O_{1/3}OH_{1/3}$ and $F_{3/9}O_{4/9}OH_{2/9}$ models appear to be optimal for the HER, the latter being stable under the working conditions of applied potential, see Pourbaix diagrams in Fig. 3.

According to the previous discussion, some of the Ti_3C_2 terminated MXenes could be competitive or even better electrocatalysts for the HER when compared to other materials

View Article Online
Journal of Materials Chemistry A Paper

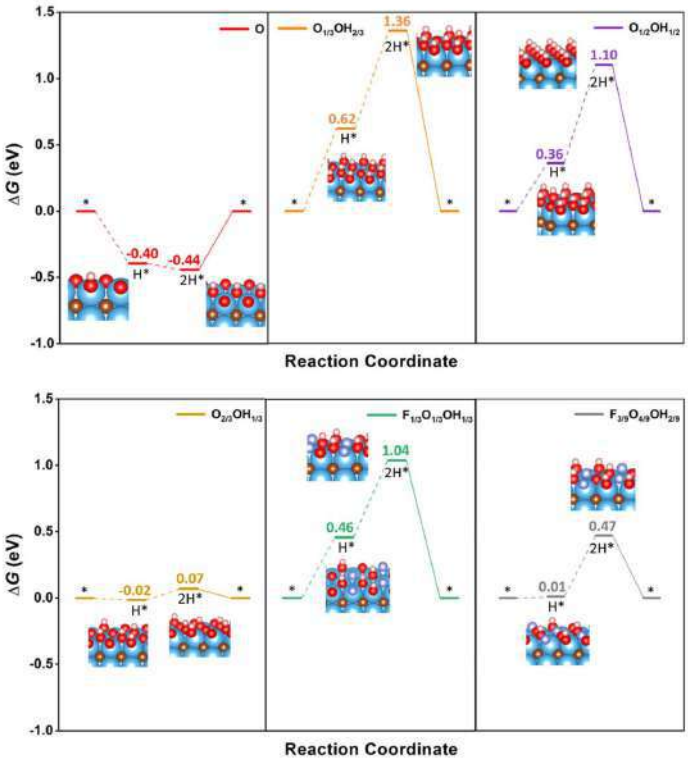

Fig. 6 Gibbs free energy, ΔG, diagram of the HER on selected binary and ternary terminations of the Ti_3C_2 (0001) surface combining –O, –OH, and –F moieties, under standard working conditions, following the standard Volmer–Tafel mechanism sequence. Solid lines represent the chemical step of the as-generated H_2 desorption, while dashed lines represent the electrochemical PCET steps. Color coding as in Fig. 4.

reported in the literature, estimated, *e.g.*, with similar DFT exchange–correlations and coverages, including Pt,[79] MoS_2,[80] WS_2,[81] graphitic carbonitride with N-doped graphene, *i.e.*, C_3N_4@NG,[82] and C_3N material,[83] to include just some of the most prominent ones. In particular, as stated above, situations corresponding to the $O_{2/3}OH_{1/3}$, $F_{1/3}O_{1/3}OH_{1/3}$, and $F_{3/9}O_{4/9}OH_{2/9}$ models appear to be the optimal cases, even if accounting for DFT inherent accuracy. Thus, proper surface terminated Ti_3C_2 MXenes emerge as a promising material for the HER, especially when accounting for their high surface area, abundance and lightness of the constituent elements, which fosters high performances per unit area or materials grams. Still, one should not consider these as definitive situations, but rather as indicative, since other stoichiometries and arrangements surely exist which are not regarded in the present study when constructing the Pourbaix diagrams, and also regarding the inherent accuracy of DFT. But, clearly, O-rich binary terminations admixing –O and –OH groups can be claimed as responsible for a good HER activity at low pH and F-free conditions, while ternary systems mixing –F, –O, and –OH groups are responsible for the same performance in F-containing situations.

Last but not least, one could attempt at understanding the main trends favoring the predicted HER mechanism. This is tackled here by calculating the Bader charges of the termination groups, as shown in Fig. 8. Let us consider first binary situations with different ratios of –O and –OH surface groups. As observed in Fig. 8, the negative net charge of –O groups increases with the –O ratio, and would reach a limit of $-1.09e$ for a fully O-terminated model. Inversely, the negative net charge of –OH groups decreases when the O concentration increases (or the OH one decreases), from an ideal value of $-0.73e$ for the fully OH-terminated case. Thus, the larger the net negative charge on –O moieties, the stronger the H^+ attraction and, consequently, the more stable the H* becomes. However, a suitable value of -0.01 eV is found for $O_{2/3}OH_{1/3}$, since fully O-terminated Ti_3C_2 attaches the H adatoms too strongly, with a ΔG_H of -0.40 eV, which is detrimental for the HER process.

Table 1 Summary of the potential determining steps, based on the calculated ΔG_H as a descriptor, on the explored Ti_3C_2 models, either pristine, or covered according to the specified terminations. The required overpotential, η, is specified, as well as the preferred Volmer–Heyrovsky (VH) or Volmer–Tafel (VT) mechanism, specifying the subtype of path, either O-TER, OH-TER, or TER–TER. In the case of pristine Ti_3C_2, note that the strong H-affinity prevents any H_2 formation, regardless of η

Model	Mechanism	Subtype	ΔG_H/eV	η/V
Pristine Ti_3C_2	—	—	−1.32	—
O	VH	—	−0.40	0.40
H	VH	—	0.63	0.63
OH	VH	—	−0.48	0.48
F	VH	—	2.62	2.62
$O_{1/3}OH_{2/3}$	VH	OH-TER	0.08	0.08
$O_{1/2}OH_{1/2}$	VH	OH-TER	0.23	0.23
$O_{2/3}OH_{1/3}$	VH	O-TER	−0.01	0.01
$F_{1/3}O_{1/3}OH_{1/3}$	VT	TER–TER	−0.01	0.01
$F_{3/9}O_{4/9}OH_{2/9}$	VH	O-TER	0.01	0.01

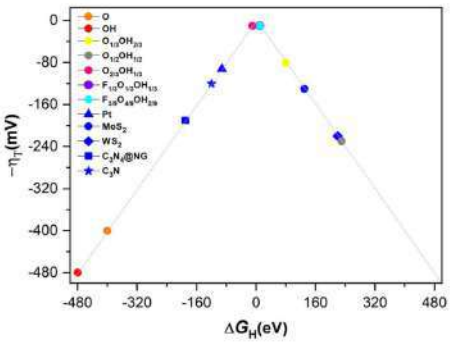

Fig. 7 Volcano plot of $-\eta$ *vs.* ΔG_H on the different terminated Ti_3C_2 surface models, including fully O- and OH-terminated cases, as well as binary situations represented by the $O_{1/3}OH_{2/3}$, $O_{1/2}OH_{1/2}$, and $O_{2/3}OH_{1/3}$ models, and ternary ones as in the $F_{1/3}O_{1/3}OH_{1/3}$ and $F_{3/9}O_{4/9}OH_{2/9}$ models. In addition, reference values for Pt, MoS_2, WS_2, C_3N_4@NG, and C_3N are included for comparison.

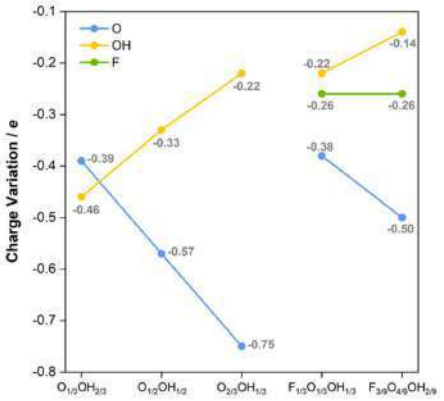

Fig. 8 Bader charges, in *e*, of –F, –O, and –OH groups on the diverse binary (admixing –O and –OH moieties) and ternary (admixing –F, –O, and –OH moieties).

The observed trends in net charges of –OH and –O groups are maintained when having –F groups at the surface. For instance, the Bader charges of –O and –OH groups in the $F_{1/3}O_{1/3}OH_{1/3}$ model are -0.38 and $-0.22e$, respectively, similar to those found for the same ratios of -0.39 and $-0.22e$ on $O_{1/3}OH_{2/3}$ and $O_{2/3}OH_{1/3}$ models, respectively. Moreover, the net charge at –O of $-0.57e$ in $O_{1/2}OH_{1/2}$ is similar and follows the observed trend when compared to the $F_{3/9}O_{4/9}OH_{2/9}$ of $-0.50e$, and actually the –OH charge of $-0.14e$ follows the trend when decreasing the OH ratio. Finally, the –F net charge is maintained constant at $-0.26e$ for both $F_{1/3}O_{1/3}OH_{1/3}$ and $F_{3/9}O_{4/9}OH_{2/9}$, thus irrespective of the –O/–OH ratio. Thus, charges on a moiety are largely independent of the presence of other moieties, in line with the information obtained from CDD plots in Fig. S11 of the ESI,† and solely affected by their surface concentration. Keeping this in mind, but also regarding the trend of ΔG_H with respect to the –O charge, one may wonder which is the origin of the small overpotentials on the F-containing models, when the charge on –O decreases. The answer seems to be related, on one hand, to the negative charge on –F groups, and, on the other hand, to the larger electronic affinity of –F. The resulting net generates a stronger attractive electric field towards the H^+ reactant, which may favor the adsorption, but in a more moderate fashion. This agrees with previous experimental results,[84,85] stating that the higher the featured –F coverage, the lower the HER activity on $Ti_3C_2T_x$, whereas compared to –O terminations, lower –F coverage promotes the H^+ adsorption and decreases the Gibbs free energy change of the HER.

4. Conclusions

In the present work we studied the potential HER performance of Ti_3C_2 MXene and, in particular, the effect of terminations by considering fully –O, –OH, –F, and –H terminations, as well as a pristine surface, but also mixed terminations, either binary or ternary, considering as well different ratios of surface moieties. To assess the most likely terminations under HER conditions of low pH and *U*, Pourbaix diagrams were built after examining the stability of *ca.* 450 different surface terminations, with variances in composition, species ratios, and topologically different arrangements. The cases with –F terminations were treated separately since there are synthetic procedures that do not use this element as the etchant. On top of that, different Volmer–Tafel and Volmer–Heyrovsky HER mechanisms were investigated on the obtained surface models, considering the initial or later involvement of surface H atoms from –H or –OH groups.

The reported results highlight that, at variance with a number of previous studies, fully –O, –OH, and –H

View Article Online
Journal of Materials Chemistry A Paper

terminations are possible, but only at very positive (–O) or negative (–OH and –H) potentials with respect to the RHE reference. Interestingly, close to the HER equilibrium conditions, binary models admixing –O and –OH moieties are predicted to be preferred for F-free situations, while ternary models also containing –F are relevant in F-containing samples. In particular, based on the $O_{2/3}OH_{1/3}$ and $F_{3/9}O_{4/9}OH_{2/9}$ models using –O moieties as the active center the Volmer–Heyrovsky mechanism is found to be optimal with almost negligible overpotential. For a lower –F content, as in the $F_{1/3}O_{1/3}OH_{1/3}$ model, a Volmer–Tafel like mechanism, where a Tafel step is initially carried out involving surface –OH groups, followed by two Volmer steps to regenerate the electrocatalysts as-generated –O centers, is also found to be optimal featuring an almost inexistent overpotential of 0.01 V. These two situations appear to be quite competitive when compared to other electrocatalysts used for the HER in the literature, such as Pt, MoS_2, or WS_2.

The analysis of electronic structure and charge density reveals that larger the concentration of –O moieties on the Ti_3C_2 surface, the more negatively charged they become with a concomitant stronger ability for H^+ reduction, reaching moderate bond strengths when the –O coverage is $\frac{2}{3}$. The presence of –F groups is not detrimental *per se*, and actually, their negative charge and the stronger electric field they generate contribute to favoring the H^+ reduction with moderate adsorption strength even when having a lower –O coverage of *ca.* $\frac{1}{3}$, as in the $F_{3/9}O_{4/9}OH_{2/9}$ and $F_{1/3}O_{1/3}OH_{1/3}$ models, which explains and reconciles previous experimental reports pointing out to better performances when having a higher presence of –O groups, and a lower presence of –F ones.[73] Finally, the present study underscores the tunability of these surface terminations to maximize the HER performance, while addressing their stability under working conditions of pH and *U*.

Conflicts of interest

There are no conflicts of interest to declare.

Acknowledgements

The research carried out at the Universitat de Barcelona has been supported by the Spanish MCIN/AEI/10.13039/501100011033 PID2021-126076NB-I00 project, funded partially by FEDER Una manera de hacer Europa, and María de Maeztu CEX2021-001202-M grants, including funding from the European Union and, in part, by COST Action CA18234. A significant part of the computational resources has been provided by the Red Española de Supercomputación (RES) QHS-2022-1-0004 and QHS-2021-3-0012. L. M. thanks the HPC-EUROPA3 (HPC17OOIBY) project supported by the EC Research Innovation Action under the H2020 Programme. L. M. thanks the China Scholarship Council (CSC) for financing her PhD (CSC202108390032).

References

1 M. Dresselhaus and I. Thomas, *Nature*, 2001, **414**, 332–337.
2 J. A. Turner, *Science*, 2004, **305**, 972–974.
3 S. Chu and A. Majumdar, *Nature*, 2012, **488**, 294–303.
4 S. E. Hosseini and M. A. Wahid, *Renewable Sustainable Energy Rev.*, 2016, **57**, 850–866.
5 J. Greeley, T. F. Jaramillo, J. Bonde, I. Chorkendorff and J. K. Nørskov, *Nat. Mater.*, 2006, **5**, 909–913.
6 X. X. Zou and Y. Zhang, *Chem. Soc. Rev.*, 2015, **44**, 5148–5180.
7 J. N. Hansen, H. Prats, K. K. Toudahl, N. M. Secher, K. Chan, J. Kibsgaard and I. Chorkendorff, *ACS Energy Lett.*, 2021, **6**, 1175–1180.
8 D. E. Brown, M. N. Mahmood, M. C. M. Man and A. K. Turner, *Electrochim. Acta*, 1984, **29**, 1551–1556.
9 I. A. Raj and K. I. Vasu, *J. Appl. Electrochem.*, 1990, **20**, 32–38.
10 M. A. Lukowski, A. S. Daniel, F. Meng, A. Forticaux, L. Li and S. Jin, *J. Am. Chem. Soc.*, 2013, **135**, 10274–10277.
11 T. F. Jaramillo, K. P. Jørgensen, J. Bonde, J. H. Nielsen, S. Horch and I. Chorkendorff, *Science*, 2007, **317**, 100–102.
12 G. Gao, Y. Jiao, F. Ma, Y. Jiao, E. Waclawik and A. Du, *J. Phys. Chem. C*, 2015, **119**, 13124–13128.
13 J. Kibsgaard, C. Tsai, K. Chan, J. D. Benck, J. K. Nørskov, F. Abild-Pedersen and T. F. Jaramillo, *Energy Environ. Sci.*, 2015, **8**, 3022–3029.
14 Y. Zheng, Y. Jiao, J. Chen, J. Liu, J. Liang, A. Du, W. Zhang, Z. Zhu, S. C. Smith, M. Jaroniec, G. Q. Lu and S. Z. Qiao, *J. Am. Chem. Soc.*, 2011, **133**, 20116–20119.
15 G. Gao, Y. Jiao, F. Ma, Y. Jiao, E. Waclawik and A. Du, *J. Catal.*, 2015, **332**, 149–155.
16 G. Gao, Y. Jiao, F. Ma, Y. Jiao, E. Waclawik and A. Du, *Phys. Chem. Chem. Phys.*, 2015, **17**, 31140–31144.
17 H. Fei, J. Dong, M. J. Arellano-Jiménez, G. Ye, N. Dong Kim, E. L. G. Samuel, Z. Peng, Z. Zhu, F. Qin, J. Bao, M. J. Yacaman, P. M. Ajayan, D. Chen and J. Tour, *Nat. Commun.*, 2015, **6**, 8668.
18 G. P. Gao, A. P. O'Mullane and A. J. Du, *ACS Catal.*, 2017, **7**, 494–500.
19 B. Anasori, M. R. Lukatskaya and Y. Gogotsi, *Nat. Rev. Mater.*, 2017, **2**, 16098.
20 M. Naguib, M. Kurtoglu, V. Presser, J. Lu, J. Niu, M. Heon, L. Hultman, Y. Gogotsi and M. W. Barsoum, *Adv. Mater.*, 2011, **23**, 4248–4253.
21 M. Ghidiu, M. R. Lukatskaya, M. Q. Zhao, Y. Gogotsi and M. W. Barsoum, *Nature*, 2014, **516**, 78–81.
22 X. Yu, X. Cai, H. Cui, S. W. Lee, X. F. Yu and B. Liu, *Nanoscale*, 2017, **9**, 17859–17864.
23 V. Kamysbayev, A. S. Filatov, H. Hu, X. Rui, F. Lagunas, D. Wang, R. Klie and D. V. Talapin, *Science*, 2020, **369**, 979–983.
24 I. Persson, J. Halim, H. Lind, T. W. Hansen, J. B. Wagner, L.-Å. Näslund, V. Darakchieva, J. Palisaitis, J. Rosen and P. O. Å. Persson, *Adv. Mater.*, 2019, **31**, 1805472.
25 X. Sang, Y. Xie, M.-W. Lin, M. Alhabeb, K. L. Van Aken, Y. Gogotsi, P. R. C. Kent, K. Xiao and R. R. Unocic, *ACS Nano*, 2016, **10**, 9193–9200.
26 J. Xie, X. Yang and Y. Xie, *Nanoscale*, 2020, **12**, 4283–4294.
27 R. He, Y. Wan, P. Zhao, P. Guo, Z. Jiang and J. Zheng, *Comput. Theor. Chem.*, 2019, **1150**, 26–39.

28 J. Peng, X. Chen, W. J. Ong, X. Zhao and N. Li, *Chem*, 2019, **5**, 18–50.
29 J. Ran, G. Gao, F. T. Li, T. Y. Ma, A. Du and S. Z. Qiao, *Nat. Commun.*, 2017, **8**, 13907.
30 C. Ling, L. Shi, Y. Ouyang and J. Wang, *Chem. Mater.*, 2016, **28**, 9026–9032.
31 Z. W. Seh, K. D. Fredrickson, B. Anasori, J. Kibsgaard, A. L. Strickler, M. R. Lukatskaya, Y. Gogotsi, T. F. Jaramillo and A. Vojvodic, *ACS Energy Lett.*, 2016, **1**, 589–594.
32 H. Pan, *Sci. Rep.*, 2016, **6**, 32531.
33 J. Xie, J. Qi, F. Lei and Y. Xie, *Chem. Commun.*, 2020, **56**, 11910–11930.
34 J. Xie and Y. Xie, *ChemCatChem*, 2015, **7**, 2568–2580.
35 M. A. Hope, A. C. Forse, K. J. Griffith, M. R. Lukatskaya, M. Ghidiu, Y. Gogotsi and C. P. Grey, *Phys. Chem. Chem. Phys.*, 2016, **18**, 5099–5102.
36 R. Ibragimova, M. J. Puska and H.-P. Komsa, *ACS Nano*, 2019, **13**, 9171–9181.
37 M. López, Á. Morales-García, F. Viñes and F. Illas, *ACS Catal.*, 2021, **11**, 12850–12857.
38 J. D. Gouveia, Á. Morales-García, F. Viñes, F. Illas and J. R. B. Gomes, *Appl. Catal., B*, 2020, **260**, 118191.
39 J. Durst, A. Siebel, C. Simon, F. Hasché, J. Herranz and H. A. Gasteiger, *Energy Environ. Sci.*, 2014, **7**, 2255–2260.
40 P. J. Rheinländer, J. Herranz, J. Durst and H. A. Gasteiger, *J. Electrochem. Soc.*, 2014, **161**, F1448.
41 S. Li, P. Tuo, J. Xie, X. Zhang, J. Xu, J. Bao, B. Pan and Y. Xie, *Nano Energy*, 2018, **47**, 512–518.
42 C. Liu, H. Wu, X. Wang, J. Fan, H. Su, D. Yang, Y. Wei, F. Du, Y. Dall'Agnese and Y. Gao, *Energy Storage Mater.*, 2023, **54**, 164–171.
43 H. Xu, J. Fan, H. Su, C. Liu, G. Chen, Y. Dall'Agnese and Y. Gao, *Nano Lett.*, 2023, **23**, 283–290.
44 S. Ma, X. L. Fan, Y. R. An, D. X. Yang, Z. F. Luo, Y. Hu and N. J. Guo, *J. Mater. Sci.*, 2019, **54**, 11378–11389.
45 H. C. Yang, Y. D. Ma, X. S. Lv, B. B. Huang and Y. Dai, *J. Catal.*, 2020, **387**, 12–16.
46 N. Li, Z. L. Zeng, Y. W. Zhang, X. Z. Chen, Z. Z. Kong, Arramel, Y. Li, P. Zhang and B. S. Nguyen, *ACS Omega*, 2021, **6**, 23676–23682.
47 G. Kresse and J. Furthmüller, *Phys. Rev. B: Condens. Matter Mater. Phys.*, 1996, **54**, 11169.
48 G. Kresse and D. Joubert, *Phys. Rev. B: Condens. Matter Mater. Phys.*, 1999, **59**, 1758.
49 J. P. Perdew, K. Burke and M. Ernzerhof, *Phys. Rev. Lett.*, 1996, **77**, 3865.
50 H. J. Monkhorst and J. D. Pack, *Phys. Rev. B: Solid State*, 1976, **13**, 5188.
51 S. Grimme, J. Antony, S. Ehrlich and H. Krieg, *J. Chem. Phys.*, 2010, **132**, 154104.
52 R. Morales-Salvador, J. D. Gouveia, Á. Morales-García, F. Viñes, J. R. B. Gomes and F. Illas, *ACS Catal.*, 2021, **11**, 11248–11255.
53 B. E. Conway and B. V. Tilak, *Electrochim. Acta*, 2002, **47**, 3571–3594.
54 X. Huang, J. Wang, H. B. Tao, H. Tian, Z. Zhang and H. Xu, *J. Catal.*, 2020, **389**, 461–467.
55 J. N. Brønsted, *Chem. Rev.*, 1928, **5**, 231–338.
56 M. G. Evans and M. Polanyi, *Trans. Faraday Soc.*, 1938, **34**, 11–24.
57 K. S. Exner, J. Anton, T. Jacob and H. Over, *Angew. Chem., Int. Ed.*, 2016, **55**, 7501–7504.
58 K. S. Exner and H. Over, *Acc. Chem. Res.*, 2017, **50**, 1240–1247.
59 J. K. Nørskov, J. Rossmeisl, A. Logadottir, L. Lindqvist, J. R. Kitchin, T. Bligaard and H. Jónsson, *J. Phys. Chem. B*, 2004, **108**, 17886–17892.
60 *NIST Standard Reference Database*, SRD Number 69, 1901, DOI: **10.18434/T4D303**.
61 Q. Li, Y. Ouyang, S. Lu, X. Bai, Y. Zhang, L. Shi, C. Ling and J. Wang, *Chem. Commun.*, 2020, **56**, 9937–9949.
62 M. Pourbaix, *Atlas of Electrochemical Equilibria in Aqueous Solutions*, National Association of Corrosion Engineers (NACE), Houston, Texas, USA, 1974.
63 M. López, K. S. Exner, F. Viñes and F. Illas, *Adv. Theory Simul.*, 2022, 2200217.
64 D. F. Sriver and P. W. Atkins, *Inorganic Chemistry*, Freeman, W.H. and Company, New York, 5th edn, 2009.
65 D. R. Lide, *CRC Handbook of Chemistry and Physics*, CRC Press, Boca Raton, Florida, 102nd edn, 2004.
66 H. A. Hansen, I. C. Man, F. Studt, F. Abild-Pedersen, T. Bligaard and J. Rossmeisl, *Phys. Chem. Chem. Phys.*, 2010, **12**, 283–290.
67 N. Xue, X. Li, L. Han, H. Zhu, X. Zhao, J. Zhuang, Z. Ga and X. Tao, *J. Mater. Chem. A*, 2022, **10**, 7960–7967.
68 S. Yang, P. Zhang, F. Wang, A. G. Ricciardulli, M. R. Lohe, P. W. M. Blom and X. Feng, *Angew. Chem., Int. Ed.*, 2018, **19**, 15717–15721.
69 S.-Y. Pang, Y.-T. Wong, S. Yuan, Y. Liu, M.-K. Tsang, Z. Yang, H. Huang, W.-T. Wong and J. Hao, *J. Am. Chem. Soc.*, 2019, **141**, 9610–9616.
70 J. Gan, F. Li, Y. Tang and Q. Tang, *ChemSusChem*, 2020, **13**, 6005–6015.
71 Y. Jiang, T. Sun, X. Xie, W. Jiang, J. Li, B. Tian and C. Su, *ChemSusChem*, 2019, **12**, 1368–1373.
72 C. Ling, L. Shi, Y. Ouyang and J. Wang, *Chem. Mater.*, 2016, **28**, 9026–9032.
73 A. D. Handoko, H. T. Chen, Y. W. Lum, Q. F. Zhang, B. Anasori and Z. W. She, *iScience*, 2020, **23**, 101181.
74 F. Viñes, C. Sousa, P. Liu, J. A. Rodriguez and F. Illas, *J. Chem. Phys.*, 2005, **122**, 174709.
75 M. Khazaei, M. Arai, T. Sasaki, C. Y. Chung, N. S. Venkataramanan, M. Estili, Y. Sakka and Y. Kawazoe, *Adv. Funct. Mater.*, 2013, **23**, 2185–2192.
76 G. P. Gao, A. P. O'Mullane and A. J. Du, *ACS Catal.*, 2017, **7**, 494–500.
77 B. Huang, N. G. Zhou, X. Z. Chen, W. J. Ong and N. Li, *Chem.–Eur. J.*, 2018, **24**, 18479–18486.
78 N. Li, Z. L. Zeng, Y. W. Zhang, X. Z. Chen, Z. Z. Kong, Arramel, Y. Li, P. Zhang and B. S. Nguyen, *ACS Omega*, 2021, **6**, 23676–23682.
79 J. K. Nørskov, T. Bligaard, A. Logadottir, J. Kitchin, J. G. Chen, S. Pandelov and U. Stimming, *J. Electrochem. Soc.*, 2005, **152**, J23–J26.

80 L. Lin, N. Miao, Y. Wen, S. Zhang, P. Ghosez, Z. Sun and D. A. Allwood, *ACS Nano*, 2016, **10**, 8929–8937.
81 J. Bonde, P. G. Moses, T. F. Jaramillo, J. K. Nørskov and I. Chorkendorff, *Faraday Discuss.*, 2009, **140**, 219–231.
82 Y. Zheng, Y. Jiao, Y. Zhu, L. H. Li, Y. Han, Y. Chen, A. Du, M. Jaroniec and S. Z. Qiao, *Nat. Commun.*, 2014, **5**, 3783.
83 S. Yao, X. Zhang, A. Chen, Z. Zhang, M. Jiao and Z. Zhou, *J. Mater. Chem. A*, 2019, **7**, 19290–19296.
84 A. D. Handoko, K. D. Fredrickson, B. Anasori, K. W. Convey, L. R. Johnson, Y. Gogotsi, A. Vojvodic and Z. W. Seh, *ACS Appl. Energy Mater.*, 2018, **1**, 173–180.
85 Y. Zhang, L. Chen, Y. Gui and L. Liu, *Appl. Surf. Sci.*, 2022, **592**, 153334.

Journal of Materials Chemistry A

ROYAL SOCIETY OF CHEMISTRY

PAPER

View Article Online
View Journal | View Issue

Check for updates

Cite this: J. Mater. Chem. A, 2024, 12, 7856

Surface termination dependent carbon dioxide reduction reaction on Ti_3C_2 MXene†

Ling Meng, [ab] Li-Kai Yan, [*b] Francesc Viñes [*a] and Francesc Illas [a]

The use of two-dimensional (2D) MXene materials as highly efficient electrocatalysts for the carbon dioxide reduction reaction (CO_2RR) has gained considerable attention in the last few years. However, current computational studies on the CO_2RR are primarily focused on MXene materials with different types of metals or displaying fully –O or –OH terminated surfaces, which fail to account for the fact that as-synthesized MXenes possess mixtures of –O, –OH, –F, and/or –H surface groups. Here, a comprehensive density functional theory (DFT) study is carried out on the stability and impact of different surface terminations and moiety distributions on CO_2RR performance done on the prototype Ti_3C_2 MXene, analyzing the possible electrocatalytic synthesis of a series of CO_2RR products, from CO to H_2CO, HCOOH, CH_3OH, and CH_4 under favorable low pH and potential, U, reaction conditions, while considering the competitive H_2 evolution reaction (HER). From *ca.* 450 distinct surface terminations, four F-free models are selected as dominant in Pourbaix surface stability diagrams under low pH and U conditions, namely –OH, $-OH_{2/3}O_{1/3}$, $-OH_{1/2}O_{1/2}$, and $-OH_{1/3}O_{2/3}$, and one F-containing model, $-F_{1/3}OH_{1/3}O_{1/3}$. Results highlight the participation of surface –OH groups as H-donors, and the benefits of simultaneous hydrogenation from proton reduction and –OH H transfer. In addition, the presence of both –OH and –O groups is beneficial, reducing limiting potential, U_L, costs, as experimentally observed. On the $-F_{1/3}OH_{1/3}O_{1/3}$ model, the presence of –F is *per se* non-detrimental, moving the limiting step to an early stage and reducing the U_L. The overall results underscore the competitiveness of MXenes in the CO_2RR with respect to a Cu electrocatalyst reference, and the tunability possibilities to maximize the selectivity towards either the CO_2RR or the HER.

Received 14th January 2024
Accepted 15th February 2024

DOI: 10.1039/d4ta00320a

rsc.li/materials-a

1. Introduction

With the steadily growing use of fossil fuels, carbon dioxide (CO_2) emissions have increased to a worrying exceedingly high level. One of the major issues facing nowadays society is climate change and the ultra-high energy prices, recently highlighted by the impressive European energy crisis in the winter of 2022.[1] Thus, the exploitation of new energy sources is crucial to avoid such energy constrains, where one very appealing way is to use carbon dioxide (CO_2) emissions as a C_1 chemical source, turning CO_2 economy into a waste-to-product model, and, by that, contributing to a carbon-neutral cycle.[2] For this, carbon reduction technologies are key, one of which is the use of electrocatalytic CO_2 reduction reaction (CO_2RR) to convert it into other useful chemicals and fuels. Most of these processes imply hydrogenation reactions, and the full technology can be thought as green when powered by renewable energy sources, such as solar and wind power, and when the used hydrogen (H_2) is produced in the same way.[3–6]

So far, despite receiving widespread attention from both theoretical and experimental research communities,[7–9] the CO_2RR is yet not widely implemented on an industrial scale due to multiple reasons, main ones being its cost and the low reaction activity reached by present catalysts, implying that novel and/or costly materials are needed, often accompanied by slow reaction kinetics, which altogether increases the process price and efficiency.[10,11] In addition to the aforementioned factors, achieving high levels of selectivity, stability, and durability is still a critical challenge in the field of the CO_2RR.[12] Over the last few years, extensive research endeavours have been focused on countless catalysts, including both non-precious metal[13,14] and non-metal catalysts.[15,16] Among them, Cu-based heterogeneous catalysts have attracted much attention due to their ability to convert CO_2 to abundant multi-carbon products, such as hydrocarbons and alcohols, while being accessible in cost.[17,18] However, using these catalysts, the formation of methane (CH_4), the main component of biogas, still starts at potentials ranging from −0.9 V to −1.1 V *vs.* the reversible

[a]Departament de Ciència de Materials i Química Física & Institut de Química Teòrica i Computacional (IQTCUB), Universitat de Barcelona, c/ Martí i Franquès 1-11, 08028, Barcelona, Spain. E-mail: francesc.vines@ub.edu

[b]Institute of Functional Material Chemistry, Key Laboratory of Polyoxometalate Science of Ministry of Education, Faculty of Chemistry, Northeast Normal University, Changchun 130024, P. R. China. E-mail: yanlk924@nenu.edu.cn

† Electronic supplementary information (ESI) available. See DOI: https://doi.org/10.1039/d4ta00320a

hydrogen electrode (RHE).[19,20] In addition, their low reaction kinetics has been found to be influenced by limitations arising from linear scaling relations between reaction intermediate binding energies, translated in a restricted stability of adsorbed carbon monoxide (CO), *i.e.* CO*, and similar reaction intermediates such as CHO*, which eventually leads to a reduced activity.[21,22] Thus, the quest for new cost-effective CO_2RR catalysts with less negative potentials is still open.

In this context, MXenes, few-layered transition metal carbides and/or nitrides, have arisen as an attractive family of materials for the CO_2RR, given their superior conductivity and hydrophilicity, making them very promising catalysts for this purpose.[23] MXenes are two-dimensional (2D) materials with $M_{n+1}X_nT_x$ general chemical formula, where M denotes an early transition metal, X generally represents C and/or N, T_x denotes the surface functional group, intrinsic to the MXene synthesis procedure, and n normally ranges from 1 to 3,[24–26] although MXenes with $n = 4$ have been already reported.[27] MXenes are normally gained by selective etching from precursor MAX phases, where *A*, normally a *p*-element like Al or Si, is removed using a hydrofluoric acid (HF) solution,[28] although *in situ* HF can be used admixing lithium fluoride (LiF) with hydrochloric acid (HCl).[29] With these methods, a mixture of –O, –H, –OH, and –F of terminations is gained.[30,31] Still, the type and quantity of such terminations are highly sensitive to synthesis conditions such as etching time, temperature, or HF concentration.[32,33] For instance, high concentrations of HF lead to a larger number of –F terminations, while when lower HF concentrations are used more –O species are found.[31,34] On top of that, successful F-free synthesis protocols have been reported,[35] even cleaning protocols[36] or new synthetic routes[37] to acquire T_x-free MXenes and even tune the T_x with many other terminations. In short, all this casuistry can be used to design MXenes to suit specific applications, playing with composition, size, and surface termination.[38]

Focusing back on the CO_2RR, recently Li *et al.*[39] computationally screened bare M_3C_2 (groups IV, V, and VI) MXenes for the CO_2RR by density functional theory (DFT) means, predicting Cr_3C_2 and Mo_3C_2 as most promising candidates, with limiting potentials of −1.05 and −1.31 V to form CH_4. Handoko *et al.*[40] and Chen *et al.*[41] accounted for surface termination exploring –O and –OH moieties, respectively, finding that O-terminated MXenes can enhance the stability of reaction intermediates by coordinating hydrogen atoms, while OH-terminated MXenes display a high reactivity owing to the already presence of hydrogen atoms. As a result, the catalysts exhibited a lower overpotential and challenged the traditional scaling relationships, while simultaneously establishing new ones. Recently, Handoko *et al.*[42] also experimentally reported that the CO_2RR activity of Ti_2CT_x is related to the proportion of surface –F and –O moieties, in the sense that a higher amount of –F leads to a lower activity and selectivity. Note that C_2 coupling is also a current research focus, although the use of pure MXene is still a challenge, and most of the recent approaches dealt with defect engineering or heterostructures,[43,44] a common strategy to boost the CO_2RR to C_2,[45] like using Cu or Fe transition metal single atoms on $Ti_3C_2T_x$ or Mo_2C, respectively,[46,47] or dioxygen vacancies on $Mo_2TiC_2O_2$.[48] The focus here is on non-modified MXenes, and, therefore, on C_1 products. Despite the numerous DFT investigations on bare or fully terminated MXenes, there is still a lack of analysis under realistic conditions, hindering the correlation between theoretical simulations and experimental results. Therefore, further comprehensive studies are required to finally elucidate and comprehend CO_2RR performance on MXenes.

This is tackled here taking the paradigmatic Ti_3C_2 MXene as a case study. This material, first synthesized in 2011,[49] is considered a MXene prototype, being the target of extensive research and development, and currently the most well-studied and mature MXene material.[50] Here we systematically analyze, by first-principles based calculations, the CO_2RR performance on Ti_3C_2 MXene with four different but realistic terminations in specific ranges of pH and potential, *U*, based on a surface stability assessment using computational Pourbaix diagrams[51,52] created by considering about 450 different surface terminations with different combinations of surface species.[53] By using these suited models, we gain valuable and detailed insights into the CO_2RR process under realistic working conditions, highlighting (i) the CO_2 activation capacity of the selected models considering the working temperature, *T*, and CO_2 partial pressure, p_{CO_2}, (ii) that the presence of –F species is unavoidable under acidic conditions when the MXene is extracted using fluorinated solvents, (iii) that, contrary to previous studies,[41,54,55] the fully –OH or –O terminated MXene models are challenged at less negative potentials, while MXene with mixed terminations would be more realistic CO_2RR electrocatalytic models under such conditions, with (iv) a new CO_2RR mechanism involving these termination groups in the hydrogenation steps, while (v) the presence of –F groups is found to be inherently not only non-detrimental, but to positively contribute when the surface coverage is limited, so that finally (vi) Ti_3C_2 with a stable ternary mixture containing –O and –OH groups with a small amount of –F exhibits one of the lowest bias-demanding CO_2RR, even if fully –OH terminated is, *a priori*, more selective, all in all showing that (vii) MXenes are, in general, improved electrocatalysts with respect to the usual Cu-electrocatalyst reference.

2. Theoretical aspects

2.1. Computational details

All the presented periodic DFT calculations were carried out using the Vienna *ab initio* simulation package (VASP).[56] The generalized gradient approximation (GGA) Perdew–Burke–Ernzerhof (PBE) exchange-correlation functional[57] was used, accurately suited in the description of MXenes energetics.[58–60] Additionally, Grimme's D3 approach was included to account for dispersive force interactions.[61] The core electron density and its impact on the valence electron density were described using the projector augmented wave (PAW) method developed by Blöchl,[62] as implemented by Kresse and Joubert.[63] Besides, the valence electron density was expanded on a plane wave basis set with a cutoff kinetic energy of 415 eV, high enough to acquire total energies converged below the chemical accuracy of 1 kcal mol^{-1}, *ca.* 0.04 eV,[64] the same order of accuracy obtained when

View Article Online
Journal of Materials Chemistry A Paper

performing test calculations using an implicit solvent model[65] and thus found to be not required in the oncoming discussion.

Different supercell models were used in the construction of Pourbaix diagrams, in particular, $p(2\times2)$ and $p(3\times3)$ supercells of Ti_3C_2, where a full monolayer (ML) coverage is defined as having one surface moiety per each surface metal atom. The $p(2\times2)$ supercell was used to evaluate the pristine, fully –O, –OH, –H, and –F covered Ti_3C_2, as well as mixed cases with $\frac{1}{2}$ ML *vs.* $\frac{1}{2}$ ML, $\frac{1}{4}$ *vs.* $\frac{3}{4}$ of a ML binary coverage, and $\frac{1}{4}$, $\frac{1}{4}$, and $\frac{1}{2}$ of a ML ternary situation, while the $p(3\times3)$ supercell was employed to investigate binary situations with $\frac{1}{3}$ *vs.* $\frac{2}{3}$ coverage, as well as ternary situations with an equal coverage of each component. For reaction mechanism evaluation, $p(3\times3)$ or $p(4\times4)$ supercells were used. A 20 Å vacuum was added to the slab models to ensure their appropriate isolation, while the Brillouin zone was sampled using an optimal 5×5×1 **k**-point **Γ**-centered Monkhorst–Pack grid,[66] achieving as well the aforementioned chemical accuracy.

During the structural optimization, a convergence criterion of 10^{-5} eV was used for the electronic self-consistent field steps, while atomic positions were relaxed until forces acting on atoms were below 0.01 eV $Å^{-1}$. Unless stated otherwise, all calculations were carried out spin polarized. The vibrational frequencies of the reaction surface species minima were determined by constructing and diagonalizing the Hessian matrix using finite differences of 0.03 Å in length to evaluate the analytical gradients,[67,68] yet only atomic displacements on the adsorbed species and terminations were considered, while substrate atoms were held fixed, *i.e.* a decoupling of surface species with the material phonons was assumed.

2.2. Surface Pourbaix diagrams

The purpose of constructing a Pourbaix diagram in this study is to identify the most thermodynamically stable surface termination of the Ti_3C_2 MXene under the realistic working conditions of pH and U during the CO_2RR. Details can be found in previous work,[53] but still let us briefly explain the procedure here. Initially, a systematic sampling approach was employed to explore various high-symmetry adsorption sites for each studied termination, as illustrated in Fig. S1 of the ESI,† revealing that the H_{T1} site was consistently the most favorable site for adsorption of any of the T_x surface terminations. This information was used to optimize and gain the free-energy of different surface terminations, either with single moieties, or with ratios in mixed situations, all as a function of the applied electrode potential, U, and pH, using to this end the computational hydrogen electrode (CHE) approach.[69] Note that diverse distributions of functional groups were accounted for, encompassing both highly regular and irregular arrangements. To account for the number of electrons (e^-), protons (H^+) and fluorine ions (F^-) involved during the adsorption processes, the stoichiometric coefficients $\nu(e^-)$, $\nu(H^+)$, and $\nu(F^-)$ were considered when constructing the reaction formation free energy equations required for the Pourbaix diagrams,[70] as;

$$\Delta G(\mathrm{pH}, U) = \Delta G(0,0) - \nu(H^+)k_B T \times \ln 10 \times \mathrm{pH} - \nu(e^-)eU - \nu(F^-)eU_F, \quad (1)$$

where $\Delta G(0,0)$ is the formation energy of a given surface termination at zero pH and U, where U refers to the applied electrode potential *vs.* the standard hydrogen electrode (SHE), e is the charge of an electron, and k_B is Boltzmann's constant. To account for the chemical potential of electron–proton pairs, we rely on the CHE model whereas the computational fluorine electrode (CFE) is used in the case of fluorine anions,[53] U_F being the reduction potential of fluorine, and the results for the different $p(2\times2)$ and $p(3\times3)$ supercells are comparable when normalizing by the surface area. By this, a Pourbaix diagram can be drawn showing, under any pH and U conditions, which surface termination exhibits the lowest ΔG, and that is shown here in Fig. S2 of the ESI,† either for F-containing situations, as expected from a MXene synthesized using HF,[71,72] or in the absence of fluorine ions, in case $Ti_3C_2T_x$ was obtained using a F-free synthesis method.[73]

Ideally, for the CO_2RR, one would pursue situations with a minimal negative potential, and with low pH, in order to prompt the reaction kinetics. Thus, taking into account the potential working conditions of $T = 298.15$ K, $p_{H_2} = 1$ bar, pH < 4, and an improved applied potential U range of -0.75 V < U < 0 V, as commonly used in the CO_2RR towards CH_4 using MXene-based electrocatalysts,[39–42,74] the most suitable and realistic $Ti_3C_2T_x$ models were F-free $OH_{2/3}O_{1/3}$, $OH_{1/2}O_{1/2}$, $OH_{1/3}O_{2/3}$, and fully OH-terminated, as well as the F-containing $F_{1/3}OH_{1/3}O_{1/3}$, as illustrated in Fig. S2 of the ESI.† Already at this stage, one should notice how mixed situations are more the rule than the exception, and that fully OH-terminated models would be realistic only at low potentials, while O-terminated models would not be accurate situations for the CO_2RR. However, one must advert that most of the previous literature on MXenes focused on bare or fully O-terminated MXenes,[75,76] with only a limited number of studies considering –OH termination, and only Chen *et al.*[41] regarded the involvement of H atoms from the –OH termination in the CO_2RR.

2.3. CO_2RR mechanism

In general, the first step of CO_2 reduction is its adsorption from the gas phase, $CO_2^{(g)}$, on a catalyst free surface site (*);

$$CO_2^{(g)} + * \rightarrow CO_2*. \quad (2)$$

After this *sine qua non* step, the rest of the reaction mechanism would imply proton-coupled electron transfer (PCET) steps, where protons, H^+, and electrons, e^-, are sequentially added. The full reduction of adsorbed CO_2 to adsorbed CH_4* and water (H_2O*) requires eight PCET electrochemical steps,[77] as:

$$CO_2* + 8H^+ + 8e^- + * \rightarrow CH_4* + 2H_2O*, \quad (3)$$

followed by the subsequent desorption of CH_4* and H_2O* to the gas and liquid phases, respectively, as:

$$CH_4* + 2H_2O* \rightarrow 2* + CH_4^{(g)} + 2H_2O_{(l)}. \quad (4)$$

For convenience, most of the earlier studies assumed that, for any precursor adsorbed species, A*, its reduction is done in

a single elementary reaction, where one H^+ and one electron e^- are directly involved in producing AH*, as:

$$A^* + H^+ + e^- \rightarrow AH^*. \quad (5)$$

However, we here contemplated as well the possible involvement of termination –OH groups as a hydrogen source. Thus, for instance, in the presence of –OH surface moieties, the A* could be hydrogenated from the –OH group, as:

$$A^* + \text{–OH} \rightarrow AH^* + \text{–O}, \quad (6)$$

leaving behind an –O moiety in a chemical step. Later, an electrochemical step can be set up, where a proton is reduced on the as-formed –O moiety, regenerating the –OH group, as;

$$\text{–O} + H^+ + e^- \rightarrow \text{–OH}. \quad (7)$$

Notice as well that, thus, –O terminations could be reducing sites for medium H^+, which would act as a reservoir. According to this, one could elaborate an alternative path, where H^+ is reduced on a –O site, as in eqn (7), and in a later step, the as-formed –OH could be involved in the chemical hydrogenation of A* species, as in eqn (6). These different ordering pathways have been contemplated here, to gain a more complete understanding and involvement of surface terminations in the course of the CO_2RR and the followed mechanism.[53]

2.4. Thermodynamic approach

To outline the reaction mechanisms, a thermodynamic approach, as extendedly used in previous studies, has been used.[78,79] It implies that only the difference in Gibbs free energies between the different reaction intermediate states are relevant, and so used in determining the necessary limiting potential, U_L, for the reaction to take place. This succinctly implies that any PCET step features a latest transition state when endergonic, and an earliest transition state when exergonic, although a proportionality could be expected when the system under study follows the Brønsted–Evans–Polanyi (BEP) relationships.[80,81] Notice, still, that approaches are available to account for the transition states in the course of the reaction,[82,83] yet here, for comparative purposes with earlier studies,[84–86] they have not been accounted for.

The first step in outlining the reaction free energy profiles is to estimate the total adsorption energies of the intermediate species, ΔE^i_{ads}, so that

$$\Delta E^i_{ads} = E_{i/sub} - (E_{sub} + E_i). \quad (8)$$

Here, E_{sub} represents the energy of the substrate, here Ti_3C_2 MXene with the explored surface termination. E_i is the energy of the i adsorbed species as optimized in the vacuum, carried out at the Γ-point in a broken-symmetry box of 9×10×11 Å^3 dimensions, to force the duly orbital occupancy. Lastly, $E_{i/sub}$ is the energy of the i moiety adsorbed on the specific studied substrate model. Thus, the more negative ΔE^i_{ads} is, the stronger is the adsorption.

When addressing the reaction ΔG calculations, one has to keep in mind that, by using the above-mentioned CHE reference,[69] under the standard equilibrium conditions of pH = 0, U = 0 V, a temperature T of 298.15 K, and a partial pressure of H_2, p_{H_2}, of 1 bar, the chemical potential of a pair of H^+ and e^- can be related to that of H_2 at 0 V *vs.* the SHE, so that

$$H_{(aq)}^+ + e^- \rightarrow \tfrac{1}{2} H_2(g);\ \Delta G^\circ = 0\ \text{eV}, \quad (9)$$

where the chemical potentials or Gibbs free energies of the initial states, $H_{(aq)}^+ + e^-$, and the final state, $\frac{1}{2} H_2^{(g)}$, are identical. Note that, at variance with thermocatalysis, where T and p_{H_2} are normally used as variables of catalytic control, in electrocatalysis one normally works under the above standard conditions, while using pH and U_L as reaction variables, instead. Having this in mind, for any elementary reaction step, one can get the ΔG as

$$\Delta G = \Delta E + \Delta E_{ZPE} - T\Delta S, \quad (10)$$

which takes into account the reaction step energy difference, ΔE, the change in zero point energy (ZPE), ΔE_{ZPE}, and in entropy, ΔS. The ΔE term can be readily obtained from the total energies computed during the optimization, exemplified in eqn (5), as follows:

$$\Delta E = E_{AH^*} - E_{A^*} - \tfrac{1}{2} E_{H_2}. \quad (11)$$

Similarly, the ΔE_{ZPE} term can be gained as:

$$\Delta E_{ZPE} = E^{ZPE}_{AH^*} - E^{ZPE}_{A^*} - \frac{1}{2} E^{ZPE}_{H_2}, \quad (12)$$

where the ZPE term is gained from the computed vibrational frequencies, so that

$$E^{ZPE} = \frac{1}{2} \sum_{i=1}^{NMV} h\nu_i, \quad (13)$$

where ν_i represents the vibrational frequencies of the normal modes of vibration (NMV), and h Planck's constant. For a linear molecule in vacuum, the number of NMV is 3N-5 for a system with N atoms, while for any other type of molecule, the NMV is 3N-6. When adsorbed, any molecule or atom has 3N NMV, since free translations and rotations become restricted vibrational modes upon adsorption. Similarly, to ΔE_{ZPE}, the entropy change, ΔS, can be calculated as follows:

$$\Delta S = S_{AH}{}^* - S_A{}^* - \tfrac{1}{2} S_{H_2}. \quad (14)$$

The entropy of gas phase molecules has been obtained from the National Institute of Standards and Technology (NIST) webbook,[87] while for the adsorbed moieties, only the vibrational entropy (S_{vib}) is considered due to the ground state character and the hindrance of translations and rotations upon adsorption.[88] Thus, for adsorbed species, one has:

$$S = S_{vib} = k_B \sum_{i=1}^{NMV} \ln\left(1 - e^{-\frac{h\nu_i}{k_B T}}\right) - \sum_{i=1}^{NMV} h\nu_i \left(\frac{1}{e^{\frac{h\nu_i}{k_B T}} - 1}\right). \quad (15)$$

View Article Online
Journal of Materials Chemistry A
Paper

Given the reaction Gibbs free energy profiles, one can assess the reaction limiting potential, U_L, defined as the minimum potential required for a specific electrochemical reaction to occur spontaneously under given reaction conditions. In the case of the CO_2RR, U_L would be the potential at which each elementary electrochemical hydrogenation step becomes exergonic, indicating the minimum energy input required for the reaction to proceed. The descriptor ΔG_{max}, a free-energy model extracting the largest free-energy difference between intermediate states of an elementary step at a given target electrode potential, is used to quantify limiting potential for the CO_2RR, as

$$U_L = -\frac{\Delta G_{max}}{e}, \quad (16)$$

where, generally, the smaller the limiting potential, the higher the reaction activity.

2.5. Adsorption/desorption rates

Apart from the previous thermodynamic approach, it is worth keeping in mind that CO_2 adsorption must occur under the reaction conditions, while ideally a product such as CH_4 should desorb easily. This can be tackled here by profiling kinetic phase diagrams as used in the past.[89,90] In this approach, the molecule adsorption rate is compared to its desorption rate at different T and molecular partial pressures, finding turning points where adsorption and desorption rates are equal, *i.e.* equilibrium points. For the adsorption rate, r_{ads}, one can use non-activated collision theory,[91] such as:

$$r_{ads} = \frac{S_0 p_i A}{\sqrt{2\pi m_i k_B T}}, \quad (17)$$

where the initial sticking coefficient is denoted by S_0, p_i represents the partial pressure of the gas-phase molecule, either CO_2 or CH_4, and A represents the surface area of an adsorption site, established by dividing the supercell area of each surface by the number of possible sites, while m_i denotes the molecular mass. For the sticking coefficients, values of 0.4 and 0.01 were used for CO_2 and CH_4, respectively, as customary used in the past.[92,93]

To estimate the desorption rates, r_{des}, transition state theory (TST)[94] is used assuming that the desorbed transition state (TS) is a late two-dimensional (2D) TS. In this case, the energy barrier is given by the desorption energy, ΔE_{des}, which is simply the negative of the adsorption energy, ΔE_{des}, here without ZPE, as this term is already accounted for in the vibrational partition function, see below. Thus, r_{des} is defined as:

$$r_{des} = \nu_{des} \exp\left(\frac{\Delta E_{ads}}{k_B T}\right); \quad \nu_{des} = \frac{k_B T}{h} \frac{q^{gas}_{trans,2D} q^{gas}_{rot} q^{gas}_{vib}}{q^{ads}_{vib}}, \quad (18)$$

The ν_{des} prefactor is obtained from various partition functions, q, including $q^{gas}_{trans,2D}$, q^{gas}_{rot}, and q^{gas}_{vib}, which refer to the 2D translational, the rotational, and the vibrational partition functions, respectively, defined as

$$q^{gas}_{trans,2D} = A\frac{2\pi m k_B T}{h^2}, \quad (19)$$

$$q^{ads/gas}_{vib} = \prod_i \frac{\exp\left(-\frac{h\nu_i}{2k_B T}\right)}{1-\exp\left(-\frac{h\nu_i}{k_B T}\right)}, \quad (20)$$

$$q^{gas}_{rot} = \frac{T}{\sigma^{sym} T_{rot}}, \quad (21)$$

where σ^{sym} is the molecular symmetry number, 2 and 12 for CO_2 and CH_4, respectively,[89,95] and T_{rot} the rotational temperature, 0.561 and 122 K for CO_2 and CH_4, respectively.[96,97] Note that the vibrational partition function of the adsorbed state, q^{ads}_{vib}, takes into account the frustrated rotations and translations as discussed above.

3. Results and discussion

3.1. MXene models, CO_2 activation, and CH_4 physisorption

The CO_2RR species have been optimized on the five considered surface-terminated $Ti_3C_2T_x$ models as depicted in Fig. 1, in turn derived from Pourbaix diagrams shown in Fig. S2 of the ESI.† Notice that according to their density of states (DOS) and projected DOS (PDOS), all models exhibit a metallic character, and generally with a large number of states at the Fermi energy, see Fig. S3 of the ESI,† which is a prerequisite for electrocatalysis, *cf.* ref. 47. One of the first aspects to tackle is whether CO_2 is attached and activated on such terminations. According to *Le Sabatier* principle,[98] CO_2 should moderately adsorb, enough to remain not strongly bound to prevent catalyst poisoning, yet not weakly enough to enable sufficient opportunities for its chemical bond breaking.[99] On the other hand, a product such as CH_4 should also moderately adsorb, enough to permit its release, and, more importantly, not too strongly, to avoid the self-poisoning of the electrocatalyst by the methane product.

In order to investigate the interaction between CO_2 and the chosen surface-terminated $Ti_3C_2T_x$ models, various adsorption sites were examined in a systematic fashion, taking into account the interaction with respect to different surface moieties (*cf.* Fig. S4a of the ESI†) and CO_2 orientations (*cf.* Fig. S4b of the ESI†), including vertical orientations, but also planar situations with different molecular orientations. This systematic procedure, here exemplified on CO_2, has been carried out for the rest of the reaction species and intermediates, with energy minima structures duly characterized by frequency analysis. The adsorptive configurations are shown in Fig. 2, and comparative adsorption energies in Fig. 3. As can be seen, generally CO_2 keeps its linear geometry on any explored surface termination, except for the full –OH termination, where the molecule has an E_{ads} of −0.71 eV, gets bent by 135.9°, negatively charged by 0.80 e, and with a mean bond elongation of C–O bonds by 1.25 Å, in full accordance with CO_2 being activated.[100,101] Clearly, the presence of surface –O groups is detrimental to activating CO_2, and only on fully –OH terminated MXene, the negatively charged CO_2, with charge mostly present on its O atoms, is stabilized with the slightly positively charged H atoms of surface –OH groups, see Fig. 2, with Bader charges of −0.73*e*, and it is also observed with the –OH group H charge depletion shown in

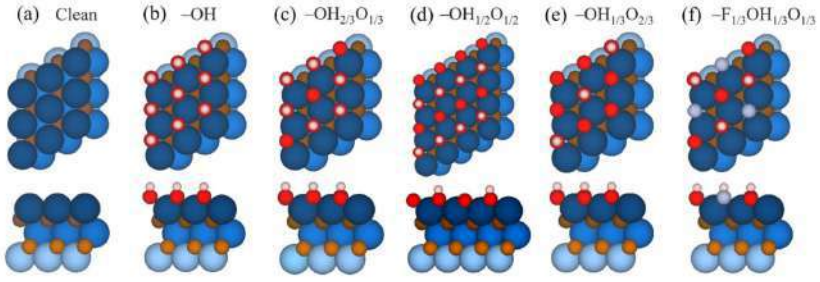

Fig. 1 Top (upper images) and side (lower images) views of the $p(3\times3)$ Ti_3C_2 MXene (0001) surface with (a) a clean surface, (b) full –OH, (c) $-OH_{2/3}O_{1/3}$, (d) $-OH_{1/2}O_{1/2}$, here of $p(4\times4)$ supercell, (e) $-OH_{1/3}O_{2/3}$, and (f) $-F_{1/3}OH_{1/3}O_{1/3}$ terminations. Termination H, O, and F atoms are represented by white, red, and light lilac spheres, respectively, while Ti and C atoms are shown as blue and brown spheres, with different levels of shading depending on their stacking position, with darker versions being closer to the shown surface.

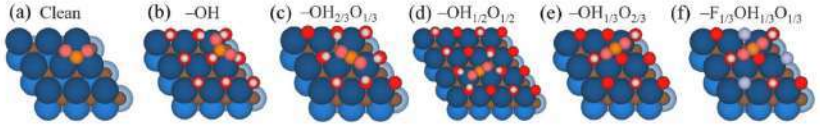

Fig. 2 Top views of optimal CO_2 adsorption sites on the Ti_3C_2 MXene model (0001) surface with (a) a clean surface, (b) full –OH, (c) $-OH_{2/3}O_{1/3}$, (d) $-OH_{1/2}O_{1/2}$, (e) $-OH_{1/3}O_{2/3}$, and (f) $-F_{1/3}OH_{1/3}O_{1/3}$ terminations. Colour coding as in Fig. 1, with CO_2 C and O atoms shown as orange and pink spheres, respectively.

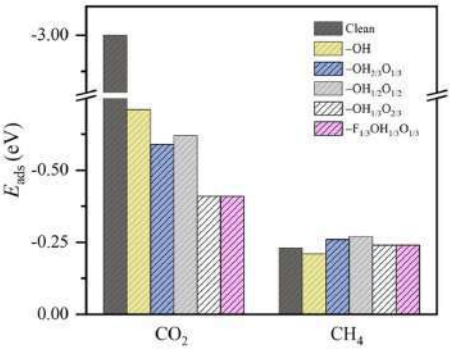

Fig. 3 Adsorption energies of CO_2 and CH_4, ΔE_{ads}, on the studied $Ti_3C_2T_x$ MXene (0001) surface models with a clean surface, full –OH, $-OH_{2/3}O_{1/3}$, $-OH_{1/2}O_{1/2}$, $-OH_{1/3}O_{2/3}$, and $-F_{1/3}OH_{1/3}O_{1/3}$ terminations. All values are given in eV.

the charge density difference (CDD) plots, see Fig. S5 of the ESI.†,[53]

This behavior contrasts with, *e.g.* CH_4 adsorption energies, see Fig. 3, where methane is physisorbed in any surface model, with E_{ads} ranging −0.21 to −0.27 eV. Here, actually, the presence of –O groups is slightly beneficial, allegedly forming H bonds with those of CH_4. Curiously, the stronger affinity towards CO_2 compared to CH_4 is in line with previous reports on pristine, surface termination free MXenes, as reported in the literature,[102] where such values were used to estimate CO_2 and CH_4 adsorption and desorption rates in the context of biogas upgrading. Note that the adsorption energies for both CO_2 and CH_4 are coincidental on $-OH_{1/3}O_{2/3}$ and $-F_{1/3}OH_{1/3}O_{1/3}$ models, since they belong to very similar local environments. Analogously, we estimated such adsorption/desorption rates as explained above, see Fig. S6 of the ESI,† in order to generate the so-called kinetic phase diagrams, present in Fig. 4.

Briefly, there, depending on the working conditions of temperature, T, and gases pressure, p, one can estimate the preference of the surfaces in adsorbing (or desorbing) such species. From them, it is evident that, *e.g.*, working at 300 K and 1 bar pressure, all surface models are favourable for attaching the CO_2 reactant, a premise of the reaction that is met. Moreover, the release of the eventual CH_4 product would be favoured in any explored model even in an atmosphere of 1 bar of CH_4, according to the kinetic phase diagrams of Fig. 4, a sought-after feature of a working electrocatalyst which underlies that no CH_4 self-poisoning is envisaged on such MXene models. From all the surface-terminated studied models, the fully –OH terminated model exhibits the strongest CO_2 adsorption and CH_4 desorption capabilities, while, as the surface concentration of –OH moiety decreases, these differences gradually diminish. Furthermore, when –F is present, as in $-F_{1/3}OH_{1/3}O_{1/3}$, similar

View Article Online
Journal of Materials Chemistry A Paper

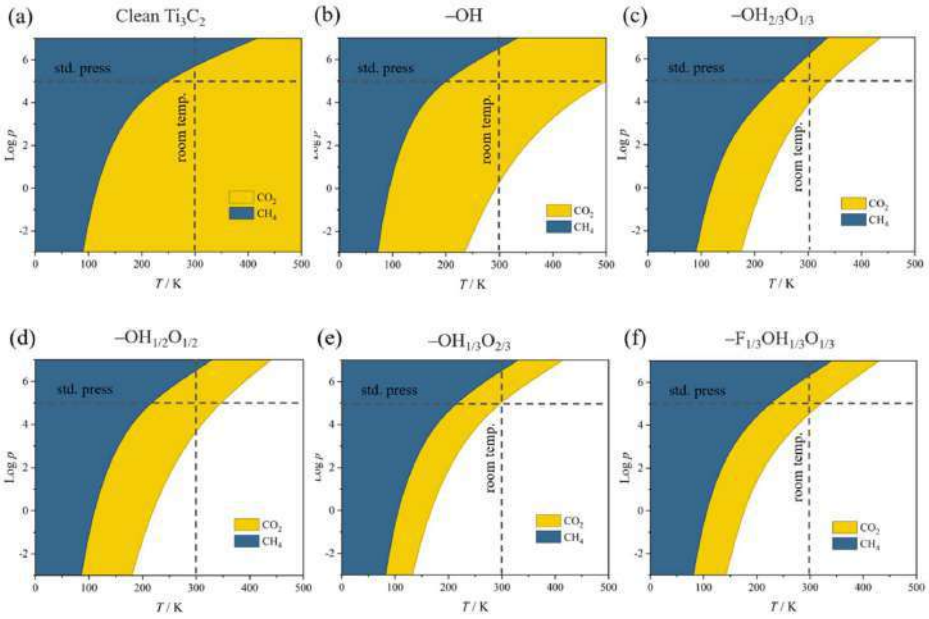

Fig. 4 Calculated adsorptive kinetic phase diagrams for CO_2 and CH_4 on (a) a clean surface, (b) full –OH, (c) $–OH_{2/3}O_{1/3}$, (d) $–OH_{1/2}O_{1/2}$, (e) $–OH_{1/3}O_{2/3}$, and (f) $–F_{1/3}OH_{1/3}O_{1/3}$ terminations as a function of the logarithm of gas pressures, p, in Pa. Coloured regions imply preference towards adsorption, while colourless areas represent regions where one would expect surfaces to be free of such molecules.

kinetic phase diagrams are gained compared to $–OH_{2/3}O_{1/3}$, implying, to some extent, a similar role of both –OH and –F groups, with similar charges of *ca.* −1 e, and comparable electric fields.

3.2. CO_2RR electrocatalysis mechanisms

After having established the suited surface-terminated MXene models for CO_2RR conditions, and the CO_2 and CH_4 adsorptive/desorptive conditions, the electrocatalytic performance is put under the inspection light, depicting the Gibbs free energy landscapes under standard working conditions, $T = 298.15$ K, $p_{H_2} = 1$ bar, pH = 0, and $U = 0$ V, to extract from them the limiting potential, U_L, as the main indicator of the electrocatalytic performance, yet the H-vacancy energetic cost, $E_{H_{vac}}$, is also used here to discuss the ease of T_x trapping H adatoms from surface –OH groups, defined as

$$E_{H_{vac}} = E_{T_x\text{-H}} + \tfrac{1}{2}E_{H_2} - E_{T_x}, \quad (22)$$

where $E_{T_x\text{-H}}$ describes the energy of MXene with a H-containing T_x termination, but with one missing H-atom, $\frac{1}{2}E_{H_2}$ accounts for the formation of a single H atom, released as half a H_2 molecule, and E_{T_x} is the energy of the H-containing T_x-terminated MXene. Within this definition, the more negative $E_{H_{vac}}$ is, the weaker H binds to the MXene surface, and so the easier is its transfer.

Let us begin the analysis with the highly active –OH surface termination, as observed with the high affinity towards CO_2, see Fig. 4. This affinity prompts the formation of stable HCO_2* during the CO_2 adsorption involving a H atom from a surface –OH group, being more stable by 2.22 eV, see Fig. 5, and energetically preferred over the direct electrochemical hydrogenation of CO_2 over an otherwise untouched –OH surface termination. It is mandatory here to note that the H transfer from the –OH group is spontaneous, and not artificial, neither in the –OH surface termination nor in the other models, as several attempts were made to prevent it. Thus, it is apparent that the resulting moiety is quite stable, and that drives the H transfer from neighboring –OH due to their proximity. Once HCO_2* is formed in a chemical step, the attention is driven towards the first PCET electrochemical step, finding that hydrogenation at the C atom is most favorable, H_2CO hydrogenation at the O atom implies at least a ΔG of 1.89 eV, yet stabilizing the system by only 0.04 eV. This step spontaneously draws two more surface H atoms from two vicinal –OH groups, forming a $H_2C(OH)_2$ compound, *i.e.* methanediol or methylene glycol. In the second PCET, the involvement of one –OH in the methylene glycol synthesis is then reverted so that

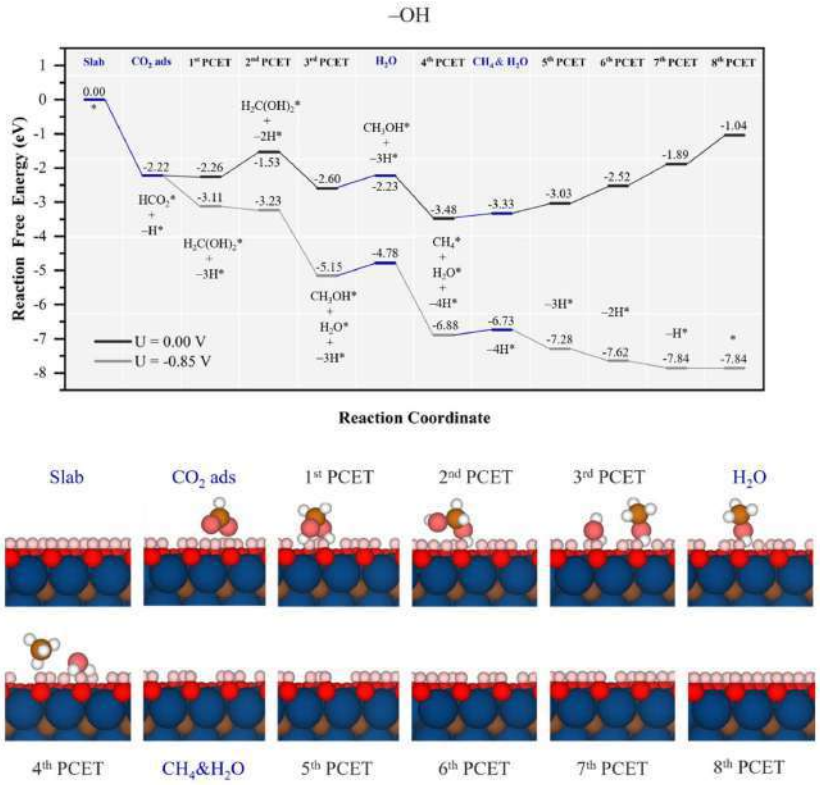

Fig. 5 Gibbs free energy, ΔG, diagram of the CO_2RR on fully –OH terminated Ti_3C_2 MXene, under standard working conditions. Blue lines represent chemical steps of as-generated H_2O or CH_4 desorption, or CO_2 adsorption, while black and grey lines represent the electrochemical proton-coupled electron transfer (PCET) steps under zero and applied $U = U_L$ calculated potential of −0.85 V *vs.* SHE, respectively. The *n*H* symbols refer to how many H atoms have been transferred from surface –OH groups at the reaction stage. Bottom panels show side views of atomic structures of different reaction stages. Colour coding as in Fig. 2.

hydrogenation of the as-formed surface –O group back to –OH proceeds with a ΔG of 0.73 eV.

Still, the regenerated –OH is able to again participate in the course of the reaction, along with the third PCET, forming methanol and water, *i.e.*

$$H_2C(OH)_2^* + H^+ + e^- + {-OH} \rightarrow H_3COH^* + H_2O^* + {-O}, \quad (23)$$

a quite favorable reaction step with a ΔG of −1.07 eV, and so thermodynamically preferred over the methylene glycol desorption. After this, the as-formed water can desorb, requiring 0.37 eV. Finally, in the fourth PCET, a similar situation occurs, where the reduced proton combines with a hydrogen from a surface –OH group, to form methane and water, as

$$H_3COH^* + H^+ + e^- + {-OH} \rightarrow CH_4^* + H_2O^* + {-O}, \quad (24)$$

with a noticeable ΔG of −1.25 eV, and preferred over the methanol desorption, requiring 0.71 eV, see Fig. S7 of the ESI.† At this point of the reaction, four PCET electrochemical steps have occurred, while four surface –OH groups have been consumed, supplying the remaining four PCET for the full methanation of CO_2. After CH_4 and H_2O desorption, requiring solely 0.15 eV, the remaining PCET steps are involved in regenerating the consumed surface –OH groups, with the subsequent ΔG values of 0.45, 0.51, 0.63, and 0.85 eV, respectively.

Notice here how energetically influential is the cooperative and simultaneous hydrogenation from solution protons and surface –OH groups, quite reducing the methylene glycol,

View Article Online
Journal of Materials Chemistry A Paper

methanol, and methane formation steps. This mechanism occurs thanks to the low $E_{H_{ins}}$ of the –OH surface termination, with a value of −0.56 eV, see Table 1, implying that such surface H atoms are relatively easy to capture and thus to participate in the reaction, and underscores the exceptionally high participation of the H atoms from the –OH groups, to the point that molecular synthesis is not the potential determining step (PDS), but the electrocatalyst surface regeneration, with a ΔG_{max} of 0.85 eV. The corresponding theoretical limiting potential U_L is −0.85 V *vs.* RHE, as depicted in Fig. 5, in which each electrochemical step is exergonic, while the chemical steps demand, at most, 0.37 eV for water release, feasible under working conditions. In addition, the U_L falls well within the stability region of the –OH model on the Pourbaix diagram in Fig. S2 of the ESI† at low pH, consistently implying the stability and recovery of the –OH terminated Ti_3C_2 electrocatalyst.

Furthermore, the selectivity of the catalyst is also, *a priori*, remarkable. As can be seen in alternative reaction paths shown in Fig. S7 of the ESI,† the two-electron synthesis of formic acid, $HCOOH_{(l)}$, is quite hindered by the formation of HCOOH* from HCO_2*, requiring 1.88 eV, while four-electron synthesis of formaldehyde, CH_2O*, from methylene glycol is disfavoured by 0.88 eV. Apart from these possible products, CO formation is avoided given the high stability of HCO_2* and the downhill formation of methylene glycol thanks to the participation of surface –OH groups transferring H atoms. Similarly, methanol synthesis is also quite hindered by the quite downhill formation of methane and water, see Fig. 5 and S7 of the ESI.† Thus, apart from the competitive hydrogen evolution reaction (HER), with an estimated U_L of −0.48 V using the very same computational scheme,[53] the synthesis of CH_4 competes with that of CH_2O in a similar fashion on fully –OH terminated Ti_3C_2 MXene, and only formic acid would be obtained at a very low potential of −1.88 V.

When –OH groups are partially replaced by –O, as in the $-OH_{2/3}O_{1/3}$ model, a different scenario unfolds, as illustrated in Fig. 6. In contrast to the full –OH coverage case, the reduced availability of surface H atoms, in line with a positive value of $E_{H_{ins}}$ of 0.12 eV, see Table 1, hampers the CO_2 molecule ability to capture surface H atoms before the electrochemical steps start, and so diminishes the involvement of surface H atoms in the oncoming PCET steps. Thus, CO_2 adsorption is mild, of −0.16 eV, and the initial formation of HCO_2* occurs by a PCET, with a ΔG of −0.35 eV, whereas the possible step related to surface H atom leading to adsorbed formic acid, HCOOH*, is disadvantageous by 0.21 eV, see Fig. S8 of the ESI.† From HCO_2*, the formation of methylene glycol is fostered by a PCET step coupled with two surface H transfers, being an uphill process of 0.71 eV, see Fig. 6, but still more favorable than formic acid formation by a second PCET, with a ΔG of 0.92 eV, see Fig. S8 of the ESI.† However, in the subsequent step, *HCO_2 captures a total of two surface H atoms, which play a crucial role in the second PCET to form methylene glycol. Here, the third PCET is similar to that occurring on the fully –OH covered model, with regeneration of a surface –OH group after methylene glycol formation, here downhill by 0.3 eV, while following regeneration is uphill by 0.24 eV.

However, from the 5th PCET on, there is a notable shift of –O termination activity, with a higher propensity for proton reduction. Thus, this reduction has a ΔG of 0.61 eV, and preferred by 0.12 eV over the proton-reduction induced methylene glycol decomposition into formaldehyde and water, see Fig. S8 of the ESI,† as:

$$H_2C(OH)_2^* \rightarrow H_2CO^* + H_2O^*, \quad (25)$$

an uphill process maintained in the 6th PCET with a ΔG of 0.76 eV. Actually, on this bifurcation, the system is much more favourable for methanol formation, as in eqn (23), a quite exergonic electrochemical step with a ΔG of −1.18 eV. After the as-formed H_2O is released, requiring 0.34 eV, the CH_3OH* can either desorb requiring 0.56 eV or get a vicinal reduced H, slightly less energy demanding by 0.06 eV. However, when this last electrochemical step occurs, eqn (24) is triggered, with a ΔG of −1.52 eV. Thus, under this picture, the methane formation PDS is this last $CH_3OH^* + H^*$ adduct formation, with a ΔG value of 0.84 eV, and a resulting U_L of −0.84 V *vs.* SHE, and so, similar to full –OH termination. Actually, the required U_L falls within the full –OH model stability according to the F-free Pourbaix diagram in Fig. S2 of the ESI† under acidic conditions, and would be viable only at neutral pH, although it is widely recognized that the electrocatalytic activity in more alkaline media is generally lower compared to acidic conditions.[103] Even if here the U_L is similar to that for the model with full –OH coverage, the PDS also corresponds to a late electrochemical stage, the $CH_3OH^* + H^*$ adduct formation, instead of –OH regeneration, and the mechanisms present similarities, including methylene glycol formation and decomposition, and methanol decomposition. The main difference between both models is the involvement of both –OH and –O groups, as H donors and acceptors, respectively. The –OH may be regarded as a H reservoir, through a Volmer step, and also as a donor, thus having a dual functionality. As per the selectivity, the chemistry involved in the $-OH_{2/3}O_{1/3}$ model appears to be less selective than that of the fully –OH terminated, since channels leading to formic acid exist, with a U_L of solely −0.21 V, −0.71 V for methylene glycol, and −0.73 V for $CH_2O_{(l)}$, and with a similar production of methanol and methane according to the competitive desorption of as-formed CH_3OH and its reaction to generate methane, see Fig. 6 and S8 of the ESI,† with no route

Table 1 Summary of the PCET PDS as well as specific electrochemical reaction step, on the explored surface-terminated Ti_3C_2 models, under CO_2RR working conditions. The required U_L in V, and surface $E_{H_{ins}}$ in eV, values are specified

Model	PCET	PDS	$E_{H_{ins}}$	U_L
–OH	8th	$-H^* \rightarrow *$	−0.56	−0.85
$-OH_{2/3}O_{1/3}$	7th	$CH_3OH^* + * \rightarrow CH_3OH^* + H^*$	0.12	−0.84
$-OH_{1/2}O_{1/2}$	6th	$CH_3OH^* + -H^* \rightarrow CH_3OH^* + *$	0.26	−0.70
$-OH_{1/3}O_{2/3}$	1st	$CO_2^* \rightarrow HCOOH^* + -H^*$	0.73	−0.37
$-F_{1/3}OH_{1/3}O_{1/3}$	2nd	$HCOOH^* + -H^* \rightarrow HCOOH^* + *$	0.31	−0.51

towards the CO formation. In addition, with such a model, the reported HER U_L is only of −0.08 V,[53] so, if any, such MXene termination would be better advisable to synthesize formic acid given the suited potential, matching the Pourbaix diagram stability shown in Fig. S2 of the ESI,† but with a competition to H_2(g) generation through the HER.

When further increasing the –O/–OH ratio as in the $-OH_{1/2}O_{1/2}$ model, again some similitudes with respect to the profile on the $-OH_{2/3}O_{1/3}$ model are kept, see Fig. 6 and 7, also in line with a similar degree of H transfer, with an $E_{H_{vac}}$ of 0.26 eV, see Table 1, similar to the value of 0.12 eV for the $-OH_{2/3}O_{1/3}$ model. Again, the reaction starts with CO_2 physisorption with an E_{ads} of −0.06 eV only, but now, given the extra room to accommodate formic acid, the 1st PCET is coupled with an –OH group H transfer leading to HCOOH*, which is exergonic by −0.3 eV, see Fig. 7. However, this formic acid is strongly adsorbed by 1.08 eV, see Fig. S9 of the ESI,† thus preventing its release. Consequently, the reaction advances through a 2nd PCET forming formate with a ΔG of −0.17 eV, *i.e.* transferring one H back to the substrate, thus reducing a nearby –O group, underscoring that formate stability is quite related to the presence of nearby –O groups.

After formate is synthesized, a 3rd PCET involves again H transfer from two nearby –OH groups and one proton reduction, to again lead to the adsorbed methylene glycol moiety, with an energy cost of 0.41 eV, followed once more by on surface –O group reduction, costly only by 0.15 eV. Similarly to the model with $-OH_{2/3}O_{1/3}$ surface terminations, the rest of the reaction follows a similar pathway; the methylene glycol decomposition, as induced by a proton reduction coupled to a surface –OH hydrogen transfer results in CH_3OH* and H_2O* in a quite exergonic electrochemical step with a ΔG of −0.77 eV, much more preferred than, *e.g.* decomposition towards formaldehyde, endergonic by 0.46 eV. After water desorption, methanol competes in between

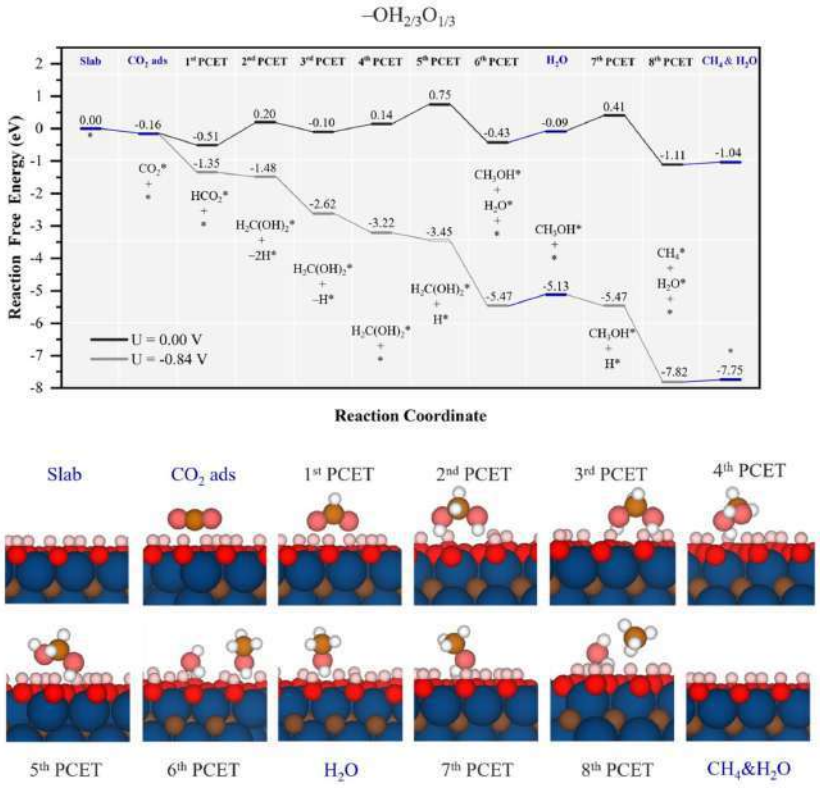

Fig. 6 Gibbs free energy, ΔG, diagram of the CO_2RR on the $-OH_{2/3}O_{1/3}$ Ti_3C_2 MXene model, under standard working conditions and at a $U = U_L$ calculated potential of −0.84 V *vs.* SHE. Colour code as in Fig. 6. The *n*H* symbols refer to how many H atoms have been reduced over surface –O groups at the given reaction stage. Bottom panels show side views of atomic structures of different reaction stages. Colour coding as in Fig. 2.

View Article Online
Journal of Materials Chemistry A
Paper

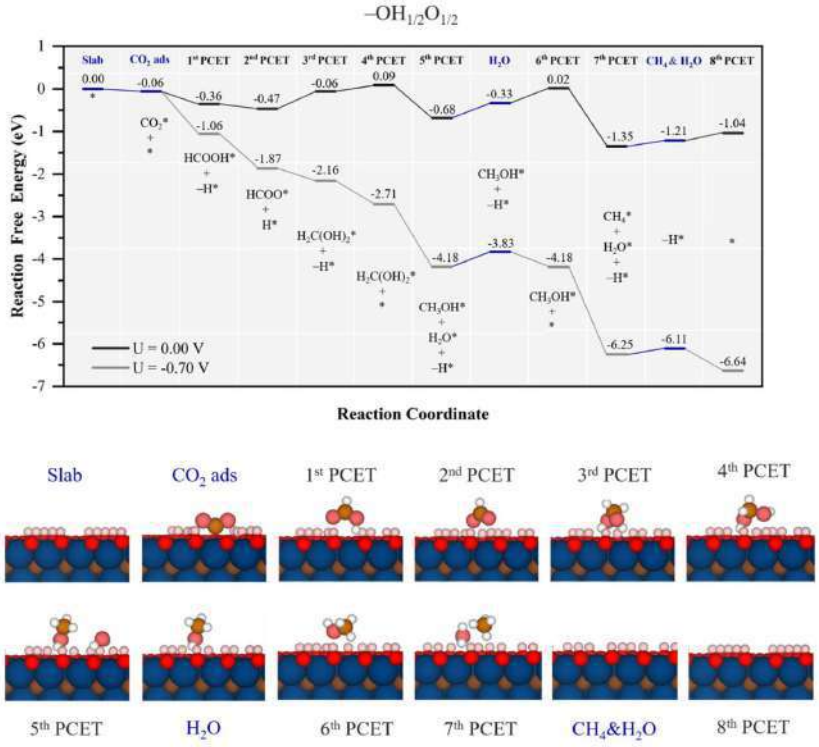

Fig. 7 Gibbs free energy, ΔG, diagram of the CO_2RR on the $-OH_{1/2}O_{1/2}$ Ti_3C_2 MXene model, under standard working conditions and at a $U = U_L$ calculated potential of −0.70 V *vs.* SHE. Colour code and notation as in Fig. 6 and 7. Bottom panels show side views of atomic structures of different reaction stages. Colour coding as in Fig. 2.

desorbing, ΔG of 0.63 eV, or refreshing the nearby lost –OH group, $\Delta G = 0.35$ eV, as shown in Fig. S9 of the ESI.† From this point on, again, methanol decomposition into CH_4* and H_2O*, implying the joint hydrogenation from a reduced proton and one H from an –OH group, results in an exergonic step with $\Delta G = -1.37$ eV, see Fig. 7, followed by product release and surface regeneration with a ΔG of 0.31 eV. Altogether, the PDS is the electrochemical step leading to adsorbed methanol, ready for its reaction towards CH_4, with a U_L of −0.7 V *vs.* SHE. This potential would lead also to full –OH termination under strongly acidic conditions, see Fig. S2 of the ESI.†

In any case, the CO_2RR mechanism is essentially kept, with a role of –O surface groups as reducing sites for protons, and later –OH groups as being H-donors, with the steps of formation and decomposition of methylene glycol and methanol, yet here with an initial formation and stabilization of formic acid triggered by the increase of surface –O groups. As per the selectivity, no path to CO is found, while formic acid release is prevented by the high desorption energy of 1.08 eV. Here, the formaldehyde path implies going through methylene glycol, whose conversion towards methanol is very exergonic by −0.77 eV, and the same applies to methanol decomposition to CH_4. Thus, a high selectivity towards CH_4 would be forecasted, although still the model would compete with the HER, with a U_L of −0.23 V,[53] H_2[g] being the main expected product.

When even increasing the surface –O content, such as in the $-OH_{1/3}O_{2/3}$ model, the reaction path mimics to some extent that of the $-OH_{1/2}O_{1/2}$ model, as shown in Fig. 8 and S10 of the ESI.† Starting from a mild physisorption of CO_2, the first PCET already combines proton reduction with H transfer from –OH, forming HCOOH*, with a ΔG value of 0.37 eV. From this point on, the 2nd and 3rd PCETs are essentially isoenergetic proton reductions on surface –O moieties, with the possibility of desorbing HCOOH, requiring 0.4 eV energy, and no more involvement of –OH groups, which may be related to the increase of $E_{H_{vac}}$ up to 0.73 eV, making the H transfer from vicinal –OH groups more difficult. In the 4th PCET, the methylene glycol formation path is essentially isoenergetic by 0.03 eV,

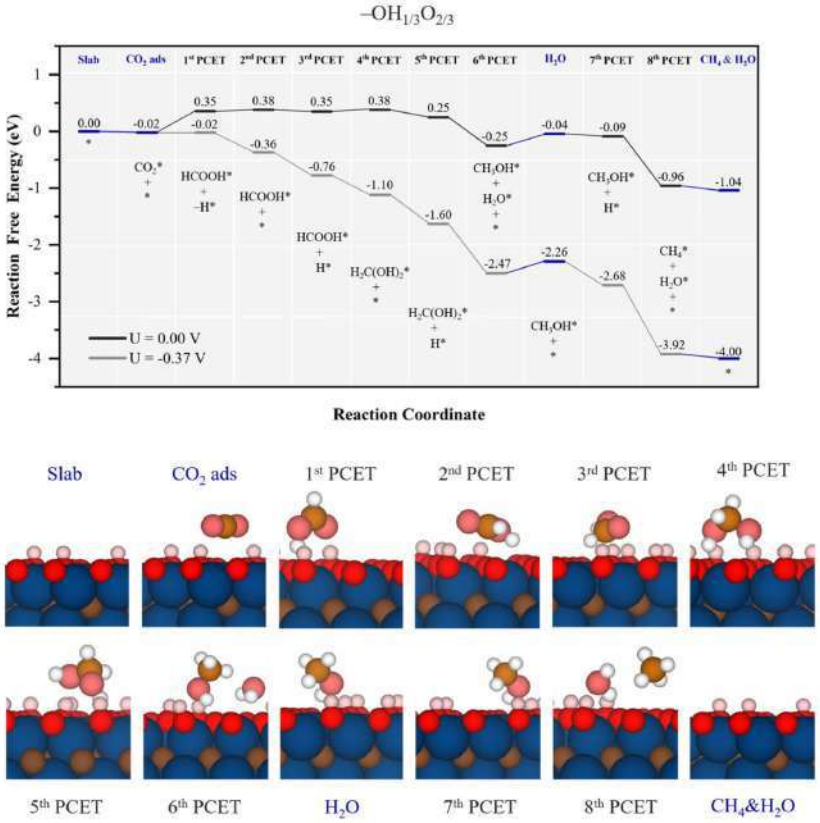

Fig. 8 Gibbs free energy, ΔG, diagram of the CO_2RR on the $-OH_{1/3}O_{2/3}$ Ti_3C_2 MXene model, under standard working conditions and at a $U = U_L$ calculated potential of −0.37 V *vs.* SHE. Colour code and notation as in Fig. 6 and 7. Bottom panels show side views of atomic structures of different reaction stages. Colour coding as in Fig. 2.

while CO formation induced by nearby –O proton reduction upon is uphill by 0.36 eV. After this point, the reaction is downhill, first by a –O proton reduction, followed later by methylene glycol decomposition into methanol, with a ΔG of −0.5 eV.

Also similar to the case of the $-OH_{1/2}O_{1/2}$ model, the formed H_2O in methanol synthesis can easily desorb, requiring 0.21 eV, see Fig. 8, while methanol desorption is more costly as it requires 0.51 eV, see Fig. S10 of the ESI.† Actually, the minimum energy path implies proton reduction nearby on an –O site, from which the proton reduction can again be coupled with –OH H transfer, turning the electrochemical step being quite exergonic by −0.87 eV, see Fig. 8. In general terms, the reaction profile is closer to the $\Delta G = 0$ eV than the other inspected models so far, and with less ups and downs in energy, which translates into reduced limiting potential. In fact, the full process can be made exergonic with a limiting potential of −0.37 V *vs.* SHE, corresponding to the initial formic acid formation in the first PCET, at variance with previous models, where the PDS is found at a late stage. Still, the U_L is too large for this surface stability, see the Pourbaix diagram in Fig. S2 of the ESI,† and the model would be valid for less acid conditions. Still, as low as the U_L of −0.37 V may seem, as per the selectivity, the $-OH_{1/3}O_{2/3}$ model has a very low U_L for the HER, of solely −0.01 V,[53] and so, the selectivity towards CH_4(g) would be low, and other reaction products, such as HCOOH, CH_3OH, and CO, would be possible with a U_L of −0.37 V, even if their detachment from the surface would be energetically more costly than further reacting towards CH_4, implying a lower content of them.

View Article Online
Journal of Materials Chemistry A Paper

From the above analysis, one could draw a general trend: namely, the U_L decreases as the –OH proportion decreases. However, no minimum would be expected at a full –O termination. Firstly, according to a previous study conducted by Handoko *et al.*,[40] a larger U_L of 0.52 V *vs.* RHE was found for Ti_2CO_2, while Morales *et al.*[104] pointed out a similar activity between Ti_3C_2 and Ti_2C MXenes. Moreover, according to the Pourbaix diagrams in Fig. S2 of the ESI,† even at zero potential, a full –O termination would require a pH larger than 7, and, as aforementioned, alkaline media is not the best case scenario for the CO_2RR electrocatalytic activity.

At this point, one may wonder what would be the effect of –F surface groups on CO_2RR performance, particularly relevant at low pH and U, see Fig. S2 of the ESI.† This is analysed on the $-F_{1/3}OH_{1/3}O_{1/3}$ model shown in Fig. 9. Actually, if one would assume –F surface groups being mere spectators, the –OH/–O ratio would be comparable to that of the $-OH_{1/2}O_{1/2}$ model, and so a similar performance would be expected, at least in U_L, even if the production rates per electrocatalyst gram would decrease as a third of the surface sites are blocked by –F groups. Mechanistically, as the $E_{H_{ads}}$ value of 0.31 eV is similar to the value of 0.26 eV for the $-OH_{1/2}O_{1/2}$ model, see Table 1, one would envisage a similar involvement of –OH/–O groups in the hydrogenation sequence. By inspecting the actual Gibbs free energy profile in Fig. 9, one observes a small physisorption of CO_2 with an E_{ads} of 0.04 eV, followed by the 1st PCET and nearby –OH H transfer to form HCOOH*, with a $\Delta G = -0.13$ eV, actually reminiscent of that found for the $-OH_{1/2}O_{1/2}$ model. However, on $-F_{1/3}OH_{1/3}O_{1/3}$ the second PCET does not lead to formate, but rather to a regeneration of the consumed –OH, here costly by 0.51 eV, again similar to that corresponding to the $-OH_{1/2}O_{1/2}$ model, with $\Delta G = 0.5$ eV,

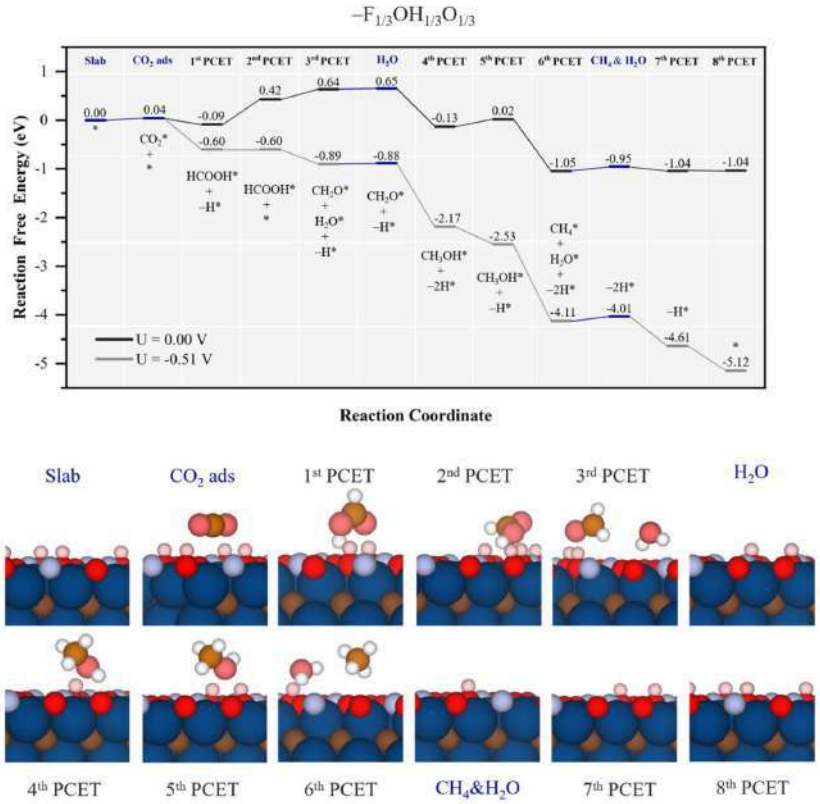

Fig. 9 Gibbs free energy, ΔG, diagram of the CO_2RR on the $-F_{1/3}OH_{1/3}O_{1/3}$ Ti_3C_2 MXene model, under standard working conditions and at a $U = U_L$ calculated potential of −0.51 V *vs.* SHE. Colour code and notation as in Fig. 6 and 7. Bottom panels show side views of atomic structures of different reaction stages. Colour coding as in Fig. 2.

see Fig. 7, and competing with methylene glycol formation, 0.08 eV more costly, see Fig. S11 of the ESI.†

Actually, the absence of the formate intermediate has consequences on the oncoming steps since, at variance with the mechanism for the $-OH_{1/2}O_{1/2}$ model, methylene glycol intermediate formation is not preferred, but the hydrogenation of formic acid coupled with a surface –OH H transfer leads to formaldehyde and water formation, as:

$$HCOOH^* + H^+ + e^- + -OH \rightarrow CH_2O^* + H_2O^* + -O, \quad (26)$$

with a mere cost of 0.22 eV, and preferred over –O reduction by 0.12 eV, and over $HCOOH_{(l)}$ formation, requiring 0.38 eV, see Fig. S11 of the ESI.† Actually, after H_2O^* removal, essentially costless by 0.01 eV, the $CH_2O^{(g)}$ release, costly only by 0.07 eV, competes though with a quite exergonic 4th PCET leading to methanol, again combining one PCTE with one –OH H transfer, with a ΔG of −0.78 eV, see Fig. 9 and S11 of the ESI.† After CH_3OH^* is formed, a vicinal –OH can be easily regenerated by requiring 0.15 eV, and after this Volmer step, methanol can decompose into CH_4^* and H_2O^* coupling H^+ reduction with one H transfer from –OH, with a ΔG of −1.07 eV, a process quite competing with the $CH_3OH_{(l)}$ release, requiring 0.44 eV, see Fig. S11 of the ESI.† Once methanol is formed, the 7th and 8th PCETs are used in regenerating two surface –OH groups, with ΔG below 0.01 eV.

Thus, the PDS corresponds to an early step of –OH regeneration right after formic acid formation, with $U_L = -0.51$ V, different from the –OH regeneration right after methanol formation on the $-OH_{1/2}O_{1/2}$ model, with $U_L = -0.70$ V. Actually, the easier reduction cost on –O groups vicinal to CH_3OH^* is the reason behind the change in the reaction profile, lowering the cost of the equivalent PDS on the $-OH_{1/2}O_{1/2}$ model, and leaving the PDS to formic acid formation, essentially unaltered by the presence of –F groups. Thus, on the $-F_{1/3}OH_{1/3}O_{1/3}$ model, the U_L is −0.51 V, close to its stability region according to Pourbaix diagrams, see Fig. S2 of the ESI.† As per the selectivity, formic acid is likely formed under the same U_L, although $CH_2O^{(g)}$ and $CH_3OH_{(l)}$ desorption compete with quite exergonic further reaction steps, moving towards more generation of methane. No channel to CO formation is found, as well. However, as happened with the $-OH_{2/3}O_{1/3}$ model, the main competition is with the HER, with a U_L of solely −0.01 V.[53]

Table 1 summarizes results for the five studied models indicating which PCET is the PDS and to which electrochemical step does it correspond to, including $E_{H_{vac}}$ and U_L values as well. As encompassed in Table 1, but also visible in the captured trends in Fig. 10, the $E_{H_{vac}}$ linearly varies with respect to the –OH/–O ratio, with similar values for the $-OH_{1/2}O_{1/2}$ and $-F_{1/3}OH_{1/3}O_{1/3}$ models. As $E_{H_{vac}}$ increases with the presence of more surface –O groups, the U_L decreases, see Fig. 10, to the point that two regions can be differentiated: one where –OH is the main surface termination site, with quite low U_L values, and the other with the participation of –O groups in reducing protons, and later transferring such H atoms, with even smaller U_L values. The higher involvement of –O surface moieties generally eases the latest PCET steps and moves PDS to an earlier stage of the reaction. Last but not least, the presence of –F groups is not *per se* detrimental, and in fact leads to a deviation of the trend, reducing U_L costs. Besides, the reaction profiles question the conventional mechanism of the sole H^+ reduction upon the reacting molecule, and unfolds (i) the sequences of Volmer steps on nearby –O surface groups, followed by H transfer to the reacting molecule from such as-formed –OH, (ii) the H transfer from already existing –OH groups, followed by proton reduction on the as-generated –O moieties, and (iii) the simultaneous hydrogenation of a moiety, coupling H^+ reduction electrochemical step with H chemical transfers from surface –OH groups. Indeed, it can be claimed that the simultaneous existence of –OH and –O groups offers a versatility of reactive paths that ultimately expresses in a reduction of the reaction bias cost.

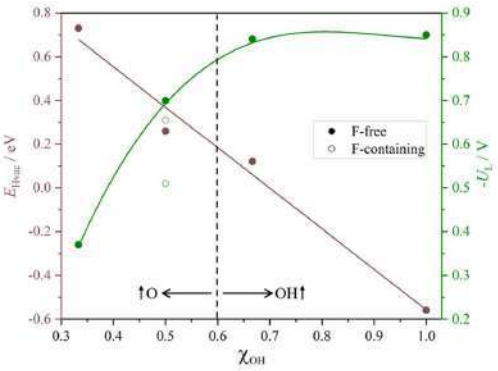

Fig. 10 Plots of H-vacancy energies, $E_{H_{vac}}$, given in eV, and minus the limiting potential, U_L, given in V, as a function of –OH group partition coefficients (χ_{OH}) with respect to –O groups.

3.3. CO_2RR electrocatalysis performance

We now focus on the CO_2RR performance of the scrutinized models keeping in mind that an optimal catalyst would feature the smallest possible U_L and that the closer the U_L to zero, the higher the activity and faster the CO_2RR kinetics. The present results are already fully consistent with previous studies,[39] in that a higher proportion of –O termination leads to a quite small U_L resulting in a higher CO_2RR activity, see Table 1. However, keeping in mind the electrocatalyst surface stability predicted in the Pourbaix diagram of Fig. S2 of the ESI,† even if certain models feature reduced U_L values, *e.g.* −0.37 V for $-OH_{1/3}O_{2/3}$ or −0.51 V for $-F_{1/3}OH_{1/3}O_{1/3}$, their range of stability implies that at low pH the surface would eventually transform into the full –OH model, or when working at higher pH would imply sluggish reaction conditions, yet to be partially compensated by a larger potential applicability. In addition, the fact that models with larger –F content do not appear in the Pourbaix diagrams helps explaining previous experimental findings,[105] particularly in that such models would make the

View Article Online
Journal of Materials Chemistry A
Paper

reaction infeasible. However, low contents such as is $-F_{1/3}OH_{1/3}O_{1/3}$ are non-detrimental *per se*, as such moieties can help in moving the PDS to an earlier stage, with a concomitant U_L reduction and, hence, operating costs. This opens the door to a control of the electrocatalyst performance by the degree of –F appearing at the surface, a point missed under F-free synthesis methodologies.[73]

Another key point of interest is the comparison of the here reported CO_2RR activity with that of other MXenes reported in the literature, such as fully OH-terminated $Mo_3C_2(OH)_2$,[39] and $Sc_2C(OH)_2$,[41] O-terminated $Mo_3C_2O_2$,[39] Zr_2NO_2,[69] $Ti_3C_2O_2$,[106] and W_2CO_2,[40] pristine surface MXene Mo_2TiC_2,[68] Mo_2CO_2-O_v model containing surface oxygen vacancies,[107] and $Cr@Nb_2NO_2$,[108] a case with a Cr single atom on a fully –O terminated Nb_2N MXene. No pure –F termination is here compared to, as shown to consistently deliver high U_L for the CO_2RR and HER on MXenes,[42,53] plus is not a reachable stable situation according to Pourbaix diagrams in Fig. S2 of the ESI.† For a more comprehensive comparison, Cu metal is also considered as it has been reported to be a highly efficient CO_2RR catalyst.[41,109] Fig. 11 clearly shows that, even if accounting from deviations from different computational approaches between present models and results in the literature, in general terms, MXene-based electrocatalysts feature lower U_L compared to the Cu reference of −0.93 V, underscoring the potential of such a family of materials for CO_2 conversion purposes. Still, one has to be critical with the display of values. For instance, some of the systems with the lowest U_L are Mo_2CO_2-O_v and W_2CO_2, with values of −0.31 and −0.35 V, respectively, while to a lower extent, other O-terminated MXenes have relatively low U_L values, like −0.45 V for Zr_2NO_2, −1.04 V for $Ti_3C_2O_2$,[106] or the value of −0.47 V for $Cr@Nb_2NO_2$. However, from the Pourbaix diagram in Fig. S2 of the ESI,† and others reported in the literature, the full O-termination is only stable at positive U_L values, and so, such surface termination gets unrealistic under CO_2RR conditions. Actually, under these conditions, more realistic values are −1.17 and −0.53 V reported for $Mo_3C_2(OH)_2$ and $Sc_2(OH)_2$, respectively, the latter representing a clear improvement with respect to the Cu reference by around 0.4 V. It is with respect to these fully OH-terminated models where we find that O-rich $-OH_{1/3}O_{2/3}$ and F-containing $-F_{1/3}OH_{1/3}O_{1/3}$ models have an U_L improvement by at least 0.16 and 0.02 V compared with $Sc_2(OH)_2$, underscoring that the slight presence of −F moieties and a balance between –OH and –O groups represent tuning points towards decreasing U_L costs.

In order to understand the differences with prior calculations, one has to note that they are regularly focused on pure –O termination. Thus, the main discrepancy is attributed to the commented involvement of –F and –OH groups, and to the strong hydrophilicity of –O groups. Based on $E_{H_{ads}}$, the strength of this H bond seems to be related to the distribution of –OH groups, which, eventually, endows the MXene surface with a new source of H atoms, making the reaction easier, a feature absent in previous studies with only –O groups. Besides, –F and –OH terminations have the same charge close to $-1e$, but as in the CDD plot in Fig. S5 of the SI,† the electron density on –F termination is more localized, leading to a stronger effective charge, and so, *a priori* more repulsion, features that may affect the MXene activity at different stages of the reaction.

Last but not least, it is worth addressing the competition between the CO_2RR, here examined with respect to methane formation, and the HER, a crucial concurrent reaction in aqueous solutions.[53,110] Even if a rigorous study of the selectivity requires addressing the kinetic barriers,[41,111] the U_L difference among both types of reactions can be used as a sound thermodynamic metric.[112] This is graphically shown in Fig. 12 as a parity plot, gaining HER values from an equivalent previous study.[53] Note that, different from previous studies focusing only on –O terminations,[113,114] we considered here the involvement of

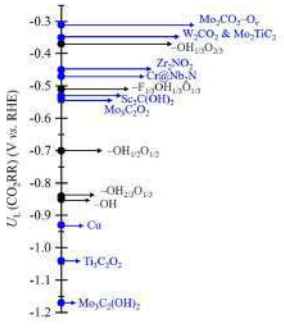

Fig. 11 Comparison of methane U_L from the presently studied terminated models on $Ti_3C_2T_x$ (black dots) along with other values reported in the literature for MXene-based systems, and Cu as a reference (blue dots). All values are given in V.

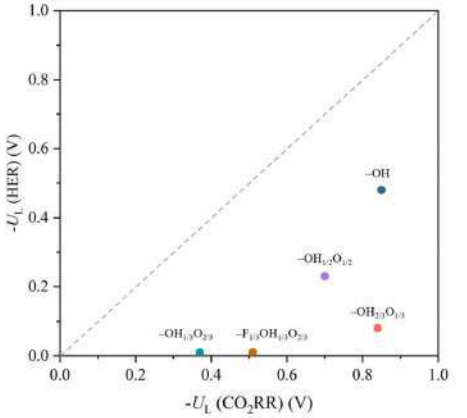

Fig. 12 Comparison of $-U_L$ for the CO_2RR *vs.* $-U_L$ for the HER on the explored terminated $Ti_3C_2T_x$ models. Values for the HER are taken from the literature.[53]

H atoms of the –OH groups, and, in the case of the HER, different reaction mechanisms have been evaluated, beyond the spreadly used, yet limitedly justified, assumption of the reaction being controlled by the first PCET;[108,115] see more details in the literature.[53] Notice that, even if none of the proposed surface terminations is more selective towards the CO_2RR than towards the HER, a general trend can be captured; the smaller the U_L needed, the less the selectivity towards the CO_2RR is. Actually, the CO_2RR selectivity seems to be improved when increasing the –OH/–O ratio, with a maximum for the fully –OH terminated model. Still, even if such models are *per se* selective towards the HER, or very selective, in the cases of the $-OH_{1/3}O_{2/3}$ and $-F_{1/3}OH_{1/3}O_{1/3}$ models, strategies are available to inhibit the HER, such as limiting H^+ transfer rates,[116–118] employing non-water proton donors,[119,120] limiting electron transfer rates,[121,122] or regulating the magnetic moment of the active site.[123]

4. Conclusions

Here we have profoundly analyzed the possible use of Ti_3C_2 MXene based materials as electrocatalysts for the CO_2RR, examining the surface composition under working conditions *via* Pourbaix diagrams and systematically studying the reaction mechanisms considering the involvement of different surface termination species, and aspects such as limiting potential towards methane production, selectivity, and competition with respect to $H_2^{(g)}$ production. Based on the surface stability dictated by the calculated Pourbaix diagrams, several surface models are investigated that may have potential interest towards the CO_2RR, namely full –OH, as well as $-OH_{2/3}O_{1/3}$, $-OH_{1/2}O_{1/2}$, and $-OH_{1/3}O_{2/3}$ models, and the F-containing $-F_{1/3}OH_{1/3}O_{1/3}$ model. Apart from their stability under working conditions, kinetic phase diagrams show that these models meet the requirement of CO_2 capture and activation, and the CH_4 product release.

The calculated reaction Gibbs free energy profiles reveal that, in general, for F-free models the reaction mechanism involves formic acid and methylene glycol formation, which decomposes into methanol and water. In subsequent steps, methanol decomposes into methane and water as well. However, on the F-containing $-F_{1/3}OH_{1/3}O_{1/3}$ model, the reaction involves the initial formation of formic acid, and its decomposition into formaldehyde, which later hydrogenates up to methanol. The present profiles help in understanding the experimental observations, in the sense that, the larger the –O content, the smaller the U_L,[42] mostly arising from the dual role of –O and –OH groups, acting as H acceptors and donors, respectively, which make the hydrogenation steps more flexible, allowing for reduction of U_L costs, and also add the possibility of reaction species to be simultaneously hydrogenated from H^+ reduction and surface –OH group H transfers, the latest fostered by a relatively low energetic cost of deprotonation. Note that the role of the –OH groups is reminiscent of the Mars-van Krevelen mechanism on oxide surfaces where the lattice O directly participates in the reaction with the left O vacancy healed by O_2 from the gas phase at a subsequent step.

Generally speaking, the presently studied $Ti_3C_2T_x$ surface MXene models, together with results from the literature, underscore the effectiveness of such materials for the CO_2RR when compared to the reference Cu electrocatalyst, with significantly improved U_L values by up to *ca.* 0.6 V. However, they still face aspects to be improved; on one hand, the required U_L in many of the models with binary and ternary terminations underscores the eventual gradual conversion into a fully –OH terminated model, which has a larger value of U_L of −0.85 V, yet lower by almost 0.1 V than the equivalent value for the Cu reference. On the other hand, the selectivity of the CO_2RR on the studied models with respect to the HER is far from optimal, yet the fully –OH terminated model is the most competitive one, and so significant degrees of the CO_2RR are to be expected when using it for this purpose. In any case, on such surface terminated $Ti_3C_2T_x$ MXenes, an optimal HER performance is to be expected at low U_L values, while a significant improvement in the CO_2RR is to be expected when reducing the U_L up to the requirements of the fully –OH terminated model. Given the vast family of possible MXene materials, and the surface tunability, the present study sheds light on the effective selection and tuning of MXenes for high performance and selective CO_2RR electrocatalysis.

Conflicts of interest

There are no conflicts of interest to declare.

Acknowledgements

The authors acknowledge financial support from the Spanish *Ministerio de Ciencia e Innovación* through grants MCIN/AEI/10.13039/501100011033 PID2021-126076NB-I00 and TED2021-129506B–C22, funded partially by FEDER *Una manera de hacer Europa*, the unit of excellence María de Maeztu CEX2021-001202 M granted to the IQTCUB, the COST Action CA18234, and the *Generalitat de Catalunya* 2021SGR00079 grant. F. V. acknowledges the ICREA Academia Award 2023 Ref. Ac2216561. L. M. thanks the China Scholarship Council (CSC) for financing her PhD (CSC202108390032). A significant part of the computational resources has been provided by the *Red Española de Supercomputación* (RES) QHS-2022-1-0004 and QHS-2021-3-0012. L. M. acknowledges the HPC-Europa3 (HPC17OOIBY) project supported by the EC Research Innovation Action under the H2020 Programme.

References

1 *International Energy Agency: CO_2 Emissions In 2022; Typeset in France by IEA - March 2023*, https://www.iea.org/.
2 *European Central Bank: Looking Through Higher Energy Prices? Monetary Policy and The Preen Transition*, https://www.ecb.europa.eu/home/html/index.en.html.
3 S. Posada-Pérez, F. Viñes, P. J. Ramirez, A. B. Vidal, J. A. Rodriguez and F. Illas, *Phys. Chem. Chem. Phys.*, 2014, **16**, 14912–14921.

4 X. Liu, C. Kunkel, P. Ramírez de la Piscina, N. Homs, F. Viñes and F. Illas, *ACS Catal.*, 2017, **7**, 4323–4335.

5 J. A. Rodriguez, J. Evans, L. Feria, A. B. Vidal, P. Liu, K. Nakamura and F. Illas, *J. Catal.*, 2013, **307**, 162–169.

6 G. Pacchioni, J. M. Ricart and F. Illas, *J. Am. Chem. Soc.*, 1994, **116**, 10152–10158.

7 S. Posada-Pérez, P. J. Ramírez, J. Evans, F. Viñes, P. Liu, F. Illas and J. A. Rodriguez, *J. Am. Chem. Soc.*, 2016, **138**, 8269–8278.

8 S. Yang, M. Jiang, W. Zhang, Y. Hu, J. Liang, Y. Wang, Z. Tie and Z. Jin, *Adv. Funct. Mater.*, 2023, **33**, 2301984.

9 C. Sun, Y. Hou, N. Lüdi, H. Hu, M. de Jesús Gálvez-Vázquez, M. Liechti, Y. Kong, M. Liu, R. Erni, A. V. Rudnev and P. Broekmann, *J. Catal.*, 2022, **407**, 198–205.

10 M. Liu, Y. Pang, B. Zhang, P. De Luna, O. Voznyy, J. Xu, X. Zheng, C. T. Dinh, F. Fan, C. Cao, F. P. G. Arquer, T. S. Safaei, A. Mepham, A. Klinkova, E. Kumacheva, T. Filleter, D. Sinton, S. O. Kelley and E. H. Sargent, *Nature*, 2016, **537**, 382–386.

11 M. J. Cheng, E. L. Clark, H. H. Pham, A. T. Bell and M. Head-Gordon, *ACS Catal.*, 2016, **6**, 7769–7777.

12 K. P. Kuhl, T. Hatsukade, E. R. Cave, D. N. Abram, J. Kibsgaard and T. F. Jaramillo, *J. Am. Chem. Soc.*, 2014, **136**, 14107–14113.

13 Y. Chen, J. Zhang, L. Yang, X. Wang, Q. Wu and Z. Hu, *Electrochem. Energy Rev.*, 2022, **5**, 11.

14 J. J. Wang, X. P. Li, B. F. Cui, Z. Zhang, X. F. Hu, J. Ding, Y. D. Deng, X. P. Han and W. B. Hu, *Rare Met.*, 2021, **40**, 3019–3037.

15 H. Hu, J. Z. Ou, X. Xu, Y. Lin, Y. Zhang, H. Zhao, D. Chen, M. He, Y. Huang and L. Deng, *J. Chem. Eng.*, 2021, **425**, 130587.

16 S. Zhou, W. Pei, Y. Zhao, X. Yang, N. Liu and J. Zhao, *Npj Comput. mater.*, 2021, **7**, 186.

17 K. P. Kuhl, E. R. Cave, D. N. Abram and T. F. Jaramillo, *Energy Environ. Sci.*, 2012, **5**, 7050–7059.

18 D. Ren, Y. Deng, A. D. Handoko, C. S. Chen, S. Malkhandi and B. S. Yeo, *ACS Catal.*, 2015, **5**, 2814–2821.

19 Y. Hori, A. Murata and R. Takahashi, *J. Chem. Soc., Faraday Trans.*, 1989, **85**, 2309–2326.

20 Y. Huang, A. D. Handoko, P. Hirunsit and B. S. Yeo, *ACS Catal.*, 2017, **7**, 1749–1756.

21 H. Shin, Y. Ha and H. Kim, *J. Phys. Chem.*, 2016, **7**, 4124–4129.

22 X. Liu, J. Xiao, H. Peng, X. Hong, K. Chan and J. K. Nørskov, *Nat. Commun.*, 2017, **8**, 15438.

23 Á. Morales-García, F. Calle-Vallejo and F. Illas, *ACS Catal.*, 2020, **10**, 13487–13503.

24 M. Naguib, J. Halim, J. Lu, K. M. Cook, L. Hultman, Y. Gogotsi and M. W. Barsoum, *J. Am. Chem. Soc.*, 2013, **135**, 15966–15969.

25 M. Naguib, V. Presser, N. Lane, D. Tallman, Y. Gogotsi, J. Lu, L. Hultman and M. W. Barsoum, *RSC Adv.*, 2011, **1**, 1493–1499.

26 M. Ahmaruzzaman, *RSC Adv.*, 2022, **12**, 34766–34789.

27 G. Deysher, C. E. Shuck, K. Hantanasirisakul, N. C. Frey, A. C. Foucher, K. Maleski, A. Sarycheva, V. B. Shenoy, E. A. Stach, B. Anasori and Y. Gogotsi, *ACS Nano*, 2020, **14**, 204–217.

28 M. Naguib, O. Mashtalir, J. Carle, V. Presser, J. Lu, L. Hultman, Y. Gogotsi and M. W. Barsoum, *ACS Nano*, 2012, **6**, 1322–1331.

29 M. Ghidiu, M. R. Lukatskaya, M.-Q. Zhao, Y. Gogotsi and M. W. Barsoum, *Nature*, 2014, **516**, 78–81.

30 X. Q. Tan, W. Mo, X. Lin, J. Y. Loh, A. R. Mohamed and W. J. Ong, *Nanoscale*, 2023, **15**, 6536–6562.

31 M. A. Hope, A. C. Forse, K. J. Griffith, M. R. Lukatskaya, M. Ghidiu, Y. Gogotsi and C. P. Grey, *Phys. Chem. Chem. Phys.*, 2016, **18**, 5099–5102.

32 B. C. Wyatt, A. Rosenkranz and B. Anasori, *Adv. Mater.*, 2021, **33**, 2007973.

33 M. Benchakar, L. Loupias, C. Garnero, T. Bilyk, C. Morais, C. Canaff, N. Guignard, S. Morisset, H. Pazniak, S. Hurand, P. Chartier, J. Pacaud, V. Mauchamp, M. W. Barsoum, A. Habrioux and S. Célérier, *Appl. Surf. Sci.*, 2020, **530**, 147209.

34 J. Sun, B. Liu, Q. Zhao, C. H. Kirk and J. Wang, *Adv. Mater.*, 2023, **35**, 2306072.

35 S. Y. Pang, Y. T. Wong, S. Yuan, Y. Liu, M. K. Tsang, Z. Yang, H. Huang, W. T. Wong and J. Hao, *J. Am. Chem. Soc.*, 2019, **141**, 9610–9616.

36 R. Meshkian, H. Lind, J. Halim, A. El Ghazaly, J. Thörnberg, Q. Tao, M. Dahlqvist, J. Palisaitis, P. O. Å. Persson and J. Rosen, *ACS Appl. Nano Mater.*, 2019, **2**, 6209–6219.

37 V. Kamysbayev, A. S. Filatov, H. Hu, X. Rui, F. Lagunas, D. Wang, R. F. Klie and D. V. Talapin, *Science*, 2020, **369**, 979–983.

38 D. Ontiveros, F. Viñes and C. Sousa, *J. Mater. Chem. A*, 2023, **11**, 13754–13764.

39 N. Li, X. Chen, W. J. Ong, D. R. MacFarlane, X. Zhao, A. K. Cheetham and C. Sun, *ACS Nano*, 2017, **11**, 10825–10833.

40 A. D. Handoko, K. H. Khoo, T. L. Tan, H. Jin and Z. W. Seh, *J. Mater. chem. A*, 2018, **6**, 21885–21890.

41 H. Chen, A. D. Handoko, J. Xiao, X. Feng, Y. Fan, T. Wang, D. Legut, Z. W. Seh and Q. Zhang, *ACS Appl. Mater. Interfaces*, 2019, **11**, 36571–36579.

42 A. D. Handoko, H. Chen, Y. Lum, Q. Zhang, B. Anasori and Z. W. Seh, *iScience*, 2020, **23**, 101181.

43 C. Y. J. Lim, A. D. Handoko and Z. W. Seh, *Diamond Relat. Mater.*, 2022, **130**, 109461.

44 G. T. M. Kadja, M. M. Ilm, N. J. Azhar, A. Febrianti, J. J. M. Siregar, N. Nurdini, U. Pratomo and M. I. Khalil, *FlatChem*, 2023, **38**, 100481.

45 X. Li, Y. Chen, X. Zhan, Y. Xu, L. Hao, L. Xu, X. Li, M. Umer, X. Tan, B. Han, A. W. Robertson and Z. Sun, *Innov. Mater.*, 2023, **1**, 100014.

46 H. Bao, Y. Qiu, X. Peng, J.-a. Wang, Y. Mi, S. Zhao, X. Liu, Y. Liu, R. Cao, L. Zhuo, J. Ren, J. Sun, J. Luo and X. Sun, *Nat. Commun.*, 2021, **12**, 238.

47 Y. Zhang and Z. Cao, *J. Phys. Chem. C*, 2021, **125**, 13331–13342.

48 X. Qian, L. Li, Y. Li, Z. Liu, Z. Tian, C. Zhan and L. Chen, *Phys. Chem. Chem. Phys.*, 2021, **23**, 12431–12438.

49 M. Naguib, M. Kurtoglu, V. Presser, J. Lu, J. Niu, M. Heon, L. Hultman, Y. Gogotsi and M. W. Barsoum, *Adv. Mater.*, 2011, **23**, 4248–4253.
50 M. Tahir, A. Ali Khan, S. Tasleem, R. Mansoor and W. K. Fan, *Energy Fuels*, 2021, **35**, 10374–10404.
51 M. Pourbaix, *Atlas of Electrochemical Equilibria in Aqueous Solutions*, National Association of Corrosion Engineers (NACE), Houston, Texas, USA, 1974.
52 M. López, K. S Exner, F. Viñes and F. Illas, *Adv. Theory Simul.*, 2023, **6**, 2200217.
53 L. Meng, L. K. Yan, F. Viñes and F. Illas, *J. Mater. Chem. A*, 2023, **11**, 6886–6900.
54 Y. Cheng, X. Xu, Y. Li, Y. Zhang and Y. Song, *Comput. Mater. Sci.*, 2022, **202**, 110971.
55 X. Qian, L. Li, Y. Li, Z. Liu, Z. Tian, C. Zhan and L. Chen, *Phys. Chem. Chem. Phys.*, 2021, **23**, 12431–12438.
56 G. Kresse and J. Furthmüller, *Phys. Rev. B*, 1996, **54**, 11169–11186.
57 J. P. Perdew, K. Burke and M. Ernzerhof, *Phys. Rev. Lett.*, 1996, **77**, 3865–3868.
58 J. D. Gouveia, Á. Morales-García, F. Viñes, J. R. B. Gomes and F. Illas, *ACS Nano*, 2022, **16**, 12541–12552.
59 V. Parey, B. M. Abraham, S. H. Mir and J. K. Singh, *ACS Appl. Mater. Interfaces*, 2021, **13**, 35585–35594.
60 G. Gao, A. P. O'Mullane and A. Du, *ACS Catal.*, 2017, **7**, 494–500.
61 S. Grimme, J. Antony, S. Ehrlich and H. Krieg, *J. Chem. Phys.*, 2010, **132**, 154104.
62 P. E. Blöchl, *Phys. Rev. B*, 1994, **50**, 17953–17979.
63 G. Kresse and D. Joubert, *Phys. Rev. B*, 1999, **59**, 1758–1775.
64 R. Morales-Salvador, J. D. Gouveia, Á. Morales-García, F. Viñes, J. R. B. Gomes and F. Illas, *ACS Catal.*, 2021, **11**, 11248–11255.
65 K. Mathew, V. S. C. Kolluru, S. Mula, S. N. Steinmann and R. G. Hennig, *J. Chem. Phys.*, 2019, **151**, 234101.
66 H. J. Monkhorst and J. D. Pack, *Phys. Rev. B*, 1976, **13**, 5188–5192.
67 M. López, Á. Morales-García, F. Viñes and F. Illas, *ACS Catal.*, 2021, **11**, 12850–12857.
68 J. D. Gouveia, Á. Morales-García, F. Viñes, F. Illas and J. R. B. Gomes, *Appl. Catal., B*, 2020, **260**, 118191.
69 J. K. Nørskov, J. Rossmeisl, A. Logadottir, L. Lindqvist, J. R. Kitchin, T. Bligaard and H. Jónsson, *J. Phys. Chem. B*, 2004, **108**, 17886–17892.
70 H. A. Hansen, I. C. Man, F. Studt, F. Abild-Pedersen, T. Bligaard and J. Rossmeisl, *Phys. Chem. Chem. Phys.*, 2010, **12**, 283–290.
71 W. Yuan, L. Cheng, Y. An, H. Wu, N. Yao, X. Fan and X. Guo, *ACS Sustain. Chem. Eng.*, 2018, **6**, 8976–8982.
72 N. A. Adibah, S. N. A. Zaine and M. F. A. Shukur, *Mater. Sci. Forum*, 2021, **1023**, 15–20.
73 T. Li, L. Yao, Q. Liu, J. Gu, R. Luo, J. Li, X. Yan, W. Wang, P. Liu, B. Chen, W. Zhang, W. Abbas, R. Naz and D. Zhang, *Angew. Chem., Int. Ed.*, 2018, **57**, 6115–6119.
74 Z. Guo, Y. Li, B. Sa, Y. Fang, J. Lin, Y. Huang, C. Tang, J. Zhou, N. Miao and Z. Sun, *Appl. Surf. Sci.*, 2020, **521**, 146436.
75 Y. Li, Y. Chen, Z. Guo, C. Tang, B. Sa, N. Miao, J. Zhou and Z. Sun, *J. Chem. Eng.*, 2022, **429**, 132171.
76 V. Parey, B. M. Abraham, M. V. Jyothirmai and J. K. Singh, *Catal. Sci. Technol.*, 2022, **12**, 2223–2231.
77 S. Nitopi, E. Bertheussen, S. B. Scott, X. Liu, A. K. Engstfeld, S. Horch, B. Seger, I. E. L. Stephens, K. Chan, C. Hahn, J. K. Nørskov, T. F. Jaramillo and I. Chorkendorff, *Chem. Rev.*, 2019, **119**, 7610–7672.
78 I. Fishtik and R. Datta, *Chem. Eng. Sci.*, 2000, **55**, 4029–4043.
79 Y. Xiao and W. Zhang, *Nanoscale*, 2020, **12**, 7660–7673.
80 J. N. Brønsted, *Chem. Rev.*, 1928, **5**, 231–338.
81 K. Niu, L. Chi, J. Rosen and J. Björk, *J. Phys. Chem. Lett.*, 2022, **13**, 2800–2807.
82 K. S. Exner and H. Over, *Acc. Chem. Res.*, 2017, **50**, 1240–1247.
83 M. López, K. S. Exner, F. Viñes and F. Illas, *J. Catal.*, 2023, **421**, 252–263.
84 H. Chen, A. D. Handoko, T. Wang, J. Qu, J. Xiao, X. Liu, D. Legut, Z. Wei Seh and Q. Zhang, *ChemSusChem*, 2020, **13**, 5690–5698.
85 N. Li, X. Wang, X. Lu, P. Zhang and W. J. Ong, *Chem.–An Euro. J.*, 2021, **27**, 17900–17909.
86 S. Baskaran and J. Jung, *Appl. Surf. Sci.*, 2022, **592**, 153339.
87 *NIST Standard Reference Database SRD Number* 69, DOI: **10.18434/T4D303**.
88 Q. Li, Y. Ouyang, S. Lu, X. Bai, Y. Zhang, L. Shi, C. Ling and J. Wang, *Chem. Commun.*, 2020, **56**, 9937–9949.
89 Á. Morales-García, A. Fernández-Fernández, F. Viñes and F. Illas, *J. Mater. Chem. A*, 2018, **6**, 3381–3385.
90 R. Morales-Salvador, Á. Morales-García, F. Viñes and F. Illas, *Phys. Chem. Chem. Phys.*, 2018, **20**, 17117–17124.
91 *Collision Theory*, Chemistry LibreTexts, Libretexts, 2017.
92 S. Pogodin and N. López, *ACS Catal.*, 2014, **4**, 2328–2332.
93 R. Bisson, M. Sacchi, T. T. Dang, B. Yoder, P. Maroni and R. D. Beck, *J. Phys. Chem. A*, 2007, **111**, 12679–12683.
94 C. Kunkel, F. Viñes and F. Illas, *Energy Environ. Sci.*, 2016, **9**, 141–144.
95 T. Shimanouchi, *Tables of Molecular Vibrational Frequencies Consolidated Volume I*, National Bureau of Standards, 1972, pp. 1–160.
96 P. W. Atkins and J. De Paula, *Atkins' Physical Chemistry*. Oxford University Press, 8th edn, 2006.
97 A. V. Leont'eva, A. Y. Zakharov and A. Y. Prokhorov, *arXiv*, 2017, preprint, arXiv:1708.08077, DOI: **10.48550/arXiv.1708.08077**.
98 H. Ooka, J. Huang and K. S. Exner, *Front. Energy Res.*, 2021, **9**, 654460.
99 J. R. Pankhurst, P. Iyengar, A. Loiudice, M. Mensi and R. Buonsanti, *Chem. Sci.*, 2020, **11**, 9296–9302.
100 A. Mazheika, Y. G. Wang, R. Valero, F. Viñes, F. Illas, L. M. Ghiringhelli, S. V. Levchenko and M. Scheffler, *Nat. Commun.*, 2022, **13**, 419.
101 M. López, L. Broderick, J. J. Carey, F. Viñes, M. Nolan and F. Illas, *Phys. Chem. Chem. Phys.*, 2018, **20**, 22179–22186.
102 H. Prats, H. McAloone, F. Viñes and F. Illas, *J. Mater. Chem. A*, 2020, **8**, 12296–12300.

103 J. D. Wiensch, J. John, J. M. Velazquez, D. A. Torelli, A. P. Pieterick, M. T. McDowell, K. Sun, X. Zhao, B. S. Brunschwig and N. S. Lewis, *ACS Energy Lett.*, 2017, **2**, 2234–2238.
104 Á. Morales-García, M. Mayans-Llorach, F. Viñes and F. Illas, *Phys. Chem. Chem. Phys.*, 2019, **21**, 23136–23142.
105 A. D. Handoko, K. D. Fredrickson, B. Anasori, K. W. Convey, L. R. Johnson, Y. Gogotsi, A. Vojvodic and Z. W. Seh, *ACS Appl. Energy Mater.*, 2018, **1**, 173–180.
106 N. H. Attanayake, H. R. Banjade, A. C. Thenuwara, B. Anasori, Q. Yan and D. R. Strongin, *Chem. Commun.*, 2021, **57**, 1675–1678.
107 S. Cao, Y. Hu, C. Yang, J. Li, H. Chen, S. Wei, S. Liu, Z. Wang, D. Sun and X. Lu, *J. CO_2 Util.*, 2022, **62**, 102074.
108 S. Lu, Y. Zhang, F. Lou and Z. Yu, *J. CO_2 Util.*, 2022, **62**, 102069.
109 A. A. Peterson, F. Abild-Pedersen, F. Studt, J. Rossmeisl and J. K. Nørskov, *Energy Environ. Sci.*, 2010, **3**, 1311–1315.
110 Z. W. Seh, K. D. Fredrickson, B. Anasori, J. Kibsgaard, A. L. Strickler, M. R. Lukatskaya, Y. Gogotsi, T. F. Jaramillo and A. Vojvodic, *ACS Energy Lett.*, 2016, **1**, 589–594.
111 C. Shi, H. A. Hansen, A. C. Lausche and J. K. Nørskov, *Phys. Chem. Chem. Phys.*, 2014, **16**, 4720–4727.
112 X. Hong, K. Chan, C. Tsai and J. K. Nørskov, *ACS Catal.*, 2016, **6**, 4428–4437.
113 Y. W. Cheng, J. H. Dai, Y. M. Zhang and Y. Song, *J. Mater. Chem. A*, 2018, **6**, 20956–20965.
114 Y. W. Cheng, J.-H. Dai, Y. M. Zhang and Y. Song, *J. Phys. Chem. C*, 2018, **122**, 28113–28122.
115 S. Lu, H. L. Huynh, F. Lou, M. Guo and Z. Yu, *J. CO_2 Util.*, 2021, **51**, 101645.
116 B. L. Sheets and G. G. Botte, *ChemComm*, 2018, **54**, 4250–4253.
117 M. A. Ortuño, O. Hollóczki, B. Kirchner and N. López, *J. Phys. Chem. Lett.*, 2019, **10**, 513–517.
118 J. M. McEnaney, A. R. Singh, J. A. Schwalbe, J. Kibsgaard, J. C. Lin, M. Cargnello, T. F. Jaramillo and J. K. Nørskov, *Energy Environ. Sci.*, 2017, **10**, 1621–1630.
119 S. Malkhandi, B. Yang, A. K. Manohar, G. K. S. Prakash and S. R. Narayanan, *J. Am. Chem. Soc.*, 2013, **135**, 347–353.
120 A. K. Manohar, S. Malkhandi, B. Yang, C. Yang, G. K. Surya Prakash and S. R. Narayanan, *J. Electrochem. Soc.*, 2012, **159**, A1209.
121 K. A. Brown, D. F. Harris, M. B. Wilker, A. Rasmussen, N. Khadka, H. Hamby, S. Keable, G. Dukovic, J. W. Peters, L. C. Seefeldt and P. W. King, *Science*, 2016, **352**, 448–450.
122 D. Zhu, L. Zhang, R. E. Ruther and R. J. Hamers, *Nat. Mater.*, 2013, **12**, 836–841.
123 X. Guo and S. Huang, *Electrochim. Acta*, 2018, **284**, 392–399.

Available online at www.sciencedirect.com

ScienceDirect

Current Opinion in Electrochemistry

ELSEVIER

Review Article

Theoretical modelling of the Hydrogen evolution reaction on MXenes: A critical review

Ling Meng, Francesc Viñes and Francesc Illas

Abstract

MXenes, two-dimensional (2D) transition-metal carbides and nitrides with diverse compositions and structures, have attracted notable attention due to their potential as promising alternatives to the conventional Pt-group catalysts for the hydrogen evolution reaction (HER). Hereby, we analyze the state-of-art approaches in theoretical modelling HER in MXenes with the aim of assessing their intrinsic activity for this crucial electrocatalytic reaction, analyze diverse thermodynamic and electronic properties proposed as descriptors, inspect kinetic aspects, and explore linear scaling relations. Ultimately, we present an overview of the challenges, perspectives, and future research of HER in MXenes.

Addresses

Departament de Ciència de Materials i Química Física & Institut de Química Teòrica i Computacional (IQTCUB), Universitat de Barcelona, c/ Martí i Franquès 1, 08028 Barcelona, Spain

Corresponding author: Illas, Francesc (francesc.illas@ub.edu)

Current Opinion in Electrochemistry 2023, **40**:101332

This review comes from a themed issue on **Fundamental and Theoretical Electrochemistry (2024)**

Edited by **Kai S. Exner**

For complete overview about the section, refer Fundamental and Theoretical Electrochemistry (2024)

Available online 7 June 2023

https://doi.org/10.1016/j.coelec.2023.101332

Introduction

The rising energy demand and depletion of natural resources require renewable energy sources [1–3]. Molecular hydrogen (H_2) shows promise as an alternative fuel [4–6]. Current industrial hydrogen production has limitations [7,8], but electrochemical processes offer a sustainable solution. Efficient and cost-effective electrocatalysts are vital for widespread use [9,10]. Two-dimensional (2D) materials, MXenes, have shown promising potential as HER electrocatalysts [11–19]. These materials exhibit a chemical formula of $M_{n+1}X_nT_x$ with $n = 1–4$, M is an early transition metal, X stands for carbon and/or nitrogen, and T_x are terminating functional groups such as O, H, OH, or F (*cf.* Figure 1a–b) [17]. MXenes are obtained from chemical etching of A elements from a MAX phase precursor using F-containing etchants like hydrofluoric acid (HF), either directly [17] or *in situ* [20*]. Surface termination can be controlled [21], and F-free synthesis [22] methods are available. Some treatments yield clean MXenes [23], allowing for adjustments in composition, thickness, and surface termination. This concise review explores MXene's HER using computational methods, discussing reaction mechanisms, activity descriptors, and future research trends.

Hydrogen evolution reaction and MXene electrocatalysts

The general mechanisms of the HER were established for most materials including MXenes [24–33]. Two possible well-agreed mechanisms for the HER reaction, Volmer-Heyrovsky and Volmer–Tafel (*cf.* Figure 1c) [25]. Both share a first electrochemical step as is Eq. (1).

$$\text{Volmer step: } H^+ + e^- + * \rightarrow H^* \quad (1)$$

where * represents an active site and H* represents an adsorbed hydrogen atom. These two mechanisms differ on the second step, represented in Eqs. (2) and (3).

$$\text{Heyrovsky step: } H^+ + e^- + H^* \rightarrow * + H_2 \quad (2)$$

$$\text{Tafel step: } 2H^* \rightarrow * + H_2 \quad (3)$$

The Heyrovsky step is electrochemical nature, whereas Tafel step involves the recombination of two previously reduced protons.

Meng et al. [26*] found that the reaction could potentially start from H atoms of −OH or −H terminations, besides the reduction of aqueous H^+ in VH or VT mechanisms. They also explored the termination effect on HER mechanism of Ti_3C_2 MXene, pointing out that models featuring mixed terminations lead closer to the HER equilibrium line with thermodynamic overpotential of 0.01. All in all, MXenes showed outstanding performance as HER electrocatalysts [34,35] and several descriptors have been proposed to evaluate their HER electrocatalytic properties [36*,37*].

Figure 1

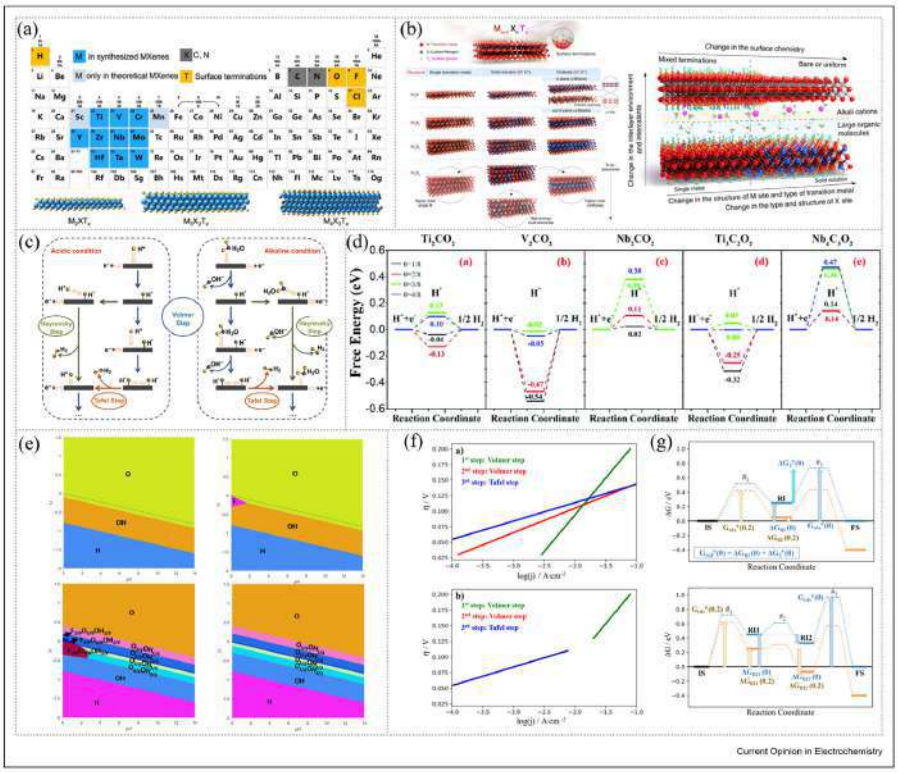

(**a**) All elements involved in different MAX phases. Reprinted with permission from Ref. [73]. (**b**) Schematic illustration of the MXene structures with $M_{n+1}X_nT_x$ general formula (see text), reprinted with permission from ref. [20]. (**c**) Schematic Volmer-Heyrovsky and Volmer–Tafel pathways for hydrogen evolution reaction (HER) under acidic and alkaline conditions. Reprinted with permission from ref. [24]. (**d**) Free energy diagram of HER processing on Ti_2CO_2, V_2CO_2, Nb_2CO_2, $Ti_3C_2O_2$, and $Nb_4C_3O_2$ under standard conditions. Reprinted with permission from ref. [65]. (e) Pourbaix diagrams for Ti_3C_2 MXene (0001) surface regarding fully –O, –OH, and –H terminated surfaces (left), or including as well fully –F terminated surfaces (right). Reprinted with permission from ref. [26]. (f–g) Schematic representation of an arbitrarily chosen Gibbs free energy profile and linear Tafel regimes based on the V_2C–H model for the Volmer-Heyrovsky and Volmer–Tafel mechanisms. Reprinted with permission from ref. [50].

Thermodynamic approach to the HER by MXenes

The calculated Gibbs free energy (ΔG) of HER intermediates is crucial for assessing the activity of electrocatalysts like MXenes as it is directly related to the potential determining step (PDS). For the equilibrium in Eq. (4) at 1 bar and 298.15 K

$$H^+_{(aq)} + e^- \leftrightarrow 1/2 \cdot H_2(g) \quad (4)$$

the computational hydrogen electrode (CHE) model, [38] allows one to estimate the chemical potential of the left-hand side and to relate it to the standard hydrogen

electrode (SHE), which takes the potential for Eq. (4) as zero. In the case of MXenes, one has

$$\Delta G_H = \Delta E_H + \Delta E_{ZPE} - T\cdot\Delta S_H, \quad (5)$$

and

$$\Delta E_H = E_{nH/MXene} - E_{(n-1)H/MXene} - 1/2\cdot E_{H_2} \quad (6)$$

where $E_{nH/MXene}$ and $E_{(n-1)H/MXene}$ are the total energy of the MXene model with n and n-1 H adatoms, respectively, E_{H_2} is the H_2 molecule energy in vacuum, the ΔE_{ZPE} and ΔS_H terms account for the difference in zero-point-energy contribution and entropy change, respectively. A variant of this descriptor has been proposed [39*,40*], that is directly related to the rate determining step (RDS) although not widely used yet (*cf.* Figure 1d).

In MXenes, the −O termination [41] is the primary active site for H adatom. However, analyzing other potential active sites requires further investigation. Here, ΔG_H appear to be a key descriptor for HER catalyzed by MXenes [42], consistent with the *Sabatier* principle. Optimal H adsorption strength is vital for efficient reaction rates at different steps. However, while the ΔG_H maximum corresponds to the HER PDS,

Figure 2

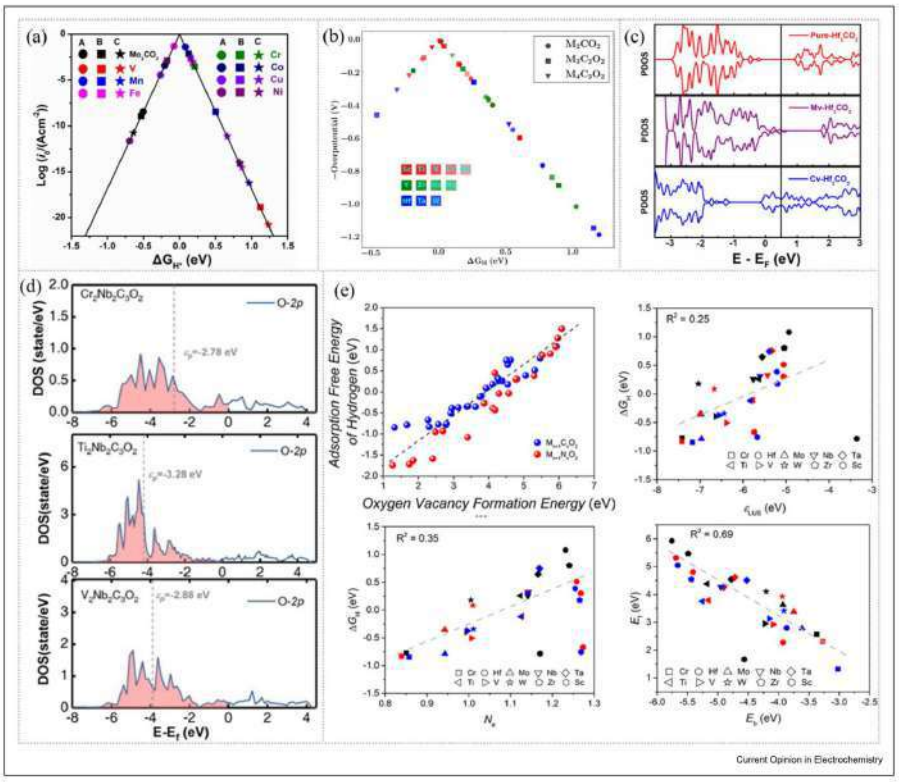

(**a**) The volcano curve of exchange current (i_0) as a function of the ΔG_{H^*}. Reprinted with permission from ref. [63]. (**b**) Negative of the overpotential of MXenes plotted versus ΔG_{H^*}. Reprinted with permission from ref. [28]. (**c**) Projected density of states (PDOS) of the O atom on Hf_2CO_2 with different vacancy types. Reprinted with permission from ref. [47]. (**d**) DOS plot of $Cr_2Nb_2C_3O_2$, $Ti_2Nb_2C_3O_2$, and $V_2Nb_2C_3O_2$. The ε_p values denote the position of O-2*p* band center with respect to the Fermi level. Reprinted with permission from ref. [32]. (**e**) Linear relationship between ΔG_{H^*} and oxygen formation energy (E_i), the lowest unoccupied state (ε_{LUS}), number of electrons gained by oxygen atom (N_e) and oxygen binding energy (E_b). Reprinted with permission from ref. [37].

Brønsted–Evans–Polanyi (BEP) relationships [43,44] justify considering it as RDS. However, more researches are required to investigate the kinetics and determine the true RDS in the HER process. Using $\Delta G_H = 0$ as a design criterion is controversial because it assumes equilibrium conditions without considering overpotential or non-thermoneutral conditions [45,46]. Additionally, there are several computationally based proposals to improve the MXenes HER through structural modifications [29,30,33,47,48].

Pourbaix diagrams are useful for determining the surface composition of an electrode under specific *pH* and potential conditions using the CHE method [38]. Analyzing Pourbaix diagrams is an essential step in computational studies. While previous works on MXenes primarily focused on the stable –O termination (*cf.* Figure 1d) [41], this may not be the most stable under electrochemical conditions. More recently, Meng et al. [26*] and López et al. [27*] considered Pourbaix diagrams for MXenes involving several terminations (*cf.* Figure 1e). Ashton et al. [49] used them to predict favorable MXene synthesis conditions.

Kinetic aspects of HER by MXenes

Studying the transition states (TSs) for the VH and VT mechanisms in HER is complex due to coupled proton-electron transfers. Some studies treated them as non-electrochemical steps. Only one study by López et al. [50*] investigated the kinetics of HER on V_2C MXene (*cf.* Figure 1f–g) and simulated the Tafel slope, which indicates the reaction rate based on current density and overpotential [31,51,52]. The Tafel also is provided about the rate from the current density (j) and as in Eq. (7) [53],

$$\log_{10} j\,(\eta) = \log_{10} j_0 + \eta/b, \tag{7}$$

where $1/b$ is the Tafel slop, j and j_0 are the current density and exchange current density, respectively [54]. The relationship between the free energy landscape and the Tafel plot is complex. Accurate measurements require quasi-equilibrium [55,56] or steady-state [57] conditions. Tafel slopes are condition-specific and influenced by several factors [58–61]. Furthermore, the role of the frequency factor (A) in MXenes HER activity also should be explored, as it is known that HER activity of noble metals involves high A values [62].

Descriptors of the Hydrogen evolution reaction by MXene electrocatalysts

Various descriptors have been proposed to evaluate the HER performance of MXenes, including the HER overpotential (η) [28], the exchange current j_0 [63], as in Eq. (7), and ΔG [64], being used to represent MXenes catalytic activity and identify important properties through volcano plots (*cf.* Fig. 2a and b). Among them, especially the *d*-band (ε_d) and *p*-band (ε_p) centers, are often used as descriptors for HER activity [65–67] (*cf.* Figure 2c and d). Anand et al. [67] suggested that a closer ε_d to the Fermi level improves charge transfer kinetics. Jin et al. [32] found a correlation between ε_p and ΔG_H, indicating the impact of the outer metal layer on HER activity and H adsorption. Further details can be found in Fig. 2e and summarized in Table 1. Exploring the linear relationship between descriptors is crucial for evaluating HER activity. It can reduce the cost of high throughput screening and facilitate the synthesis of MXenes with enhanced HER activity based on theoretical principles.

Table 1

Overview of potential linear relations for HER on MXenes proposed in recent years. These involve various properties such as Bond Length (BL), the Bader charge variation (N_e), Gibbs free energy of hydrogen adsorption (ΔG_H), binding and formation energy of modified MXenes (E_b and E_f), Fermi level energy (E_{Fermi}), the lowest unoccupied state (ε_{LUS}), the highest peak position (E_p), *p*-band centre (ε_p) of density of state (DOS), overpotential (η), exchange current (j_0), the number of valence electrons, atom radius, and electronegativity of doped atoms of MXenes. The corresponding references are also indicated.

Relevance	BL	N_e	ΔG_H	E_b	E_f	E_{fermi}	Ref.
BL		√	√			√	[32,33,36*]
N_e	√		√	√	√		[33,36*,37*]
ΔG_H	√	√		√	√		[32,36*,37*]
E_b		√	√		√		[29,37*]
E_f		√	√	√			[29,37*]
E_{Fermi}	√						[37*]
ε_{LUS}			√				[37*]
E_p/ε_p			√				[32,47]
η							[28]
j_0							[63]
H-coverage	√	√	√				[30,65,71]
Atom Radius	√			√			[72*]
Valence Electron Num.			√				[72*]
Electronegativity			√				[72*]

Summary and outlook

MXenes are promising candidates as efficient electrocatalysts for hydrogen production. Screening MXenes through experiments or modeling using grounded descriptors simplifies evaluation and design. However, a comprehensive overview of recent developments and expanded descriptors is missing. Further research is needed to explore the role of mixed surface terminations under realistic conditions, as most studies have focused on specific terminations. Also, advanced approaches, like explicit inclusion of solvation effects [68] and making used grand-canonical DFT [69], reshape the understanding of electron transfer reactions and catalytic activity on MXene materials. HER kinetics and appropriate modeling with descriptors have received limited attention. Further exploration is needed in this

area. Additionally, machine learning [70*] is widely used to accelerate the discovery and design of catalytic materials, but its development is ongoing.

Declaration of competing interest

The authors declare that they have no known competing financial interests or personal relationships that could have appeared to influence the work reported in this paper.

Data availability

Data will be made available on request.

Acknowledgements

The present study has been supported by the Spanish MCIN/AEI/10.13039/501100011033 PID2021-126076NB-I00 and TED2021-129506B-C22 projects, funded partially by FEDER, *una manera de hacer Europa*, and *María de Maeztu* CEX2021-001202-M grants, including funding from European Union and, in part, by and COST Action CA18234. The authors also thank Generalitat de Catalunya for financing consolidated research groups (2021SGR79). L.M. thanks the China Scholarship Council for financing her PhD (CSC202108390032). F.V. thanks the ICREA Academia Award 2023 Ref. Ac2216561.

References

Papers of particular interest, published within the period of review, have been highlighted as:

* of special interest

1. Dresselhaus MS, Thomas IL: **Alternative energy technologies**. *Nature* 2001, **414**:332–337.
2. Turner JA: **Sustainable hydrogen production**. *Science* 2004, **305**:972–974.
3. Deng F, Olvera-Vargas H, Zhou M, Qiu S, Sirés I, Brillas E: **Critical review on the mechanisms of Fe^{2+} regeneration in the electro-fenton process: fundamentals and boosting strategies**. *Chem Rev* 2023, https://doi.org/10.1021/acs.chemrev.2c00684.
4. Chu S, Majumdar A: **Opportunities and challenges for a sustainable energy future**. *Nature* 2012, **488**:294–303.
5. Hosseini SE, Wahid MA: **Hydrogen production from renewable and sustainable energy resources: promising green energy carrier for clean development**. *Renew Sustain Energy Rev* 2016, **57**:850–866.
6. Crabtree GW, Dresselhaus MS, Buchanan MV: **The Hydrogen economy**. *Phys Today* 2004, **57**:39–44.
7. Nnabuife SG, Ugbeh-Johnson J, Okeke NE, Ogbonnaya C: **Present and projected developments in Hydrogen production: a technological review**. *Carbon Capture Sci Technol* 2022, **3**:100042.
8. Xu JG, Froment GF: **Methane steam reforming, methanation and water-gas shift. 1. Intrinsic kinetics**. *AIChE J* 1989, **35**:88–96.
9. Suryanto BHR, Wang Y, Hocking RK, Adamson W, Zhao C: **Overall electrochemical splitting of water at the heterogeneous interface of nickel and iron oxide**. *Nat Commun* 2019, **10**:5599.
10. Raveendran A, Chandran M, Dhanusuraman R: **A comprehensive review on the electrochemical parameters and recent material development of electrochemical water splitting electrocatalysts**. *RSC Adv* 2023, **13**:3843–3876.
11. Li C, Baek JB: **Recent advances in noble metal (Pt, Ru, and Ir)-based electrocatalysts for efficient Hydrogen evolution reaction**. *ACS Omega* 2020, **5**:31–40.
12. Xiong W, Yin H, Wu T, Li H: **Challenges and opportunities of transition metal oxides as electrocatalysts**. *Chem Eur J* 2023, **29**, e202202872.
13. Gao G, Jiao Y, Ma F, Jiao Y, Waclawik E, Du A: **Structures and phase transition of a MoS_2 monolayer**. *J Phys Chem C* 2015, **119**:13124–13128.
14. Kibsgaard J, Tsai C, Chan K, Benck JD, Nørskov JK, Abild-Pedersen F, Jaramillo TF: **Designing an improved transition metal phosphide catalyst for hydrogen evolution using experimental and theoretical trends**. *Energy Environ Sci* 2015, **8**:3022–3029.
15. Lukowski MA, Daniel AS, Meng F, Forticaux A, Li L, Jin S: **Enhanced Hydrogen evolution catalysis from chemically exfoliated metallic MoS_2 nanosheets**. *J Am Chem Soc* 2013, **135**:10274–10277.
16. Jaramillo TF, Jørgensen KP, Bonde J, Nielsen JH, Horch S, Chorkendorff I: **Identification of active edge sites for electrochemical H_2 evolution from MoS_2 nanocatalysts**. *Science* 2007, **317**:100–102.
17. Naguib M, Kurtoglu M, Presser V, Lu J, Niu J, Heon M, Hultman L, Gogotsi Y, Barsoum MW: **Two-dimensional nanocrystals produced by exfoliation of Ti_3AlC_2**. *Adv Mater* 2011, **23**:4248–4253.
18. Gogotsi Y, Anasori B: **The rise of MXenes**. *ACS Nano* 2019, **13**:8491–8494.
19. Morales-García Á, Calle-Vallejo F, Illas F: **MXenes new horizons in catalysis**. *ACS Catal* 2020, **10**:13487–13503.
20. * Mohammadi AV, Rosen J, Gogotsi Y: **The world of two-dimensional carbides and nitrides (MXenes)**. *Science* 2021, **372**, eabf1581.
A forward-looking review of the field of MXenes, with information related to structure and composition of MXenes, the theoretical and experimental demonstration of MXene properties, synthesis and processing, energy storage, harvesting, and electrocatalysis, and discusses pending challenges that will deepen the fundamental understanding of MXenes properties and enable their use in a variety of emerging technologies for hybridization with other 2D materials.
21. Sardar S, Jana A: **Covalent surface alteration of MXenes and its effect on superconductivity**. *Matter* 2020, **3**:1397–1399.
22. Yu X, Cai X, Cui H, Lee SW, Yu XF, Liu B: **Fluorine-free preparation of titanium carbide MXene quantum dots with high near-infrared photothermal performances for cancer therapy**. *Nanoscale* 2017, **9**:17859–17864.
23. Kamysbayev V, Filatov AS, Hu H, Rui X, Lagunas F, Wang D, Klie R, Talapin DV: **Covalent surface modifications and superconductivity of two-dimensional metal carbide MXenes**. *Science* 2020, **369**:979–983.
24. Wei J, Zhou M, Long A, Xue Y, Liao HB, Wei C, Xu ZJ: **Heterostructured electrocatalysts for hydrogen evolution reaction under alkaline conditions**. *Nano-Micro Lett* 2018, **10**:5148–5180.
25. Handoko AD, Steinmann SN, Seh ZW: **Theory-guided materials design: two-dimensional MXenes in electro- and photocatalysis**. *Nanoscale Horiz* 2019, **4**:809–827.
26. * Meng L, Yan LK, Viñes F, Illas F: **Effect of terminations on the Hydrogen evolution reaction mechanism on Ti_3C_2 MXene**. *J Mater Chem* 2023, **11**:6886–6900.
A comprehensive analysis of the effects of MXene terminations on HER from DFT calculations, exploring the mechanism changes compared to traditional studies but also presenting an overpotential volcano plot that highlights the most promising candidates for HER.
27. * López M, Exner KS, Viñes F, Illas F: **Computational Pourbaix diagrams for MXenes: a key ingredient toward proper theoretical electrocatalytic studies**. *Adv Theory Simul* 2022: 2200217.
A detailed description of the computational procedure leading to Pourbaix diagrams, that are required to construct suitable, thermodynamically stable, surface models representative of the situation at specific pH and potential conditions. Several representative MXenes were studied, highlighting the importance of selecting appropriate

models for theoretical electrocatalysis investigations, especially in catalysis.

28. Pandey M, Thygesen KS: **Two-dimensional MXenes as catalysts for electrochemical Hydrogen evolution: a computational screening study**. *J Phys Chem C* 2017, **121**: 13593–13598.

29. Cheng YW, Dai JH, Zhang YM, Song Y: **Two-dimensional, ordered, double transition metal carbides (MXenes): a new family of promising catalysts for the Hydrogen evolution reaction**. *J Phys Chem C* 2018, **122**:28113–28122.

30. Cheng YW, Dai JH, Zhang YM, Song Y: **Transition metal modification and carbon vacancy promoted Cr_2CO_2 (MXenes): a new opportunity for a highly active catalyst for the hydrogen evolution reaction**. *J Mater Chem* 2018, **6**: 20956–20965.

31. Sahoo SK, Ye Y, Lee S, Park J, Lee H, Lee J, Han JW: **Rational design of TiC-supported single-atom electrocatalysts for Hydrogen evolution and selective Oxygen reduction reactions**. *ACS Energy Lett* 2019, **4**:126–132.

32. Jin D, Johnson LR, Raman AS, Ming X, Gao Y, Du F, Wei Y, Chen G, Vojvodic A, Gogotsi Y, Meng X: **Computational screening of 2D ordered double transition-metal carbides (MXenes) as electrocatalysts for Hydrogen evolution reaction**. *J Phys Chem C* 2020, **124**:10584–10592.

33. Su Y, Song M, Wang X, Jiang J, Si X, Zhao T, Qian P: **System theoretical study on the effect of variable nonmetallic doping on improving catalytic activity of 2D-$Ti_3C_2O_2$ for Hydrogen evolution reaction**. *Nanomaterials* 2021, **11**:2497.

34. Kang Z, Cai J, Ye D, Zhao H, Luo J, Zhang J: **Three-dimensional nitrogen-doped MXene as support to form high-performance platinum catalysts for water-electrolysis to produce hydrogen**. *J Chem Eng* 2022, **446**:137443.

35. Bai S, Yang M, Jiang J, He X, Zou J, Xiong Z, Liao G, Liu S: **Recent advances of MXenes as electrocatalysts for hydrogen evolution reaction**. *NPJ 2D Mater Appl* 2021, **5**:78.

36. * Wang C, Wang X, Zhang T, Qian P, Lookman T, Su Y: **A descriptor for the design of 2D MXene hydrogen evolution reaction electrocatalyst**. *J Mater Chem* 2022, **10**:18195–18205.
An analysis of the HER properties of the Ti_2CO_2 MXene, with a focus on condutivity, stability, and electronic structure theory, developing simple descriptors, then using high-throughput calculations and machine learning processes to find highly active HER catalysts more efficiently.

37. * Jiang W, Zou X, Du H, Gan L, Xu C, Kang F, Duan W, Li J: **Universal descriptor for large-scale screening of high-performance MXene-based materials for energy storage and conversion**. *Chem Mater* 2018, **30**:2687–2693.
A proposal and testing of a series of descriptors related to the MXene HER process, and accurately related to the ΔG_H trend. This include the lowest occupation state (εLUS), the number of electrons gained by the oxygen atom (Ne), the oxygen vacancy formation energy (Ef), to name a few. This faciliates efficient searches of eficient electrodes based on MXenes and as energy storage devices.

38. Nørskov JK, Rossmeisl J, Logadottir A, Lindqvist L, Kitchin JR, Bligaard T, Jónsson H: **Origin of the overpotential for Oxygen reduction at a fuel-cell cathode**. *J Phys Chem B* 2004, **108**: 17886–17892.

39. * Kozuch S, Shaik S: **How to conceptualize catalytic cycles? The energetic span model**. *Acc Chem Res* 2011, **44**:101–110.
A key article presenting the energy span model that establishes a direct relationship between experimental and theoretical results. The turnover frequency (TOF) is thoroughly defined from a theoretical perspective, and a change in the conceptualization of catalytic cycles is in order: In catalysis, there are no rate-determining steps, but rather rate-determining states.

40. * Exner KS: **A universal descriptor for the screening of electrode materials for multiple-electron processes: beyond the thermodynamic overpotential**. *ACS Catal* 2020, **10**: 12607–12617.
A thoroughly analsysis of the linear scaling relationship leading to the volcano plot constructed using the traditional thermodynamic overpotential activity descriptor η_{TD}. The role of kinetics is also presented which leads to the proposal of the alternative activity $G_{max}(\eta)$ descriptor for multi-electron processes. This approach incorporates both applied overpotential and kinetic effects for a more comprehensive evaluation of catalytic activity.

41. Liu J, Peng W, Li Y, Zhang F, Fan X: **2D MXene-based materials for electrocatalysis**. *Trans Tianjin Univ* 2020, **26**:149–171.

42. Ooka H, Huang J, Exner KS: **The *Sabatier* principle in electrocatalysis: basics, limitations, and extensions**. *Front Energy Res* 2021, **9**:654460.

43. Koper MTM: **Theory of multiple proton–electron transfer reactions and its implications for electrocatalysis**. *Chem Sci* 2013, **4**:2710–2723.

44. Yang Q, Li G, Manna K, Fan F, Felser C, Sun Y: **Topological engineering of Pt-group-metal-based chiral crystals toward high-efficiency Hydrogen evolution catalysts**. *Adv Mater* 2020, **32**:1908518.

45. Ooka H, Nakamura R: **Shift of the optimum binding energy at higher rates of catalysis**. *J Phys Chem Lett* 2019, **10**: 6706–6713.

46. Exner KS: **Does a thermoneutral electrocatalyst correspond to the apex of a volcano plot for a simple two-electron process?** *Angew Chem Int Ed* 2020, **59**:10236–11024.

47. Gan J, Li F, Tang Q: **Vacancies-engineered M_2CO_2 MXene as an efficient Hydrogen evolution reaction electrocatalyst**. *J Phys Chem Lett* 2021, **12**:4805–4813.

48. Parey V, Abraham BM, Jyothirmai MV, Singh JK: **Mechanistic insights for electrochemical reduction of CO_2 into hydrocarbon fuels over O-terminated MXenes**. *Catal Sci Technol* 2022, **12**:2223–2231.

49. Ashton M, Trometer N, Mathew K, Suntivich J, Freysoldt C, Sinnott SB, Hennig RG: **Predicting the electrochemical synthesis of 2D materials from first principles**. *J Phys Chem C* 2019, **123**:3180–3187.

50. * López M, Exner KS, Viñes F, Illas F: **Theoretical study of the mechanism of the hydrogen evolution reaction on the V_2C MXene: thermodynamic and kinetic aspects**. *J Catal* 2023, https://doi.org/10.1016/j.jcat.2023.03.027.
A comprehensive evaluation of the thermodynamics and kinetics of HER on MXene from DFT based calculation, in contrast to the traditional reliance on the well-known ΔG_H thermodynamic descriptor. In addition, a theoretical evaluation of Tafel plots bridges theory and experiment, reporting a potential-depending switching of the preferred mechanism from the Volmer–Heyrovsky to the Volmer–Tafel.

51. Yuan W, Huang Q, Yang X, Cui Z, Zhu S, Li Z, Du S, Qiu N, Liang Y: **Two-dimensional lamellar Mo_2C for electrochemical Hydrogen production: insights into the origin of Hydrogen evolution reaction activity in acidic and alkaline electrolytes**. *ACS Appl Mater Interfaces* 2018, **10**:40500–40508.

52. Yan Y, Zhang R, Yu Y, Sun Z, Che R, Wei B, LaGrow AP, Wang Z, Zhou W: **Interfacial optimization of PtNi octahedrons@Ti_3C_2 MXene with enhanced alkaline hydrogen evolution activity and stability**. *Appl Catal B Environ* 2021, **291**: 120100.

53. Parsons R: **General equations for the kinetics of electrode processes**. *Trans Faraday Soc* 1951, **47**:1332–1344.

54. Tafel J: **Über die Polarisation bei Kathodischer Wasserstoffentwicklung**. *Z fur Phys Che* 2017, **905**:641–712.

55. Atkins P, Paula JD: *Physical chemistry for the life sciences*. New York, NY: W. H. Freeman and Company; 2006:275–276.

56. Chang R: *Physical chemistry for the biosciences*. Sausalito, CA: University Science Books; 2005:368–369.

57. Reimers AM, Reimers AC: **The steady-state assumption in oscillating and growing systems**. *J Theor Biol* 2016, **406**: 176–186.

58. Bai SH, Zhang SQ, Yu Y, Li JF, Yang Y, Wei H, Chu HB: **Fabricating nitrogen-rich Fe–N/C electrocatalysts through CeO_2-assisted pyrolysis for enhanced oxygen reduction reaction**. *Chemelectrochem* 2019, **6**:4040–4048.

59. Exner KS: **Why the microkinetic modeling of experimental tafel plots requires knowledge of the reaction intermediate's binding energy?** *Electrochem Sci Adv* 2022, **2**, e2100037.

60. Shinagawa T, Esparza ATG, Takanabe K: **Insight on Tafel slopes from a microkinetic analysis of aqueous electrocatalysis for energy conversion**. *Sci Rep* 2015, **5**:13801.

61. Geng J, Wu R, Bai H, Chan IN, Ng KW, Ip WF, Pan H: **Design of functionalized double-metal MXenes ($M_2M'C_2T_2$: M = Cr, Mo, M' = Ti, V) for magnetic and catalytic applications**. *Int Hydrog. Energy* 2022, **47**:18725–18737.

62. Zeradjanin AR, Narangoda P, Masa J, Schlögl R: **What controls activity trends of electrocatalytic hydrogen evolution Reaction?—Activation energy *versus* frequency factor**. *ACS Catal* 2022, **12**:11597–11605.

63. Gan J, Li F, Tang Y, Tang Q: **Theoretical study of transition-metal-modified Mo_2CO_2 MXene as a catalyst for the Hydrogen evolution reaction**. *ChemSusChem* 2020, **13**:6005.

64. Ekspong J, Gracia-Espino E, Wågberg T: **Hydrogen evolution reaction activity of heterogeneous materials: a theoretical model**. *J Phys Chem C* 2020, **124**:20911–20921.

65. Gao G, O'Mullane AP, Du A: **2D MXenes: a new family of promising catalysts for the hydrogen evolution reaction**. *ACS Catal* 2017, **7**:494–500.

66. Jiao Y, Zheng Y, Davey K, Qiao SZ: **Activity origin and catalyst design principles for electrocatalytic hydrogen evolution on heteroatom-doped graphene**. *Nat Energy* 2016, **1**:16130.

67. Anand R, Ram B, Umer M, Zafari M, Umer S, Lee G, Kim KS: **Doped MXene combinations as highly efficient bifunctional and multifunctional catalysts for water splitting and metal–air batteries**. *J Mater Chem* 2022, **10**:22500–22511.

68. Abidi N, Skrzypczak AB, Steinmann SN: **Revisiting the active sites at the MoS_2/H_2O interface via grand-canonical DFT: the role of water dissociation**. *ACS Appl Mater Interfaces* 2020, **12**: 31401–31410.

69. Abidi N, Skrzypczak AB, Steinmann SN: **How stable are 2H-MoS_2 edges under hydrogen evolution reaction conditions?** *J Phys Chem C* 2021, **125**:17058–17067.

70. * Abraham BM, Sinha P, Halder P, Singh JK: **Fusing machine learning strategy with density functional theory to hasten the discovery of 2D MXene based catalysts for hydrogen generation**. *J Mater Chem* 2023, https://doi.org/10.1039/D3TA00344B.
A robust and broadly applicable multistep workflow using supervised machine learning (ML) algorithms to construct well-trained data-driven models to predict the HER activity from DFT based calculations. The physically meaningful predictions and insights of the developed ML/DFT-based multistep workflow will open new avenues for accelerated screening, rational design and discovery of potential HER catalysts.

71. Yang H, Ma Y, Lv X, Huang B, Dai Y: **Prediction of intrinsic electrocatalytic activity for hydrogen evolution reaction in Ti_4X_3 (X = C, N)**. *J Catal* 2020, **387**:12–16.

72. * Wang X, Su Y, Song M, Song K, Chen M, Qian P: **Design single nonmetal atom doped 2D Ti_2CO_2 electrocatalyst for hydrogen evolution reaction by coupling electronic descriptor**. *Appl Surf Sci* 2021, **556**:149778.
A descriptor based study of the coupling of valence electrons and charge transfer to predict the catalytic activity trend of the 2D NM-Ti_2CO_2. The systematic analysis of the electronic structure, not only explains the rationality of this simple coupling descriptor, but also reveals the regulation origin of HER catalytic activity. Furthermore, this provides a theoretical basis for the design and high-throughput screening of HER catalysts.

73. Gogotsi Y, Huang Q: **MXenes: two-dimensional building blocks for future materials and devices**. *ACS Nano* 2021, **15**: 5775–5780.

ChemElectroChem | Concept
doi.org/10.1002/celc.202300598
Chemistry Europe
European Chemical Societies Publishing
www.chemelectrochem.org

MXenes as Electrocatalysts for the CO_2 Reduction Reaction: Recent Advances and Future Challenges

Ling Meng,[a] Ebrahim Tayyebi,[b] Kai S. Exner,*[b] Francesc Viñes,*[a] and Francesc Illas[a]

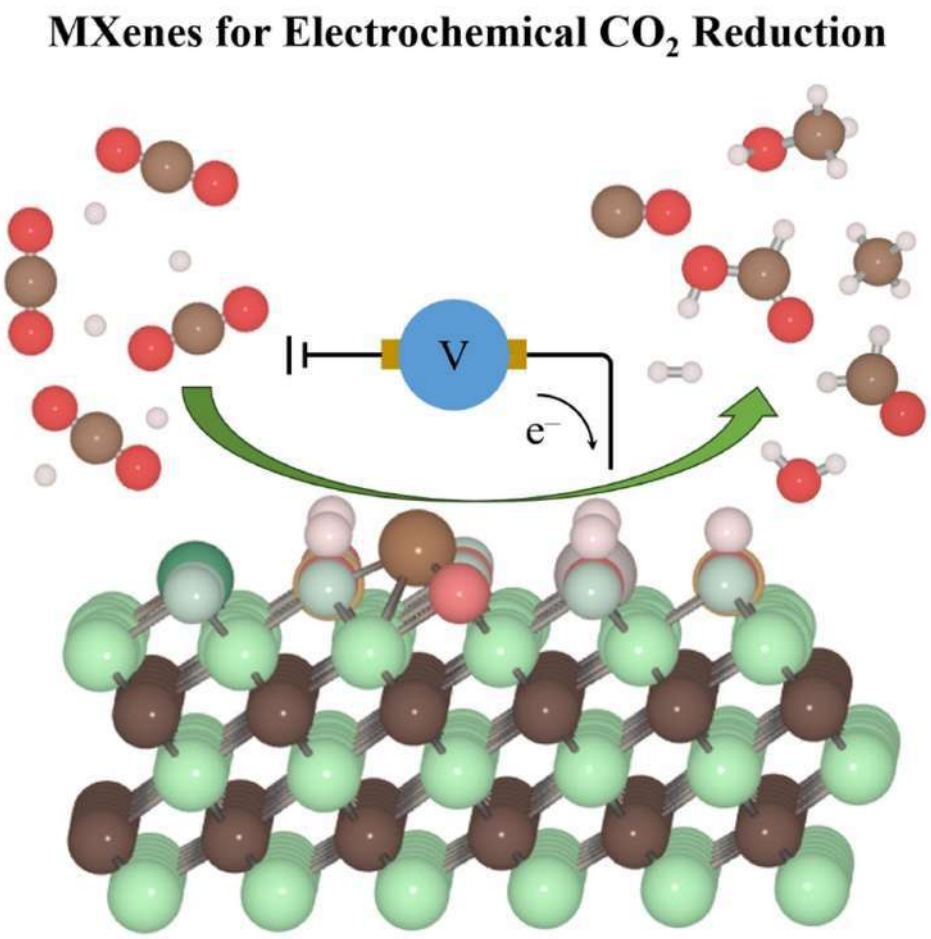

ChemElectroChem | Concept | doi.org/10.1002/celc.202300598 | Chemistry Europe | European Chemical Societies Publishing

Electrochemical carbon dioxide reduction (CO_2RR) is gaining momentum as an effective process to capture and convert CO_2 into valuable chemicals and fuels, as well as to contribute reducing greenhouse gas emissions. Two-dimensional transition metal carbides and/or nitrides (MXenes) are increasingly attracting attention as CO_2RR electrocatalysts due to their enhanced chemical activity and selectivity, overcoming limitations of traditional metal CO_2RR electrocatalysts, and likely breaking the scaling relations of reaction intermediates toward the desired product. The present concept reviews the state-of-the-art in the computational description of CO_2RR on MXenes, going from CO_2 activation on pristine models to different surface terminations, and discuss possible ways to tune the catalytic activity and selectivity, including doping, defects, supported single metal atoms, solvent effects, and electric field effects, while putting in the spotlight prospects by including kinetic aspects.

1. Introduction

The excessive use of fossil fuels has led to an increase in the atmospheric carbon dioxide (CO_2) concentration, causing global warming and climate change. CO_2 capture and usage (CCU) is an appealing strategy to counteract it, using CO_2 as a C_1 chemical feedstock, and turning the CO_2 economy into a waste-to-product model, closing the C-cycle when using sustainable energy resources.[1,2] Here, the use of electrocatalysts for CO_2 reduction reactions (CO_2RR) is gaining momentum, with research endeavors aimed at finding or developing active and selective electrocatalysts working at a low reduction overpotentials.[3]

Currently, the primary focus is on transition metal (TM) catalysts such as oxide-derived Cu electrocatalysts, having a unique reactivity in converting CO_2 to hydrocarbons and alcohols.[4,5] Still, on such TM catalysts, the bonding similarity of C-based moieties makes it difficult to independently stabilize certain intermediates such as CO* or CHO*, eventually severely limiting their chemical activity and overpotential.[6,7] For instance, on Cu, methane (CH_4) production is observed at an applied electrode potential, U, of -0.9 V *vs.* the reversible hydrogen electrode (RHE) with a slow reaction kinetics. While kinetics is facilitated at U below -1.1 V *vs* RHE, the increase in activity is accompanied with a concomitant lower selectivity due to the competing hydrogen evolution reaction (HER) as a detrimental side process.[8] Clearly, there is still room for improvement with the ultimate target of finding economic electrocatalytic materials with improved kinetics and selectivity while operating at lower cathodic overpotentials; that is, toward more positive electrode potentials.

Recently, a growing interest has evolved on using two-dimensional (2D) transition metal carbides and/or nitrides (MXenes)[9] for CO_2RR. MXenes, with general formula $M_{n+1}X_nT_x$ ($n=1$–3), are made of early TMs (M), carbon and/or nitrogen (X), and, as a result of their synthesis conditions, normally display terminal functional groups T_x, typically $-O$, $-H$, $-OH$, or $-F$, as well including $-Cl$, $-I$, $-Br$, $-S$, $-Se$, $-Te$, $-NH$, and $-NH_2$.[10–12] MXenes feature high surface areas, abundant active sites, excellent conductivities, structural stability, corrosion resistance, and hydrophilicity.[13] Interestingly, MXenes have the potential to, to some extent, circumvent Cu-based electrocatalysts conductivity, stability, and selectivity issues, and are thus appealing for CO_2RR.[14]

Many advances in CO_2RR by MXenes have been spurred by computational studies carried out in the framework of density functional theory (DFT). Nevertheless, there is still a lack of comprehensive understanding even if it has been gradually increasing over the last years. Here, we present a comprehensive review of the most significant DFT advances in the CO_2RR electrocatalysis by MXenes, critically discussing the model evolution and impact, with the eye put on the still unresolved research questions and future prospects.

2. First Generation of MXene Models for CO_2RR (2017–2018)

Some of the earliest DFT studies focused just on the CO_2 capture by clean MXenes.[15–18] These first studies revealed a very high chemical activity of MXenes, irrespective of n in $M_{n+1}X_n$, being able to capture CO_2 even at adverse working conditions of temperature and CO_2 partial pressure, and to activate it by charge transfer, leading to a negatively charged, bent, adsorbed CO_2^- molecule with elongated C–O bonds (*cf.* Figure 1a). The model computations forecasted high, yet conservative, CO_2 loading capacities up to 8.25 mol kg^{-1}. These predictions were experimentally confirmed, reaching values of 12 mol CO_2 kg^{-1}, paving the way toward the use of MXene in CO_2RR electrocatalysis.[19] Indeed, Li *et al.*[20] focused on M_3C_2 MXene models and proposed Cr_3C_2 and Mo_3C_2 (*cf.* Figure 1b) as likely the most selective toward CH_4. Their finding reveals that, except for the initial two adsorbates (COO* and COOH*), reaction intermediates primarily attach to MXenes via an

[a] L. Meng, Prof. F. Viñes, Prof. Dr. F. Illas
Departament de Ciència de Materials i Química Física & Institut de Química Teòrica i Computacional (IQTCUB), Universitat de Barcelona, c/Martí i Franquès 1–11, 08028 Barcelona, Spain
E-mail: francesc.vines@ub.edu

[b] Dr. E. Tayyebi, Prof. K. S. Exner
University Duisburg-Essen, Faculty of Chemistry, Theoretical Inorganic Chemistry, Universitätsstraße 5, 45141 Essen, Germany;
and
Cluster of Excellence RESOLV, ■■■postcode missing■■■Bochum, Germany;
and
Center for Nanointegration (CENIDE) Duisburg-Essen, ■■■postcode missing■■■Duisburg, Germany
E-mail: kat.exner@uni-due.de

ChemElectroChem | Concept doi.org/10.1002/celc.202300598 | Chemistry Europe European Chemical Societies Publishing

oxygen (O*) atom. The diverse configurations in which intermediates are adsorbed suggest the possibility of a different scaling relation for MXenes.

In contrast to Cu-based electrocatalysts, where the potential-determining step (PDS);[21] that is, the elementary reaction step with highest free-energy change under equilibrium conditions, is primarily influenced by the early stages of the proton-coupled transfer processes in CO_2RR. Li *et al.* observed a PDS shift toward later stages of mechanistic description due to the removal of O* by water formation identified as the PDS.[22] This goes along with previous studies[23–25] indicating that the higher the degree of bending of chemisorbed CO_2, the higher its chemical activity, eventually easing the difficult initial hydrogenation steps. However, the electrocatalytic activity approximated by means of the limiting potential (U_L) analysis, indicating the electrode potential at which all elementary steps are exergonic or downhill in free energy,[26] was found to be still small due to $U_L < -1$ V. The PDS was related to water or hydroxyl formation on Mo_3C_2 and Cr_3C_2, respectively, in line with a rather high hydrophilicity of pristine MXenes.[27] This prompted the authors to evaluate the performance of terminated MXenes, such as $Mo_3C_2O_2$ and $Mo_3C_2(OH)_2$, revealing that $Mo_3C_2O_2$ exhibited a reduced U_L of −0.54 V (*cf.* Figure 1c) while the PDS shifted to the step CHO*→CH_2O*. On the other hand, the CO_2 adsorption Gibbs free energy weakens from −0.86 to +0.23 eV (*cf.* Figures 1b,c), implying a difficult transition from chemisorption to physisorption. Consequently, a balance between small overpotential in conjunction with chemisorbed CO_2 would be desirable for an enhanced CO_2RR.

In summary, the first generation of MXene theoretical models were oversimplified, often overlooking the presence of surface terminations in terms of the limiting potential analyses. Albeit cleaning protocols to gain pristine MXenes exist, and synthetic procedures have been developed to obtain such MXenes absent of surface terminations,[28–29] researchers moved to a second generation of models, where surface terminations were explicitly accounted for to emphasize their important role in CO_2RR.

Ling Meng obtained her bachelor and Master's degree from Northeast Normal University (China, 2013–2020), and is currently a PhD candidate at the University of Barcelona (Spain, 2021–2024) under the supervision of Prof. Dr. Francesc Illas and Prof. Francesc Viñes. Her research interests lie in the fields of computational chemistry, energy storage, electrocatalysis, and materials science, with a focus on catalytic reactions and their mechanisms, aimed at designing advanced catalytic material. Her current work includes developing catalysts for green energy production and the conversion of greenhouse gases into useful materials.

Ebrahim Tayyebi earned his Bachelor's in Chemical Engineering from the University of Arak, Iran, in 2009, followed by a Master's at Amirkabir University of Technology in 2012. He completed his PhD in Chemical Engineering at the University of Iceland in 2020. Currently, he works as a postdoctoral researcher in the group led by Prof. Kai Exner at the University of Duisburg-Essen. His expertise lies in ab initio simulations in electrocatalysis and electrochemistry, specifically focusing on electrochemical reactions at electrified solid/electrolyte interfaces.

Kai S. Exner began his chemistry studies in 2008 at Justus-Liebig-University (JLU) Giessen, Germany, and received his PhD at the same university in 2015. In 2021, he was appointed tenure-track Professor (W1) at the University of Duisburg-Essen (UDE), Germany. Exner has received numerous awards including the Carl Duisberg Memorial Prize 2023 from the German Chemical Society. His research focuses on the application of ab initio methods in electrocatalysis and batteries, method development in electrochemistry, descriptor-based approaches for materials screening, microkinetic approaches for catalytic processes at electrified interfaces, as well as the investigation of biomolecules for drug delivery or biocatalytic applications.

Francesc Illas is a Full Professor in the Materials Science and Physical Chemistry department of the University of Barcelona. He spent several periods at IBM Almaden Research Center and Los Alamos National Laboratory and was invited professor at Universitá della Calabria (Italy) and Université Pierre et Marie Curie (France). He received several awards, was elected Fellow of the European Academy of Sciences (2009), of the Academia Europeae (2017) and is the recipient of the 2022 Medal of the Spanish Royal Society of Chemistry. His research involves application of theoretical and computational chemistry methods to surface chemistry and heterogeneous catalysis.

Francesc Viñes obtained his PhD in Chemistry at the Universitat de Barcelona (UB) in 2008, where he became an Associate Professor in the Materials Science and Physical Chemistry department in 2019. He is an Alexander von Humboldt foundation fellow since 2008, beginning with his postdoctoral time in the Friedrich-Alexander University of Erlangen-Nuremberg up to 2011. From 2023 on, he is an awardee of the Catalan Institute of Advanced Research (ICREA) Academia. His research is based in the theoretical and computational description of heterogeneously thermo-, photo-, or electroacatalyzed processes and the descriptor of catalyst and materials through computational materials science.

ChemElectroChem | Concept doi.org/10.1002/celc.202300598 | Chemistry Europe European Chemical Societies Publishing

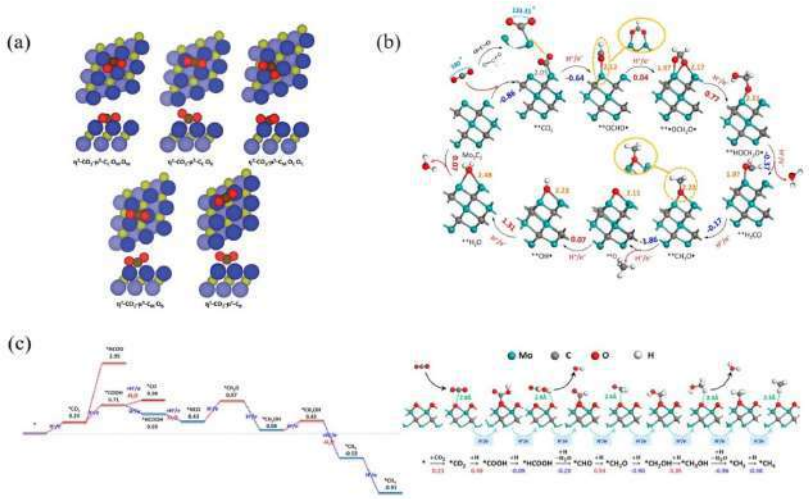

Figure 1. (a) Side and top views of CO_2 adsorbed on MXene (0001) surfaces from ref. [15] Copyright (2018), with permission from Royal Society of Chemistry. (b–c) Minimum energy pathway for the CO_2 conversion into CH_4 and H_2O catalyzed by Mo_3C_2 and $Mo_3C_2O_2$, respectively, from ref. [20] Copyright (2017), with permission from American Chemical Society.

3. Second Generation of MXene Models for CO_2RR (2018–2020)

The second generation of MXene models for CO_2RR first emerged in 2018 when Handoko *et al.*[30] screened 19 types of O-terminated M_2XO_2 MXenes (*cf.* Figure 2a). There, at variance with TMs – with a strong CO* bonding and the presence of only –C coordination – the surface O moieties allow the stabilization of reaction intermediates through –H coordination, energetically favoring *e.g.* formic acid product; this is, along the minimum energy pathway, the MXene catalyst relies less on –C coordinated intermediates such as COOH*, and alternates with –H coordinated intermediates, such as HCOOH* (*cf.* Figure 2b). This implies that U_L can be independently tuned with respect to the adsorption free energies of COOH* or HCOOH* to achieve higher electrocatalytic activities. In addition, compared to Cu as electrocatalyst,[31] the most promising W_2CO_2 and Ti_2CO_2 MXenes show significantly lower theoretical overpotential of −0.52 and −0.69 V (*cf.* Figure 2a).

Subsequently, Chen *et al.*[32] investigated the thermodynamic and kinetic catalytic properties of –OH terminated MXenes (*cf.* Figure 2c), revealing that $Sc_2C(OH)_2$ exhibited the lowest U_L of −0.53 V. The high CO_2RR activity was attributed to the key role of –OH moieties in stabilizing the adsorbed intermediates, *e.g.* facilitating H_2CO* and HCOOH* intermediates by making use of surface –H. There, U_L for each elementary step is established as a linear function of the H vacancy formation energy, E_{Hvac}, as $U_L = U_0 + \alpha^*H \cdot E_{Hvac}$, where U_0 is the limiting potential when $E_{Hvac} = 0$, α^*H is the slope that describes how much E_{Hvac} is impacting U_L (*cf.* Figure 2d), while E_{Hvac} and the Bader charges were primary descriptive indicators of the CO_2RR performance.

Furthermore, while theoretical studies often focus on determining the most viable routes leading to more highly reduced hydrocarbons like CH_4, experimental investigations involving MXenes commonly reveal less reduced products such as formate or CO. For example, Handoko *et al.*[33] established the influence of surface terminations on CO_2RR, where the catalytic activity correlates with the proportion of –F and –O terminations on Ti_2CT_x and Mo_2CT_x (*cf.* Figs. 3ab), so that a higher –F proportion on Ti_2CT_x showed less catalytic activity and selectivity. The lowest U_L for selective HCOOH formation was observed on Mo_2CT_x with a small –F fraction of 3.8% (*cf.* Figure 3c–f). This model change is backed up by the fact that the synthesis of single/pure surface-terminated MXenes is quite challenging, and, even though the successful synthesis of pure $Mo_2TiC_2O_2$ has been reported,[34] mixed terminations are still prevalent. Without any further ado, future research should focus on such mixed surface functional groups on MXenes, defining more realistic models to get more accurate and in-depth analysis of the CO_2RR.

4. Third Generation of MXene Models for CO_2RR (2020–present)

The third generation of MXene models primarily focused on structural modifications, including not only T_x components, but also, doping, single atoms, and defect engineering. As far as

ChemElectroChem | Concept
doi.org/10.1002/celc.202300598
Chemistry Europe
European Chemical Societies Publishing

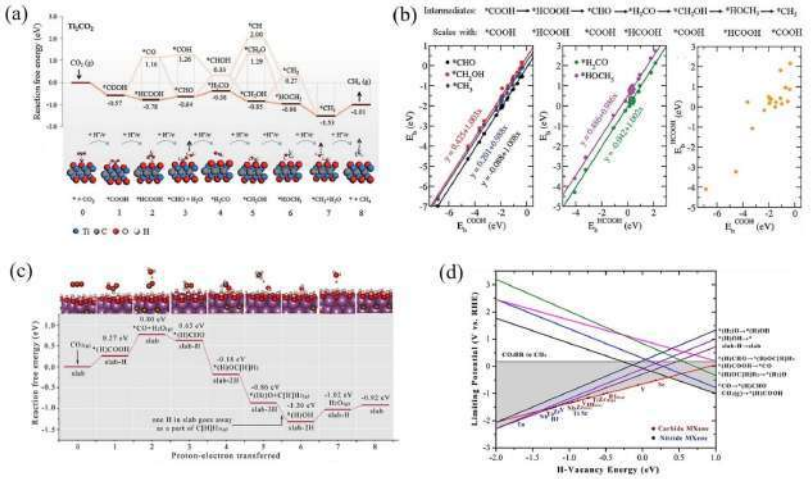

Figure 2. (a) Free energy diagram and ball-and-stick models representing the various possible pathways for CO_2RR to CH_4 on O-terminated Ti_2CO_2 MXene, and (b) various linear regression fits of CO_2RR reaction intermediates binding energies on M_2XO_2 MXene surfaces, from ref. [30] Copyright (2018), with permission from Royal Society of Chemistry. (c) Free energy diagrams for the lowest energy pathways to CH_4 on $Sc_2C(OH)_2$ and (d) volcano curve of OH-terminated MXenes related to elementary steps from ref. [32] Copyright (2019), with permission from American Chemical Society.

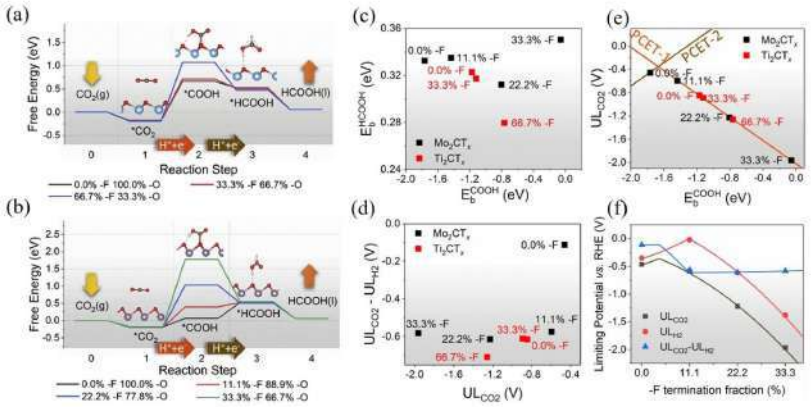

Figure 3. Calculated free energy diagram at U_L 0 V for CO_2RR to formic acid on (a) Ti_2CT_x and (b) Mo_2CT_x with varying fractions of –F and –O surface terminating groups. (c–e) Relations between different CO_2RR reaction intermediates binding energies on Ti_2CT_x and Mo_2CT_x. (f) The corresponding limiting potentials (U_L) for CO_2RR, HER, and the difference between the two; $U_L(CO_2)$-$U_L(H_2)$, on Mo_2CT_x at varying –F T_x fraction, from ref. [33] Copyright (2020), with permission from Elsevier.

surface defects are concerned, Chen *et al.*[35] investigated the effects of M atom (V_M) or C/N atom (V_X) vacancies on the U_L of M_2XO_2 MXenes studying the distinct response on intermediates such as COOH* or CHO* and adsorbed molecular products such as HCOOH* or H_2CO* (*cf.* Figure 4a). Their study revealed that V_M and V_X significantly influence the reaction intermediates bonding while this effect was less pronounced for CO_2 adsorption (*cf.* Figure 4b). In addition, V_M seemed to strengthen the binding while the opposite effect was found on V_X, thus opening a path for the regulation of U_L. Aside, binding energies linearly correlated with Fermi level shift (ΔE_{Ferm}), which can be a good indicator of the electrocatalytic activity (*cf.* Figure 4c). This point was proven later on borides[36] while a posterior study

ChemElectroChem | Concept doi.org/10.1002/celc.202300598 | Chemistry Europe European Chemical Societies Publishing

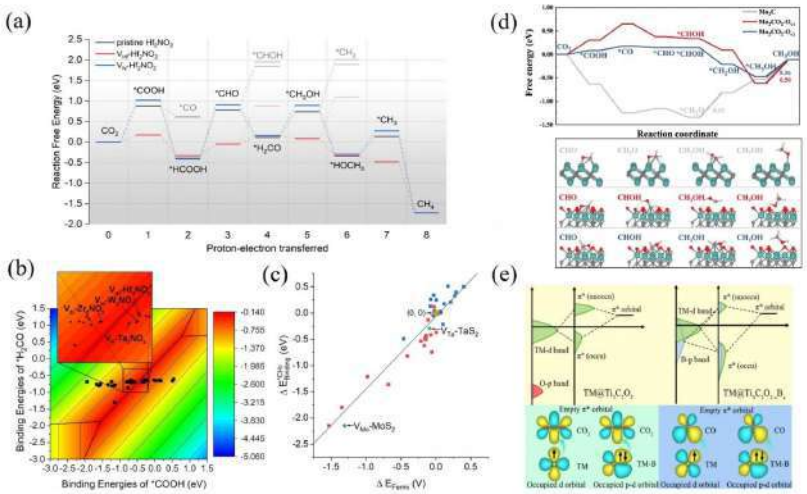

Figure 4. (a) Free-energy diagram for pristine Hf_2NO_2, V_{Hf}–Hf_2NO_2, and V_N–Hf_2NO_2, (b) $U_L(CO_2)$ contour map as a function of COOH* and H_2CO* binding energy and (c) relationship between the change of the Fermi level and change of CH_3* binding energy on M_2XO_2 MXenes, from ref. [35] Copyright (2020), with permission from Wiley-VCH. (d) Free energy profiles of CO_2RR to CH_4 and corresponding intermediates adsorption configurations on Mo_2C, Mo_2CO_2–O_{V1}, and Mo_2CO_2–O_{V2}, from ref. [37] Copyright (2022), with permission from Elsevier. (e) Schematic diagrams of CO_2 molecule and CO intermediate activation mechanisms on $TM@Ti_3C_2O_2$ and $TM@Ti_3C_2O_{2-x}B_x$, from ref. [42] Copyright (2023), with permission from Royal Society of Chemistry.

pointed out further improvements by adjusting the surface vacancies number and position (*cf.* Figure 4d).[37]

Similarly, doping can be used to engineer the catalytic activity as it influences the MXenes electronic structure. Li *et al.*[38] found that metal doping resulted in an upward *d*-band center shift on Mo_3C_2, unbalancing the scaling relationship between the adsorption energies of H_2CO_2* and H_2COOH* as well as intermediates associated with the PDS, while displaying surface-located lone electrons that enhance the catalytic activity. Later, Cheng *et al.*[39] found that Nb_2CO_2, not catalytically active towards CO_2RR, improved the U_L when substitutionally doping C by *p* block elements in that metal doping not only reduced the U_L, but also improved the selectivity toward a certain product.

Finally, surface single-atom engineering has become key in regulating the MXenes electrocatalytic activity. By controlling atomic positions and compositions, MXene catalysts can be customized and optimized, offering new prospects for CO_2RR. Apart from Zhou *et al.*[40] who studied single atoms catalysts (SACs) on $Ti_3C_2O_2$, all other studies highlighted the synergy between single atoms and surface terminations. In this line, Li *et al.*[41] found that TMs single atoms on O-terminated Ti_2C, $TM@Ti_2CO_2$, was more likely to activate CO_2 compared to the S-terminated case of $TM@Ti_2CS_2$, however, the latter featured a smaller U_L. This unfolds the advantages of combining mixed –O and –S surface terminations.

Likewise, Peng *et al.*[42] and Cao *et al.*[43] reported the synergistic effect between SACs and dopants. In the former, a B dopant, $TM@Ti_3C_2O_{1-x}B_x$, gains electrons from the substrate by leaving a partially electron-deficient 2*p* orbital. Aside, the empty 2*p* orbitals facilitate electron donation from the TM to B, resulting in a strongly polarized covalent TM–B bond with enhanced structural stability compared to O atoms. The occupied B orbitals foster electron density donation to the π-antibonding CO_2 orbital, assisting the TM in activating CO_2 (*cf.* Figure 4e). All in all, the research field is moving toward improving MXene CO_2RR electrocatalysts activity and selectivity by considering mixed terminations, doping, vacancies, single-atoms, or a combination of such factors. The most prominent studied cases, comprising U_L and formation of the main product, are listed in Table 1.

5. Evolution of the MXene Generation in Reaction Mechanisms

As far as DFT-predicted CO_2RR mechanisms are concerned, Figure 5 briefly illustrates the main differences depending on the employed models, while we guide the reader to the preceding sections and subsequent references for a more comprehensive understanding. In first generation models (*cf.* Figure 5),[15,20,44,45] CO_2 undergoes activation through strong chemical bonds *via* C and/or O atoms, while solely through O atoms in subsequent reduction stages. The latest O* electrochemical protonation steps towards water are endergonic in

ChemElectroChem | Concept | doi.org/10.1002/celc.202300598 | Chemistry Europe European Chemical Societies Publishing

Table 1. Summary of recent results on CO_2RR by MXene-based electrocatalyst, where only the system that exhibits optimal performance in each study is here listed. Second column encompasses the various methods used to modify the structure, including the introduction of different metals (M), carbides/nitrides (X), surface termination (T_x), as well as doping and vacancy and single atom catalyst (SAC) engineering. The activity is represented by the limiting potential (U_L). The main products as well as the corresponding literature reference are also shown.

Electrocatalyst	Modulation mode	Activity	PDS	Product	Ref.
$Mo_3C_2O_2$	Fully –O term	$U_L = -0.54$ V	$CHO^* \rightarrow CH_2O^*$	CH_4	[20]
W_2CO_2	Fully –O term	$U_L = -0.35$ V	$CO_2^* \rightarrow COOH^*$	CH_4	[30]
$Sc_2C(OH)_2$	Fully –OH term	$U_L = -0.53$ V	$(H)COOH^* \rightarrow CO^*$	CH_4	[32]
Mo_2CT_x	Mixed –O and 3.8% –F term	$U_L \approx -0.37$ V	$CO_2^* \rightarrow COOH^*$	HCOOH	[33]
V_{Hf}–Hf_2NO_2[a]	M vacancy	$U_L = -0.28$ V	$HCOOH^* \rightarrow CHO^*$	CH_4	[35]
Zr_2NO_2	Various M and X	$U_L \approx -0.45$ V	$CO_2^* \rightarrow COOH^*$	CH_4	[36]
Mo_2CO_2–O_{V2}[b]	O vacancy	$U_L = -0.31$ V	$CH_3^* \rightarrow CH_4^*$	CH_4	[37]
Mo_3TiC_2	M doping	$U_L = -0.35$ V	$OCH_3O^* \rightarrow HOCH_2O^*$	CH_4	[38]
V@Nb_2CO_2	SAC	$U_L = -0.11$ V	$CO_2^* \rightarrow COOH^*$	HCOOH	[39]
Co@$Ti_3C_2O_2$	SAC	$U_L = -0.21$ V	$OCHO^* \rightarrow OCH_2O^*$	CH_4	[40]
Cr@Ti_2CT_x	SAC & Mixed –O and –S term	$U_L = -0.44$ V	$H_2COOH^* \rightarrow CH_2O$	CH_4	[41]
Fe@$Ti_3C_2O_{2-x}B_x$	T_x doping	$U_L = -0.40$ V	$CH_2O^* \rightarrow CH_3O^*$	CH_4	[42]
Ru@NS–$Ti_3C_2O_2$	SAC & M doping	$U_L \approx 0$ V	$CO_2^* \rightarrow COOH^*$	CO	[43]
Mo_3TiC_2	M doping	$U_L \approx 0$ V	$CO^* \rightarrow CHO^*$	CH_4	[44]
Mo_2C	–	$U_L = -1.19$ V	$OH^* \rightarrow H_2O^*$	CH_4	[45]
Fe@W_2CS_2	SAC & Fully –S term	$U_L = -0.245$ V	$COOH^* \rightarrow CO^*$	CO	[47]
Ru@Mo_2CS_2	SAC & Fully –S term	$U_L = -0.07$ V	$OCHOH^* \rightarrow CHO^*$	CH_4	[48]
V@Ti_2CN_2	SAC & Fully –N term	$U_L = -0.06$ V	$COOH^* \rightarrow CO^*$	CO	[49]

[a] V_{Hf} stands for Hf vacancy, [b] O_{V2} stands for O vacancy.

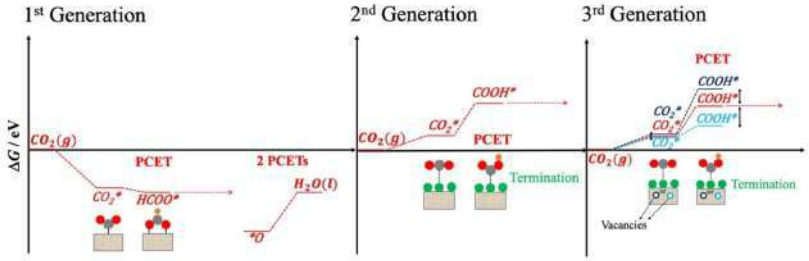

Figure 5. Scheme illustrating distinct reaction mechanisms for CO_2 reduction on various generations of MXene models. The binding free energies (ΔG) here are arbitrary, and only the first proton-coupled electron transfer (PCET) is generally shown, except for latest two PCETs for O* conversion into H_2O^* on 1st generation MXenes. MXene substrate is shown as brown rectangle, while red, grey, and orange circles denote reaction moieties C, O, and H atoms, respectively. Surface termination species are shown as green circles.

free energy (ΔG), and thus, limit the activity in the thermodynamic picture.[20,45] On second generation MXene models (*cf.* Figure 5), the termination groups such as –O, –OH, –S, or –F alter the CO_2 and other intermediates binding energies.[20,30,35,46] Thus, in a hypothetical CO_2* weakened scenario (*cf.* Figure 5), diverse intermediates may interact with surface groups through H, C, or O atoms, contingent on the specific group present, while interaction *via* H atoms of the –OH termination may either facilitate proton-coupled electron transfers or stabilize intermediates by as-generated surface –O group upon H atom removal from –OH.[20,32] Regarding third generation models,[35,37,39–43,47,49] the presence, *e.g.* of different vacancies can modify the binding energy of intermediates, schematically shown in Figure 5, benefitting or making more adverse some H^+ reduction steps, while this effect has been demonstrated to have a comparatively lesser impact on CO_2 binding energy in comparison to other intermediates.

6. Future Prospects and Outlook

The present concept shows that DFT calculations have been crucial to establish MXenes for CO_2RR. The continued improvement of models indicate that these materials have the potential

ChemElectroChem | Concept doi.org/10.1002/celc.202300598 | Chemistry Europe European Chemical Societies Publishing

for the formation of valuable carbon-based products by the electrocatalytic reduction of CO_2 with a small U_L and tuned selectivity. Improved modeling has highlighted how, in addition to the inherent MXene activity, the presence of certain surface terminations or mixed situations can affect the free energies of key CO_2RR intermediates or open new reaction pathways, ultimately resulting in a reduction of the energetic costs of the PDS.

Further consideration of structural modification, including defect and doping, and SAC anchoring, place MXene-based electrocatalyst under the spotlight of CO_2RR. Nevertheless, several challenges remain, and careful experimental work is urgently needed, especially since their performance is predicted to be highly sensitive to surface terminations. Additional theoretical investigations of CO_2RR by MXenes at working condition using realistic mixed surface terminations is also needed following pioneering work for the hydrogen evolution reaction (HER).[46] Another rock-in-the-shoe is that some theoretical works[20,38] ignore the high energy of recovery steps, *e.g.* on $Mo_3C_2(OH)_2$, the PDS of the reaction would not be determined by the ΔG of CO_2 activation (0.35 eV), but rather the release of H_2O, $*OH \rightarrow * + H_2O$, with ΔG of 1.17 eV.[20] Focusing on the first elementary reaction steps of CO_2RR *vs.* HER only is also a limitation, and thus one should always inspect the entire free-energy landscape rather than a selected step to render predictions on the electrocatalytic activity.[38,42,48] The recently introduced free-energy span model[49,50] offers the opportunity to track the entire free-energy landscape at low computational costs and to identify limiting reaction steps in a potential-dependent fashion. Such advanced frameworks appear of importance due to the opportunity of a change in the mechanistic pathway and limiting step with increasing overpotential,[51] indicating the need to go beyond the potential-independent contemplation of the energetics by means of the limiting potential analysis.

In the early early-stage of catalyst design one should also consider the synthetic feasibility, with negative formation energies, $E_f < 0$, and the electrochemical stability, with positive dissolution potentials, $U_{diss} > 0$ V.[43] Pourbaix diagrams should be also utilized to determine the catalyst surface composition and stability.[49,52] In the SAC context, the TM adsorption energy is far from being sufficient,[47] and a comparison between the TM adsorption and bulk TM cohesive energies is needed to properly evaluate the TM SAC thermodynamic stability, and better when accounting for dynamic stability when inspecting the TM adatom diffusion energy.[49,53,54] Finally, the effect of the external electric field can be regarded,[43,49] as an additional way of tuning CO_2RR products efficiency.

Furthermore, recent research has highlighted the pivotal role of the electrolyte composition in shaping CO_2RR selectivity and activity. Large alkali cations have been identified to improve the selectivity and activity of CO_2RR, though the precise mechanisms are still a subject of intense debate.[55–57] A recent experimental work[58] has shown that the performance of a $Ti_3C_2T_x$ modified glassy carbon electrode improves as the concentration of $KHCO_3$ in the electrolyte increases. When a 0.1 M $KHCO_3$ solution was present, they observed negligible product formation. However, when using a 0.5 M $KHCO_3$ electrolyte, a variety of different CO_2RR products, comprising CO, methanol, ethanol, and acetone, were quantified.

Clearly, the future use of MXenes for CO_2RR is continuously spurred by computational simulations that slowly but steadily include more ingredients in the models, aimed at either tuning the performance and/or selectivity, and to deliver more accurate estimates. This requires modeling and modulating the type and ratio of mixed surface groups, an explicit inclusion of the electrolyte, and a potential-dependent assessment of the reaction energetics to identify critical reaction steps, either from the thermodynamic point of view, but also when possible incorporating a kinetic assessment, as recently done for the HER over V_2C MXene by the simulation of Tafel plots.[59] These advanced predictions, when duly accounting for the surface hydration and the presence of ions in the electrolyte medium, will be the cornerstone for the design of efficient CO_2RR MXene-based electrocatalysts.

Acknowledgements

The authors acknowledge financial support from the Spanish Ministerio de Ciencia e Innovación through grants MCIN/AEI/10.13039/501100011033 PID2021-126076NB-I00 and TED2021-129506B-C22, funded partially by FEDER Una manera de hacer Europa, the unit of excellence María de Maeztu CEX2021-001202-M granted to the IQTCUB, the COST Action CA18234, and the Generalitat de Catalunya 2021SGR00079 grant. F.V. thanks the ICREA Academia Award 2023 Ref. Ac2216561. L.M. thanks the China Scholarship Council (CSC) for financing her PhD (CSC202108390032). K.S.E. acknowledges funding by the Ministry of Culture and Science of the Federal State of North Rhine-Westphalia (NRW Return Grant). K.S.E. is associated with the CRC/TRR247: "Heterogeneous Oxidation Catalysis in the Liquid Phase" (Project number 388390466-TRR 247), the RESOLV Cluster of Excellence, funded by the Deutsche Forschungsgemeinschaft under Germany's Excellence Strategy – EXC 2033-390677874 – RESOLV, and the Center for Nanointegration (CENIDE).

Conflict of Interests

The authors declare no conflict of interest.

Data Availability Statement

Data sharing is not applicable to this article as no new data were created or analyzed in this study.

Keywords: CO_2RR · Density functional theory · Modeling · MXenes · Surface terminations

[1] N. Armaroli, V. Balzani, *Angew. Chem. Int. Ed.* **2007**, *46*, 52–66.

ChemElectroChem | Concept | doi.org/10.1002/celc.202300598 | Chemistry Europe European Chemical Societies Publishing

[2] H. Yang, Z. Xu, M. Faan, R. Gupta, R. B. Slimane, A. E. Bland, I. Wright, *J. Environ. Sci.* **2008**, *20*, 14–27.
[3] K. P. Kuhl, T. Hatsukade, E. R. Cave, D. N. Abram, J. Kibsgaard, T. F. Jaramillo, *J. Am. Chem. Soc.* **2014**, *136*, 14107–14113.
[4] K. P. Kuhl, E. R. Cave, D. N. Abram, T. F. Jaramillo, *Energy Environ. Sci.* **2012**, *5*, 7050–7059.
[5] D. Ren, Y. Deng, A. D. Handoko, C. S. Chen, S. Malkhandi, B. S. Yeo, *ACS Catal.* **2015**, *5*, 2814–2821.
[6] A. A. Peterson, J. K. Nørskov, *J. Phys. Chem. Lett.* **2012**, *3*, 251–258.
[7] Y. X. Liu, J. Xiao, H. Peng, X. Hong, K. Chan, J. K. Nørskov, *Nat. Commun.* **2017**, *8*, 15438.
[8] K. J. P. Schouten, Z. Qin, E. Pérez Gallent, M. T. M. Koper, *J. Am. Chem. Soc.* **2012**, *134*, 9864–9867.
[9] Á. Morales-García, F. Calle-Vallejo, F. Illas, *ACS Catal.* **2020**, *10*, 13487–13503.
[10] Y. Gogotsi, Q. Huang, *ACS Nano* **2021**, *15*, 5775–5780.
[11] A. VahidMohammadi, J. Rosen, Y. Gogotsi, *Science* **2021**, *372*, eabf1581.
[12] F. A. Janjhi, I. Ihsanullah, M. Bilal, R. Castro-Muñoz, G. Boczkaj, F. Gallucci, *Water Resour. Ind.* **2023**, *29*, 100202.
[13] M. Naguib, M. Kurtoglu, V. Presser, J. Lu, J. Niu, M. Heon, L. Hultman, Y. Gogotsi, M. W. Barsoum, *Adv. Mater.* **2011**, *23*, 4248–4253.
[14] X. Zhan, C. Si, J. Zhou, Z. Sun, *Nanoscale Horiz.* **2020**, *5*, 235–258.
[15] X.-Q. Tan, W. Mo, X. Lin, J. Y. Loh, A. R. Mohamed, W.-J. Ong, *Nanoscale* **2023**, *15*, 6536–6562.
[16] Á. Morales-García, A. Fernández-Fernández, F. Viñes, F. Illas, *J. Mater. Chem. A.* **2018**, *6*, 3381–3385.
[17] R. Morales-Salvador, Á. Morales-García, F. Viñes, F. Illas, *Phys. Chem. Chem. Phys.* **2018**, *20*, 17117–17124.
[18] Á. Morales-García, M. Mayans-Llorach, F. Viñes, F. Illas, *Phys. Chem. Chem. Phys.* **2019**, *21*, 23136–23142.
[19] A. Jurado, K. Ibarra, Á. Morales-García, F. Viñes, F. Illas, *ChemPhysChem* **2021**, *22*, 2456–2463.
[20] L. Persson, J. Hallim, H. Lind, T. W. Hansen, J. B. Wagner, L.-Á. Näslund, V. Darakchieva, J. Palisaitis, J. Rosen, P. O. Å. Persson, *Adv. Mater.* **2019**, *31*, 1805472.
[21] N. Li, X. Chen, W.-J. Ong, D. R. MacFarlane, X. Zhao, A. K. Cheetham, C. Sun, *ACS Nano* **2017**, *11*, 10825–10833.
[22] M. T. M. Koper, *J. Solid State Electrochem.* **2013**, *17*, 339–344.
[23] A. A. Peterson, F. Abild-Pedersen, F. Studt, J. Rossmeisl, J. K. Nørskov, *Energy Environ. Sci.* **2010**, *3*, 1311–1315.
[24] P. B. Kelemen, J. Matter, *Proc. Nat. Acad. Sci.* **2008**, *105*, 17295–17300.
[25] E. Eikeland, A. B. Blichfeld, C. Tyrsted, A. Jensen, B. B. Iversen, *ACS Appl. Mater. Interfaces* **2015**, *7*, 5258–5264.
[26] A. Mazheika, Y.-G. Wang, R. Valero, F. Viñes, F. Illas, L. M. Ghiringhelli, S. V. Levchenko, M. Scheffler, *Nat. Commun.* **2022**, *13*, 419.
[27] J. K. Nørskov, J. Rossmeisl, A. Logadottir, L. Lindqvist, J. R. Kitchin, T. Bligaard, H. Jónsson, *J. Phys. Chem. B* **2004**, *108*, 17886–17892.
[28] J. D. Gouveia, Á. Morales-García, F. Viñes, F. Illas, J. R. B. Gomes, *Appl. Catal. B* **2020**, *260*, 118191.
[29] M. Naguib, *ACS Cent. Sci.* **2020**, *6*, 344–346.
[30] M. Wu, B. Wang, Q. Hu, L. Wang, A. Zhou, *Materials* **2018**, *11*, 2112.
[31] A. D. Handoko, K. H. Khoo, T. L. Tan, H. Jin, Z. W. Seh, *J. Mater. Chem. A.* **2018**, *6*, 21885–21890.
[32] A. Javier, B. Chmielowiec, J. Sanabria-Chinchilla, Y.-G. Kim, J. H. Baricuatro, M. P. Soriaga, *Electrocatalysis* **2015**, *6*, 127–131.
[33] H. Chen, A. D. Handoko, J. Xiao, X. Feng, Y. Fan, T. Wang, D. Legut, Z. W. She, Q. Zhang, *ACS Appl. Mater. Interfaces* **2019**, *11*, 36571–36579.
[34] A. D. Handoko, H. Chen, Y. Lum, Q. Zhang, B. Anasori, Z. W. Seh, *iScience* **2020**, *23*, 101181.
[35] J. L. Hart, K. Hantanasirisakul, A. C. Lang, B. Anasori, D. Pinto, Y. Pivak, J. T. van Omme, S. J. May, Y. Gogotsi, M. L. Taheri, *Nat. Commun.* **2019**, *10*, 522.
[36] H. Chen, A. D. Handoko, T. Wang, J. Qu, J. Xiao, X. Liu, D. Legut, Z. Wei Seh, Q. Zhang, *ChemSusChem* **2020**, *13*, 5690–5698.
[37] V. Parey, B. M. Abraham, M. V. Jyothirmai, J. K. Singh, *Catal. Sci. Technol.* **2022**, *12*, 2223–2231.
[38] S. Cao, Y. Hu, C. Yang, J. Li, H. Chen, S. Wei, S. Liu, Z. Wang, D. Sun, X. Lu, *J. CO_2 Util.* **2022**, *62*, 102074.
[39] Y. Li, Y. Chen, Z. Guo, C. Tang, B. Sa, N. Miao, J. Zhou, Z. Sun, *Chem. Eng. J.* **2022**, *429*, 132171.
[40] Y. Cheng, X. Xu, Y. Li, Y. Zhang, Y. Song, *Comput. Mater. Sci.* **2022**, *202*, 110971.
[41] Y. Zhou, H. Cao, Z. An, M. Li, Y. Huo, J. Jiang, J. Xie, M. He, *Appl. Surf. Sci.* **2023**, *616*, 156492.
[42] N. Li, J. Peng, Z. Shi, P. Zhang, X. Li, *Chin. J. Catal.* **2022**, *43*, 1906–1917.
[43] J. Peng, Z. Shi, J. Jiang, P. Zhang, J.-P. Hsu, N. Li, *Mater. Horiz.* **2023**, ■■■*Dear Author, if the journal has volumes, please add the journal number*■■■, DOI: 10.1039/D3MH00503H.
[44] S. Cao, H. Chen, Y. Hu, J. Li, C. Yang, Z. Chen, S. Wei, S. Liu, Z. Wang, D. Sun, X. Lu, *Chem. Eng. J.* **2023**, *461*, 141936.
[45] Y. Xiao, W. Zhang, *Nanoscale* **2020**, *12*, 7660–7673.
[46] Z. Guo, Y. Li, B. Sa, Y. Fang, J. Lin, Y. Huang, C. Tang, J. Zhou, N. Miao, Z. Sun, *Appl. Surf. Sci.* **2020**, *521*, 146436.
[47] N. Li, X. Wang, X. Lu, P. Zhang, W.-J. Ong, *Chem. Eur. J.* **2021**, *27*, 17900–17909.
[48] S. Baskaran, J. Jung, *Appl. Surf. Sci.* **2022**, *592*, 153339.
[49] F. Li, H. Ai, C. Shi, K. H. Lo, H. Pan, *Int. J. Hydrogen Energy* **2021**, *46*, 12886–12896.
[50] K. S. Exner, *ACS Catal.* **2020**, *10(21)*, 12607–12617.
[51] S. Razzaq, K. S. Exner, *ACS Catal.* **2023**, *13(3)*, 1740–1758.
[52] K. S. Exner, *Mater. Horiz.* **2023**, *10*, 2086–2095.
[53] M. López, K. S. Exner, F. Viñes, F. Illas, *Adv. Theory Simul.* **2022**, ■■■*Dear Author, if the journal has volumes, please add the journal number*■■■, DOI: 10.1002/adts.202200217.
[54] H. Oschinski, Á. Morales-García, F. Illas, *J. Phys. Chem. C* **2021**, *125*, 2477–2484.
[55] M. Keyhanian, D. Farmanzadeh, Á. Morales-García, F. Illas, *J. Mater. Chem. A* **2022**, *10*, 8846–8855.
[56] M. C. O. Monteiro, F. Dattila, B. Hagedoorn, R. García-Muelas, N. López, M. T. M. Koper, *Nat. Catal.* **2021**, *4*, 654–662.
[57] J. Gu, S. Liu, W. Ni, W. Ren, S. Haussener, X. Hu, *Nat. Catal.* **2022**, *5(4)*, 268–276.
[58] M. Liu, Y. Pang, B. Zhang, P. De Luna, O. Voznyy, J. Xu, X. Zheng, C. T. Dinh, F. Fan, C. Cao, F. P. G. De Arquer, T. S. Safaei, A. Mepham, A. Klinkova, E. Kumacheva, T. Filleter, D. Sinton, S. O. Kelley, E. H. Sargent, *Nature* **2016**, *537*, 382–386.
[59] S. Krishnan, S. Marimuthu, M. K. Singh, D. K. Rai, *Energy Adv.* **2023**, *2*, 1166–1175.
[60] M. López, K. S. Exner, F. Viñes, F. Illas, *J. Catal.* **2023**, *421*, 252–263.

Manuscript received: October 26, 2023
Revised manuscript received: December 15, 2023
Version of record online: ■■, ■■

Unveiling the Synergy between Surface Terminations and Boron Configuration in Boron-Based Ti_3C_2 MXenes Electrocatalysts for Nitrogen Reduction Reaction

Ling Meng, Francesc Viñes, and Francesc Illas*

Departament de Ciència de Materials i Química Física & Institut de Química Teòrica i Computacional (IQTCUB), Universitat de Barcelona, c/ Martí i Franquès 1-11, 08028, Barcelona, Spain

Abstract

The performance of B-containing Ti_3C_2 MXenes as catalysts for the nitrogen reduction reaction (NRR) is scrutinized using density functional theory (DFT) methods on realistic models and accounting for working-conditions. The present models include substituted and adsorbed boron along with various mixed surface terminations, primarily comprising –O and –OH groups, while considering the competitive hydrogen evolution reaction (HER) as well. The results highlight that substituted and low-coordinated adsorbed boron atoms exhibit a very high N_2 adsorption capability. For NRR, adsorbed B atoms yield lower overpotentials, especially for surfaces with mixed –O/–OH surface groups, where the latter participate in the reaction lowering the hydrogenation reaction energy costs. The NRR does also benefit of having B adsorbed on the surface which on moderate –OH terminated model display the lowest limiting potential of -0.83 V, competitive to reference Ru, and to HER. The insights derived from this comprehensive study provide guidance in formulating novel and effective MXene-based electrocatalysts for NRR.

*corresponding author: francesc.illas@ub.edu

1. Introduction

Gas phase nitrogen (N_2), having a strong triple bond, is one of the most abundant nitrogen containing compounds on Earth and it is heavily utilized in the chemical industry for the conventional Haber-Bosch process to synthesize ammonia (NH_3). Ammonia can then become oxidized to nitric acid, which constitutes a key component in global fertilizer production.[1,2] The Haber-Bosch industrial process requires the presence of a catalyst but also high temperatures (above 350 °C) and high pressures (above 150 atm) conditions, implying a huge amount of energy consumption with concomitant serious carbon dioxide (CO_2) emissions.[3,4] Therefore, in the pursuit of long-term sustainability, alternative NH_3 synthesis technologies working at softer conditions are being actively explored.[5,6]

Inspired by natural biological N_2 fixation,[7] finding ammonia synthesis procedures working at mild conditions (room temperature and atmospheric pressure) constitutes a challenge and an exciting alternative.[8,9] Particularly, the electrocatalytic nitrogen reduction reaction (NRR) has garnered significant attention as an appealing carbon-neutral methods,[10,11] especially when electricity can be obtained from renewable sources.[12] Ammonia electrosynthesis typically involves a coordinated transfer of protons and electrons, with protons sourced from aqueous medium, and electrons from renewable electrical resources,[12] thus avoiding CO_2 emissions as well.[13] However, this technological appealing process is hampered by the lack of efficient electrocatalysts fulfilling the strict limitations of NRR.[14] Therefore, the development of efficient and highly selective NRR electrocatalysts holds significant economic importance and urgency.

In recent years, a new class of 2D materials known as MXenes[15-17] have emerged as a frontier with ever-growing technological applications.[18] MXenes are new types of two-dimensional (2D) transition metal carbides, nitrides, and carbonitrides, with general $M_{n+1}X_nT_x$ (n = 1–3) formula, consisting of early transition metals (M), carbon and/or nitrogen (X), and typically with terminal functional groups, T_x, usually –O, –H, –OH,–F[16,19,20] or a combination of them.[21,22] Recently, there has been considerable interest in using MXenes as catalyst for the NRR.[23,24] For instance, it has been reported that the $M_2C(0001)$ surface of several MXenes readily adsorb and dissociate N_2.[8,25] Azofra *et al.*[26] conducted a computational analysis of the NRR on M_3C_2 MXenes aimed at evaluating their capability in capturing, activating, and electrochemically transforming N_2 into NH_3. These authors identified V_3C_2 and Nb_3C_2 as the most promising candidates, with associated overpotentials of 0.64 and 0.90 V, respectively.

However, one must advert that these predictions were obtained from models involving the clean, bare, surface of these MXene materials, which do not appropriately represent the systems in which the reactions are taking place which involve an electrochemical environment.[21,24,27] Explicitly accounting for a given termination in the M_2XT_x of T_x = –H, –O, –N, Johnson *et al.*[24] reported a strong influence of the termination on the predicted free energy profiles. However, mixed terminations need to be considered in real-world scenarios.[21,22,28,29] In fact, the type and quantity of surface terminations of MXene are highly sensitive to synthesis conditions such as etching time, temperature, or etchant concentration.[30,31] For instance, typically, hydrofluoric acid (HF) is used as the etchant, however, higher concentrations of HF tend to result in more –F terminations, while lower concentrations lead to the prevalence of –O species.[32] Furthermore, successful synthesis protocols with F-free and gaining T_x-free MXenes have also been reported.[33-36]

There is experimental evidence that surface engineering of MXenes, particularly the types and concentrations of surface terminations, is crucial in facilitating electron transfer, surface adsorption, and activation of N_2. For instance, Xia *et al.*[37] have found that NH_3 production is enhanced with the increase of –OH groups at the Ti_3C_2 MXene surface; furthermore, Ding *et al.*[38] reported experimentally that $Ti_3C_2T_x$ MXene with medium density F-functionalized terminations could enhance the adsorption and activation of N_2. Clearly, the aforementioned theoretical studies not considering the role of terminations are not realistic and more in-depth studies are needed to fill this knowledge gap and better understanding the intricate details of MXene surface engineering in the context of NRR.

The present work focus is on Ti_3C_2, the first MXene ever synthesized.[15] Previous research indicated that the uneven distribution of surface functional groups on MXenes can result in the introduction of numerous oxygen vacancies on the MXene surface that can be occupied by other elements.[39,40] The case of boron atoms is particularly attractive since there is evidence that it exhibits a great potential for N_2 fixation.[41,42] In fact, several B-based NRR electrocatalysts, based on g-C_3N_4, graphene, and 2D boron sheets, have been reported,[43-45] and some studies have been conducted on B-based MXenes for NRR.[46-48] However, these previous studies used oversimplified models, considering scenarios where B substitutes the –O surface termination only, but where its existence, vicinity of terminations, and B quantity were not adequately represented, which calls for more elaborated studies.

There is, regretfully, no current research specifically demonstrating the potential adsorption of boron atoms on the terminal groups of MXenes. Therefore, following earlier studies of single-boron MXene NRR catalysts, we address the present research using ten unique models based on $Ti_3C_2T_x$, specifically encompassing different types of situations for B atoms as shown in Figure 1, with additional details given below and also in Table S1 of the Supporting Information (SI). By using these models, one can obtain detailed insights of the NRR process under realistic working conditions. In particular, the present results highlight *i)* that the stability of the catalysts is influenced by the arrangement of B (substituted/adsorbed), which may result in completely opposite stability behavior at the same termination; *ii)* the N_2 activation capacity of the selected models considering the working temperature, T, and N_2 partial pressure, p_{N_2}, as well as the influence of the coordination number and surface groups on them; *iii)* the effects of –O and –OH groups on NRR under acidic conditions, assuming that MXene is synthesized through a F-free method. In addition, *iv)* we propose a new NRR mechanism that involves different terminations and B-scenarios, where, *v)* contrary to previous works where only substituted B were considered, situations with adsorbed B are not only more stable but also exhibit enhanced performance in NRR. Finally, *vi*) the situations with moderate –OH coverage exhibit most excellent NRR activity and selectivity, with feasibility points in their experimental synthesis and use.

2. Computational Details

2.1. Models and Methods

The Vienna *ab initio* simulation package (VASP)[49] was used to carry out all the needed periodic density functional theory (DFT) calculations. The generalized gradient approximation (GGA) Perdew-Burke-Ernzerhof (PBE) [50] exchange-correlation functional was employed, found to describe the electronic structure and related properties of MXenes with sufficient accuracy.[51-53] Furthermore, the D3 approach proposed by Grimme et *al.*[54] was used to account for interactions involving dispersion. The valence electron density was expanded using a plane wave basis set, with a cutoff kinetic energy of 415 eV, to ensure that the total energies obtained were converged below the chemical accuracy of 1 kcal·mol^{-1} —*ca.* 0.04 eV,[55] whereas the projector augmented wave (PAW) method,[56] as implemented by Kresse and Joubert,[57] was employed to describe the effect of core electrons on the valence electron density.

Utilizing a $p(3\times3)$ supercell, see Figure 1, a F-free experimental protocol is assumed to initially lead to fully –O or –OH covered Ti_3C_2. Subsequently, considering the superior stability of –OH termination according to Pourbaix diagrams, and the above-mentioned influence of the vicinity of B, the mixed –O and –OH cases with $^2/_9$ *vs.* $^7/_9$ of a monolayer (ML), $^1/_3$ *vs.* $^2/_3$ ML, and $^4/_9$ *vs.* $^5/_9$ ML were also explored, respectively. Note that here a full ML is defined as having one surface moiety per surface metal atom. In addition, a 20 Å vacuum was added to the periodically repeated slabs to ensure their appropriate isolation. Numerical integration in the Brillouin zone was carried out on an optimized $5\times5\times1$ **k**-point **Γ**-centered Monkhorst-Pack grid,[58] providing numerical convergence within 0.05 eV, very close to the accepted chemical accuracy value of *ca.* 0.04 eV. The energy of isolated atoms and of molecules at the equilibrium geometry in vacuum was determined by carrying calculations in a broken symmetry large cell of $10\times10\times10$ Å dimensions to ensure due orbital occupancy, carried out spin-polarized for systems with unpaired electrons, and performed at **Γ**-point only.

During the structural optimizations, the convergence of the electronic self-consistent field steps was controlled using a criterion of 10^{-5} eV, and the relaxation of atomic positions was performed until the forces exerted on the atoms were below 0.01 $eV\cdot Å^{-1}$. It should be noted that, unless specified otherwise, all calculations were conducted taking spin polarization into account. The vibrational frequencies of the stationary points related to surface species were determined by constructing and diagonalizing the corresponding block of the Hessian matrix using finite differences of analytical gradients with steps of 0.03 Å in length as done in previous works.[59,60] Thus, only degrees of freedom involving the adsorbed species and terminations were accounted for, while the substrate atoms were kept fixed, assuming a decoupling of the surface species from the materials phonons.

On the above models, adsorbed (**a**) and substituted (**s**) B situations with single B or B pairs were examined, also considering two different B coordination types on H_C or B_O sites, plus different surface situations for the terminating groups. The complete set of models used and the corresponding notation are displayed in Figure 1. To better follow the employed notation, let us take the **s**B@$Ti_3C_2O_{8/9}$ and **a**2B@$Ti_3C_2O_{4/9}OH_{5/9}$ cases as examples. There one can readily see that single B substitutes one surface –O group on $Ti_3C_2O_{8/9}$, whereas two B are adsorbed on the $Ti_3C_2O_{4/9}OH_{5/9}$ model. For each model, the symbols in parentheses in Figure 1 are used as shortcut for notation simplification.

2.2. NRR Mechanism

The initial, *sine qua non*, step in the NRR is gas phase, $N_2^{(g)}$, adsorption onto a catalyst free surface site, *, as;

$$N_2^{(g)} + * \rightarrow N_2* \quad (1).$$

The subsequent reaction mechanism involves a series of concerted proton-electron transfer (CPET) steps, where protons (H^+) and electrons (e^-) are added together, but in a sequential manner up to ammonia (NH_3) product.[61] Thus;

$$N_2* + 6H^+ + 6e^- + * \rightarrow 2NH_3* \quad (2).$$

Next, it is highly likely that NH_3* will dissolve in water, resulting in the formation of $NH_4OH_{(l)}$,[62,63] as;

$$NH_3* + H_2O_{(l)} \rightarrow NH_4OH_{(l)} \quad (3),$$

and, because of this, NH_3 desorption is not considered a determining step.

For convenience, it is often assumed that the reduction of precursor adsorbed species, A*, occurs in a single elementary reaction step,[64,65] in which H^+ and e^- are directly involved in the production of AH* as

$$A* + H^+ + e^- \rightarrow AH* \quad (4).$$

In addition, we also considered the potential contribution of –OH termination as a source of hydrogen. Thus, A* also could undergo hydrogenation through the –OH group, as

$$A* + -OH \rightarrow AH* + -O \quad (5),$$

leaving the –O moiety behind in the chemical step. Subsequently, a CPET electrochemical step can regenerate the –OH group, as;

$$-O + H^+ + e^- \rightarrow -OH \quad (6).$$

The present study explores various pathways to enhance the comprehension and engagement of surface terminations during the NRR in the Ti_3C_2 MXene and its subsequent mechanism.

2.3. Stability of B-Based Models

To gain information on the experimental synthetic feasibility, the thermodynamic stability of the B-based MXene models was assessed. Typically, the structural stability of these

concept-electrocatalysts can be evaluated using parameters such as the B mean adsorption energy, E_{ads}, estimated as;

$$E_{ads} = \frac{E_{nB/MXene} - E_{MXene} - n*E_B}{n} \quad (7),$$

where $E_{nB/MXene}$, E_{MXene}, and E_B are the total energies of MXene with and without n B atoms, and the isolated B atom energy. As commonly done in the literature, one can compare E_{ads} to the computed boron bulk cohesive energy, E_{coh},[66-68] in order to assess the thermodynamic stability —sometimes referred as $E_{diff} = E_{ads} - E_{coh}$—, so that an adsorption stronger than cohesive energy would energetically drive the presence of isolated B atoms. The B bulk cohesive energy was computed here optimizing bulk boron using a 5×5×1 **k**-point mesh, and the obtained value of -6.45 eV/atom was used in the comparison for consistence, even if slightly overbinding compared to the experimental value of -5.81 eV/atom.[69] Furthermore, the catalyst stability can be assessed by calculating the formation energy, E_f, taking bulk Ti, graphite, O_2, and H_2 as constituent reactants in their standard state, being Ti and graphite computed likewise as done for B bulk.

2.4. Thermodynamic Approach to the Limiting Potential

To provide a comprehensive picture of the NRR mechanism, we rely on the well-known thermodynamic approach as proposed by Nørskov *et al.*,[70] widely used in previous studies related to electrocatalysis by MXenes.[21,71-73] Within this approach, the focus is on the Gibbs free energy differences between different reaction intermediate states, which helps determining the required limiting potential, U_L, of the reaction. Strictly speaking, every CPET step involves a transition state which can be approximated as shown by Exner,[74] and applied to the hydrogen evolution reaction (HER) on the V_2C MXene.[75] However, there overwhelming evidence that relevant information can be extracted by relying on the thermodynamic picture only.[61,76]

Within the thermodynamic approach, one relies on the free energy profiles which, in turn, requires to first make an estimation of the total adsorption energies of the intermediate species, E^i_{ads}, obtained as

$$E^i_{ads} = E_{i/sub} - (E_{sub} + E_i) \quad (8).$$

Here, E_{sub} and $E_{i/sub}$ are the total energy of the corresponding MXene model, featuring a variety of mixed surface terminations as shown in Figure 1, without and with the adsorbed

i-species, respectively, and E_i is the total energy of the *i* adsorbed species in vacuum. With this definition, the more negative E^i_{ads}, the stronger the adsorption is.

To estimate the reaction Gibbs free energy change, ΔG, at each electrochemical step, we rely on the aforementioned computational hydrogen electrode (CHE) model,[70] assuming that under standard equilibrium conditions of $pH = 0$, $U = 0$ V, temperature, T, of 298.15 K, and a partial pressure of H_2, p_{H_2}, of 1 bar, the chemical potential of a pair of H^+ and e^- can be correlated to that of H_2 at 0 V *vs.* the reversible hydrogen electrode (RHE), as;

$$H^+_{(aq)} + e^- \rightarrow \tfrac{1}{2}\cdot H_2^{(g)};\ \Delta G^\circ = 0\ \text{eV} \qquad (9).$$

Keeping in mind that the chemical potentials or Gibbs free energies of the initial states, $H^+_{(aq)} + e^-$, and the final state, $\tfrac{1}{2}\cdot H_2^{(g)}$, are equal, it turns out that the Gibbs free energy of the proton-electron pair is just half the free energy of the hydrogen molecule. Thus, one can calculate ΔG for any elementary reaction step as

$$\Delta G = \Delta E + \Delta E_{ZPE} - T\cdot\Delta S \qquad (10),$$

where ΔE is the total energy change of the electrochemical step, ΔE_{ZPE} is the change in zero point energy change between initial and final states of this step, estimated from the calculated harmonic frequencies, and ΔS is the corresponding entropy change which for adsorbed species involves the vibrational partition function only —explicit formulas for ZPE and ΔS can be found in the literature.[21,73,77] The entropy of gas phase N_2, H_2, and NH_3 species has been sourced from the National Institute of Standards and Technology (NIST) webbook.[78] Note also that the ΔG values obtained from Eq. 10 correspond $pH = 0$ and $U = 0$ V, while ΔG values at finite pH and U can be easily derived as well, as detailed in the literature.[76,79]

From the Gibbs free energy profiles of a given reaction, it becomes possible to evaluate the reaction limiting potential, denoted as U_L, defined as the minimum potential required for a particular electrochemical reaction to proceed successfully under specified reaction conditions.[70] In the context of NRR, the U_L signifies the electrochemical potential at which each elementary electrochemical hydrogenation step step in the reaction becomes exergonic, indicating the minimum energy input necessary for the reaction to advance successfully. The descriptor ΔG_{max} defined as the largest free-energy difference between initial and final state for each concerted proton-electron transfer (CPET) step. computed at U=0 , is employed here to extract U_L for NRR, as;

$$U_L = -\frac{\Delta G_{max}}{e} \quad (12),$$

where, generally, the lower U_L —the closer to zero overpotential—, the higher the reaction activity.

2.5. Adsorption Rates

As aforementioned, under reaction condition, $N_2^{(g)}$ adsorption is a necessary occurrence, while desorption of $NH_3^{(g)}$ likely to be fostered by dissolution as $NH_4OH_{(l)}$. To include the $N_2^{(g)}$ adsorption necessary step, we rely on kinetic phase diagrams (KPD), as introduced in previous studies.[80,81] These require a thorough evaluation comparing the molecular adsorption/desorption rates, r_{ads} and r_{des}, respectively, under different temperatures and partial pressures. This allows one to determine the critical turning points at which the adsorption and desorption rates reach equilibrium. The adsorption rates are estimated from non-activated collision theory while desorption rates are gained using transition state theory (TST), assuming latest transitions states. Details on the employed formulas are well detailed in the literature.[82]

3. Results and Discussion

3.1. Models and Stability of B-based MXenes

Firstly, a systematic sampling search was carried out to investigate the four highly symmetric adsorption sites, including top (T) and bridge (B), hollow carbon (H_C), and hollow metal (H_M) of pristine Ti_3C_2, as shown in Figure 1a, where H_M was found to be always the most favourable adsorption site, consistent with previous studies.[59,83] In the case of Ti_3C_2O, the three possible high-symmetry adsorption sites were also sampled (*cf.* Figure 1b), being H_C site the most favourable adsorption site, closely followed by B_O site, being most stable on **a**B-O_2, **a**B-B_O-O3, and **a**B-B_O-O_4 (*cf.* Figure 1). When having B_2 dimers, see Figures 1k and 1l, a semi-bridge situation is found, with a molecular display resembling that of ethene.

As far as the stability of each model is concerned, the calculated E_{ads}, E_{diff}, and E_f values are listed in Table S1 of the Supporting Information (SI). Note that all the models display a negative formation energy per atom, ranging from -0.37 eV/atom for **s**B-OH to -0.54 eV/atom for **a**B-O, implying that all the studied casuistry is stable with respect their elemental components. Aside, the B adsorption energies can be also substantial, ranging from -2.53 eV for **s**B-O to -7.66 eV for **a**B-O. As expected, the more negative the E_f, the more negative the E_{ads} is. Interestingly, the structural stability is apparently related to

changes in boron arrangement and termination. For the B-substituted (**s**B) models, the stability gradually increases with decreasing number of –O groups and concomitant increasing number of –OH groups, while for B-adsorbed (**a**B) cases the stability gradually decreases. In addition, the adsorption site and atomic coordination has a certain impact on the stability, since B on H_C sites is usually more stable than on B_O sites. Increasing the amount of boron (B) as in the explored dimers leads to less stable systems. More importantly, few cases display E_{ads} larger than the B-bulk cohesive energy, this is, negative E_{diff} values. In particular, **a**B-O, **a**B-H_C-O_4 and **a**2B-O, while **a**B-H_C-O_3 E_{diff} value is close to zero. It is clear, that B adsorption is favoured by a full or large coverage of O adatoms.

The Bader charge of the different compound parts is also listed in Table S1 of the SI. Generally, the Ti_3C_2 MXene donates electrons to the T_x groups, being either –O or –OH, given their larger electronegativity, and in accordance with previous reports,[73] and charge density difference (CDD) plots in Figure S1 of the SI. As far as B is concerned, it becomes slightly reduced on **s**B models yet slightly oxidized in **a**B ones, a trend that becomes more significant as the ratio of –O groups increases and accentuated on H_C conversely to B_O sites. In the case of **s**B models, their substitution to a –O or –OH implies a certain electron density maintenance, to better embed in the T_x layer. In the case of **a**B situations, the B atoms gets slightly positively charged. In fact, for the most stable aforementioned situations, **a**B-O and **a**B-H_C-O_4, even **a**B-H_C-O_3, the B atom gets its maximum charge of +0.24 *e*, while on the B_2 dimer of **a**2B-O, the charge per B atom is +0.16 *e*.

Aside, CDD plots shown in Figure S1 of the SI visually confirm the aforementioned results, in that Ti_3C_2 donates electron density to –O and –OH terminating groups and B and **s**B situations, while for **a**B even **a**2B situations, the B atoms become positively charged. Before discussing NRR, the conductivity of these materials should be considered, since a semiconductor like band gap would handicap electron transfer.[84] To address this issue, the density of states (DOS) and projected density of states (PDOS) were gained and shown in Figure S2 of the SI. Briefly, these reveal that all systems exhibit a metallic behaviour with the participation of Ti *d* orbitals, C, B, T_x = O, OH *p* orbital, and H *s* orbitals close to the Fermi level. Notice that **s**B and **a**B exhibit significant differences, the former with limited interaction with atomic orbitals from other elements, while the latter involves a strong, covalent mixing with the *p* orbitals of –O groups, shown in the -6 to -10 eV region.

3.2. N_2 Adsorption

It has been pointed out[85] that surface doping with B can enhance the activation of CO_2 adsorption, since C atoms of adsorbed CO_2 gain more electrons on B-doped MXene. This trend should also be applicable to N_2, given the structural and property similarities between CO_2 and N_2 molecules. Furthermore, experimental results have also shown[86] that the NH_3 generation rate of B-doped Ti_3C_2 is significantly higher than that in the non-doped cases. Thus, here, B-doped MXene is expected to facilitate NRR, and surpass in activity those non-doped scenarios.

The N_2 adsorption is a *sine qua non* requirement for the NRR, and one can envisage physisorbed and chemisorbed situations. In the first case, the interaction between doping B and N_2 is almost negligible, with essentially no charge-transfer, whereas for chemisorption *end-on* and *side-on* structures can be found,[87] as well *bridge* configurations,[65] see Figure 2. The optimized geometries for each conformation are shown in Figure S3 of the SI. Additionally, we also considered adsorption at a single B active centre, either **a**B and **s**B, as well as on B_2 dimers. The N_2 adsorption energies, E_{ads}, N_2 Bader charges, Q_{N_2}, and closest bond lengths between surface B and N_2, *d*(BN), and of N_2 molecule, *d*(NN), are reported in Table S2 of the SI.

First of all, the physisorbed (-*p* states) are easily recognized by small E_{ads} values ranging from -0.09 (**a**B-O-*p*) to -0.30 eV (**a**2B-OH-*p*), with essentially no charge transfer between the catalyst and the physisorbed N_2 molecule. The *d*(BN) distances are large, from 3.26 (**a**B-O-*p*) to 3.51 Å (**a**2B-OH-*p*), and the *d*(NN) distance remains always 1.12 Å; the value of the gas phase molecule calculated in vacuum. When it comes to the chemisorbed identified states, the interaction between N_2 and an active B centre may involve σ donation from N_2 or B back-donation to the empty $2\pi^*$ molecular orbital of N_2 as suggested in the literature.[88,89] Compared to **a**B, **s**B exhibits significantly stronger N_2 adsorption ability, with adsorption energy ranging from -1.43 (**s**B-O-*s*) to -2.79 eV (**s**B-OH-*e*), quite in the line of the reported inherent N_2 affinity of pristine MXenes.[20] However, **a**B situations display a less strong chemisorption, with adsorption energy values ranging from -0.37 (**a**B-B_O-O_4-*s*) to -1.19 eV (**a**B-O_2-*s*).

The difference towards N_2 interaction between **a**B and **s**B may be attributed to the negative Bader charge of **s**B as shown in Table S1 of the SI, easing the back-donation of electron density to the N_2 $2\pi^*$ orbital, also in line with the negative Bader charges on N_2 for **s**B, Q_{N_2}, from -0.08 (**s**B-O-*e*) to -0.20 *e* (**s**B-OH-*s*), see Table S2 of the SI, and

mirrored by a positive charge change on B atoms, ΔQ_B, see Table S2 of the SI. This charge change is also present on **a**B, but to a lesser extent, with Q_{N_2} values ranging from -0.07 (**a**B-B$_O$-O$_4$-*e*) to -0.18 *e* (**a**2B-OH-*bs*). For the chemisorbed states one finds, as expected, relatively small *d*(BN) bond lengths, from 1.35 (**s**B-OH-*e*) to 1.62 Å (**a**2B-O-*be*), and slightly elongated N_2 bonds, from 1.16 (**s**B-O-*e*) to 1.40 Å (**s**B-OH-*s*). Clearly, the exploration yielded a handful of chemisorbed minima, prone to N_2 activation and posterior reduction.

Furthermore, the analysis also suggests that –OH environment and the *side-on* adsorption mode strengthen the N_2 interaction on **s**B models, while for **a**B, when B is adsorbed on H$_C$ site, its three sp^3 hybridized orbitals and three electrons are used for –O coordination, leaving one empty sp^3 orbital as possible acceptor, and not prone to back-donation, which explains why these sites lead to physisorption. For **a**2B dimers, the *bridge-side-on* maximizes the interaction with N_2, where each B has one free electron to bond each of the N atoms in the N_2 molecule, ultimately weakening the molecular bond. Thus, the donation and back-donation mechanism, the B electron charge, and the coordination mode freeing sp^3 electrons are found to be key in the N_2 adsorption and activation.

To further confirm the existence of a direct bond between B doping atoms and the N_2 molecule, insights are withdrawn from the minima PDOS shown in Figure S4-6 of the SI. The plots for the physisorbed state show no significant overlap between B and N_2 sp^3 orbitals, where **a**B-H$_C$-O$_4$-*p* is clear example. The opposite occurs for the chemisorbed states with clear orbital overlap (see *e.g.* the cases of N_2 on **s**B-O-*s* or **a**B-B$_O$-O$_4$-*s*) with localized discrete states with contributions both from B and N atoms, in line with covalent-like bonds. The charge density differences (CDD), shown in Figure S7 of the SI, are in line with the mentioned donation-acceptation picture.

Last but not least, to go beyond the static adsorption picture, and to inspect whether $N_2^{(g)}$ would get adsorbed on the catalyst, we compared the adsorption and desorption rates, r_{ads} and r_{des}, respectively, for all models and adsorption modes, much following the employed procedure used in the past to acquire the kinetic phase diagrams (KPD).[90,91] As seen in Figure 3, under reaction working condition of $T = 300$ K and 1 bar of $N_2^{(g)}$ partial pressure, a number of models and sites feature an adsorption rate superior to the desorption rate, in particular, **a**2B-O-*bs*, **a**B-B$_O$-O$_4$-*e*, **a**B-B$_O$-O$_3$-*e*, **a**B-O$_2$-*e*, **a**B-O$_2$-*s*, **s**B-O-*s*, **s**B-OH-*s*, **s**B-O-*e*, and **s**B-OH-*e*; thus, in all cases chemically bound,

activated N_2, with an adsorption energy stronger than -0.67 eV, in concordance with values listed in Table S2 of the SI, and so, underscoring the viability of **s**B modes than **a**B ones. Note also that since NRR typically takes place in aqueous solution where the produced NH_3 reacts with $H_2O_{(l)}$ to form $NH_4OH_{(l)}$, there is no need to consider the adsorptive and desorptive landscape for $NH_3^{(g)}$.

By correlating the N_2 adsorptive capacities, and doping model stabilities, the only model with a priori kinetic stability capable of adsorbing and activating $N_2^{(g)}$ would be the B dimer on O-terminated MXene, the **a**2B-O, see Table S1 of the SI and plots in Figure 3. Still, the NRR Gibbs energy profile will be studied for other close models, since such systems could be kinetically metastable, and to capture trends and mechanism variations with respect the model composition, see below.

3.3. NRR Mechanisms

Before delving into the NRR free energy profiles, it is mandatory to define the possible mechanisms, and to keep in mind the possible competition with the hydrogen evolution reactions (HER) would be.[92] Previous research suggested that NRR predominantly occurs through *distal* and *alternating* mechanisms in *end-on*, or *enzymatic* mechanism in *side-on* adsorption modes,[93] as illustrated in Figure 4. However, in the present study, apart from the three mechanisms, physisorption is also considered as a possible step. The *distal* mechanism has its name since it assumes that the CPET first attacks the N atom farthest from the catalyst surface, and continues in subsequent CPET steps until a first $NH_3^{(g)}$ is synthesized and released, leaving a N* moiety on the catalyst surface, which gets later fully reduced until the second $NH_3^{(g)}$ is gained. At variance, in the *alternating* mechanism, the CPET alternate in between the two N atoms of the *end-on* situation. Finally, the *enzymatic* mechanism mimics biological mechanisms of N_2 fixation, where one departs from an activated *side-on* adsorption mode, favouring an alternating pattern of CPET for the two N atoms.

Before focusing in the reaction free energy profiles, it is worth stating here that, in the case of **a**2B exhibiting dual active sites, the NH_2NH_2* does not appear in the *enzymatic* mechanism since optimizations consistently showed that the N–N bond breaks during the hydrogenation of $NHNH_2$*, directly forming two NH_2* species. Furthermore, *mixed* situations can occur, where $NHNH_2$* is formed when reducing NNH_2* instead of gaining $NH_3^{(g)}$ and N* adatoms through the *distal* pathway, see Figure 4, or when, in the *enzymatic* path, the $NHNH_2$* hydrogenates to NH* and $NH_3^{(g)}$ instead of forming

NH_2NH_2*. Thus, these mixed paths connecting distal with alternating or enzymatic paths are also regarded in the following.

3.4. NRR Reaction Free Energy Profiles

Let us finally analyse the three possible mechanisms for the electrochemical reduction of N_2 into NH_3, with the ultimate aim of determining the most favourable pathway, while investigating the influence of B doping site, **a**B *vs.* **s**B, having B single atoms or dimers, *i.e.* **a**B *vs.* **a**2B, and the effect of nearby functional groups. To this end, we start with substitutional B situations (**s**B), with surface –O or –OH groups, shown in Figure 5. In these models, and as mentioned above, a prominent feature is the exceptionally strong N_2 adsorption capability. On **s**B-O, except for the $NHNH_2$* and final NH_3* generation steps, the other CPET are exergonic. Indeed, ΔG_{max} corresponds to the final CPET with a value of 1.40 eV as the potential-determining step (PDS), and the most favourable pathway is *mixed*; mainly following *distal* mechanism, except for the $NHNH_2$* formation which correspond to *alternating* one. On the **s**B-OH model, the NH_2* → NH_3* is also the PDS with ΔG_{max} of 1.47 eV, and also follows the *distal* mechanism, except for the hydrogenation of $NHNH_2$* species, which follows the *mixed* route to generate NH* and NH_3* directly. Here, at variance with **s**B-O, all steps are endergonic or in equilibrium except for the $NHNH_2$* hydrogenation step. Note that, as observed in, *e.g.* CO_2RR on $Ti_3C_2T_x$ models,[73] the surface –OH groups can transfer H atoms, and that is found in the *alternating* path when reducing N_2H*, where $NHNH_2$* is formed, at the same time one vicinal –OH group transfers its H to form this moiety, see Figure 5, being a much more stable intermediate. Still, accounting for energetic preferences on path bifurcations, the *distal-alternating mixed* mechanism is, in principle, preferred.

In the situations with adsorbed B, **a**B, one may have B on bridge sites, B_O, or hollow sites, H_C, and the reaction may imply changes in the adsorption mode. In the case of **a**B-O, see Figure 6, the B atom is on a H_C site, see Figure 1. There, the reaction sequence after N_2 physisorption leads to N_2H*, the PDS with a ΔG of 1.37 eV, where situations having B at H_C or B_O are nearly equivalent. From there on the reaction primarily follows the NHNH* *via* the *alternating* mechanism, alternating also B being between H_C and B_O. This is due to the fact that, when the H addition implies a N-N bond breaking, and the freed lone pair is used to make a new covalent bond with B, at the expense as well of breaking a B-O bond, and adopting a B_O conformation. By adding a new H bond, the

generated extra B-N bond gets broken to use the N lone pair in the new N-H bond, and then B goes back to a Hc conformation maximizing bonds with surface O atoms.

The next model with highest concentration of –O groups is the **a**B-O_4, with $^4/_9$ of the surface being –O groups, and the rest –OH groups. The NRR free energy reaction profile is shown in Figure 7, which departs from B in Hc as this is the more stable situation, see Table S1 of the SI. Here, a first step that is costly is the first CPET to form N_2H* on a Bo mode, with a ΔG of 0.93 eV. However, after keeping B in Bo and following the *mixed* pathway, the PDS is on the last NH_3* formation, similar to the **s**B models, with a ΔG of 1.19 eV.

The situation changes, though, when increasing the number of –OH groups nearby that can participate in the reaction. This is visible on the **a**B-O_3 model in Figure 8. There, the initial free energy profile is similar to that of **a**B-O_4, departing from Hc site for B, up to the formation of N_2H* with a ΔG of 0.52 eV. From this point on, the further hydrogenation through *distal-alternating mixed* path implies the simultaneous transfer of one H from a vicinal –OH group to form $NHNH_2$*, being this step quite exergonic by -1.66 eV. From this point on, the next CPET implies the formation of the first NH_3* leaving behind NH*, endergonic by 0.37 eV, and the subsequent CPET on NH* to form NH_2*, again quite exergonic by -1.6 eV. At this point, the as-generated –O can be hydrogenated to recover the former –OH group with a ΔG of 0.60 eV, and the formation of –OH group from the pre-existing –O group becomes the costliest CPET and thus constitutes the PDS with a ΔG of 0.83 eV. From this point, the reaction ends up with the second NH_3 molecule formation.

Finally, on the **a**B-O_2 model, the reaction proceeds mostly with B on Bo site, as expected, see Figure 9. There N_2* initially follow the *enzymatic* pathway, and further hydrogenation from $NHNH_2$* after the first three CPET has a very stable jump towards NH_2* placing into the *distal* path, involving one H atom transfer from a vicinal surface –OH groups, with a ΔG of -2.11 eV. From this point on, the as generated –O group is compensated, and next the second NH_3 formation is achieved with a ΔG of 1.14 eV. After NH_3 desorption, the final CPET back-recovers the Bo site for B and also regenerates a second surface –OH, becoming the PDS with ΔG = 2.01 eV. Thus, in general, for large –OH coverage, as in **a**B-O_2 and **a**B-O_3, the participation of surface –OH groups is to be highlighted, modulating the reaction profile, since on both the PDS involve the –OH participation. However, the results of **a**B-O_2 indicate that an excessive amount of surface –OH is not necessary, and a moderate amount of –OH can therefore improve the reaction

as in **a**B-O_3. Aside, even if **s**B models exhibit excellent N_2 adsorption, their performance is generally poorer compared to **a**B models, which seems to benefit from a high surface presence of –OH groups, as seen in **a**B-O_3 with ΔG_{max} of 0.83 eV, the smallest so far.

At this point one may wonder what the effect of having B dimers would be. Compared to **a**B, on double adsorbed B sites (*cf.* **a**2B in Figure 10) two additional $N_2^{(g)}$ adsorption modes are possible, *be* and *bs*, as shown in Figure 2. These are also viable for hydrogenated species in the course of the NRR. However, since in **a**2B-O *bs* N_2 adsorption is faster, as seen in Figure 3, we depart from this mode to generate the reaction free energy profile which is presented in Figure 10, where T_N denotes adsorption on top of a nitrogen atom and T_B denotes adsorption on a bridge between two nitrogen atoms. There, the B_2 surface dimer prompts following the *enzymatic* pathway downhill up to $NHNH_2$*, and then *mixed* shortcut to get on *distal* to form NH* and NH_2*, which bounds two B atoms, and finalizes the reaction being formation of last NH_3* the PDS with a ΔG of 1.51 eV. Interestingly, in the **a**2B-OH model, the reaction route is more complex. Despite the slightly more favourable N_2* *bs*, the high stability of reaction intermediates along the *mixed* path from the *enzymatic* path leads the final NH_3* formation as the PDS with ΔG of 2.1 eV. However, it can be argued that a route in which the bridge and top sites on B_2 makes the reaction route go through *alternating* path could be possible, as shown in Figure S8 with PDS being the last NH_3 formation, with ΔG of 0.99 eV, but the thermodynamic will be larger when all sites were occupied by the most favourable mechanism.

In summary, from the studied reaction paths and as summarized in Figure 11a one can clearly state that *i*) **a**B generally features slightly smaller U_L compared to **s**B, *ii*) that having a combination of surface –O and –OH groups also generally reduces the U_L, with *iii*) the free energy reaction path sometimes affected by the involvement of vicinal surface –OH transferring simultaneously their H atoms, *iv*) that actually, having **a**B is best when B being on H_C surrounded by –OH, *v*) that *distal*, *alternating*, *enzymatic*, and *mixed* paths are often visited, and, finally, *vi*) that having adsorbed B with moderate –OH groups is best for reducing U_L. At this point, still, one has to consider that upon reduction conditions, the NRR will compete with hydrogen evolution reaction (HER), as happens as well with CO_2RR.[73] The HER and the selectivity towards NRR, and a comparison with literature is treated in the next section.

3.5. Performance and NRR vs. HER

The present assessment of the overall performance relies on the calculated ΔG_{max} value alongside its respective U_L. Figure 11a compares the Boron doped $Ti_3C_2T_x$ models as NRR electrocatalyst to the Ru (0001) reference of having ΔG = -1.08 V,[94] yet gained using revised PBE functional with no dispersion correction interactions, so one should avoid making clear differences for ΔG differences within the DFT standard accuracy of ca. 0.2 eV. In any case, Figure 11a evidences a clear benefit possibly extendable to other MXene compositions. Moreover, the HER is a major competing side reaction to the NRR, which may decrease the faradaic efficiency (FE) in experiments. HER is usually evaluated using a three-state diagram,[21] which includes the initial CPET to form H*, and a second one which directly generates the H_2 product. Within this scheme, the closer the absolute value of ΔG_{max} of HER is to zero, the closer is the material to the ideal HER catalyst. As shown in Figure 11b, the studied models catalysts perform significantly different, with **a**2B-O demonstrating excellent HER performance, with $|\Delta G_{HER}|$ of 0.1 eV, while **a**B-O_3 is worst with a $|\Delta G_{HER}|$ of 1.75 eV, see values in Table S3 of the SI. At this point, one can compare the U_L of NRR, U_L(NRR) to that of HER, U_L(HER), as illustrated in Figure 11c. Here, the competition between NRR is evident, as in some cases, the HER is more easily achieved than NRR on fully –O covered adsorbed **a**B-O and **a**2B-O. However, for adsorbed situations with mixed quantities of surface –O and –OH groups, **a**B-O_3 and **a**B-O_4, the NRR is more favored than HER, see Figure 11b. Finally, on substituted **s**B-O and **s**B-OH, and B adsorbed on high –OH covered, **a**B-O_2, the competition between NRR and HER is more evident. Looking for low U_L, and relatively good performance of NRR *vs.* HER, the **a**B-O_3 situation would be optimal. Note that strategies exist to inhibit HER, including limiting proton concentration or transfer rate,[94-96] using non-aqueous proton donors to inhibit hydrogen adsorption on catalysts, and providing protective layers to prevent proton transfer to the surface.[97,98]

Finally, it is worth addressing the experimental synthesis feasibility of the above raised NRR electrocatalysts candidates. The preparation of B-doped $Ti_3C_2T_x$ involves placing the solution into a Teflon-lined autoclave and a hydrothermal treatment at 180 °C for 24 hours.[99] However, previous studies[44, 100] have shown that high-temperature treatment may lead to the removal of surface –OH groups, which poses a challenge in maintaining a high –OH state, if willing to get highly selective **a**B-O_4, and best performing **a**B-O_3. Still, previous studies on computational Pourbaix diagrams[79, 101]

indicate the stability of surface terminations as a factor of *pH* and *U*, where pure –O, –OH, and mixed –O/–OH situations are reachable at low *pH* and slightly positive, negative, and close to zero overpotential, respectively, solving stability issues under low *pH* and potential operating conditions.

4. Conclusions

In this study, we investigated the potential performance of B-based Ti_3C_2 MXene for the NRR, with a specific focus on different boron configurations, including substituted/adsorbed boron (**s**B/**a**B), the distinct B coordination (H_C/B_O), and the number of boron atoms, as well as the impact of different surface terminations ratios on catalytic activity, including two **s**B and eight **a**B models. The N_2 adsorption energy and activation rate was considered to determine whether the catalytic reaction could proceed. Moreover, we also analyzed the involvement of hydrogen atoms from the –OH terminating groups, especially for mixed –O/–OH terminations in **a**B-O_2 and **a**B-O_3 models.

The present DFT calculations revealed that, despite **s**B models have the strongest N_2 adsorption capacity, followed by low-coordinated **a**B, the NRR performance of **s**B is significantly lower than that corresponding to **a**B situations. From the present models it appears that a moderate number of –OH groups at the catalyst surface, neither excessive nor too low, is better for NRR performance, especially for **a**B-O_3, which exhibited significantly higher NRR performance than cases fully –O terminated, such as **s**B-O, **a**B-O, and **a**2B-O, and the cases with high –O-terminated presence **a**B-O_2, and **a**B-O_4 with low –OH coverage. In addition, **a**B-O_3 is predicted to outperform Ru (0001) which is the reference electrocatalyst, and to be selective to NRR as it shows very poor activity towards the HER reaction. It is worth pointing out that the better performance of this system normally is due to the participation of hydrogen atoms of –OH groups, stabilizing reaction intermediates, and thereby helping at reducing the energetic costs of the reaction. Note in addition that, according to computationally-derived Pourbaix diagrams, such situations are predicted to be stable under working conditions.

Acknowledgments

The research carried out at the *Universitat de Barcelona* has been supported by the Spanish MCIN/AEI/10.13039/501100011033 PID2021-126076NB-I00 and TED2021-129506B-C22, partially funded by FEDER *Una manera de hacer Europa*, and *María de Maeztu* CEX2021-001202-M grants, including funding from European Union. The authors acknowledge partial support from COST Action CA18234 and from the *Generalitat de Catalunya* grant 2021SGR79. L.M. thanks the China Scholarship Council (CSC) for financing her PhD (CSC202108390032). F.V. thanks the ICREA Academia Award 2023 with Ref. Ac2216561.

AUTHOR INFORMATION

Corresponding Author

Francesc Illas - *Departament de Ciència de Materials i Química Física & Institut de Química Teòrica i Computacional (IQTCUB), Universitat de Barcelona, c/ Martí i Franquès 1-11, 08028 Barcelona, Spain.*

Authors

Ling Meng - *Departament de Ciència de Materials i Química Física & Institut de Química Teòrica i Computacional (IQTCUB), Universitat de Barcelona, c/ Martí i Franquès 1-11, 08028 Barcelona, Spain.*

Francesc Viñes - *Departament de Ciència de Materials i Química Física & Institut de Química Teòrica i Computacional (IQTCUB), Universitat de Barcelona, c/ Martí i Franquès 1-11, 08028 Barcelona, Spain.*

ASSOCIATED CONTENT

Supporting Information

The supporting information is available free of charge at DOI:

Stability-related energies and Bader charge of different moieties; N_2 adsorption models, energies and bond lengths, Bader charge changes between after N_2 adsorption; limiting potential (U_L) and steps for the studied models; charge density difference (CDD) plots of inspected models; geometric structures of N_2 adsorption; total and partial density of states of inspected models.

COMPETING INTERESTS

There are no conflicts of interest to declare.

Figure 1. Top (upper images) and side (lower images) views of the ten models derived from the employed $p(3\times3)$ MXene supercells, including; (a) pristine Ti_3C_2 (0001) with the top (T), bridge (B), hollow carbon (H_C), and hollow metal (H_M) four high-symmetry sites tagged; (b) Ti_3C_2O (0001) with T, H_C, and O-bridge (B_O) three high-symmetry sites tagged; (c) **s**B@$Ti_3C_2O_{8/9}$ (**s**B-O); (d) **s**B@$Ti_3C_2OH_{8/9}$ (**s**B-OH); (e) **a**B@Ti_3C_2O with B on H_C (**a**B-O); (f) **a**B@$Ti_3C_2O_{4/9}OH_{5/9}$ with B on H_C (**a**B-H_C-O_4); (g) **a**B@$Ti_3C_2O_{4/9}OH_{5/9}$ with B on B_O (**a**B-B_O-O_4); (h) **a**B@$Ti_3C_2O_{1/3}OH_{2/3}$ with B on H_C (**a**B-H_C-O_3); (i) **a**B@$Ti_3C_2O_{1/3}OH_{2/3}$ with B on B_O (**a**B-B_O-O_3); (j) **a**B@$Ti_3C_2O_{2/9}OH_{7/9}$ (**a**B-O_2); (k) **a**2B@Ti_3C_2O (**a**2B-O), and (l) **a**2B@$Ti_3C_2O_{4/9}OH_{5/9}$ (**a**2B-O_4). H and O atoms in the termination groups are represented by light pink and red spheres, respectively, while the B atoms are represented by white spheres. Ti and C atoms are shown as blue and brown spheres, with different levels of shading depending on their stacking position, with darker versions being closer to the shown surface.

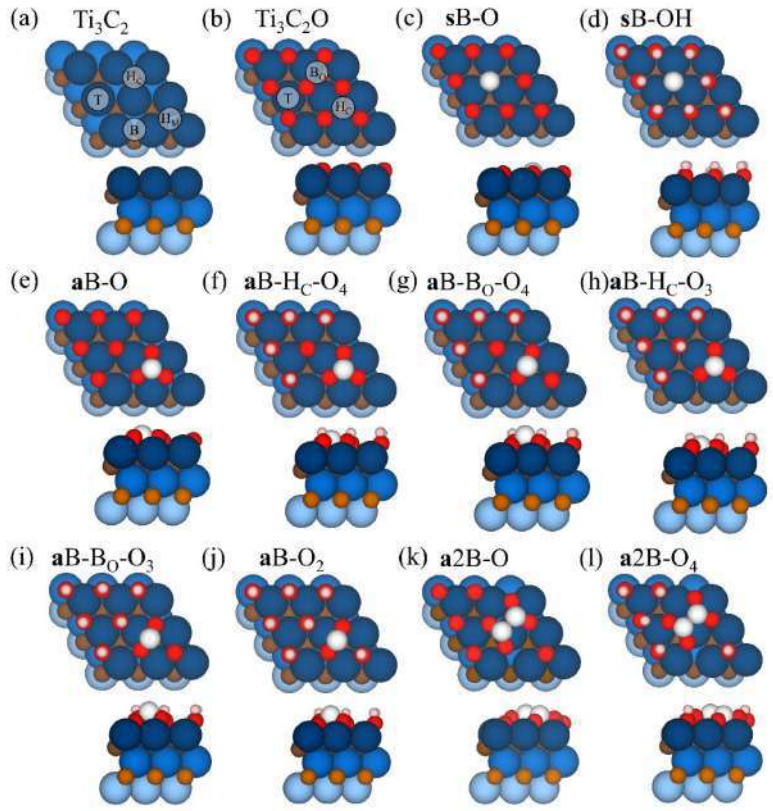

21

Figure 2. Various adsorption configurations for N_2 adsorption, including chemisorption and physisorption for (a) single boron and (b) B_2 dimer models shown in Figure 1.

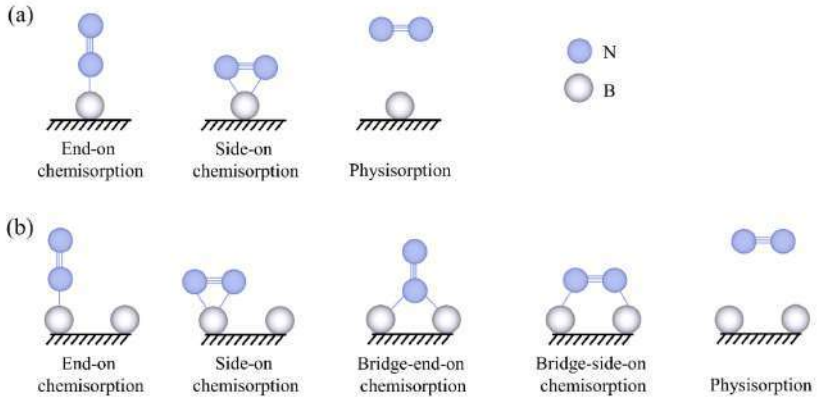

Figure 3. Calculated adsorption, r_{ads}, and desorption, r_{des}, N_2 rates on studied models shown in Fig. S5 of the SI, as a function of temperature, T, and the gas partial pressure, p, here shown for 1 bar. Black dashes line represents r_{ads} for *end-on* (*e*) and *side-on* (*s*), as well as *bridge-end-on* (*b-e*) and *bridge-side-on* (*b-s*) chemisorption, and red dashed line represents r_{ads} for physisorption.

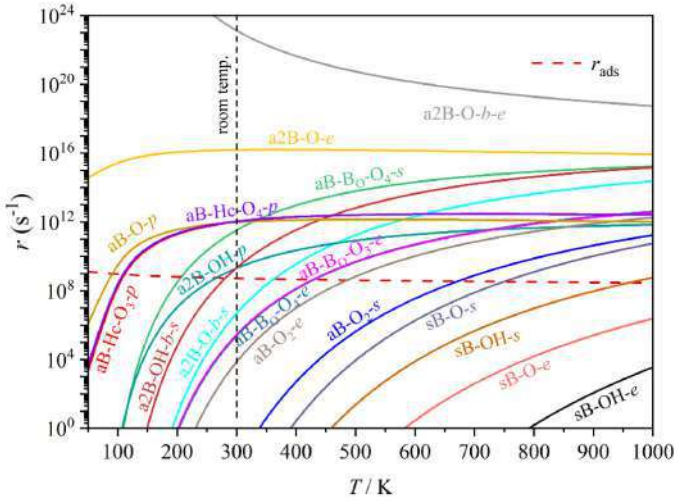

Figure 4. Schematic diagram of possible reaction pathways for NRR on B-based Ti_3C_2 MXene. The black, grey, and blue solid arrows represent the *distal*, *alternating*, and *enzymatic* pathways, respectively. The black dashed arrows represent the *mixed* pathway.

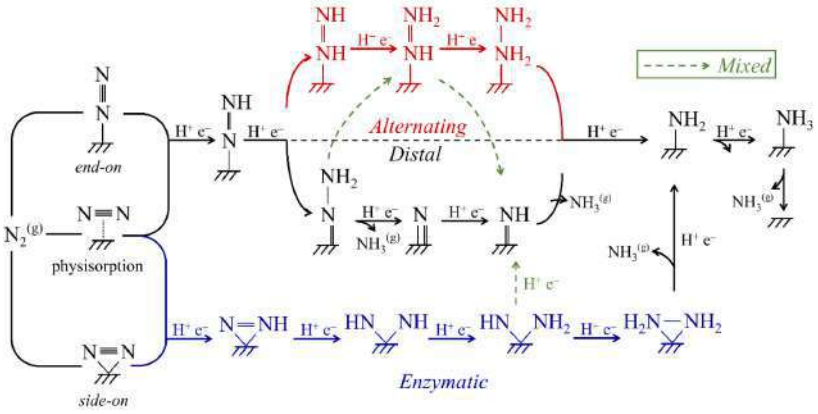

Figure 5. Gibbs free energy, ΔG, diagrams of NRR on (a) **s**B-O (top), and (b) **s**B-OH (bottom), under standard working conditions of $T = 300$ K, partial gases pressures of 1 bar, $pH = 0$, and $U = 0$ V. Solid lines represent chemical steps such as $N_2^{(g)}$ adsorption or as-generated $NH_3^{(g)}$ desorption, while dashed lines represent CPET steps. The –H* notation implies the H transfer from surface –OH group. Below the reaction paths, side views of the atomic models for the different reaction steps are shown. N and B atoms are shown in light blue and white colour respectively, the H atoms of –OH group and the proton of CPET are represented by light pink and dark pink respectively, while the rest of the colour coding is as in Figure 1. Black numbers and symbols indicate the optimal path, while gray ones indicate non-optimal.

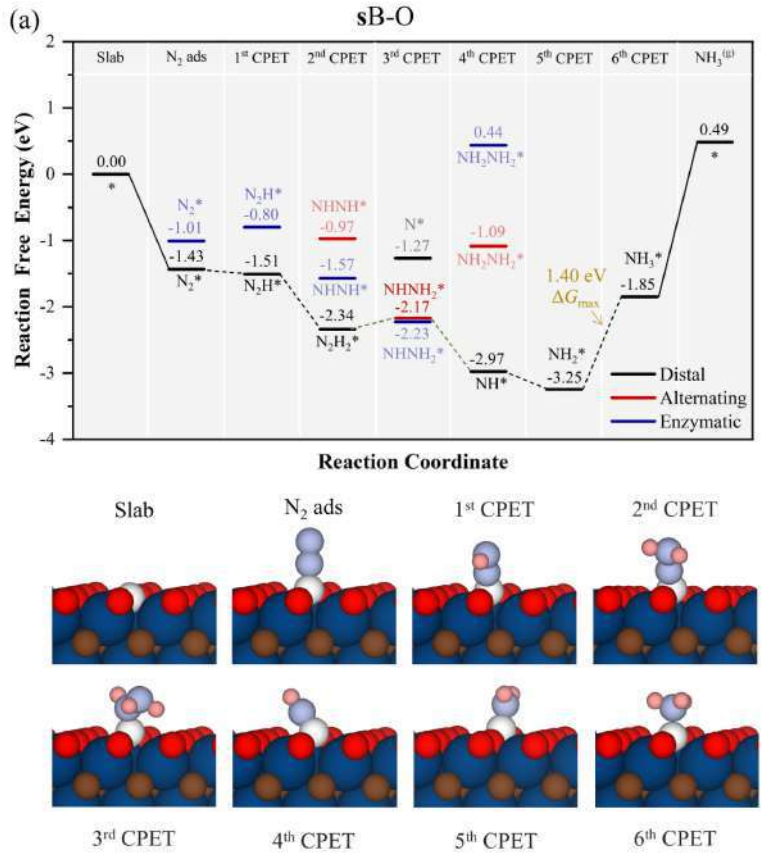

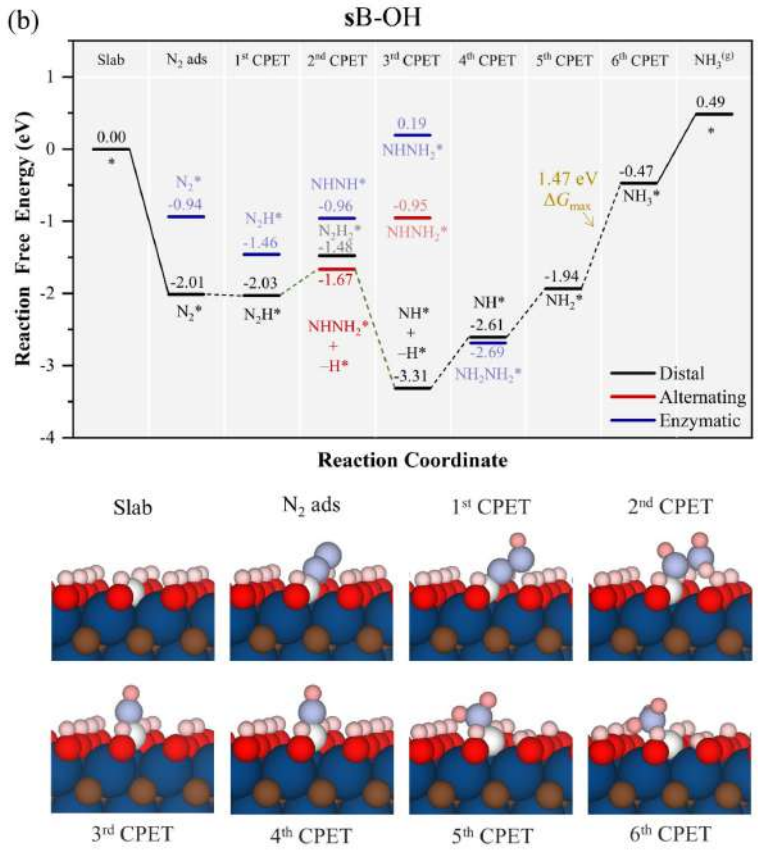
(b)
sB-OH
Slab
N2 ads
1st CPET
2nd CPET
3rd CPET
4th CPET
5th CPET
6th CPET
NH3(g)
Reaction Free Energy (eV)
Reaction Coordinate
0.00
*
N2*
-0.94
-2.01
N2*
N2H*
-1.46
-2.03
N2H*
NHNH*
-0.96
N2H2*
-1.48
-1.67
NHNH2*
+
–H*
0.19
NHNH2*
-0.95
NHNH2*
NH*
+
–H*
-3.31
NH*
-2.61
-2.69
NH2NH2*
1.47 eV
ΔGmax
-1.94
NH2*
-0.47
NH3*
0.49
*
Distal
Alternating
Enzymatic
Slab
N2 ads
1st CPET
2nd CPET
3rd CPET
4th CPET
5th CPET
6th CPET

Figure 6. Gibbs free energy, ΔG, diagrams of NRR on **a**B-O under standard working conditions of $T = 300$ K, partial gases pressures of 1 bar, $pH = 0$, and $U = 0$ V. Solid lines represent chemical steps such as $N_2^{(g)}$ adsorption or as-generated $NH_3^{(g)}$ desorption, while dashed lines represent CPET steps. Below the reaction paths, side views of the atomic models for the different reaction steps are shown, colour-coded as in Figure 5.

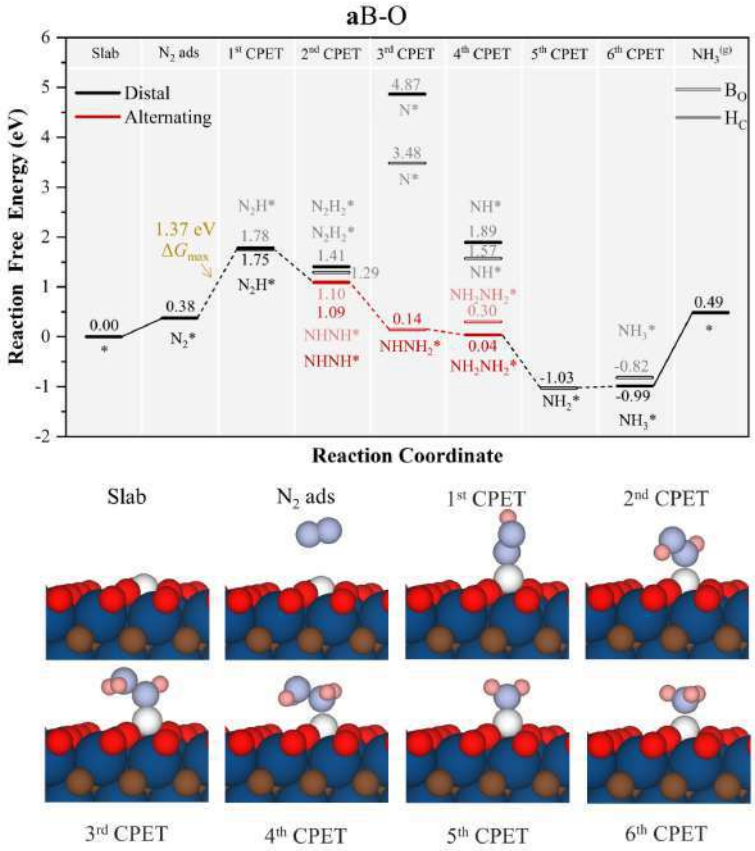

Figure 7. Gibbs free energy, ΔG, diagrams of NRR on **a**B-O_4 under standard working conditions of $T = 300$ K, partial gases pressures of 1 bar, $pH = 0$, and $U = 0$ V. Solid lines represent chemical steps such as $N_2^{(g)}$ adsorption or as-generated $NH_3^{(g)}$ desorption, while dashed lines represent CPET steps. Below the reaction paths, side views of the atomic models for the different reaction steps are shown, colour-coded as in Figure 5.

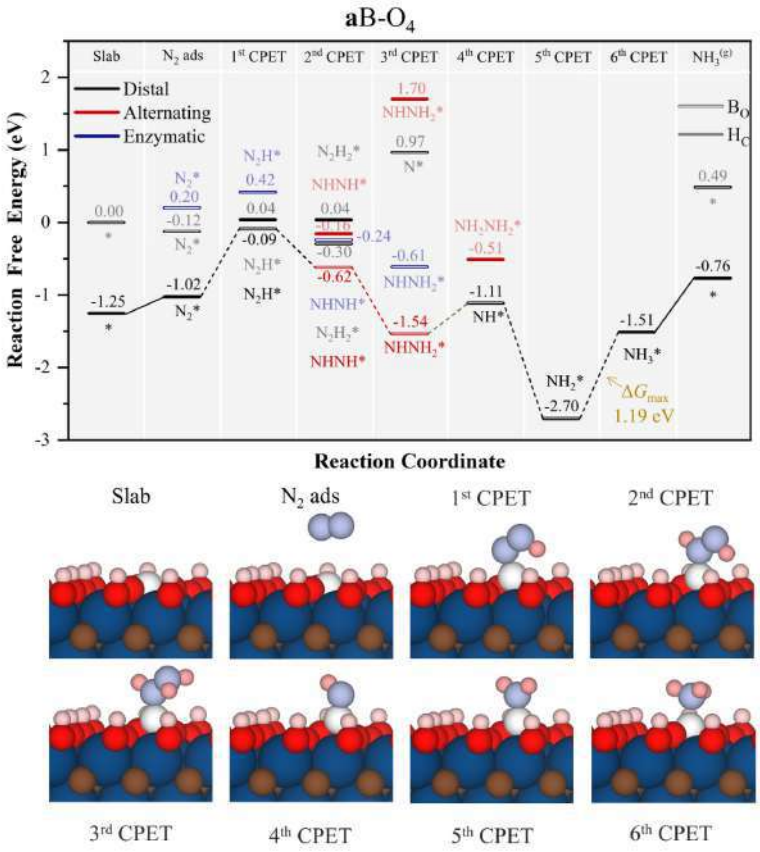

Figure 8. Gibbs free energy, ΔG, diagrams of NRR on **a**B-O_3 under standard working conditions of $T = 300$ K, partial gases pressures of 1 bar, $pH = 0$, and $U = 0$ V. Solid lines represent chemical steps such as $N_2^{(g)}$ adsorption or as-generated $NH_3^{(g)}$ desorption, while dashed lines represent CPET steps. Below the reaction paths, side views of the atomic models for the different reaction steps are shown, colour-coded as in Figure 5. Notation as in Figure 5.

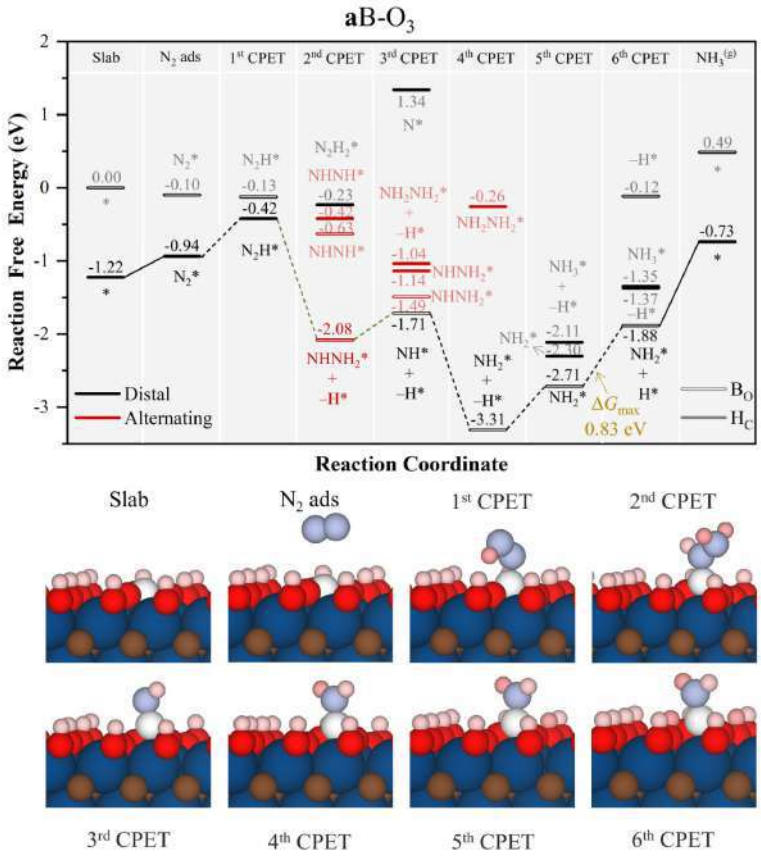

Figure 9. Gibbs free energy, ΔG, diagrams of NRR on **a**B-O_2 under standard working conditions of $T = 300$ K, partial gases pressures of 1 bar, $pH = 0$, and $U = 0$ V. Solid lines represent chemical steps such as $N_2^{(g)}$ adsorption or as-generated $NH_3^{(g)}$ desorption, while dashed lines represent CPET steps. Below the reaction paths, side views of the atomic models for the different reaction steps are shown, colour-coded as in Figure 5. Notation as in Figure 5.

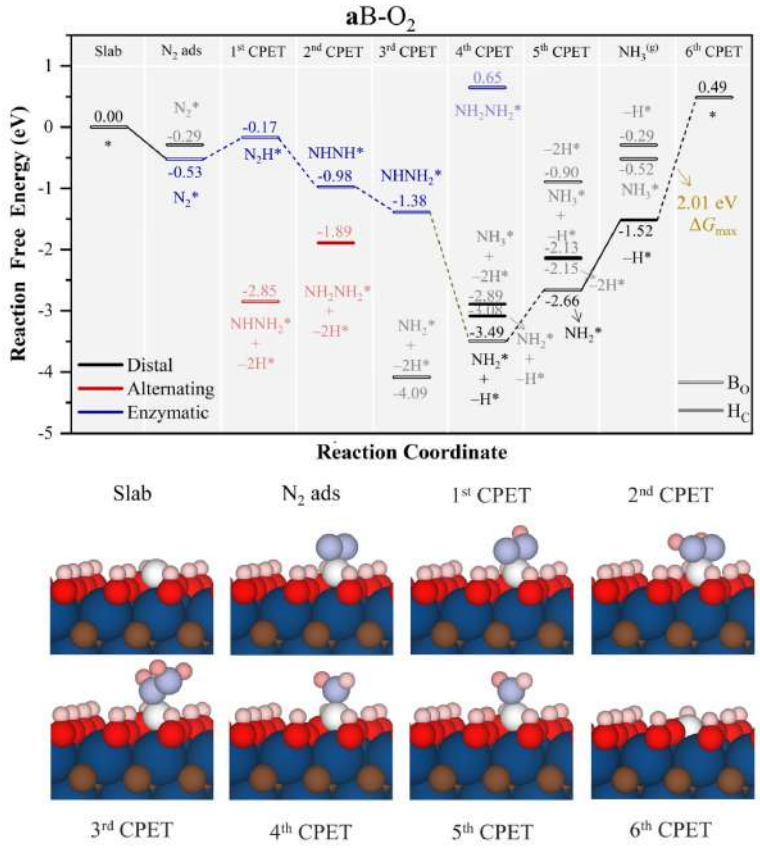

Figure 10. Gibbs free energy, ΔG, diagrams of NRR on (a) **a**2B-O (top), and (b) **a**2B-OH (bottom), under standard working conditions of $T = 300$ K, partial gases pressures of 1 bar, $pH = 0$, and $U = 0$ V. Solid lines represent chemical steps such as $N_2^{(g)}$ adsorption or as-generated $NH_3^{(g)}$ desorption, while dashed lines represent CPET steps. T_N represents adsorption on top of a nitrogen atom and T_B represents adsorption on a bridge between two nitrogen atoms. Below the reaction paths, side views of the atomic models for the different reaction steps are shown. Colour coding is as in Figure 5.

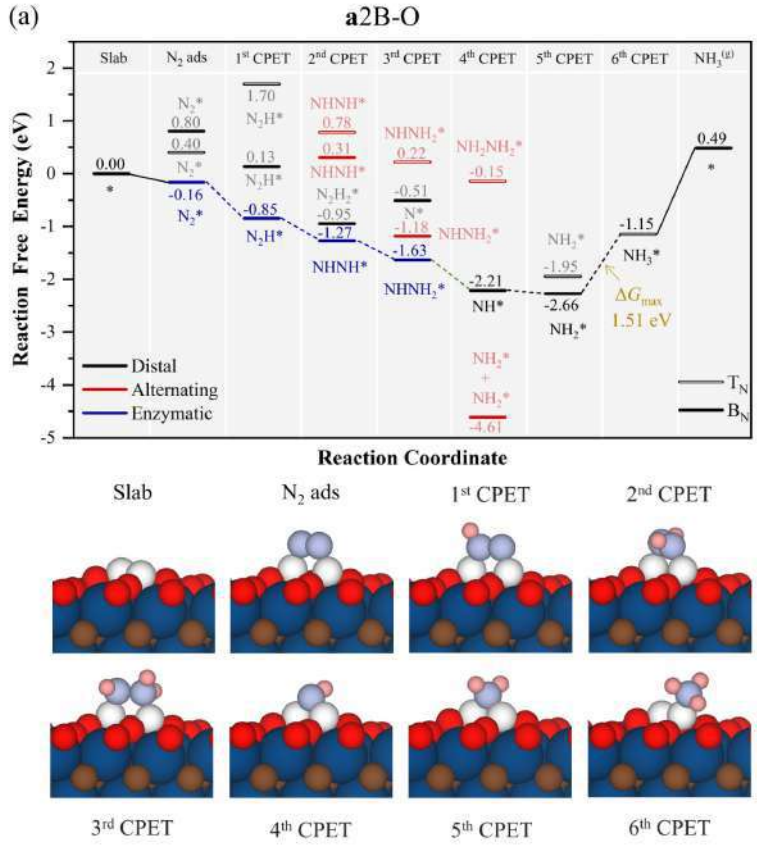

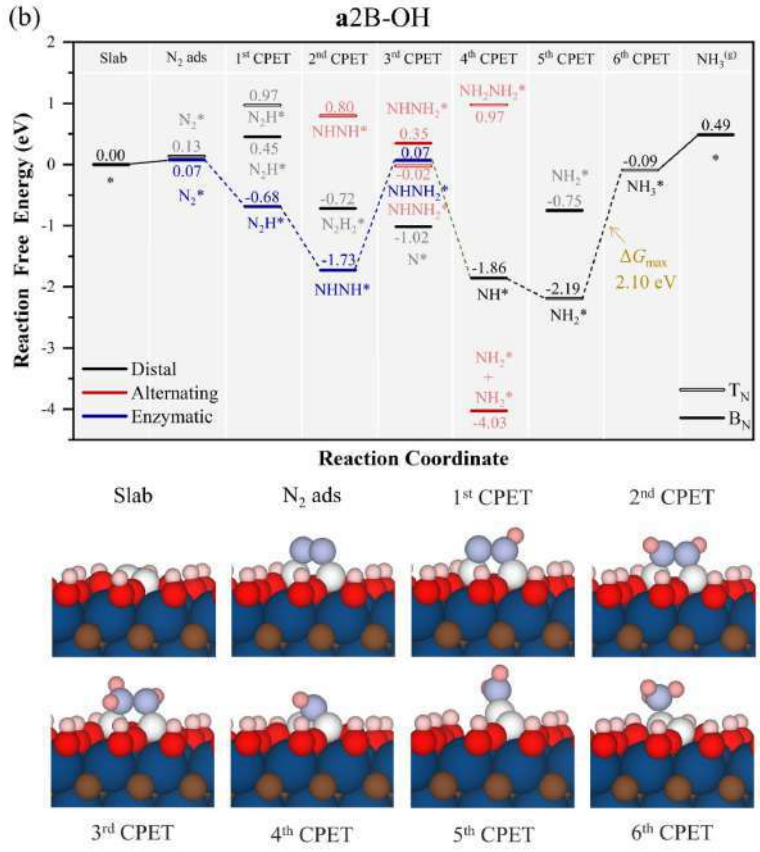
(b)
a2B-OH
Slab
N2 ads
1st CPET
2nd CPET
3rd CPET
4th CPET
5th CPET
6th CPET
NH3(g)
Reaction Free Energy (eV)
Reaction Coordinate
Distal
Alternating
Enzymatic
0.00
0.13
0.07
-0.68
-1.73
0.97
0.45
0.80
-0.72
0.35
0.07
-0.02
-1.02
0.97
-1.86
-2.19
-0.75
-0.09
0.49
ΔGmax
2.10 eV
-4.03
TN
BN
Slab
N2 ads
1st CPET
2nd CPET
3rd CPET
4th CPET
5th CPET
6th CPET

Figure 11. (a) Comparison of U_L(NRR) of the different models with respect to Ru (0001) reference, (b) free energy change for HER on the studied catalysts, and (c) U_L(NRR) *vs.* U_L(HER).

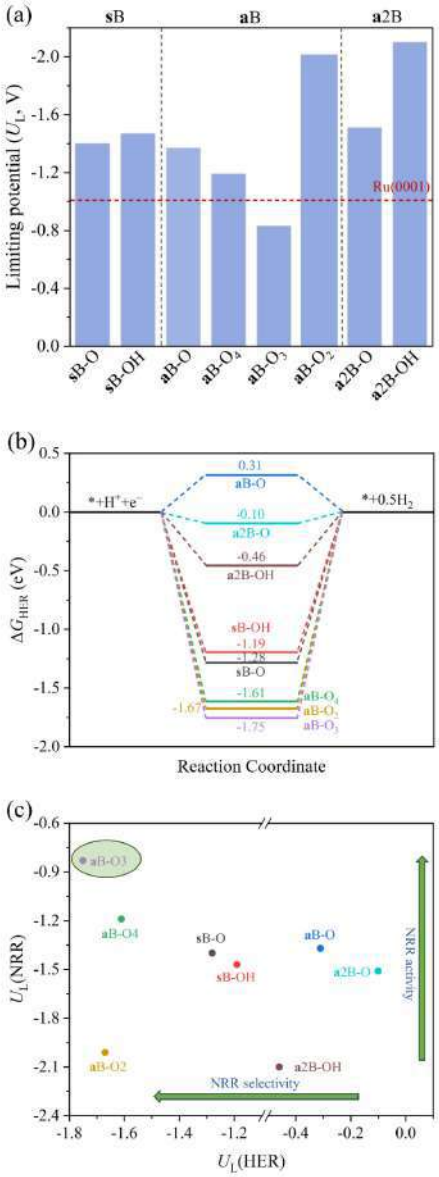

33

References

(1) Erisman, J. W.; Sutton, M. A.; Galloway, J.; Klimont, Z.; Winiwarter, W. How a Century of Ammonia Synthesis Changed the World. *Nat. Geosci.* **2008,** *1*, 636–639.

(2) Chirik, P. J. One Electron at a Time. *Nat. Chem.* **2009,** *1*, 520–522.

(3) Suryanto, B. H. R.; Du, H.-L.; Wang, D.; Chen, J.; Simonov, A. N.; MacFarlane, D. R. Challenges and Prospects in the Catalysis of Electroreduction of Nitrogen to Ammonia. *Nat. Catal.* **2019,** *2*, 290–296

(4) Soloveichik, G. Electrochemical Synthesis of Ammonia as a Potential Alternative to the Haber-Bosch Process. *Nat. Catal.* **2019,** *2*, 377–380.

(5) Machaj, K.; Kupecki, J.; Malecha, Z.; Morawski, A. W.; Skrzypkiewicz, M.; Stanclik, M.; Chorowski, M. Ammonia as a Potential Marine Fuel: A Review. *Energy Strat. Rev.* **2022,** *44*, 100926.

(6) Hasan, M. H.; Mahlia, T. M.; Mofijur, M.; Rizwanul Fattah, I. M.; Handayani, F.; Ong, H. C.; Silitonga, A. S. A Comprehensive Review on the Recent Development of Ammonia as a Renewable Energy Carrier. *Energies* **2021**, *14*, 3732.

(7) Cleveland, C. C.; Townsend, A. R.; Schimel, D. S.; Fisher, H.; Howarth, R. W.; Hedin, L. O.; Perakis, S. S.; Latty, E. F.; Von Fischer, J. C.; Elseroad, A.; Wasson, M. F. Global Patterns of Terrestrial Biological Nitrogen (N_2) Fixation in Natural Ecosystems. *Global Biogeochem. Cycles* **1999,** *13*, 623–645.

(8) Gouveia, J. D.; Morales-García, Á.; Viñes, F.; Gomes, J. R. B.; Illas, F. Facile Heterogeneously Catalyzed Nitrogen Fixation by MXenes. *ACS Catal.* **2020,** *10*, 5049–5056.

(9) Qiu, W.; Xie, X.-Y.; Qiu, J.; Fang, W.-H.; Liang, R.; Ren, X.; Ji, X.; Cui, G.; Asiri, A. M.; Cui, G.; Tang, B.; Sun, X. High-Performance Artificial Nitrogen Fixation at Ambient Conditions Using a Metal-Free Electrocatalyst. *Nat. Commun.* **2018,** *9*, 3485.

(10) Kaiprathu, A.; Velayudham, P.; Teller, H.; Schechter, A. Mechanisms of Electrochemical Nitrogen Gas Reduction to Ammonia Under Ambient Conditions: A Focused Review. *J. Solid State Electrochem.* **2022,** *26*, 1897–1917.

(11) He, H.; Wen, H.-M.; Li, H.-K.; Zhang, H.-W. Recent Advances in Metal-Organic Frameworks and their Derivatives for Electrocatalytic Nitrogen Reduction to Ammonia. *Coord. Chem. Rev.* **2022,** *471*, 214761.

(12) Nocera, D. G. Proton-Coupled Electron Transfer: The Engine of Energy Conversion and Storage. *J. Am. Chem. Soc.* **2022,** *144*, 1069–1081.

(13) Adams, S.; Acheampong, A. O., Reducing Carbon Emissions: The Role of Renewable Energy and Democracy. *J. Clean. Prod.* **2019,** *240*, 118245.

(14) Cui, Y.; Sun, C.; Qu, Y.; Dai, T.; Zhou, H.; Wang, Z.; Jiang, Q. The Development of Catalysts for Electrochemical Nitrogen Reduction toward Ammonia: Theoretical and Experimental Advances. *Chem. Comm.* **2022,** *58*, 10290–10302.

(15) Naguib, M.; Kurtoglu, M.; Presser, V.; Lu, J.; Niu, J. J.; Heon, M.; Hultman, L.; Gogotsi, Y.; Barsoum, M. W. Two-Dimensional Nanocrystals Produced by Exfoliation of Ti_3AlC_2. *Adv. Mater.* **2011**, *23*, 4248–4253.

(16) Gogotsi, Y.; Anasori, B. The Rise of MXenes. *ACS Nano* **2019**, *13*, 8491–8494.

(17) Anasori, B.; Gogotsi, Y. MXenes: Trends, Growth, and Future Directions. *Graphene 2D Mater.* **2022**, *7*, 75−79.

(18) Gogotsi, Y. The Future of MXenes. *Chem. Mater.* **2023**, *35*, 8767−8770.

(19) VahidMohammadi, A.; Rosen, J.; Gogotsi, Y. The World of Two-Dimensional Carbides and Nitrides (MXenes). *Science* **2021,** *372*, eabf1581.

(20) Gouveia, J. D.; Morales-García, Á.; Viñes, F.; Gomes, J. R. B.; Illas, F. MXenes *à la Carte*: Tailoring the Epitaxial Growth Alternating Nitrogen and Transition Metal Layers. *ACS Nano* **2022,** *16*, 12541−12552.

(21) Meng, L.; Yan, L.-K.; Viñes, F.; Illas, F. Effect of Terminations on the Hydrogen Evolution Reaction Mechanism on Ti_3C_2 MXene. *J. Mater. Chem. A* **2023,** *11*, 6886−6900.

(22) Ibragimova, R.; Puska, M. J.; Komsa, H.-P. pH-Dependent Distribution of Functional Groups on Titanium-Based MXenes. *ACS Nano* **2019,** *13*, 9171−9181.

(23) Zhang, X.; Wang, S.; Yan, L.; Su, Z. Mo_3C_2: Active Electrocatalysts for Spontaneous Nitrogen Reduction Reaction. *J. Phys. Chem. C* **2023**, *127*, 22530−22536.

(24) Johnson, L. R.; Sridhar, S.; Zhang, L.; Fredrickson, K. D.; Raman, A. S.; Jang, J.; Leach, C.; Padmanabhan, A.; Price, C. C.; Frey, N. C.; Raizada, A.; Rajaraman, V.; Saiprasad, S. A.; Tang, X.; Vojvodic, A. MXene Materials for the Electrochemical Nitrogen Reduction —Functionalized or Not? *ACS Catal.* **2020,** *10*, 253−264

(25) Gouveia, J. D.; Viñes, F.; Illas, F.; Gomes, J. R. B. MXenes Atomic Layer Stacking Phase Transitions and their Chemical Activity Consequences. *Phys. Rev. Mater.* **2020,** *4*, 054003.

(26) Azofra, L. M.; Li, N.; MacFarlane, D. R.; Sun, C. Promising Prospects for 2D d^2–d^4 M_3C_2 Transition Metal Carbides (MXenes) in N_2 Capture and Conversion into Ammonia. *Energy Environ. Sci.* **2016,** *9*, 2545−2549.

(27) Wang, Y.; Xu, Y.; Hu, M.; Ling, H.; Zhu, X. MXenes: Focus on Optical and Electronic Properties and Corresponding Applications. *Nanophotonics* **2020,** *9*, 1601−1620.

(28) Caffrey, N. M. Effect of Mixed Surface Terminations on the Structural and Electrochemical Properties of Two-Dimensional $Ti_3C_2T_2$ and V_2CT_2 MXenes Multilayers. *Nanoscale* **2018,** *10*, 13520−13530.

(29) Meng, L.; Tayyebi, E.; Exner, K. S.; Viñes, F.; Illas, F. MXenes as Electrocatalysts for the CO_2 Reduction Reaction: Recent Advances and Future Challenges. *ChemElectroChem* **2024,** DOI: 10.1002/celc.202300598.

(30) Biswas, S.; Alegaonkar, P. S. MXene: Evolutions in Chemical Synthesis and Recent Advances in Applications. *Surfaces* **2022,** *5*, 1−34.

(31) Wyatt, B. C.; Rosenkranz, A.; Anasori, B. 2D MXenes: Tunable Mechanical and Tribological Properties. *Adv. Mater.* **2021**, *33*, 2007973

(32) Abdolhosseinzadeh, S.; Jiang, X.; Zhang, H.; Qiu, J.; Zhang, C. Perspectives on Solution Processing of Two-Dimensional MXenes. *Mater. Today* **2021,** *48*, 214−240

(33) Pang, S.-Y.; Wong, Y.-T.; Yuan, S.; Liu, Y.; Tsang, M.-K.; Yang, Z.; Huang, H.; Wong, W.-T.; Hao, J. Universal Strategy for HF-Free Facile and Rapid Synthesis of Two-dimensional MXenes as Multifunctional Energy Materials. *J. Am. Chem. Soc.* **2019**, *141*, 9610−9616.

(34) Meshkian, R.; Lind, H.; Halim, J.; El Ghazaly, A.; Thörnberg, J.; Tao, Q.; Dahlqvist, M.; Palisaitis, J.; Persson, P. O. Å.; Rosen, J. Theoretical Analysis, Synthesis, and Characterization of 2D $W_{1.33}C$ (MXene) with Ordered Vacancies. *ACS Appl. Nano Mater.* **2019**, *2*, 6209−6219.

(35) Kamysbayev, V.; Filatov, A. S.; Hu, H.; Rui, X.; Lagunas, F.; Wang, D.; Klie, R. F.; Talapin, D. V. Covalent Surface Modifications and Superconductivity of Two-Dimensional Metal Carbide MXenes. *Science* **2020,** *369*, 979−983.

(36) Zhou, H.; Chen, Z.; Kountoupi, E.; Tsoukalou, A.; Abdala, P. M.; Florian, P.; Fedorov, A.; Müller, C. R. Two-Dimensional Molybdenum Carbide 2D-Mo_2C as a Superior Catalyst for CO_2 Hydrogenation. *Nat. Commun.* **2021,** *12*, 5510.

(37) Xia, J.; Yang, S.-Z.; Wang, B.; Wu, P.; Popovs, I.; Li, H.; Irle, S.; Dai, S.; Zhu, H. Boosting Electrosynthesis of Ammonia on Surface-Engineered MXene Ti_3C_2. *Nano Energy* **2020,** *72*, 104681.

(38) Ding, Y.; Zhang, J.; Guan, A.; Wang, Q.; Li, S.; Al-Enizi, A. M.; Qian, L.; Zhang, L.; Zheng, G. Promoting N_2 Electroreduction to Ammonia by Fluorine-Terminating $Ti_3C_2T_x$ MXene. *Nano Converg.* **2021,** *8*, 14.

(39) Xie, Y.; Naguib, M.; Mochalin, V. N.; Barsoum, M. W.; Gogotsi, Y.; Yu, X.; Nam, K.-W.; Yang, X.-Q.; Kolesnikov, A. I.; Kent, P. R. C. Role of Surface Structure on Li-Ion Energy Storage Capacity of Two-Dimensional Transition-Metal Carbides. *J. Am. Chem. Soc.* **2014,** *136*, 6385−6394.

(40) Karlsson, L. H.; Birch, J.; Halim, J.; Barsoum, M. W.; Persson, P. O. Å. Atomically Resolved Structural and Chemical Investigation of Single MXene Sheets. *Nano Lett.* **2015,** *15*, 4955−4960.

(41) Légaré, M.-A.; Bélanger-Chabot, G.; Dewhurst, R. D.; Welz, E.; Krummenacher, I.; Engels, B.; Braunschweig, H. Nitrogen Fixation and Reduction at Boron. *Science* **2018,** *359*, 896−900.

(42) Ma, F.; Jiao, Y.; Gao, G.; Gu, Y.; Bilic, A.; Chen, Z.; Du, A. Graphene-like Two-Dimensional Ionic Boron with Double Dirac Cones at Ambient Condition. *Nano Lett.* **2016,** *16*, 3022−3028.

(43) Yu, X.; Han, P.; Wei, Z.; Huang, L.; Gu, Z.; Peng, S.; Ma, J.; Zheng, G., Boron-Doped Graphene for Electrocatalytic N_2 Reduction. *Joule* **2018,** *2*, 1610−1622.

(44) Ling, C.; Niu, X.; Li, Q.; Du, A.; Wang, J. Metal-Free Single Atom Catalyst for N_2 Fixation Driven by Visible Light. *J. Am. Chem. Soc.* **2018,** *140*, 14161−14168.

(45) Liu, C.; Li, Q.; Zhang, J.; Jin, Y.; MacFarlane, D. R.; Sun, C. Theoretical Evaluation of Possible 2D Boron Monolayer in N_2 Electrochemical Conversion into Ammonia. *J. Phys. Chem. C.* **2018,** *122*, 25268−25273.

(46) Zhang, N.; Wang, M.-y.; Liu, J.-Y. Prediction of Single-Boron Anchored on MXene Catalysts for High-Efficient Electrocatalytic Nitrogen Reduction Reaction. *Mol. Catal.* **2022,** *531*, 112658.

(47) Wang, Y.; Qian, X.; Zheng, G.; Tian, Z.; Zhang, Q. Boron-Doped MXenes as Electrocatalysts for Nitrogen Reduction Reaction: A Theoretical Study. *Front. Chem. Eng.* **2021,** *3*, 702129.

(48) Zheng, S.; Li, S.; Mei, Z.; Hu, Z.; Chu, M.; Liu, J.; Chen, X.; Pan, F. Electrochemical Nitrogen Reduction Reaction Performance of Single-Boron Catalysts Tuned by MXene Substrates. *J. Phys. Chem. Lett.* **2019,** *10*, 6984−6989.

(49) Kresse, G.; Furthmüller, J. Efficient Iterative Schemes for Ab Initio Total-Energy Calculations Using a Plane-Wave Basis Set. *Phys. Rev. B.* **1996**, *54*, 11169−11186.

(50) Perdew, J. P.; Burke, K.; Ernzerhof, M. Generalized Gradient Approximation Made Simple. *Phys. Rev. Lett.* **1996**, *77*, 3865−3868.

(51) Parey, V.; Abraham, B. M.; Mir, S. H.; Singh, J. K., High-Throughput Screening of Atomic Defects in MXenes for CO_2 Capture, Activation, and Dissociation. *ACS Appl. Mater. Interfaces* **2021,** *13*, 35585−35594.

(52) Gao, G.; O'Mullane, A. P.; Du, A., 2D MXenes: A New Family of Promising Catalysts for the Hydrogen Evolution Reaction. *ACS Catal.* **2017,** *7*, 494−500.

(53) Ontiveros, D.; Viñes, F.; Sousa, F. Bandgap Engineering of MXene Compounds for Water Splitting. *J. Mater. Chem. A* **2023**, *11*, 13754–13764.

(54) Grimme, S.; Antony, J.; Ehrlich, S.; Krieg, H. A Consistent and Accurate *Ab Initio* Parametrization of Density Functional Dispersion Correction (DFT-D) for the 94 Elements H-Pu. *J. Chem. Phys.* **2010**, *132*, 154104

(55) Morales-Salvador, R.; Gouveia, J. D.; Morales-Garcia, Á.; Viñes, F.; Gomes, J. R. B.; Illas, F. Carbon Capture and Usage by MXenes. *ACS Catal.* **2021**, *11*, 11248–11255.

(56) Blöchl, P. E. Projector Augmented-Wave Method. *Phys. Rev. B* **1994**, *50*, 17953–17979.

(57) Kresse, G.; Joubert, D. From Ultrasoft Pseudopotentials to the Projector Augmented-Wave Method. *Phys. Rev. B.* **1999**, *59*, 1758–1775.

(58) Monkhorst, H. J.; Pack, J. D. Special Points for Brillouin-Zone Integrations. *Phys. Rev. B.*, **1976**, *13*, 5188–5192.

(59) López, M.; Morales-Garcia, Á.; Viñes, F.; Illas, F. Thermodynamics and Kinetics of Molecular Hydrogen Adsorption and Dissociation on MXenes: Relevance to Heterogeneously Catalyzed Hydrogenation Reactions. *ACS Catal.* **2021**, *11*, 12850–12857.

(60) Gouveia, J. D.; Morales-García, Á.; Viñes, F.; Illas, F.; Gomes, J. R. B. MXenes as Promising Catalysts for Water Dissociation. *Appl. Catal. B: Environ* **2020**, *260*, 118191.

(61) Nitopi, S.; Bertheussen, E.; Scott, S. B.; Liu, X.; Engstfeld, A. K.; Horch, S.; Seger, B.; Stephens, I. E. L.; Chan, K.; Hahn, C.; Nørskov, J. K.; Jaramillo, T. F.; Chorkendorff, I. Progress and Perspectives of Electrochemical CO_2 Reduction on Copper in Aqueous Electrolyte. *Chem. Rev.* **2019**, *119*, 7610–7672.

(62) Chun, H. J.; Apaja, V.; Clayborne, A.; Honkala, K.; Greeley, J. Atomistic Insights into Nitrogen-Cycle Electrochemistry: A Combined DFT and Kinetic Monte Carlo Analysis of NO Electrochemical Reduction on Pt(100). *ACS Catal.* **2017**, *7*, 3869−3882.

(63) Katsounaros, I.; Figueiredo, M. C.; Chen, X.; Calle-Vallejo, F.; Koper, M. T. M., Structure- and Coverage-Sensitive Mechanism of NO Reduction on Platinum Electrodes. *ACS Catal.* **2017,** *7*, 4660−4667.

(64) Zijlstra, B.; Zhang, X.; Liu, J.-X.; Filot, I. A. W.; Zhou, Z.; Sun, S.; Hensen, E. J. M., First-Principles Microkinetics Simulations of Electrochemical Reduction of CO_2 over Cu catalysts. *Electrochim. Acta* **2020,** *335*, 135665.

(65) Ye, K.; Hu, M.; Li, Q.-K.; Luo, Y.; Jiang, J.; Zhang, G., Cooperative Single-Atom Active Centers for Attenuating the Linear Scaling Effect in the Nitrogen Reduction Reaction. *J. Phys. Chem. Lett.* **2021,** *12*, 5233−5240.

(66) Kim, S.; Ruiz-Puigdollers, A.; Gamallo, P.; Viñes, F.; Lee, J. Y., Functionalization of γ-Graphyne by Transition Metal Adatoms. *Carbon* **2017,** *120*, 63−70.

(67) Oschinski, H.; Morales-García, Á.; Illas, F., Interaction of First Row Transition Metals with M_2C (M = Ti, Zr, Hf, V, Nb, Ta, Cr, Mo, and W) MXenes: A Quest for Single-Atom Catalysts. *J. Phys. Chem. C* **2021,** *125*, 2477−2484.

(68) Kim, S.; Gamallo, P.; Viñes, F.; Lee, J. Y.; Illas, F., Substrate-Mediated Single-Atom Isolation: Dispersion of Ni and La on γ-Graphyne. *Theor. Chem. Acc.* **2017,** *136*, 80.

(69) Kittel, C., Introduction to Solid State Physics. 8th ed., John Wiley & Sons Inc., New York, NY, USA, **2005**, 59.

(70) Nørskov, J. K.; Rossmeisl, J.; Logadottir, A.; Lindqvist, L.; Kitchin, J. R.; Bligaard, T.; Jónsson, H., Origin of the Overpotential for Oxygen Reduction at a Fuel-Cell Cathode. *J. Phys. Chem. B* **2004**, *108*, 17886−17892.

(71) Li, N.; Chen, X.; Ong, W.-J.; MacFarlane, D. R.; Zhao, X.; Cheetham, A. K.; Sun, C., Understanding of Electrochemical Mechanisms for CO_2 Capture and Conversion into Hydrocarbon Fuels in Transition-Metal Carbides (MXenes). *ACS Nano* **2017,** *11*, 10825−10833.

(72) Guo, Z.; Li, Y.; Sa, B.; Fang, Y.; Lin, J.; Huang, Y.; Tang, C.; Zhou, J.; Miao, N.; Sun, Z., M_2C-Type MXenes: Promising Catalysts for CO_2 Capture and Reduction. *Appl. Surf. Sci.* **2020,** *521*, 146436.

(73) Meng, L.; Yan, L.-K.; Viñes, F.; Illas, F., Surface Termination Dependent Carbon Dioxide Reduction Reaction on Ti_3C_2 MXene. *J. Mater. Chem. A* **2024**, *12*, 7856−7874.

(74) Exner, K. S.; Over, H., Kinetics of Electrocatalytic Reactions from First-Principles: A Critical Comparison with the *Ab Initio* Thermodynamics Approach. *Acc. Chem. Res.* **2017,** *50*, 1240−1247.

(75) López, M.; Exner, K. S.; Viñes, F.; Illas, F., Theoretical Study of the Mechanism of the Hydrogen Evolution Reaction on the V_2C MXene: Thermodynamic and Kinetic Aspects. *J. Catal.* **2023,** *421*, 252−263.

(76) Kulkarni, A.; Siahrostami, S.; Patel, A.; Nørskov, J. K. Understanding Catalytic Activity Trends in the Oxygen Reduction Reaction. *Chem. Rev.* **2018**, *118*, 2302–2312.

(77) Li, Q.; Ouyang, Y.; Lu, S.; Bai, X.; Zhang, Y.; Shi, L.; Ling, C.; Wang, J. Perspective on Theoretical Methods and Modeling Relating to Electrocatalysis Processes. *Chem. Commun.* **2020**, *56*, 9937−9949.

(78) *NIST Standard Reference Database SRD Number 69*, DOI: 10.18434/T4D303.

(79) López, M.; Exner, K. S.; Viñes, F.; Illas, F., Computational Pourbaix Diagrams for MXenes: A Key Ingredient toward Proper Theoretical Electrocatalytic Studies. *Adv. Theory Simul.* **2023,** *6*, 2200217.

(80) Morales-García, Á.; Fernández-Fernández, A.; Viñes, F.; Illas, F. CO_2 Abatement Using Two-Dimensional MXene Carbides. *J. Mater. Chem . A.* **2018,** *6*, 3381−3385.

(81) Morales-Salvador, R.; Morales-García, Á.; Viñes, F.; Illas, F. Two-Dimensional Nitrides as Highly Efficient Potential Candidates for CO_2 Capture and Activation. *Phys. Chem. Chem. Phys.* **2018,** *20*, 17117−17124.

(82) Kunkel, C.; Viñes, F.; Illas, F. Transition Metal Carbides as Novel Materials for CO_2 Capture, Storage, and Activation. *Energy Environ. Sci.* **2016**, *9*, 141−144.

(83) Jurado, A.; Morales-García, Á.; Viñes, F.; Illas, F. Molecular Mechanism and Microkinetic Analysis of the Reverse Water Gas Shift Reaction Heterogeneously Catalyzed by the Mo_2C MXene. *ACS Catal.* **2022,** *12*, 15658−15667.

(84) Zhu, S.; Drazkowski, M.; Boukamp, B. A.; Bouwmeester, H. J. M. On the Effect of Electrode Material in Electrical Conductivity Relaxation - An Alternative Interpretation of the Two-Fold Relaxation Behavior in $La_{5.4}WO_{11.1-\delta}$. *Solid State Ion.* **2022,** *384*, 115994.

(85) Peng, J.; Shi, Z.; Jiang, J.; Zhang, P.; Hsu, J.-P.; Li, N., Charge–Orbital Synergistic Engineering of TM@$Ti_3C_2O_{1-x}B_x$ for highly selective CO_2 electrochemical reduction. *Mater. Horiz.*, **2023,** *10*, 4278–4292.

(86) Leiming, T.; Kui, P.; Wen, Q.; Liming, H.; Linhai, D.; Guanhua, Z.; Qiuye, L.; Changlin, Y., Facile Fabrication of Boron-Doped Titanium Carbide for Efficient Electrocatalytic Nitrogen Reduction. *Catal. Sci. Technol.*, **2023,** *13*, 4517–4524.

(87) Chen, J.; Cheng, H.; Ding, L.-X.; Wang, H. Competing Hydrogen Evolution Reaction: A Challenge in Electrocatalytic Nitrogen Fixation. *Mater. Chem. Front.* **2021,** *5*, 5954−5969.

(88) Ling, C.; Niu, X.; Li, Q.; Du, A.; Wang, J. Metal-Free Single Atom Catalyst for N_2 Fixation Driven by Visible Light. *J. Am. Chem. Soc.* **2018,** *140*, 14161−14168.

(89) Fan, M.; Liang, X.; Li, Q.; Cui, L.; He, X.; Zou, X. Boron: A Key Functional Component for Designing High-Performance Heterogeneous Catalysts. *Chin. Chem. Lett.* **2023,** *34*, 107275.

(90) Vázquez-Parga, D.; Jurado, A.; Roldán, A.; Viñes, F. A Computational Map of the Probe CO Molecule Adsorption and Dissociation on Transition Metal Low Miller Indices Surfaces. *Appl. Surf. Sci.*, **2023**, *618*, 156581.

(91) Viñes, F.; Calzada, A.; Gamallo, P. Thermodynamic, Kinetic and Dynamic Aspects of Biogas Upgrading Using Nano-Engineered Grazynes. *Appl. Surf. Sci.*, **2023**, *71*, 102459.

(92) Chen, S.; Liu, X.; Xiong, J.; Mi, L.; Li, Y. Engineering Strategies for Boosting the Nitrogen Reduction Reaction Performance of MoS_2-Based Electrocatalysts. *Mater. Today Nano* **2022,** *18*, 100202.

(93) Wei, Z.; Feng, Y.; Ma, J. Co-Doped Graphene Edge for Enhanced N_2-to-NH_3 Conversion. *J. Energy Chem.* **2020,** *48*, 322−327.

(94) Sheets, B. L.; Botte, G. G. Electrochemical Nitrogen Reduction to Ammonia Under Mild Conditions Enabled by a Polymer Gel Electrolyte. *Chem. Commun.* **2018,** *54*, 4250−4253.

(95) Ortuño, M. A.; Holloczki, O.; Kirchner, B.; López, N. Selective Electrochemical Nitrogen Reduction Driven by Hydrogen Bond Interactions at Metal–Ionic Liquid Interfaces. *J. Phys. Chem. Lett.* **2019**, *10*, 513−517.

(96) McEnaney, J. M.; Singh, A. R.; Schwalbe, J. A.; Kibsgaard, J.; Lin, J. C.; Cargnello, M.; Jaramillo, T. F.; Nørskov, J. K., Ammonia Synthesis from N_2 and H_2O Using a Lithium Cycling Electrification Strategy at Atmospheric Pressure. *Energy Environ. Sci.* **2017,** *10*, 1621−1630.

(97) Malkhandi, S.; Yang, B.; Manohar, A. K.; Prakash, G. K. S.; Narayanan, S. R. Self-Assembled Monolayers of n-Alkanethiols Suppress Hydrogen Evolution and Increase the Efficiency of Rechargeable Iron Battery Electrodes. *J. Am. Chem. Soc.* **2013,** *135*, 347−353.

(98) Manohar, A. K.; Malkhandi, S.; Yang, B.; Yang, C.; Surya Prakash, G. K.; Narayanan, S. R. A High-Performance Rechargeable Iron Electrode for Large-Scale Battery-Based Energy Storage. *J. Electrochem. Soc.* **2012,** *159*, A1209−A1214.

(99) Tekalgne, M. A.; Do, H. H.; Nguyen, T. V.; Le, Q. V.; An, J.; Hong, S. H.; Ahn, S. H.; Kang, H.; Kim, J. S.; Kim, S. Y. Efficient Electrocatalysts for Hydrogen Evolution Reaction Using Heteroatom-Doped MXene Nanosheet. *Int. J. Energy Res.* **2023,** *2023*, 8980888.

(100) Xie, Y.; Naguib, M.; Mochalin, V. N.; Barsoum, M. W.; Gogotsi, Y.; Yu, X.; Nam, K.-W.; Yang, X.-Q.; Kolesnikov, A. I.; Kent, P. R. C. Role of Surface Structure on Li-Ion Energy Storage Capacity of Two-Dimensional Transition-Metal Carbides. *J. Am. Chem. Soc.* **2014,** *136*, 6385−6394.

(101) Meng, L.; Viñes, F.; Illas, F. Theoretical Modelling of the Hydrogen Evolution Reaction on MXenes: A Critical Review. *Curr. Opin. Electrochem.* **2023,** *40*, 101332.

Graphic for TOC

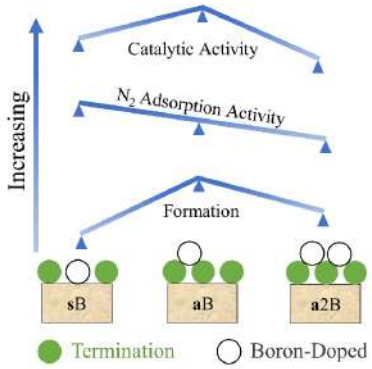

ACS Catalysis

pubs.acs.org/acscatalysis
Research Article

Contrasting Metallic (Rh^0) and Carbidic (2D-Mo_2C MXene) Surfaces in Olefin Hydrogenation Provides Insights on the Origin of the Pairwise Hydrogen Addition

Ling Meng, Ekaterina V. Pokochueva, Zixuan Chen, Alexey Fedorov,* Francesc Viñes,* Francesc Illas, and Igor V. Koptyug

Cite This: ACS Catal. 2024, 14, 12500−12511

ABSTRACT: Kinetic studies are vital for gathering mechanistic insights into heterogeneously catalyzed hydrogenation of unsaturated organic compounds (olefins), where the Horiuti−Polanyi mechanism is ubiquitous on metal catalysts. While this mechanism envisions nonpairwise H_2 addition due to the rapid scrambling of surface hydride (H*) species, a pairwise H_2 addition is experimentally encountered, rationalized here based on density functional theory (DFT) simulations for the ethene (C_2H_4) hydrogenation catalyzed by two-dimensional (2D) MXene $Mo_2C(0001)$ surface and compared to Rh(111) surface. Results show that ethyl (C_2H_5*) hydrogenation is the rate-determining step (RDS) on $Mo_2C(0001)$, yet C_2H_5* formation is the RDS on Rh(111), which features a higher reaction rate and contribution from pairwise H_2 addition compared to 2D-$Mo_2C(0001)$. This qualitatively agrees with the experimental results for propene hydrogenation with parahydrogen over 2D-Mo_2C_{1-x} MXene and Rh/TiO_2. However, DFT results imply that pairwise selectivity should be negligible owing to the facile H* diffusion on both surfaces, not affected by H* nor C_2H_4* coverages. DFT results also rule out the Eley−Rideal mechanism appreciably contributing to pairwise addition. The measurable contribution of the pairwise hydrogenation pathway operating concurrently with the dominant nonpairwise one is proposed to be due to the dynamic site blocking at higher adsorbate coverages or another mechanism that would drastically limit the diffusion of H* adatoms.

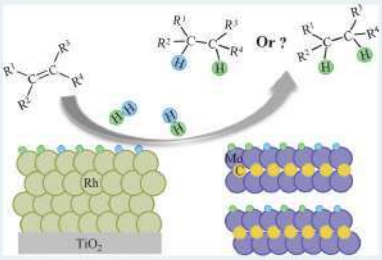

KEYWORDS: *2D-Mo_2C, Rh^0, MXenes, ethene, parahydrogen, pairwise hydrogenation*

1. INTRODUCTION

Hydrogenation reactions are at the core of heterogeneous catalysis, spanning from environmental treatments and the petrochemical industry to the synthesis of fine chemicals.[1] Regardless of a particular application, the surface of a heterogeneous catalyst provides active sites for weakening the H_2 bond, leading ultimately to the dissociative chemisorption that yields active surface H adatoms (H*).[2] Subsequently, H* species are transferred to a substrate, *e.g.*, in the hydrogenation of unsaturated hydrocarbons such as alkynes and alkenes.[3] The catalytic hydrogenation of alkenes has nearly a centenary-long research history, owing to a high practical relevance.[4] A textbook example is the hydrogenation of ethene, *i.e.*, $C_2H_4^{(g)} + H_2^{(g)} \rightarrow C_2H_6^{(g)}$, perhaps, the most extensively studied alkene hydrogenation reaction. From the mechanism proposed by Horiuti and Polanyi (*cf.* Scheme 1), which is widely recognized as the prevalent route for alkene hydrogenation,[5,6] it follows that the addition of H_2 to ethene is nonpairwise, *i.e.*, the added H atoms generally come from different H_2 molecules. In the Horiuti−Polanyi mechanism, the rapid surface diffusion of the H* species plays a crucial role in randomly adding hydrogen atoms to a substrate (ethene).[7]

That being said, it is now conclusively established that various types of heterogeneous catalysts can achieve pairwise hydrogen addition, whereby the two H atoms that end up in the hydrogenation product molecule originate from the same H_2 molecule.[8] The unambiguous evidence for this is provided by experiments that use parahydrogen (p-H_2), the nuclear spin isomer of H_2 with the opposite spin orientation of its two H atoms (more rigorously, it is a state with zero total nuclear spin). The addition of p-H_2 to various alkenes or alkynes leads, when the addition proceeds in a pairwise manner, to a nonequilibrium population of nuclear spin states in the product(s), resulting in a major (*i.e.*, orders of magnitude)

Received: April 28, 2024
Revised: July 1, 2024
Accepted: July 22, 2024
Published: August 6, 2024

https://doi.org/10.1021/acscatal.4c02534
ACS Catal. 2024, 14, 12500−12511

Scheme 1. Horiuti–Polanyi (Nonpairwise) and Farkas (Pairwise) Hydrogen Addition Mechanisms

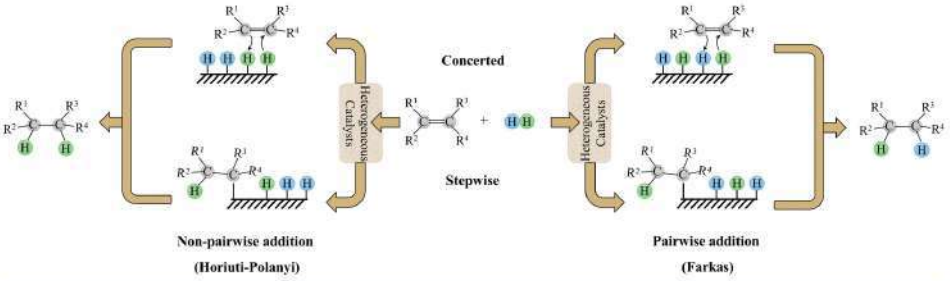

signal enhancement in NMR spectra of the reaction products. Parahydrogen-induced polarization (PHIP) is a method that allows one to evaluate the selectivity of a catalyst to the pairwise addition of H_2 as the detected NMR signal enhancement is directly proportional to the pairwise selectivity,[9,10] aided by the high sensitivity of PHIP as a mechanistic tool that identifies reliably the contribution of the pairwise hydrogenation pathway of merely *ca.* 0.01%.[8]

Using the PHIP approach, various metal-based catalysts have been demonstrated to provide pairwise selectivity in an order of several percent. Pairwise addition of H_2 has been observed for catalysts based on Rh,[11] Pd,[12] Pt,[13,14] Ir,[15] V,[16] Cu,[10] and Co,[17] among others. Furthermore, the hexagonal close-packed (hcp) phase of Mo_2C also exhibited a significant selectivity in the pairwise hydrogen addition, resulting in approximately a 150-fold increase in signal intensity, compared to the face-centered-cubic (fcc) MoC phase containing C-vacancies.[18]

These experiments involving p-H_2 demonstrate unambiguously the feasibility of the pairwise addition on metal and metal carbide surfaces, which generally disagrees with the commonly accepted Horiuti–Polanyi mechanism that assumes a rapid diffusion of H* species.[9,10] Yet, an alternative reaction route proposed by Farkas entails a slow diffusion of H* and allows for the pairwise addition pathway (*cf.* Scheme 1).[20] Note that, in principle, both concerted and stepwise hydrogen additions can follow pairwise and nonpairwise routes, as presented in Scheme 1.[21]

The arguments above notwithstanding, it remains challenging to predict (and even rationalize) the selectivity preference to the pairwise hydrogen addition pathway for a given catalytic surface. To understand the interplay between the diffusion rate of H* species, the energy barriers on the hydrogenation pathway, and the contribution from the pairwise addition to the overall hydrogenation rate, we relied on the density functional theory (DFT) computations of a model ethene (C_2H_4) hydrogenation to ethane (C_2H_6). Rh was chosen for this study as it is one of the most active catalysts in the hydrogenation of unsaturated substrates, with Rh/TiO_2 demonstrating pairwise selectivities of up to 8%.[11] Metal carbides are also efficient hydrogenation catalysts and, as mentioned above, can produce pronounced PHIP effects. It was anticipated that the presence of carbide phases or carbidic species would affect the rate of hydrogenation and significantly modify the diffusive mobility of surface H* species. As the diffusive separation of H* species highly favors nonpairwise H_2 addition, it was deemed instructive to consider such effects in this study. Given the known instability of Rh_2C under hydrogenation conditions,[22] 2D-Mo_2C(0001) appears to be a more suitable carbide owing to its higher thermal stability (relative to noble metal carbides such as Rh_2C or PdC_x) and well-defined nature (the presence of single surface termination in MXenes). Consequently, we have explored a well-defined 2D-Mo_2C MXene exhibiting predominantly the basal (0001) surface,[23] and contrasted the results to those obtained for the Rh(111) surface. Both 2D-Mo_2C and C-deficient 2D-Mo_2C_{1-x} can be obtained experimentally by a reductive defunctionalization of Mo_2CT_x (T_x are surface functional groups) of the MXene family.[24,25] Worthy of note, hydrogenation reactions of unsaturated hydrocarbons on MXenes are largely understudied.[26]

To shed light on the origin of PHIP effects, we considered thermodynamic and kinetic aspects of H_2 addition in both concerted and stepwise pathways when departing from H* as generated upon H_2 adsorption and dissociation on the catalyst surface. Note that the energetics associated with the two mechanisms are almost identical. Thus, to ease the upcoming discussion, only the stepwise mechanism is presented in detail here, using a pool of diffusing H* adatoms on the 2D-Mo_2C(0001) and the Rh(111) surfaces. The DFT predictions were then assessed experimentally using parahydrogen addition to propene on 2D-Mo_2C_{1-x} and Rh/TiO_2 catalysts.[27] The use of a simpler ethene model instead of propene in the DFT calculations is supported by the observation that H_2 activation mainly originates from the electrostatic potential and charge on metal sites on the catalyst surface, with only a limited influence from the substrate.[27] Ethene and propene are homologous olefins with a single double bond and so a similar reactive site.[28] The ethene hydrogenation rate was reported to be ca. an order of magnitude higher than that of propene,[29,30] implying a difference of only 0.06–0.1 eV in the activation energy barrier according to the Arrhenius equation. Thus, using a simpler ethene structure reduces computational complexity and time without compromising the value of insights for propene hydrogenation. The study reveals that, upon H_2 dissociation, H* species undergo diffusion before transferring to alkenes and emphasizes the effect of surface coverage (including hydrides and alkene adsorbates) on the rate of ethene hydrogenation (with only a minor effect found when considering 3/4 monolayer of H* or C_2H_4* species), demonstrating the vastly dominant nonpairwise mechanism for both Rh(111) and 2D-Mo_2C(0001), regardless of a stacking motif (ABA or ABC). Overall, our results demonstrate that, within the range of surface coverages explored, the inherently nonpairwise nature

https://doi.org/10.1021/acscatal.4c02534
ACS Catal. 2024, 14, 12500–12511

of the Horiuti–Polanyi mechanism cannot be reconciled with the pronounced contribution of the pairwise hydrogenation pathway observed experimentally. Therefore, alternative possibilities for the pairwise H_2 addition on the surface of heterogeneous catalysts need to be considered.

2. EXPERIMENTAL AND THEORETICAL ASPECTS

2.1. Computational Details. Periodic DFT calculations were carried out using the Vienna *ab initio* simulation package (VASP).[31] The exchange-correlation interaction was approximated within the generalized gradient approximation (GGA) using the formalism proposed by Perdew–Burke–Ernzerhof (PBE),[32] including Grimme's D3 approach to account for dispersive interactions.[33] The projector-augmented wave (PAW) method,[34] as implemented in VASP by Kresse and Joubert,[35] was chosen to describe the density of core electrons and their effect on the valence electron density. The valence electron density was expanded on a plane wave basis set with a cutoff kinetic energy of 415 eV.

The Rh reference (111) surface, the most stable one of Rh,[36] was modeled using a $p(4 \times 4)$ slab with four fully optimized layers constructed from the optimized geometry of Rh bulk, as described in ref 36. A vacuum region of at least 16 Å was used perpendicular to the surface direction to avert interactions between the periodically repeated models. Likewise, the 2D-Mo_2C MXene(0001) basal surfaces, featuring either the regular ABC stacking, or the energetically more stable ABA stacking,[37] were modeled using a $p(4 \times 4)$ supercell. For such models, an optimal $4 \times 4 \times 1$*k*-point **Γ**-centered Monkhorst–Pack grid was used to sample the Brillouin zone for the necessary numerical integration in the reciprocal space.[38] During the geometry optimization of the models, either pristine or with adsorbates, a convergence criterion of 10^{-5} eV was used for the electronic self-consistent field steps, while the relaxation of atomic positions finalized when forces acting on atoms were below 0.01 eV·Å^{-1}. Based on previous calculations, differences in computational details, such as operation thresholds, *k*-points densities, and basis set sizes, resulted in variations in total energy below the chemically meaningful precision threshold of *ca.* 0.04 eV.[39]

The obtained optimized structures of surface species on the reaction coordinate were characterized as minima via vibrational frequency analysis, gained Hessian matrix diagonalization involving adsorbate degrees of freedom only, with elements obtained from finite differences of analytical gradients with steps of 0.03 Å in length,[40] thus assuming vibrational decoupling from surface phonons, following reported approaches.[41−43] For each adsorbate, different high-symmetry adsorption sites were sampled, see Figure S1 of the Supporting Information (SI), and for each adsorbate, various orientations and connectivities were considered systematically. For each species, *i*, and for each found minimum, adsorption energies, ΔE^i_{ads}, were calculated as

$$\Delta E^i_{ads} = E_{i/surf} - (E_{surf} + E_i) \quad (1)$$

where $E_{i/surf}$ is the energy of the surface with the adsorbate, E_{surf} stands for the energy of the clean surface, *i.e.*, ABC- or ABA-stacked 2D-Mo_2C MXene(0001) surface, or Rh(111) surface models, and E_i is the energy of the *i* species in the gas phase as optimized in vacuum considering the **Γ**-point only within a box of broken-symmetry dimensions of $9 \times 10 \times 11$ Å^3. Notice that, strictly speaking, such energies can be regarded as adsorption energies for the species existing in the gas phase, namely, H_2, C_2H_4, and C_2H_6, while for H and C_2H_5, these would be interaction energies, but in what follows, they are discussed indistinctly as adsorption energies. Within this definition, the more negative the ΔE^i_{ads}, the stronger the interaction is. In addition, the adsorption Gibbs free energies at a given temperature, *T*, and gas partial pressure, *p*, were gained. The details are provided in Section S1 of the SI.

Once reactants are adsorbed, and as far as the stepwise ethene hydrogenation mechanism is concerned, we regarded the following reaction steps

(i) H_2 dissociation, ΔE_{diss}:

$$H_2{}^* + {}^* \rightleftharpoons 2\cdot H^* \quad (2)$$

(ii) First hydrogen transfer, ΔE^{1st}_H:

$$C_2H_4{}^* + H^* \rightleftharpoons C_2H_5{}^* + {}^* \quad (3)$$

(iii) Second hydrogen transfer, ΔE^{2st}_H:

$$C_2H_5{}^* + H^* \rightleftharpoons C_2H_6{}^* + {}^* \quad (4)$$

including also adsorption and desorption steps of H_2, C_2H_4, and C_2H_6. In addition, diffusion of surface species has been investigated. For the reactive and diffusive paths, transition states (TSs) have been located using the climbing-image nudged elastic band (CI-NEB) and the improved dimer approaches,[44,45] applied on the most stable structures of initial states (ISs) and final states (FSs). As was described above for the identified minima, the TSs are characterized as well as saddle points, thus featuring zero gradients and a single imaginary frequency, consistent with the reaction path. Adsorption, desorption, diffusive, and reactive rates have been obtained as detailed in Section S2 of the SI. The span model used is described in Section S3 of the SI.

2.2. Experimental Details. Rh/TiO_2 with 1 wt % of Rh (determined with an X-ray fluorescence method) was prepared by the incipient impregnation method. Before use, TiO_2 (Hombifine N, phase-pure anatase, S_{BET} = 103 m^2 g^{-1}) was calcined at 550 °C for 2 h and dried at 120 °C for 6 h prior to impregnation. The support was impregnated with a solution of rhodium(III) nitrate (Sigma-Aldrich), thoroughly mixed, and left in air for 24 h, followed by drying in air for 3 h at 120 °C, calcination in air for 2 h at 600 °C and a treatment with H_2 for 3 h at 330 °C. The size of Rh particles in the resulting Rh/TiO_2 was assessed with transmission electron microscopy and was found to be *ca.* 1.4 nm. The particle dispersion, calculated from CO chemisorption measurements, was 77%, consistent with the previous report.[11] Mo_2CT_x was obtained by etching Mo_2Ga_2C with concentrated hydrofluoric acid (HF) as described previously.[24,46,47] The same batch of Mo_2CT_x was used for experiments in this work, as reported in ref 24. For the hydrogenation experiments, 100 mg of Mo_2CT_x was loaded in a 1:4″ OD stainless steel reactor and held in place using two pieces of a fiberglass tissue. Hydrogen gas was enriched with parahydrogen up to *ca.* 95% using a *p*-H_2 generator based on a closed-cycle helium cryostat (Cryotrade engineering CryoPribor, model CFA-200-H2cell) and a cryo-compressor (Vacree Technologies Co., Ltd., model C100A). Propene and *p*-H_2 were supplied separately through Bronkhorst mass-flow controllers and were mixed directly in the gas lines with a volume ratio of 1:4. The resulting mixture was supplied through a 1:16″ OD PTFE capillary via a Y-connector from PEEK polymer to the reactor, and then to the 10 mm NMR

https://doi.org/10.1021/acscatal.4c02534
ACS Catal. 2024, 14, 12500−12511

tube placed inside the NMR spectrometer (300 MHz). A valve added between the line from the reactor and a bypass line allowed for a facile acquisition of NMR spectra with the complete nuclear spin relaxation without termination of the gas flow through the catalyst layer. The reactor was heated with a tubular furnace. The Mo_2CT_x precursor was pretreated in an H_2 flow of 60 mL min^{-1} at 500 °C for 2 h (heating ramp was 10 °C min^{-1}), to give a material denoted as Mo_2CT_{x-500}, and then cooled down to 150 °C without termination of the gas flow. Subsequently, the catalyst was tested in the temperature range from 165 to 375 °C and at a gas flow rate of 26, 156, and 240 mL min^{-1}. Alternatively, 5 mg of Rh/TiO_2 was mixed with 20 mg of SiC (S_{BET} ca. 6 m^2 g^{-1}) and pretreated before the catalytic test in an H_2 flow of 30 mL min^{-1} at 200 °C for 1 h, then cooled down to 43 °C without termination of the gas flow. In this case, the catalytic test was performed in the temperature range from 43 to 150 °C using the same gas flow rates of 26, 156, and 240 mL min^{-1}.

Conversion of propene ($X_{C_3H_6}$) was calculated from the ratio of the integral of propane (*i.e.*, hydrogenation product) NMR signal ($S_{C_3H_8}$) to the sum of the integrals of propane and unreacted propene (*i.e.*, substrate) signals ($S_{C_3H_6}$), determined from the spectra acquired after relaxation of nuclear spins to the thermal equilibrium

$$X_{C_3H_6} = \frac{S_{C_3H_8}}{S_{C_3H_8} + S_{C_3H_6}} \cdot 100\% \quad (5)$$

Signal enhancement (SE) for CH_3-groups of propane was evaluated as

$$SE = \frac{|S_{PHIP} - S_{thermal} \cdot C|}{S_{thermal}/6} \quad (6)$$

where S_{PHIP} is the integral of the NMR signal of hyperpolarized propane (acquired during gas flow), $S_{thermal}$ is the integral of the NMR signal of propane after relaxation to thermal equilibrium, and 6 is the number of protons in the two CH_3 groups of propane. C is the coefficient of NMR signal suppression at high flow rates caused by a fast inflow of reagents from the Earth's magnetic field to the NMR probe due to an insufficient time for the nuclear magnetization to achieve its high-field equilibrium value. $S_{thermal}$ is evaluated after complete thermalization and is thus not affected by flow, whereas its contribution to the enhanced NMR signal is reduced by flow, *i.e.*, $C < 1$.

3. RESULTS AND DISCUSSION

3.1. Computational Assessment. The reactants (C_2H_4* and H_2*), the product (C_2H_6*), and the intermediates (H* and C_2H_5*) have been evaluated on high symmetry sites of the ABC- or ABA-stacked 2D-Mo_2C(0001) surface, as well as on the Rh(111) surface, and the optimal adsorption sites are presented in Figure S2. The observed H_2* minima on the 2D-Mo_2C MXene model are in line with the previous report.[48] The adsorption Gibbs free energies, ΔG_{ads}, for reactants and product, plotted in Figure 1—values are provided in Table S1—reveal that, regardless of the stacking, the ΔG_{ads} energies of MXene-derived 2D-Mo_2C are comparable to that of Rh, even though there are certain differences, *i.e.*, with the exception of C_2H_6, the ΔG_{ads} energies are larger on the 2D-Mo_2C models relative to Rh(111). Among the 2D-Mo_2C models, the Gibbs free energies of adsorption are larger for

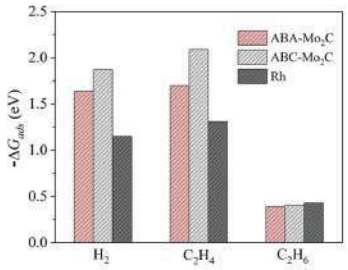

Figure 1. Adsorption free energies of H_2 (assuming the spontaneous dissociation into 2H*), C_2H_4, and C_2H_6 on the ABA-Mo_2C, ABC-Mo_2C and Rh(111) surfaces under 1 bar of gas pressure and 250 or 60 °C for the 2D-Mo_2C and Rh(111) models, respectively.

ABC-Mo_2C than for ABA-Mo_2C, consistent with a lower stability of the ABC-stacking relative to the ABA-stacking.[37]

The computed adsorption energies were used to estimate adsorption and desorption rates as a function of the gas pressure, p, and temperature, T (*cf.* Figure S3). In turn, the rates can be used to derive the so-called kinetic phase diagrams (KPD),[43] presented in Figure 2. Given the easiness of H_2* dissociation, see below, the formation of H_2* from 2 H* and its subsequent desorption have been used for the KPD. With this in mind, a slightly higher affinity of the surfaces for C_2H_4 is found with respect to H_2. It is clear that reactants, C_2H_4 and H_2 (undergoing the dissociation to 2 H*), can be adsorbed on all three surfaces at the working conditions, while C_2H_6 would be prone to facile desorption; a favorable feature for the catalyst performance.

As briefly introduced, the dissociation of one H_2* into 2 H* on the studied surfaces was assessed also in the vicinity of a single C_2H_4* species. H* adsorbs preferentially on the H_B and H_M sites for the ABA-Mo_2C and ABC-Mo_2C models, respectively (*cf.* Figure S1). However, on Rh(111), despite H_{fcc} being the most stable site for the H* adsorption, the adsorption of H* on H_{hcp} is energetically less exothermic by merely 0.03 eV (*cf.* Figure S1), implying both sites compete for the H* species. The number of conceivable intermediates for two vicinal H* is larger for the Rh(111) surface; see Figure S4 and Table S2 for the coadsorption energies. Competitive minima are used as final states for the H_2* dissociation (*cf.* Figure S5), with the estimated dissociation energy barriers, E_b, of only 0.28 and 0.11 eV for the ABA- and ABC-Mo_2C models, respectively, and only 0.06 eV for Rh(111)—toward vicinal H_{fcc} and H_{hcp} sites—, and 0.08 eV toward two vicinal H_{fcc} sites. Thus, H_2 dissociation is a low-energy barrier elementary step on all three pristine surfaces and slightly more difficult on 2D-Mo_2C(0001) than on Rh(111).

Considering the notably stronger interaction of C_2H_4 compared to H_2 molecule on all three surfaces, one can anticipate the dissociation of H_2 to proceed also in the presence of C_2H_4*. To this end, the H_2* adsorption sites and 2 H* coadsorption sites were probed, see Figures S6 and S7 for the respective structures, and Tables S3–S6 for the adsorption energies. The presence of C_2H_4* has only a moderate impact on the H_2 dissociation energy barriers, E_b (cf. Table S7). In the presence of C_2H_4*, the E_b values decrease to 0.19 and 0.09 eV for ABA- and ABC-Mo_2C, respectively, and to only 0.01 eV for the Rh(111) surface—ISs, TSs, and FSs corresponding to the

https://doi.org/10.1021/acscatal.4c02534
ACS Catal. 2024, 14, 12500−12511

ACS Catalysis pubs.acs.org/acscatalysis Research Article

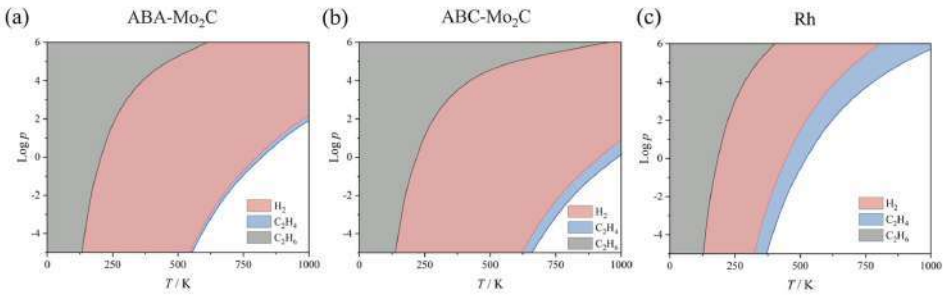

Figure 2. Calculated kinetic phase diagrams for H_2, C_2H_4, and C_2H_6 on the (a) ABA-Mo_2C, (b) ABC-Mo_2C, and (c) Rh(111) models as a function of temperature T, in K, and standard logarithmic function of the gas pressures, p, in Pa. Colored regions imply a preference toward adsorption, while white areas represent regions where pristine surfaces are preferred.

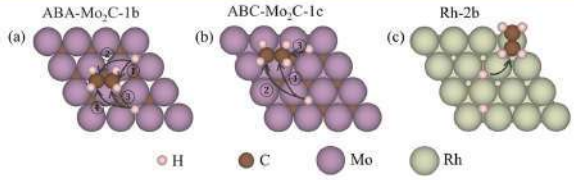

Figure 3. Potential routes of the first step of the C_2H_4 hydrogenation reaction on (a) ABA-Mo_2C-1b, (b) ABC-Mo_2C-1c, and (c) Rh-2b. See Figure S7 for the definition of notations.

paths with the lowest E_b are presented in Figure S8. To summarize, 2D-Mo_2C and Rh(111) dissociate H_2 easily, regardless of the presence or absence of the C_2H_4* species.

As aforementioned, the accepted mechanisms for the hydrogenation of alkenes over heterogeneous transition metal catalysts involve the dissociative chemisorption of H_2.[49] Upon H_2 dissociation and prior to the H* transfer to an unsaturated hydrocarbon such as an alkene, the diffusion of H* adatoms may take place.[50] The diffusion of H* adatoms was computationally explored considering the presence or absence of C_2H_4*, following the paths depicted in Figure S1, and, in the Rh(111) case, involving both H_{fcc} and H_{hcp} competitive sites. The preferred paths on the pristine surfaces, shown in Figure S9, reveal diffusion energy barriers E_b of 0.35 and 0.27 eV for the ABA- and ABC-Mo_2C models and of 0.16 eV for the Rh(111) surface; these values vary slightly in the presence of C_2H_4* (cf. Figure S10), with the E_b values of 0.37 and 0.28 eV for the ABA- and ABC-Mo_2C models, and 0.10 eV for Rh(111). Altogether, the results show that regardless of the absence or presence of C_2H_4*, the E_b of H_2 dissociation is lower than that of H* diffusion (cf. Table S8).

Next, the energetics of the ethene hydrogenation steps were evaluated. The reactive pathways for the first H* transfer are shown in Figure 3, while reaction energy changes, ΔE, and energy barriers, E_b, are presented in Table S9. The ΔE to form C_2H_5* from C_2H_4* and H* on the 2D-Mo_2C models range from 0.28 to 0.57 eV, which is generally comparable to the ΔE of 0.39 eV on Rh(111). Similarly, the E_b range from 0.64 to 0.84 eV on the 2D-Mo_2C models, which are slightly lower than 0.91 eV found for Rh(111). Thus, the first H* transfer step to C_2H_4* is more facile on 2D-Mo_2C regardless of the stacking when compared to Rh(111).

The second hydrogenation step that converts C_2H_5* and H* to C_2H_6* is slightly exothermic, by −0.11 eV, for Rh(111), with a moderate E_b of 0.55 eV. However, on the 2D-Mo_2C models, this step is endothermic, in the range of 0.86−1.32 eV, leading to higher E_b values varying from 1.77 to 2.11 eV (*cf.* Table S9). Thus, the significant endothermicity of the second H* transfer step on both 2D-Mo_2C models distinguishes them from the Rh(111) model. The higher energy barrier for the second hydrogenation step on both 2D-Mo_2C(0001) surfaces is due to the similarly stronger bonding of C_2H_4* and C_2H_5* species on 2D-Mo_2C compared to the adsorption energy of C_2H_6*, at variance with Rh, where bonding energies are more similar. The similarly high adsorption energies for C_2H_4* and C_2H_5* species on 2D-Mo_2C lead to a relatively low barrier for the first hydrogenation step but make the second hydrogenation barrier higher, in agreement with the Brønsted−Evans−Polanyi (BEP) relationships. Overall, the hydrogenation of C_2H_4* to C_2H_6* is moderately endothermic on Rh(111) by 0.27 eV and has an energy barrier of 0.94 eV according to the span model,[51] while on ABA- and ABC-Mo_2C the reaction is endothermic by 1.20 and 1.70 eV, with the span model energy barriers of 2.06 and 2.40 eV, respectively (*cf.* Table S9). These results suggest a more facile hydrogenation of ethene to ethane on Rh(111) relative to both 2D-Mo_2C models, see Figure 4.

Substrate coverage effects may change the energy barriers, for instance, by lateral interactions. In this context, the high coverage of C_2H_4* and H* adatoms under the reaction conditions can be prompted by a stronger ethene adsorption and low barriers for the H_2 dissociation; see Figures 1, 2, and Table S8, in addition to a higher partial pressure of H_2 compared to C_2H_4. To probe the substrate coverage effects,

https://doi.org/10.1021/acscatal.4c02534
ACS Catal. 2024, 14, 12500−12511

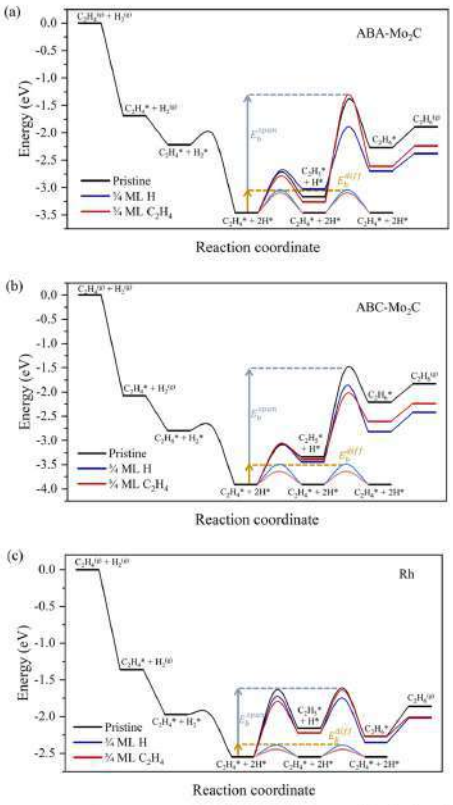

Figure 4. Total reaction energy profiles on the pristine (black) (0001) surfaces of (a) ABA-Mo_2C and (b) ABC-Mo_2C, and (c) Rh(111). From C_2H_4* + 2H* state, the forward paths are superimposed for 3/4 ML H* (blue), and 3/4 ML C_2H_4* (red). The diffusive paths of H* adatoms are shown in lighter shades of the respective colored traces. Note that the pristine diffusive path (gray) and that of the 3/4 ML C_2H_4* model (pink) essentially superimpose. All energy values are corrected by the zero energy term (ZPE).

we considered surface models with 3/4 of a monolayer (ML) of either C_2H_4* or H*. Here, coverage is defined based on H* ML with full occupancy of active hollow sites; that is, a H* per 6.9 or 6.4 Å^2 for 2D-Mo_2C or Rh, respectively, while assuming C_2H_4* occupies a projected area of *ca.* 27.7 Å^2 on 2D-Mo_2C, see Figure S2, similar to four sites of H*, a situation copycatted on Rh as well. On the 3/4 ML C_2H_4* model, the most stable sampled situation minimized the lateral repulsion between moieties, while in the 3/4 ML H* situation, the simultaneous placement of a C_2H_4* moiety left only two empty hollow sites, located near the C_2H_4* to allow assessing H_2 adsorption, dissociation, and C_2H_4* hydrogenation steps. Thus, in the 3/4 ML H* model 12 H* adatoms reside on the modeled surface, including the two H* atoms obtained from the H_2 dissociation. On the 3/4 ML C_2H_4* model, there are three C_2H_4* molecules, one of which engages in the hydrogenation reaction.

Before addressing ethene hydrogenation at these high coverages, it is worth analyzing H_2 dissociation at a such higher H* coverage, remembering that, *e.g.*, on Pt(111), the dissociation enthalpy of H_2 declines at high coverages of H*.[52] To this end, we removed two vicinal H* adatoms from the 3/4 ML H* model, achieving a $^5/_8$ ML H* coverage. On that surface, H_2 adsorption energy slightly decreases to −0.46 and −0.62 eV, and so does the dissociation energy, which decreases to −0.88 and −0.94 eV, with E_b declining to 0.10 and 0.01 eV, for ABA- and ABC-Mo_2C, respectively, compared to low-coverage values, see Tables S3 and S8 of the SI. On Rh(111), the E_{ads} and dissociation energy reduces to −0.02 and −1.14 eV, as well, with a negligible energy barrier close to 0 eV. Thus, H* coverage seems to reduce the adsorption strength and ease the H_2 dissociation, yet the effect is much smaller compared to, *e.g.*, the reported data on Pt(111).[52] With this in mind, the reaction energies, energy barriers, full process energy change, and E_b values of the span model are listed in Table S10 for the ABA- and ABC-Mo_2C, and Rh(111) surfaces. The transition states and reaction pathways are presented in Figures S11–S13. These results show that the 3/4 ML coverage of either C_2H_4* or H* adatoms has only a minor impact on certain steps (*vide infra*), and so, the full reaction profile is essentially unchanged, see Figure 4, generally unaffected by whether the high coverage situation is found with C_2H_4* or H* moieties, also due to the similar surface occupancy of the 3/4 ML C_2H_4* or H* models, see above, and expected similar lateral interactions between these surface moieties. This non-dependency of activation energies on coverage has been observed, *e.g.*, in allyl alcohol hydrogenation on Rh(111), although for some other hydrogenation reactions, *e.g.*, cyclohexene hydrogenation, the H* coverage was reported to reduce the hydrogenation energy barriers significantly.[53] On Rh(111), the impact is negligible, making the reaction less endothermic by merely 0.1 eV, and with an E_b reduced by 0.14 eV in the case of the 3/4 ML H* coverage. The coverage effect on the energy profile of the 2D-Mo_2C models is similar yet with more pronounced changes; at the 3/4 ML H*-coverage, the span E_b decreases by 0.49 and 0.35 eV for the ABA-Mo_2C and ABC-Mo_2C, respectively. However, for the 3/4 ML C_2H_4* coverage, the span E_b increases by 0.1 eV in ABA-Mo_2C, yet it decreases by 0.53 eV for ABC-Mo_2C, a difference attributed to distinct C_2H_4* arrangements for the different stackings presented in Figures S11 and S12. Overall, full hydrogenation of C_2H_4* is more endothermic, and the reaction barriers are higher on 2D-Mo_2C compared to Rh(111), regardless of the effects of the stacking or coverages of H* and C_2H_4*. The H* adatoms diffusion energy barriers on the 3/4 ML models of C_2H_4*, shown in Figure S14, are generally similar to those of the pristine surfaces, with the E_b variations in the 0.01 eV range for any of the explored Mo_2C models. Still, for the 3/4 ML coverage of H*, shown in Figure S15, larger diffusion E_b values of 0.42 eV on ABA- and ABC-Mo_2C compared to respective values of 0.37 and 0.28 eV on the pristine cases are found, see Table S11.

At this point, one can assess, based on the presented DFT results, the relative fractions of the expected pairwise *vs* nonpairwise hydrogenation pathways, the latter governed by H* diffusion energy barriers. This assessment is based on the estimation of the reaction rates as a function of the working temperature, T, *via* the span model energy barriers and the

https://doi.org/10.1021/acscatal.4c02534
ACS Catal. 2024, 14, 12500−12511

ACS Catalysis pubs.acs.org/acscatalysis Research Article

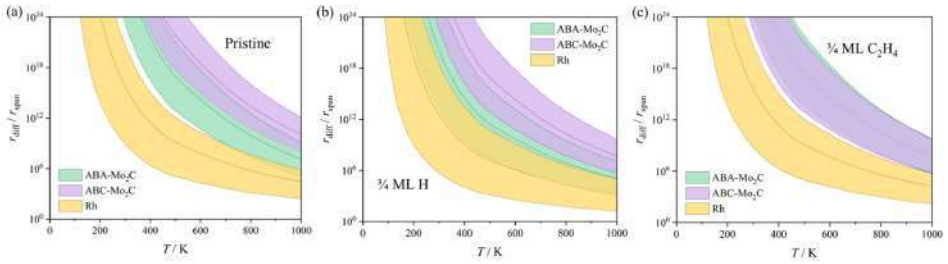

Figure 5. Calculated ratio between the rates of H* diffusion, r_{diff}, and the reaction rate obtained using the span model energy barrier, r_{span}, on ABA- and ABC-2D-Mo_2C (0001) surfaces, and Rh(111) surface, using (a) pristine surfaces, (b) a surface with coverage of 3/4 ML of H* or (c) 3/4 ML of C_2H_4*. Shaded regions reflect the DFT uncertainty of ±0.2 eV on the estimated energy barriers.

diffusion rates, obtained using transition state theory (TST) and considering 1 bar of reactants. Note that, since the competition of pairwise vs nonpairwise mechanisms relies on reaction vs diffusion rates, microkinetic modeling could provide estimates of reaction rate, although inclusion of diffusion, even if possible, would not affect reaction rate. Thus, as posed, microkinetic modeling would deliver no extra information from estimated rates. Effect of diffusion could be implemented by *ab initio* molecular dynamics, although here one should consider thousands of trajectories, which entails excessive computational costs. A more affordable approach would be kinetic Monte Carlo, although yet with difficulties in tagging spin on H adatom and spin scrambling by diffusion. With this information in hand, one can calculate the ratio between the diffusion rate, r_{diff}, and the reaction rate obtained using the span model, r_{span}, *i.e.*, r_{diff}/r_{span}. A ratio larger than unity indicates that H* diffusion is faster than the hydrogenation reaction. The obtained r_{diff}/r_{span} ratios for the ABA- and ABC-Mo_2C(0001) surfaces and that for Rh(111) as a function of temperature are shown in Figure 5.

DFT results show that the nonpairwise mechanism is expected to dominate on any of the model catalytic surfaces studied and that the pairwise mechanism is more likely on Rh(111) than on the 2D-Mo_2C (0001) surfaces, independent of the H* and C_2H_4* coverage of the surfaces. Note, however, that one should account for the DFT accuracy limits of ±0.2 eV. Thus, accuracy limits were added to Figure 5 assuming that the employed PBE-D3 level of calculation is underestimating or overestimating certain E_b values, in particular, overestimating diffusion barriers E_b on Rh(111) and the span model E_b barriers for the hydrogenation reaction on the 2D-Mo_2C(0001) surfaces, underestimating the diffusion E_b on the Mo_2C(0001) surfaces, and hydrogenation span model E_b barriers on Rh(111). Still, the trends discussed above remain unchanged also after accounting for the accuracy of our DFT approach.

Alternatively, a mechanism based on a concerted addition of H_2 to C_2H_4* that avoids the formation of H* adatoms, if operative, would result in a high selectivity toward pairwise H_2 addition. Therefore, we have considered also the contribution of an Eley−Rideal mechanism, where the H_2 molecule reacts with C_2H_4* directly from the gas phase, contributing to a pairwise addition via this single-step mechanism. However, all the computational attempts exploring the Eley−Rideal mechanism yielded high DFT energy barriers, *i.e.*, at least 4.84, 5.12, and 2.28 eV for ABA- and ABC-2D-Mo_2C(0001) and Rh(111) surfaces, respectively, thus larger than the most-demanding energy barrier of the stepwise mechanism (see Table S9 and Figure S16 of the SI). Therefore, a competitive pairwise hydrogenation mechanism that follows the Eley−Rideal kinetics can be discarded.

In what follows, we will discuss experimental results for the estimates of the pairwise and nonpairwise addition pathways obtained in the experiments with parahydrogen addition to propene on Rh/TiO_2 and Mo_2CT_{x-500} catalysts.

3.2. Experimental Results. As discussed above, the observation of the NMR signal enhancement (SE) in PHIP experiments requires that the two H atoms of the same p-H_2 molecule add to an unsaturated bond of a reactant (propene in this case) in a pairwise manner. The SE value is defined by eq 6, with higher SE values corresponding to a higher contribution of pairwise addition pathway to the overall product formation rate. Because the SE is normalized by the amount of product produced in the reaction (see eq 6), the SE values can be directly compared for different conversion levels.

While ethene was used to simplify the DFT calculations described above, PHIP experiments were performed with propene as a substrate. We note that the hydrogenation of ethene with *p*-H_2, even if entirely pairwise, would not produce observable NMR signal enhancement for the product ethane and thus could not be used to reveal a possible contribution of the pairwise H_2 addition. This is because the two hydrogen atoms incorporated in ethane upon hydrogenation of ethene are chemically and magnetically equivalent (as in *p*-H_2), while observation of signal enhancement requires breaking this equivalence in the reaction product. Since the latter condition is satisfied in propane, our hydrogenation experiments use propene. Worthy of note, it is unlikely that the underlying hydrogenation pathways (including the respective adsorption and diffusion properties, *vide supra*) predicted by our DFT calculations for ethene would be significantly different for propene. Therefore, the use of these two homologous olefins is not expected to affect the conclusions of this study.

Mo_2CT_{x-500} catalyst was prepared in situ by a 2 h pretreatment of Mo_2CT_x (100 mg) in the undiluted H_2 flow at 500 °C, i.e., in conditions that are known to fully reductively defunctionalize the surface termination groups of Mo_2CT_x (and concurrently generate some C vacancies by removing the carbidic carbon as methane) and provide a 2D-Mo_2C_{1-x} material.[25] Mo_2CT_{x-500} was cooled down to 150 °C after the pretreatment without termination of H_2 flow and then tested in propene hydrogenation with p-H_2 using the volume ratio of

https://doi.org/10.1021/acscatal.4c02534
ACS Catal. 2024, 14, 12500−12511

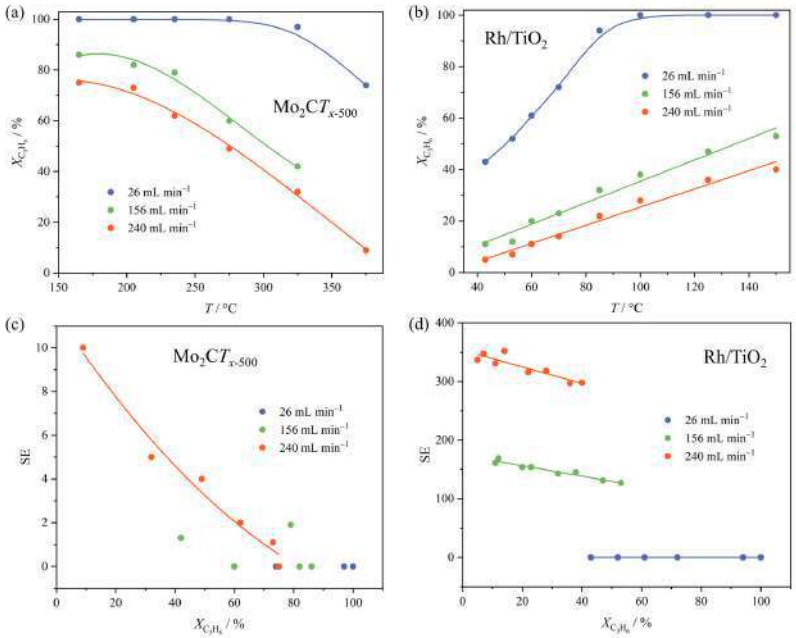

Figure 6. Conversion of propene ($X_{C_3H_6}$) in its hydrogenation with *p*-H_2 (1:4 volume ratio) as a function of temperature over (a) Mo_2CT_{x-500} and (b) Rh/TiO_2 catalysts, and (c,d) NMR signal enhancement, SE, as a function of conversion, for the three flow rates used. The lines are added to guide the eye. Note that the metal-based weight-over-flow (W/F) ratios were notably different, i.e., W/F = 2.8, 0.47, 0.30 mg_{Mo} min mL^{-1} and 1.9 × 10^{-3}, 3.2 × 10^{-4}, 2.1 × 10^{-4} mg_{Rh} min mL^{-1} for the flow rates of 26, 156, and 240 mL min^{-1}, respectively.

propene to p-H_2 of 1:4. Mo_2CT_{x-500} showed complete propene conversion at 165 °C when using a flow rate of 26 mL min^{-1}; propene conversion decreased to 75% upon increasing the flow rate to 240 mL min^{-1} (Table S12). Noteworthy, propene conversion on Mo_2CT_{x-500} declined with increasing temperature, possibly due to the formation of surface carbon deposits. Yet notably low signal enhancements were observed for the reaction product (propane) with Mo_2CT_{x-500} across the entire temperature range tested (165−375 °C). More specifically, at temperatures lower than 235 °C, the observed signal enhancements did not exceed 2-fold, indicating an almost entirely nonpairwise H_2 addition on Mo_2CT_{x-500}. A slight increase to a (still low yet unambiguously detectable) 10-fold SE with an increase in temperature to 375 °C was observed.

As mentioned above, Rh/TiO_2 is one of the most efficient catalysts to enable relatively high levels of SE in PHIP experiments at high conversion, *i.e.*, selectivity to the pairwise addition route of up to 8% and a 200-fold SE has been reported previously.[15] To compare Mo_2CT_{x-500} to Rh/TiO_2 at similar conversions, we mixed 1 wt % Rh/TiO_2 with a SiC diluent (to help dissipate the heat released of the exothermic propene hydrogenation reaction) and used hydrogenation temperatures in the range of *ca.* 43−150 °C. The obtained propene conversion and SE for Rh/TiO_2 are presented in Table S12. At low temperatures (*ca.* 43−75 °C), the observed signal enhancements were generally higher for Rh/TiO_2, with the SE values at ca. 276- to 390-fold. Overall, Mo_2CT_{x-500} shows at 150 °C a *ca.* twice higher conversion at the two higher flow rates than Rh/TiO_2, while SE values differ by *ca.* 2 orders of magnitude (*viz.*, 261−301 for Rh/TiO_2 *vs* 10 for Mo_2CT_{x-500}).

We note that the observed SE values are systematically larger at higher flow rates. This is due to the relaxation of nuclear spins that drives the nuclear spin system to thermal equilibrium, thereby significantly attenuating the NMR signal enhancement created initially by the pairwise addition of *p*-H_2. Lower gas flow rates result in longer gas travel time from the reactor to the NMR probe, leading to larger losses of nuclear polarization and lower apparent SE values. To obtain the true SE values, an extrapolation of SE to an infinite flow rate (*i.e.*, zero travel time) is required, yet in practice, this approach may introduce significant uncertainties. Therefore, the SE values obtained at the highest gas flow rate used in the experiments (*i.e.*, 240 mL min^{-1}) are taken here as the proxy for the extent of the pairwise hydrogen addition in propene hydrogenation on Mo_2CT_{x-500} and Rh/TiO_2, as presented in Figure 6. At the same time, higher flow rates result in reduced reactant residence time in the reactor and, thus, in lower conversions. For completeness, Table S12 reports both SE and conversion values at all three flow rates used.

https://doi.org/10.1021/acscatal.4c02534
ACS Catal. 2024, 14, 12500−12511

3.3. Discussion. As shown above, the selectivity to the pairwise hydrogen addition assessed via the experimentally observed NMR signal enhancements is notably larger for the Rh/TiO_2 relative to Mo_2CT_{x-500}. Assuming that the hydrogenation proceeds via dissociative chemisorption of H_2 on a catalyst surface, obtained pairwise selectivities are qualitatively in line with the results of DFT calculations. Indeed, lower ratios between the rates of H* surface diffusion and the hydrogenation reaction (r_{diff}/r_{span}) for the Rh(111) compared to those for the 2D-Mo_2C(0001) surface (representing experimental Rh/TiO_2 and Mo_2CT_{x-500}, respectively) imply a higher likelihood for the pairwise addition on Rh(111). However, in quantitative terms, the DFT calculations predict the diffusion to be 4−12 orders of magnitude faster than the hydrogenation reaction under typical experimental conditions. The disparity between the two rates appears too significant to be affected notably by any reasonable fine-tuning of the employed calculational models and the associated computational errors. Furthermore, the calculations additionally suggest that even if an H_2 molecule would dissociate in the immediate vicinity of an adsorbed ethene molecule, the diffusive separation of H* adatoms is notably faster than their transfer to ethene, and therefore the likelihood of the pairwise hydrogen addition is not increased appreciably.

The observation of PHIP effects on metal surfaces is sometimes ascribed to the presence of adsorbates that lower significantly the diffusive mobility of H* adatoms, favoring thereby the pairwise hydrogen addition.[54] Indeed, a number of surface sites can be blocked or become blocked if associated with the simultaneous diffusion of H*, both factors slowing down H* diffusion considerably and potentially prompting the pairwise addition. In this context, the present DFT calculations demonstrated no significant changes in the diffusive and reactive rates due to high surface coverages of coadsorbates (3/4 ML of H* or C_2H_4*). Within this static picture, the diffusive and reactive channels are not blocked, making the presence of adsorbates an unlikely decisive factor for the emergence of PHIP effects. While the presence of other adsorbates (such as $CH_3CH{=}CH_2$*) may feature a more pronounced influence on the r_{diff}/r_{span} ratio, the disparity of several orders of magnitude in the r_{diff}/r_{span} ratio observed for the hydrogenation of ethene strongly suggests that adsorbates present at the catalyst surface cannot explain the contribution of the pairwise hydrogenation mechanism, at least for the range of surface coverages addressed in this work.

Alternative explanations of pairwise H_2 addition thus need to be considered. In particular, the reaction of an H_2 molecule directly from the gas phase with an adsorbed C_2H_4* molecule through an Eley−Rideal mechanism would be expected to result in high pairwise selectivity. However, very high energy barriers revealed by DFT calculations for this mechanism exclude this as a possibility, see Figure S16 of the SI. A few other hydrogenation mechanisms sometimes advanced in catalytic literature generally cannot explain pairwise hydrogenation either because, similar to the Horiuti−Polanyi mechanism, random H* atoms are involved even when the reaction of an alkene or an alkyne with either $H_2^{(g)}$ or H_2* (instead of H*) is considered.[7,55,56] For instance, in the associative mechanism of the partial alkyne hydrogenation, the reaction between adsorbed propyne and H_2 adds one H atom to propyne but places the second one on the metal surface as H*.[55] Our DFT results demonstrate that, for the similar configuration C_2H_5* + H*, the second H* adatom is much more likely to diffuse away than to complete the hydrogenation cycle, *i.e.*, the underlying substrate-assisted hydrogenation mechanism is also nonpairwise.

Therefore, the quantitative results cannot be reconciled with the theoretically predicted preference for the Horiuti−Polanyi mechanism and other nonpairwise mechanisms of heterogeneous hydrogenations. At the same time, the experimental observations clearly reveal the presence of the pairwise reaction pathway for Rh/TiO_2 and even for Mo_2CT_{x-500} catalysts, for which the calculated r_{diff}/r_{span} ratios are particularly unfavorable. Moreover, this and other experimental studies of PHIP effects demonstrate that pairwise hydrogen addition is essentially omnipresent in hydrogenations catalyzed by various heterogeneous catalysts.[8] It is thus reasonable to conclude that the results point to the existence of additional reaction route(s) that inherently favor pairwise reaction pathway, operating concurrently with the dominant Horiuti−Polanyi mechanism and contributing measurably to the overall reaction yield. When such a concurrent mechanism involves the dissociation of H_2, the migration (and therefore, the randomization) of the formed H* species should be strongly suppressed, as is, for instance, the case for molecular transition metal catalysts that operate via the oxidative addition of H_2, olefin insertion, and reductive elimination steps. In the case of Rh/TiO_2, the presence of such "pairwise-selective" sites could result from an strong metal-support interaction (SMSI) effect. When SMSI effects are not available, a plausible mechanism could rely on a blocked diffusion of H* adatoms arising from occupied sites and the simultaneous competing diffusion of many H* adatoms, dynamically preventing diffusion until a nearby site is freed, an aspect not considered in the computation of diffusion rates. This would imply that H* adatoms formed after H_2 adsorption and dissociation nearby C_2H_4* cannot diffuse away as fast as predicted due to the dynamic site blocking, particularly for coverages higher than the explored 0.75 ML coverage. In such a situation, H* would have fewer chances to diffuse, and concomitantly, both generated H* atoms from p-H_2 would be more likely added in a pairwise manner to C_2H_4*.[57] Alternatively, a mechanism based on a concerted addition of H_2* to a substrate that completely avoids the formation of H* adatoms and features competitive reaction barriers relative to the Horiuti−Polanyi pathway would result in a high selectivity toward pairwise H_2 addition in the hydrogenation of unsaturated hydrocarbons. Future studies should explore the possibilities outlined above.

4. CONCLUSIONS

Here, first-principles DFT calculations were used to elucidate a more detailed reaction mechanism of the ethene hydrogenation on the well-defined model Rh(111) surface and 2D-Mo_2C(0001) with ABC- and ABA-stacking. Consistent results from both DFT calculations and experimental observations indicate that these catalysts are capable of effectively catalyzing the hydrogenation of ethene, which aligns with predictions based on adsorption rates that decrease sequentially for C_2H_4, H_2, and C_2H_6. Furthermore, the DFT results show that although 2D-Mo_2C and Rh(111) surfaces adsorb H_2, dissociate H_2, and diffuse H* adatoms with comparable barriers, regardless of the surface coverage with H* and C_2H_4* adsorbates in a model ethene hydrogenation reaction, the H* transfer steps for the hydrogenation of C_2H_5* to C_2H_6* are distinct. Specifically, while the first hydrogen transfer, to form C_2H_5* from C_2H_4* and H*, proceeds with similar barriers on

https://doi.org/10.1021/acscatal.4c02534
ACS Catal. 2024, 14, 12500−12511

Rh(111) and 2D-Mo_2C, the hydrogenation of ethyl species to ethane is endothermic on 2D-Mo_2C models and features significantly higher energy barriers than on Rh(111). This leads to a lower predicted rate of the ethene hydrogenation reaction on 2D-Mo_2C (in agreement with the experiment).

The DFT calculations were combined, for the first time, with experimental studies of hydrogenation with parahydrogen to address the origin of the nonpairwise vs pairwise H_2 addition. The hydrogenation of propene on 2D-Mo_2C_{1-x} and Rh/TiO_2 catalysts at comparable conversions resulted in an appreciable enhancement of the NMR signals of the reaction product (propane), which indicates unambiguously that the pairwise addition of H_2 to propene contributes measurably to the reaction rate, in line also with the previous studies that relied on parahydrogen to demonstrate the existence of the pairwise hydrogenation pathway on various surfaces. Importantly, our DFT study highlighted that diffusive migration of H* adatoms on a catalyst surface, which is an essential part of the Horiuti−Polanyi hydrogenation mechanism, is notably faster relative to the rate of H* addition to ethene, such that only randomized H* adatoms are added to the alkene. This inference is not altered measurably when considering significantly high catalyst surface coverages and other reaction conditions, implying no adsorbate lateral interaction hindrances.

While the experimentally established preference for the pairwise mechanism on Rh relative to 2D-Mo_2C is qualitatively explained based on the inherent H* diffusion differences between these catalysts, in more quantitative terms, the pairwise H_2 addition, with both H atoms of the same H_2 molecule ending up in the same product molecule, is predicted to be markedly less probable on any studied catalyst. Therefore, this combined theoretical and experimental study clearly demonstrates the predominance of the widely accepted Horiuti−Polanyi hydrogenation mechanism, which cannot explain the measurable contribution of the pairwise hydrogenation pathway as experimentally observed. Alternative reaction pathways, such as the identified concerted transition states for the H_2 addition following the Eley−Rideal pathway, were ruled out based on their high reaction barriers. One remaining plausible explanation is the diffusion hindrance of H* adatoms due to a dynamic surface site blocking at coverages higher than the currently explored 0.75 ML of H* or C_2H_4*, potentially prompting the pairwise addition. However, this remains to be confirmed in subsequent studies. Overall, the underlying pairwise hydrogenation mechanism avoids the randomization of hydrogen atoms either by preventing diffusion and scrambling of H* adatoms or by excluding entirely the involvement of H* adatoms in the reaction pathway.

■ ASSOCIATED CONTENT

Supporting Information

The Supporting Information is available free of charge at https://pubs.acs.org/doi/10.1021/acscatal.4c02534.

Configurations of catalysts, adsorbates, and the lowest-energy surface sites; Gibbs free/total adsorption energies of adsorbates; estimations of rates; reaction energies, energy barriers, and atomic structure view for H diffusion, H_2 dissociation and reaction process; conversion of propene, $X_{C_3H_6}$, and NMR signal enhancement of propane, SE (PDF)

■ AUTHOR INFORMATION

Corresponding Authors

Alexey Fedorov − *Department of Mechanical and Process Engineering, ETH Zürich, Zürich 8092, Switzerland;* orcid.org/0000-0001-9814-6726; Email: fedoroal@ethz.ch

Francesc Viñes − *Departament de Ciència de Materials i Química Física & Institut de Química Teòrica i Computacional (IQTCUB), Universitat de Barcelona, 08028 Barcelona, Spain;* orcid.org/0000-0001-9987-8654; Email: francesc.vines@ub.edu

Authors

Ling Meng − *Departament de Ciència de Materials i Química Física & Institut de Química Teòrica i Computacional (IQTCUB), Universitat de Barcelona, 08028 Barcelona, Spain*

Ekaterina V. Pokochueva − *International Tomography Center SB RAS, Novosibirsk 630090, Russian Federation;* Present Address: Université Claude Bernard Lyon 1, CRMN UMR-5082, CNRS, ENS Lyon, Villeurbanne 69100, France; orcid.org/0000-0003-0444-6619

Zixuan Chen − *Department of Mechanical and Process Engineering, ETH Zürich, Zürich 8092, Switzerland;* orcid.org/0000-0002-3882-3016

Francesc Illas − *Departament de Ciència de Materials i Química Física & Institut de Química Teòrica i Computacional (IQTCUB), Universitat de Barcelona, 08028 Barcelona, Spain;* orcid.org/0000-0003-2104-6123

Igor V. Koptyug − *International Tomography Center SB RAS, Novosibirsk 630090, Russian Federation;* orcid.org/0000-0003-3480-7649

Complete contact information is available at: https://pubs.acs.org/10.1021/acscatal.4c02534

Notes

The authors declare no competing financial interest.

■ ACKNOWLEDGMENTS

The authors acknowledge financial support from the Spanish *Ministerio de Ciencia e Innovación* through grants MCIN/AEI/10.13039/501100011033 PID2021-126076NB-I00 and TED2021-129506B−C22, funded partially by FEDER *Una manera de hacer Europa*, the unit of excellence María de Maeztu CEX2021-001202-M granted to the IQTCUB, the COST Action CA18234, and the *Generalitat de Catalunya* 2021SGR00079 grant. F.V. thanks the ICREA Academia Award 2023 ref Ac2216561. L.M. thanks the China Scholarship Council (CSC) for financing her PhD (CSC202108390032). A significant part of the computational resources has been provided by the *Red Española de Supercomputación* (RES) QHS-2023-1-0014 and QHS-2022-3-0016. ETH Zürich supported this work through a doctoral fellowship to Z.C. (ETH-40 17-2). This work was financially supported by the Russian Science Foundation (grant #22-43-04426). I.V.K. and E.V.P. thank the Russian Ministry of Science and Higher Education for access to NMR equipment and L.M. Kovtunova for providing the Rh/TiO_2 catalyst.

■ REFERENCES

(1) Zhang, L.; Zhou, M.; Wang, A.; Zhang, T. Selective Hydrogenation over Supported Metal Catalysts: From Nanoparticles to Single Atoms. *Chem. Rev.* **2020**, *120*, 683−733.

(2) Aireddy, D. R.; Ding, K. Heterolytic Dissociation of H_2 in Heterogeneous Catalysis. *ACS Catal.* **2022**, *12*, 4707−4723.
(3) Thomas, S. P.; Greenhalgh, M. D. Heterogeneous Hydrogenation of C=C and C≡C Bonds. In *Comprehensive Organic Synthesis*, Vol. *1*; Knochel, P., Molander, J. A., Eds. Elsevier: Amsterdam, 2014; pp 564−604.
(4) Mattson, B.; Foster, W.; Greimann, J.; Hoette, T.; Le, N.; Mirich, A.; Wankum, S.; Cabri, A.; Reichenbacher, C.; Schwanke, E. Heterogeneous Catalysis: The Horiuti−Polanyi Mechanism and Alkene Hydrogenation. *J. Chem. Educ.* **2013**, *90*, 613−619.
(5) Horiuti, J.; Polanyi, M. A Catalysed Reaction of Hydrogen with Water. *Nature* **1933**, *132*, 819.
(6) Horiuti, I.; Polanyi, M. Exchange Reactions of Hydrogen on Metallic Catalysts. *Trans. Faraday Soc.* **1934**, *30*, 1164−1172.
(7) Yang, B.; Burch, R.; Hardacre, C.; Hu, P.; Hughes, P. Selective Hydrogenation of Acetylene over Cu(211), Ag(211) and Au(211): Horiuti−Polanyi Mechanism vs. Non-Horiuti−Polanyi Mechanism. *Catal. Sci. Technol.* **2017**, *7*, 1508−1514.
(8) Pokochueva, E. V.; Burueva, D. B.; Salnikov, O. G.; Koptyug, I. V. Heterogeneous Catalysis and Parahydrogen-Induced Polarization. *ChemPhysChem* **2021**, *22*, 1421−1440.
(9) Kovtunov, K. V.; Beck, I. E.; Bukhtiyarov, V. I.; Koptyug, I. V. Observation of Parahydrogen-Induced Polarization in Heterogeneous Hydrogenation on Supported Metal Catalysts. *Angew. Chem., Int. Ed.* **2008**, *47*, 1492−1495.
(10) Salnikov, O. G.; Liu, H. J.; Fedorov, A.; Burueva, D. B.; Kovtunov, K. V.; Copéret, C.; Koptyug, I. V. Pairwise Hydrogen Addition in the Selective Semihydrogenation of Alkynes on Silica-Supported Cu Catalysts. *Chem. Sci.* **2017**, *8*, 2426−2430.
(11) Pokochueva, E. V.; Burueva, D. B.; Kovtunova, L. M.; Bukhtiyarov, A. V.; Gladky, A. Y.; Kovtunov, K. V.; Koptyug, I. V.; Bukhtiyarov, V. I. Mechanistic In Situ Investigation of Heterogeneous Hydrogenation over Rh/TiO_2 Catalysts: Selectivity, Pairwise Route and Catalyst Nature. *Faraday Discuss.* **2021**, *229*, 161−175.
(12) Kovtunov, K. V.; Barskiy, D. A.; Salnikov, O. G.; Burueva, D. B.; Khudorozhkov, A. K.; Bukhtiyarov, A. V.; Prosvirin, I. P.; Gerasimov, E. Y.; Bukhtiyarov, V. I.; Koptyug, I. V. Strong Metal−Support Interactions for Palladium Supported on TiO_2 Catalysts in the Heterogeneous Hydrogenation with Parahydrogen. *ChemCatChem* **2015**, *7*, 2581−2584.
(13) Zhou, R.; Zhao, E. W.; Cheng, W.; Neal, L. M.; Zheng, H.; Quiñones, R. E.; Hagelin-Weaver, H. E.; Bowers, C. R. Parahydrogen-Induced Polarization by Pairwise Replacement Catalysis on Pt and Ir Nanoparticles. *J. Am. Chem. Soc.* **2015**, *137*, 1938−1946.
(14) Salnikov, O. G.; Burueva, D. B.; Gerasimov, E. Y.; Bukhtiyarov, A. V.; Khudorozhkov, A. K.; Prosvirin, I. P.; Kovtunova, L. M.; Barskiy, D. A.; Bukhtiyarov, V. I.; Kovtunov, K. V.; Koptyug, I. V. The Effect of Oxidative and Reductive Treatments of Titania-Supported Metal Catalysts on the Pairwise Hydrogen Addition to Unsaturated Hydrocarbons. *Catal. Today* **2017**, *283*, 82−88.
(15) Zhao, E. W.; Zheng, H.; Ludden, K.; Xin, Y.; Hagelin-Weaver, H. E.; Bowers, C. R. Strong Metal−Support Interactions Enhance the Pairwise Selectivity of Parahydrogen Addition over Ir/TiO_2. *ACS Catal.* **2016**, *6*, 974−978.
(16) Zhivonitko, V. V.; Skovpin, I. V.; Szeto, K. C.; Taoufik, M.; Koptyug, I. V. Parahydrogen-Induced Polarization Study of the Silica-Supported Vanadium Oxo Organometallic Catalyst. *J. Phys. Chem. C* **2018**, *122*, 4891−4900.
(17) Parastaev, A.; Muravev, V.; Osta, E. H.; Kimpel, T. F.; Simons, J. F. M.; van Hoof, A. J. F.; Uslamin, E.; Zhang, L.; Struijs, J. J. C.; Burueva, D. B.; Pokochueva, E. V.; Kovtunov, K. V.; Koptyug, I. V.; Villar-Garcia, I. J.; Escudero, C.; Altantzis, T.; Liu, P.; Béché, A.; Bals, S.; Kosinov, N.; Hensen, J. M. Breaking Structure Sensitivity in CO_2 Hydrogenation by Tuning Metal−Oxide Interfaces in Supported Cobalt Nanoparticles. *Nat. Catal.* **2022**, *5*, 1051−1060.
(18) Burueva, D. B.; Smirnov, A. A.; Bulavchenko, O. A.; Prosvirin, I. P.; Gerasimov, E. Y.; Yakovlev, V. A.; Kovtunov, K. V.; Koptyug, I. V. Pairwise Parahydrogen Addition Over Molybdenum Carbide Catalysts. *Top. Catal.* **2020**, *63*, 2−11.
(19) Boudart, M.; Djega-Mariadassou, G. *Kinetics of Heterogeneous Catalytic Reactions*. Princeton University Press, 1984.
(20) Farkas, A. Part. II.—Catalytic Reactions of Hydrocarbons. The Activation of Hydrogen in Catalytic Reactions of Hydrocarbons. *Trans. Faraday Soc.* **1939**, *35*, 906−917.
(21) Baráth, E. Hydrogen Transfer Reactions of Carbonyls, Alkynes, and Alkenes with Noble Metals in the Presence of Alcohols/Ethers and Amines as Hydrogen Donors. *Catalysts* **2018**, *8*, No. 671.
(22) Pokochueva, E. V.; Kountoupi, E.; Janák, M.; Kuznetsov, D. A.; Prosvirin, I. P.; Müller, C.; Fedorov, A.; Koptyug, I. V. Implications for the Hydrogenation of Propyne and Propene with Parahydrogen due to the *in situ* Transformation of Rh_2C to Rh^0/C. *ChemPhysChem* **2024**, No. e202400270, DOI: 10.1002/cphc.202400270.
(23) Anasori, B.; Lukatskaya, M. R.; Gogotsi, Y. 2D Metal Carbides and Nitrides (MXenes) for Energy Storage. *Nat. Rev. Mater.* **2017**, *2*, No. 16098.
(24) Zhou, H.; Chen, Z.; Kountoupi, E.; Tsoukalou, A.; Abdala, P. M.; Florian, P.; Fedorov, A.; Müller, C. R. Two-Dimensional Molybdenum Carbide 2D-Mo_2C as a Superior Catalyst for CO_2 Hydrogenation. *Nat. Commun.* **2021**, *12*, No. 5510.
(25) Kountoupi, E.; Barrios, A. J.; Chen, Z.; Müller, C. R.; Ordomsky, V. V.; Comas-Vives, A.; Fedorov, A. The Impact of Oxygen Surface Coverage and Carbidic Carbon on the Activity and Selectivity of Two-Dimensional Molybdenum Carbide (2D-Mo_2C) in Fischer−Tropsch Synthesis. *ACS Catal.* **2024**, *14*, 1834−1845.
(26) Yan, Y.; Sall, D.; Loupias, L.; Célérier, S.; Aouine, M.; Bargiela, P.; Prévot, M.; Morfin, F.; Piccolo, L. MXene-Supported Single-Atom and Nano Catalysts for Effective Gas-Phase Hydrogenation Reactions. *Mater. Today Catal.* **2023**, *2*, No. 100010.
(27) Koptyug, I. V.; Kovtunov, K. V.; Burt, S. R.; Anwar, M. S.; Hilty, C.; Han, S. I.; Pines, A.; Sagdeev, R. Z. *para*-Hydrogen-Induced Polarization in Heterogeneous Hydrogenation Reactions. *J. Am. Chem. Soc.* **2007**, *129*, 5580−5586.
(28) Wade, L. G. *Organic Chemistry*, 6th ed.; Pearson Prentice Hall, 2006; p 279.
(29) Mao, Z.; Xie, Z.; Chen, J. G. Comparison of Heterogeneous Hydroformylation of Ethylene and Propylene over $RhCo_3$/MCM-41 Catalysts. *ACS Catal.* **2021**, *11*, 14575−14585.
(30) Liu, R. Ideal Site Geometry for Heterogeneous Catalytic Reactions: A DFT Study. *Catalysts* **2024**, *14*, No. 34.
(31) Kresse, G.; Furthmüller, J. Efficient Iterative Schemes for Ab Initio Total-Energy Calculations Using a Plane-Wave Basis Set. *Phys. Rev. B* **1996**, *54*, No. 11169.
(32) Perdew, J. P.; Burke, K.; Ernzerhof, M. Generalized Gradient Approximation Made Simple. *Phys. Rev. Lett.* **1996**, *77*, No. 3865.
(33) Grimme, S.; Antony, J.; Ehrlich, S.; Krieg, H. A Consistent and Accurate Ab Initio Parametrization of Density Functional Dispersion Correction (DFT-D) for the 94 Elements H-Pu. *J. Chem. Phys.* **2010**, *132*, No. 154104.
(34) Blöchl, P. E. Projector Augmented-Wave Method. *Phys. Rev. B* **1994**, *50*, No. 17953.
(35) Kresse, G.; Joubert, D. From Ultrasoft Pseudopotentials to the Projector Augmented-Wave Method. *Phys. Rev. B* **1999**, *59*, No. 1758.
(36) Vega, L.; Ruvireta, J.; Viñes, F.; Illas, F. Jacob's Ladder as Sketched by Escher: Assessing the Performance of Broadly Used Density Functionals on Transition Metal Surface Properties. *J. Chem. Theory Comput.* **2018**, *14*, 395−403.
(37) Gouveia, J. D.; Viñes, F.; Illas, F.; Gomes, J. R. B. MXenes Atomic Layer Stacking Phase Transitions and Their Chemical Activity Consequences. *Phys. Rev. Mater.* **2020**, *4*, No. 054003.
(38) Monkhorst, H. J.; Pack, J. D. Special Points for Brillouin-Zone Integrations. *Phys. Rev. B* **1976**, *13*, No. 5188.
(39) Zhang, Y.; Kitchaev, D. A.; Yang, J.; Chen, T.; Dacek, S. T.; Sarmiento-Pérez, R. A.; Marques, M. A. L.; Peng, H.; Ceder, G.; Perdew, J. P.; Sun, J. Efficient First-Principles Prediction of Solid Stability: Towards Chemical Accuracy. *npj Comput. Mater.* **2018**, *4*, No. 9.

(40) Li, Q.; Ouyang, Y.; Lu, S.; Bai, X.; Zhang, Y.; Shi, L.; Ling, C.; Wang, J. Perspective on Theoretical Methods and Modeling Relating to Electro-Catalysis Processes. *Chem. Commun.* **2020**, *56*, 9937−9949.
(41) Cho, J.; Lim, T.; Kim, H.; Meng, L.; Kim, J.; Lee, S.; Lee, J. H.; Jung, G. Y.; Lee, K. S.; Viñes, F.; Illas, F.; Exner, K. S.; Joo, S. H.; Choi, C. H. Importance of Broken Geometric Symmetry of Single-Atom Pt Sites for Efficient Electrocatalysis. *Nat. Commun.* **2023**, *14*, No. 3233.
(42) Gouveia, J. D.; Morales-García, Á.; Viñes, F.; Illas, F.; Gomes, J. R. B. MXenes as Promising Catalysts for Water Dissociation. *Appl. Catal., B* **2020**, *260*, No. 118191.
(43) Morales-Salvador, R.; Gouveia, J. D.; Morales-García, Á.; Viñes, F.; Gomes, J. R. B.; Illas, F. Carbon Capture and Usage by MXenes. *ACS Catal.* **2021**, *11*, 11248−11255.
(44) Henkelman, G.; Jónsson, H. A Dimer Method for Finding Saddle Points on High Dimensional Potential Surfaces Using only First Derivatives. *J. Chem. Phys.* **1999**, *111*, 7010−7022.
(45) Reuter, K.; Scheffler, M. Composition, Structure, and Stability of RuO_2(110) as a Function of Oxygen Pressure. *Phys. Rev. B* **2001**, *65*, No. 035406.
(46) Halim, J.; Kota, S.; Lukatskaya, M. R.; Naguib, M.; Zhao, M. Q.; Moon, E. J.; Pitock, J.; Nanda, J.; May, S. J.; Gogotsi, Y.; Barsoum, M. W. Synthesis and Characterization of 2D Molybdenum Carbide (MXene). *Adv. Funct. Mater.* **2016**, *26*, 3118−3127.
(47) Deeva, E. B.; Kurlov, A.; Abdala, P. M.; Lebedev, D.; Kim, S. M.; Gordon, C. P.; Tsoukalou, A.; Fedorov, A.; Müller, C. R. In Situ XANES/XRD Study of the Structural Stability of Two-Dimensional Molybdenum Carbide Mo_2CT_x: Implications for the Catalytic Activity in the Water−Gas Shift Reaction. *Chem. Mater.* **2019**, *31*, 4505−4513.
(48) Jurado, A.; Morales-García, Á.; Viñes, F.; Illas, F. Molecular Mechanism and Microkinetic Analysis of the Reverse Water Gas Shift Reaction Heterogeneously Catalyzed by the Mo_2C MXene. *ACS Catal.* **2022**, *12*, 15658−15667.
(49) Bond, G. C. *Metal-Catalysed Reactions of Hydrocarbons*; Springer: Boston, MA, USA, 2005.
(50) Pozzo, M.; Alfè, D.; Amieiro, A.; French, S.; Pratt, A. Hydrogen Dissociation and Diffusion on Ni- and Ti-Doped Mg(0001) Surfaces. *J. Chem. Phys.* **2008**, *128*, No. 094703.
(51) Kozuch, S.; Shaik, S. How to Conceptualize Catalytic Cycles? The Energetic Span Model. *Acc. Chem. Res.* **2011**, *44*, 101−110.
(52) Podkolzin, S. G.; Watwe, R. M.; Yan, Q.; de Pablo, J. J.; Dumesic, J. A. DFT Calculations and Monte Carlo Simulations of the Co-Adsorption of Hydrogen Atoms and Ethylidyne Species on Pt(111). *J. Phys. Chem. B* **2001**, *105*, 8550−8562.
(53) Li, H.; Ding, Z. Hydrogen Coverage Dependent C═C Hydrogenation Activity on Rh(111). *Chem. Phys. Lett.* **2020**, *746*, No. 137287.
(54) McCormick, J.; Korchak, S.; Mamone, S.; Ertas, Y.; Liu, Z.; Verlinsky, L.; Wagner, S.; Gloggler, S.; Bouchard, L. Over 12% Polarization and 20 minute Lifetime of ^{15}N on Choline Derivative Utilizing Parahydrogen and Rh Nanocatalyst in Water. *Angew. Chem., Int. Ed.* **2018**, *57*, 10692−10696.
(55) Vilé, G.; Baudouin, D.; Remediakis, I. N.; Copéret, C.; López, N.; Pérez-Ramírez, J. Silver Nanoparticles for Olefin Production: New Insights into the Mechanistic Description of Propyne Hydrogenation. *ChemCatChem* **2013**, *5*, 3750−3759.
(56) Yang, B.; Gong, X.-Q.; Wang, H.-F.; Cao, X.-M.; Rooney, J. J.; Hu, P. Evidence To Challenge the Universality of the Horiuti−Polanyi Mechanism for Hydrogenation in Heterogeneous Catalysis: Origin and Trend of the Preference of a Non-Horiuti−Polanyi Mechanism. *J. Am. Chem. Soc.* **2013**, *135*, 15244−15250.
(57) Dong, Y.; Ebrahimi, M.; Tillekaratne, A.; Zaera, F. Direct Addition Mechanism during the Catalytic Hydrogenation of Olefins over Platinum Surfaces. *J. Phys. Chem. Lett.* **2016**, *7*, 2439−2443.

https://doi.org/10.1021/acscatal.4c02534
ACS Catal. 2024, 14, 12500−12511

3.6. References

1. Kabeyi, M. J. B.; Olanrewaju, O. A., Sustainable Energy Transition for Renewable and Low Carbon Grid Electricity Generation and Supply. *Front. Energy Res.* **2022,** *9*, 743114.
2. Strielkowski, W.; Civín, L.; Tarkhanova, E.; Tvaronavičienė, M.; Petrenko, Y., Renewable Energy in the Sustainable Development of Electrical Power Sector: A Review. *Energies* **2021,** *14*, 8240.
3. Dresselhaus, M. S.; Thomas, I. L., Alternative Energy Technologies. *Nature* **2001,** *414*, 332–337.
4. Turner, J. A., Sustainable Hydrogen Production. *Science* **2004,** *305*, 972–4.
5. Pareek, A.; Dom, R.; Gupta, J.; Chandran, J.; Adepu, V.; Borse, P. H., Insights into Renewable Hydrogen Energy: Recent Advances and Prospects. *Mater. Sci. Energy Technol.* **2020,** *3*, 319–327.
6. Jones, M. W.; Peters, G. P.; Gasser, T.; Andrew, R. M.; Schwingshackl, C.; Gütschow, J.; Houghton, R. A.; Friedlingstein, P.; Pongratz, J.; Le Quéré, C., National Contributions to Climate Change Due to Historical Emissions of Carbon Dioxide, Methane, and Nitrous Oxide Since 1850. *Sci. Data* **2023,** *10*, 155.
7. Zhang, X.; Guo, S.-X.; Gandionco, K. A.; Bond, A. M.; Zhang, J., Electrocatalytic Carbon Dioxide Reduction: From Fundamental Principles to Catalyst Design. *Mater. Today Adv.* **2020,** *7*, 100074.
8. Naguib, M.; Mochalin, V. N.; Barsoum, M. W.; Gogotsi, Y., 25th Anniversary Article: MXenes: A New Family of Two-Dimensional Materials. *Adv. Mater.* **2014,** *26*, 992–1005.
9. Hope, M. A.; Forse, A. C.; Griffith, K. J.; Lukatskaya, M. R.; Ghidiu, M.; Gogotsi, Y.; Grey, C. P., NMR Reveals the Surface Functionalisation of Ti_3C_2 MXene. *Phys. Chem. Chem. Phys.* **2016,** *18*, 5099–5102.
10. Handoko, A. D.; Khoo, K. H.; Tan, T. L.; Jin, H.; Seh, Z. W., Establishing New Scaling Relations on Two-Dimensional MXenes for CO_2 Electroreduction. *J. Mater. Chem. A* **2018,** *6*, 21885–21890.
11. Chen, H.; Handoko, A. D.; Xiao, J.; Feng, X.; Fan, Y.; Wang, T.; Legut, D.; Seh, Z. W.; Zhang, Q., Catalytic Effect on CO_2 Electroreduction by Hydroxyl-

Terminated Two-Dimensional MXenes. *ACS Appl. Mater. Interfaces* **2019,** *11*, 36571–36579.

12. Naguib, M.; Kurtoglu, M.; Presser, V.; Lu, J.; Niu, J.; Heon, M.; Hultman, L.; Gogotsi, Y.; Barsoum, M. W., Two-Dimensional Nanocrystals Produced by Exfoliation of Ti_3AlC_2. In *MXenes*, Jenny Stanford Publishing: **2011**; pp 15–29.
13. Olabi, A. G.; Abdelkareem, M. A.; Al-Murisi, M.; Shehata, N.; Alami, A. H.; Radwan, A.; Wilberforce, T.; Chae, K. J.; Sayed, E. T., Recent Progress in Green Ammonia: Production, Applications, Assessment; Barriers, and Its Role in Achieving the Sustainable Development Goals. *Energy Convers. Manag.* **2023,** *277*, 116594.
14. Pattabathula, V.; Richardson, J., Introduction to Ammonia Production. *Chem. Eng. Prog*, **2016,** *112*, 69–75.
15. Qing, G.; Ghazfar, R.; Jackowski, S. T.; Habibzadeh, F.; Ashtiani, M. M.; Chen, C. P.; Smith III, M. R.; Hamann, T. W., Recent Advances and Challenges of Electrocatalytic N_2 Reduction to Ammonia. **2020,** *120*, 5437–5516.
16. Liu, S.; Wang, M.; Qian, T.; Ji, H.; Liu, J.; Yan, C., Facilitating Nitrogen Accessibility to Boron-Rich Covalent Organic Frameworks via Electrochemical Excitation for Efficient Nitrogen Fixation. *Nat. Commun.* **2019,** *10*, 3898.
17. Shi, L.; Yin, Y.; Wang, S.; Sun, H., Rational Catalyst Design for N_2 Reduction under Ambient Conditions: Strategies toward Enhanced Conversion Efficiency. *ACS Catal.* **2020,** *10*, 6870–6899.
18. Machado, R. M.; Heier, K. R.; Broekhuis, R. R., Developments in Hydrogenation Technology for Fine-Chemical and Pharmaceutical Applications. **2001,** *4*, 745–755.
19. Gao, G.; O'Mullane, A. P.; Du, A., 2D MXenes: A New Family of Promising Catalysts for the Hydrogen Evolution Reaction. *ACS Catal.* **2017,** *7*, 494–500.
20. Ran, J.; Gao, G.; Li, F. T.; Ma, T. Y.; Du, A.; Qiao, S. Z., Ti_3C_2 MXene Co-Catalyst on Metal Sulfide Photo-Absorbers for Enhanced Visible-Light Photocatalytic Hydrogen Production. *Nat. Commun.* **2017,** *8*, 13907.
21. Ling, C.; Shi, L.; Ouyang, Y.; Wang, J., Searching for Highly Active Catalysts for Hydrogen Evolution Reaction Based on O-Terminated MXenes through a Simple Descriptor. *Chem. Mater.* **2016,** *28*, 9026–9032.
22. Li, N.; Chen, X.; Ong, W. J.; MacFarlane, D. R.; Zhao, X.; Cheetham, A. K.;

Sun, C., Understanding of Electrochemical Mechanisms for CO_2 Capture and Conversion into Hydrocarbon Fuels in Transition-Metal Carbides (MXenes). *ACS Nano* **2017,** *11*, 10825–10833.

23. Handoko, A. D.; Chen, H.; Lum, Y.; Zhang, Q.; Anasori, B.; Seh, Z. W., Two-Dimensional Titanium and Molybdenum Carbide MXenes as Electrocatalysts for CO_2 Reduction. *iScience* **2020,** *23*, 101181.
24. Kamysbayev, V.; Filatov, A. S.; Hu, H.; Rui, X.; Lagunas, F.; Wang, D.; Klie, R. F.; Talapin, D. V., Covalent Surface Modifications and Superconductivity of Two-Dimensional Metal Carbide MXenes. *Science* **2020,** *369*, 979–983.
25. Persson, I.; Halim, J.; Hansen, T. W.; Wagner, J. B.; Darakchieva, V.; Palisaitis, J.; Rosen, J.; Persson, P. O. Å., How Much Oxygen Can a MXene Surface Take Before It Breaks? *Adv. Funct. Mater.* **2020,** *30*, 1909005.
26. Naguib, M.; Kurtoglu, M.; Presser, V.; Lu, J.; Niu, J.; Heon, M.; Hultman, L.; Gogotsi, Y.; Barsoum, M. W., Two-Dimensional Nanocrystals Produced by Exfoliation of Ti_3AlC_2. *Adv. Mater.* **2011,** *23*, 4248–4253.
27. Ghidiu, M.; Lukatskaya, M. R.; Zhao, M. Q.; Gogotsi, Y.; Barsoum, M. W., Conductive Two-Dimensional Titanium Carbide 'Clay' with High Volumetric Capacitance. *Nature* **2014,** *516*, 78–81.
28. Yu, X.; Cai, X.; Cui, H.; Lee, S.-W.; Yu, X.-F.; Liu, B., Fluorine-Free Preparation of Titanium Carbide MXene Quantum Dots with High Near-Infrared Photothermal Performances for Cancer Therapy. *Nanoscale* **2017,** *9*, 17859–17864.
29. Tan, X. Q.; Mo, W.; Lin, X.; Loh, J. Y.; Mohamed, A. R.; Ong, W. J., Retrospective Insights into Recent MXene-Based Catalysts for CO_2 Electro/Photoreduction: How Far Have We Gone? *Nanoscale* **2023,** *15*, 6536–6562.
30. Pandey, M.; Thygesen, K. S., Two-Dimensional MXenes as Catalysts for Electrochemical Hydrogen Evolution: A Computational Screening Study. *J. Phys. Chem. C* **2017,** *121*, 13593–13598.
31. Meng, L.; Yan, L. K.; Viñes, F.; Illas, F., Effect of Terminations on the Hydrogen Evolution Reaction Mechanism on Ti_3C_2 MXene. *J. Mater. Chem. A* **2023,** *11*, 6886–6900.

32. Meng, L.; Yan, L. K.; Viñes, F.; Illas, F., Surface Termination Dependent Carbon Dioxide Reduction Reaction on Ti_3C_2 MXene. *J. Mater. Chem. A* **2024,** *12*, 7856–7874.
33. Meng, L.; Viñes, F.; Illas, F., Theoretical Modelling of the Hydrogen Evolution Reaction on MXenes: A Critical Review. *Curr. Opinion. Electrochem.* **2023,** *40*, 101332.
34. Meng, L.; Tayyebi, E.; Exner, K. S.; Viñes, F.; Illas, F., MXenes as Electrocatalysts for the CO2 Reduction Reaction: Recent Advances and Future Challenges. *ChemElectroChem* **2024,** *11*, e202300598.
35. Sriver D. F.; and Atkins P. W., *Inorganic Chemistry*, 5th ed., Freeman, W.H. and Company, New York, **2009**.
36. Nørskov, J. K.; Rossmeisl, J.; Logadottir, A.; Lindqvist, L.; Kitchin, J. R.; Bligaard, T.; Jónsson, H., Origin of the Overpotential for Oxygen Reduction at a Fuel-Cell Cathode. *J. Phys. Chem. B* **2004,** *108*, 17886–17892.
37. Conway, B. E.; Tilak, B. V., Interfacial Processes Involving Electrocatalytic Evolution and Oxidation of H_2, and the Role of Chemisorbed H. *Electrochim. Acta* **2002,** *47*, 3571–3594.
38. López, M.; Exner, K. S.; Viñes, F.; Illas, F., Theoretical Study of the Mechanism of the Hydrogen Evolution Reaction on the V_2C MXene: Thermodynamic and Kinetic Aspects. *J. Catal.* **2023,** *421*, 252–263.
39. Wu, J.; Huang, Y.; Ye, W.; Li, Y., CO_2 Reduction: From the Electrochemical to Photochemical Approach. *Adv. Sci.* **2017,** *4*, 1700194.
40. Xiao, Y.; Zhang, W., High Throughput Screening of M_3C_2 MXenes for Efficient CO_2 Reduction Conversion into Hydrocarbon Fuels. *Nanoscale* **2020,** *12*, 7660–7673.
41. M. Pourbaix, *Atlas of Electrochemical Equilibria in Aqueous Solutions*. National Association of Corrosion Engineers (NACE), Houston, Texas, USA, **1974.**
42. Xue, N.; Li, X.; Han, L.; Zhu, H.; Zhao, X.; Zhuang, J.; Gao, Z.; Tao, X., Fluorine-Free Synthesis of Ambient-Stable Delaminated Ti_2CT_x (MXene). *J. Mater. Chem. A* **2022,** *10*, 7960–7967.
43. Yang, S.; Zhang, P.; Wang, F.; Ricciardulli, A. G.; Lohe, M. R.; Blom, P. W.; Feng, X. J. A. C., Fluoride-Free Synthesis of Two-Dimensional Titanium Carbide

(MXene) Using a Binary Aqueous System. *Angew. Chem. Int. Ed.* **2018,** *130*, 15717–15721.

44. Pang, S. Y.; Wong, Y. T.; Yuan, S.; Liu, Y.; Tsang, M. K.; Yang, Z.; Huang, H.; Wong, W. T.; Hao, J., Universal Strategy for HF-Free Facile and Rapid Synthesis of Two-dimensional MXenes as Multifunctional Energy Materials. *J. Am. Chem. Soc.* **2019,** *141*, 9610–9616.
45. Anasori, B.; Lukatskaya, M. R.; Gogotsi, Y., 2D Metal Carbides and Nitrides (MXenes) for Energy Storage. *Nat. Rev. Mater.* **2017,** *2*, 16098.
46. Gan, J.; Li, F.; Tang, Y.; Tang, Q., Theoretical Study of Transition-Metal-Modified Mo_2CO_2 MXene as a Catalyst for the Hydrogen Evolution Reaction. *ChemSusChem* **2020,** *13*, 6005–6015.
47. López, M.; Exner, K. S.; Viñes, F.; Illas, F., Computational Pourbaix Diagrams for MXenes: A Key Ingredient toward Proper Theoretical Electrocatalytic Studies. *Theory Simul.* **2023,** *6*, 2200217.
48. Guo, Z.; Li, Y.; Sa, B.; Fang, Y.; Lin, J.; Huang, Y.; Tang, C.; Zhou, J.; Miao, N.; Sun, Z., M_2C-Type MXenes: Promising Catalysts for CO_2 Capture and Reduction. *Appl. Surf. Sci.* **2020,** *521*, 146436.
49. Viñes, F.; Sousa, C.; Liu, P.; Rodriguez, J. A.; Illas, F., A Systematic Density Functional Theory Study of the Electronic Structure of Bulk and (001) Surface of Transition-Metals Carbides. *J. Chem. Phys.* **2005,** *122*, 174709.
50. Ooka, H.; Huang, J.; Exner, K. S., The Sabatier Principle in Electrocatalysis: Basics, Limitations, and Extensions. *Front. Energy Res.* **2021,** *9*, 654460.
51. Pankhurst, J. R.; Iyengar, P.; Loiudice, A.; Mensi, M.; Buonsanti, R., Metal–Ligand Bond Strength Determines the Fate of Organic Ligands on the Catalyst Surface During the Electrochemical CO_2 Reduction Reaction. *Chem. Sci.* **2020,** *11*, 9296–9302.
52. Mazheika, A.; Wang, Y. G.; Valero, R.; Viñes, F.; Illas, F.; Ghiringhelli, L. M.; Levchenko, S. V.; Scheffler, M., Artificial-Intelligence-Driven Discovery of Catalyst Genes with Application to CO_2 Activation on Semiconductor Oxides. *Nat. Commun.* **2022,** *13*, 419.

53. López, M.; Broderick, L.; Carey, J. J.; Viñes, F.; Nolan, M.; Illas, F., Tuning Transition Metal Carbide Activity by Surface Metal Alloying: A Case Study on CO_2 Capture and Activation. *Phys. Chem. Chem. Phys.* **2018,** *20*, 22179–22186.
54. Morales-García, Á.; Mayans-Llorach, M.; Viñes, F.; Illas, F., Thickness biased capture of CO_2 on carbide MXenes. *Phys. Chem. Chem. Phys.* **2019,** *21*, 23136–23142.
55. Wiensch, J. D.; John, J.; Velazquez, J. M.; Torelli, D. A.; Pieterick, A. P.; McDowell, M. T.; Sun, K.; Zhao, X.; Brunschwig, B. S.; Lewis, N. S., Comparative Study in Acidic and Alkaline Media of the Effects of pH and Crystallinity on the Hydrogen-Evolution Reaction on MoS_2 and $MoSe_2$. *ACS Energy Lett.* **2017,** *2*, 2234–2238.
56. Huang, B.; Zhou, N.; Chen, X.; Ong, W.-J.; Li, N., Insights into the Electrocatalytic Hydrogen Evolution Reaction Mechanism on Two-Dimensional Transition-Metal Carbonitrides (MXene). *Chem. Eur. J.* **2018,** *24*, 18479–18486.
57. Nørskov, J. K.; Bligaard, T.; Logadottir, A.; Kitchin, J. R.; Chen, J. G.; Pandelov, S.; Stimming, U., Trends in the Exchange Current for Hydrogen Evolution. *J. Electrochem. Soc.* **2005,** *152*, J23−J26.
58. Lin, L.; Miao, N.; Wen, Y.; Zhang, S.; Ghosez, P.; Sun, Z.; Allwood, D. A., Sulfur-Depleted Monolayered Molybdenum Disulfide Nanocrystals for Superelectrochemical Hydrogen Evolution Reaction. *ACS Nano* **2016,** *10*, 8929–8937.
59. Bonde, J.; Moses, P. G.; Jaramillo, T. F.; Nørskov, J. K.; Chorkendorff, I., Hydrogen Evolution on Nano-Particulate Transition Metal Sulfides. *Faraday Discuss.* **2009,** *140*, 219–231.
60. Zheng, Y.; Jiao, Y.; Zhu, Y.; Li, L. H.; Han, Y.; Chen, Y.; Du, A.; Jaroniec, M.; Qiao, S. Z., Hydrogen Evolution by a Metal-Free Electrocatalyst. *Nat. Commun.* **2014,** *5*, 3783.
61. Cai, X.; Yi, W.; Chen, J.; Lu, L.; Sun, B.; Ni, Y.; Redfern, S. A. T.; Wang, H.; Chen, Z.; Chen, Y., A Novel 2D Porous C_3N_2 Framework as a Promising Anode Material with Ultra-High Specific Capacity for Lithium-Ion Batteries. *J. Mater. Chem. A* **2022,** *10*, 6551–6559.

62. Handoko, A. D.; Fredrickson, K. D.; Anasori, B.; Convey, K. W.; Johnson, L. R.; Gogotsi, Y.; Vojvodic, A.; Seh, Z. W., Tuning the Basal Plane Functionalization of Two-Dimensional Metal Carbides (MXenes) To Control Hydrogen Evolution Activity. *ACS Appl. Energy Mater.* **2018,** *1*, 173–180.
63. Zhang, Y.; Chen, L.; Gui, Y.; Liu, L., Catalytic Transfer Hydrogenation of Nitrobenzene Over Ti_3C_2/Pd Nanohybrids Boosted by Electronic Modification and Hydrogen Evolution Inhibition. *Appl. Surf. Sci.* **2022,** *592*, 153334.
64. Li, T.; Yao, L.; Liu, Q.; Gu, J.; Luo, R.; Li, J.; Yan, X.; Wang, W.; Liu, P.; Chen, B.; Zhang, W.; Abbas, W.; Naz, R.; Zhang, D., Fluorine-Free Synthesis of High-Purity $Ti_3C_2T_x$ (T=OH, O) via Alkali Treatment. *Angew. Chem. Int. Ed.* **2018,** *57*, 6115–6119.
65. Attanayake, N. H.; Banjade, H. R.; Thenuwara, A. C.; Anasori, B.; Yan, Q.; Strongin, D. R., Electrocatalytic CO_2 Reduction on Earth Abundant 2D Mo_2C and Ti_3C_2 MXenes. *Chem. Commun.* **2021,** *57*, 1675–1678.
66. Gouveia, J. D.; Morales-García, Á.; Viñes, F.; Illas, F.; Gomes, J. R. B., MXenes as Promising Catalysts for Water Dissociation. *Appl. Catal. B: Environ* **2020,** *260*, 118191.
67. Cao, S.; Hu, Y.; Yang, C.; Li, J.; Chen, H.; Wei, S.; Liu, S.; Wang, Z.; Sun, D.; Lu, X., Constructing Surface Vacancy to Activate the Stuck MXenes for High-Performance CO_2 Reduction Reaction. *J. CO_2 Util.* **2022,** *62*, 102074.
68. Lu, S.; Zhang, Y.; Lou, F.; Yu, Z., Theoretical Study of Single Transition Metal Atom Catalysts Supported on Two-Dimensional Nb_2NO_2 for Efficient Electrochemical CO_2 Reduction to CH_4. *J. CO_2 Util.* **2022,** *62*, 102069.
69. Peterson, A. A.; Abild-Pedersen, F.; Studt, F.; Rossmeisl, J.; Nørskov, J. K., How Copper Catalyzes the Electroreduction of Carbon Dioxide into Hydrocarbon Fuels. *Energy Environ. Sci.* **2010,** *3*, 1311–1315.
70. Hong, X.; Chan, K.; Tsai, C.; Nørskov, J. K., How Doped MoS_2 Breaks Transition-Metal Scaling Relations for CO_2 Electrochemical Reduction. *ACS Catal.* **2016,** *6*, 4428–4437.
71. Sheets, B. L.; Botte, G. G., Electrochemical Nitrogen Reduction to Ammonia under Mild Conditions Enabled by a Polymer Gel Electrolyte. *Chem. Comm.* **2018,** *54*, 4250–4253.

72. Ortuño, M. A.; Hollóczki, O.; Kirchner, B.; López, N., Selective Electrochemical Nitrogen Reduction Driven by Hydrogen Bond Interactions at Metal–Ionic Liquid Interfaces. *J. Phys. Chem. Lett.* **2019,** *10*, 513–517.
73. McEnaney, J. M.; Singh, A. R.; Schwalbe, J. A.; Kibsgaard, J.; Lin, J. C.; Cargnello, M.; Jaramillo, T. F.; Nørskov, J. K., Ammonia Synthesis from N_2 and H_2O using a Lithium Cycling Electrification Strategy at Atmospheric Pressure. *Energy Environ. Sci.* **2017,** *10*, 1621–1630.
74. Malkhandi, S.; Yang, B.; Manohar, A. K.; Prakash, G. K.; Narayanan, S. R., Self-Assembled Monolayers of N-Alkanethiols Suppress Hydrogen Evolution and Increase the Efficiency of Rechargeable Iron Battery Electrodes. *J. Am. Chem. Soc.* **2013,** *135*, 347–353.
75. Manohar, A. K.; Malkhandi, S.; Yang, B.; Yang, C.; Prakash, G. S.; Narayanan, S. R., A High-Performance Rechargeable Iron Electrode for Large-Scale Battery-Based Energy Storage. *J. Electrochem. Soc.* **2012,** *159*, A1209.
76. Brown, K. A.; Harris, D. F.; Wilker, M. B.; Rasmussen, A.; Khadka, N.; Hamby, H.; Keable, S.; Dukovic, G.; Peters, J. W.; Seefeldt, L. C.; King, P. W., Light-Driven Dinitrogen Reduction Catalyzed by a CdS: Nitrogenase MoFe Protein Biohybrid. *Science* **2016,** *352*, 448–450.
77. Zhu, D.; Zhang, L.; Ruther, R. E.; Hamers, R. J., Photo-Illuminated Diamond as a Solid-State Source of Solvated Electrons in Water for Nitrogen Reduction. *Nat. Mater.* **2013,** *12*, 836–841.
78. Guo, X.; Huang, S. J. E. A., Tuning Nitrogen Reduction Reaction Activity via Controllable Fe Magnetic Moment: A Computational Study of Single Fe Atom Supported on Defective Graphene. *Electrochim. Acta* **2018,** *284*, 392–399.
79. Kang, Z.; Cai, J.; Ye, D.; Zhao, H.; Luo, J.; Zhang, J., Three-Dimensional Nitrogen-Doped MXene as Support to Form High-Performance Platinum Catalysts for Water-Electrolysis to Produce Hydrogen. *J. Chem. Eng.* **2022,** *446*, 137443.
80. Bai, S.; Yang, M.; Jiang, J.; He, X.; Zou, J.; Xiong, Z.; Liao, G.; Liu, S., Recent Advances of MXenes as Electrocatalysts for Hydrogen Evolution Reaction. *npj 2D Mater. Appl.* **2021,** *5*, 78.

81. Wang, C.; Wang, X.; Zhang, T.; Qian, P.; Lookman, T.; Su, Y., A Descriptor for the Design of 2D MXene Hydrogen Evolution Reaction Electrocatalysts. *J. Mater. Chem. A* **2022,** *10*, 18195–18205.
82. Jiang, W.; Zou, X.; Du, H.; Gan, L.; Xu, C.; Kang, F.; Duan, W.; Li, J., Universal Descriptor for Large-Scale Screening of High-Performance MXene-Based Materials for Energy Storage and Conversion. *Chem. Mater.* **2018,** *30*, 2687–2693.
83. Abidi, N.; Bonduelle-Skrzypczak, A.; Steinmann, S. N., Revisiting the Active Sites at the MoS_2/H_2O Interface via Grand-Canonical DFT: The Role of Water Dissociation. *ACS Appl. Mater. Interfaces* **2020,** *12*, 31401–31410.
84. Abidi, N.; Bonduelle-Skrzypczak, A.; Steinmann, S. N., How Stable Are 2H-MoS_2 Edges under Hydrogen Evolution Reaction Conditions? *J. Phys. Chem. C* **2021,** *125*, 17058–17067.
85. Ekspong, J.; Gracia-Espino, E.; Wågberg, T., Hydrogen Evolution Reaction Activity of Heterogeneous Materials: A Theoretical Model. *J. Phys. Chem. C* **2020,** *124*, 20911–20921.
86. Jiao, Y.; Zheng, Y.; Davey, K.; Qiao, S. Z., Activity Origin and Catalyst Design Principles for Electrocatalytic Hydrogen Evolution on Heteroatom-Doped Graphene. *Nat. Energy* **2016,** *1*, 16130.
87. Anand, R.; Ram, B.; Umer, M.; Zafari, M.; Umer, S.; Lee, G.; Kim, K. S., Doped MXene Combinations as Highly Efficient Bifunctional and Multifunctional Catalysts for Water Splitting and Metal–Air Batteries. *J. Mater. Chem. A* **2022,** *10*, 22500–22511.
88. Abraham, B. M.; Sinha, P.; Halder, P.; Singh, J. K., Fusing a Machine Learning Strategy with Density Functional Theory to Hasten the Discovery of 2D MXene-Based Catalysts for Hydrogen Generation. *J. Mater. Chem. A* **2023,** *11*, 8091–8100.
89. Erisman, J. W.; Sutton, M. A.; Galloway, J.; Klimont, Z.; Winiwarter, W. How a Century of Ammonia Synthesis Changed the World. *Nat. Geosci.* **2008,** *1*, 636–639.
90. Chirik, P. J. One Electron at a Time. *Nat. Chem.* **2009,** *1*, 520–522.
91. Suryanto, B. H. R.; Du, H.-L.; Wang, D.; Chen, J.; Simonov, A. N.; MacFarlane, D. R. Challenges and Prospects in the Catalysis of Electroreduction of Nitrogen to Ammonia. *Nat. Catal.* **2019,** *2*, 520–296.

92. Soloveichik, G. Electrochemical Synthesis of Ammonia as a Potential Alternative to the Haber-Bosch Process. *Nat. Catal.* **2019,** *2*, 377–380.
93. Machaj, K.; Kupecki, J.; Malecha, Z.; Morawski, A. W.; Skrzypkiewicz, M.; Stanclik, M.; Chorowski, M. Ammonia as a Potential Marine Fuel: A Review. *Energy Strat. Rev.* **2022,** *44*, 100926.
94. Hasan, M. H.; Mahlia, T. M.; Mofijur, M.; Rizwanul Fattah, I. M.; Handayani, F.; Ong, H. C.; Silitonga, A. S. A Comprehensive Review on the Recent Development of Ammonia as a Renewable Energy Carrier. *Energies* **2021***, 14,* 3732.
95. Cleveland, C. C.; Townsend, A. R.; Schimel, D. S.; Fisher, H.; Howarth, R. W.; Hedin, L. O.; Perakis, S. S.; Latty, E. F.; Von Fischer, J. C.; Elseroad, A.; Wasson, M. F. Global Patterns of Terrestrial Biological Nitrogen (N_2) Fixation in Natural Ecosystems. *Global Biogeochem. Cycles* **1999,** *13*, 623–645.
96. Bennaamane, S.; Rialland, B.; Khrouz, L.; Fustier-Boutignon, M.; Bucher, C.; Clot, E.; Mézailles, N., Ammonia Synthesis at Room Temperature and Atmospheric Pressure from N_2: A Boron-Radical Approach. *Angew. Chem. Int. Ed.* **2023,** *62*, e202209102.
97. Qiu, W.; Xie, X.-Y.; Qiu, J.; Fang, W.-H.; Liang, R.; Ren, X.; Ji, X.; Cui, G.; Asiri, A. M.; Cui, G.; Tang, B.; Sun, X. High-Performance Artificial Nitrogen Fixation at Ambient Conditions Using a Metal-Free Electrocatalyst. *Nat. Commun.* **2018,** *9*, 3485.
98. Kaiprathu, A.; Velayudham, P.; Teller, H.; Schechter, A. Mechanisms of Electrochemical Nitrogen Gas Reduction to Ammonia Under Ambient Conditions: A Focused Review. *J. Solid State Electrochem.* **2022,** *26*, 1897–1917.
99. He, H.; Wen, H.-M.; Li, H.-K.; Zhang, H.-W. Recent Advances in Metal-Organic Frameworks and their Derivatives for Electrocatalytic Nitrogen Reduction to Ammonia. *Coord. Chem. Rev.* **2022,** *471*, 214761.
100. Gouveia, J. D.; Morales-García, Á.; Viñes, F.; Gomes, J. R. B.; Illas, F. Facile Heterogeneously Catalyzed Nitrogen Fixation by MXenes. *ACS Catal.* **2020,** *10*, 5049–5056.
101. Azofra, L. M.; Li, N.; MacFarlane, D. R.; Sun, C. Promising Prospects for 2D *d*2–*d*4 M_3C_2 Transition Metal Carbides (MXenes) in N2 Capture and Conversion into Ammonia. *Energy Environ. Sci.* **2016,** *9*, 2545−2549.

102. Wang, Y.; Xu, Y.; Hu, M.; Ling, H.; Zhu, X. MXenes: Focus on Optical and Electronic Properties and Corresponding Applications. *Nanophotonics* **2020,** *9*, 1601−1620.
103. Ibragimova, R.; Puska, M. J.; Komsa, H.-P. pH-Dependent Distribution of Functional Groups on Titanium-Based MXenes. *ACS Nano* **2019,** *13*, 9171−9181.
104. Caffrey, N. M. Effect of Mixed Surface Terminations on the Structural and Electrochemical Properties of Two-Dimensional $Ti_3C_2T_2$ and V_2CT_2 MXenes Multilayers. *Nanoscale* **2018,** *10*, 13520−13530.
105. Johnson, L. R.; Sridhar, S.; Zhang, L.; Fredrickson, K. D.; Raman, A. S.; Jang, J.; Leach, C.; Padmanabhan, A.; Price, C. C.; Frey, N. C.; Raizada, A.; Rajaraman, V.; Saiprasad, S. A.; Tang, X.; Vojvodic, A. MXene Materials for the Electrochemical Nitrogen Reduction —Functionalized or Not? *ACS Catal.* **2020,** *10*, 253−264
106. Xia, J.; Yang, S.-Z.; Wang, B.; Wu, P.; Popovs, I.; Li, H.; Irle, S.; Dai, S.; Zhu, H. Boosting Electrosynthesis of Ammonia on Surface-Engineered MXene Ti_3C_2. *Nano Energy* **2020,** *72*, 104681.
107. Ding, Y.; Zhang, J.; Guan, A.; Wang, Q.; Li, S.; Al-Enizi, A. M.; Qian, L.; Zhang, L.; Zheng, G. Promoting N2 Electroreduction to Ammonia by Fluorine-Terminating $Ti_3C_2T_x$ MXene. *Nano Converg.* **2021,** *8*, 14.
108. Légaré, M.-A.; Bélanger-Chabot, G.; Dewhurst, R. D.; Welz, E.; Krummenacher, I.; Engels, B.; Braunschweig, H. Nitrogen Fixation and Reduction at Boron. *Science* **2018,** *359*, 896−900.
109. Ma, F.; Jiao, Y.; Gao, G.; Gu, Y.; Bilic, A.; Chen, Z.; Du, A. Graphene-like Two-Dimensional Ionic Boron with Double Dirac Cones at Ambient Condition. *Nano Lett.* **2016,** *16*, 3022−3028.
110. Xie, Y.; Naguib, M.; Mochalin, V. N.; Barsoum, M. W.; Gogotsi, Y.; Yu, X.; Nam, K.-W.; Yang, X.-Q.; Kolesnikov, A. I.; Kent, P. R. C. Role of Surface Structure on Li-Ion Energy Storage Capacity of Two-Dimensional Transition-Metal Carbides. *J. Am. Chem. Soc.* **2014,** *136*, 6385−6394.
111. Karlsson, L. H.; Birch, J.; Halim, J.; Barsoum, M. W.; Persson, P. O. Å. Atomically Resolved Structural and Chemical Investigation of Single MXene Sheets. *Nano Lett.* **2015,** *15*, 4955−4960.

112. Zhang, N.; Wang, M.-y.; Liu, J.-Y. Prediction of Single-Boron Anchored on MXene Catalysts for High-Efficient Electrocatalytic Nitrogen Reduction Reaction. *Mol. Catal.* **2022,** *531*, 112658.
113. Wang, Y.; Qian, X.; Zheng, G.; Tian, Z.; Zhang, Q. Boron-Doped MXenes as Electrocatalysts for Nitrogen Reduction Reaction: A Theoretical Study. *Front. Chem. Eng.* **2021,** *3*, 702129.
114. Zheng, S.; Li, S.; Mei, Z.; Hu, Z.; Chu, M.; Liu, J.; Chen, X.; Pan, F. Electrochemical Nitrogen Reduction Reaction Performance of Single-Boron Catalysts Tuned by MXene Substrates. *J. Phys. Chem. Lett.* **2019,** *10*, 6984−6989.
115. Meng, L.; Viñes, F.; Illas, F., Unveiling the Synergy between Surface Terminations and Boron Configuration in Boron-Based Ti_3C_2 MXenes Electrocatalysts for Nitrogen Reduction Reaction. *ACS Catal.* **2024,** Under Review.
116. Chen, S.; Liu, X.; Xiong, J.; Mi, L.; Li, Y. Engineering Strategies for Boosting the Nitrogen Reduction Reaction Performance of MoS2-Based Electrocatalysts. *Mater. Today Nano* **2022,** *18*, 100202.
117. Wei, Z.; Feng, Y.; Ma, J. Co-Doped Graphene Edge for Enhanced N2-to-NH3 Conversion. *J. Energy Chem.* **2020,** *48*, 322−327.
118. López, M.; Morales-García, Á.; Viñes, F.; Illas, F. Thermodynamics and Kinetics of Molecular Hydrogen Adsorption and Dissociation on MXenes: Relevance to Heterogeneously Catalyzed Hydrogenation Reactions. *ACS Catal.* **2021**, *11*, 12850–12857.
119. Jurado, A.; Morales-García, Á.; Viñes, F.; Illas, F. Molecular Mechanism and Microkinetic Analysis of the Reverse Water Gas Shift Reaction Heterogeneously Catalyzed by the Mo2C MXene. *ACS Catal.* **2022,** *12*, 15658−15667.
120. Chen, J.; Cheng, H.; Ding, L.-X.; Wang, H. Competing Hydrogen Evolution Reaction: A Challenge in Electrocatalytic Nitrogen Fixation. *Mater. Chem. Front.* **2021,** *5*, 5954−5969.
121. Ye, K.; Hu, M.; Li, Q.-K.; Luo, Y.; Jiang, J.; Zhang, G., Cooperative Single-Atom Active Centers for Attenuating the Linear Scaling Effect in the Nitrogen Reduction Reaction. *J. Phys. Chem. Lett.* **2021,** *12*, 5233−5240.
122. Ling, C.; Niu, X.; Li, Q.; Du, A.; Wang, J. Metal-Free Single Atom Catalyst for N2 Fixation Driven by Visible Light. *J. Am. Chem. Soc.* **2018,** *140*, 14161−14168.

123. Fan, M.; Liang, X.; Li, Q.; Cui, L.; He, X.; Zou, X. Boron: A Key Functional Component for Designing High-Performance Heterogeneous Catalysts. *Chin. Chem. Lett.* **2023,** *34*, 107275.
124. Gouveia, J. D.; Morales-García, Á.; Viñes, F.; Gomes, J. R. B.; Illas, F. MXenes *à la Carte*: Tailoring the Epitaxial Growth Alternating Nitrogen and Transition Metal Layers. *ACS Nano* **2022,** *16*, 12541−12552.
125. Vázquez-Parga, D.; Jurado, A.; Roldán, A.; Viñes, F. A Computational Map of the Probe CO Molecule Adsorption and Dissociation on Transition Metal Low Miller Indices Surfaces. *Appl. Surf. Sci.*, **2023**, *618*, 156581.
126. Viñes, F.; Calzada, A.; Gamallo, P. Thermodynamic, Kinetic and Dynamic Aspects of Biogas Upgrading Using Nano-Engineered Grazynes. *Appl. Surf. Sci.*, **2023**, *71*, 102459.
127. Tekalgne, M. A.; Do, H. H.; Nguyen, T. V.; Le, Q. V.; An, J.; Hong, S. H.; Ahn, S. H.; Kang, H.; Kim, J. S.; Kim, S. Y. Efficient Electrocatalysts for Hydrogen Evolution Reaction Using Heteroatom-Doped MXene Nanosheet. *Int. J. Energy Res.* **2023,** *2023*, 8980888.
128. Zhang, L.; Zhou, M.; Wang, A.; Zhang, T. Selective Hydrogenation over Supported Metal Catalysts: From Nanoparticles to Single Atoms. *Chem. Rev.* **2020**, *120*, 683–733.
129. Aireddy, D. R.; Ding, K. Heterolytic Dissociation of H2 in Heterogeneous Catal sis. *ACS Catal.* **2022**, *12*, 4707–4723.
130. Horiuti, J.; Polanyi, M. A Catalysed Reaction of Hydrogen with Water. *Nature* **1933**, *132*, 819–819.
131. Horiuti, I.; Polanyi, M. Exchange Reactions of Hydrogen on Metallic Catalysts. *Trans. Faraday Soc.* **1934**, *30*, 1164–1172.
132. Yang, B.; Burch, R.; Hardacre, C.; Hu, P.; Hughes, P. Selective Hydrogenation of Acetylene over Cu(211), Ag(211) and Au(211): Horiuti–Polanyi Mechanism vs. Non-Horiuti–Polanyi Mechanism. *Catal. Sci. Technol.* **2017**, *7*, 1508–1514.
133. Pokochueva, E. V.; Burueva, D. B.; Salnikov, O. G.; Koptyug, I. V. Heterogeneous Catalysis and Parahydrogen-Induced Polarization. *ChemPhysChem* **2021**, *22*, 1421–1440.
134. Kovtunov, K. V.; Beck, I. E.; Bukhtiyarov, V. I.; Koptyug, I. V. Observation of

Parahydrogen-Induced Polarization in Heterogeneous Hydrogenation on Supported Metal Catalysts. *Angew. Chem. Int. Ed.* **2008**, *47*, 1492–1495.

135. Salnikov, O. G.; Liu, H.J.; Fedorov, A.; Burueva, D. B.; Kovtunov, K. V.; Copéret, C.; Koptyug, I. V. Pairwise Hydrogen Addition in the Selective Semihydrogenation of Alkynes on Silica-Supported Cu Catalysts. *Chem. Sci.* **2017**, *8*, 2426–2430.
136. Augustine, R. L.; Yaghmaie, F. Heterogeneous Catalysis in Organic Chemistry. 7. Stereochemistry of the Hydrogenation of 1, 3, 5-Trimethylcyclohexene. *J. Org. Chem.* **1987**, *52*, 1862–1863.
137. Farkas, A. Part. II.—Catalytic Reactions of Hydrocarbons. The Activation of Hydrogen in Catalytic Reactions of Hydrocarbons. *Trans. Faraday Soc.* **1939**, *35*, 906–917.
138. Baráth, E. Hydrogen Transfer Reactions of Carbonyls, Alkynes, and Alkenes with Noble Metals in the Presence of Alcohols/Ethers and Amines as Hydrogen Donors. *Catalysts* **2018**, *8*, 671.
139. Pokochueva, E. V.; Burueva, D. B.; Kovtunova, L. M.; Bukhtiyarov, A. V.; Gladky, A. Y.; Kovtunov, K. V.; Koptyug, I. V.; Bukhtiyarov, V. I. Mechanistic In Situ Investigation of Heterogeneous Hydrogenation over Rh/TiO_2 Catalysts: Selectivity, Pairwise Route and Catalyst Nature. *Faraday Discuss.* **2021**, *229*, 161–175.
140. Koptyug, I. V.; Kovtunov, K. V.; Burt, S. R.; Anwar, M. S.; Hilty, C.; Han, S. I.; Pines, A.; Sagdeev, R. Z. *para*-Hydrogen-Induced Polarization in Heterogeneous Hydrogenation Reactions. *J. Am. Chem. Soc.* **2007**, *129* (17), 5580–5586.
141. Wade, L.G. (**2006**). Organic Chemistry (6th ed.). Pearson Prentice Hall. pp. 279. ISBN 978-1-4058-5345-3.
142. Mao, Z.; Xie, Z.; Chen, J. G., Comparison of Heterogeneous Hydroformylation of Ethylene and Propylene over RhCo3/MCM-41 Catalysts. *ACS Catal.* **2021,** *11*, 14575–14585.
143. Liu, R., Ideal Site Geometry for Heterogeneous Catalytic Reactions: A DFT Study. *Catalysts* **2024,** *14*, 34.
144. Meng, L.; Pokochueva, E. V.; Chen, Z.; Fedorov A.; Viñes, F.; Illas, F.; Koptyug, I. V., Contrasting Metallic (Rh^0) and Carbidic (2D-Mo_2C MXene) Surfaces in Olefin Hydrogenation Provides Insights on the Origin of the Pairwise Hydrogen Addition. *ACS Catal.* **2024,** Accepted, DOI:10.1021/acscatal.4c02534.

145. Gouveia, J. D.; Viñes, F.; Illas, F.; Gomes, J. R. B. MXenes Atomic Layer Stacking Phase Transitions and their Chemical Activity Consequences. *Phys. Rev. Mater.* **2020,** *4*, 054003.
146. Morales-Salvador, R.; Gouveia, J. D.; Morales-García, Á.; Viñes, F.; Gomes, J. R. B.; Illas, F. Carbon Capture and Usage by MXenes. *ACS Catal.* **2021**, *11*, 11248–11255.
147. Bond, G. C. Metal-Catalysed Reactions of Hydrocarbons; Springer, Boston, MA, USA, 2005.
148. Pozzo, M.; Alfè, D.; Amieiro, A.; French, S.; Pratt, A. Hydrogen Dissociation and Diffusion on Ni- and Ti-Doped Mg(0001) Surfaces. *J. Chem. Phys.* **2008**, *128*, 094703.
149. Cheng, J.; Hu, P.; Ellis, P.; French, S.; Kelly, G.; Lok, C. M. Brønsted−Evans−Polanyi Relation of Multistep Reactions and Volcano Curve in Heterogeneous Catalysis. *J. Phys. Chem. C* **2008**, *112*, 1308–1311.
150. McCormick, J.; Korchak, S.; Mamone, S.; Ertas, Y.; Liu, Z.; Verlinsky, L.; Wagner, S.; Gloggler, S.; Bouchard, L. Over 12% Polarization and 20 Minute Lifetime of 15N on Choline Derivative Utilizing Parahydrogen and Rh Nanocatalyst in Water. *Angew. Chem. Int. Ed.* **2018,** *57*, 10692–10696.
151. Vile, G.; Baudouin, D.; Remediakis, I. N.; Copéret, C.; López, N.; Pérez-Ramírez, J. Silver Nanoparticles for Olefin Production: New Insights into the Mechanistic Description of Propyne Hydrogenation. *ChemCatChem* **2013**, *5*, 3750–3759.
152. Yang, B.; Gong, X.-Q.; Wang, H.-F.; Cao, X.-M.; Rooney, J. J.; Hu, P. Evidence To Challenge the Universality of the Horiuti–Polanyi Mechanism for Hydrogenation in Heterogeneous Catalysis: Origin and Trend of the Preference of a Non-Horiuti–Polanyi Mechanism. *J. Am. Chem. Soc.* **2013**, *135*, 15244–15250.
153. Dong, J.; Ebrahimi, M.; Tillekaratne, A.; Zaera, F. Direct Addition Mechanism during the Catalytic Hydrogenation of Olefins over Platinum Surfaces. *J. Phys. Chem. Lett.* **2016**, *7*, 2439–2443.

Chapter 4

2D-Nitrogen-Doped Graphene Supported Single Metal Atom Catalysts in Electrochemistry

4.1. Introduction

Downsizing bulk metal catalysts to the atomic level, specifically as Single Atom Catalysts (SACs), represents a cutting-edge strategy for achieving high catalytic activity and reducing costs.[1,2] SACs mark a significant advancement in the field of catalysis, their unique properties combine the advantages of both homogeneous and heterogeneous catalysis,[3,4] making them particularly attractive for various applications. This chapter will present two studies that investigate the characteristics and applications of non-precious metal SACs, as well the role of geometric symmetry in their catalytic performance.

The first study focuses on identifying viable non-precious metal SACs for the Oxygen Reduction Reaction (ORR) in alkaline environments[5] to improve the performance of chlor-alkali electrolysis. This research employs computational screening methods to evaluate various potential catalysts, aiming to find cost-effective alternatives to precious metal catalysts. The study highlights key parameters affecting ORR catalytic performance, including the binding energies of intermediates and the electronic properties of catalyst sites. Through theoretical calculations and experimental validation, identifying several non-precious metal SACs that exhibit excellent catalytic performance in alkaline environments, offering new possibilities for practical applications.

The second study goes beyond the traditional symmetric platinum single atom[6] supported by nitrogen-doped graphene model, to explore the impact of geometric symmetry on the catalytic performance of SACs in the Chlorine Evolution Reaction (CER).[7] It reveals that geometric symmetry and coordination environment significantly influence catalytic performance. Moreover, using advanced spectroscopic techniques, the coordination structures of platinum active sites was characterized and the competitive Oxygen Eevolution Reaction (OER)[8] was also analysed under the same operating conditions, demonstrating the exceptional catalytic performance of SACs in CER and provides a profound understanding of their coordination characteristics.

These studies emphasize the importance of designing efficient SACs. By exploring non-precious metal alternatives and the geometric factors affecting precious metal catalysts, a comprehensive understanding of the factors driving catalytic performance were provided, paving the way for the development of more efficient and cost-effective industrial application catalysts.

4.2. Computationally Screening Non-Precious Single Atom Catalysts for Oxygen Reduction in Alkaline Media

4.2.1. Introduction

The chlor-alkali industry aims to produce chlorine gas, sodium hydroxide, and/or potassium hydroxide through the electrolysis of saltwater solutions, ranking as the second-largest electrochemical process after the Hall-Héroult process used in aluminum production.[9-11] Unfortunately, these processes are energy-intensive, using mercury electrodes or asbestos-containing membranes, leading to significant environmental issues.[12-14] Therefore, advanced chlor-alkali processes,[15,16] such as Oxygen Depolarized Cathodes (ODCs) used at the cathode of membrane electrolysis cells, promote water formation through ORRs instead of HERs constitute a newly developed method to reduce energy consumption, which has been implemented on an industrial scale. This process offers significant advantages from a thermodynamic perspective compared to traditional processes with a decreasing of approximately 1 V in the equilibrium potential difference between the anode CERs and cathode ORRs,[17,18] enabling an easy achievement of 30% energy savings.[19,20] To enhance the performance of chlor-alkali electrolysis, a suitable electrocatalyst capable of catalysing ORR in alkaline solutions (as sodium hydroxide solution) is required, such as carbon-supported platinum[21] and silver,[22] metalloporphyrins,[16] phthalocyanines, and perovskites.[23]

In recent decades, extensive research has been conducted to replace high-activity but scarce and expensive platinum-based catalysts.[24,25] Non-precious metal catalysts have garnered attention due to their promising ORR activity and low cost in electrochemical technologies.[26,27] Among the studied catalysts,[28,29] SACs involving single metal atoms dispersed and anchored on specific substrates have gained widespread attention for their high efficient and low cost performance, exhibiting high catalytic activity even in slow reaction kinetics like ORR. Therefore, the search for active and stable ORR SACs is inevitable.

Utilizing first-principles theoretical methods to screen potential material has become a powerful tool for predicting the electrocatalytic activity of ORR catalysts.[30-32] While experimental studies[33,24] have extensively examined the performance of a series of N-doped graphene supported single non-precious metal atom (NG-SAC) in chlor-alkali

electrolysis, the theoretical understanding of ORR in alkaline media remains to be addressed. Thus, NG-SACs (SAC = Sc, Ti, V, Mn, Fe, Ni, Cu) for ORR activity in alkaline media have been explored, as shown in Figure 4.1, with Pt as a reference case.

This work produced the publication of one research article in *Catalysis Today*, titled "*Computationally screening non-precious single atom catalysts for oxygen reduction in alkaline media*",[34] the supporting information for can be found in Appendix E, which are provided at the end of this thesis. Subsequent pages contain a summary of this article. My contributions to this research article comprise: (a) Conceptualization of reaction and formal analysis, (b) methodology and data curation, (c) surveying and summarizing the relevant publications, and (d) joining the initial manuscript of paper and making the corresponding figure. A full description of the work done can be found in Ref. 34.

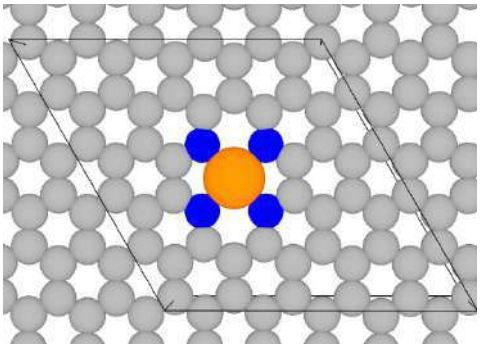

Figure 4.1. Schematic representation of the model used to represent the SAC electrocatalysts used in the present work. Grey, blue, and orange balls denote C, N, and the metal atom, respectively.[34]

4.2.2. Oxygen Reduction Reaction (ORR) System in Alkaline Media

The ORR in alkaline medium can be represented as Eq. 4.1:

$$O_{2(g)} + 2H_2O + 4e^- \rightarrow 4OH^- \quad (4.1).$$

Liang *et al.*[35] has proposed an ORR mechanism in alkaline medium, with the following steps of Eqs. 4.2-5:

$$O_2 + * + H_2O + e^- \rightarrow *OOH + OH^- \quad (4.2),$$

$$*OOH + e^- \rightarrow *O + OH^- \quad (4.3),$$

$$*O + H_2O + e^- \rightarrow *OH + OH^- \quad (4.4),$$

$$*OH + e^- \rightarrow OH^- + * \quad (4.5).$$

Moreover, the expression ($OH^- - e^-$) can be expressed as Eq. 4.6 when consider the reaction energy,

$$OH^- - e^- = H_2O - H^+ - e^- = H_2O - \tfrac{1}{2} H_2 \quad (4.6).$$

It also should be noted that the ORR is accompanied by the corresponding half-reaction of HER, $2H_2 \rightarrow 4H^+ + 4e^-$, under standard conditions, with respect to the SHE,

the equilibrium potential is taken as zero. The overall reaction is the production of water, under these conditions, the standard equilibrium electrode potential (E°) is –0.40 eV at *pH*=14.

4.2.3. Results

4.2.3.1. Stability of the SAC Models

Transition metal atoms deposited on carbon materials often interact by forming clusters and large nanoparticles, which can hinder catalysis and consequently catalytic performance. Therefore, when studying SACs, evaluating their stability is essential. In this work, we considered the formation energy (E_f), binding energy (E_b), cohesive energy (E_{coh}) and net Bader charge (Q) of the SAC models studied, as shown in Table 4.1. The E_f of SAC models, defined as the energy required to decompose the catalyst into its individual components, is directly related to stability, a more negative E_f value indicates greater thermodynamic stability of the catalyst. The E_b is defined as the binding energy of a single atom. The E_f values in Table 4.1 demonstrate that the SAC models used are thermodynamically stable, with E_b consistently greater than E_{coh}, indicating metal sintering is thermodynamically unfavourable. Additionally, the net Q of metal atoms in each SAC model in Table 4.1 shows positive values, suggesting the oxidation of the metal components, and decreasing gradually from Sc to Cu, with Pt having the lowest value, confirming the suitability of single metal atoms as active sites, leading to significant charge transfer between the substrate and oxygen molecules.

Table 4.1. Calculated formation energy (E_f), binding energy (E_b), and cohesive energies (E_{coh}) of the different SAC model in eV. The rightmost column corresponds to the calculated Bader net charges (Q) at the M center in the isolated SAC models.[34]

SAC	E_f	E_b	E_{coh}	Q
Sc	-3.85	-8.54	-4.64	1.82
Ti	-2.05	-8.52	-3.67	1.43
V	-1.51	-7.73	-2.42	1.32
Mn	-2.54	-6.77	-3.85	1.29
Fe	-1.75	-7.68	-2.81	1.08
Ni	-2.48	-7.99	-3.12	0.83
Cu	-0.40	-5.26	-1.78	0.90
Pt	-1.67	-7.81	-2.31	0.72

Moreover, the adsorption energy (E_{ads}) of key reaction intermediates such as O_2, OOH*, O*, and OH* largely determines the Gibbs free energy values that control the catalytic performance of ORR. Negative E_{ads} values indicate that the adsorption process is energetically favourable. By considering different adsorption modes and optimizing the structure of each mode, the optimal E_{ads} values were obtained as shown in Figure 4.2 and Table 4.2. Finally, the DOSs and PDOSs in Figure S1 of Appendix E exhibit metallic or near-metallic characteristics in all systems, making them excellent candidates for electrode applications.

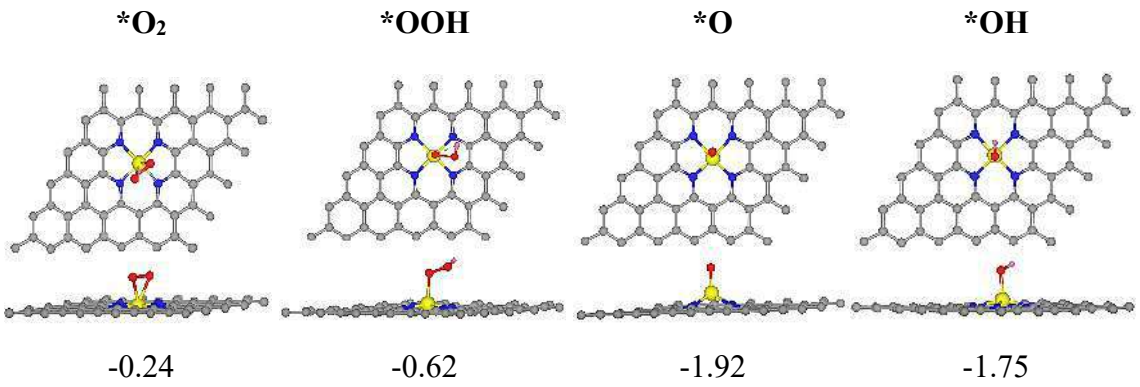

Figure 4.2. Top (top) and side (bottom) atomic structures for *O_2, *OOH, *O, and *OH at the Cu SAC catalyst with their corresponding adsorption energy (E_{ads}, in eV). The information for the rest of systems can be found in Table S1. O and H atoms are shown as red and white spheres, respectively, while the rest of the color-coding is as in Figure 4.4.[34]

Table 4.2. Calculated Gibbs free energies (ΔG_i, in eV), the overpotentials (η), and the limiting potentials (U_L) of different catalysts at $U = 0$ V, $pH = 14$.[34]

SAC	ΔG_{OOH*}	ΔG_{O*}	ΔG_{OH*}	ΔG_{OH^-}	η_{theo} (V)	U_L(V)
Ideal	-0.40	-0.40	-0.40	-0.40	0.00	0.00
Sc	-0.23	-1.35	2.90	-2.92	3.30	-2.90
Ti	-0.04	0.69	3.05	-5.30	3.45	-3.05
V	-0.17	1.23	2.39	-5.05	2.79	-2.39
Mn	-1.61	0.27	0.47	-0.73	0.87	-0.47
Fe	-1.15	0.07	0.41	-0.93	0.81	-0.41
Ni	0.09	-1.07	-0.97	0.35	0.75	-0.35
Cu	0.13	-1.24	-0.8	0.31	0.71	-0.31
Pt	0.37	-1.37	-1.29	0.69	1.09	-0.69

4.2.3.2. ORR Electrocatalysis Performance

Four-electron pathway for the ORR was analysed to determine the highest electrocatalytic activity of NG-SACs in alkaline medium. The free-energy profile for each model at U = 0 V and pH = 14 was shown in Figure 4.3, with an ideal catalyst as comparison. The equilibrium potential (E°) of ORR at pH = 14 is 0.4 V, relative to the standard hydrogen electrode (SHE), thus the total energy change ΔG at U = 0 V should be $E^{\circ} \times 4e^{-}$, *i.e.*, -1.60 eV. Here the potential-determining step (PDS) is defined by the maximum positive ΔG_{max} for all steps in the mechanism. The corresponding limiting potential (U_L) is the specific value at which Gibbs free energy becomes thermoneutral or negative for each electrochemical step, as well the theoretical overpotential (η_{theo}), which is the difference between the equilibrium potential (E° = 0.4 V *vs.* SHE) and the limiting potential (U_L), all serving as major criterion for evaluating catalytic performance in ORR.

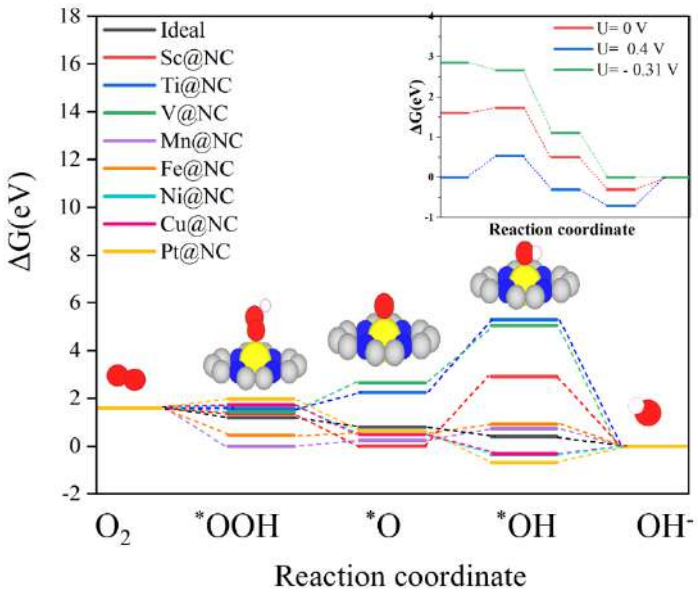

Figure 4.3. Gibbs free energy diagrams for ORR at U = 0 V and pH = 14 for the Sc, Ti, V, Mn, Fe, Ni, Cu, and Pt SACs with the ideal catalysts included for comparison. The inset corresponds to the plots for the Cu SAC at pH = 14 and U = 0 V, at the equilibrium potential (0.4 V) and at U_L V *vs.* SHE, which is system dependent. Inset images colour-coding as in Figure 4.2.[34]

The calculated U_L values for Sc, Ti, V, Mn, Fe, Ni, Cu, and Pt are -2.91, -3.05, -2.39, -0.47, -0.35, -0.35, -0.31, and -0.69 V *vs.* SHE, respectively, and the η_{theo} values are 3.30, 3.45, 2.79, 0.87, 0.81, 0.75, 0.71, and 1.09 V *vs.* SHE, respectively. It was shown that transition metals with fewer *d* electrons exhibit larger U_L, and this drastically decreases once the *d* shell is half-filled, identifying Cu as the best candidate among the studied NG-SACs models.

To gain deeper insights into the mechanism, we explored the Electrochemical-Step Symmetry Index (*ESSI*),[36] which is often defined for OERs and allows us to determine how close a catalyst is to the ideal case.[37,38] For convenience, *ESSI* for the OER can be defined as:

$$\text{ESSI} = \frac{1}{n}\sum_{1}^{n}\left(\frac{\Delta G_i^+}{e^-} - E^\circ\right) \quad (4.7),$$

where ΔG_i^+ corresponds to reaction energies that are greater than or equal to the E° in each electrochemical step, which can be potential limiting step. Obviously, for the ideal catalyst, $n = 4$, and $\frac{\Delta G_i^+}{e^-} = E^\circ$ for all steps, thus *ESSI* = 0 V. The relationship between *ESSI* for the OER and ORR has been previously derived by Govindarajan *et al.*,[36] so here it suffices to state that for $n = 3, 2, 1$ in the OER, one has $n = 1, 2, 3$ in the ORR, and *ESSI*(ORR) = -3*ESSI*(OER), *ESSI*(ORR) = -*ESSI*(OER), and *ESSI*(ORR) = -1/3*ESSI*(OER). Note that the case of $n = 4$ corresponds to the ideal catalysts, and *ESSI*(ORR) = *ESSI*(OER) = 0. Now, let us discuss the *ESSI*(ORR) values for the present systems, for the case of SAC of Cu, one has ΔG_{OOH^*} = 0.13 eV, ΔG_{O^*} = -1.24 eV, ΔG_{OH^*} = -0.80 eV, and ΔG_{OH^-} = 0.31 eV. In this case, there are two steps with ΔG_i smaller than -0.4 eV, so $n = 2$ in either OER or ORR, and *ESSI*(ORR) = (-1.24 - 0.80)/2 + 0.4 = -0.62 V. For the case of Ti, ΔG_{OOH^*} = -0.04 eV, ΔG_{O^*} = 0.69 eV, ΔG_{OH^*} = 3.05 eV, and ΔG_{OH^-} = -5.30 eV. Here, for the OER n = 1, therefore, *ESSI*(ORR) = 1/3 [(-5.30/1) + 0.4] = -1.63.

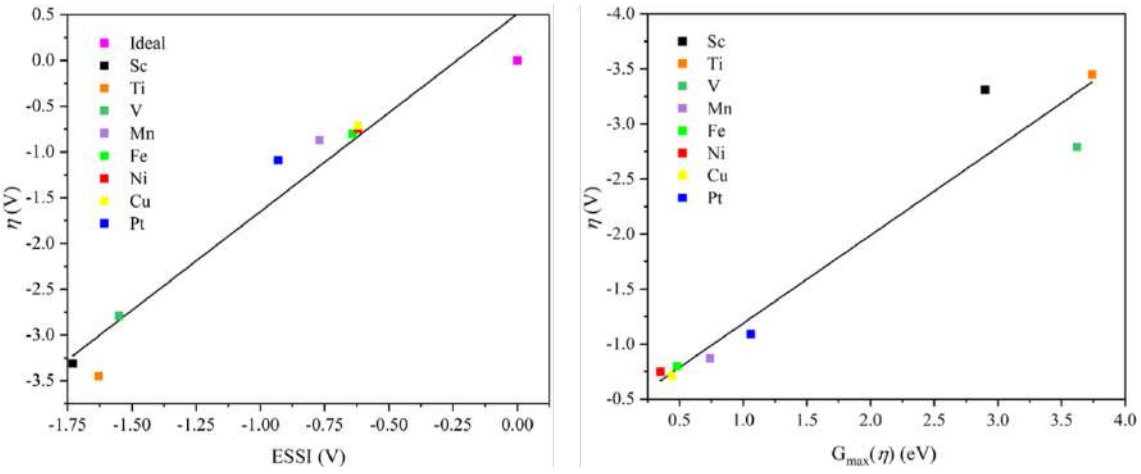

Figure 4.4. Plot of predicted overpotentials (η) versus the electrochemical-step symmetry index (*ESSI*) for the ORR reaction at U = 0 V and *pH* = 14 (left panel) and *vs.* the $G_{max}(\eta)$ descriptor in eV (right panel). The ideal catalyst, for which η_{theo} = ESSI = 0 is shown for comparison.[34]

Next, in Figure 4.4, we plot *ESSI* against η_{theo} of ORR and note that, from Table 4.2, n for ORR is equal to 2 for Sc, Mn, Fe, Ni, Cu, and Pt, while it appears to be 1 for Ti and V. Clearly, catalysts with $n = 2$ displayed low values of η_{theo} and are close to the ideal

catalyst, thus supporting previous findings for other systems.[38] Additionally, we evaluated the so-called $G_{max}(\eta)$ descriptor,[39,40] which indicates the maximum positive span for all reactions involving intermediate species from O_2 molecule to OH^- in the proposed mechanism, as shown in Figure 4.3. For Sc, at $pH = 14$, $G_{max}(\eta)$ is determined by ΔG_{OH*}, while for Ti, V, Mn, and Fe, it is determined by $\Delta G_{O*} + \Delta G_{OH*}$, for Ni by ΔG_{OH^-}, and finally for Cu and Pt by $\Delta G_{OOH*} + \Delta G_{OH^-}$. Therefore, $G_{max}(\eta)$ values can be directly obtained from Table 4.2, but are reported in Table 4.3 for convenience. In principle, high activity is associated with small $G_{max}(\eta)$ values, but unlike *ESSI*, a precise value for the ideal catalyst cannot be defined. From the values in Table 4.2 and, especially from the plot in Figure 4.4, it can be readily seen that the two descriptors provide a similar description, even though *ESSI* is based on thermodynamics and $G_{max}(\eta)$ derived from the span model proposed by Kozuch and Shaik[41] based on kinetic arguments. In fact, the span governing $G_{max}(\eta)$ provides an approximation of the rate-determining step if a suitable value for the Tafel slope (typically 40 mV/dec or 120 mV/dec) is adopted.

Table 4.3. Electrochemical-step symmetry index (*ESSI*) and $G_{max}(\eta)$ descriptor for the explored systems at $U = 0$ V and $pH = 14$.[34]

SAC	*ESSI* (V)	$G_{max}(\eta)$ (eV)
Ideal	0.00	---
Sc	-1.73	2.90
Ti	-1.63	3.74
V	-1.55	3.62
Mn	-0.77	0.74
Fe	-0.64	0.48
Ni	-0.62	0.35
Cu	-0.62	0.44
Pt	-0.93	1.06

Therefore, by considering these the *ESSI* and $G_{max}(\eta)$ descriptors analyses, we gain a deeper understanding of the performance of these NG-SACs systems in the ORR and identify Cu as a particularly promising catalyst candidate.

4.2.4. Conclusions

These findings, coupled with additional data and analyses presented in the research articles below, lead to the following conclusions:

- The studied NG-SAC catalysts are thermodynamically stable against sintering with the metal atoms being partially oxidized by considering their formation energy (E_f), binding energy (E_b) and cohesive energy (E_{coh}).
- A plausible ORR mechanism that can proceed in an alkaline medium condition ($pH = 14$) was proposed.
- The catalytic performance was analysed using the electrochemical-step symmetry index (*ESSI*) and $G_{max}(\eta)$ descriptors.
- Among all the NG-SACs, Cu shows the best performance in alkaline conditions ($pH = 14$).

4.3. Importance of Broken Geometric Symmetry of Single-Atom Pt Sites for Efficient Electrocatalysis

4.3.1. Introduction

Increasing literatures indicate significant heterogeneity in the active sites of single-atom catalysts (SACs),[42-44] posing challenges in identifying the genuine active sites and quantifying the intrinsic activity through Turnover Frequency (TOF) or similar metrics for the rational design of improved SACs. Typically, Pt SACs exhibit a wide range of applications in various electro-, photo-, and heterogeneous,[45,46] tending to stabilize through approximately perfect square planar geometry (D_{4h}) as expected by ligand field theory,[6] such as Pt-N_4 and Pt-S_4, where *p*-block elements doped as surface pockets to anchor a single atom.[47,48]

However, theoretically, these model structures predict a significant weakening of axial coordination, resulting in lower catalytic activity.[49,50] The reported experimental electrocatalytic performance of carbon-supported Pt SACs, differ from theoretical computational models, suggesting possible asymmetric coordination geometries for the active site in the experiments like Pt-N_xC_{4-x}.[51,52] Although there is theoretical evidence that catalytic performance of Pt sites with symmetric D_{4h} geometry is poor or moderate, the impact of geometric symmetry breaking of Pt SACs and its crucial role in experiments in electrocatalysis remains unclear. In fact, not all possible configuration environment of active sites are equally active in the studied electrochemical reactions. Unfortunately, even with the assistance of Extended X-ray Absorption Fine Structure (EXAFS) analysis in experiment, it is also challenging to differentiate various Pt moieties that may coexist in SACs. Hence, the synthesis of SACs containing homogenous catalyst-like single active sites is essential for clearly identifying the genuine active sites in Pt SACs.

To elucidate the critical role of structural symmetry and coordination geometry in SACs in electrocatalysis, this study utilizes N-doped graphene-supported single platinum metal atoms (NG-SACs), with different Pt configuration scenarios, *i.e.*, different Pt–N coordination number (CN), such as high(four)-coordinated symmetric Pt-N_4 with square planar, low-coordinated symmetric and asymmetric Pt-N_3 and Pt-N_3V configurations, with trigonal planar and T-shape, respectively, as shown in Figure 4.5. Therefore, three models, Pt-N_4, Pt-N_3 and Pt-N_3V, are utilized to investigate the catalysis of CERs through a combination of experimental and theoretical methods, while also analysing the potential

simultaneous side reaction of OER, aim to disclose the influence of geometric symmetry. I was not involved in experiments.

This work produced the publication of one research article in *Nature Communication*, titled "*Importance of Broken Geometric Symmetry of Single-Atom Pt Sites for Efficient Electrocatalysis*",[53] the supporting information for can be found in Appendix F, provided at the end of this section. Subsequent pages contain a summary of this article. My contributions to this research article comprise (a) Carrying out the DFT calculations and data treatment, (b) analysis of the calculations results, (c) surveying and summarizing the relevant publications, and (d) writing the initial manuscript of paper. A full description of the work done can be found in Ref. 53.

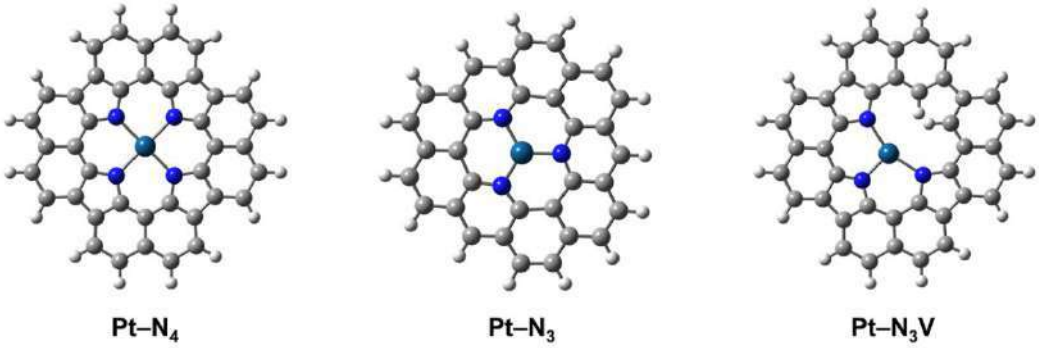

Figure 4.5. Three active site models, square planar Pt–N_4, trigonal planar Pt–N_3, and T-shaped Pt–N_3V, used for the DFT calculations.[53]

4.3.2. CERs and OERs

Building on insights from previous research,[48,54] it was assumed that the CER follows the Volmer–Heyrovsky mechanism.[55,56] Two distinct pathways within the Volmer–Heyrovsky framework involving dissimilar intermediates (*i.e.*, *Cl or *OCl) were explored,[57] as (I) and (II) Pathway of Eqs. 4.8-11:

(I) Pathway mediated by the *Cl intermediate:

$$* + Cl^- (aq) \rightleftharpoons *Cl + e^- \quad (4.8),$$

$$*Cl + Cl^- (aq) \rightleftharpoons Cl_2 (g) + e^- \quad (4.9),$$

(II) Pathway mediated by the *OCl intermediate:

$$*O + Cl^- (aq) \rightleftharpoons *OCl + e^- \quad (4.10),$$

$$*OCl + Cl^- (aq) \rightleftharpoons *O + Cl_2 (g) + e^- \quad (4.11).$$

The Cl^-_{aq} chemical potential is related to that of the Cl_2 gas molecule as Eq. 4.12:

$$Cl^- (aq) \rightleftharpoons 1/2\ Cl_2 (g) + e^-, E^\circ = 1.36\ V\ vs.\ RHE \quad (4.12).$$

For the OER side reaction, $2H_2O\ (aq) \rightarrow O_{2(g)} + 4H^+\ (aq) + 4e^-$, $E°_{OER}$ = 1.23 *vs.* RHE, was modelled by assuming the mononuclear mechanism[58] of Eqs. 4.13-16:

$$* + H_2O\ (l) \rightleftharpoons *OH + H^+ + e^- \quad (4.13),$$

$$*OH \rightleftharpoons *O + H^+ + e^- \quad (4.14),$$

$$*O + H_2O\ (l) \rightleftharpoons *OOH + H^+ + e^- \quad (4.15),$$

$$*OOH \rightleftharpoons O_{2(g)} + H^+ + e^- \quad (4.16),$$

The proton-electron pair, $H^+ + e^-$, chemical potential can be related to the Gibbs free energy of the H_2 gas molecule using the CHE approach as Eq. 4.17:

$$H^+ + e^- \rightleftharpoons 1/2H_{2(g)},\ E^\circ = 0\ V\ vs.\ RHE \quad (4.17).$$

4.3.3. Results

4.3.3.1. Active Site Structure and CER Free Energy Profiles of the Pt SACs

Building on experimental foundations, we further explore the detailed mechanisms of Pt-N_4, Pt-N_3 and Pt-N_3(V) in the CER pathway and their catalytic active Pt site structures, which were characterized under CER conditions (U > 1.36 V_{SHE}) by constructing Pourbaix diagrams.[59]

For the Pt-N_4 model, we find that the axially unoccupied Pt site (*) is more favourable, as shown in Figure 4.6, whereas Pt-N_3 and Pt-N_3(V) are capped by oxygen (*O), together with the underneath Pt atom serving as the active site. These results indicate that the CER reaction on Pt-N_4 and Pt-N_3(V) proceeds through *Cl or *OCl intermediates, respectively. Then both pathways for all three sites were simulated and results plotted in Figure 4.7. Next, the maximum free energy difference for each step was quantified, *i.e.*, $G_{max}\ (U)$,[39] as a function of applied electrode potential, where $G_{max}\ (U) = \max[G_{\#k}(U), k = 1, \ldots, n]$, which is also similar to the energy descriptors in Chapter 4.2, in addition, we also refer the reader to recent publications by the authors.[60,61]

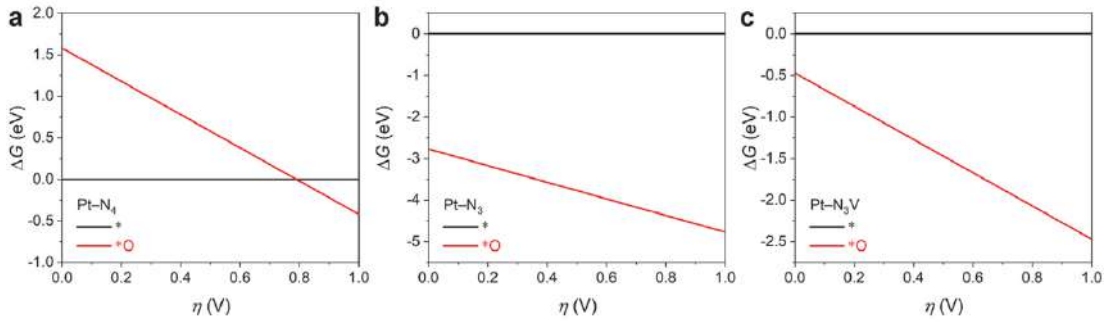

Figure 4.6. Pourbaix-like diagrams for **a** square planar Pt–N_4, **b** trigonal planar Pt–N3, and **c** T-shaped Pt–N_3V models.[53]

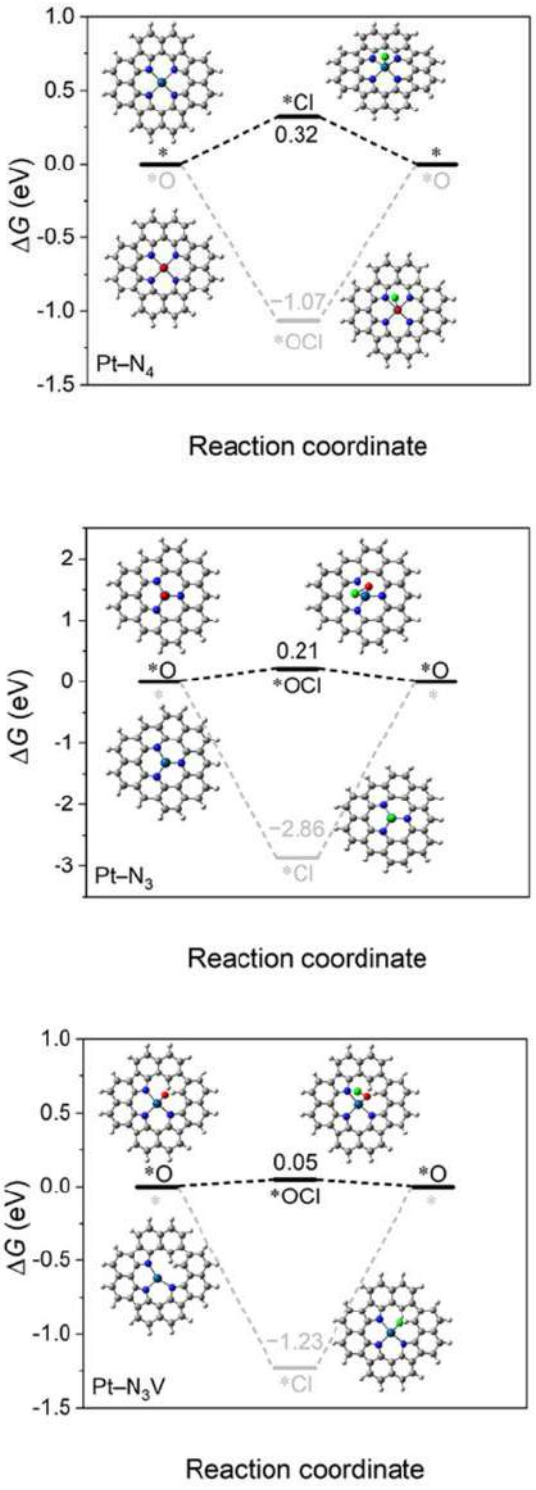

Figure 4.7. Free-energy diagrams of the CER *via* the *Cl and *OCl pathways at 1.36 V_{SHE} for Pt–N_4, Pt–N_3, and Pt–N_3V.[53]

Consistent with our previous findings,[48,54,62] the square planar Pt-N_4 prefers the *Cl pathway (G_{max} (U) = 0.32 eV) over the *OCl pathway (G_{max} (U) = 1.07 eV) at U = 1.36 V_{SHE}. However, for Pt-N_3 or Pt-N_3V, the *OCl pathway is energetically favoured over

the *Cl mechanism. Notably, the $G_{max}(U)$ for Pt-N_3 and Pt-N_3V are 0.21 and 0.05 eV, respectively, confirming the experimental finding that Pt-N_3(V) sites are more active in CER than Pt-N_4.

4.3.3.2. Selectivity of the Pt SACs

Additionally, we described the competitive oxygen evolution reaction (OER)[63] for Pt-N_4, Pt-N_3 and Pt-N_3(V), through a widely accepted mononuclear mechanism involving *OH, *O, and *OOH adsorbates, and identified the activity descriptor $G_{max}(U)$, as shown in Table 4.4 and Figure 4.8. Furthermore, two selectivity models of competition between CER and OER were explored using the data from Table 4.4, one is $G_{sel}(U)$,[63] defined as Eq. 4.18,

$$G_{sel}(U) = G_{max}(U)^{OER} - G_{max}(U)^{CER} \quad (4.18),$$

the second model is a more quantitative one that precisely determines the percentage of CER selectivity,[57,63] as Eq. 4.19,

$$\text{selectivity } (U) = \frac{exp\left(\frac{G_{sel}}{k_B.T}\right)}{exp\left(\frac{G_{sel}}{k_B.T}\right)+1} \quad (4.19).$$

The results show that CER selectivity can reach up to 100%, as illustrated in Figure 4.9, and is unaffected by the applied electrode potential or the chemical nature of the active sites, which is consistent with experimental results.

Table 4.4. Summary of $G_{max}(U)$ for the CER and OER over Pt–N_4 and Pt–N_3V at pH = 0.[53]

$G_{max}(U)$ (eV)	Pt–N_4	Pt–N_3	Pt–N_3V
CER	0.32[a] (0.28[b])	0.21 (0.17)	0.05 (0.01)
OER	1.56 (1.48)	2.25 (2.17)	0.35 (0.31)

[a] U = 1.36 V_{SHE}

[b] U = 1.40 V_{SHE}

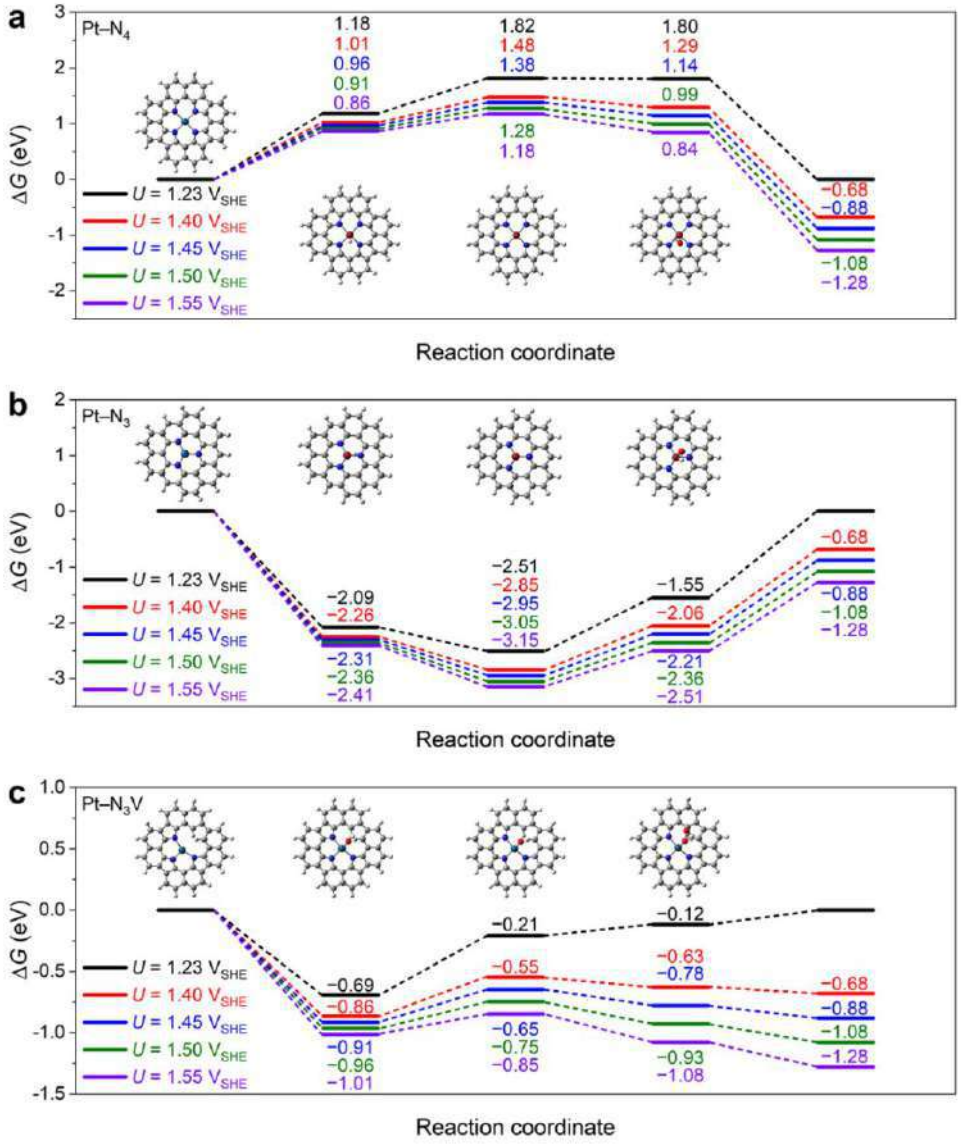

Figure 4.8. Free-energy diagrams of the OER, assuming the mononuclear mechanism *via* the *OH, *O, and *OOH adsorbates, for Pt–N_4 (**a**), Pt–N_3 (**b**), and Pt–N_3V (**c**).[53]

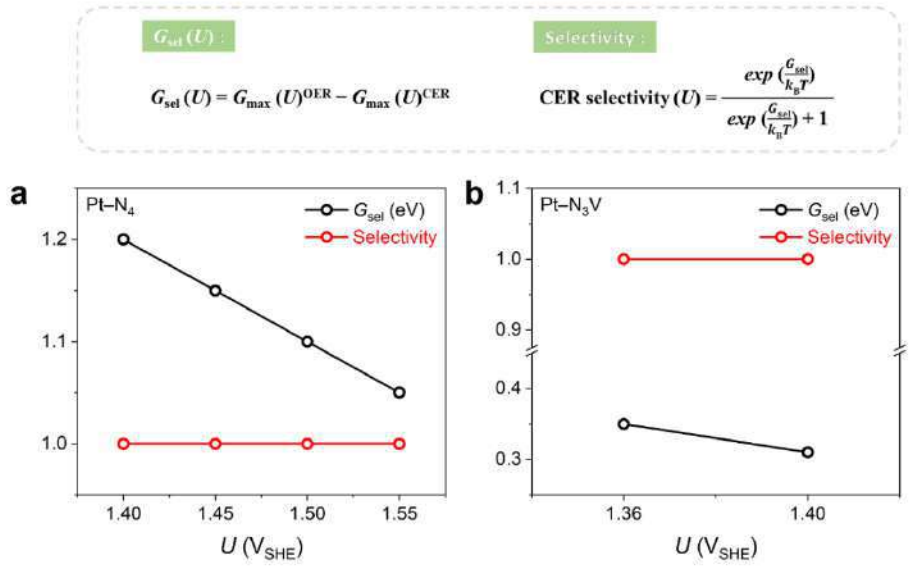

Figure 4.9. Selectivity analysis for the competing CER and OER processes over the **a**, Pt–N_4 and **b**, Pt–N_3V sites.[53]

4.3.3.3. Stability of the Pt SACs

Finally, the stability of Pt-N_4 and Pt-N_3V systems under CER conditions was studied. To this end, the equilibrium potential (U_{diss}) for oxidation and demetallation of central Pt species to PtO_2 was introduced as a descriptor of catalyst stability,[64] defined as Eq. 4.20:

$$U_{diss} = \frac{\Delta G_{stab}}{4} \quad (4.20).$$

Here, ΔG_{stab} is related to the equation [Pt] + $2H_2O$ → [ ] + PtO_2 + $4H^+$ + $4e^-$, note that [ ] denotes the empty pocket of the Pt SACs, to analyse the tendency of the active Pt site to oxidize and demetallize to form PtO_2, which is considered to be the energetically favoured phase under CER conditions according to the Pourbaix diagram. The results showed that U_{diss} values for Pt-N_4, Pt-N_3V, and Pt-N_3 are 2.98, 1.99, and 0.78 V_{SHE}, respectively, which are consistent with experimental results, indicating that Pt-N_3V is less stable than Pt-N_4 under CER conditions at U > 1.36 V_{SHE}. Additionally, considering that the U_{diss} for Pt-N_3 is 0.78 V_{SHE}, which is significantly lower than the CER equilibrium potential, we conclude that the trigonal planar Pt-N_3 site cannot stably exist under CER conditions. In contrast, the T-shaped Pt-N_3V structure explains the excellent activity and selectivity of Pt SACs catalysts in CER.

4.3.4. Conclusions

- The heterogeneity of SACs may be related to their geometric symmetry.

- In CER, for Pt-N_4, * is the genuine Pt active site structure, while for PtN_3 it is *O, which results in the CER reaction pathway of * → Cl → * + Cl_2, for Pt-N_4, whereas O → *OCl → *O + Cl_2 for Pt-N_3 and Pt-N_3V.
- Under CER conditions, the Pt-N_4 structure is more stable than Pt-N_3V, and also exhibits higher selectivity for CER, however, the low-coordinated structure Pt-N_3V shows higher CER activity than the high-coordinated structure PtN_4.
- Modulating the geometric symmetry to find the optimal coordination field strength that stabilizes the Pt sites and corresponding intermediates, such as *Cl or *OCl, is crucial, involving a balance between stability and activity.

4.4. Publications

Catalysis Today 431 (2024) 114560

Contents lists available at ScienceDirect

Catalysis Today

journal homepage: www.elsevier.com/locate/cattod

Computationally screening non-precious single atom catalysts for oxygen reduction in alkaline media

Tahereh Jangjooye Shaldehi [a], Ling Meng [b], Soosan Rowshanzamir [a,*], Mohammad Javad Parnian [c], Kai Exner [d], Francesc Viñes [b], Francesc Illas [b,*]

[a] Hydrogen & Fuel Cell Research Laboratory, School of Chemical, Petroleum and Gas Engineering, Iran University of Science and Technology, Narmak, Tehran 16846-13114, Iran
[b] Departament de Ciència de Materials i Química Física & Institut de Química Teòrica i Computacional (IQTCUB), Universitat de Barcelona, c/ Martí i Franquès 1-11, 08028 Barcelona, Spain
[c] Department of Chemical and Petroleum Engineering, University of Calgary, 2500 University Dr. NW, Calgary, Alberta T2N 1N4, Canada
[d] University Duisburg-Essen, Faculty of Chemistry, Theoretical Inorganic Chemistry, Universitätsstraße 5, 45141 Essen, Germany; Cluster of Excellence RESOLV, Bochum, Germany; Center for Nanointegration (CENIDE) Duisburg-Essen, Duisburg, Germany

ARTICLE INFO

Keywords:
Oxygen reduction reaction
ORR
Alkaline media
Single atom catalyst
DFT

ABSTRACT

The performance of single-atom catalysts (SACs) containing Sc, Ti, V, Mn, Fe, Ni, Cu, and Pt on N-doped carbon (NC) as possible cathodes in advanced chlor-alkali electrolysis has been investigated by means of density functional theory (DFT) with the aim of finding candidates to improve the sluggish kinetics of the oxygen reduction reaction (ORR). A plausible mechanism is proposed for the ORR that allows making use of the computational hydrogen electrode (CHE) approach in this environment, and suitable models have been used to estimate the free-energy changes corresponding to the elementary reaction steps. The performance of the different catalysts has been analyzed in terms of the electrochemical-step symmetry index (ESSI) and G_{max} descriptors. From these descriptors, the Cu-containing SAC is predicted to exhibit the highest catalytic activity which is consistent with a theoretical overpotential of 0.71 V, indicating that this type of catalysts in oxygen depolarized cathodes (ODCs) may overcome the limitations of the high cost and low abundance of Pt and other precious metals.

1. Introduction

The chlor-alkali industrial process, the second largest electrochemical process after the Hall–Héroult process for Al production, aims at producing gaseous chlorine, sodium, and/or potassium hydroxide by the electrolysis of brine solutions [1–3]. Unfortunately, these processes are energy costly, use mercury electrodes or asbestos-containing membranes with evident concomitant environmental issues, harmful effects, and economic problems [4–8]. Consequently, the petrochemical industry is interested in finding alternative, more sustainable, processes to produce caustic soda and gaseous chlorine. In this sense, the so-called advanced chlor-alkali process [9,10] is one of the latest developed approaches aimed at reducing energy consumption, which is working at the industrial scale. In this process, oxygen depolarized cathodes (ODCs) are used in the membrane electrochemical cell at the cathode to facilitate water formation *via* oxygen reduction reaction (ORR) rather than hydrogen evolution reaction (HER). From a thermodynamic point of view, it is a clear advantage to apply ODCs in membrane electrochemical cells as the equilibrium potential difference between the anode (chlorine evolution) and the cathode is reduced by about 1 V compared to the conventional process with the HER at the cathode [11,12]. Therefore, the use of ODCs in membrane cells easily leads to a 30% saving in energy consumption [13,14].

Being a type of gas diffusion electrodes (GDEs), the ODCs consist of a micro/nano-particule catalyst and a hydrophobic material [15,16]. The reaction site in the ODC involves a three-phase boundary with oxygen, water, and electrons at the gas, liquid, and solid phases, respectively. In the ODCs, the ORR suffers from a sluggish reaction kinetics due to the transfer of four electrons for the reduction of a single oxygen molecule [17]. To enhance the performance of chlor-alkali electrolysis, a suitable electrocatalyst is needed, which is able to catalyze ORR in a sodium hydroxide solution at 80–90 °C. Common catalysts for ODCs are

* Corresponding authors.
E-mail addresses: rowshanzamir@iust.ac.ir (S. Rowshanzamir), francesc.illas@ub.edu (F. Illas).

https://doi.org/10.1016/j.cattod.2024.114560
Received 8 October 2023; Received in revised form 25 January 2024; Accepted 30 January 2024
Available online 3 February 2024

carbon-supported platinum [18–20] and silver [21–23], metal porphyrins, phthalocyanins, and perovskites [24,25].

In the last decades, significant research has been carried out to substitute the highly active but scarce and expensive Pt-based catalysts [26,27]. In particular, non-precious metal catalysts have attracted attention because of their promising ORR activity in electrochemical technologies [28–36]. Among the investigated catalysts, transition metal single-atom catalysts (SACs) are promising in speeding up the slow ORR kinetics with high efficiency and low cost. SACs involve single metal atoms dispersed and anchored on a given substrate, have been used in several electrocatalytic processes, in energy storage [37–42] and have shown high catalytic performance for ORR in acidic or alkaline media [43,44].

The search for active and stable SACs for the ORR involves screening a large number of potential material motifs. To render such screening in an efficient fashion, first principles based theoretical approaches such as density functional theory (DFT) in conjunction with the computational hydrogen electrode (CHE) model [45] have become a powerful tool to predict the electrocatalytic activity of ORR catalysts [46–49]. Nevertheless, most theoretical investigations of the ORR have focused on acid solutions, and only a few studies have been reported on alkaline environments. Yu *et al.* [50] have studied the ORR catalyzed by N-doped graphene on the cathode of fuel cells by DFT calculations and showed that this system is promising to partially replace the conventionally used Pt in the alkaline medium.

For the ORR in alkaline medium, the performance of ODC single-atom electrocatalyst in the chlor- alkali electrolysis has been studied in detail from the experimental point of view [51–55]. However, to properly interpret and understand experimental results, and, more importantly, to predict the properties of new materials before synthesis, a detailed analysis from theory is needed. In this work, the ORR activity in alkaline medium of a selection of non-precious single atoms from the 3d transition series (Sc, Ti, V, Mn, Fe, Ni, Cu) supported on N-doped graphene is explored computationally by means of DFT calculations and the CHE model, including Pt as a reference case.

2. ORR mechanism

The ORR mechanism is complex and includes intermediates that depend on the nature of the electrode, electrocatalyst, electrolyte, and on the pH, with significant differences in the proposed mechanism in acid or alkaline media.

2.1. The ORR mechanism in acid media

In acid media, the overall reaction is.

$$O_2\,(g) + 4\,H^+ + 4e^- \rightarrow 2\,H_2O \tag{1}$$

with an equilibrium potential of U = 1.23 V *vs.* RHE (reversible hydrogen electrode). It is common to postulate that there are three adsorbed intermediates in the pathway from O_2 to H_2O [48,56–60], namely *O, *OH, and *OOH that are formed as in Eqs. 2–5.

$$O_2\,(g) + H^+ + e^- + * \rightarrow *OOH \tag{2}$$

$$*OOH + H^+ + e^- \rightarrow *O + H_2O\,(l) \tag{3}$$

$$*O + H^+ + e^- \rightarrow *OH \tag{4}$$

$$*OH + H^+ + e^- \rightarrow H_2O\,(l) + * \tag{5}$$

where O_2 and H_2O are in the gas and liquid phase, respectively. One must point out that Eqs. (2–5) are reconciled with the "mononuclear ORR mechanism", which is the reverse pathway for the mononuclear OER mechanism. This mechanism is likely operative in the ORR when the respective electrocatalyst binds *OH strongly (left leg of the volcano) as discussed in Ref. [61]. Note also that there are several other mechanistic pathways for ORR feasible, including various chemical and electrochemical steps which make the ORR mechanistic description more complex than originally anticipated, and different mechanistic pathways can be operative for different catalysts.

For reactions (2–5) the changes in Gibbs free energy (ΔG_i, i = 2–5) can be computed as detailed extensively in the literatures [48,62] and briefly reviewed in the next section. The calculated ΔG_i provides an estimate of the equilibrium potential required for each step (E_i^o) to take place on a given substrate simply because $E_i^o = -\frac{\Delta G_i}{e_0}$ where e_0 is the electron charge [45]. Note in addition that, irrespective of the catalyst used, the sum of ΔG_i values must be the − 4.92 eV, the equilibrium Gibbs free energy for the reaction at U = 0 V *vs.* RHE. Therefore, it is believed that an ideal catalyst reveals $\Delta G_i = -1.23$ eV for any i at U = 0 V *vs.* RHE —or $\Delta G_i = 0$ eV for any i at U = 1.23 V *vs.* RHE—, and the maximum deviation from this value defines the theoretical overpotential or limiting potential as explained in detail in the next section [63].

From the preceding discussion, it turns out that from the calculated equilibrium potential one can predict the corresponding overpotential, and thus be able to screen different materials in the search for the improved catalyst. Regarding the estimate of the ΔG_i values, here it suffices to state that for the adsorbed species, the vibrational contribution to entropy is estimated from harmonic frequencies, the free energy of O_2 is taken relative to the experimental H_2O (l) formation free energy $-\Delta G^{f,exp}$ (H_2O)— and H_2O and H_2 gas phase molecules calculated free energies with the entropy contribution taken from thermodynamic tables,

$$G(O_2) = 2(\Delta G^{f,exp}(H_2O) - G(H_2O)) - 2\,G(H_2) \tag{6}$$

and that, from the CHE it follows that at $pH = 0$ and 1 bar and 298.15 K.

$$G(H^+ + e^-) = 1/2\,G(H_2) \tag{7}$$

Finally, whenever needed, the free energy of liquid water can be estimated by adding an appropriate entropy correction to the gas phase value [45]. It is worth pointing out that the "mononuclear" mechanism discussed above has been questioned by Barlocco *et al.* [41] who showed that the oxygen evolution reaction (OER) on SACs can follow an alternative pathway. These authors studied a set of 30 SACs involving different carbon-based materials and found that intermediates such as M$(OH)_2$, M(O)(OH), M$(O)_2$, and M(O_2), where M stands for the metal atom in the SAC, exhibit larger adsorption free energy and, hence, may play a role in the OER and ORR mechanisms.

2.2. The ORR mechanism in alkaline media

The ORR reaction in alkaline media can be written as in Eq. (8).

$$O_2(g) + 2\,H_2O + 4e^- \rightarrow 4OH^- \tag{8}$$

and its mechanism has been less studied with some issues remaining open. For instance, it is sometimes postulated that the first step is as in Eq. (9).

$$O_2 + e^- + * \rightarrow *O_2^- \tag{9}$$

and that, at high pH values, *OOH is never formed from a coupled proton-electron transfer (CPET) step [64]. In fact, Smickler *et al.* [65] have argued that the electron transfer in Eq. (9) occurs at the outer sphere which agrees with the fact that the overall reaction takes place a similar speed in different metallic electrodes such a silver and gold. The mechanism that, according to Smickler *et al.* [65] follows from Eq. (9) involves adsorbed charged species which are difficult to accurately model with periodic DFT approaches and makes the overall approach difficult to apply for systematic screening potential electrocatalysts.

Recently, an alternative mechanism has been proposed by Liang *et al.* [66] for the OER in basic media that, while not involving CPET, allows

the use of the CHE model. Since the OER and ORR are reverse processes, the proposed steps for the ORR are as follows:

$$O_2 + * + H_2O + e^- \rightarrow *OOH + OH^- \quad (10)$$

$$*OOH + e^- \rightarrow *O + OH^- \quad (11)$$

$$*O + H_2O + e^- \rightarrow *OH + OH^- \quad (12)$$

$$*OH + e^- \rightarrow OH^- + * \quad (13)$$

which involves the *O, *OH, and *OOH intermediates as in the mononuclear mechanism in acidic media. Now, following the procedure by Liang *et al.* [66], as summarized in the next section, one can compute the change in Gibbs free energy (ΔG_i, $i = 10$–13) and estimate the equilibrium potential of each step, to ultimately predict the theoretical overpotential or other activity descriptors for a given catalyst.

To end up this section, three remarks are necessary. First, note that the ORR reaction as in Eq. (8) is accompanied by the corresponding hydrogen oxidation half reaction $2\,H_2 \rightarrow 4\,H^+ + 4e^-$ for which, at standard conditions, the equilibrium potential *vs.* SHE is taken as zero. Second, one must be aware that alternative mechanisms with different intermediates may need to be considered as discussed in the recent review by Di Liberto and Pacchioni [67]; and third, one should not forget that the models discussed involve some limitations as they neglect the presence of the solvent which may also become an active reaction species [67].

3. Electrode models, theoretical framework, and computational details

As mentioned in the introduction, the focus of the present work is on screening SAC models that can serve as ODC in chlor-alkali electrolyzers. To represent the active sites, we consider graphene-like patch models where a single metal atom is coordinated to four N atoms as indicated in Fig. 1. The models are similar to those used previously by Calle-Vallejo *et al.* [68] but with a considerably larger unit cell. The present model can also be seen as a periodic version of the one used in recent work investigating the chlorine evolution reaction [69]. Thus, a sufficiently large $5 \times 5 \times 1$ supercell of the one-layer pristine graphene is chosen with starting C-C bond length of 1.42 Å as in pristine graphene and lattice parameters of $a = b = 12.3$ Å and $c = 20$ Å, the latter value being chosen to prevent interaction between periodic replicas. Next, the N-doped graphene model was generated by replacing four C with four N atoms and, finally, the SAC model is obtained by adding a metal atom (Sc, Ti, V, Mn, Fe, Ni, Cu, and Pt) to the cavity surrounding the atoms. In this way, the metal atom forms two five- and two six-membered rings, as seen in Fig. 1. The final unit cell contains 44 C atoms, 4 N atoms, and one single metal atom.

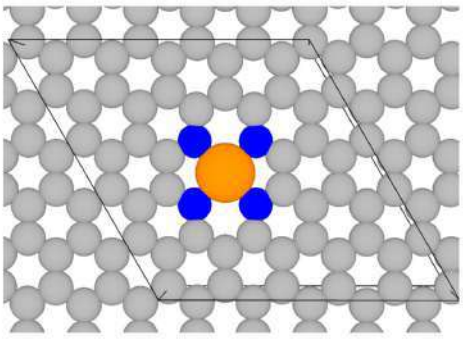

Fig. 1. Schematic representation of the model used to represent the SAC electrocatalysts used in the present work. Grey, blue, and orange balls denote C, N, and the metal atom, respectively.

Herein, we discuss the ORR under alkaline conditions by adapting the mechanism from Liang et *al.* [66]. By using the RHE as a reference electrode under standard conditions of hydrogen gas pressure $p_{H_2} = 1$ bar and $T = 298.15$ K, the necessary ΔG_i ($i = 10$–13) values are calculated as follows:

$$\Delta G_{10} = [G(*OOH) + G(OH^-)] - [G(O_2) + G(*) + G(H_2O) + G(e^-)] \quad (14)$$

$$\Delta G_{11} = [G(*O) + G(OH^-)] - [G(*OOH) + G(e^-)] \quad (15)$$

$$\Delta G_{12} = [G(*OH) + G(OH^-)] - [G(*O) + G(H_2O) + G(e^-)] \quad (16)$$

$$\Delta G_{13} = [G(*) + G(OH^-)] - [G(*OH) + G(e^-)] \quad (17)$$

Following the literature [48,62], G^* is just estimated from the total energy of the clean electrode model, in our case that of the model in Fig. 1, so that G(*) = E*, whereas for the adsorbed species (A = *OOH, *OH, *O).

$$G(\mathrm{A}) = E(\mathrm{A}) + E_{ZPE}(\mathrm{A}) - TS(\mathrm{A}) \quad (18)$$

where E(A) represents the total energy of the electrode model of Fig. 1 with the adsorbed species A, E_{ZPE}(A) is the corresponding vibrational zero-point energy (ZPE) considering only the adsorbate degrees of freedom, and S(A) stands for the entropy of the adsorbed species which includes the vibrational contribution only. In addition, the chemical potential of O_2 can be obtained by assuming the equilibrium in Eq. (6). The only remaining terms are $G(OH^-)$ and $G(e^-)$ and more precisely their difference, namely $G(OH^-) - G(e^-)$. To calculate this term, we also follow Liang *et al.* [66] who used the equilibrium as in Eq. (19).

$$H_2O(l) \rightarrow H^+ + OH^- \quad (19)$$

for which it holds that.

$$G(OH^-) + G(H^+) = G(H_2O(l)) \quad (20)$$

adding and subtracting $G(e^-)$ in the left-hand side one has.

$$G(OH^-) - G(e^-) + G(H^+) + G(e^-) = G(H_2O(l)) \quad (21)$$

which finally leads to.

$$G(OH^-) - G(e^-) = G(H_2O) - [G(H^+) + G(e^-)] = G(H_2O) - 1/2\,G(H_2) \quad (22)$$

Substituting Eq. (22) into Eqs. (14)–(17), one gets.

$$\Delta G_{10} = G(*OOH) - [G(O_2) + G(*) + G(H_2O)] + G(H_2O) - 1/2\,G(H_2) \quad (23)$$

$$\Delta G_{11} = G(*O) - G(*OOH) + G(H_2O) - 1/2\,G(H_2) \quad (24)$$

$$\Delta G_{12} = G(*OH) - [G(*O) + G(H_2O)] + G(H_2O) - 1/2\,G(H_2) \quad (25)$$

$$\Delta G_{13} = G(*) - G(*OH) + G(H_2O) - 1/2\,G(H_2) \quad (26)$$

So far all ΔG values are referred to standard conditions or zero pH and zero potential which is often indicated as $\Delta G(0,0)$. To obtain the corresponding expressions at finite pH and potential relative to the SHE, it suffices to recall that for an elementary step involving a single CPET one can write [70,71].

$$\Delta G(pH, U) = \Delta G(0,0) - \nu(H^+)k_BT(\ln 10)pH - \quad - \nu(e^-)eU \quad (27)$$

where e is the elementary charge of an electron and U is the applied electrode potential with respect to the SHE with $\nu(H^+)$ and $\nu(e^-)$ being the number of transferred protons and electrons, respectively. Using Eq. (27) one easily gets the equivalent of ΔG_i ($i = 10$–13) for a given pH and potential. In acidic conditions, $pH = 0$, we can use SHE or RHE, because.

$$\Delta G(pH, U) = \Delta G(0,0 \quad (28)$$

$$eU(RHE) = eU(SHE) \quad (29)$$

However, under alkaline conditions, *i.e.* at $pH = 14$, then.

$$\Delta G(pH, U) = \Delta G(0,0) - k_B T(\ln 10) pH - eU =$$

$$= \Delta G(0,0) - 0.83 - eU \quad (30)$$

Consequently, for $U = 0$ *vs.* SHE one has $\Delta G(14,U) = \Delta G(0,0) - 0.83$, which simply means that for each elementary reaction step, one just need to subtract 0.83 eV from data in the acidic medium. In other words;

$$eU(\mathrm{RHE}) = eU(\mathrm{SHE}) - k_B T(\ln 10) pH = eU(\mathrm{SHE}) - 0.83 \quad (31)$$

That is, for $\Delta G(pH,U)$ under acidic $pH = 0$ and $U = 0$ V *vs.* SHE, $\Delta G(0,0) = U_0 \times 4 = -1.23$ V (*vs.* SHE) $\times 4 = -4.92$ eV, whereas for alkaline $pH = 14$, $\Delta G(14,0) = U_0 \times 4 = (1.23 - 0.83)$ V (*vs.* SHE) $\times 4 = -1.6$ eV. In the context of the CHE model and for a real catalyst, the highest potential at which all reaction steps are exergonic is termed the thermodynamic limiting potential (U_L) [48] and is defined as

$$U_L = U_0 - \frac{1}{e} \left[\max(\Delta G_i)_{|_{pH=0-13}}\right] \quad (32)$$

The difference between the equilibrium potential U_0 and the limiting potential (U_L) defines the theoretical overpotential (η_{theo}), this is.

$$\eta_{theo} = U_0 - U_L \quad (33)$$

For the ORR in acidic and alkaline conditions U_0 is + 1.23 V and + 0.4 V *vs.* SHE, respectively. Note also that, for the ideal catalyst, all steps have the same ΔG_i, and U_L matches U_0 leading to $\eta = 0$. It is also important to note that η (as well as U_L) serves as an indicator of the effectiveness of a given catalyst activity and cannot be directly compared to a measured overpotential, which is inherently influenced by the current density.

The set of equations above, similar to those in the original work of Nørskov *et al.* [45] for the reaction in acid media, allows one to predict the potential of each step just from DFT based calculation. At this point, it is worth pointing out that, because of the approximate character of the exchange-correlation functionals, the DFT calculated energy of gas phase molecules suffers from rather large errors which, severely affect the equilibrium potential predictions [63,72]. To a large extent, the DFT intrinsic error can be minimized by means of a semiempirical correction. In the case of the ORR, the error, measured as the Gibbs free energy difference between the experimental (−4.92 eV) and the calculated value for the ideal catalyst is almost entirely due to the energy of the gas phase O_2 molecule and depends on the chosen exchange-correlation functional [63].

The DFT calculations were carried out allowing for spin polarization with the Perdew–Burke–Ernzerhof (PBE) exchange-correlation functional [73], with dispersion effects included through the D3 approach of Grimme [74]. This choice is justified by the good performance of PBE in describing the transition metal series and it provides a good description of closed-shell metallic systems [75–78]. Note in passing that some authors have suggested that the implicit more accurate hybrid functionals or its cheaper PBE+U version provide a slightly different and, hence, expectedly more accurate description of SAC systems of interest in electrocatalysis [79,80]. Nevertheless, one must also be aware of the intrinsic errors of the available functionals in describing the gas phase thermochemistry [81] as reactants and products are gas phase molecules. The gas phase errors of PBE are known and can be corrected as indicated below. Also, using the same method for the different systems permits to catch the main trends which is the main goal of the present work.

The valence electron density was expressed using a plane-wave basis set with a kinetic energy cut-off of 415 eV and the projector augmented wave (PAW) method of Bloch [82], as implemented by Kresse and Joubert [83], was used to account for the effect of the core electrons on the valence electron density. The necessary numerical integrations in the reciprocal space were carried out using a 4 × 4 × 1 mesh of special **k**-points [84]. The optimization of the structures was finalized until the maximum force on any atom in the supercell were all below 0.01 eV $Å^{-1}$. The criterion of convergence of the total energy along the optimization was set to 10^{-5} eV. For the gas phase species, the total energy was obtained by placing it in a large asymmetric box. Finally, $G(O_2)$ in Eq. (23), has been corrected by the estimated PBE error of 0.46 eV as reported by Sargeant *et al.* [63], so that the PBE calculated Gibbs free energy for the ORR, for which the PBE value is 4.46 eV, matches the experimental value. All calculations have been carried out using the Vienna *ab initio* simulation package (VASP) [85,86].

4. Stability of the SAC models

It is well-known that transition metal atoms deposited on carbon materials tend to interact ultimately by forming clusters and large nanoparticles, which is detrimental to catalysis and, consequently, reduce their performance. Hence, when investigating possible SACs, it is necessary to first assess their stability. In the present work, we consider formation energy, binding energy, and cohesive energy of the considered models. The formation energy (E_f) of the SAC model can be defined as the energy required to dissociate the catalyst into its individual components, which is directly related to stability, and can be estimated as:

$$E_f = [E_{SAC} + 2\,E_C] - [E_M + E_{CN}] \quad (34)$$

where E_{SAC} and E_{CN} are the total energies of the optimized SAC model in Fig. 1 and the (5 ×5) pristine N-graphene supercell with four appropriately located N atoms; E_C is the energy of the carbon atom calculated from graphene and E_M is chemical potential of M atom calculated from its corresponding bulk structure. The factor 2 in Eq. (34) arises from the fact that two C atoms have to be removed to accommodate the M atom in the SAC. Obviously, the more negative the calculated E_f, the more thermodynamically stable the catalyst is. The E_f values summarized in Table 1 indicate that the SAC models used are thermodynamically stable. The binding energy (E_b) is defined as;.

$$E_b = E_{SAC} - E_{support} - E_M \quad (35)$$

where $E_{support}$ and E_M are the total energies of the SAC model without M atom and single M atom. Comparing the obtained E_b values in Table 1 with the corresponding cohesive energy (E_{coh}) values of the bulk metal (3.90, 4.85, 5.31, 2.92, 4.87, 4.87, 3.48, and 5.50 eV for Sc, Ti, V, Mn, Fe, Ni, Cu, and Pt, respectively), taken from Ref. [76], which were calculated using the same approach, it appears that, in all cases, $E_b > E_{coh}$, clearly indicating that metal sintering is not thermodynamically favored.

To a large extent, the adsorption energy (E_{ads}) of key reaction intermediates such as O_2, OOH, O, and OH determines the magnitude of the Gibbs free energy values that govern the catalytic performance of the ORR, as discussed above. Therefore, it is interesting to analyze the main trends just for the adsorption energy of the different species X defined as:

$$E_{ads} = E_{SAC\_X} - E_{SAC} - E_X \quad (36)$$

Table 1
Calculated formation energy (E_f), binding energy (E_b), and cohesive energies (E_{coh}) of the different SAC model in eV. The rightmost column corresponds to the calculated Bader net charges (Q) at the M center in the isolated SAC models.

SAC	E_f	E_b	E_{coh}	Q
Sc	-3.85	-8.54	-4.64	1.82
Ti	-2.05	-8.52	-3.67	1.43
V	-1.51	-7.73	-2.42	1.32
Mn	-2.54	-6.77	-3.85	1.29
Fe	-1.75	-7.68	-2.81	1.08
Ni	-2.48	-7.99	-3.12	0.83
Cu	-0.40	-5.26	-1.78	0.90
Pt	-1.67	-7.81	-2.31	0.72

where $E_{SAC\,X}$ and E_X are the total energy of X species adsorbed on the SAC and on the gas phase, respectively, computed in the supercell. Negative E_{ads} values indicate that the adsorption process is energetically favorable. The optimal E_{ads} values were obtained by explicitly considering all different adsorption modes and, for each, carrying out its structural optimization. Fig. 2 and Table S1 summarizes the obtained values including a schematic representation of the final optimized structures. Finally, Table 1 also reports the net Bader charges of the metal atoms in each SAC model, all values are positive indicating that the metal gets partially oxidized with the net charge decreasing from Sc to Cu as expected, the lowest value is for Pt which is includes as reference. This confirms that single metal atoms are suitable active sites that lead to considerable differences in charge transfer between substrates and oxygen molecules. Finally, we briefly discuss the density of states (DOS) and projected DOS (PDOS) of all systems with the corresponding plots reported in Fig. S1. The plots show that all systems exhibit a metallic or nearly metallic character that makes them good candidates for electrode. The plots also show a clear overlap between the metal 3*d* (5*d* for Pt) and the N 2*p* levels due to the strong bonding between the metal atoms and the anchoring N atoms.

5. Gibbs free energy profiles and ORR electrocatalysis performance

Here we analyze the four-electron pathway for the ORR in alkaline condition to determine the SAC with the highest electrocatalytic activity. Fig. 3 shows the free-energy profile for each SAC model at zero potential and $pH = 14$, obtained according to Eqs. (23) to (26), and includes the values for the ideal catalyst for comparison. For completeness, the calculated E, E_{ZPE}, TS, and G values for *OOH, *OH, *O on each metal are reported in Tables S2 to S4, respectively. The steps with a positive ΔG value are thermodynamically hindered and determine the theoretical overpotential [87,88]. Fig. S2 shows that in the case of Sc, there is only one step with positive ΔG that corresponds to *O to *OH conversion. For V, Ti, Fe, and Mn, there are two steps with positive ΔG but again with the *O to *OH conversion is thermodynamically most uphill, and thus, defines the potential-determining step (PDS). Interestingly, for Ni, Cu, and Pt, there is only one step with positive ΔG, but it corresponds to *OOH formation as the PDS.

At $pH = 14$, the equilibrium ΔG_{ORR} at $U = 0$ V is -1.60 eV —*i.e.* -0.40×4— as opposite to $\Delta G_{ORR} = -4.92$ eV from -1.23×4 at $pH = 0$. Thus, at $pH = 14$, the equilibrium potential *vs.* SHE is $U = 0.4$ V and, under this condition, ΔG_{ORR} becomes obviously zero as from Eq. (27) it turns out that Gibbs adsorption energies are shifted by $+ n_e U$, depending on the number of electrons corresponding to each step. Obviously, for all catalysts, $\Delta G_{ORR} = 0$ eV is met a $U = 0.4$ V *vs.* SHE and $pH = 14$. One must note that, for the ideal catalyst at $U = 0.4$ V *vs.* SHE

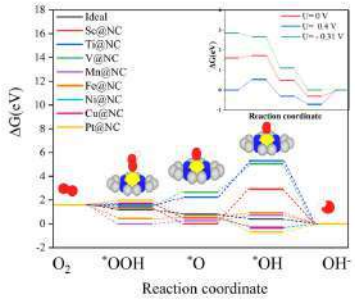

Fig. 3. Gibbs free energy diagrams for ORR at $U = 0$ V and $pH = 14$ for the Sc, Ti, V, Mn, Fe, Ni, Cu, and Pt SACs with the ideal catalysts included for comparison. The inset corresponds to the plots for the Cu SAC at $pH = 14$ and $U = 0$ V, at the equilibrium potential (0.4 V) and at U_L V *vs.* SHE, which is system dependent. Inset images colour-coding as in Fig. 2.

and $pH = 14$, the four steps have $\Delta G_i = 0$. However, for real catalysts under these conditions, the respective ΔG_i values of the elementary steps are not zero and one needs to consider the limiting potential $-U_L$ as defined in Eq. (32) —, that is, the specific value for each system at which the Gibbs free energies in each electrochemical step become thermoneutral or negative. The calculated U_L values of Sc, Ti, V, Mn, Fe, Ni, Cu, and Pt are -2.91, -3.05, -2.39, -0.47, -0.35, -0.35, -0.31, and -0.69 V, *vs.* SHE, respectively. According to Eq. (32), the difference between the equilibrium potential ($U = 0.4$ V *vs.* SHE) and the limiting potential (U_L) defines the theoretical overpotential η_{theo} —*cf.* Eq. (33)— with values of 3.30, 3.45, 2.79, 0.87, 0.81, 0.75, 0.71, and 1.09 V *vs.* SHE, in the same order, respectively. From this set of results, it is clear that transition metal with few *d* electrons exhibit large limiting potential and this decreases drastically once the d shell is half filled with Cu being identified as the best candidate among the considered SAC systems.

To reach a deeper insight into the mechanism, we explored the electrochemical-step symmetry index (*ESSI*) [89] which allows concluding how close a catalyst is to the ideal case [90,91]. For convenience, the *ESSI* is usually defined for the OER as

$$ESSI = \frac{1}{n}\sum_{i}^{n}\left(\frac{\Delta G_i^{+}}{e^{-}} - E^{0}\right) \quad (37),$$

where ΔG_i^{+} corresponds to the opposite of reaction energies in Eqs. (23–26) larger or equal than the equilibrium potential E^0as only the corresponding steps can be potential-limiting; recall that at the present

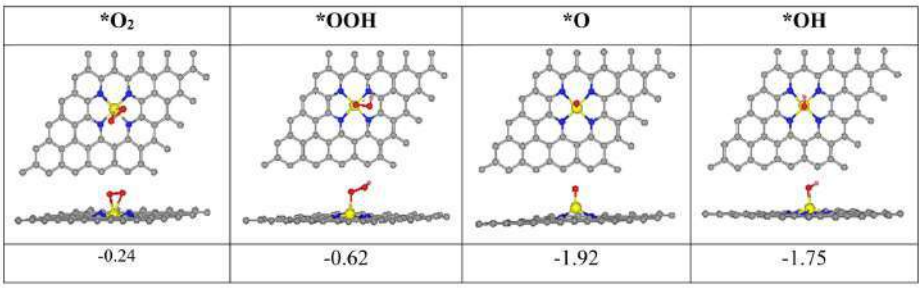

Fig. 2. Top (top) and side (bottom) atomic structures for $*O_2$, *OOH, *O, and *OH at the Cu SAC catalyst with their corresponding adsorption energy (E_{ads}, in eV). The information for the rest of systems can be found in Table S1. O and H atoms are shown as red and white spheres, respectively, while the rest of the color-coding is as in Fig. 1.

alkaline conditions, E^0 is + 0.4 V *vs.* SHE. Obviously, for the ideal catalyst, $n = 4$, $\Delta G_i^+/e^- = E^0$ for all steps i, and thus, *ESSI* = 0 V. The relationship between the *ESSI* for the OER and ORR, hereafter denoted as *ESSI(OER)* and *ESSI(ORR)* has been previous derived by Govindarajan *et al.* [92], so here it suffices to state that for $n = 3, 2, 1$ in the OER one has $n = 1, 2, 3$ in the ORR and *ESSI(ORR)* = −3 *ESSI(OER)*, *ESSI (ORR)* = - *ESSI(OER)* and *ESSI(ORR)* = −1/3 *ESSI(OER)*; note that the case of n = 4 corresponds to the ideal catalysts and one has *ESSI(ORR)* = *ESSI(OER)* = 0. Now let us know, discuss the *ESSI(ORR)* values for the present systems which are also collected in Table 3. For the case of Cu, from Eqs. (23) to (26) one has $\Delta G_{10} = 0.13$ eV, $\Delta G_{11} = -1.24$ eV, $\Delta G_{12} = -0.80$ eV, and $\Delta G_{13} = 0.31$ eV. In this case there are two steps with ΔG smaller than − 0.4 eV, so $n = 2$, either in OER or ORR, and *ESSI (ORR)* = (−1.24 - 0.80)/2 + 0.4 = - 0.62 V. For the case of Ti, $\Delta G_{10} = -0.04$ eV, $\Delta G_{11} = 0.69$ eV, $\Delta G_{12} = 3.05$ eV, and $\Delta G_{13} = -5.30$ eV, here for the OER $n = 1$ therefore, *ESSI(ORR)* = 1/3 [(−5.30/1) + 0.4] = −1.63. Next, in Fig. 4, we plot *ESSI(ORR)* against $-\eta_{ORR}$ and note that, from Table 2, *n* for ORR is equal to 2 for Sc, Mn, Fe, Ni, Cu, Pt while it appears to be 1 for Ti and V. Clearly, catalysts with $n = 2$ displayed low values of η_{ORR} and are close to the ideal catalyst thus supporting previous findings for other systems [91].

To end up the discussion on the obtained results, we briefly comment on the so-called $G_{max}(\eta)$ descriptor [93,94] defined as the largest positive span for all possible reactions between the intermediate species in the mechanism corresponding to Eqs. (10)-(13). This implies computing the Gibbs free energy spans from all possible starting reactants or intermediates to the next ones in the reaction mechanism. Here, one starts by computing the Gibbs free energy from $O_{2(g)}$ to *OOH, *O, *OH or OH^-, and the next step involves computing the Gibbs free energy from *OOH to *O, *OH or OH^-. It continues by computing the Gibbs free energy from *O to *OH or OH^-, and, finally, computing the Gibbs free energy from *OH or OH^-. $G_{max}(\eta)$ just corresponds to the largest of all these values, *i.e.* the largest span. For a more detailed discussion, the reader is referred to reference [95]. For instance, for Sc $G_{max}(\eta)$ at $U = 0$ and $pH = 14$ is determined by ΔG_{12} while for Ti, V, Mn and Fe it is determined by $\Delta G_{11} + \Delta G_{12}$, by ΔG_{13} for Ni and; finally by $\Delta G_{10} + \Delta G_{13}$ for Cu and Pt. Thus, the $G_{max}(\eta)$ values can be directly obtained from the values in Table 2 but are reported in Table 3 for convenience. In principle, high activity is associated to small $G_{max}(\eta)$ values but contrarily, to ESSI, a precise value for the ideal catalyst cannot be defined. From the values in Table 2 and, especially from the plot in Fig. 4, one readily see that the two descriptors lead to a similar description even in ESSI is based on thermodynamics and $G_{max}(\eta)$ comes from the span model proposed by Kozuch and Shaik [96] on the basis of kinetics arguments. In fact, the span governing $G_{max}(\eta)$ provides an approximation of the rate-determining step if a suitable value for the Tafel slope (typically 40 mV/dec or 120 mV/dec) is adopted.

Table 2
Calculated Gibbs free energies (ΔG_i, i = 10–13, in eV), the overpotentials (η), and the limiting potentials (U_L) of different catalysts at $U = 0$ V, $pH = 14$.

SAC	ΔG_{10}	ΔG_{11}	ΔG_{12}	ΔG_{13}	η_{theo} (V)	U_L (V)
Ideal	-0.40	-0.40	-0.40	-0.40	0.00	0.00
Sc	-0.23	-1.35	2.90	-2.92	3.30	-2.90
Ti	-0.04	0.69	3.05	-5.30	3.45	-3.05
V	-0.17	1.23	2.39	-5.05	2.79	-2.39
Mn	-1.61	0.27	0.47	-0.73	0.87	-0.47
Fe	-1.15	0.07	0.41	-0.93	0.81	-0.41
Ni	0.09	-1.07	-0.97	0.35	0.75	-0.35
Cu	0.13	-1.24	-0.8	0.31	0.71	-0.31
Pt	0.37	-1.37	-1.29	0.69	1.09	-0.69

Table 3
Electrochemical-step symmetry index (*ESSI*) and $G_{max}(\eta)$ descriptor for the explored systems at $U = 0$ V and $pH = 14$.

SAC	*ESSI* (V)	G_{max} (η) (eV)
Ideal	0.00	—
Sc	-1.73	2.90
Ti	-1.63	3.74
V	-1.55	3.62
Mn	-0.77	0.74
Fe	-0.64	0.48
Ni	-0.62	0.35
Cu	-0.62	0.44
Pt	-0.93	1.06

6. Conclusions

In the present work, we studied the ORR performance of a series of single-atom catalysts (Sc, Ti, V, Mn, Fe, Ni, Cu, and Pt) in alkaline media as possible candidates for cathodes in advanced chlor-alkali electrolysis, in which the single atoms being anchored at the hollow sites of N-doped graphene. Using periodic density functional theory calculations on a suitable supercell, a four-electron mechanism is proposed that allows studying the Gibbs free-energy profiles and deriving the thermodynamic overpotential invoking the computational hydrogen electron model. The

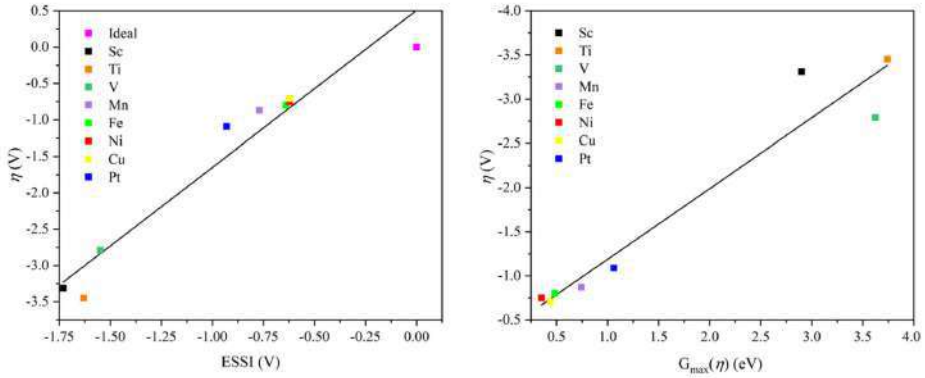

Fig. 4. Plot of predicted overpotentials (η) *versus* the electrochemical-step symmetry index (*ESSI*) for the ORR reaction at U = 0 V and $pH = 14$ (left panel) and *vs.* the $G_{max}(\eta)$ descriptor in eV (right panel). The ideal catalyst, for which η_{ORR} = ESSI = 0 is shown for comparison.

present results show that the N-doping and vacancy effect can create a strong bond between the metal and the substrate. The studied catalysts are stable against sintering with the metal atoms being partially oxidized. From all metals, Cu is predicted to exhibit the best performance with a relatively low theoretical overpotential of 0.71 V in alkaline condition ($pH = 14$). The electrochemical-step symmetry index (ESSI) has been obtained for the ORR in the different systems and plotted against the overpotential. The plot evidences that catalysts with more than one step above the equilibrium potential approach the conditions of the ideal catalysts, in agreement with previous findings for a variety of systems and putting this index as an excellent descriptor of the catalytic activity. This work not only enhances our understanding of graphene-based single-atom catalysts for ORR in alkaline media but also provides an example of the rational design of high-performance ORR catalysts using DFT calculations and theory derived descriptors.

CRediT authorship contribution statement

Shaldehi Tahereh Jangjooye: Data curation, Investigation, Writing – original draft, Formal analysis, Validation. **Rowshanzamir Soosan:** Funding acquisition, Supervision, Writing – review & editing. **Meng Ling:** Conceptualization, Data curation, Formal analysis, Methodology, Writing – original draft, Writing – review & editing, Validation, Visualization. **Exner Kai:** Conceptualization, Formal analysis, Investigation, Methodology, Writing – review & editing, Supervision. **Parnian Mohammad Javad:** Supervision, Writing – review & editing. **Illas Francesc:** Conceptualization, Formal analysis, Funding acquisition, Investigation, Methodology, Resources, Supervision, Writing – original draft, Writing – review & editing, Validation. **Viñes Francesc:** Supervision, Validation, Writing – review & editing, Conceptualization, Investigation, Methodology, Resources.

Declaration of Competing Interest

The authors declare that they have no known competing financial interests or personal relationships that could have appeared to influence the work reported in this paper.

Data availability

Data will be made available on request.

Acknowledgments

The authors are thankful to Dr. Federico Calle-Vallejo for fruitful discussions regarding the electrochemical-step symmetry index. The present study has been supported by the Spanish MCIN/AEI/10.13039/501100011033 PID2021–126076NB-I00 and TED2021–129506B-C22 projects, funded partially by FEDER, *una manera de hacer Europa*, and *María de Maeztu* CEX2021–001202-M grants, including funding from European Union. In addition, the work has been supported in part by COST Action CA18234 and the *Generalitat de Catalunya* financial support to research groups grant 2021SGR79. K.S.E. acknowledges funding by the Ministry of Culture and Science of the Federal State of North Rhine-Westphalia (NRW Return Grant). K.S.E. is associated with the CRC/TRR247: "Heterogeneous Oxidation Catalysis in the Liquid Phase" (Project number 388390466-TRR 247), the RESOLV Cluster of Excellence, funded by the Deutsche Forschungsgemeinschaft under Germany's Excellence Strategy – EXC 2033 – 390677874 – RESOLV, and the Center for Nanointegration (CENIDE). T. Jangjooye Shaldehi special thanks to the Ministry of Science, Research and Technology (MSRT) of the Islamic Republic of Iran for financing her research visit; L.M. thanks the China Scholarship Council (CSC) for financing her PhD (CSC202108390032; and F.V. thanks the ICREA Academia Award 2023 Ref. Ac2216561.

Appendix A. Supporting information

Supplementary data associated with this article can be found in the online version at doi:10.1016/j.cattod.2024.114560.

References

[1] K. Li, Q. Fan, H. Chuai, H. Liu, S. Zhang, X. Ma, Trans. Tianjin Univ. 27 (2021) 202–216.
[2] Y. Liu, Y. Wang, S. Zhao, J. Curr. Opin. Electrochem 37 (2023) 101202.
[3] S. Lakshmanan, T. Murugesan, J. Clean. Technol. Environ. Policy 16 (2014) 225–234.
[4] J.A. Rosales Huamani, Z.M. Díaz Cordova, J.A. Montaño Pisfil, J. Batteries 7 (2021) 1–11.
[5] T.F. O'Brien, T.V. Bommaraju, F. Hine, Handb. Chlor-Alkali Technol. (2005) 17–36.
[6] P. Millet, Handb. Membr. React. 2 (2013) 384–415.
[7] J. Crook, A. Mousavi, J. Environ. Forensics 17 (2016) 211–217.
[8] M. Paidar, V. Fateev, K. Bouzek, J. Electrochim. Acta 209 (2016) 737–756.
[9] J. Jung, S. Postels, A. Bardow, J. Clean. Prod. 80 (2014) 46–56.
[10] Y. Kiros, M. Pirjamali, M. Bursell, J. Electrochim. Acta 51 (2006) 3346–3350.
[11] T. Morimoto, K. Suzuki, T. Matsubara, N. Yoshida, J. Electrochim. Acta 45 (2000) 4257–4262.
[12] M. Sudoh, T. Kondoh, N. Kamiya, T. Ueda, K. Okajima, J. Electrochem. Soc. 147 (2000) 3739.
[13] J. Kintrup, M. Millanuelo, V. Trieu, A. Bulán, E.S. Mojica, J. Electrochem. Soc. 26 (2017) 73–76.
[14] I. Moussallem, J. Jörissen, U. Kunz, S. Pinnow, T. Turek, J. Appl. Electrochem 38 (2008) 1177–1194.
[15] A. Botz, J. Clausmeyer, D. Öhl, T. Tarnev, D. Franzen, T. Turek, W. Schuhmann, J. Angew 57 (2018) 12285–12289.
[16] F. Kubannek, T. Turek, U. Krewer, J. Chem. Ing. –Tech. 91 (2019) 720–733.
[17] W.S.A. Ignaczak, R. Nazmutdinov, A. Goduljan, L.M. de Campos Pinto, F. Juarez, P. Quaino, E. Santos, J. Nano, Energy 29 (2016) 362–368.
[18] N. Ramaswamy, S. Mukerjee, J. Adv. Phys. Chem. 2012 (2012) 491604.
[19] T.R. Ralph, M.P. Hogarth, J. Platin. Met. Rev. 46 (2002) 3–14.
[20] F. Farzami, E. Joudaki, S.J. Hashemi, J. Eng. 3 (2011) 836–841.
[21] Y. Kiros, T. Quatrano, P. Bj, J. Electrochem Commun. 6 (2004) 526–530.
[22] N. Furuya, H. Aikawa, J. Electrochim. Acta 45 (2000) 4251–4256.
[23] F. Bienen, M. Paulisch, T. Mager, J. Osiewacz, M. Nazari, M. Oseberg, B. Ellendorff, Th Turek, U. Nieken, I. Manke, K. Friedrich, J. EISA 3 (2022) 1–12.
[24] Y. Kiros, M. Pirjamali, M. Bursell, J. Electrochim. Acta 51 (2006) 3346–3350.
[25] Y. Kiros, M. Bursell, Int. J. Electrochem 3 (2008) 444–451.
[26] M.G. Hosseini, P. Zardari, J. Appl. Surf. Sci. 345 (2015) 223–231.
[27] F. Farzami, E. Joudaki, S.J. Hashemi, J. Eng. 3 (2011) 836–841.
[28] P. Zardari, M.G. Hosseini, Int. J. Hydrog. Energy 41 (2016) 8803–8818.
[29] M.G. Hosseini, P. Zardari, I. Ariankhah, J. Iran. Chem. Soc. 16 (2019) 1749–1760.
[30] K. Fujimoto, Y. Ueda, T. Ishida, Y. Fujii, M. Nakayama, J. Electrochem. Soc. 168 (2021) 086510.
[31] X. Zhai, W. Yang, M. Li, G. Lv, J. Liu, X. Zhang, J. Carbon 65 (2013) 277–286.
[32] A. Zhao, J. Masa, W. Schuhmann, W. Xia, J. Phys. Chem. C. 117 (2013) 24283–24291.
[33] Y. Liang, Y. Li, H. Wang, H. Dai, J. Am. Chem. Soc. 44 (2013) 2013–2036.
[34] J. Schosseler, A. Trentmann, B. Friedrich, K. Hahn, H. Wotruba, J. Met 9 (2019).
[35] U. Tylus, et al., J. APPL CATAL B ENVIRON 198 (2016) 318–324.
[36] T. Donga, G.B. Noumi, M.J. Sieliechi, J.B. Tchatchueng, J. Carbon Trends 4 (2021) 100043.
[37] L. Jiao, H.L. Jiang, J. Chem. 5 (2019) 786–804.
[38] H. Huang, K. Shen, F. Chen, Y. Li, J. ACS Catal. 10 (2020) 6579–6586.
[39] S. Dang, Q.L. Zhu, Q. Xu, J. Nat. Rev. Mater. 3 (2017).
[40] Y. Shang, X. Duan, S. Wang, Q. Yue, B. Gao, X. Xu, J. CCL 33 (2022) 663–673.
[41] I. Barlocco, L.A. Cipriano, G. Di Liberto, G. Pacchioni, J. Catal. 417 (2023) 351–359.
[42] S. Tosoni, G. Di Liberto, I. Matanovic, G. Pacchioni, J. Power Sources 556 (2023) 232492.
[43] P. Jiao, Sh Wu, C. Zhu, D. Ye, C. Qin, C. An, N. Hu, Q. Deng, J. Nanoscale 14 (2022) 14322–14340.
[44] Y. Wang, F. Hu, Y. Mi, C. Yan, S. Zhao, J. Chem. Eng. 406 (2020) 127135.
[45] J.K. Nørskov, J. Rossmeisl, A. Logadottir, L. Lindqvist, J.R. Kitchin, T. Bligaard, H. Jónsson, J. Phys. Chem. B 108 (2004) 17886–17892.
[46] C. Fu, C. Liu, T. Li, X. Zhang, F. Wang, J. Yang, Y. Jiang, P. Cui, H. Li, J. Comput. Mater. Sci. 170 (2019) 109202.
[47] S. Maheshwari, Y. Li, N. Agrawal, M.J. Janik, Adv. Catal. 63 (2018) 117–167.
[48] A. Kulkarni, S. Siahrostami, A. Patel, J.K. Nørskov, J. Chem. Rev. 118 (2018) 2302–2312.
[49] H.Y. Zhuo, X. Zhang, J.X. Liang, Q. Yu, H. Xiao, J. Li, J. Chem. Rev. 120 (2020) 12315–12341.
[50] L. Yu, X. Pan, X. Cao, P. Hu, X. Bao, J. Catal. 282 (2011) 183–190.
[51] M.G. Hosseini, F. Hosseinzadeh, P. Zardari, M. Darbandi, Int. J. Hydrog. Energy 46 (2021) 28513–28526.
[52] M.G. Hosseini, P. Zardari, J. Appl. Surf. Sci. 345 (2015) 223–231.
[53] M.G. Hosseini, P. Zardari, Int. J. Hydrog. Energy 41 (2016) 8803–8818.
[54] R.S. Figueiredo, R. Bertazzoli, C.A. Rodrigues, J. Ind. Eng. Chem. 52 (2013) 5611–5615.

[55] M.G. Hosseini, F. Hosseinzadeh, P. Zardari, O. Mermer, J. Fuller Nanotub Car N. 26 (2018) 675–687.
[56] X. Zhao, Y. Liu, J. Am. Chem. Soc. 143 (2021) 9423–9428.
[57] S. Siahrostami, G.L. Li, V. Viswanathan, J.K. Nørskov, J. Phys. Chem. Lett. 8 (2017) 1157–1160.
[58] V. Viswanathan, H.A. Hansen, J.K. Nørskov, J. Phys. Chem. Lett. 6 (2015) 4224–4228.
[59] C. Zhang, S. Yu, Y. Xie, W. Zhang, K. Zheng, N.E. Drewett, S.J. Yoo, Z. Wang, L. Shao, H. Tian, J. G. Kim, W. Zheng, J. Carbon 140 (2019) 370–379.
[60] C. Zhang, W. Zhang, S. Yu, D. Wang, W. Zhang, W. Zheng, M. Wen, H. Tian, K. Huang, S. Feng, J.J. Bentzen, J. ChemElectroChem 4 (2017) 1269–1273.
[61] K. Exner, ChemCatChem 15 (2023) e202201222.
[62] I. Man, H. Su, F. Calle-Vallejo, H. Hansen, J. Martínez, N. Inoglu, J. Kitchin, T. Jaramillo, J. Nørskov, J. Rossmeisl, J, Chemcatchem 3 (2011) 1159–1165.
[63] E. Sargeant, F. Illas, P. Rodríguez, F. Calle-Vallejo, J. ChemElectroChem 896 (2021) 115178.
[64] M.T.M. Koper, J. Chem. Sci. 4 (2013) 2710–2723.
[65] A. Ignaczak, R. Nazmutdinov, A. Goduljan, L.Moreira de Campos Pinto, F. Juarez, P. Quaino, G. Belletti, E. Santos, W. Schmickler, J. Electro 8 (2017) 554–564.
[66] Q. Liang, G. Brocks, A. Bieberle-Hütter, J. Phys. Energy 3 (2021) 026001.
[67] G. Di Liberto, G. Pacchioni, Adv. Mater. 35 (2023) 2307150.
[68] F. Calle-Vallejo, J.I. Martínez, J.M. García-Lastra, E. Abad, M.T.M. Koper, J. Surf, Sci 607 (2013) 47–53.
[69] J. Cho, T. Lim, H. Kim, L. Meng, J. Kim, J.H. Lee, G.Y. Jung, F. Viñes, F. Illas, K. S. Exner, S.H. Joo, C.H. Choi, Nat. Commun. 14 (2023) 3233.
[70] K.S. Exner, J. Anton, T. Jacob, Electrochim. Acta 120 (2014) 460–466.
[71] M. López, K.S. Exner, F. Viñes, F. Illas, Adv. Theory Simul. 6 (2023) 2200217.
[72] I. Granda-Marulanda, A. Rendon-Calle, S. Builes, F. Illas, F. Calle-Vallejo, M.T. M. Koper, ACS Catal. 10 (2020) 6900–6907.
[73] J.P. Perdew, K. Burke, M. Ernzerhof, Rev. Lett. 77 (1996) 3865.
[74] S. Grimme, J. Antony, S. Ehrlich, H. Krieg, J. Chem. Phys. 132 (2010) 154104.
[75] P. Janthon, S. Luo, S.M. Kozlov, F. Viñes, J. Limtrakul, D.G. Truhlar, F. Illas, J. Chem. Theory Comput. 10 (2014) 3832–3839.
[76] P. Janthon, S.M. Kozlov, F. Viñes, J. Limtrakul, F. Illas, J. Chem. Theory Comput. 9 (2013) 1631–1640.
[77] L. Vega, F. Viñes, J. Comput. Chem. 41 (2020) 2598–2603.
[78] D. Vázquez-Parga, A. Fernández-Martínez, F. Viñes, J. Chem. Theory Comput. 19 (2023) 198285–198292.
[79] I. Barlocco, L.A. Cipriano, G. Di Liberto, G. Pacchioni, Adv. Theory Simul. 6 (2023) 2200513.
[80] G. Di Liberto, L.A. Cipriano, G. Pacchioni, A CS Catal. 12 (2022), 5846–585.
[81] R. Urrego-Ortiz, S. Builes, F. Illas, F. Calle-Vallejo, EES Catal. 2 (2024) 157–179.
[82] P.E. Blöch, J. Phys. Rev. B 50 (1994) 17953.
[83] G. Kresse, D. Joubert, J. Phys. Rev. B 59 (1999) 1758.
[84] H.J. Monkhorst, J.D. Pack, J. Phys. Rev. B 13 (1976) 5188.
[85] G. Kresse, J. Furthmüller, Phys. Rev. B Condens. Matter Mater. Phys. 54 (1996) 11169.
[86] J.P. Perdew, K. Burke, M. Ernzerhof, J. Phys. Rev. Lett. 77 (1996) 3865.
[87] M.T.M. Koper, J. Solid, State Electrochem 17 (2013) 339–344.
[88] J.K. Nørskov, J. Rossmeisl, A. Logadottir, L. Lindqvist, J.R. Kitchin, T. Bligaard, H. Jónsson, J. Phys. Chem. B 108 (2004) 17886–17892.
[89] N. Govindarajan, J.M. García-Lastra, E.J. Meijer, F. Calle-Vallejo, Curr. Opin. Electrochem.. 8 (2018) 110–117.
[90] O. Piqué, F. Illas, F. Calle-Vallejo, J. Phys. Chem. Chem. Phys. 22 (2020) 6797–6803.
[91] E. Romeo, F. Illas, F. Calle-Vallejo, J. Chem. Sci. 14 (2023) 3622–3629.
[92] N. Govindarajan, J.M. García-Lastra, E.Jan Meijer, F. Calle-Vallejo, J. Curr. Opin. Electrochem 8 (2018) 110–117.
[93] K. Exner, ACS Catal. 10 (2020) 12607–12617.
[94] S. Razzaq, K. Exner, J. ACS Catal. 13 (2023) 1740–1758.
[95] K.S. Exner, ACS Phys. Chem. Au 3 (2023) 190–198.
[96] S. Kozuch, S. Shaik, J. Acc. Chem. Res. 44 (2011) 101–110.

nature communications

Article

https://doi.org/10.1038/s41467-023-38964-x

Importance of broken geometric symmetry of single-atom Pt sites for efficient electrocatalysis

Received: 6 January 2023

Accepted: 24 May 2023

Published online: 03 June 2023

Check for updates

Junsic Cho[1,10], Taejung Lim[2,10], Haesol Kim[1,10], Ling Meng[3], Jinjong Kim[2,4], Seunghoon Lee[1], Jong Hoon Lee[5], Gwan Yeong Jung[6], Kug-Seung Lee[7], Francesc Viñes[3], Francesc Illas[3], Kai S. Exner[8] ✉, Sang Hoon Joo[2,4] ✉ & Chang Hyuck Choi[1,9] ✉

Platinum single-atom catalysts hold promise as a new frontier in heterogeneous electrocatalysis. However, the exact chemical nature of active Pt sites is highly elusive, arousing many hypotheses to compensate for the significant discrepancies between experiments and theories. Here, we identify the stabilization of low-coordinated Pt^{II} species on carbon-based Pt single-atom catalysts, which have rarely been found as reaction intermediates of homogeneous Pt^{II} catalysts but have often been proposed as catalytic sites for Pt single-atom catalysts from theory. Advanced online spectroscopic studies reveal multiple identities of Pt^{II} moieties on the single-atom catalysts beyond ideally four-coordinated Pt^{II}–N_4. Notably, decreasing Pt content to 0.15 wt.% enables the differentiation of low-coordinated Pt^{II} species from the four-coordinated ones, demonstrating their critical role in the chlorine evolution reaction. This study may afford general guidelines for achieving a high electrocatalytic performance of carbon-based single-atom catalysts based on other d^8 metal ions.

Downsizing bulk metal catalysts to the atomic level, alias single-atom catalysts (SACs), is a promising strategy for realizing superior catalytic activity and reducing costs[1–3]. SACs are often considered bridges between heterogeneous and homogeneous catalysis, and ideally, they bring hope to realize a uniform active site distribution, as encountered in homogeneous catalysis, in the realm of heterogeneous catalysts[4,5]. However, increasing literature suggests that SACs exhibit a significant degree of heterogeneity in their active sites[6–8]. Consequently, this heterogeneity hinders the identification of the genuine active site and the precise quantification of the intrinsic activity of the catalysts by turnover frequency (TOF) or similar metrics, thus causing formidable challenges for the rational design of better SACs.

In this work, we focus on archetypical Pt SACs, which have found broad utility in a variety of electro-, photo-, and heterogeneous catalytic reactions[9–12]. In general, Pt SACs are composed of Pt ions in an oxidation state of +2[11–14]. Because Pt^{II} has a d^8 electronic configuration,

[1]Department of Chemistry, Pohang University of Science and Technology (POSTECH), Pohang 37673, Republic of Korea. [2]Department of Chemistry, Ulsan National Institute of Science and Technology (UNIST), Ulsan 44919, Republic of Korea. [3]Departament de Ciència de Materials i Química Física & Institut de Química Teòrica i Computacional (IQTCUB), Universitat de Barcelona, c/ Martí i Franquès 1-11, 08028 Barcelona, Spain. [4]Department of Chemistry, Seoul National University, Seoul 08826, Republic of Korea. [5]UNIST Central Research Facilities (UCRF), Ulsan National Institute of Science and Technology (UNIST), Ulsan 44919, Republic of Korea. [6]School of Energy and Chemical Engineering, Ulsan National Institute of Science and Technology (UNIST), Ulsan 44919, Republic of Korea. [7]Beamline Department, Pohang Accelerator Laboratory, Pohang University of Science and Technology (POSTECH), Pohang 37673, Republic of Korea. [8]Faculty of Chemistry, Theoretical Inorganic Chemistry, University of Duisburg-Essen, 45141 Essen, Germany; Cluster of Excellence RESOLV, 44801 Bochum, Germany; Center for Nanointegration Duisburg-Essen (CENIDE), 47057 Duisburg, Germany. [9]Institute for Convergence Research and Education in Advanced Technology (I-CREATE), Yonsei University, Seoul 03722, Republic of Korea. [10]These authors contributed equally: Junsic Cho, Taejung Lim, Haesol Kim. ✉e-mail: kai.exner@uni-due.de; shjoo1@snu.ac.kr; chchoi@postech.ac.kr

it strongly prefers to be stabilized by a near-perfect square planar geometry (D_{4h}), as expected from the ligand field theory[15]. Thus, based on conventional extended X-ray absorption fine structure (EXAFS) analyses, the coordination environments of Pt^{II} in carbon-supported Pt SACs are typically accepted as a porphyrin-like geometry, such as $Pt–N_4$ and $Pt–S_4$, where *p*-block elements doped in carbon substrates function as surface pockets for immobilizing Pt ions[16–19]. However, in theory, these model structures predict substantially weakened axial coordination and, consequently, poor catalytic activity, while broken or unsaturated ones are expected to offer more optimized axial coordination leading to high catalytic activity[12,20–23]. These phenomena originate from a significant ligand field splitting (Δ), which effectively upshifts the energy level of the empty $d_{x^2-y^2}$ orbital, but lowers that of the fully occupied other *d* orbitals. Thus, a considerable energy cost is required for the charge redistribution of Pt^{II} for its strong axial bond formation. Therefore, discrepancies between the experimentally observed electrocatalytic performance of carbon-supported Pt SACs and theoretically computed models have been reported in the literature[24].

Extensive efforts have thus been made to identify the chemical nature of the catalytic sites in Pt SACs. Possible asymmetric coordination geometries such as $Pt–N_xC_{4-x}$ have been proposed by density functional theory (DFT) calculations[19,25,26]. Additionally, in situ modifications of the symmetric coordination geometries, formed by partial ligand exchange of the four equivalent ligands with electrolyte components (e.g., water) or by changes in the oxidation state of the central Pt^{II} ions under realistic electrochemical conditions, have also been considered[12,19,27]. Despite previous achievements, which indicate the poor or moderate catalytic performance of Pt sites with symmetric D_{4h} geometry, the broken geometric symmetry of Pt SACs and their key roles in electrocatalysis have not been clarified thus far. This uncertainty primarily originates from the possible heterogeneity of isolated Pt sites, considering that not all sites are necessarily equally active toward the investigated electrochemical reaction. Unfortunately, even EXAFS analysis, which is likely the most powerful and extensively used technique for studying the structure of a single site, cannot conclusively distinguish between different Pt moieties that coexist in SACs. Thus, the synthesis of SACs containing homogeneous catalyst-like single active sites is crucial for the clear identification of the genuine active sites in Pt SACs.

This study reveals the presence of low-coordinated Pt^{II} species in carbon-based Pt SACs and their vital roles in electrocatalysis. The chlorine evolution reaction (CER) is taken as a model reaction, of which the product, Cl_2, is practically important due to extensive applications in the chemical industry, typically produced via the chlor-alkali process with Ru/Ir-based dimensionally stable anode (DSA) electrodes[28,29]. We quantify the extent of Pt demetallation from Pt SACs in operando using advanced online inductively coupled plasma-mass spectrometry coupled with an electrochemical flow cell (EFC/ICP-MS) and compare the result with the simultaneous electrochemical activity loss during the CER. No singular Pt identity is confirmed from the considerable discrepancy between these two parameters, i.e., Pt dissolution vs. CER activity loss, without significant modification of the TOF. In addition to the common symmetric D_{4h} geometry, low-coordinated Pt^{II} species is clearly observed in the EXAFS spectrum of a control Pt SAC with an ultralow Pt loading of 0.15 wt.%. Structure-dependent studies of the catalytic activity, selectivity, and stability by combining experimental and theoretical approaches verify the central role of the low-coordinated Pt^{II} sites in Pt SACs for boosting the CER.

Results

A model catalyst was prepared by heat treatment of a powder mixture of Pt^{II} meso-tetraphenylporphine (PtTPP) and acid-treated carbon nanotubes (CNTs) at 700 °C under N_2 flow. The prepared catalyst was characterized as in our previous studies using high-angle annular dark-field scanning transmission electron microscopy (HAADF-STEM), X-ray diffraction (XRD), X-ray absorption spectroscopy (XAS), and X-ray photoelectron spectroscopy (XPS)[17,30]. The catalyst is composed of abundant porphyrin-like $Pt^{II}–N_4$ moieties, which are covalently embedded on the CNT support (cf. Supplementary Note 1 for a detailed discussion; Supplementary Figs. 1–5). The Pt content is approximately 3 wt.%, as determined by inductively coupled plasma-optical emission spectroscopy (ICP-OES). This model catalyst is hereafter named '$Pt_1(3)$/CNT', where the subscript '1' indicates the atomic isolation of Pt, and the number in parenthesis indicates the Pt content in wt.%.

The catalytic performance of $Pt_1(3)$/CNT was evaluated for the CER, the anodic reaction of chlor–alkali electrolysis to produce gaseous chlorine by a two-electron process — $2Cl^- \rightarrow Cl_2 + 2e^-$, $U^0_{CER} = 1.36$ V vs. standard hydrogen electrode (SHE)[31,32] — that competes with the oxygen evolution reaction (OER; $2H_2O \rightarrow O_2 + 4H^+ + 4e^-$, $U^0_{OER} = 1.23$ V vs. reversible hydrogen electrode (RHE)). $Pt_1(3)$/CNT shows an excellent CER activity (Fig. 1a). While no significant Faradaic current is observed in a NaCl-free 0.1 M $HClO_4$ electrolyte, with the addition of 1 M NaCl into the 0.1 M $HClO_4$ electrolyte, the catalyst records an onset potential of 1.36 V_{RHE} and an oxidation current density (*j*) of 53 mA cm^{-2} at 1.45 V_{RHE}. The online differential electrochemical mass spectrometry (DEMS) measurement reveals a predominant ionic current for $m/z = 35$ (Cl^+) in 0.1 M $HClO_4$ + 1 M NaCl electrolyte (Fig. 1b), which corresponds to the fragmentation of Cl_2 and its hydrolyzed derivatives from the following equation: $Cl_2 + H_2O \rightarrow HCl + HOCl$[32,33]. Concomitantly, distinct ionic currents for $m/z = 36$ and 51 (HCl^+ and OCl^+, respectively) are detected, indicating the formation of HCl and HOCl during CER. An insignificant ionic current for $m/z = 32$ (O_2^+) may attribute to the further decomposition of HOCl forming O_2 via the following equation: $2HOCl \rightarrow 2HCl + O_2$ (cf. Supplementary Note 2 for a detailed discussion of non-Faradaic O_2 formation)[32,33]. In NaCl-free 0.1 M $HClO_4$ electrolyte, the O_2 is not detected within the CER-relevant potential window, inferring that the $Pt_1(3)$/CNT catalyzes CER selectively against competitive OER (Fig. 1c). The DEMS results are further corroborated by the rotating ring disk electrode (RRDE) measurement, which exhibits approximately 100% CER selectivity (Supplementary Fig. 6). Notably, this CER activity outperforms that of the commercial DSA (Supplementary Fig. 7) and most of the previously reported CER catalysts (Supplementary Table 1)[34–39].

The high catalytic activity of $Pt_1(3)$/CNT is primarily attributed to the presence of Pt sites. CNT and N-doped CNT — the latter was synthesized with a Pt-free TPP precursor — exhibit much smaller oxidation currents than $Pt_1(3)$/CNT (Fig. 1a). In addition, the CER activity of $Pt_1(3)$/CNT deteriorates considerably in a CO-saturated electrolyte (Fig. 1d), a well-known poisoning agent with a high binding affinity for atomically isolated Pt^{II} ions[27,40]. This result further confirms the catalytic role of Pt sites in the efficient CER. The polarization curves measured in the Ar- or CO-saturated electrolytes without NaCl are almost identical, indicating that the decrease in CER activity is not an artifact induced by the competitive CO oxidation reaction under anodic polarization conditions.

After confirming the high CER activity of $Pt_1(3)$/CNT and the chemical nature of its catalytic site, the durability of this catalyst was evaluated by measuring 500 iterative cyclic voltammograms (CVs) from 1.0 to 1.6 V_{RHE} (Fig. 1e). We adopted iterative CVs for accelerating catalyst degradation, as this catalyst exhibits promising stability under constant potential conditions relevant to real CER electrolysis conditions (Supplementary Fig. 8). After 500 CVs, $Pt_1(3)$/CNT exhibits a significant decrease in CER activity, and the *j* value measured at 1.45 V_{RHE} decreases by 61% from 53 to 21 mA cm^{-2} (Fig. 1f). The CER activity decreases rapidly at the beginning of the durability test, but then it becomes gradually alleviated.

To reveal the fundamental origin of the observed deactivation, real-time Pt dissolution from $Pt_1(3)$/CNT was analyzed using online

Article https://doi.org/10.1038/s41467-023-38964-x

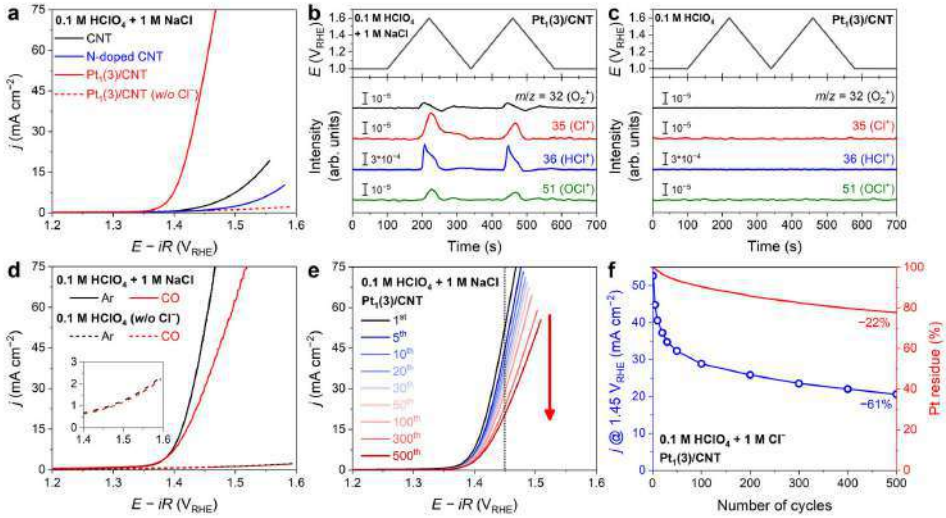

Fig. 1 | CER performance of $Pt_1(3)$/CNT. a CER polarization curves of the CNT, N-doped CNT, and $Pt_1(3)$/CNT catalysts obtained in Ar-saturated 0.1 M $HClO_4$ with 1 M NaCl. The polarization curve of $Pt_1(3)$/CNT measured in an NaCl-free electrolyte is also shown (dotted line). **b**, **c** Online DEMS results of m/z = 32, 35, 36, and 51 of $Pt_1(3)$/CNT during two consecutive slow CVs obtained in Ar-saturated 0.1 M $HClO_4$ with 1 M NaCl (**b**) and NaCl-free electrolytes (**c**). **d** The polarization curves of $Pt_1(3)$/CNT in Ar/CO-saturated 0.1 M $HClO_4$ with and without 1 M NaCl. **e** The durability test of $Pt_1(3)$/CNT performed by measuring CER polarization curves during iterative 500 CVs from 1.0 and 1.6 V_{RHE}. **f** Comparison between the CER activity decrement and Pt loss measured during the durability test.

EFC/ICP-MS in an Ar-saturated 0.1 M $HClO_4$ electrolyte containing 1 M NH_4Cl (Supplementary Figs. 9 and 10). By applying the same CV conditions as those used for the durability study, the Pt sites remaining on the $Pt_1(3)$/CNT were estimated by subtracting the accumulated amount of dissolved Pt ions from the initial Pt content (Supplementary Fig. 11). The total Pt loss after 500 CVs is only 22% (Fig. 1f), which hardly corresponds to the considerable CER activity loss of 61%. Indeed, the Pt dissolution profile reveals relatively no significant Pt demetallation at the beginning of these experiments.

Consequently, we considered a possible TOF modification of the aged $Pt_1(3)$/CNT along with Pt dissolution. It is important to note that the apparent catalytic activity is not only governed by the active site density but also by the TOF of each catalytic site[41–43]. TOF modification of SACs typically originates from structural changes in the local coordination geometry or the introduction of new heteroatoms or functional groups near their catalytic metal sites[20,44,45]. However, the k^3-weighted Pt L_3-edge EXAFS spectrum measured after 500 CVs reveals an almost identical Pt–N bond length and Pt–N coordination number (CN) to those of the pristine $Pt_1(3)$/CNT (Supplementary Fig. 12), indicating no significant structural change in the active Pt sites after the durability test.

On the other hand, the XPS spectrum pinpoints substantial alternations in the chemical composition of $Pt_1(3)$/CNT after 500 CVs. The XPS O 1*s* spectrum shows a new peak at 532.3 eV, indicating the formation of C=O (531.5 eV) and C–O (532.6 eV) functionalities on $Pt_1(3)$/CNT after the durability test (Fig. 2a and Supplementary Fig. 13)[46]. Also, the aged $Pt_1(3)$/CNT shows a redox couple at 0.56 V_{RHE}, which is a fingerprint of oxygen functional groups (e.g., quinone) on the carbon surface[47,48], and this peak intensifies as the number of CV cycles increases (Fig. 2b). In addition to oxygen functionalities, chlorine functional groups are also formed. The XPS Cl 2*p* spectrum of the aged $Pt_1(3)$/CNT reveals peaks at 200.4 eV with a spin-orbit splitting of 1.6 eV (Fig. 2c). This peak corresponds to the core level spectra of organochlorine compounds, not residual alkali chloride (199 eV)[49], indicating the cogeneration of chlorine functional groups on the carbon support after 500 CVs.

To identify whether the newly generated functional groups are responsible for the decrease in the TOF of $Pt_1(3)$/CNT, two model catalysts with abundant oxygen (O-$Pt_1(3)$/CNT) and chlorine (Cl-$Pt_1(3)$/CNT) functionalities were additionally prepared by post-treatment of $Pt_1(3)$/CNT with O_3 and SO_2Cl_2, respectively[50]. ICP-OES analysis revealed no detectable Pt loss after these post-treatments. In contrast, XPS O 1*s*/Cl 2*p* spectra (and electrochemical redox signals at 0.56 V_{RHE} for O-$Pt_1(3)$/CNT) confirm the successful introduction of the oxygen and chlorine functional groups onto the CNT support (Fig. 2a–c). Despite the introduction of the functional groups, the CER polarization curves for O-$Pt_1(3)$/CNT and Cl-$Pt_1(3)$/CNT are almost identical to that of pristine $Pt_1(3)$/CNT (Fig. 2d). These results indicate that the catalytic degradation of aged $Pt_1(3)$/CNT is likely not attributable to the TOF modification induced by the newly generated oxygen or chlorine functional groups.

In addition to the functional group generation, the other considerable change in $Pt_1(3)$/CNT after 500 CVs was the decrease in the Pt content of the catalysts (Fig. 1f). Although Pt moieties are the catalytic sites for the CER, their electronic structures can be affected by their content. Since the Pt moieties are implanted on the CNT surface, their conjugation can disturb the electronic structure of the carbon support (e.g., electron withdrawing/donating properties) and consequently tune the TOF of the Pt sites[51]. Besides the carbon support modifications, a recent study on Fe SACs also suggested direct electronic interactions among adjacent Fe moieties, namely TOF modifications, induced by the spatial proximity of the Fe sites as the Fe loading increased[52]. Therefore, a decrease in the Pt active site density may be responsible for the TOF decay, possibly leading to a rapid decrease in the CER activity.

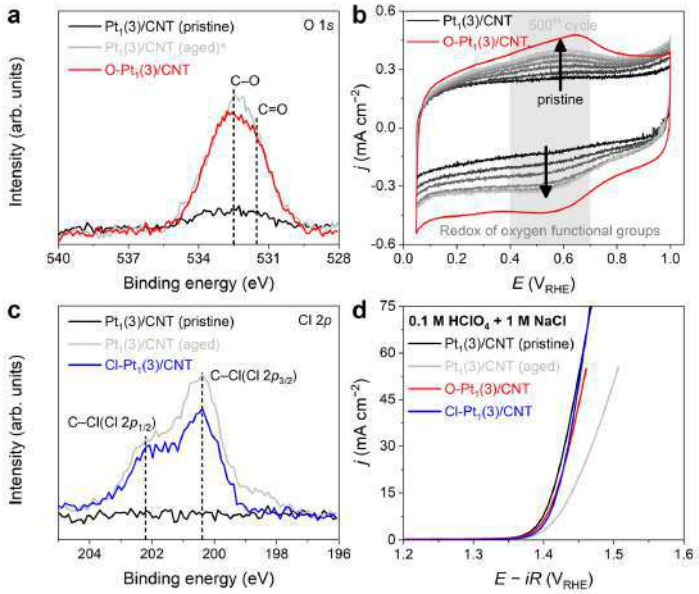

Fig. 2 | In/ex situ surface modifications of $Pt_1(3)$/CNT. a The XPS O 1*s* spectra of $Pt_1(3)$/CNT, aged $Pt_1(3)$/CNT, and O-$Pt_1(3)$/CNT. (*Nafion contribution-subtracted spectrum; See Supplementary Fig. 13). **b** CV responses of pristine and aged $Pt_1(3)$/CNT measured in Ar-saturated 0.1 M $HClO_4$. The CV response of O-$Pt_1(3)$/CNT is also shown. **c** The XPS Cl 2*p* spectra of $Pt_1(3)$/CNT, aged $Pt_1(3)$/CNT, and Cl-$Pt_1(3)$/CNT. **d** CER polarization curves of the $Pt_1(3)$/CNT, aged $Pt_1(3)$/CNT, O-$Pt_1(3)$/CNT, and Cl-$Pt_1(3)$/CNT catalysts obtained in Ar-saturated 0.1 M $HClO_4$ with 1 M NaCl.

Based on this deduction, Pt_1/CNTs were synthesized with different Pt loadings of 1 and 0.15 wt.%, which were denoted as '$Pt_1(1)$/CNT' and '$Pt_1(0.15)$/CNT', respectively. The structures of the two catalysts were extensively characterized (Supplementary Figs. 1–5), showing the formation of Pt SACs as $Pt_1(3)$/CNT. Interestingly, despite the substantial decrease in Pt loading, $Pt_1(1)$/CNT and $Pt_1(0.15)$/CNT exhibit only a slight decrease in CER activity compared with $Pt_1(3)$/CNT (Fig. 3a). The polarization curves show *j* values of 53, 49, and 39 mA cm^{-2} at 1.45 V_{RHE} as the Pt content decreases from 3 wt.% to 1 and 0.15 wt.%, respectively. Independent of Pt loading, the CER selectivity is almost 100% (Supplementary Figs. 6 and 14). Notably, the Pt-loading-dependent CER activity can be translated into three and fifteen times higher TOF values for $Pt_1(1)$/CNT and $Pt_1(0.15)$/CNT, respectively, compared with $Pt_1(3)$/CNT. The observed TOF trend contradicts our deduction, which was that the TOF decreases with decreasing Pt content. Thus, the control experiments suggest that the TOF decay, induced either by newly generated oxygen-/chlorine-functional groups or the loss of Pt moieties, is not the main cause of Pt_1/CNT deactivation.

Therefore, we searched for the origin of the unexpected TOF trend, and the XAS spectra of $Pt_1(1)$/CNT and $Pt_1(0.15)$/CNT provided a decisive clue (Fig. 3b). Similar to $Pt_1(3)$/CNT, the X-ray absorption near edge structure (XANES) spectra of $Pt_1(1)$/CNT and $Pt_1(0.15)$/CNT show the +2 oxidation state of Pt (Supplementary Fig. 4). Their EXAFS spectra also specify a strong Pt–N scattering at 2.0 Å without Pt–Pt scattering at 2.8 Å (Supplementary Fig. 3 and Supplementary Table 2). Interestingly, the Pt–N peak intensity decreases as the Pt loading decreases, indicating the different coordination natures of the Pt sites in the three control catalysts. Their fitting parameters show lowered CN values from 4.0 for $Pt_1(3)$/CNT to 3.4 for $Pt_1(1)$/CNT and further to 3.0 for $Pt_1(0.15)$/CNT (Fig. 3c and Supplementary Table 2). Considering that the d^8 configuration of Pt^{II} prefers a four-coordinated square planar structure (e.g., Pt^{II}–N_4)[15], the CN value of 3.0 indicates an unusual stabilization of isolated Pt^{II} in the form of either trigonal-planar-like Pt^{II}–N_3 or T-shaped Pt^{II}–N_3V (where V denotes a vacancy). Notably, these coordinatively unsaturated Pt^{II} complexes are very rarely found so far but have often been proposed as key reaction intermediates in homogeneous catalysis[53]. Hence, the coexistence of the coordinatively unsaturated Pt–N_3(V) sites (i.e., Pt–N_3 and/or Pt–N_3V) with Pt–N_4 on the heterogeneous CNT support emphasizes the failure of all earlier discussions to understand the fundamental origin of $Pt_1(3)$/CNT deactivation because the assumption of a singular catalytic site corresponding to Pt–N_4 is violated.

Notably, the considerable CER activity of $Pt_1(0.15)$/CNT demonstrates that Pt–N_3(V) rather than the symmetric Pt–N_4 site is responsible for the excellent CER activity. Thus, the apparent CER activity of Pt_1/CNT catalysts depends neither on the total Pt content nor on the total number of Pt–N_4 sites but is mainly governed by the number of Pt–N_3(V) sites. Therefore, we approximately predicted the Pt–N_3(V) contents of $Pt_1(1)$/CNT and $Pt_1(3)$/CNT by linear extrapolation to the corresponding *j* values of an extended line defined from zero current with no Pt–N_3(V) content to *j* value and Pt–N_3(V) content of $Pt_1(0.15)$/CNT (Fig. 3d). By subtracting the Pt–N_3(V) content from the total Pt content, the Pt–N_4 contents of $Pt_1(1)$/CNT and $Pt_1(3)$/CNT can also be derived. The calculation determines the Pt–N_3(V)/Pt–N_4 contents to be 0.19/0.81 and 0.2/2.8 wt.% for $Pt_1(1)$/CNT and $Pt_1(3)$/CNT, respectively. Based on these approximations, which are only valid when the TOFs of the active Pt–N_3(V) sites for all Pt_1/CNT catalysts are identical, the average CN values can be inversely estimated to be 3.8 and 3.9 for $Pt_1(1)$/CNT and $Pt_1(3)$/CNT, respectively. These values are within the error range of the EXAFS fitting parameters (Fig. 3c).

Article https://doi.org/10.1038/s41467-023-38964-x

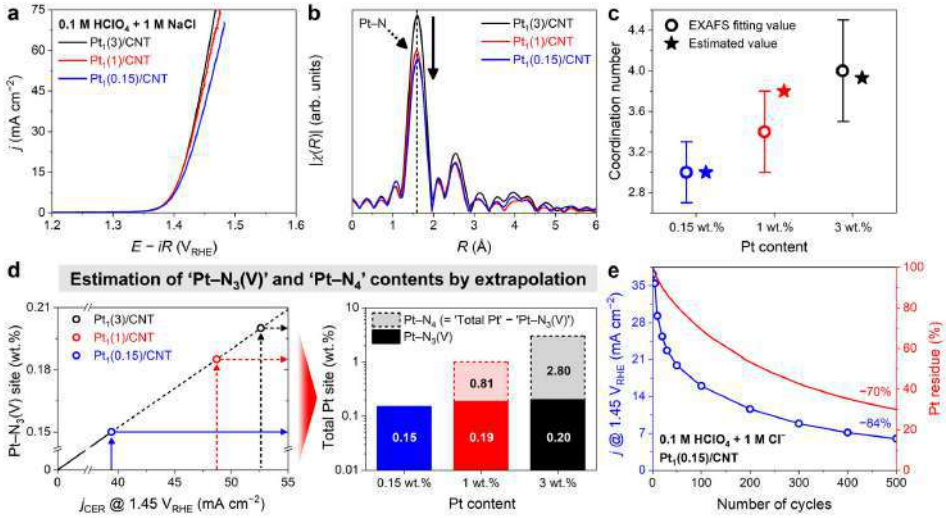

Fig. 3 | Pt loading effects on CER activity of Pt_1/CNTs. a CER polarization curves of the $Pt_1(3)$/CNT, $Pt_1(1)$/CNT, and $Pt_1(0.15)$/CNT catalysts obtained in Ar-saturated 0.1 M $HClO_4$ with 1 M NaCl. **b** The k^3-weighted Pt L_3-edge EXAFS spectra of the Pt_1/CNT catalysts without phase correction and **c** their Pt–N coordination numbers obtained by EXAFS fitting. The error bars indicate the error ranges of the EXAFS fitting parameter. **d** Estimation of Pt–N_3(V) contents in $Pt_1(1)$/CNT and $Pt_1(3)$/CNT by linear extrapolation to their corresponding j values of an extended line defined from zero current with no Pt–N_3(V) content to j value and Pt–N_3(V) content of $Pt_1(0.15)$/CNT. **e** Comparison between the CER activity decrement and Pt loss of $Pt_1(0.15)$/CNT during the durability test.

In addition, the critical role of Pt–N_3(V) in catalyzing CER is further corroborated by in situ XAS measurements. In the Pt L_3-edge XANES spectra, which were measured in an Ar-saturated 0.1 M $HClO_4$ + 1 M NaCl electrolyte, the white line (WL) intensity marginally increases after immersing the catalyst into the electrolyte, and the increment further intensifies at 1.45 V_{RHE} (Supplementary Fig. 15). This result agrees well with our previous study and infers the adsorption of CER intermediates on the Pt sites[30]. Interestingly, the intensified WL at 1.45 V_{RHE} is slightly higher for $Pt_1(0.15)$/CNT and decreases with increasing Pt content in the catalysts, indicating higher coverage of CER intermediates as a proportion of Pt–N_3(V) sites in the catalysts increases. The same conclusion is also made with in situ EXAFS spectra that show an increasing Pt–Cl scattering peak at 2.3 Å as Pt content in the catalysts decreases (Supplementary Fig. 15 and Supplementary Table 3). We further note that CN_{Pt-N} of $Pt_1(0.15)$/CNT increases from 3 for the powdery sample (Fig. 3c) to 4 under the electrochemical conditions and attribute this change to in situ formation of an additional Pt–O bond, which will be discussed again in the DFT section. The ratio between $CN_{Pt-N/O}$ and CN_{Pt-Cl} of $Pt_1(0.15)$/CNT is approximately 4 : 1, and this supports the predominant presence of Pt–N_3(V) sites in $Pt_1(0.15)$/CNT and their high catalytic activity towards CER.

The identification of the main catalytic site leads to a much-alleviated disparity between the extent of CER activity drop and accumulated Pt loss, as observed in the example of $Pt_1(0.15)$/CNT during its durability test (Fig. 3e). After 500 CVs, the initial CER activity and Pt content of $Pt_1(0.15)$/CNT decrease by 84 and 70%, respectively, and their profiles over time are also comparable. In addition, the Pt loss of $Pt_1(X)$/CNTs (X = 0.15, 1, and 3) after 500 CVs becomes intensified as the proportion of the Pt–N_3(V) increases (Supplementary Fig. 16). These results further corroborate that the Pt–N_3(V) site is the genuine catalytic site and further indicate that the decrease in CER activity after the durability test primarily originates from the loss of Pt–N_3(V) sites. Therefore, for $Pt_1(3)$/CNT, the significant discrepancy between the activity drop (~61%) and Pt loss (~22%) can now be accounted by the coexistence of the Pt–N_3(V) minority and Pt–N_4 majority moieties; the former site is more active but also more labile than the latter.

To comprehend the detailed CER path on the Pt_1/CNT catalysts and their catalytic structure, we apply electronic structure calculations in the framework of DFT. Based on the EXAFS fitting parameters, we consider three different models, namely square planar Pt–N_4, trigonal planar Pt–N_3, and T-shaped Pt–N_3V (Fig. 4a). For all these models, the structures of the catalytically active Pt site were characterized under CER conditions ($U > 1.36$ V_{SHE}) by the construction of Pourbaix diagrams[54]. While an axially unoccupied Pt site (*) is favored for Pt–N_4 (Supplementary Figs. 17 and 18), Pt–N_3 and Pt–N_3V are capped by oxygen, *O, which, together with the Pt atom underneath, serves as the active site (Supplementary Fig. 18). These results suggest that the CER over Pt–N_4 and Pt–N_3(V) proceeds via *Cl or *OCl intermediates, respectively. We have modeled both pathways for all three sites and quantified the largest free-energy span between the intermediate states in dependence on applied electrode potential by referring to the descriptor G_{max} (U)[55]. The compilation of the free-energy diagrams at $U = 1.36$ V_{SHE} reveals that, in agreement with our previous works[17,30,56], square planar Pt–N_4 prefers the *Cl (G_{max} (U) = 0.32 eV) rather than the *OCl path (G_{max} (U) = 1.07 eV) (Fig. 4b). However, the *OCl path is energetically favored over the *Cl mechanism for Pt–N_3 or Pt–N_3V (Fig. 4c, d), inferring the different CER mechanisms for the Pt–N_4 and Pt–N_3(V) moieties. Notably, the activity descriptor G_{max} (U) amounts to 0.21 and 0.05 eV for Pt–N_3 and Pt–N_3V at $U = 1.36$ V_{SHE}, respectively, confirming the experimental result that the Pt–N_3(V) sites are more active than Pt–N_4 in the CER. In addition, the competing OER for the three different sites was described by assuming the well-accepted mononuclear mechanism via the *OH, *O, and *OOH adsorbates, and G_{max} (U) as a measure for the electrocatalytic activity was determined (Supplementary Fig. 19 and Supplementary Table 4)[57].

Article https://doi.org/10.1038/s41467-023-38964-x

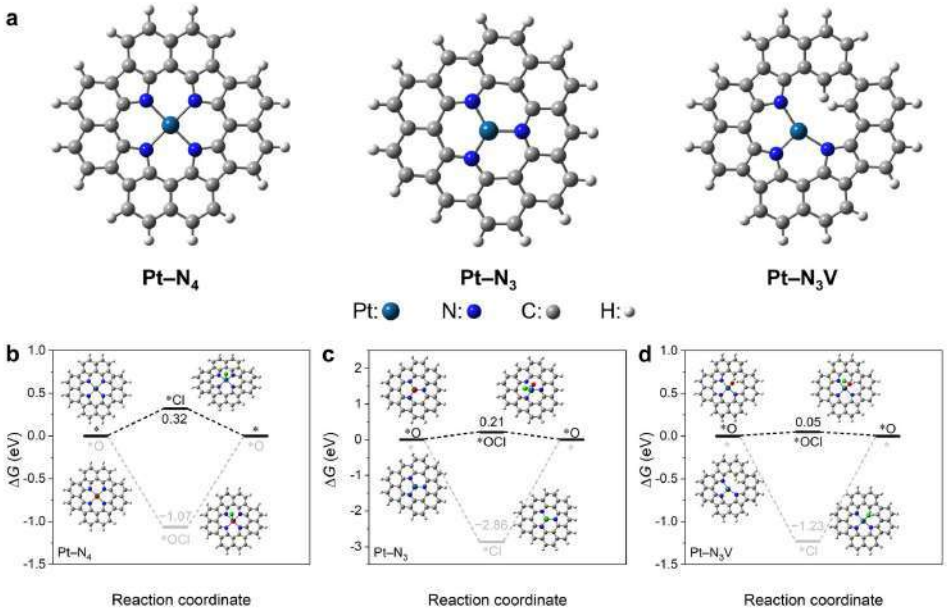

Fig. 4 | Identification of the catalytic sites by DFT calculations. a Three active site models, square planar Pt–N_4, trigonal planar Pt–N_3, and T-shaped Pt–N_3V, used for the DFT calculations. **b**–**d** Free-energy diagrams of the CER via the *Cl and *OCl pathways at 1.36 V_{SHE} for Pt–N_4 (**b**), Pt–N_3 (**c**), and Pt–N_3V (**d**).

By applying a selectivity model for the competing CER and OER[58], we demonstrate that CER selectivity amounts to 100% (Supplementary Fig. 20), independent of the applied electrode potential or chemical nature of the active sites, which coincides with the experimental results (Fig. 1b and Supplementary Figs. 6 and 14).

Finally, we study the stability of the Pt–N_4 and Pt–N_3(V) moieties under the CER conditions. For this purpose, the equilibrium potential (U_{diss}) for the oxidative demetallation of central Pt species to PtO_2 is introduced as a catalyst stability descriptor (cf. DFT calculation section in Methods and Supplementary Note 3). It is of note that PtO_2 is the energetically favored phase under CER conditions, according to the Pourbaix diagram[59]. The results show U_{diss} of 2.98, 1.99, and 0.78 V_{SHE} for Pt–N_4, Pt–N_3V, and Pt–N_3, respectively. Consistent with the experimental results, the descriptor U_{diss} indicates the poorer stability of Pt–N_3(V) compared with Pt–N_4 under CER conditions of $U > 1.36$ V_{SHE}. Considering the U_{diss} for Pt–N_3 amounts to 0.78 V_{SHE}, which is significantly below the CER equilibrium potential, we conclude that the trigonal planar Pt–N_3 site cannot be stable under the CER conditions, but instead, T-shaped Pt–N_3V is responsible for the excellent CER activity and selectivity of the Pt_1/CNT catalysts.

In this work, we have unraveled the fundamental origin of the high CER activity of Pt_1/CNT catalysts. The heterogeneity of central Pt^{II} ions and the key role of three-coordinated Pt^{II} with broken D_{4h} symmetry in CER electrocatalysis were demonstrated. Thus, the development of new synthetic strategies to maximize the site density of three-coordinated Pt with a broken symmetric geometry will become an upcoming challenge. This originates from the limited amount of Pt–N_3(V) on the catalyst surface, which apparently converges to 0.2 wt.% only, regardless of the increasing total Pt content on Pt_1/CNT. Indeed, tailoring the coordination geometry will also be critical to find optimal ligand-field strength for stabilizing the Pt sites and *OCl intermediate, owing to the trade-off relation between stability and activity. Otherwise, more practical approaches, such as engineering the catalyst-electrolyte interface or finding optimal operating conditions (e.g., well-regulated potential excursions) to promote the longevity of labile Pt–N_3(V) sites, will be the subject of another future research direction. Before answering these questions, however, understanding the underlying fundamental origins of the (quasi-)stabilization of the rarely found Pt–N_3(V) species on the supporting substrates should be prioritized. Considering the cases of Ni^{II} SACs for electrochemical CO_2 reduction[20], these guidelines might be general tasks for other metal ions with a d^8 electronic configuration in SACs, not limited to Pt^{II} catalytic sites. Therefore, the present findings will provide a foundation for the rational design of next-generation SACs with excellent electrocatalytic performances.

Methods

Preparation of the Pt_1/CNT catalysts

Before synthesizing the catalysts, multiwalled CNTs (MR99, Carbon Nano-material Technology Co., Ltd.) with an average diameter of 10 nm and an average length of 10 μm were heated and subsequently acid washed to remove metallic impurities[60]. In detail, CNTs (38.0 g) were calcined at 500 °C for 1 h in a box furnace at a heating rate of 7.9 °C min^{-1}. The heat-treated CNT powder was then acid washed at 80 °C for 12 h in 810 g of 6 M HNO_3 (diluted from 60% HNO_3, Samchun Chemicals) under vigorous stirring. After filtration and washing with excess deionized (DI) water, the powder was treated with 720 g of 6 M HCl (diluted from 36% HCl, Samchun Chemicals) under vigorous stirring. The acid-treated CNTs were collected after drying overnight in an oven at 60 °C.

Pt_1/CNT catalysts with various Pt contents (Pt_1(X)/CNT, where X = nominal wt.% of Pt) were synthesized by solid-state mixing of CNT and Pt-macrocycle precursor followed by annealing[17]. The acid-treated

CNT (500 mg) and PtTPP (95%, Frontier Scientific) were ground in an agate mortar over 20 min until the color and texture became constant. The PtTPP contents in the precursor mixtures were 71.0, 21.6, and 2.1 mg for $Pt_1(3)$/CNT, $Pt_1(1)$/CNT, and $Pt_1(0.15)$/CNT, respectively. Subsequently, the powder mixture was pyrolyzed at 700 °C for 3 h under an N_2 flow (5 N, 1 L min^{-1}) at a heating rate of 2.1 °C min^{-1}. N-doped CNT was synthesized by a similar method, but 54.0 mg of TPP (1 – 3% Chlorin, Frontier Scientific), which is equivalent to 71.0 mg of PtTPP, was used as a precursor.

Two model catalysts with abundant oxygen (O-$Pt_1(3)$/CNT) or chlorine (Cl-$Pt_1(3)$/CNT) functionalities were prepared by post-treatment of $Pt_1(3)$/CNT. O-$Pt_1(3)$/CNT (150 mg) was prepared by ozone treatment at 25 °C for 1 h using an ozone generator (LAB-I, Ozonetech Inc.). Cl-$Pt_1(3)$/CNT was prepared by sequential H_2O_2 and SO_2Cl_2 treatments[50]. $Pt_1(3)$/CNT (75 mg) was mixed with a 12.7 wt.% H_2O_2 solution (1.5 L; diluted from 29–32% H_2O_2, Alfa Aesar), and the mixture was stirred at 70 °C for 2 h. The catalyst powder was collected by filtration and washed several times with DI water. Subsequently, H_2O_2-treated $Pt_1(3)$/CNT (70 mg) was dispersed in 4.2 mL of acetonitrile (99.8%, Sigma-Aldrich), and 280 mg of SO_2Cl_2 (97%, Sigma-Aldrich) was added. The mixture was stirred for 2 h at 75 °C and subsequently, heated and refluxed for 5 h at 75 °C. Cl-$Pt_1(3)$/CNT was collected via filtration and washed several times with DI water.

Physical characterizations

HAADF-STEM images were obtained using a Titan³ G2 60-300 microscope (FEI Company) equipped with a double-sided spherical aberration (Cs) corrector operated at an accelerating voltage of 200 kV. XRD patterns were obtained using a high-power X-ray diffractometer (D/MAX2500V/PC, Rigaku) equipped with Cu Kα radiation operated at 40 kV and 200 mA. The XRD patterns were measured in the 2θ range from 10° to 90° at a scan rate of 2° min^{-1}. XRD samples were prepared by pelletizing 50 mg of the catalyst in a sample holder (13 mm in width) under 8 tons of hydraulic pressure. XPS measurements were performed using a K-Alpha spectrometer (Thermo Fisher Scientific) equipped with a monochromatic Al Kα X-ray source (1486.6 eV). XPS Pt 4*f* and N 1*s* spectra were analyzed using the XPSPeak41 software with a mixed Gaussian (70)–Lorentzian (30) function after applying Shirley-type background correction. The spin-orbit components of the XPS Pt 4*f* spectra were fixed at 3.34 eV. To quantify the Pt content in the catalysts, a microwave digestion system (Mars 6, CEM) was used to completely dissolve Pt in aqua regia (36% HCl:60% HNO_3 = 3:1, v/v) at 220 °C for 40 min (600 W, heating rate of 6.7 °C min^{-1}). Subsequently, the resulting solution was analyzed by ICP-OES (700-ES, Varian).

Ex situ Pt L_3-edge XAS spectra were collected at the 6D beamline of the Pohang Accelerator Laboratory (PAL). The XAS spectra of the samples were obtained in the transmission mode after pelletizing the catalysts in a sample holder (1 cm in width). Background removal and normalization of the absorption coefficient for XANES spectra and fitting for the Fourier-transformed k^3-weighted EXAFS spectra were performed using the Athena and Artemis software with 1.1–1.2 of Rbkg in a Hanning-type window[61]. A modified Victoreen equation was applied to normalize the post-edge signal to the step of one[62]. For the quantitative XANES fitting, a combination of the Gaussian function and arctangent function was used (Eq. (1)–(3))[63].

$$I(E) = a_1(E) + g_1(E) + g_2(E) \quad (1)$$

$$a_{i=1}(E) = h_i[0.5 + \pi^{-1}\tan^{-1}[(E - E_i)/w_i]] \quad (2)$$

$$g_{j=1,2}(E) = h_j \exp[-\ln 2(E - E_j)^2)/w_j^2] \quad (3)$$

where I, E, $a(E)$, $g(E)$, h, w, E_i, and E_j represent the normalized intensity, X-ray energy (eV), arctangent function, Gaussian function, the height of peak, the width of peak, inflection point (eV), and peak position (eV), respectively. The $a_1(E)$ indicated a fundamental transition from 2*p* to 5*d* orbitals. The h_1 in $a_1(E)$ should be fixed as 1, as all fittings were conducted with normalized XANES spectra. Two Gaussian functions ($g_1(E)$ and $g_2(E)$) were used to fit the $p \rightarrow d$ transitions, indicating the WL peak and the post-edge peak, respectively (Supplementary Fig. 4). The post-edge peaks generally exhibit the electron transfer from 2*p* to the unoccupied *d*-orbitals hybridized with ligands[64]. The average oxidation numbers were estimated using the equation ($y = 0.5367\,x + 0.6549$, x is the normalized WL area) by interpolating the plot of Pt references in our previous report[30]. For EXAFS fitting, the amplitude reduction factor (S_0^2) of Pt was fixed at 0.84 after calibration using a standard Pt foil, while the details of fitting were listed (Supplementary Table 2). Crystallographic data for the PtTPP molecule were used for multishell fitting with the first-shell of Pt–N and the second-shell of Pt–C[65].

Electrochemical characterizations

Electrochemical measurements were conducted in a conventional three-electrode H-type cell using a potentiostat (VMP3, Bio-Logic Science Inc.). A homemade rotating disk electrode (RDE) with mirror-polished glassy carbon (5 mm diameter), Pt wire (CE-100, EC Frontier), and saturated Ag/AgCl (RE-T1A, EC Frontier) electrodes were used as the working, counter, and reference electrodes, respectively. The counter electrode was separated from the working and reference electrodes using a glass frit. To prevent unexpected contamination from the reference electrode[66], it was doubly separated from the electrolyte using a glass tube equipped with a glass frit. Ar-saturated 0.1 M $HClO_4$ solutions with and without 1 M NaCl (or 1 M NH_4Cl), which were prepared using DI water (≥18.2 Ω, Arium Mini, Sartorius), concentrated $HClO_4$ solution (70%, Sigma-Aldrich), NaCl (99%, Sigma-Aldrich), and NH_4Cl (99.5%, Sigma-Aldrich), were used as electrolytes. All potentials are given relative to the RHE scale after calibration of the reference electrode with a Pt wire electrode in an H_2-saturated electrolyte before each electrochemical measurement.

A thin-film electrode was fabricated by drop-casting the catalyst ink (10 μL) onto an RDE. The catalyst loading was 100 μg cm^{-2}. The catalyst ink was prepared by dispersing 5 mg of the catalyst in a mixed solution of DI water (2122 μL), isopropyl alcohol (374 μL), and 5 wt.% Nafion solution (50 μL). Before measuring the CER activity, the working electrode was electrochemically activated by 50 cycles of CV in the potential range of 0.05–1.2 V_{RHE} at a scan rate of 500 mV s^{-1} in an Ar-saturated 0.1 M $HClO_4$ electrolyte. CER polarization curves were obtained in the potential range of 1.0–1.6 V_{RHE} at a scan rate of 10 mV s^{-1} in Ar-saturated 0.1 M $HClO_4$ with 1 M NaCl (or 1 M NH_4Cl). During the measurements, the working electrode was rotated at 1600 rpm using a rotor (RRDE-3A, ALS). Durability tests were performed using 500 CV cycles in the potential range of 1.0–1.6 V_{RHE} at a scan rate of 100 mV s^{-1}. In this study, the onset potential of the CER was defined as the potential at 1 mA cm^{-2} during CER polarization. All electrochemical results were shown after 85% *iR* compensation correction, which was conducted by electrochemical impedance spectroscopy (EIS) at a fixed potential of 0.9 V_{RHE} in the frequency range of 100 kHz–1 Hz with a potential amplitude of 10 mV.

The electrochemical Cl_2 formation was analyzed by chronoamperometry (CA) using a RRDE (012613, ALS). The catalyst loading on the disk electrode was 100 μg cm^{-2}. The CER selectivity was measured for 120 s at an electrode rotation speed of 1600 rpm; this step was repeated five times with an intermittent break of 1 min. The applied disk potential was adjusted to generate a current density of ≥10 mA cm^{-2}, but the applied Pt ring potential was fixed at 0.95 V_{RHE}[67]. Prior to the RRDE study, the background currents of the disk and ring electrodes were stabilized at 0.95 V_{RHE} with an electrode rotation of 1600 rpm. The net CER current (i_{CER}) at the disk electrode and CER

selectivity were calculated using the following equations.

$$i_{CER} = |\frac{i_r}{N}| \quad (4)$$

$$Cl_2\ \text{selectivity}(\%) = 100 \cdot \frac{2 \cdot i_{CER}}{i_d + i_{CER}} = 100 \cdot \frac{2 \cdot |\frac{i_r}{N}|}{i_d + |\frac{i_r}{N}|} \quad (5)$$

where i_r, N, and i_d denote the background-corrected ring current, collection efficiency (0.35–0.37, calibrated using $K_3[Fe(CN)_6]$), and background-corrected disk current, respectively.

Online EFC/ICP-MS measurements

Online Pt dissolution was analyzed by ICP-MS (iCAP RQ, Thermo-Fisher Science) coupled with a homemade EFC. The EFC was composed of a U-shaped channel (1 mm diameter) and two openings (3 mm diameter). On one opening side, a mirror-polished 3 mm glassy carbon electrode (002012, ALS) made electrochemical contact with the electrolyte (Supplementary Fig. 9). On the other opening side, a 3 mm Teflon tube, which was sealed with a polytetrafluoroethylene (PTFE) membrane (WP-020-80, Sumitomo Electric Ind., Ltd.) at one end, was approached to the working electrode to extract any evolved gas products by vacuum. The counter electrode was a graphite rod separated from the electrolyte by a Nafion 115 membrane (DuPont). The reference electrode was a saturated Ag/AgCl electrode that was directly connected to the outlet of the EFC. The electrolyte was Ar-saturated 0.1 M $HClO_4$ with 1 M NH_4Cl, which continuously flowed to the EFC at a flow rate of 400 µL min^{-1} (Note: we avoided using 1 M NaCl due to significant damage on the sampler and skimmer cones of the ICP-MS instrument; Supplementary Fig. 10). Prior to introducing the electrolyte to the ICP-MS instrument, it was mixed with 0.5 M HNO_3 containing 5 ppb ^{187}Re as an internal standard at a mixing ratio of 1:1 using a Y-connector. Online Pt dissolution was estimated using the ratio of ^{195}Pt to ^{187}Re signals during the electrochemical treatments. The catalyst loading on the working electrode was 100 µg cm^{-2}. After stabilizing the online ICP-MS signals for 30 min at an open-circuit potential (OCP), the working electrode was electrochemically activated by 50 CV cycles at a scan rate of 500 mV s^{-1} in the potential range of 0.05–1.2 V_{RHE}. Subsequently, Pt dissolution was monitored over 500 CV cycles at a scan rate of 100 mV s^{-1} in the potential range of 1.0–1.6 V_{RHE}.

Online EFC/DEMS measurements

The gaseous products were analyzed online by DEMS. The EFC connected to a mass spectrometer (Max 300 LG, Extrel) was constructed for DEMS analysis. The EFC equipped a U-shaped channel with a 10 mm opening diameter at the bottom, which allowed for electrical contact with the 3 mm glassy carbon working electrode (A-011169, Bio-Logic). To collect volatile and gaseous products, a porous PTFE membrane (WP-010-80, Sumitomo Electric Ind., Ltd.) was positioned approximately 100 µm above the working electrode. The graphite tube (inner diameter = 3 mm) and saturated Ag/AgCl reference electrodes were electrically connected to the outlet of the EFC. The catalyst loading on the working electrode was 560 µg cm^{-2}. Ar-saturated 0.1 M $HClO_4$ and 0.1 M $HClO_4$ + 1 M NaCl were used as electrolytes. The online EFC/DEMS measurements were conducted using two consecutive CVs at a scan rate of 5 mV s^{-1} in the potential range of 1.0–1.6 V_{RHE}. The electrolyte flow rate was set to 0.07 mL min^{-1} using a syringe pump (TYD01-01, LEADFLUID). The mass signals of O_2^+ (m/z = 32), Cl^+ (m/z = 35), HCl^+ (m/z = 36), and OCl^+ (m/z = 51) were collected simultaneously during the electrode polarizations.

In situ XAS measurements

The in situ Pt L_3-edge XAS measurements were conducted at the 8 C beamline of the PAL, utilizing a flow-type in situ XAS cell equipped with an electrolyte flow channel and a window for X-ray radiation. The window was a carbon-coated Kapton film (200RS100, DuPont) with a thickness of 0.05 mm and an area of 0.503 cm^2, which was used as a working electrode. A thin-film electrode was fabricated by drop-casting of the concentrated catalyst ink with targeted loadings of 5 mg cm^{-2} for $Pt_1(3)$/CNT and $Pt_1(1)$/CNT and 7 mg cm^{-2} for $Pt_1(0.15)$/CNT. Pt wire counter and Ag/AgCl reference electrodes were directly connected to the outlet of the electrolyte stream. The fluorescence mode was used to collect the XAS spectra after calibration with a Pt foil reference. Ar-saturated 0.1 M $HClO_4$ + 1 M NaCl electrolyte was used as electrolyte, and the spectra were collected at the OCP and 1.45 V_{RHE}, respectively. Background removal and normalization of the absorption coefficient for XANES spectra and fitting for the Fourier-transformed k^3-weighted EXAFS spectra were performed using the Athena and Artemis software with 1.2 of Rbkg in a Hanning-type window. For EXAFS fitting, the S_0^2 value of Pt was fixed at 0.84 after calibration using a standard Pt foil, while the details of fitting were listed (Supplementary Table 3).

DFT calculations

Electronic structure calculations for periodically replicated appropriate models were performed using the Vienna ab initio simulation package (VASP 5.4.1) based on the framework of DFT[68]. Full computational details can be found in Supplementary Note 3.

Data availability

The data generated in this study have been deposited in the Zenodo repository database without accession code [https://zenodo.org/record/7936631#.ZGH5O3ZByUk][69].

Code availability

The DFT codes generated in this study have been deposited in the Zenodo repository database without accession code [https://zenodo.org/record/7936174#.ZGHd2XZByUk][70].

References

1. Wang, A., Li, J. & Zhang, T. Heterogeneous single-atom catalysis. *Nat. Rev. Chem.* **2**, 65–81 (2018).
2. Ji, S. et al. Chemical synthesis of single atomic site catalysts. *Chem. Rev.* **120**, 11900–11955 (2020).
3. Kim, J. H., Sa, Y. J., Lim, T., Woo, J. & Joo, S. H. Steering catalytic selectivity with atomically dispersed metal electrocatalysts for renewable energy conversion and commodity chemical production. *Acc. Chem. Res.* **55**, 2672–2684 (2022).
4. Cui, X., Li, W., Ryabchuk, P., Junge, K. & Beller, M. Bridging homogeneous and heterogeneous catalysis by heterogeneous single-metal-site catalysts. *Nat. Catal.* **1**, 385–397 (2018).
5. Mitchell, S., Vorobyeva, E. & Pérez-Ramírez, J. The multifaceted reactivity of single-atom heterogeneous catalysts. *Angew. Chem. Int. Ed.* **57**, 15316–15329 (2018).
6. Christopher, P. Single-atom catalysts: are all sites created equal? *ACS Energy Lett.* **4**, 2249–2250 (2019).
7. Zitolo, A. et al. Identification of catalytic sites for oxygen reduction in iron- and nitrogen-doped graphene materials. *Nat. Mater.* **14**, 937–942 (2015).
8. Luo, F. et al. Kinetic diagnostics and synthetic design of platinum group metal-free electrocatalysts for the oxygen reduction reaction using reactivity maps and site utilization descriptors. *J. Am. Chem. Soc.* **144**, 13487–13498 (2022).
9. Cheng, N. et al. Platinum single-atom and cluster catalysis of the hydrogen evolution reaction. *Nat. Commun.* **7**, 13638 (2016).
10. Gao, G., Jiao, Y., Waclawik, E. R. & Du, A. Single atom (Pd/Pt) supported on graphitic carbon nitride as an efficient photocatalyst for visible-light reduction of carbon dioxide. *J. Am. Chem. Soc.* **138**, 6292–6297 (2016).

11. Qiao, B. et al. Single-atom catalysis of CO oxidation using Pt_1/FeO_x. *Nat. Chem.* **3**, 634–641 (2011).
12. Choi, C. H. et al. Tuning selectivity of electrochemical reactions by atomically dispersed platinum catalyst. *Nat. Commun.* **7**, 10922 (2016).
13. Bruix, A. et al. Maximum noble-metal efficiency in catalytic materials: atomically dispersed surface platinum. *Angew. Chem. Int. Ed.* **53**, 10525–10530 (2014).
14. Yang, M. et al. A common single-site Pt(II)–$O(OH)_x$– species stabilized by sodium on "active" and "inert" supports catalyzes the water-gas shift reaction. *J. Am. Chem. Soc.* **137**, 3470–3473 (2015).
15. Krogmann, K. Planar complexes containing metal-metal bonds. *Angew. Chem. Int. Ed.* **8**, 35–42 (1969).
16. Yan, Q.-Q. et al. Reversing the charge transfer between platinum and sulfur-doped carbon support for electrocatalytic hydrogen evolution. *Nat. Commun.* **10**, 4977 (2019).
17. Lim, T. et al. Atomically dispersed Pt–N_4 sites as efficient and selective electrocatalysts for the chlorine evolution reaction. *Nat. Commun.* **11**, 412 (2020).
18. Zhao, J. et al. Manipulating the oxygen reduction reaction pathway on Pt-coordinated motifs. *Nat. Commun.* **13**, 685 (2022).
19. Fang, S. et al. Uncovering near-free platinum single-atom dynamics during electrochemical hydrogen evolution reaction. *Nat. Commun.* **11**, 1029 (2020).
20. Kim, H. et al. Identification of single-atom Ni site active toward electrochemical CO_2 conversion to CO. *J. Am. Chem. Soc.* **143**, 925–933 (2021).
21. Rong, X., Wang, H.-J., Lu, X.-L., Si, R. & Lu, T.-B. Controlled synthesis of a vacancy-defect single-atom catalyst for boosting CO_2 electroreduction. *Angew. Chem. Int. Ed.* **59**, 1961–1965 (2020).
22. Xiao, G. et al. Coordination environments tune the activity of oxygen catalysis on single atom catalysts: a computational study. *Nano Res.* **15**, 3073–3081 (2022).
23. Li, R. & Wang, D. Understanding the structure-performance relationship of active sites at atomic scale. *Nano Res.* **15**, 6888–6923 (2022).
24. Hossain, M. D., Huang, Y., Yu, T. H., Goddard, W. A. III & Luo, Z. Reaction mechanism and kinetics for CO_2 reduction on nickel single atom catalysts from quantum mechanics. *Nat. Commun.* **11**, 2256 (2020).
25. Tiwari, J. N. et al. Multicomponent electrocatalyst with ultralow Pt loading and high hydrogen evolution activity. *Nat. Energy* **3**, 773–782 (2018).
26. Song, Z. et al. Engineering the low coordinated Pt single atom to achieve the superior electrocatalytic performance toward oxygen reduction. *Small* **16**, 2003096 (2020).
27. Kwon, H. C. et al. Carbon monoxide as a promoter of atomically dispersed platinum catalyst in electrochemical hydrogen evolution reaction. *J. Am. Chem. Soc.* **140**, 16198–16205 (2018).
28. Brinkmann, T., Santonja, G. G., Schorcht, F., Roudier, S. & Sancho, L. D. Best available techniques (BAT) reference document for the production of chlor-alkali. *Publ. Off. Eur. Union*. https://doi.org/10.2791/13138 (2014).
29. World Chlorine Council, Sustainable progress. *World Chlorine Council* https://worldchlorine.org/wp-content/uploads/2018/10/WCC_Sustainable-Progress_Version-3-2017.pdf (2017).
30. Lim, T. et al. General efficacy of atomically dispersed Pt catalysts for the chlorine evolution reaction: potential-dependent switching of the kinetics and mechanism. *ACS Catal.* **11**, 12232–12246 (2021).
31. Trasatti, S. Electrocatalysis in the anodic evolution of oxygen and chlorine. *Electrochim. Acta* **29**, 1503–1512 (1984).
32. Karlsson, R. K. B. & Cornell, A. Selectivity between oxygen and chlorine evolution in the chlor-alkali and chlorate processes. *Chem. Rev.* **116**, 2982–3028 (2016).
33. Macounová, K. M., Simic, N., Ahlberg, E. & Krtil, P. Electrocatalytic aspects of the chlorate process: a voltammetric and DEMS comparison of RuO_2 and DSA anodes. *J. Electrochem. Soc.* **165**, E751 (2018).
34. Sohrabnejad-Eskan, I. et al. Temperature-dependent kinetic studies of the chlorine evolution reaction over RuO_2(110) model electrodes. *ACS Catal.* **7**, 2403–2411 (2017).
35. Zeradjanin, A. R., Menzel, N., Schuhmann, W. & Strasser, P. On the faradaic selectivity and the role of surface inhomogeneity during the chlorine evolution reaction on ternary Ti–Ru–Ir mixed metal oxide electrocatalysts. *Phys. Chem. Chem. Phys.* **16**, 13741–13747 (2014).
36. Chen, R. et al. Microstructural impact of anodic coatings on the electrochemical chlorine evolution reaction. *Phys. Chem. Chem. Phys.* **14**, 7392–7399 (2012).
37. Menzel, N., Ortel, E., Mette, K., Kraehnert, R. & Strasser, P. Dimensionally stable Ru/Ir/TiO_2-anodes with tailored mesoporosity for efficient electrochemical chlorine evolution. *ACS Catal.* **3**, 1324–1333 (2013).
38. Yang, J. et al. Regulating the tip effect on single-atom and cluster catalysts: forming reversible oxygen species with high efficiency in chlorine evolution reaction. *Angew. Chem. Int. Ed.* **61**, e202200366 (2022).
39. Moreno-Hernandez, I. A., Brunschwig, B. S. & Lewis, N. S. Crystalline nickel, cobalt, and manganese antimonates as electrocatalysts for the chlorine evolution reaction. *Energy Environ. Sci.* **12**, 1241–1248 (2019).
40. Ding, K. et al. Identification of active sites in CO oxidation and water-gas shift over supported Pt catalysts. *Science* **350**, 189–192 (2015).
41. Choi, C. H. et al. The Achilles' heel of iron-based catalysts during oxygen reduction in an acidic medium. *Energy Environ. Sci.* **11**, 3176–3182 (2018).
42. Anantharaj, S., Karthik, P. E. & Noda, S. The significance of properly reporting turnover frequency in electrocatalysis research. *Angew. Chem. Int. Ed.* **60**, 23051–23067 (2021).
43. Kim, J. H. et al. Reversible ligand exchange in atomically dispersed catalysts for modulating the activity and selectivity of the oxygen reduction reaction. *Angew. Chem. Int. Ed.* **60**, 20528–20534 (2021).
44. Wang, M. et al. CO_2 electrochemical catalytic reduction with a highly active cobalt phthalocyanine. *Nat. Commun.* **10**, 3602 (2019).
45. Cai, Y. et al. Insights on forming N,O-coordinated Cu single-atom catalysts for electrochemical reduction CO_2 to Methane. *Nat. Commun.* **12**, 586 (2021).
46. Yue, Z. R., Jiang, W., Wang, L., Gardner, S. D. & Pittman, C. U. Surface characterization of electrochemically oxidized carbon fibers. *Carbon* **37**, 1785–1796 (1999).
47. Huynh, M. T., Anson, C. W., Cavell, A. C., Stahl, S. S. & Hammes-Schiffer, S. Quinone 1 e^- and 2 e^-/2 H^+ reduction potentials: identification and analysis of deviations from systematic scaling relationships. *J. Am. Chem. Soc.* **138**, 15903–15910 (2016).
48. Yi, Y. et al. Electrochemical corrosion of a glassy carbon electrode. *Catal. Today* **295**, 32–40 (2017).
49. Moulder, J. F. & Chastain, J. *Handbook of X-ray Photoelectron Spectroscopy: A Reference Book of Standard Spectra for Identification and Interpretation of XPS Data*. (Physical Electronics Division, Perkin-Elmer Corporation, 1992).
50. Wang, C., Zhou, J. & Chu, L. Chlorine-functionalized reduced graphene oxide for methylene blue removal. *RSC Adv.* **5**, 52466–52472 (2015).
51. Ramaswamy, N., Tylus, U., Jia, Q. & Mukerjee, S. Activity descriptor identification for oxygen reduction on nonprecious electrocatalysts: linking surface science to coordination chemistry. *J. Am. Chem. Soc.* **135**, 15443–15449 (2013).

52. Jin, Z. et al. Understanding the inter-site distance effect in single-atom catalysts for oxygen electroreduction. *Nat. Catal.* **4**, 615–622 (2021).
53. Ortuño, M. A., Conejero, S. & Lledós, A. True and masked three-coordinate T-shaped platinum(II) intermediates. *Beilstein J. Org. Chem.* **9**, 1352–1382 (2013).
54. López, M., Exner, K. S., Viñes, F. & Illas, F. Computational Pourbaix diagrams for MXenes: a key ingredient toward proper theoretical electrocatalytic studies. *Adv. Theory Simul.* 2200217 https://doi.org/10.1002/adts.202200217 (2022).
55. Exner, K. S. A universal descriptor for the screening of electrode materials for multiple-electron processes: beyond the thermodynamic overpotential. *ACS Catal.* **10**, 12607–12617 (2020).
56. Exner, K. S., Lim, T. & Joo, S. H. Circumventing the OCl versus OOH scaling relation in the chlorine evolution reaction: beyond dimensionally stable anodes. *Curr. Opin. Electrochem.* **34**, 100979 (2022).
57. Rossmeisl, J., Qu, Z. W., Zhu, H., Kroes, G. J. & Nørskov, J. K. Electrolysis of water on oxide surfaces. *J. Electroanal. Chem.* **607**, 83–89 (2007).
58. Exner, K. S. Controlling stability and selectivity in the competing chlorine and oxygen evolution reaction over transition metal oxide electrodes. *ChemElectroChem* **6**, 3401–3409 (2019).
59. Goeke, R. S., Datye, A. K., Atanassov, P. & St-Pierre, J. Model electrode structures for studies of electrocatalyst degradation. *ECS Trans.* **33**, 361 (2010).
60. Sa, Y. J. et al. A general approach to preferential formation of active Fe–N_x sites in Fe–N/C electrocatalysts for efficient oxygen reduction reaction. *J. Am. Chem. Soc.* **138**, 15046–15056 (2016).
61. Ravel, B. & Newville, M. ATHENA, ARTEMIS, HEPHAESTUS: data analysis for X-ray absorption spectroscopy using IFEFFIT. *J. Synchrotron Radiat.* **12**, 537–541 (2005).
62. Iwasawa, Y. *X-ray Absorption Fine Structure for Catalysts and Surfaces*. Vol. 2 (World Scientific, 1996).
63. Yoshida, H., Nonoyama, S., Yazawa, Y. & Hattori, T. Quantitative determination of platinum oxidation state by XANES analysis. *Phys. Scr.* **2005**, 813 (2005).
64. Ankudinov, A. L., Rehr, J. J. & Bare, S. R. Hybridization peaks in Pt–Cl XANES. *Chem. Phys. Lett.* **316**, 495–500 (2000).
65. Hazell, A. Structure of (5,10,15,20-tetraphenyl-21*H*,23*H*-porphinato) platinum(II), $C_{44}H_{28}N_4Pt$. *Acta Cryst.* **40**, 751–753 (1984).
66. Ji, S. G., Kim, H., Choi, H., Lee, S. & Choi, C. H. Overestimation of photoelectrochemical hydrogen evolution reactivity induced by noble metal impurities dissolved from counter/reference electrodes. *ACS Catal.* **10**, 3381–3389 (2020).
67. Vos, J. G. & Koper, M. T. M. Measurement of competition between oxygen evolution and chlorine evolution using rotating ring-disk electrode voltammetry. *J. Electroanal. Chem.* **819**, 260–268 (2018).
68. Li, N. et al. Double transition metal carbides MXenes (D-MXenes) as promising electrocatalysts for hydrogen reduction reaction: Ab initio calculations. *ACS Omega* **6**, 23676–23682 (2021).
69. Cho, J. et al. Importance of broken geometric symmetry of single-atom Pt sites for efficient electrocatalysis. *Datasets of the main figure* https://doi.org/10.5281/zenodo.7936631 (2023).
70. Cho, J. et al. Importance of broken geometric symmetry of single-atom Pt sites for efficient electrocatalysis. *DFT code* https://doi.org/10.5281/zenodo.7936174 (2023).

Acknowledgements
This work was supported by the National Research Foundation (NRF) of Korea grant funded by the Ministry of Science and ICT (MSIT) (Nos. 2021R1A5A1030054 and 2022K1A4A7A04095893 to C.H.C.; 2019M3D1A1079306 and 2021R1A2C2007495 to S.H.J.). K.S.E. is associated with the CRC/TRR247: "Heterogeneous Oxidation Catalysis in the Liquid Phase" (Project number 388390466-TRR 247), the RESOLV Cluster of Excellence, funded by the Deutsche Forschungsgemeinschaft under Germany's Excellence Strategy – EXC 2033–390677874–RESOLV, and the Center for Nanointegration (CENIDE). Experiments at PLS-II were supported in part by MSIT and POSTECH.

Author contributions
C.H.C., S.H.J. and K.S.E. concevied and directed the project. T.L. synthesized and characterized the catalysts. J.C. and H.K. performed the electrochemical studies. L.M., F.V. and F.I. conducted computational calculations. J.K., S.L., J.H.L., G.Y.J. and K.S.L. contributed to part of the experimental and theoretical studies. J.C., T.L., H.K., K.S.E., S.H.J. and C.H.C. wrote the manuscript with contribution from all authors.

Competing interests
The authors declare no competing interests.

Additional information
Supplementary information The online version contains supplementary material available at https://doi.org/10.1038/s41467-023-38964-x.

Correspondence and requests for materials should be addressed to Kai S. Exner, Sang Hoon Joo or Chang Hyuck Choi.

Peer review information *Nature Communications* thanks Yun Wang, and the other, anonymous, reviewer(s) for their contribution to the peer review of this work. A peer review file is available.

4.5. References

1. Wang, A.; Li, J.; Zhang, T., Heterogeneous Single-Atom Catalysis. *Nat. Rev. Chem.* **2018,** *2*, 65–81.
2. Ji, S.; Chen, Y.; Wang, X.; Zhang, Z.; Wang, D.; Li, Y., *Chem. Rev.* Chemical Synthesis of Single Atomic Site Catalysts. **2020,** *120*, 11900–11955.
3. Cui, X.; Li, W.; Ryabchuk, P.; Junge, K.; Beller, M. J. N. C., Bridging Homogeneous and Heterogeneous Catalysis by Heterogeneous Single-Metal-Site Catalysts. *Nat. Catal.* **2018,** *1*, 385–397.
4. Mitchell, S.; Vorobyeva, E.; Pérez-Ramírez, J., The Multifaceted Reactivity of Single-Atom Heterogeneous Catalysts. *Angew. Chem. Int. Ed.* **2018,** *57*, 15316–15329.
5. Ignaczak, A.; Nazmutdinov, R.; Goduljan, A.; de Campos Pinto, L. M.; Juarez, F.; Quaino, P.; Belletti, G.; Santos, E.; Schmickler, W. J. E., Oxygen Reduction in Alkaline Media—A Discussion. *Electrocatalysis* **2017,** *8*, 554–564.
6. Krogmann, K., Planar Complexes Containing Metal-Metal Bonds. *Angew. Chem. Int. Ed.* **1969,** *8*, 35–42.
7. Exner, K. S.; Anton, J.; Jacob, T.; Over, H., Microscopic Insights into the Chlorine Evolution Reaction on RuO_2(110): A Mechanistic Ab Initio Atomistic Thermodynamics Study. *Electrocatalysis* **2015,** *6*, 163–172.
8. Vos, J. G.; Liu, Z.; Speck, F. D.; Perini, N.; Fu, W.; Cherevko, S.; Koper, M. T. M., Selectivity Trends Between Oxygen Evolution and Chlorine Evolution on Iridium-Based Double Perovskites in Acidic Media. *ACS Catal.* **2019,** *9*, 8561–8574.
9. Li, K.; Fan, Q.; Chuai, H.; Liu, H.; Zhang, S.; Ma, X., Revisiting Chlor-Alkali Electrolyzers: From Materials to Devices. *Trans. Tianjin Univ.* **2021,** *27*, 202–216.
10. Liu, Y.; Wang, Y.; Zhao, S., Journey of Electrochemical Chlorine Production: From Brine to Seawater. *Curr. Opin. Electrochem.* **2023,** *37*, 101202.
11. Lakshmanan, S.; Murugesan, T. J. C. T.; Policy, E., The Chlor-Alkali Process: Work in Progress. **2014,** *16*, 225–234.
12. Rosales-Huamani, J. A.; Medina-Collana, J. T.; Diaz-Cordova, Z. M.; Montaño-Pisfil, J. A., Factors Influencing the Formation of Sodium Hydroxide by an Ion Exchange Membrane Cell. *Batteries* **2021,** *7*, 34.

13. O'Brien, T. F.; Bommaraju, T. V.; Hine, F.; *Handb. Chlor-Alkali Technol.* **2005**, 17–36.
14. Millet, P., *Handb. Membr. React.* **2013,** *2*, 384–415.
15. Jung, J.; Postels, S.; Bardow, A., Cleaner Chlorine Production Using Oxygen Depolarized Cathodes? A Life Cycle Assessment. *J. Clean. Prod.* **2014,** *80*, 46–56.
16. Kiros, Y.; Pirjamali, M.; Bursell, M., Oxygen Reduction Electrodes for Electrolysis in Chlor-Alkali Cells. *Electrochim. Acta* **2006,** *51*, 3346–3350.
17. Morimoto, T.; Suzuki, K.; Matsubara, T.; Yoshida, N., Oxygen Reduction Electrode in Brine Electrolysis. *Electrochim. Acta* **2000,** *45*, 4257–4262.
18. Sudoh, M.; Kondoh, T.; Kamiya, N.; Ueda, T.; Okajima, K., Impedance Analysis of Gas-Diffusion Electrode Coated with a Thin Layer of Fluoro Ionomer to Enhance Its Stability in Oxygen Reduction. *Electrochem. Soc.* **2000,** *147*, 3739.
19. Kintrup, J.; Millaruelo, M.; Trieu, V.; Bulan, A.; Mojica, E. S., Gas Diffusion Electrodes for Efficient Manufacturing of Chlorine and Other Chemicals. *Electrochem. Soc. Interface.* **2017,** *26*, 73–76.
20. Moussallem, I.; Jörissen, J.; Kunz, U.; Pinnow, S.; Turek, T., Chlor-Alkali Electrolysis with Oxygen Depolarized Cathodes: History, Present Status and Future Prospects. *J. Appl. Electrochem.* **2008,** *38*, 1177–1194.
21. Ramaswamy, N.; Mukerjee, S., Fundamental Mechanistic Understanding of Electrocatalysis of Oxygen Reduction on Pt and Non-Pt Surfaces: Acid versus Alkaline Media. *J. Adv. Phys. Chem.* **2012,** *2012*, 491604.
22. Kiros, Y.; Quatrano, T.; Björnbom, P., Determination of the Thicknesses of the Active Layer and Cathode Limiting Currents in AFC. *Electrochem. Commu*n. **2004,** *6*, 526–530.
23. Kiros, Y.; Bursell, M., Low Energy Consumption in Chlor-Alkali Cells Using Oxygen Reduction Electrodes. *Int. J. Electrochem. Sci.* **2008,** *3*, 444–451.
24. Hosseini, M.; Zardari, P. J. A. S. S., Electrocatalytical Study of Carbon Supported Pt, Ru and Bimetallic Pt–Ru Nanoparticles for Oxygen Reduction Reaction in Alkaline Media. *Appl. Surf. Sci.* **2015,** *345*, 223–231.
25. Farzami, F.; Joudaki, E.; Hashemi, S. J. J. E., Comparative Study on Application of Bimetallic Pt-Based Alloy Electrocatalysts in Advanced Chlor-Alkali Electrolysis. *Eng.* **2011,** *3*, 836–841.

26. Hosseini, M. G.; Zardari, P., Electrocatalysis of Oxygen Reduction on Multi-Walled Carbon Nanotube Supported Ru-Based Catalysts in Alkaline Media. *Int. J. Hydrog. Energy* **2016,** *41*, 8803–8818.
27. Hosseini, M.; Zardari, P.; Ariankhah, I., RuO_2, RuO_2–TiO_2 and RuO_2–TiO_2–IrO_2 Nanoparticles Supported on Ni Mesh as Mixed Metal Oxide Electrodes for Oxygen Reduction Reaction. *J. Iran. Chem. Soc.* **2019,** *16*, 1749–1760.
28. Jiao, P.; Ye, D.; Zhu, C.; Wu, S.; Qin, C.; An, C.; Hu, N.; Deng, Q., Non-Precious Transition Metal Single-Atom Catalysts for the Oxygen Reduction Reaction: Progress and Prospects. *Nanoscale* **2022,** *14*, 14322–14340.
29. Wang, Y.; Hu, F. L.; Mi, Y.; Yan, C.; Zhao, S., Single-Metal-Atom Catalysts: An Emerging Platform for Electrocatalytic Oxygen Reduction. *J. Chem. Eng.* **2021,** *406*, 127135.
30. Fu, C.; Liu, C.; Li, T.; Zhang, X.; Wang, F.; Yang, J.; Jiang, Y.; Cui, P.; Li, H., DFT Calculations: A Powerful Tool for Better Understanding of Electrocatalytic Oxygen Reduction Reactions on Pt-Based Metallic Catalysts. *Comput. Mater. Sci.* **2019,** *170*, 109202.
31. Maheshwari, S.; Li, Y.; Agrawal, N.; Janik, M. J., Density Functional Theory Models for Electrocatalytic Reactions. *Adv. Catal.* **2018,** *63*, 117–167.
32. Kulkarni, A.; Siahrostami, S.; Patel, A.; Nørskov, J. K. J. C. r., Understanding Catalytic Activity Trends in the Oxygen Reduction Reaction. *Chem. Rev.* **2018,** *118*, 2302–2312.
33. Hosseini, M. G.; Hosseinzadeh, F.; Zardari, P.; Darbandi, M., Pd–Co Nanoparticles Decorated on Different Carbon Based Substrates as Electrocatalyst for O_2 Reduction Reaction. *Int. J. Hydrog. Energy* **2021,** *46*, 28513–28526.
34. Shaldehi, T. J.; Meng, L.; Rowshanzamir, S.; Parnian, M. J.; Exner, K.; Viñes, F.; Illas, F., Computationally Screening Non-Precious Single Atom Catalysts for Oxygen Reduction in Alkaline Media. *Catal. Today* **2024,** *431*, 114560.
35. Liang, Q.; Brocks, G.; Bieberle-Hütter, A. J. J. o. P. E., Oxygen Evolution Reaction (OER) Mechanism under Alkaline and Acidic Conditions. *J. Phys. Energy* **2021,** *3*, 026001.

36. Govindarajan, N.; García-Lastra, J. M.; Meijer, E. J.; Calle-Vallejo, F., Does the Breaking of Adsorption-Energy Scaling Relations Guarantee Enhanced Electrocatalysis? *Curr. Opin. Electrochem.* **2018,** *8*, 110–117.
37. Piqué, O.; Illas, F.; Calle-Vallejo, F., Designing Water Splitting Catalysts Using Rules of Thumb: Advantages, Dangers and Alternatives. *Phys. Chem. Chem. Phys.* **2020,** *22*, 6797–6803.
38. Romeo, E.; Illas, F.; Calle-Vallejo, F., A General but Still Unknown Characteristic of Active Oxygen Evolution Electrocatalysts. *Chem. Sci.* **2023,** *14*, 3622–3629.
39. Exner, K. S., A Universal Descriptor for the Screening of Electrode Materials for Multiple-Electron Processes: Beyond the Thermodynamic Overpotential. *ACS Catal.* **2020,** *10*, 12607–12617.
40. Razzaq, S.; Exner, K. S., Materials Screening by the Descriptor Gmax(η): The Free-Energy Span Model in Electrocatalysis. *ACS Catal.* **2023,** *13* (3), 1740–1758.
41. Kozuch, S.; Shaik, S., How to Conceptualize Catalytic Cycles? The Energetic Span Model. *Acc. Chem. Res.* **2011,** *44*, 101–110.
42. Christopher, P., Single-Atom Catalysts: Are All Sites Created Equal? *ACS Energy Lett.* **2019,** *4*, 2249–2250.
43. Zitolo, A.; Goellner, V.; Armel, V.; Sougrati, M.-T.; Mineva, T.; Stievano, L.; Fonda, E.; Jaouen, F., Identification of Catalytic Sites for Oxygen Reduction in Iron- and Nitrogen-Doped Graphene Materials. *Nat. Mater.* **2015,** *14*, 937–942.
44. Luo, F.; Wagner, S.; Ju, W.; Primbs, M.; Li, S.; Wang, H.; Kramm, U. I.; Strasser, P., Kinetic Diagnostics and Synthetic Design of Platinum Group Metal-Free Electrocatalysts for the Oxygen Reduction Reaction Using Reactivity Maps and Site Utilization Descriptors. *J. Am. Chem. Soc.* **2022,** *144*, 13487–13498.
45. Cheng, N.; Stambula, S.; Wang, D.; Banis, M. N.; Liu, J.; Riese, A.; Xiao, B.; Li, R.; Sham, T. K.; Liu, L. M.; Botton, G. A.; Sun, X., Platinum Single-Atom and Cluster Catalysis of the Hydrogen Evolution Reaction. *Nat. Commun.* **2016,** *7*, 13638.
46. Gao, G.; Jiao, Y.; Waclawik, E. R.; Du, A., Single Atom (Pd/Pt) Supported on Graphitic Carbon Nitride as an Efficient Photocatalyst for Visible-Light Reduction of Carbon Dioxide. *J. Am. Chem. Soc.* **2016,** *138*, 6292–6297.

47. Yan, Q. Q.; Wu, D. X.; Chu, S. Q.; Chen, Z. Q.; Lin, Y.; Chen, M. X.; Zhang, J.; Wu, X. J.; Liang, H. W., Reversing the Charge Transfer between Platinum and Sulfur-Doped Carbon Support for Electrocatalytic Hydrogen Evolution. *Nat. Commun.* **2019,** *10*, 4977.
48. Lim, T.; Jung, G. Y.; Kim, J. H.; Park, S. O.; Park, J.; Kim, Y. T.; Kang, S. J.; Jeong, H. Y.; Kwak, S. K.; Joo, S. H., Atomically Dispersed Pt–N_4 Sites as Efficient and Selective Electrocatalysts for the Chlorine Evolution Reaction. *Nat. Commun.* **2020,** *11*, 412.
49. Choi, C. H.; Kim, M.; Kwon, H. C.; Cho, S. J.; Yun, S.; Kim, H. T.; Mayrhofer, K. J. J.; Kim, H.; Choi, M., Tuning Selectivity of Electrochemical Reactions by Atomically Dispersed Platinum Catalyst. *Nat. Commun.* **2016,** *7*, 10922.
50. Kim, H.; Shin, D.; Yang, W.; Won, D. H.; Oh, H.-S.; Chung, M. W.; Jeong, D.; Kim, S. H.; Chae, K. H.; Ryu, J. Y.; Lee, J.; Cho, S. J.; Seo, J.; Kim, H.; Choi, C. H., Identification of Single-Atom Ni Site Active toward Electrochemical CO_2 Conversion to CO. *J. Am. Chem. Soc.* **2021,** *143*, 925–933.
51. Fang, S.; Zhu, X.; Liu, X.; Gu, J.; Liu, W.; Wang, D.; Zhang, W.; Lin, Y.; Lu, J.; Wei, S.; Li, Y.; Yao, T., Uncovering Near-Free Platinum Single-Atom Dynamics During Electrochemical Hydrogen Evolution Reaction. *Nat. Commun.* **2020,** *11*, 1029.
52. Tiwari, J. N.; Sultan, S.; Myung, C. W.; Yoon, T.; Li, N.; Ha, M.; Harzandi, A. M.; Park, H. J.; Kim, D. Y.; Chandrasekaran, S. S.; Lee, W. G.; Vij, V.; Kang, H.; Shin, T. J.; Shin, H. S.; Lee, G.; Lee, Z.; Kim, K. S., Author Correction: Multicomponent Electrocatalyst with Ultralow Pt Loading and High Hydrogen Evolution Activity. *Nat. Energy* **2019,** *4*, 249–249.
53. Cho, J.; Lim, T.; Kim, H.; Meng, L.; Kim, J.; Lee, S.; Lee, J. H.; Jung, G. Y.; Lee, K.-S.; Viñes, F.; Illas, F.; Exner, K. S.; Joo, S. H.; Choi, C. H., Importance of Broken Geometric Symmetry of Single-Atom Pt Sites for Efficient Electrocatalysis. *Nat. Commun.* **2023,** *14*, 3233.
54. Lim, T.; Kim, J. H.; Kim, J.; Baek, D. S.; Shin, T. J.; Jeong, H. Y.; Lee, K.-S.; Exner, K. S.; Joo, S. H., General Efficacy of Atomically Dispersed Pt Catalysts for the Chlorine Evolution Reaction: Potential-Dependent Switching of the Kinetics and Mechanism. *ACS Catal.* **2021,** *11*, 12232−12246.

55. Janssen, L. J. J.; Starmans, L. M. C.; Visser, J. G.; Barendrecht, E., Mechanism of the Chlorine Evolution on a Ruthenium Oxide/Titanium Oxide Electrode and on a Ruthenium Electrode. *Electrochim. Acta* **1977,** *22*, 1093–1100.
56. Trasatti, S. Electrodes of Conductive Metallic Oxides, Part B, Studies in Physical & Theoretical Chemistry, Elsevier Science Ltd, Amsterdam-Oxford-New York, **1981**.
57. Exner, K. S., Design Criteria for the Competing Chlorine and Oxygen Evolution Reactions: Avoid the OCl Adsorbate to Enhance Chlorine Selectivity. *Phys. Chem. Chem. Phys.* **2020,** *22*, 22451–22458.
58. Man, I. C.; Su, H.-Y.; Calle-Vallejo, F.; Hansen, H. A.; Martínez, J. I.; Inoglu, N. G.; Kitchin, J.; Jaramillo, T. F.; Nørskov, J. K.; Rossmeisl, J., Universality in Oxygen Evolution Electrocatalysis on Oxide Surfaces. *ChemCatChem* **2011,** *3*, 1159–1165.
59. López, M.; Exner, K. S.; Viñes, F.; Illas, F., Computational Pourbaix Diagrams for MXenes: A Key Ingredient toward Proper Theoretical Electrocatalytic Studies. *Adv. Theory Simul.* **2023,** *6*, 2200217.
60. Razzaq, S.; Exner, K. S., Method to Determine the Bifunctional Index for the Oxygen Electrocatalysis from Theory. *ChemElectroChem* **2022,** *9*, e202101603.
61. Exner, K. S., Beyond the Thermodynamic Volcano Picture in the Nitrogen Reduction Reaction over Transition-Metal Oxides: Implications for Materials Screening. *Chin. J. Catal.* **2022,** *43*, 2871–2880
62. Exner, K. S.; Lim, T.; Joo, S. H., Circumventing the OCl versus OOH Scaling Relation in the Chlorine Evolution Reaction: Beyond Dimensionally Stable Anodes. *Curr. Opin. Electrochem.* **2022,** *34*, 100979.
63. Exner, K. S., Controlling Stability and Selectivity in the Competing Chlorine and Oxygen Evolution Reaction over Transition Metal Oxide Electrodes. *ChemElectroChem* **2019,** *6*, 3401–3409.
64. Goeke, R. S.; Datye, A. K.; Atanassov, P.; St-Pierre, J., Model Electrode Structures for Studies of Electrocatalyst Degradation. *ECS Trans.* **2010,** *33*, 361.

Conclusions

In the present doctoral thesis, I utilized DFT based calculation to investigate the reactivity of widely studied 2D materials, particularly MXene and N-doped graphene with single atom, in the fields of electrocatalysis of hydrogenation evolution (HER), CO_2 reduction (CO_2RR), nitrogen reduction (NRR), chlorine evolution (CER), oxygen reduction (ORR), as well thermocatalysis of olefin hydrogenation to alkene, with a focus on issues related to energy and environmental sustainability.

Utilizing the tool of the Pourbaix diagram to refine the models with functional groups towards realism, the synergistic interaction of MXene surface functional groups significantly enhances reaction activity while reducing energy costs. Furthermore, a comprehensive analysis on MXene doping structures, including doping strategies, coordination numbers, doping environments, and quantities, as well the origin of the PHIP effect, which often overlooked in previous studies, were conducted. For nitrogen-doped graphene with single-atom, novel descriptors were introduced, in addition, a detailed examination was also conducted on the impact of different single-atom coordination numbers on reactions, revealing the structural symmetry factors influencing catalytic reactions.

These works clarify the underlying reasons behind key experimental observations, leading to predictions and determinations of the characteristic parameters of catalytic activities. In general, I have shown that:

1. The utilization of Pourbaix Diagram is eeffective to investigate the stability of catalytic surfaces under specified reaction conditions. The stable surface configuration of Ti_3C_2 MXene should be mixed termination rather than fully termination.
2. The mixed presence of –O, –OH, and –F groups on MXene can improve and reduce the energy costs.
3. On the Ti_3C_2 surface, a high-concentration of –O groups enhance its capability for H^+ reduction in HER, with moderate bond strengths observed when –O coverage is at 2/3. The presence of –F groups can promote HER especially when combined with higher concentrations of –O groups.
4. The –OH groups on Ti_3C_2 MXene can act as hydrogen donors involved in proton reduction in CO_2RR, –O group can serve as a reservoir for proton reduction, while the presence of –F is not only non-detrimental.

5. Substituted B-doped Ti_3C_2 MXene exhibits the strongest N_2 adsorption capability but typically lower NRR catalytic activity, whereas adsorbed B-doped Ti_3C_2 MXene exhibits inversely.
6. A moderate number of –OH groups on surface benefits the performance of nitrogen reduction reactions (NRR), especially when boron is surrounded by –OH groups in the H_C site.
7. 2D-Mo_2C(0001) and Rh(111) effectively catalyze olefins (ethene) hydrogenation to alkanes (ethane), with surface coverage being a factor affecting the rate of hydrogeneration. The energy barrier for the first hydrogenation from C_2H_4* to C_2H_5* is similar, however, the hydrogenation of C_2H_5* to C_2H_6* is more thermodynamically endothermic and features a significantly higher energy barrier on 2D-Mo_2C(0001).
8. DFT calculations rule out the widely accepted Horiuti-Polanyi and Eley-Rideal pairwise hydrogenation mechanisms, proposing that dynamic site blocking due to high adsorbate coverage or other mechanisms may significantly restrict hydrogen diffusion and further enhance pairwise hydrogenation.
9. A plausible ORR mechanism at alkaline pH (pH = 14) is proposed for NG-SAC material, with the descriptor of electrochemical step symmetry index (*ESSI*) introduced to evaluate the catalytic performance.
10. The heterogeneity in active site of Pt SACs may relate to their geometric symmetry. Under CER conditions, PtN_4 with symmetry shows higher structural stability and selectivity than symmetry-broken PtN_3V, although PtN_3V exhibits higher catalytic activity.
11. The actual active site of PtN_4 is Pt, whereas PtN_3 involves *O, resulting in different CER reaction pathways.
12. Adjusting geometric symmetry enhances the discovery of optimal coordination field strengths, thereby balancing stability and activity

List of Publications

Published articles in refereed journals included in this doctoral thesis:

Author contributions to the research articles comprise: (a) carrying out the DFT calculations and data treatment, (b) analysis of the calculations results, (c) surveying and summarizing the relevant publications, and (d) writing the initial manuscripts of papers as the first author, the computational part as the second author, as well making the corresponding figures.

- **Meng, L.**; Yan, L. K.; Viñes, F.; Illas, F., Effect of Terminations on the Hydrogen Evolution Reaction Mechanism on Ti_3C_2 MXene. *J. Mater. Chem. A* **2023**, 11, 6886–6900.
- **Meng, L.**; Yan, L. K.; Viñes, F.; Illas, F., Surface Termination Dependent Carbon Dioxide Reduction Reaction on Ti_3C_2 MXene. *J. Mater. Chem. A* **2024**, 12, 7856–7874.
- **Meng, L.**; Viñes, F.; Illas, F., Theoretical Modelling of the Hydrogen Evolution Reaction on MXenes: A Critical Review. *Curr. Opinion. Electrochem.* **2023**, 40, 101332.
- **Meng, L.**; Tayyebi, E.; Exner, K. S.; Viñes, F.; Illas, F., MXenes as Electrocatalysts for the CO_2 Reduction Reaction: Recent Advances and Future Challenges. *ChemElectroChem* **2024**, 11, e202300598.
- **Meng, L.**; Pokochueva, E. V.; Chen, Z.; Fedorov A.; Viñes, F.; Illas, F.; Koptyug, I. V., Contrasting Metallic (Rh^0) and Carbidic (2D-Mo_2C MXene) Surfaces in Olefin Hydrogenation Provides Insights on the Origin of the Pairwise Hydrogen Addition. *ACS Catal.* **2024**, 14, 12500–12511.
- **Meng, L.**; Viñes, F.; Illas, F., Unveiling the Synergy between Surface Terminations and Boron Configuration in Boron-Based Ti_3C_2 MXenes Electrocatalysts for Nitrogen Reduction Reaction. *ACS Catal.* **2024**, Under Review.
- Cho, J.; Lim, T.; Kim, H.; **Meng, L.**; Kim, J.; Lee, S.; Lee, J. H.; Jung, G. Y.; Lee, K.-S.; Viñes, F.; Illas, F.; Exner, K. S.; Joo, S. H.;

Choi, C. H., Importance of Broken Geometric Symmetry of Single-Atom Pt Sites for Efficient Electrocatalysis. *Nat. Commun.* **2023,** *14*, 3233.

Author contributions: (a) Conceptualization of reaction and formal analysis, (b) methodology and data curation, (c) surveying and summarizing the relevant publications, and (d) joining the initial manuscript of paper and making the corresponding figure.

- Shaldehi, T. J.; **Meng, L.**; Rowshanzamir, S.; Parnian, M. J.; Exner, K.; Viñes, F.; Illas, F., Computationally Screening Non-Precious Single Atom Catalysts for Oxygen Reduction in Alkaline Media. *Catal. Today* **2024,** *431*, 114560.

Appendix A

Supporting Information for "Effect of Terminations on the Hydrogen Evolution Reaction Mechanism on Ti_3C_2 MXene"

Effect of Terminations on the Hydrogen Evolution Reaction Mechanism on Ti_3C_2 MXene

Ling Meng,[a,b] Li-Kai Yan,[*,b] Francesc Viñes,[*,a] Francesc Illas[a]

[a] *Departament de Ciència de Materials i Química Física & Institut de Química Teòrica i Computacional (IQTCUB), Universitat de Barcelona, c/ Martí i Franquès 1-11, 08028 Barcelona, Spain*

[b] *Institute of Functional Material Chemistry, Key Laboratory of Polyoxometalate Science of Ministry of Education, Faculty of Chemistry, Northeast Normal University, Changchun 130024, P. R. China.*

[*] Corresponding authors: Francesc Viñes (francesc.vines@ub.edu), Li-Kai Yan (yanlk924@nenu.edu.cn)

Table S1. Summary of the potential determining steps, based on the calculated ΔG_H as a descriptor, on the explored Ti_3C_2 models, either pristine, or covered according to the specified terminations. The required overpotential, η, is specified, as well as the preferred Volker-Heyrovsky (VH) or Volmer-Tafel (VT) mechanism, specifying the subtype of path, either O-TER, OH-TER, or TER-TER. In the case of pristine Ti_3C_2, note that the strong H-affinity prevents any H_2 formation, regardless of η.

Model	Mechanism	Subtype	ΔG_H / eV	η / V
Pristine Ti_3C_2	—	—	-1.32	□
O	**VH**	—	-0.40	0.40
	VT[a]	—	-0.44*	0.44*
H	**VH**	—	0.63	0.63
	VT	—	2.30*	2.30*
OH	**VH**	—	-0.48	0.48
	VT	—	0.75	0.75
F	**VH**	—	2.62	2.62
$O_{1/3}OH_{2/3}$	**VH**	OH-TER	0.08	0.08
	VH	O-TER	0.62	0.62
	VT	TER-TER	0.19	0.19
	VT	O-TER	0.74	0.74
$O_{1/2}OH_{1/2}$	**VH**	OH-TER	0.23	0.23
	VH	O-TER	0.36	0.36
	VT[a]	TER-TER	0.44*	0.44*
	VT	O-TER	0.74	0.74
$O_{2/3}OH_{1/3}$	**VH**	O-TER	-0.01	0.01
	VH	OH-TER	0.66	0.66
	VT[a]	TER-TER	0.82*	0.82*
	VT	O-TER	0.09	0.09
$F_{1/3}O_{1/3}OH_{1/3}$	**VT**	TER-TER	-0.01	0.01
	VH	OH-TER	0.66	0.66
	VH	O-TER	0.46	0.46
	VT	TER-TER	0.58	0.58
$F_{3/9}O_{4/9}OH_{2/9}$	**VH**	O-TER	0.01	0.01

VH	OH-TER	0.32	0.32
VT[a]	TER-TER	0.29*	0.29*
VT	O-TER	0.46	0.46

[a] Not a real Volmer-Tafel mechanism, but similar to the Tafel step, *i.e.*, the formation of H_2 from two H atoms of the –OH surface group.

* For those the main energy impediment comes from only chemical step, *i.e.*, Tafel step, where two adjacent –OH termination groups react to form two –O groups and $H_{2(g)}$ molecule.

Figure. S1 Schematic of $Ti_3C_2T_x$ modelled by (a) full –OH and (b) $O_{2/3}OH_{1/3}$ termination towards H_C and H_{Ti} sites, respectively, with the total energy.

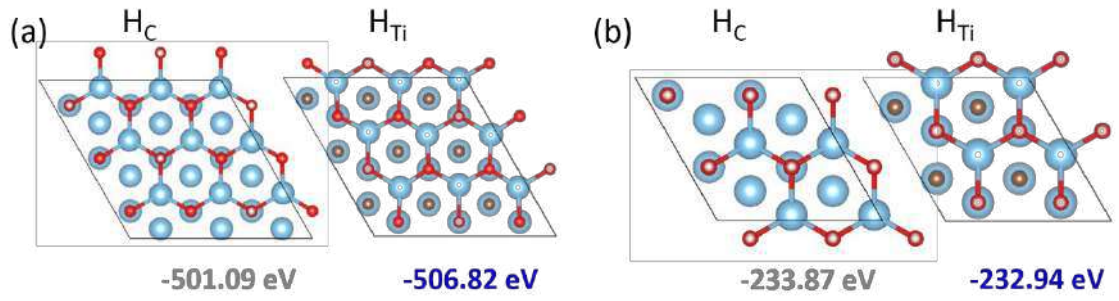

Figure. S2 Schematic arrangement of the fully –O, –OH, –H, and –F terminated Ti_3C_2 (0001) p(2×2) supercell, where moieties occupy H_{Ti} sites. The free (*) and occupied sites are colour-coded.

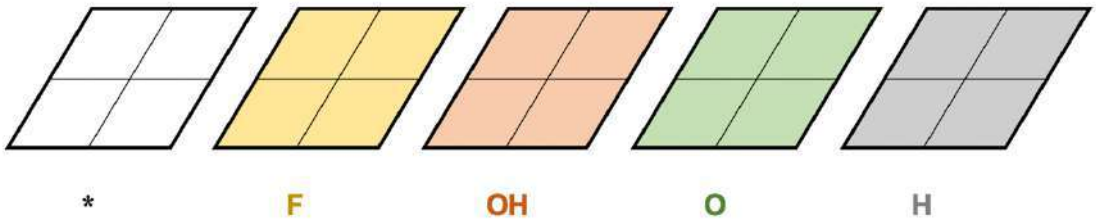

Figure. S3 Schematic arrangement of the binary ½ ML vs. ½ ML situations admixing –O, –OH, –H, and –F terminations, as well as * free sites, on the Ti_3C_2 (0001) p(2×2) supercell, exemplified on the $OH_{1/2}O_{1/2}$ case. Colour coding as in Fig. S1.

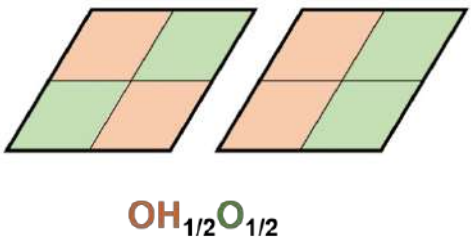

Figure. S4 Schematic arrangement of the binary $^{1}/_{4}$ ML *vs.* $^{3}/_{4}$ ML situation admixing –O, –OH, –H, and –F terminations, as well as * free sites, on the Ti_3C_2 (0001) *p*(2×2) supercell, exemplified on the $OH_{1/4}O_{3/4}$ case. Colour coding as in Fig. S1.

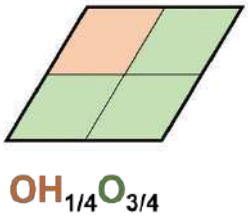

Figure. S5 Schematic arrangement of the binary $^{2}/_{3}$ ML *vs.* $^{1}/_{3}$ ML situations admixing –O, –OH, –H, and –F terminations, as well as * free sites, on the Ti_3C_2 (0001) *p*(3×3) supercell, exemplified on the $OH_{1/3}O_{2/3}$ case. Colour coding as in Fig. S1.

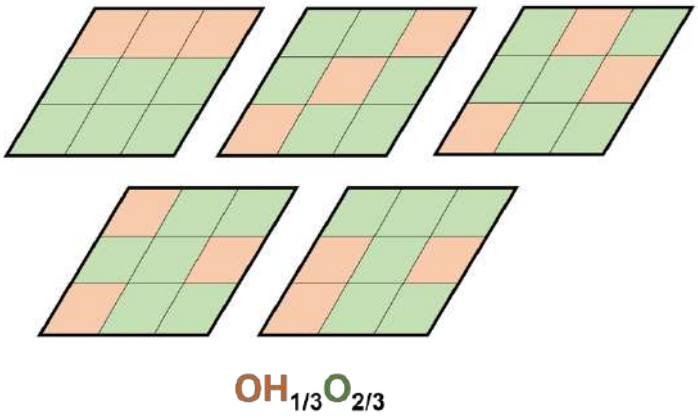

Figure. S6 Schematic arrangement of the ternary ¼, ¼, ½ ML situations admixing –O, –OH, –H, and –F terminations, as well as * free sites, on the Ti_3C_2 (0001) *p*(2×2) supercell, exemplified on the $F_{1/4}OH_{1/4}O_{1/2}$ case. Colour coding as in Fig. S1.

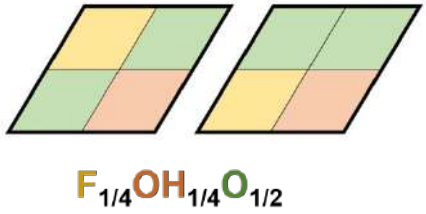

Figure. S7 Schematic arrangement of the ternary ⅓, ⅓, ⅓ ML situations admixing –O, –OH, –H, and –F terminations, as well as * free sites, on the Ti_3C_2 (0001) *p*(3×3) supercell, exemplified on the $F_{1/3}OH_{1/3}O_{1/3}$ case. Colour coding as in Fig. S1.

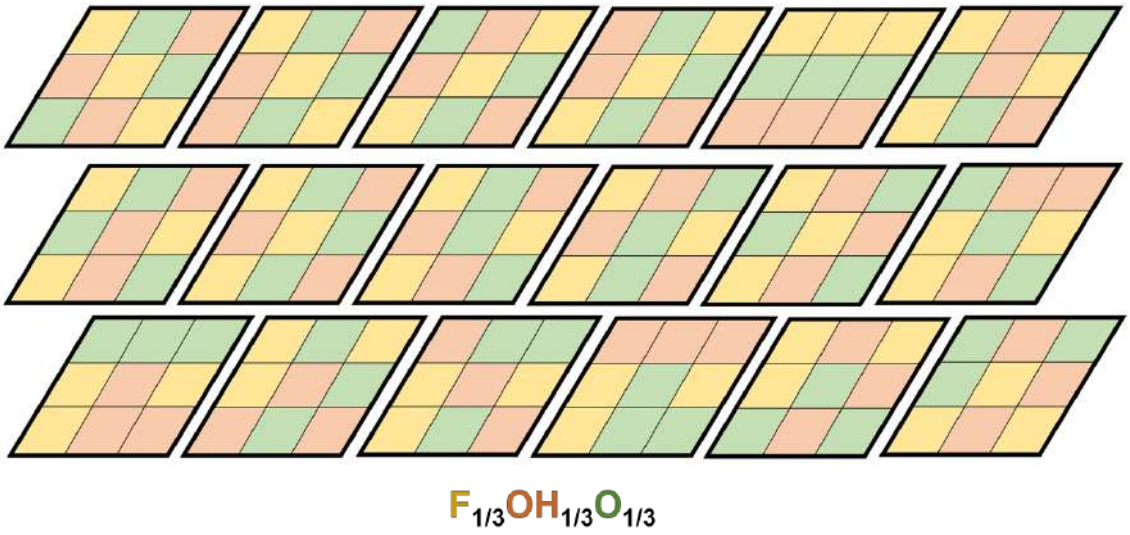

Figure. S8 Schematic arrangement of the ternary $^{3}/_{9}$, $^{4}/_{9}$, $^{2}/_{9}$ ML situations admixing –O, –OH, –H, and –F terminations, as well as * free sites, on the Ti_3C_2 (0001) *p*(3×3) supercell, exemplified on the $F_{3/9}OH_{4/9}O_{2/9}$ case. Colour coding as in Fig. S1.

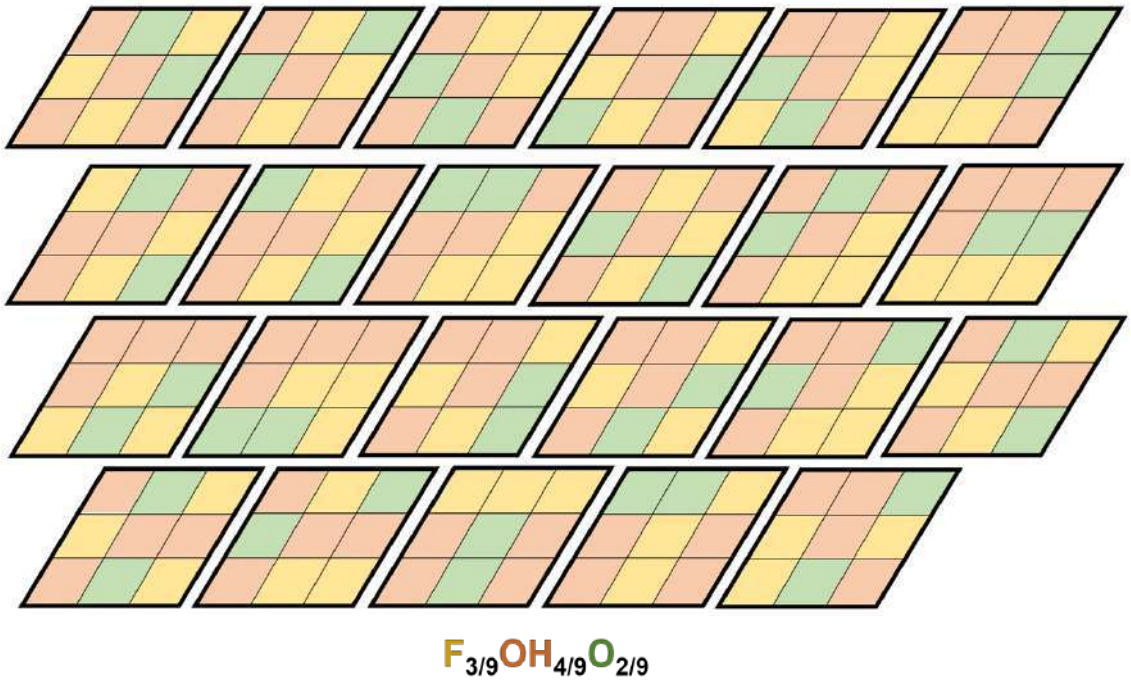

Figure. S9 Schematic arrangement of the ternary $^{3}/_{9}$, $^{5}/_{9}$, $^{1}/_{9}$ ML situations admixing –O, –OH, –H, and –F terminations, as well as * free sites, on the Ti_3C_2 (0001) p(3×3) supercell, exemplified on the $F_{3/9}OH_{5/9}O_{1/9}$ case. Colour coding as in Fig. S1.

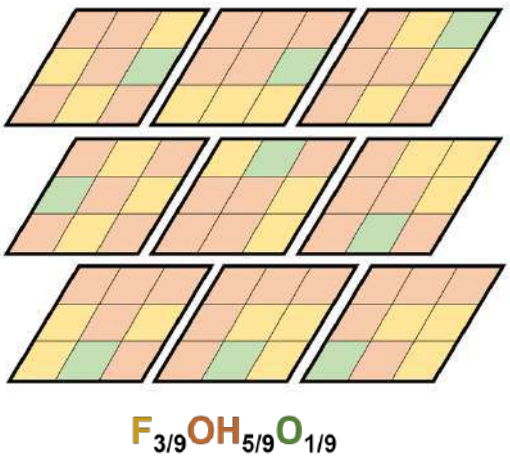

Figure. S10 Total and PDOS of the pristine Ti_3C_2 (0001) model, as those fully –O, –OH, –H, and –F terminated, and having different mixtures according to HER conditions and Pourbaix diagrams found in Figs. 2 and 3 of the main text. Energy levels are referred to the Fermi energy, E_F.

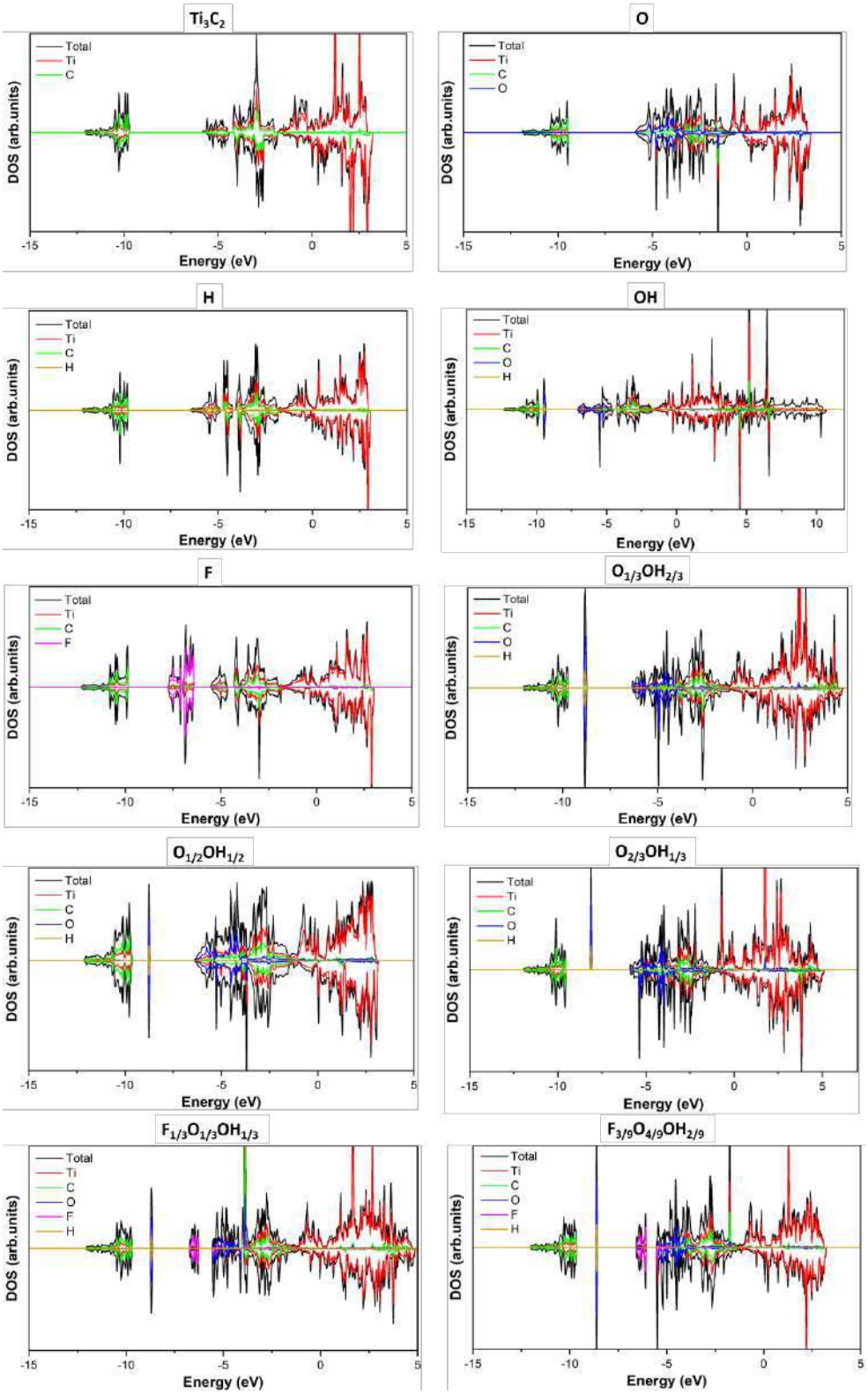

Figure. S11 Top view of the charge density difference (CDD) plots of the Ti_3C_2 (0001) fully –O, –OH, –H, and –F terminated, and having different mixtures according to HER conditions and Pourbaix diagrams found in Figs. 2 and 3 of the main text. Yellowish regions denote electron depletion, and the formation of positively charged regions, while blueish regions denote electron accumulation, and the formation of negatively charged regions. The contour intervals range up to 0.005 $e \cdot Å^{-3}$.

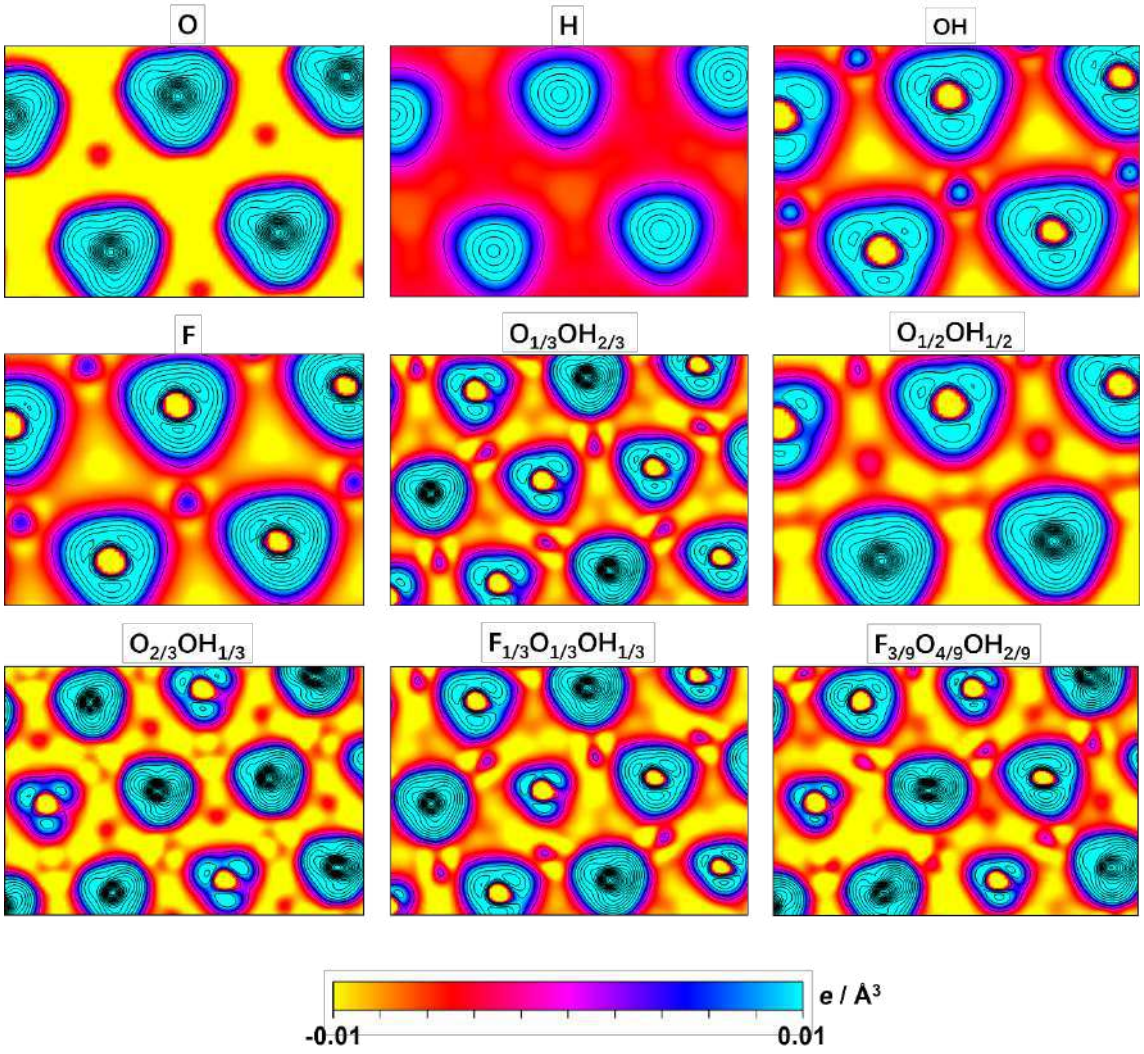

Appendix B

Supporting Information for "Surface Termination Dependent Carbon Dioxide Reduction Reaction on Ti_3C_2 MXene"

Surface Termination Dependent Carbon Dioxide Reduction Reaction on Ti_3C_2 MXene

Ling Meng,[a,b] Li-Kai Yan,[*,b] Francesc Viñes,[*,a] Francesc Illas[a]

[a] *Departament de Ciència de Materials i Química Física & Institut de Química Teòrica i Computacional (IQTCUB), Universitat de Barcelona, c/ Martí i Franquès 1-11, 08028, Barcelona, Spain*

[b] *Institute of Functional Material Chemistry, Key Laboratory of Polyoxometalate Science of Ministry of Education, Faculty of Chemistry, Northeast Normal University, Changchun 130024, P. R. China.*

[*] Corresponding authors: Francesc Viñes (francesc.vines@ub.edu), Li-Kai Yan (yanlk924@nenu.edu.cn)

Figure. S1 Top view of the Ti_3C_2 (0001) surface model, where brown spheres denote C atoms, and three different Ti layers are shown with different shades of blue, being the topmost one the darkest. High-symmetry sites are tagged, including top (T) and bridge (B) sites, and three-fold hollow carbon (H_C) and hollow metal (H_M) sites.

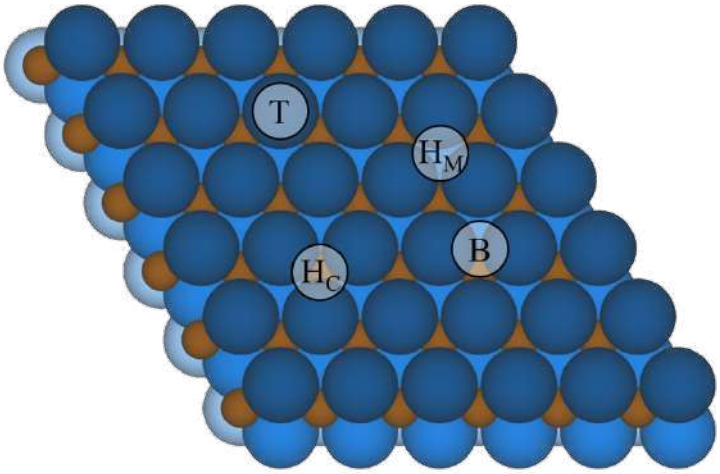

Figure. S2 Predicted Pourbaix diagrams for Ti_3C_2 MXene (0001) surface regarding all single, binary, and ternary surface compositions including –O, –OH, –H, and –F terminations, as well as free sites. Left image corresponds to situations without any –F termination, while right image corresponds to situations when regarding–F termination. The black, dashed line indicates the HER equilibrium potential with respect RHE reference.

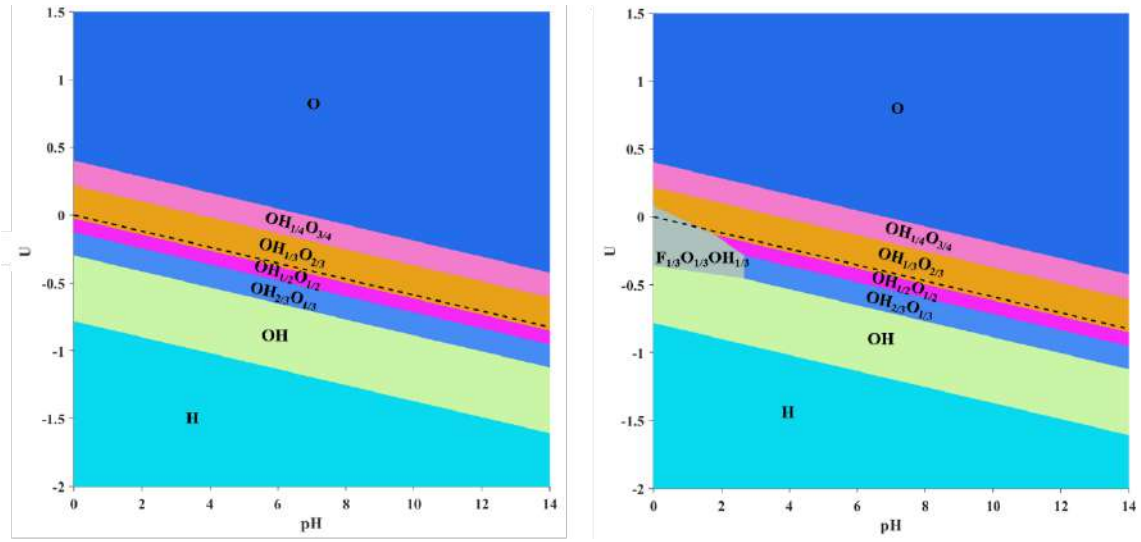

Figure. S3 Total and projected density of states (PDOS) of the pristine Ti_3C_2 (0001) surface model, as well as of the fully –OH terminated model, and of the rest of binary and ternary models explored in the present work, derived from Pourbaix diagrams shown in Fig. 1 of the main text. Energy levels are referred to the Fermi energy, E_F, set to zero.

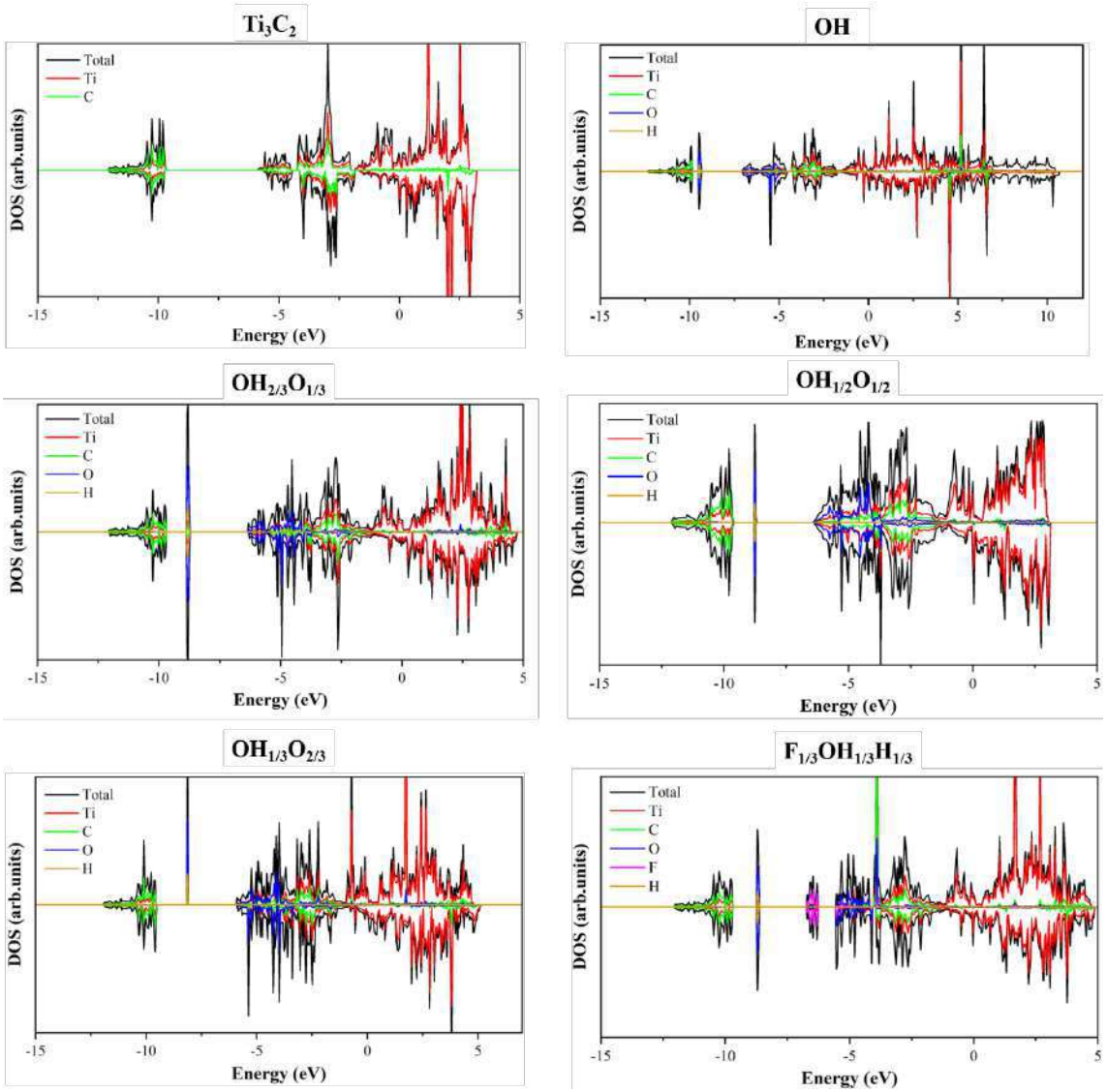

Figure. S4 Details regarding the bonding modes of CO_2 adsorption on the Ti_3C_2(0001) surface with $F_{1/3}OH_{1/3}O_{1/3}$ termination, encompassing (a) the exploration of various hexagonal centre configurations to elucidate distinct CO_2 adsorption environments, and (b) the investigation of different orientations for CO_2 adsorption.

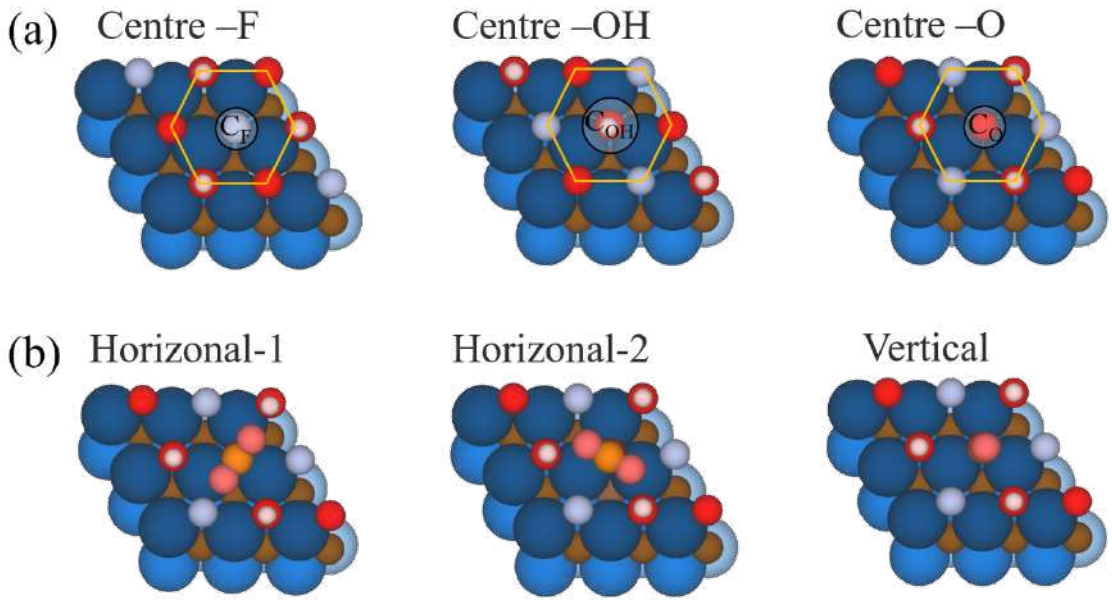

Figure. S5 Top view of the charge density difference (CDD) plots of the studied Ti_3C_2 (0001) MXene models. Yellowish regions denote electron depletion, *i.e.* the formation of positively charged regions, while blueish regions denote electron accumulation, and the formation of negatively charged regions. The contour intervals range to 0.005 $e \cdot Å^{-3}$ increments.

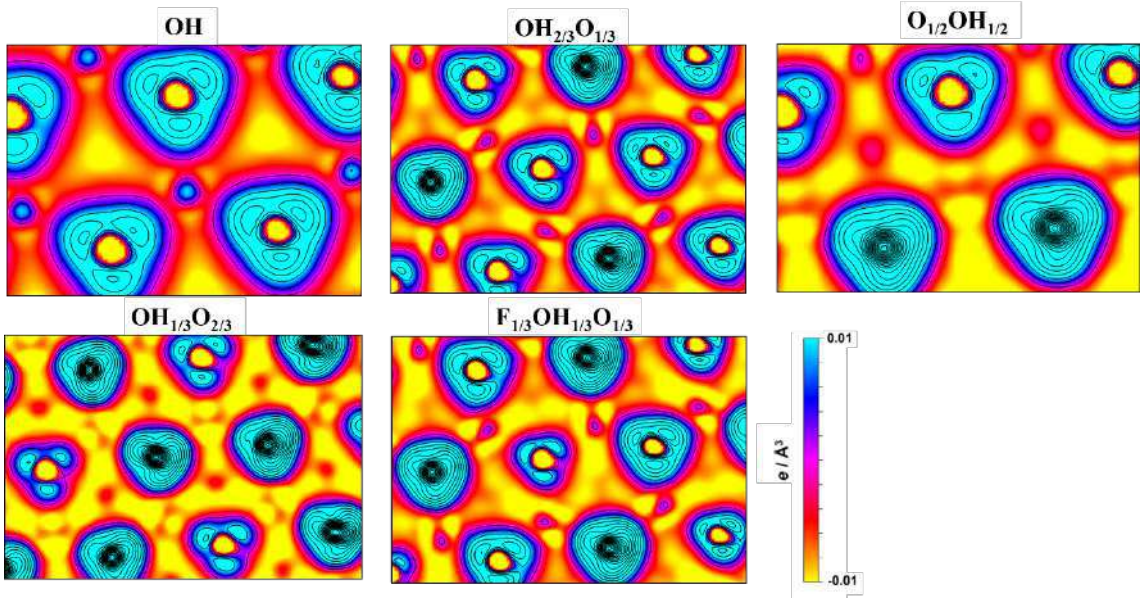

Figure. S6 Calculated rates of adsorption, r_{ads}, and desorption, r_{des}, of CO_2 and CH_4 on (a) clean surface, (b) full –OH, (c) $–OH_{2/3}O_{1/3}$, (d) $–OH_{1/2}O_{1/2}$, (d) $–OH_{1/3}O_{2/3}$, (e) $–F_{1/3}OH_{1/3}O_{1/3}$ terminations, as a function of temperature, T, and the gas partial pressure, p, here shown for 1 bar.

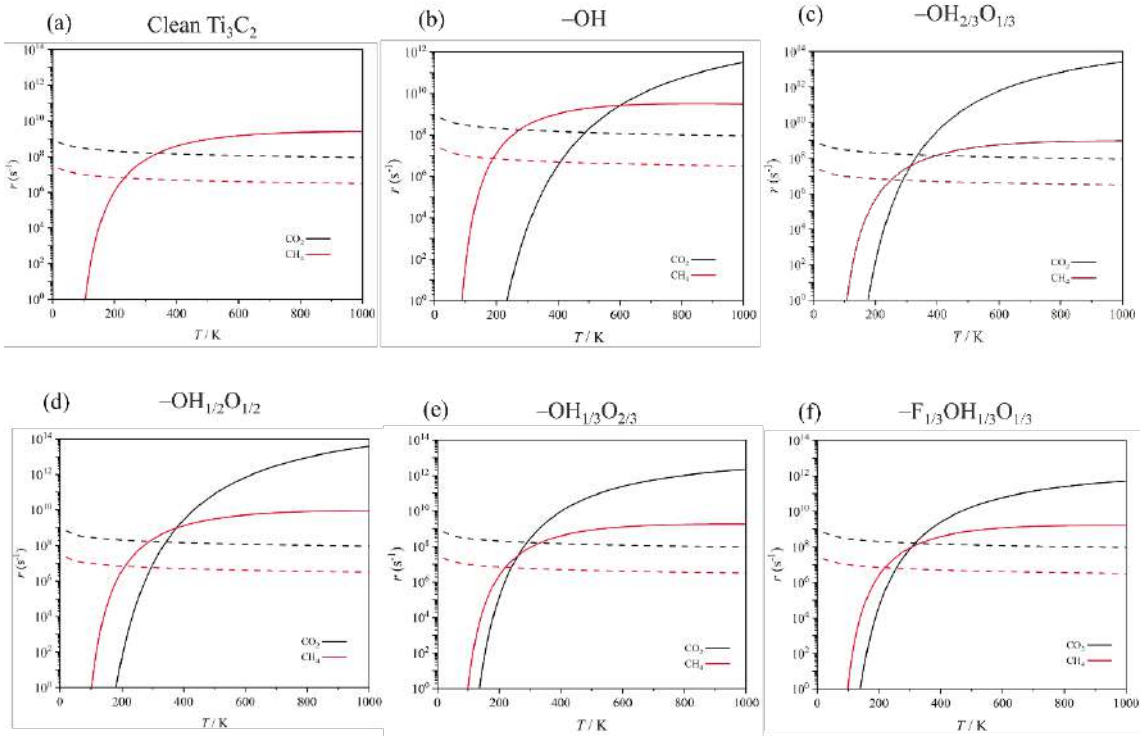

Figure. S7 Complete Gibbs free energy, Δ*G*, diagram of CO_2RR on fully –OH terminated Ti_3C_2 MXene, under standard working conditions. Blue lines represent chemical steps of as-generated H_2O or CH_4 desorptions, or CO_2 adsorption, while black and grey lines represent the electrochemical proton-coupled electron transfer (PCET) steps at zero potential *vs.* SHE. The –nH* symbols refer to how many H atoms have been transferred from surface –OH groups at the reaction stage.

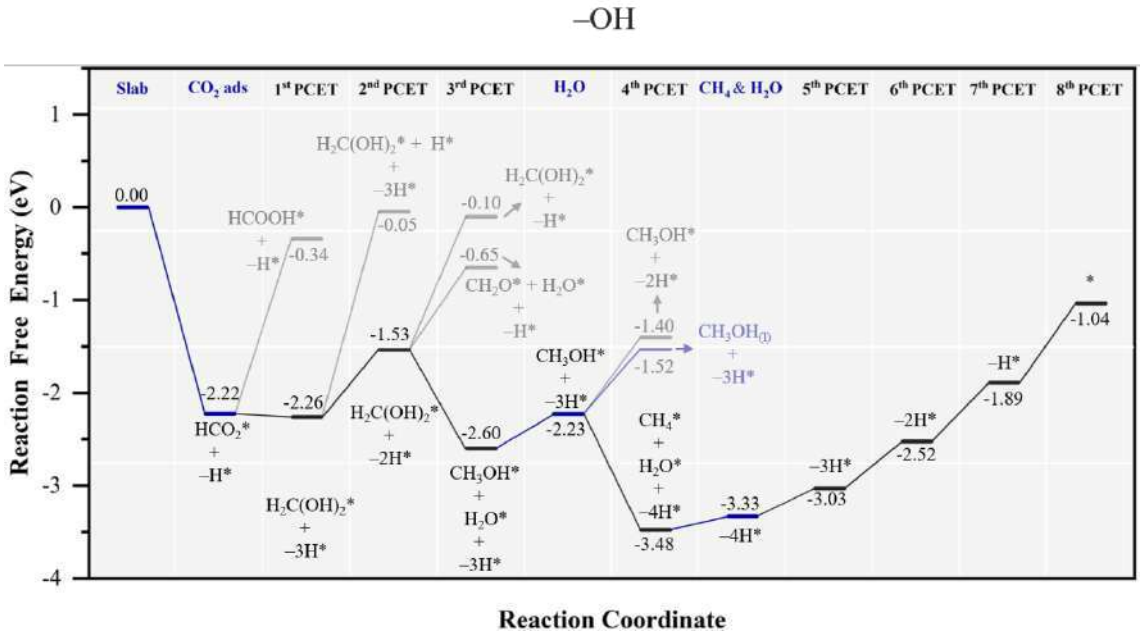

Figure. S8 Complete Gibbs free energy, Δ*G*, diagram of CO_2RR on $–OH_{2/3}O_{1/3}$ Ti_3C_2 MXene model, under standard working conditions at zero potential *vs.* SHE. Colour code as in Figure S6. nH* symbols refer to how many H atoms have been reduced over surface –O groups at the given reaction stage.

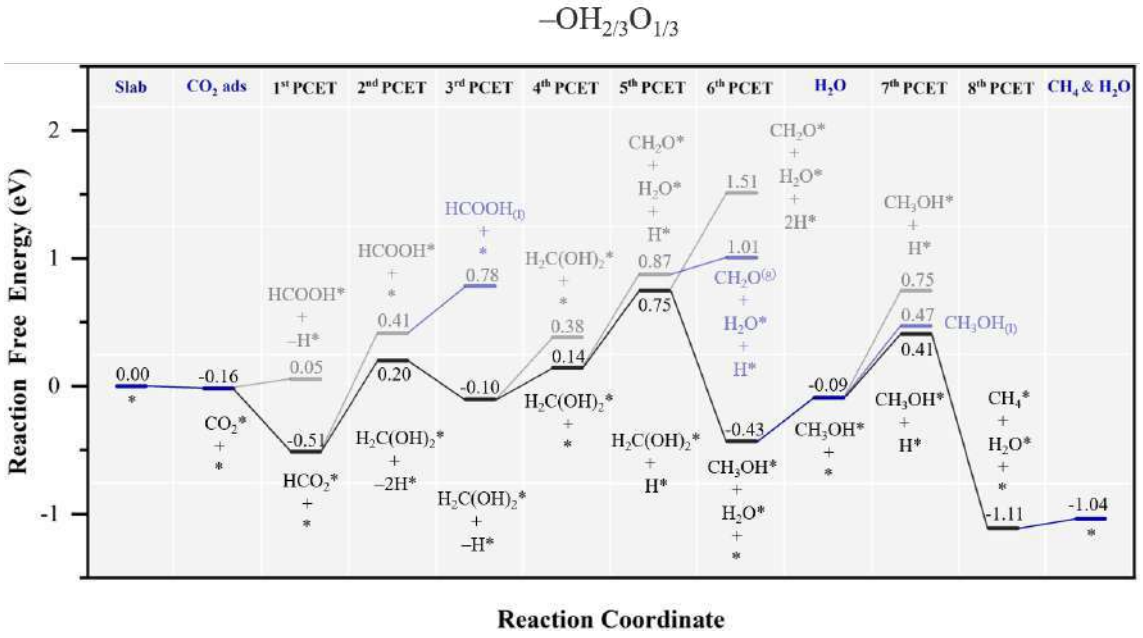

Figure. S9 Complete Gibbs free energy, ΔG, diagram of CO_2RR on $-OH_{1/2}O_{1/2}$ Ti_3C_2 MXene model, under standard working conditions at zero potential *vs.* SHE. Colour code and notation as in Figures S6 and S7.

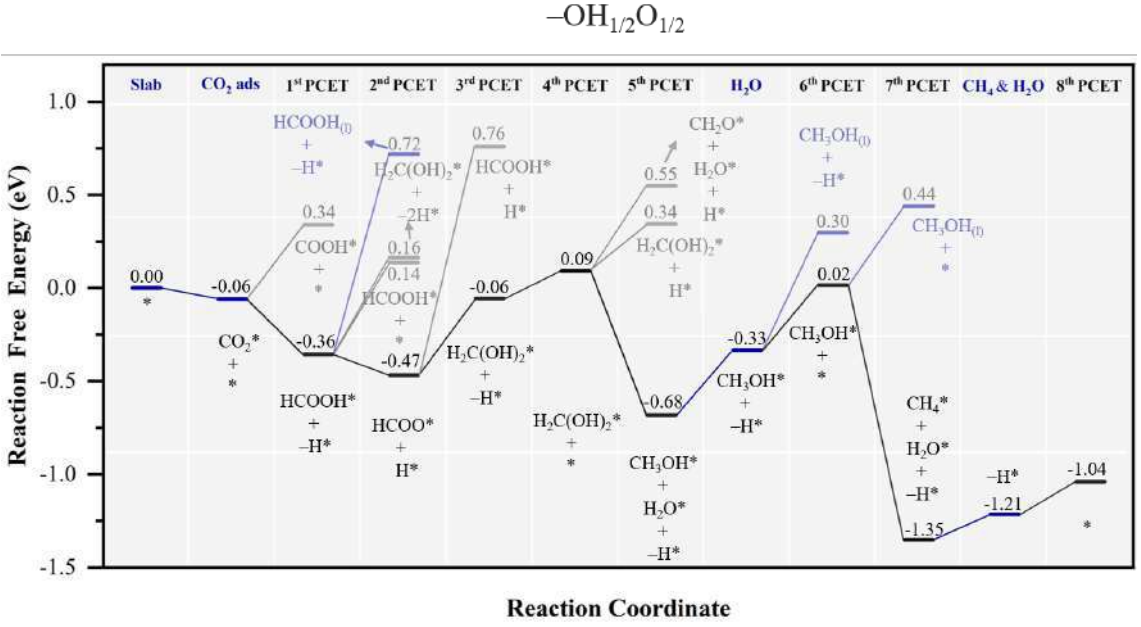

Figure. S10 Complete Gibbs free energy, Δ*G*, diagram of CO_2RR on $–OH_{1/3}O_{2/3}$ Ti_3C_2 MXene model, under standard working conditions at zero potential *vs.* SHE. Colour code and notation as in Figures S6 and S7.

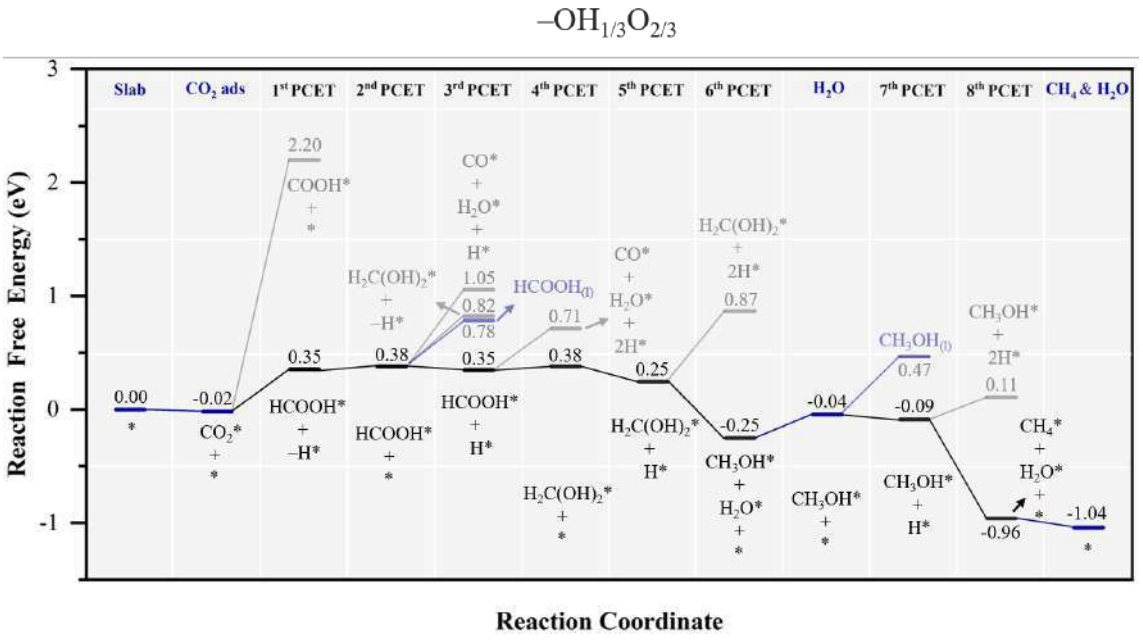

Figure. S11 Complete Gibbs free energy, ΔG, diagram of CO_2RR on $-F_{1/3}OH_{1/3}O_{1/3}Ti_3C_2$ MXene model, under standard working conditions at zero potential *vs.* SHE. Colour code and notation as in Figures S6 and S7.

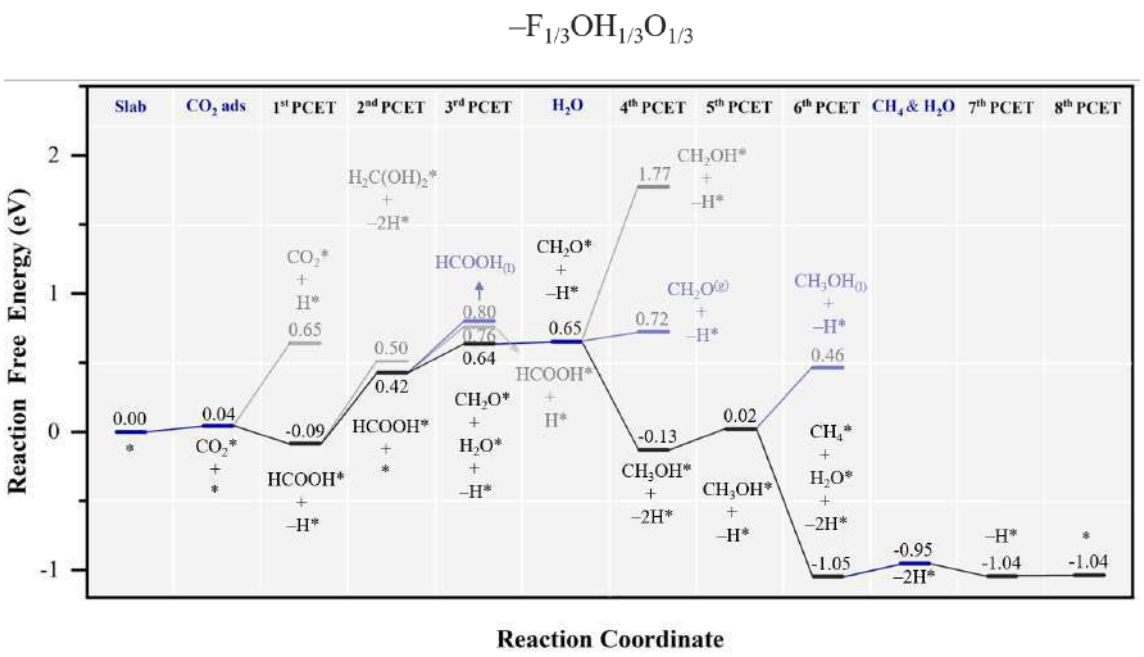

Appendix C

Supporting Information for "Unveiling the Synergy between Surface Terminations and Boron Configuration in Boron-Based Ti_3C_2 MXenes Electrocatalysts for Nitrogen Reduction Reaction."

Unveiling the Synergistic Engineering of Terminations and Boron Arrangements in Boron-Based MXene Catalysts for Nitrogen Reduction Reaction[†]

Ling Meng,[†] Francesc Viñes,[†,*] Francesc Illas[†]

[†] *Departament de Ciència de Materials i Química Física & Institut de Química Teòrica i Computacional (IQTCUB), Universitat de Barcelona, c/ Martí i Franquès 1-11, 08028, Barcelona, Spain*

[*] Corresponding authors: Francesc Illas (francesc.illas@ub.edu)

Table S1. Calculated formation energy (E_f), adsorption energy (E_{ads}), and the sum of E_{ads} and cohesive energy of boron (E_{coh}), as well as the bader charge of different models, e_B, e_{Term} and $e_{Ti_3C_2}$ represents the charge of B, termination, and substrate Ti_3C_2. Negative values indicate gain of electrons compared to isolated atoms. 3c and 2c represent three- and two-coordination of B, respectively. All values are given in eV.

Models	**Symbols**	E_f	E_{ads}	$E_{ads}+E_{coh}$	$e_{Ti_3C_2}$	e_{Term}	e_B
sB@$Ti_3C_2O_{8/9}$	**s**B-O	3.93	-2.53	3.28	1.03	-0.98	-0.06
sB@$Ti_3C_2OH_{8/9}$	**s**B-OH	2.16	-4.30	1.51	0.74	-0.62	-0.12
aB@Ti_3C_2O	**a**B-O	-1.20	-7.66	-1.85	0.96	-1.20	0.24
aB@$Ti_3C_2O_{4/9}OH_{5/9}$(3C)	**a**B-3c-O4	0.37	-4.73	-0.28	0.75	-0.99	0.24
aB@$Ti_3C_2O_{4/9}OH_{5/9}$(2C)	**a**B-2c-O4	1.73	-6.09	1.08	0.78	-0.96	0.18
aB@$Ti_3C_2O_{1/3}OH_{2/3}$(3C)	**a**B-3c-O3	0.68	-5.77	0.04	0.70	-0.94	0.24
aB@$Ti_3C_2O_{1/3}OH_{2/3}$(2C)	**a**B-2c-O3	1.99	-4.47	1.34	0.75	-0.92	0.17
aB@$Ti_3C_2O_{2/9}OH_{7/9}$	**a**B-O2	2.42	-4.04	1.77	0.71	-0.87	0.16
a2B@Ti_3C_2O	**a2**B-O	0.04	-6.42	-0.61	0.90	-1.23	0.16
a2B@$Ti_3C_2O_{4/9}OH_{5/9}$	**a2**B-OH	1.07	-5.39	0.21	0.71	-1.00	0.15

Table S2. Calculated various N_2 adsorption types, including physisorption (*p*) and chemisorption, in which encompasses end-on (*e*), side-on (*s*), bridge-end-on (*b*-*e*) and bridge-side-on (*b*-*s*). Analysed N_2 adsorption energy (E_{ads}) and charge differences of the moiety of Ti_3C_2 ($e_{Ti_3C_2}$), termination (e_{Term}) and N_2 molecule (e_B), as well as the variation (Δ) between before and after N_2 adsorption. The bond length between B and N, and adsorbed N_2. Negative values indicate gain of electrons compared to isolated atoms. The 3c and 2c represent three- and two-coordination of B, respectively, with energy in eV and distances in Å, where $N_{2(g)}$ has a bond length of 1.12 Å.

Models	**N_2 ads**	**Symbols**	**E_{ads} (N_2)**	**$e_{Ti_3C_2}$**	**$\Delta e_{Ti_3C_2}$**	**e_{Term}**	**Δe_{Term}**	**e_B**	**Δe_B**	**e_{N2}**	**BD_{B-N}**	**BD_{N-N}**
sB-O	end	**s**B-O-*e*	-1.87	1.04	0.01	-0.98	0.00	0.02	0.08	-0.08	1.38	1.16
	side	**s**B-O-*s*	-1.43	1.03	0.00	-0.98	0.00	0.06	0.12	-0.12	1.48	1.26
sB-OH	end	**s**B-OH-*e*	-2.79	0.75	0.01	-0.60	0.02	0.00	0.12	-0.15	1.35	1.21
	side	**s**B-OH-*s*	-1.52	0.74	0.00	-0.60	0.02	0.06	0.18	-0.20	1.47	1.40
aB-O	physis	**a**B-O-*p*	-0.09	0.96	0.00	-1.20	0.00	0.24	0.00	0.00	— 3.26	1.12
aB-3c-O4	physis	**a**B-3c-O4-*p*	-0.12	0.74	-0.01	-0.98	0.01	0.24	0.00	0.00	— 3.30	1.12
aB-2c-O4	end	**a**B-2c-O4-*e*	-0.68	0.79	0.01	-0.96	0.00	0.24	0.06	-0.07	1.46	1.16
	side	**a**B-2c-O4-*s*	-0.37	0.82	0.04	-0.94	0.02	0.23	0.05	-0.12	1.56	1.24
aB-3c-O3	physis	**a**B-3c-O3-*p*	-0.12	0.70	0.00	-0.94	0.00	0.24	0.00	0.00	— 3.26	1.12
aB-2c-O3	end	**a**B-2c-O3-*e*	-0.67	0.75	0.00	-0.91	0.01	0.24	0.07	-0.08	1.44	1.17

aB-O2	end	**a**B-O2-*e*	-0.78	0.73	0.02	-0.86	0.01	0.23	0.07	-0.10	1.42	1.18
	side	**a**B-O2-*s*	-1.19	0.76	0.05	-0.84	0.03	0.23	0.07	-0.15	1.52	1.27
a2B-O	end	**a**2B-O-*e*	-0.07	0.90	0.00	-1.23	0.00	0.17	0.01	-0.02	1.60	1.12
	bridge-end	**a**2B-O-*b*-*e*	0.30	0.90	0.00	-1.22	0.01	0.22	0.06	-0.12	1.62	1.21
	bridge-side	**a**2B-O-*b*-*s*	-0.71	0.91	0.01	-1.25	-0.02	0.25	0.09	-0.14	1.52	1.25
a2B-OH	physis	**a**2B-OH-*p*	-0.30	0.71	0.00	-1.00	0.00	0.14	0.00	0.00	— 3.51	1.12
	bridge-side	**a**2B-OH-*b*-*s*	-0.55	0.71	0.00	-1.02	-0.02	0.24	0.09	-0.18	1.49	1.29

Table S3. Calculated limiting potential (U_L) of PDS in NRR, adsorption energy of *H (E(*H)) and NRR intermediate *N_2H (E(*N_2H)), as well as U_L of HER.

Symbols	PDS	U_L	E(*N_2H)	E(*H)	U_L(HER)
sB-O	*NH_2 → *NH_3	-1.40	-4.92	-1.41	-1.28
sB-OH	*NH_2 → *NH_3	-1.47	-5.70	-1.42	-1.19
aB-O	*N_2 → *N_2H	-1.37	-1.57	0.07	-0.31
aB-O4	*NH_2 → *NH_3	-1.19	-3.58	-1.97	-1.61
aB-O3	(–H*) → *	-0.61	-2.64	-2.09	-1.75
aB-O2	(–H*)NH(H) → (–H*)NH_2(H)	-0.83	-3.76	-2.00	-1.67
a2B-O	*NH_2 → *NH_3	-0.80	-3.40	-0.36	-0.10
a2B-OH	*NH_2 → *NH_3	-0.66	-3.09	-0.78	-0.46

Figure S1. Calculated formation energy (E_f), adsorption energy (E_{ads}), and the sum of E_{ads} and cohesive energy ($E_{ads} + E_{coh}$), of **s**B@$Ti_3C_2O_{8/9}$ (**s**B-O); **s**B@$Ti_3C_2OH_{8/9}$ (**s**B-OH); **a**B@Ti_3C_2O(3C) (**a**B-O); **a**B@$Ti_3C_2O_{4/9}OH_{5/9}$(3C) (**a**B-3c-O4); **a**B@$Ti_3C_2O_{4/9}OH_{5/9}$(2C) (**a**B-2c-O4); **a**B@$Ti_3C_2O_{1/3}OH_{2/3}$(3C) (**a**B-3c-O3); **a**B@$Ti_3C_2O_{1/3}OH_{2/3}$(2C) (**a**B-2c-O3); **a**B@$Ti_3C_2O_{2/9}OH_{7/9}$(2C) (**a**B-O2); **a**2B@Ti_3C_2O (**a**2B-O) and **a**2B@$Ti_3C_2O_{4/9}OH_{5/9}$ (**a**2B-OH).

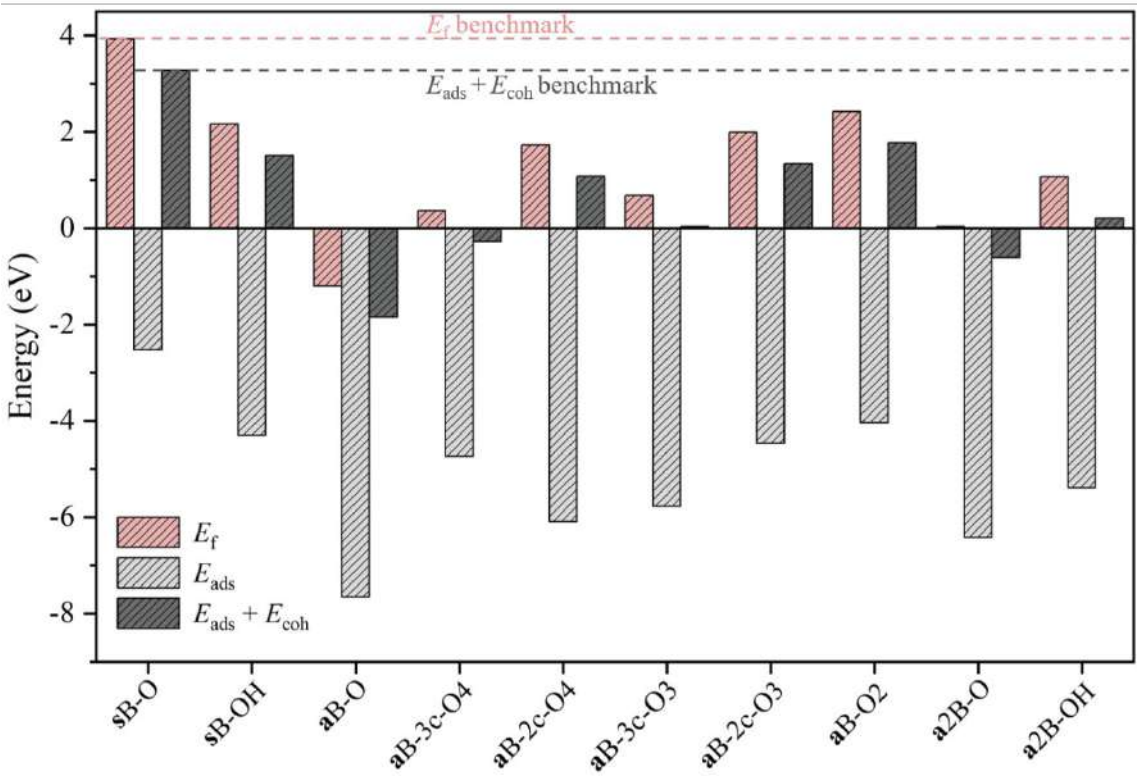

Figure S2. Bader charge of **s**B@$Ti_3C_2O_{8/9}$ (**s**B-O); **s**B@$Ti_3C_2OH_{8/9}$ (**s**B-OH); **a**B@Ti_3C_2O(3C) (**a**B-O); **a**B@$Ti_3C_2O_{4/9}OH_{5/9}$(3C) (**a**B-3c-O4); **a**B@$Ti_3C_2O_{1/3}OH_{2/3}$(3C) (**a**B-3c-O3); **a**B@$Ti_3C_2O_{2/9}OH_{7/9}$(2C) (**a**B-O2); **a**2B@Ti_3C_2O (**a**2B-O) and **a**2B@$Ti_3C_2O_{4/9}OH_{5/9}$ (**a**2B-OH).

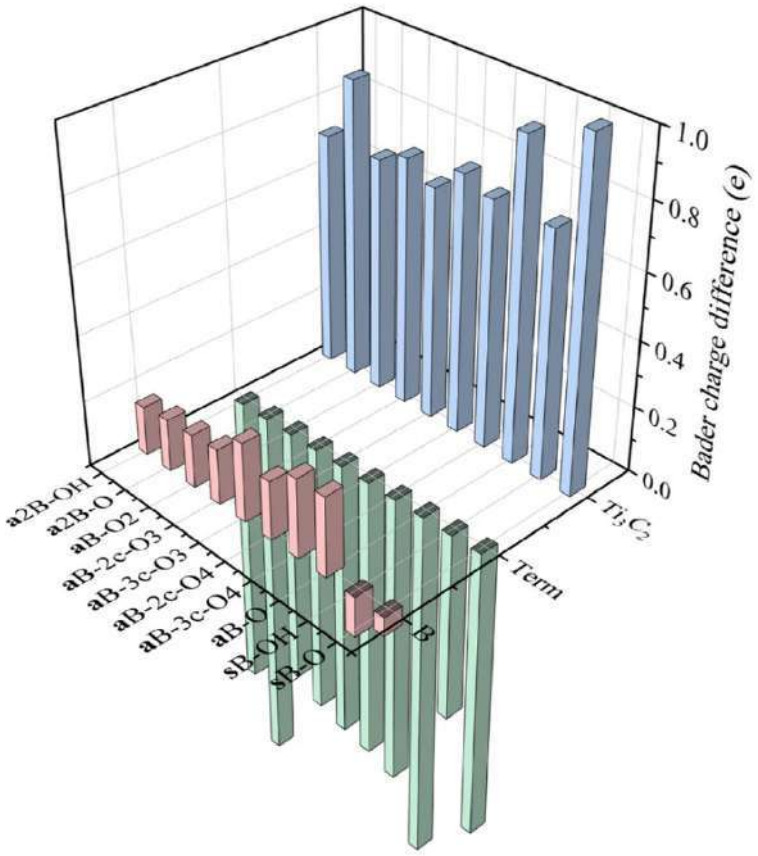

Figure S3. Top view of the charge density difference (CDD) plots of the studied models derived from Fig. 1 of the main text. Yellowish regions denote electron depletion, *i.e.* the formation of positively charged regions, while blueish regions denote electron accumulation, and the formation of negatively charged regions. The contour intervals range up to 0.01 e·Å^{-3}.

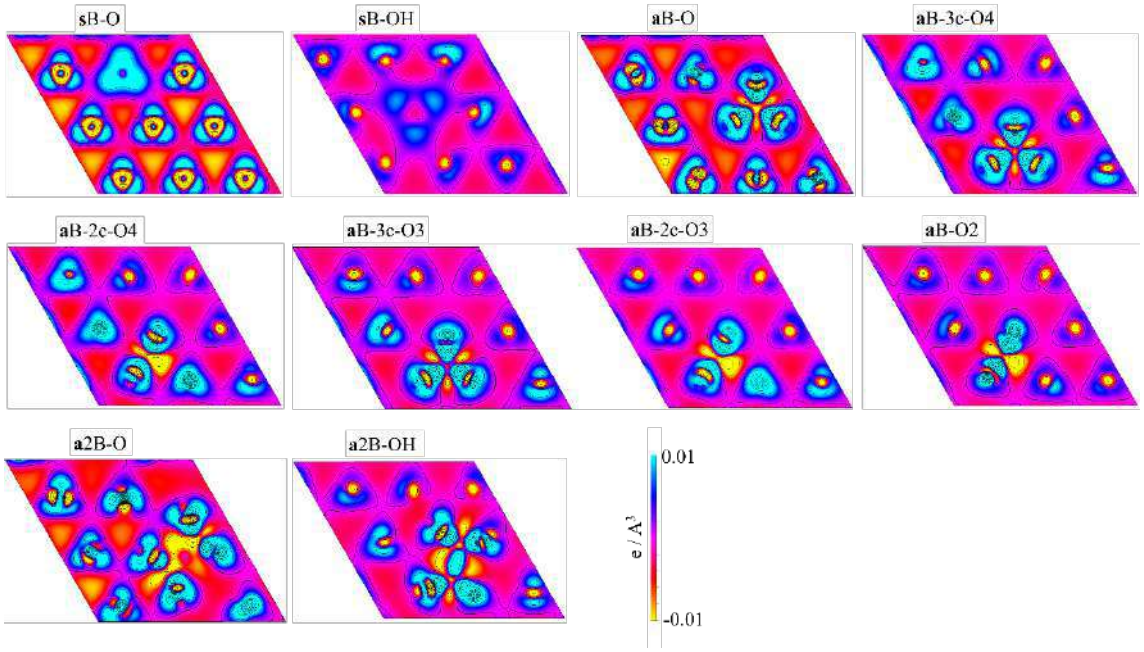

Figure S4. Total and projected density of states (PDOS) of the studied models derived from Fig. 1 of the main text. Energy levels are referred to the Fermi energy, E_F, set to zero.

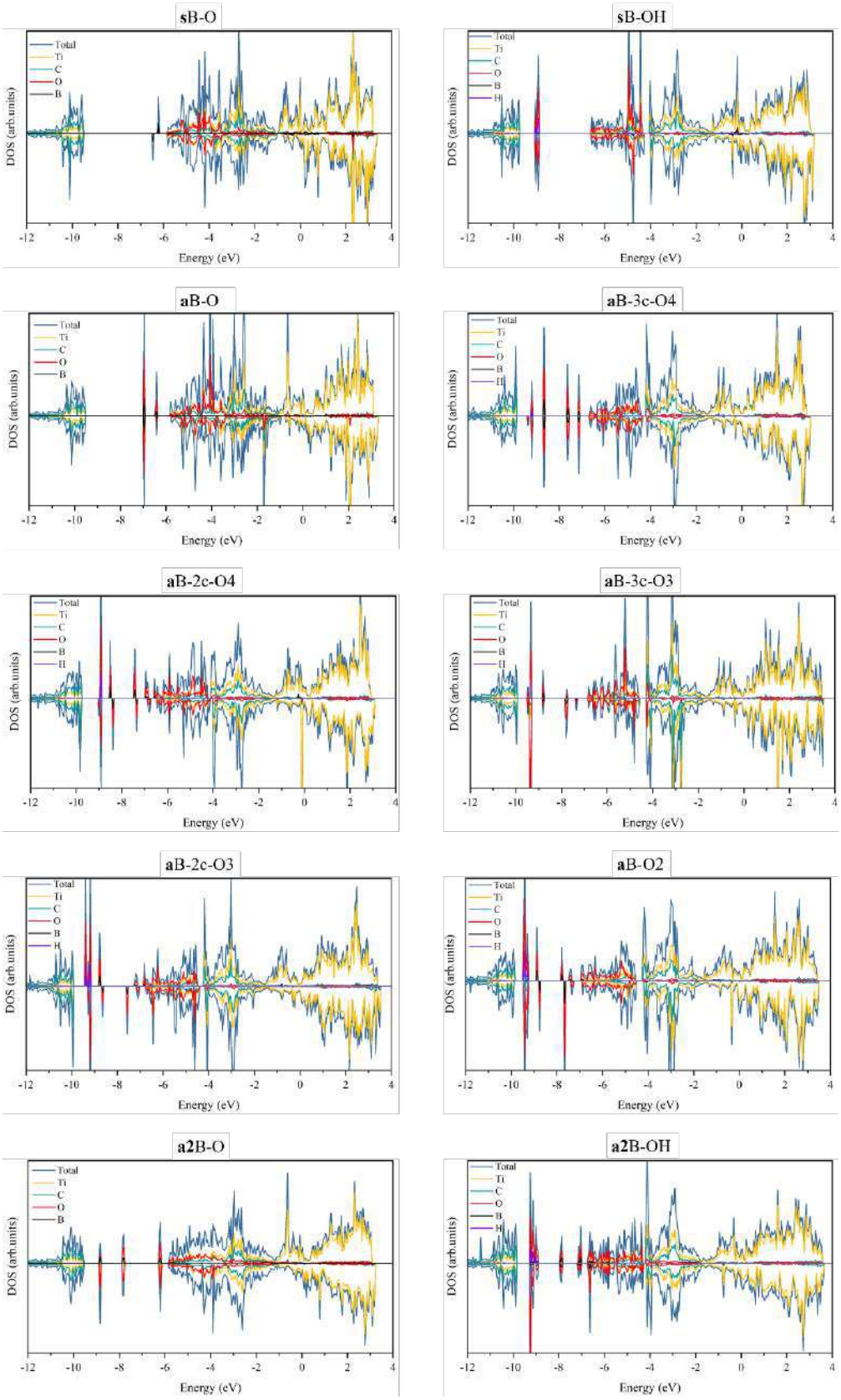

Figure S5. Optimized geometric structures of N_2 adsorbed on studied models shown in Fig. 1 of the main text. N_2 adsorption types in italics: *e* (end-on), *s* (side-on), *b-e* (bridge-end-on) and *b-s* (bridge-side-on) for chemisorption, and *p* for physisorption.

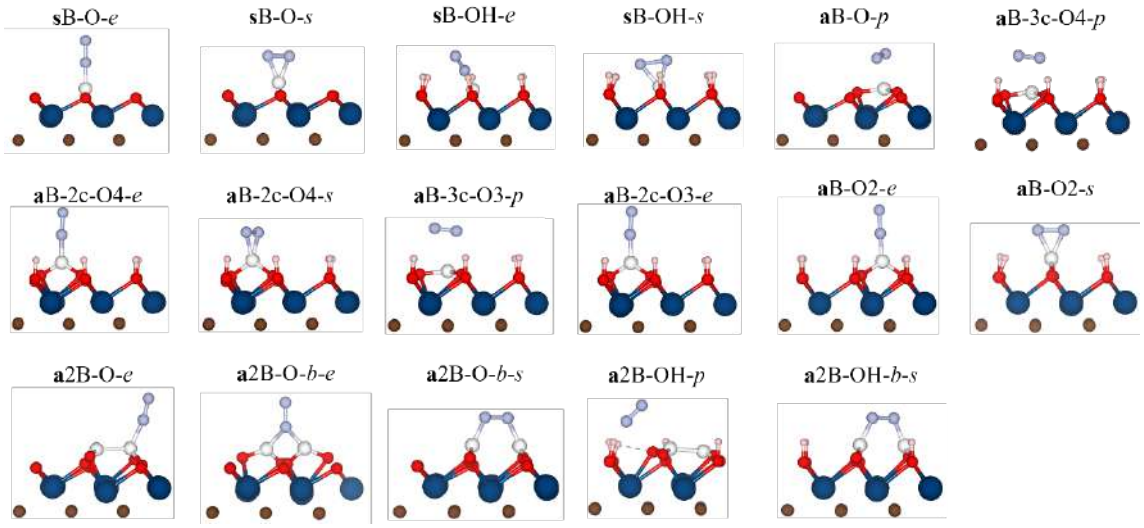

Figure S6. Bader charge of studied models shown in Fig. S5 of SI.

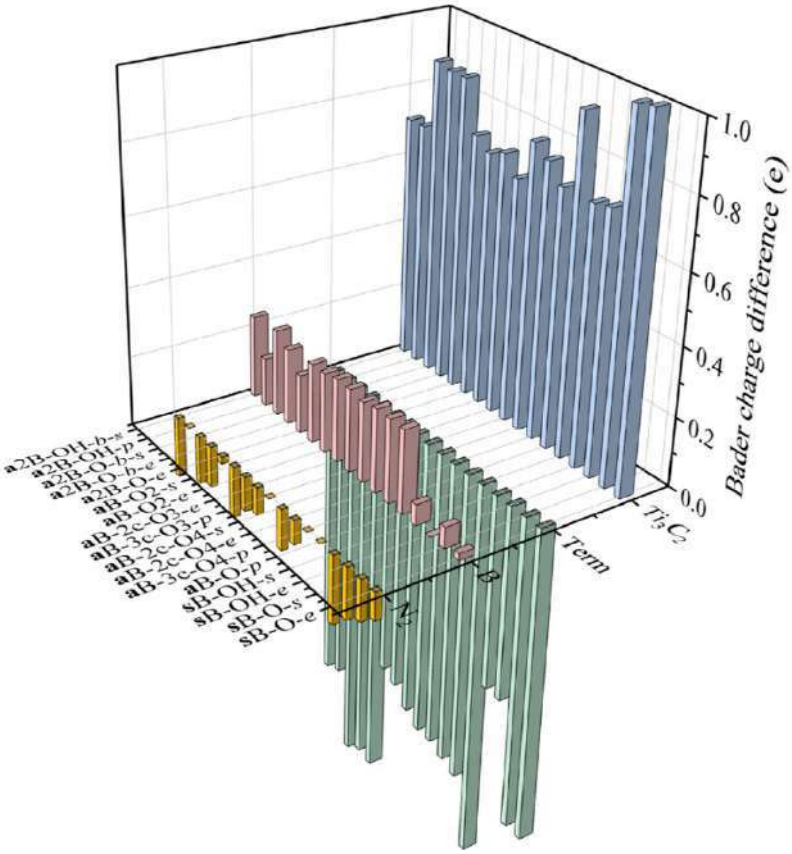

Figure S7. Total and projected density of states (PDOS) of the studied models shown in Fig. S5 of SI. Energy levels are referred to the Fermi energy, E_F, set to zero.

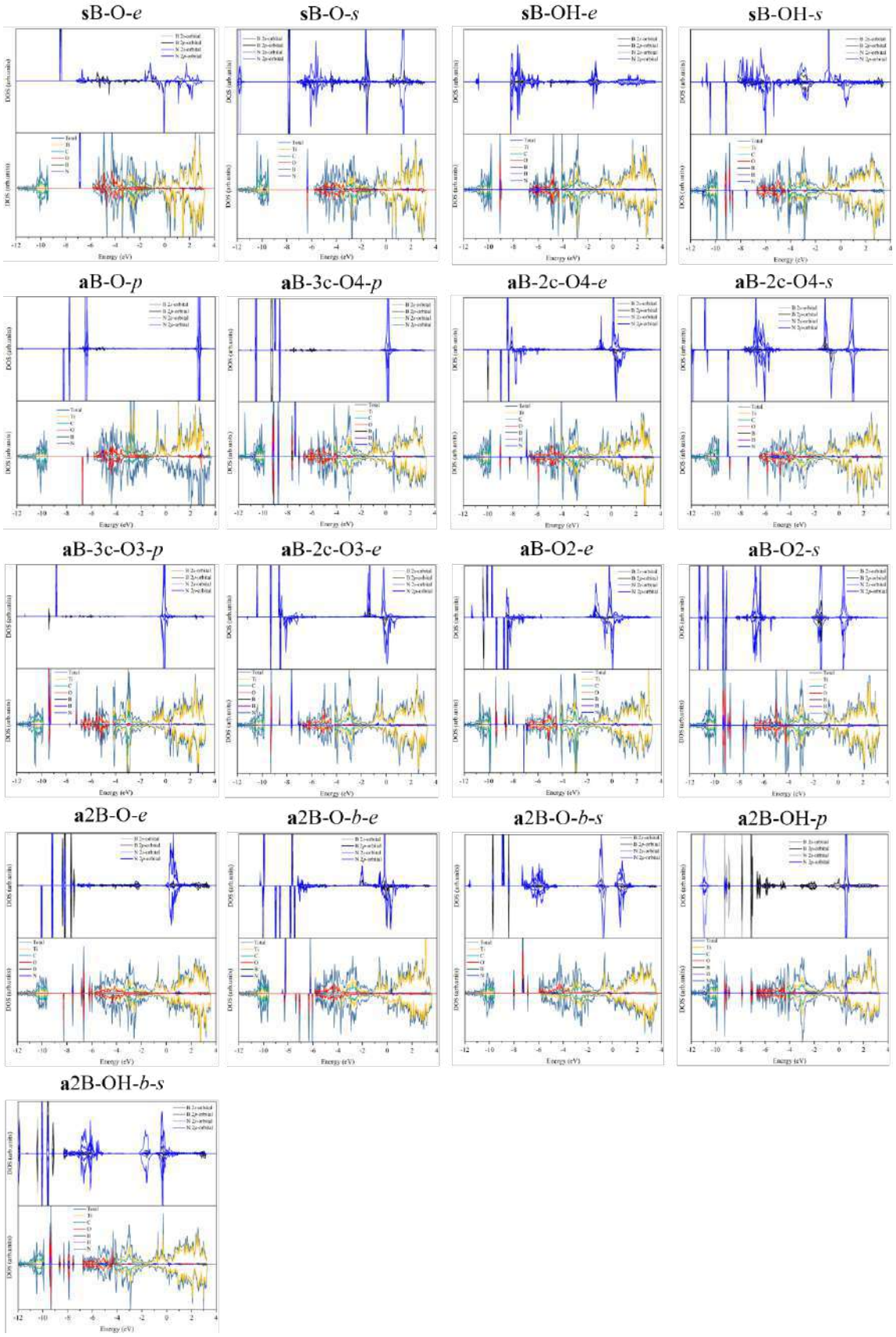

Figure S8. The charge density difference (CDD) plots of the studied models shown in Fig. S5 of SI. Yellowish regions denote electron depletion, *i.e.* the formation of positively charged regions, while blueish regions denote electron accumulation, and the formation of negatively charged regions.

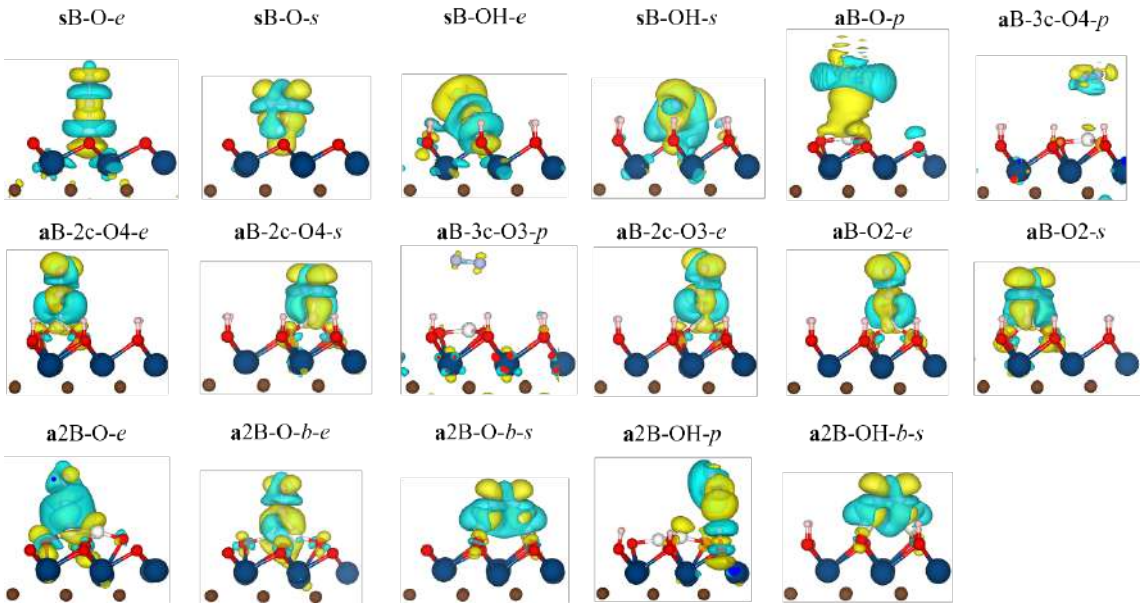

Figure S9. Volcano diagram for NRR using the adsorption energy of N_2 subtract by that on Ru(0001) as the benchmark (-4.0 eV) and the ΔG_{max} as descriptors.

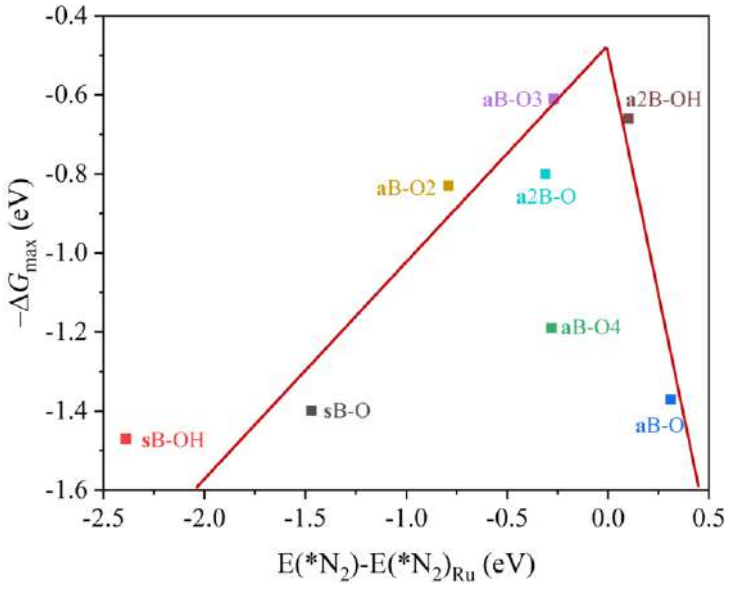

Figure S10. Pourbaix diagrams for Ti_3C_2 MXene (0001) surface regarding single and binary surface compositions including –O, –OH, and –H terminations. The black, dashed line indicates the HER equilibrium potential with respect RHE reference.

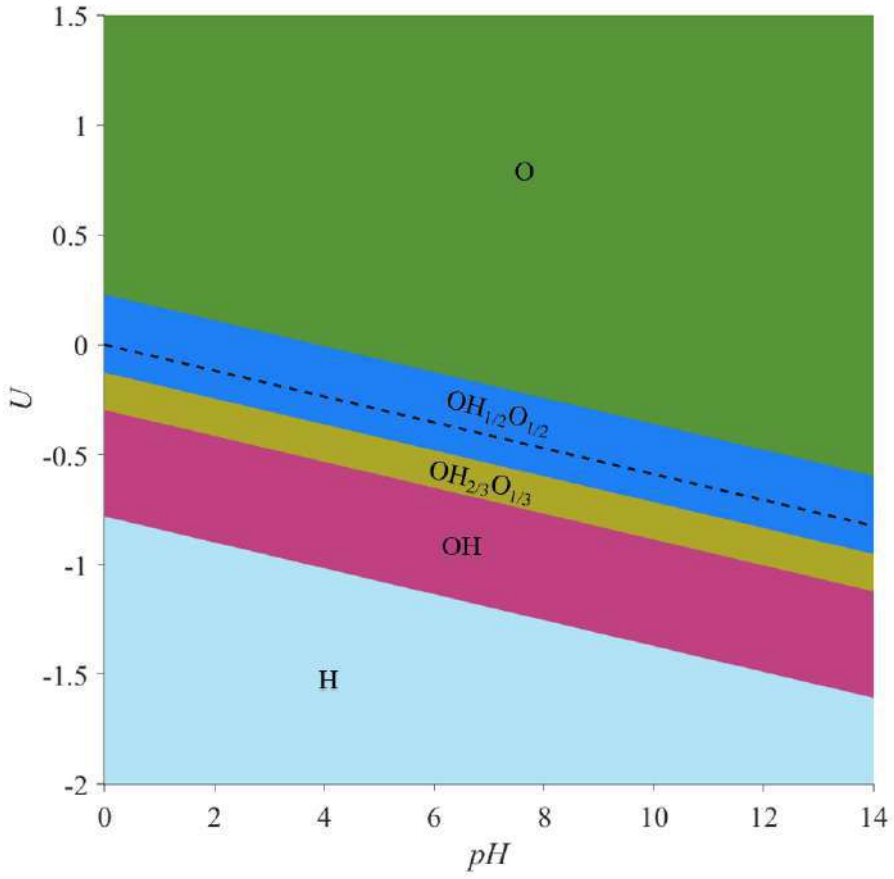

Appendix D

Supporting Information for "Contrasting Metallic (Rh^0) and Carbidic (2D-Mo_2C MXene) Surfaces in Olefin Hydrogenation Provides Insights on the Origin of the Pairwise Hydrogen Addition."

Contrasting Metallic (Rh^0) and Carbidic (2D-Mo_2C MXene) Surfaces in Olefin Hydrogenation Provides Insights on the Origin of the Pairwise Hydrogen Addition

Ling Meng,[1] Ekaterina V. Pokochueva,[2,+] Zixuan Chen,[3] Alexey Fedorov,[3,*] Francesc Viñes,[1,*] Francesc Illas,[1] Igor V. Koptyug[3]

[1]*Departament de Ciència de Materials i Química Física & Institut de Química Teòrica i Computacional (IQTCUB), Universitat de Barcelona, c/ Martí i Franquès 1-11, 08028 Barcelona, Spain.*

[2]*International Tomography Center SB RAS, 3A Institutskaya St., Novosibirsk, 630090, Russian Federation.*

[3]*Department of Mechanical and Process Engineering, ETH Zürich, Leonhardstrasse 21, Zürich, 8092, Switzerland.*

[+]*Current address: Université Claude Bernard Lyon 1, CRMN UMR-5082, CNRS, ENS Lyon, Villeurbanne 69100 France.*

*Corresponding authors: Alexey Fedorov (fedoroal@ethz.ch), Francesc Viñes (francesc.vines@ub.edu)

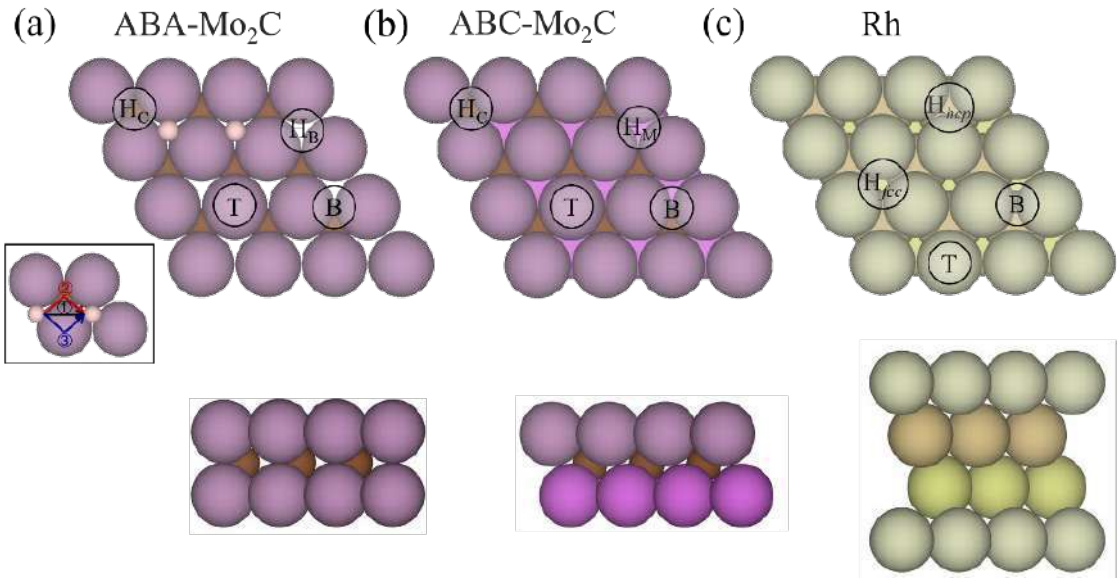

Figure S1. Top (upper images) and side (lower images) views of *p*(4×4) MXene-derived 2D-Mo_2C (0001) surface with (a) ABA stacking and (b) ABC stacking, as well as (c) Rh (111) surface. High symmetry sites are specified, including top (T) and bridge (B) sites for all surface models, hollow carbon (H_C), hollow blank (H_B), and hollow metal (H_M) for ABA- and ABC-stacked 2D-Mo_2C (0001), and hexagonal close-packed hollow (H_{hcp}) and face-centred cubic hollow (H_{fcc}) on Rh (111). C and H atoms are represented by brown and white spheres, respectively, while Mo and Rh atoms are shown as pinkish and greenish spheres, with different levels of shading depending on their stacking position. The red, black and blue lines represent the three modes of H adatom diffusion explored departing from any competitive hollow site minimum.

Section S1: Gibbs Free Energies of Adsorption

The reaction species Gibbs free energies of adsorption, ΔG^{ad}, as a function of the working temperature, T, and the species partial pressure, p, are approximated as:

$$\Delta G^{ad}(T,\ p) \approx\ [E^{total}(N_i, N_M) +\ E^{ZPE}_{(N_i,N_M)}] - E^{total}(0, N_M) - N_i[E_i^{total}\ +\ E_i^{ZPE}]\ - N_i \Delta\mu_i(T,p) \quad \text{(S1)},$$

where N_i denotes the count of adsorbed species, normally one in the studied system, while E_i^{total}, $E^{ZPE}_{(N_i,N_M)}$ and E_i^{ZPE} represent the total energy, and the zero point energy (ZPE) contributions of the adsorbed species, and that species in vacuum, respectively. N_M, for instance, would be the number of metal atoms, *e.g.* in the Rh (111) slab model, while for the Mo_2C models, this would be the number of each of substrate atom types. Since the number of substrate atoms is invariant in our study, $E^{total}(N_i, N_M) = E_{i/sub}$, and $E^{total}(0, N_M) = E_{sub}$, where E_{sub} and $E_{i/\text{sub}}$ are the total energies of the pristine surface model and of the surface model with the i^{th} species adsorbed upon, respectively. Aside, $\Delta\mu_i(T,p)$ is the chemical potential change of the adsorbed species with respect to the gas phase, where details on how to estimate it are provided below. E_i^{ZPE} can be obtained from vibrational frequencies, *viz.*:

$$E_i^{ZPE} = \frac{1}{2}\sum_{n=1}^{NMV} h\nu_n \quad \text{(S2)},$$

where h is the Planck's constant, and ν_n is the vibrational frequency for each normal mode n of vibration (NMV), *i.e.*, $3N-5$ for linear molecules in vacuum, $3N-6$ for non-linear molecules in vacuum, and $3N$ for adsorbed atoms/molecules, where N is the number of atoms (taking into account the loss of free translations and rotations that are effectively converted into vibrations upon adsorption). For C_2H_4, C_2H_6, and H_2 molecules, the gas reference is well-defined. For radical species such as C_2H_5 and H adatoms it is convenient to express its chemical potential as a combination of gas phase species, *i.e.*, $\mu_H(T,p) = 1/2\ \mu_{H_2}(T,p)$, and $\mu_{C_2H_5}(T,p) = \mu_{C_2H_4}(T,p) + 1/2\ \mu_{H_2}(T,p)$. Consequently, one can use *ab initio* thermodynamics (AIT) to express the chemical potential variations $\Delta\mu_i(T,p)$ as a product containing kinetic, rotational, vibrational, and electronic contributions according to:

$$\Delta\mu_i(T,p) = -k_BT\left\{ln\left[\left(\frac{2\pi m_i}{h^2}\right)^{3/2}\frac{(k_BT)^{5/2}}{p_i}\right] + ln\left(\frac{k_BT}{\sigma_i^{sym}B_{0,i}}\right) - \sum_{n=1}^{NMV} ln\left[1-exp\left(\frac{-\hbar\nu_{n,i}}{k_BT}\right)\right] + ln\left(I_i^{spin}\right)\right\} \quad \text{(S3)},$$

where k_B is the Boltzmann's constant, m_i the mass of the i^{th} molecule, p_i denotes the partial pressure of the i^{th} species, σ_i^{sym} is the symmetry number of i^{th} molecule —2 for H_2, 4 for C_2H_4, and 6 for C_2H_6,[1] $B_{0,i}$ is the rotational constant, computed as $B_{0,i} = \frac{\hbar^2}{2I_i}$, where I_i corresponds to the moment of inertia of the molecule, given by $I_i = \sum_a m_a {r_a}^2$, where m_a is the mass of the atoms composing the i^{th} molecule and r_a refers to the distance of the a atom centre to the molecular centre of mass. Moreover, each of the vibrational normal modes of the i^{th} molecule is assigned by $\nu_{n,i}$, while I_i^{spin} is the electronic spin degeneracy of the ground state. Since all the molecules considered here feature a singlet ground state, this term was neglected in the present study.

Section S2: Estimations of Rates

The non-activated adsorption rate of a species (r_{ads}) can be gained using collision theory,[2] as;

$$r_{ads} = \frac{S_0 \cdot p_i \cdot A}{\sqrt{2\pi \cdot m_i \cdot k_B \cdot T}} \quad \text{(S4)},$$

where S_0 is the initial sticking coefficient, p_i the partial pressure of H_2, C_2H_4, or C_2H_6 in the gas phase, and A represents the surface area of an adsorption site, estimated by dividing the surface supercell area, see Figure S1, by the number of possible adsorption sites.

The desorption rate, r_{des}, is estimated from the transition state theory (TST) and assuming that the desorbed TS is a late two-dimensional (2D) transition state,[3] where the energy barrier is the desorption energy, ΔE^i_{des}, which is simply a negative of the adsorption energy, ΔE^i_{ads}, see main text. Thus, *viz.*:

$$r_{des} = v_{des} \cdot exp\left(\frac{\Delta E^i_{\text{ads}}}{k_B \cdot T}\right);\ v_{des} = \frac{k_B \cdot T}{h} \frac{q^{gas}_{trans,2D} \cdot q^{gas}_{rot} \cdot q^{gas}_{vib}}{q^{ads}_{vib}} \quad \text{(S5)},$$

where ΔE^i_{ads} is, here, non-ZPE corrected. Note that in such rates definitions, ZPE is accounted for in the vibrational partition function. Indeed, the pre-factor v_{des} is given by various partition functions, q, including those in Equations (10-12).

$$q^{gas}_{trans,2D} = A \cdot \frac{2\pi \cdot m \cdot k_B \cdot T}{h^2} \quad \text{(S6)},$$

$$q^{ads/gas}_{vib} = \prod_n \frac{exp\left(-\frac{h \cdot \nu_n}{2 \cdot k_B \cdot T}\right)}{1 - exp\left(-\frac{h \cdot \nu_n}{k_B \cdot T}\right)} \quad \text{(S7)},$$

$$q^{gas}_{rot} = \frac{T}{\sigma^{sym} \cdot T_{rot}} \quad \text{(S8)}.$$

The $q^{gas}_{trans,2D}$, q^{gas}_{rot}, and q^{gas}_{vib} refer to the gas phase translational partition function including just 2D degrees of freedom (as the third dimension is the reaction coordinate for desorption), the rotational partition function, and the vibrational partition function, respectively, computed in a large box. The q^{ads}_{vib} is the vibrational partition function of the adsorbed molecule where six degrees of freedom correspond to frustrated rotations and translations, *vide supra*. Finally, for the rotational partition functions, see Eq. (S8), T_{rot} is the rotational temperature of the adsorbed species.

For the reactive and diffusive steps, the corresponding rates, r_j, have been obtained as well by TST,[4] defined as:

$$r_j = v \cdot exp\left(-\frac{\Delta E_{TS}}{k_B \cdot T}\right);\ v = \frac{k_B \cdot T}{h}\frac{q_{vib}^{TS}}{q_{vib}^{IS}} \quad \text{(S9)},$$

where ΔE_{TS} represents the non-ZPE corrected energy barrier, the pre-factor for v can be determined by the partition function, which refers to the vibrational partition functions in the initial state (IS) or the transition state (TS) on the surface; $q_{vib}^{TS/IS}$ denotes the vibrational partition given by:

$$q_{vib}^{TS/IS} = \prod_n \frac{exp\left(-\frac{h \cdot v_n}{2 \cdot k_B \cdot T}\right)}{1 - exp\left(-\frac{h \cdot v_n}{k_B \cdot T}\right)} \quad \text{(S10)}.$$

Section S3: The Span Model

The energy span model has been widely used to assess activity beyond traditional methods, which consider all individual transition states.[5,6] Within the span model, the rate-determining transition state (RDTS) is identified as the transition state with the highest energy, which influences the reaction rate significantly. The rate-determining intermediate (RDI), i.e., the one with the lowest energy, is used to seize the energy span.[7] The span energy barrier, E_b^{span}, captures the energetic requirement of the reaction, defined as:

$$E_b^{span} = E_{highest}^{RDTS} - E_{lowest}^{RDI} \quad \text{(S11)}.$$

Further details on the applicability of the span model are found in the literature.[41,8]

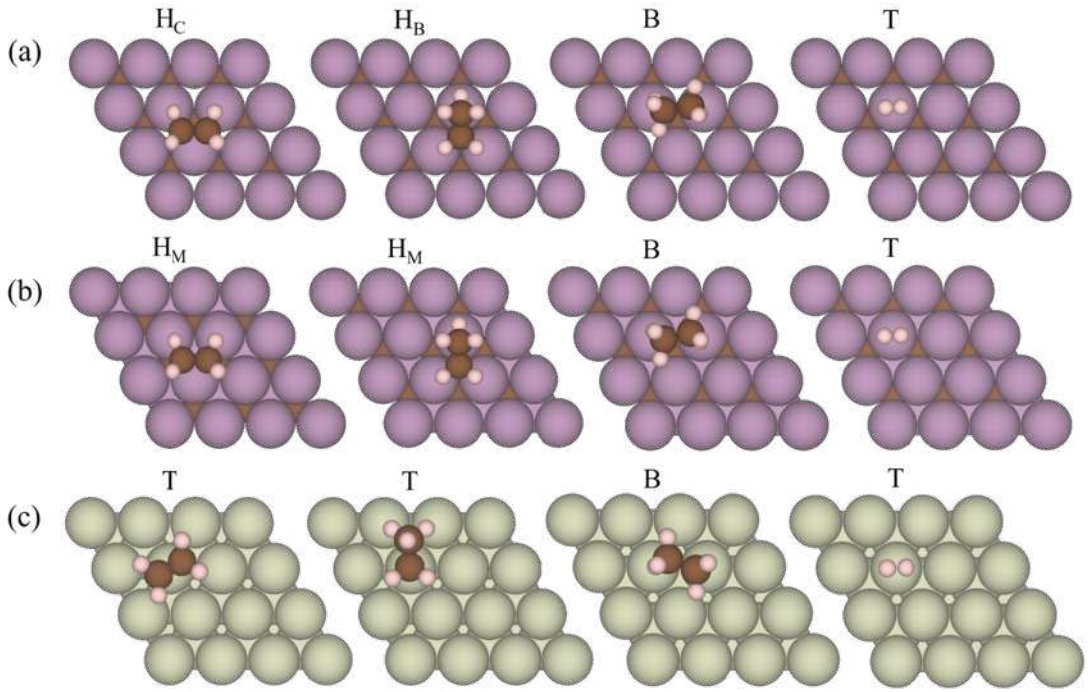

Figure S2. Top views of the lowest-energy high-symmetry surface sites of $C_2H_4^*$, $C_2H_5^*$, $C_2H_6^*$, and H_2^* species on (a) ABA-Mo_2C (0001), (b) ABC-Mo_2C (0001), and (c) Rh (111). Notations above the calculated structures denote the most stable adsorption site, being top (T), bridge (B), or hollow sites with a C underneath (H_C) or a metal (H_M), or being a mixed bridge sites (H_B).

Table S1. Adsorption Gibbs free energies of H_2, C_2H_4, and C_2H_6 on ABA and ABC-Mo_2C (0001) surfaces, and on Rh (111) surfaces, at the experimental reaction conditions of 1 bar gas partial pressure, p, and a temperature, T, of 250 °C for Mo_2C MXenes, and 60 °C for Rh. All values are given in eV.

$\Delta G^{ad}(T, p)$	H_2	C_2H_4	C_2H_6
ABA-Mo_2C	−1.02	−1.07	0.32
ABC-Mo_2C	−1.25	−1.47	0.31
Rh	−0.51	−0.68	0.28

Table S2. Adsorption energies of two H adatoms on ABA- and ABC-Mo_2C and Rh surfaces on different sites as specified in Figure S4. All values are given in eV, and do not include the ZPE term. The bold font represents the lowest energy case.

	1	2	3	4	5	6	7
ABA-Mo_2C	−1.73	**−1.75**	−1.72	—	—	—	—
ABC-Mo_2C	−1.93	**−1.97**	−1.95	—	—	—	—
Rh	**−1.19**	−1.19	−1.18	−0.95	**−1.16**	−1.17	−1.16

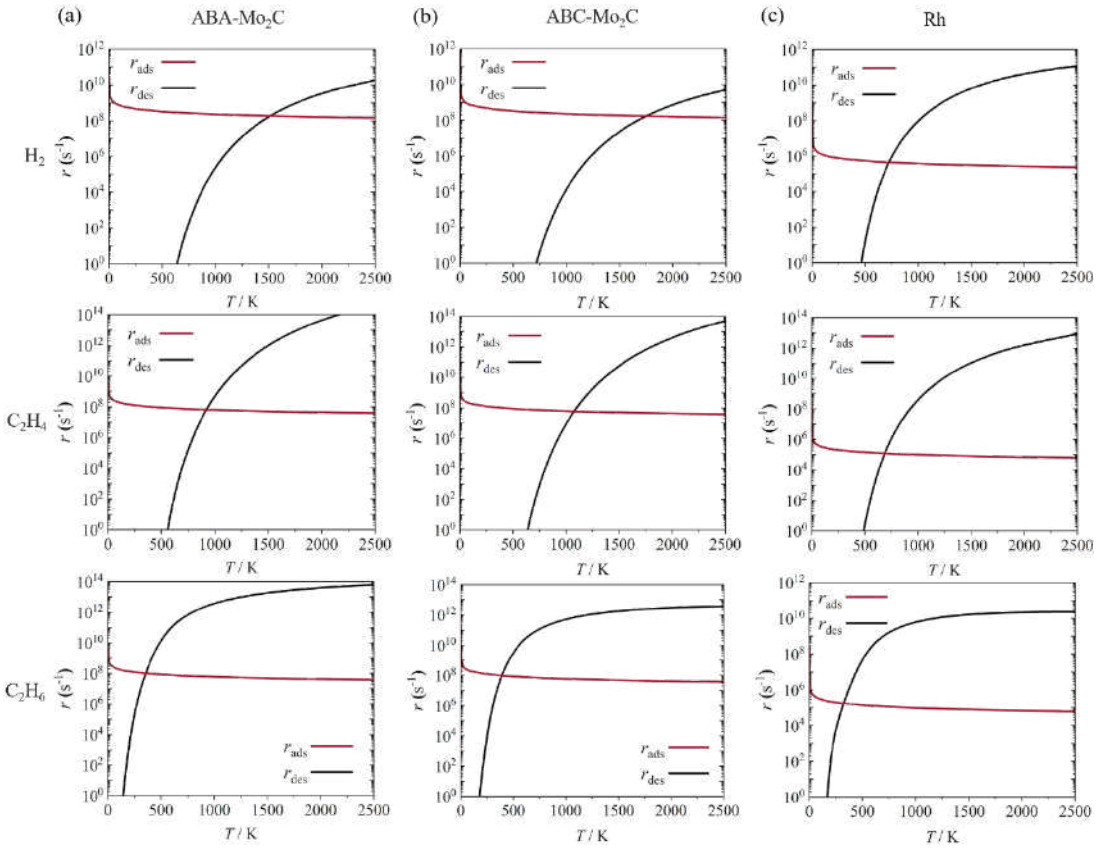

Figure S3. Calculated rates of adsorption, r_{ads}, and desorption, r_{des}, of H_2, C_2H_4, and C_2H_6 on (a) ABA-Mo_2C, (b) ABC-Mo_2C, and (c) Rh (111) models as a function of temperature, *T,* at the total gas pressure of 1 bar.

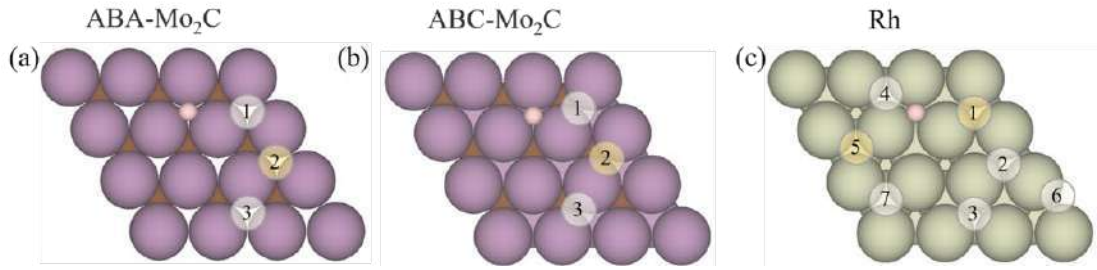

Figure S4. The lowest-energy high-symmetry surface sites of two vicinal H adatoms on (a) ABA-Mo_2C and (b) ABC-Mo_2C (0001) surfaces, and (c) Rh (111) surface. Numbered circles represent the potential high-symmetry positions for the second H adatom, while orange circles represent the final most stable positions.

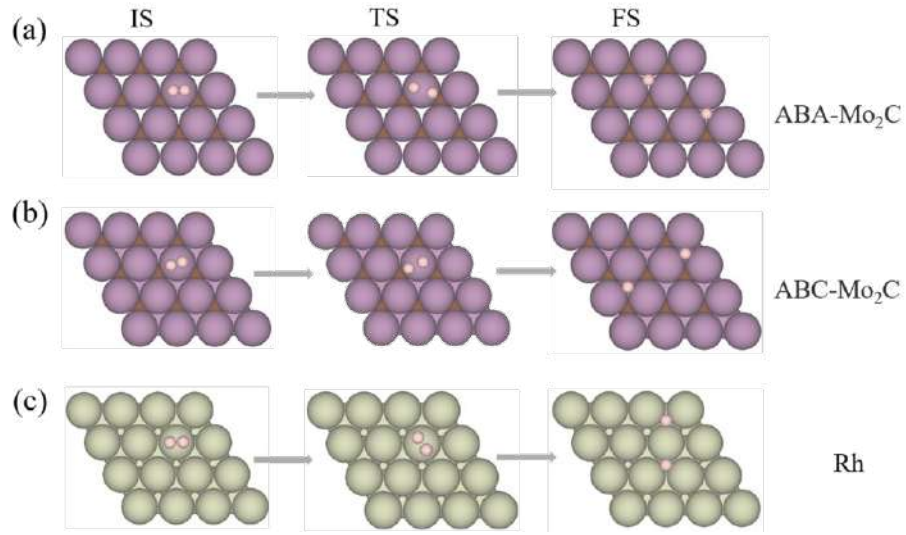

Figure S5. Top view of the H_2 dissociation on (a) ABA-Mo_2C, (b) ABC-Mo_2C, and (c) Rh (111) pristine surfaces, including initial states (ISs), transition states (TSs), and final states (FSs).

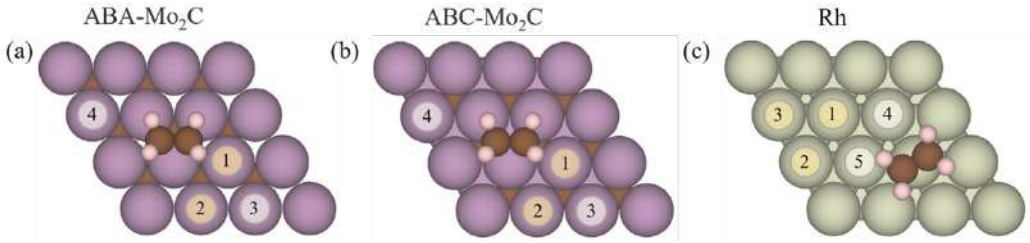

Figure S6. The lowest-energy co-adsorption sites of H_2 nearby of the adsorbed C_2H_4* on (a) ABA-Mo_2C, (b) ABC-Mo_2C, and (c) Rh (111) surfaces. Numbered circles represent potential high-symmetry positions for the co-adsorption of H_2, while orange circles represent the final most stable positions.

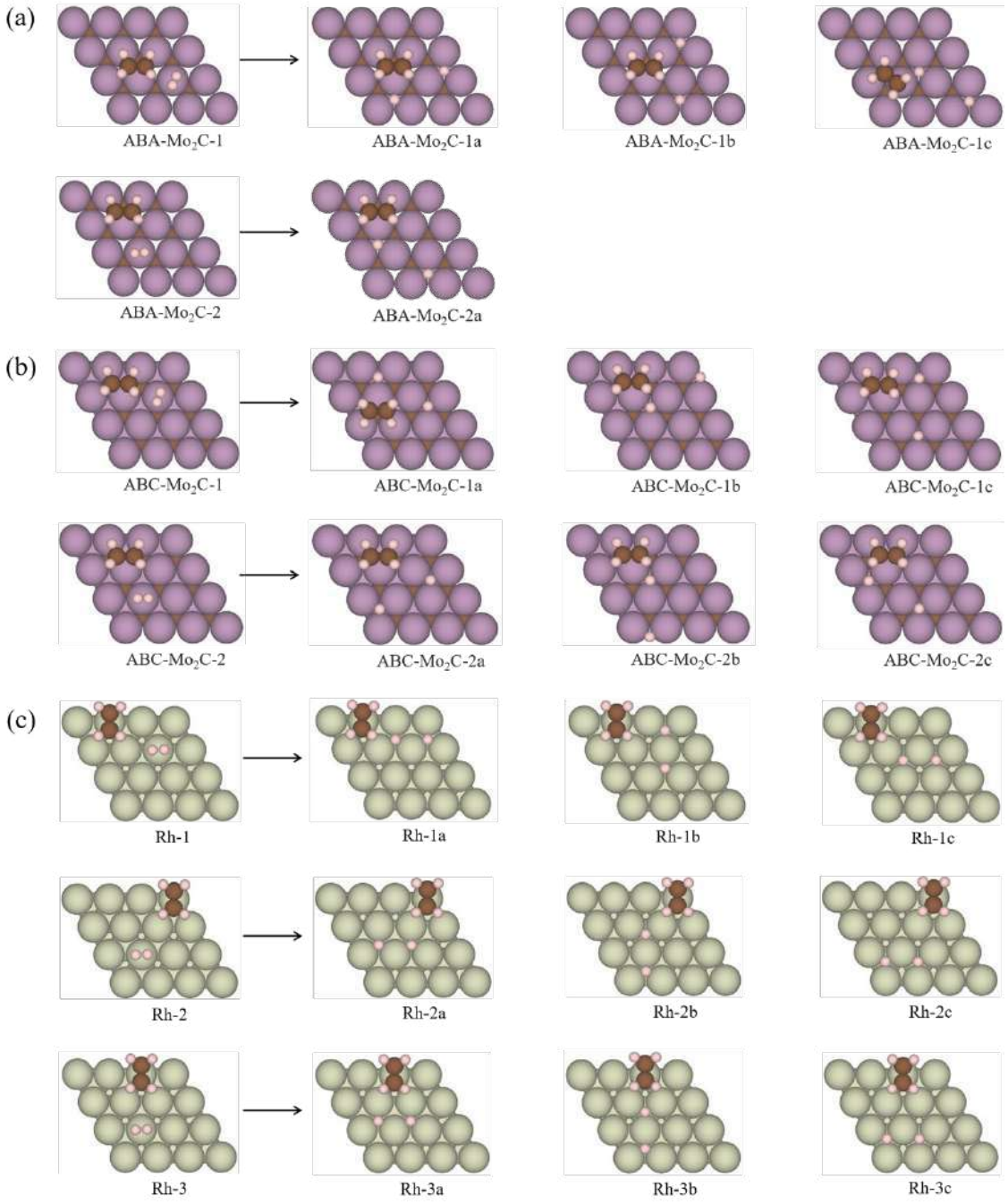

Figure S7. The main high-symmetry surface sites for the H_2 adsorption and two vicinal H* adatoms produced as a result of the H_2 dissociation on (a) ABA-Mo_2C-1 and ABA-Mo_2C-2, (b) ABC-Mo_2C-1 and ABC-Mo_2C-2, and (c) Rh-1, Rh-2, and Rh-3 surfaces in the presence of C_2H_4. For details on the notations used, see Figure S6.

Table S3. H_2 adsorption energies on ABA-Mo_2C, ABC-Mo_2C, and Rh surface models with different relative sites with respect to a pre-adsorbed C_2H_4 as specified in Figure S6. All values are given in eV. The bold font represents the ones selected to study H_2 dissociation forward.

	1	2	3	4	5
Mo_2C_{ABA}	**−0.42**	**−0.55**	−0.51	−0.55	—
Mo_2C_{ABC}	**−0.67**	**−0.77**	−0.72	−0.76	—
Rh	**−0.52**	**−0.53**	**−0.53**	—	—

Table S4. Total adsorption energies of two H adatoms on ABA-Mo_2C (0001) surface on different sites with respect to pre-adsorbed C_2H_4 as specified in Figure S7a. All values are given in eV. The bold font represents the one selected on the study.

	a	b	c
ABA-Mo_2C-1	**−1.67**	**−1.66**	−1.54
ABA-Mo_2C-2	**−1.64**	—	—

Table S5. Total adsorption energies of two H adatoms on ABC-Mo_2C (0001) surface on different sites with respect to pre-adsorbed C_2H_4 as specified in Figure S7b. All values are given in eV. The bold font represents the one selected on the study.

	a	b	c
ABC-Mo_2C-1	−1.84	−1.61	**−1.77**
ABC-Mo_2C-2	**−1.91**	−1.59	−1.61

Table S6. Total adsorption energies of two H adatoms on Rh (111) surface on different sites with respect to pre-adsorbed C_2H_4 as specified in Figure S7c. All values are given in eV. The bold font represents the one selected on the study.

	a	b	c
Rh-1	**−1.11**	**−1.11**	−1.09
Rh-2	**−1.13**	**−1.11**	−1.08
Rh-3	**−1.13**	−1.07	−1.08

Table S7. The energy barriers, E_b, for H_2 dissociation on ABA- and ABC-Mo_2C (0001) surface models, and on Rh (111) surface, according to the ISs and FSs depicted in Figures S7 and S8. All values are given in eV. The bold font represents the H_2 dissociating path with the lowest E_b.

	a	b	c
ABA-Mo_2C-1	0.20	**0.19**	—
ABA-Mo_2C-2	—	0.25	—
ABC-Mo_2C-1	—	—	**0.09**
ABC-Mo_2C-2	0.10	—	—
Rh-1	0.01	0.01	—
Rh-2	0.01	**0.01**	—
Rh-3	0.01	—	—

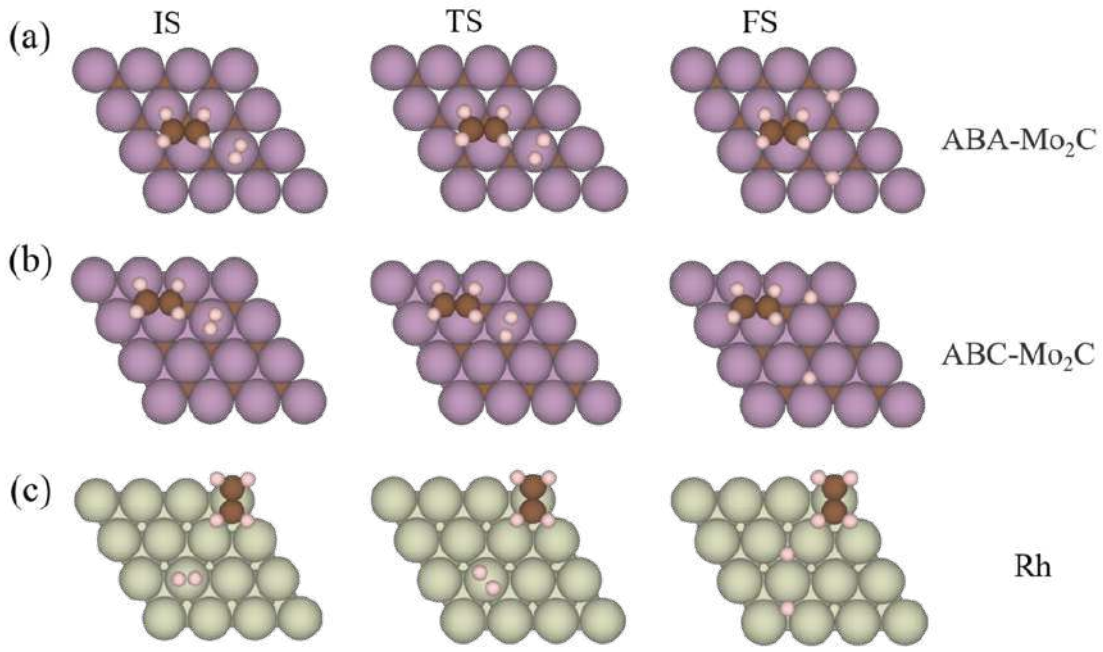

Figure S8. Top views of the different stages of H_2 dissociation on (a) ABA-Mo_2C, (b) ABC-Mo_2C, and (c) Rh (111) surfaces in the presence of C_2H_4*, including initial states (ISs), transition states (TSs), and final states (FSs) with the lowest energy barriers (E_b, see Table S7).

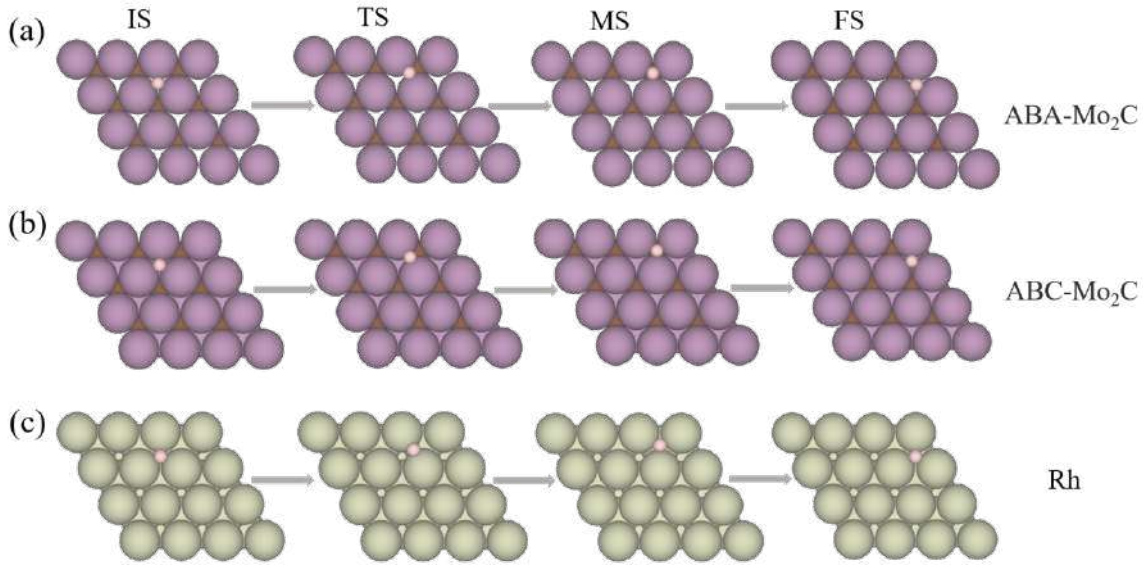

Figure S9. Top views of the different stages of H* diffusion on (a) ABA-Mo_2C, (b) ABC-Mo_2C, and (c) Rh (111) pristine surfaces, including the initial states (ISs), transition states (TSs), middle states (MSs), and final states (FSs).

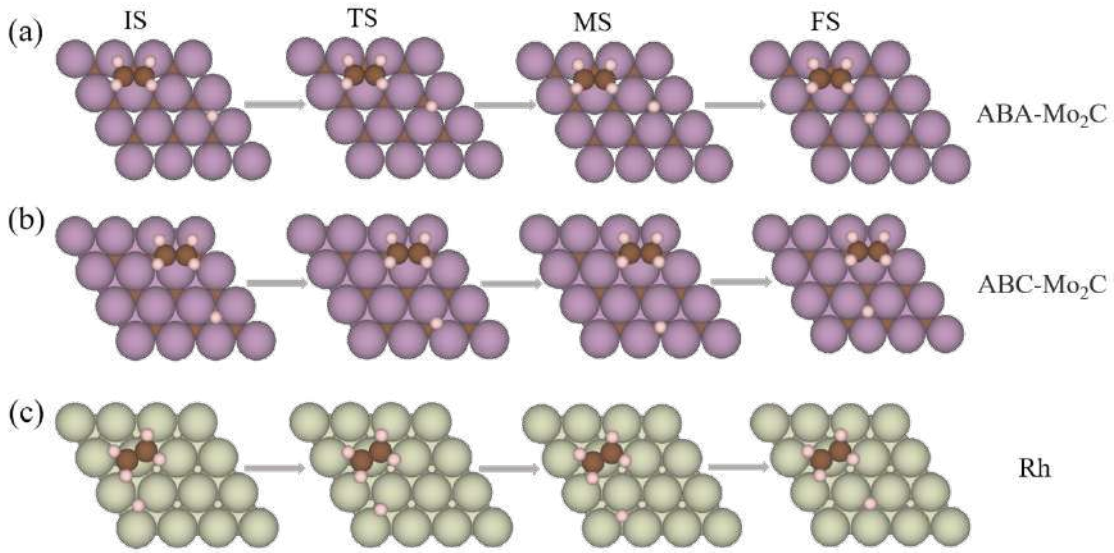

Figure S10. Top views of the different stages of H* diffusion on (a) ABA-Mo_2C, (b) ABC-Mo_2C, and (c) Rh (111) surfaces in the presence of C_2H_4*, including initial states (ISs), transition states (TSs), middle states (MSs), and final states (FSs).

Table S8. Energy barriers, E_b, for H diffusion and H_2 dissociation on ABA-Mo_2C, ABC-Mo_2C, and Rh surfaces, when pristine or in the presence C_2H_4, plus the H_2 adsorption energies. All values are given in eV.

	Pristine			With C_2H_4		
	$E_b^{H\ diff}$	$E_b^{H_2\ diss}$	$E_{ads}^{H_2}$	$E_b^{H\ diff}$	$E_b^{H_2\ diss}$	$E_{ads}^{H_2}$
ABA-Mo_2C	0.35	0.28	−0.53	0.37	0.19	−0.55
ABC-Mo_2C	0.27	0.11	−0.72	0.28	0.09	−0.77
Rh	0.16	0.06	−0.61	0.10	0.01	−0.53

Table S9. Reaction energies, ΔE, and energy barriers, E_b, of the first and second hydrogenation reaction steps on C_2H_4, as well as the full ΔE and the energy barrier according to the span model, E_b^{span}, on the ABA- and ABC-Mo_2C surface models depicted in Figure 3 of the main text, and on Rh (111). All values are given in eV.

	ΔE_H^{1st}	$E_b^{H-1^{st}}$	ΔE_H^{2nd}	$E_b^{H-2^{nd}}$	ΔE_{full}	E_b^{span}
ABA-Mo_2C-1b@1	0.28	0.73	0.92	2.03	1.20	2.30
ABA-Mo_2C-1b@2	0.33	0.79	0.87	1.90	1.20	2.22
ABA-Mo_2C-1b@3	**0.29**	**0.74**	**0.91**	**1.77**	**1.20**	**2.06**
ABA-Mo_2C-1b@4	0.34	0.84	0.86	2.07	1.20	2.40
ABC-Mo_2C-1c@1	0.38	0.64	1.32	1.98	1.70	2.36
ABC-Mo_2C-1c@2	**0.57**	**0.81**	**1.13**	**1.83**	**1.70**	**2.40**
ABC-Mo_2C-1c@3	0.50	0.78	1.31	2.11	1.70	2.51
Rh_2b	**0.39**	**0.91**	**-0.11**	**0.55**	**0.27**	**0.94**

Table S10. Reaction energies, ΔE, and energy barriers, E_b, of the first and second hydrogenation reaction steps on C_2H_4, as well as the full ΔE^{span} and the energy barrier according to the span model, E_b^{span}, on the ABA- and ABC-Mo_2C surface models, and on Rh (111) surface, either on their pristine models, or having ¾ ML of H or C_2H_4 depicted in Figures S11-S13.

		ΔE_H^{1st}	E_b^{H-1st}	ΔE_H^{2nd}	E_b^{H-2nd}	ΔE^{span}	E_b^{span}
Clean	ABA-Mo_2C-1b@3	0.29	0.74	0.91	1.77	1.20	2.06
	ABC-Mo_2C-1c@2	0.57	0.81	1.13	1.83	1.70	2.40
	Rh-2b	0.39	0.91	-0.11	0.55	0.27	0.94
¾ ML H	ABA-Mo_2C-1b@3	0.44	0.78	0.32	1.13	0.76	1.57
	ABC-Mo_2C-1c@2	0.48	0.83	0.62	1.57	1.09	2.05
	Rh-2b	0.33	0.82	-0.13	0.48	0.20	0.80
¾ ML C_2H_4	ABA-Mo_2C-1b@3	0.21	0.67	0.65	1.95	0.85	2.16
	ABC-Mo_2C-1c@2	0.52	0.84	0.78	1.35	1.30	1.87
	Rh-2b	0.32	0.75	-0.04	0.59	0.28	0.91

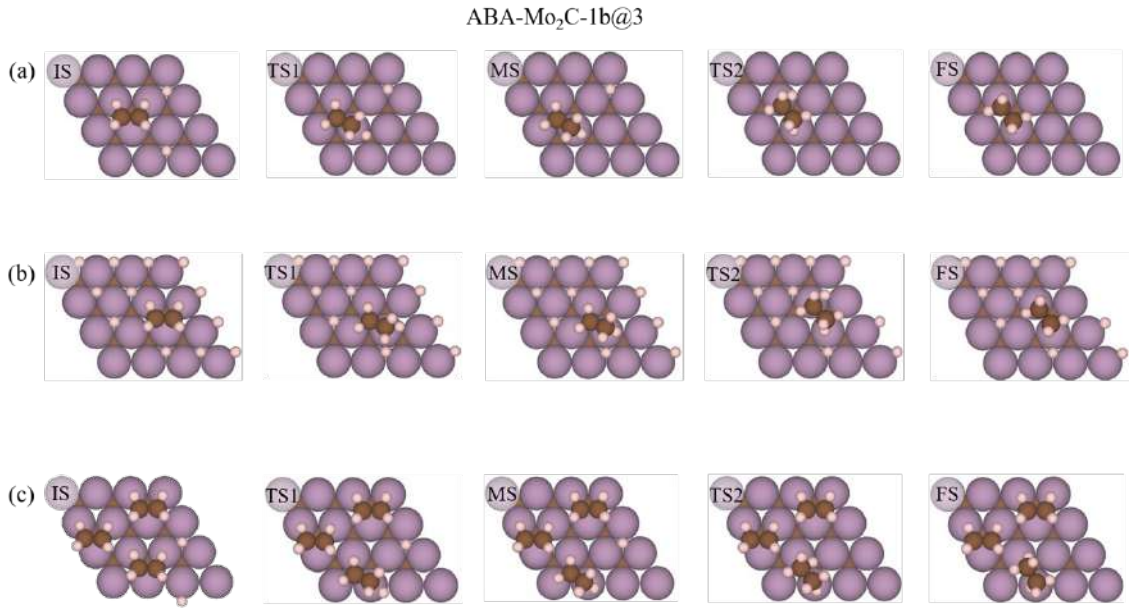

Figure S11. Top views of the IS, MS, FS of C_2H_4 hydrogenation on ABA-Mo_2C (0001) surface, including first (TS1) and second (TS2) hydrogenation transition states on (a) pristine surface, (b) ¾ ML H*, and (c) ¾ ML C_2H_4* models.

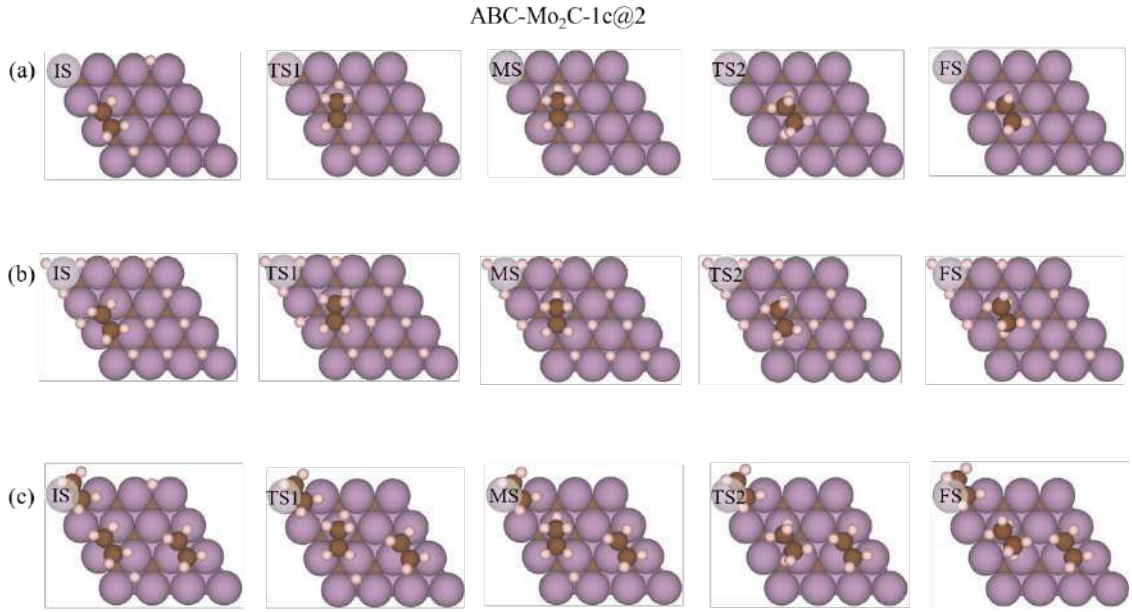

Figure S12. Top views of the IS, MS, FS of C_2H_4 hydrogenation on ABC-Mo_2C (0001) surface, including first (TS1) and second (TS2) hydrogenation transition states on (a) pristine surface, (b) ¾ ML H*, and (c) ¾ ML C_2H_4* models.

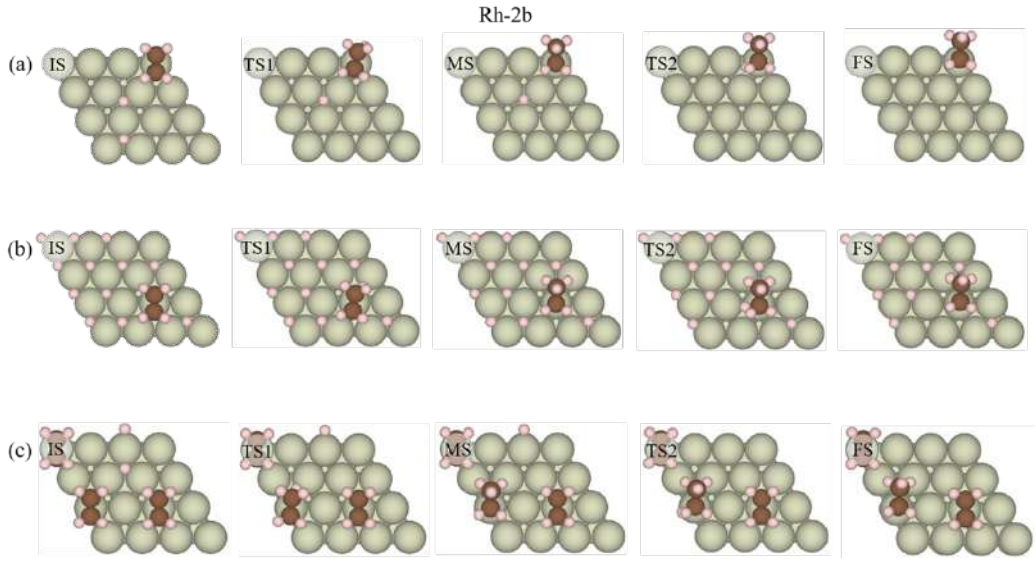

Figure S13. Top views of the IS, MS, FS of C_2H_4 hydrogenation on Rh (111) surface, including first (TS1) and second (TS2) hydrogenation transition states on (a) pristine surface, (b) ¾ ML H*, and (c) ¾ ML C_2H_4* models.

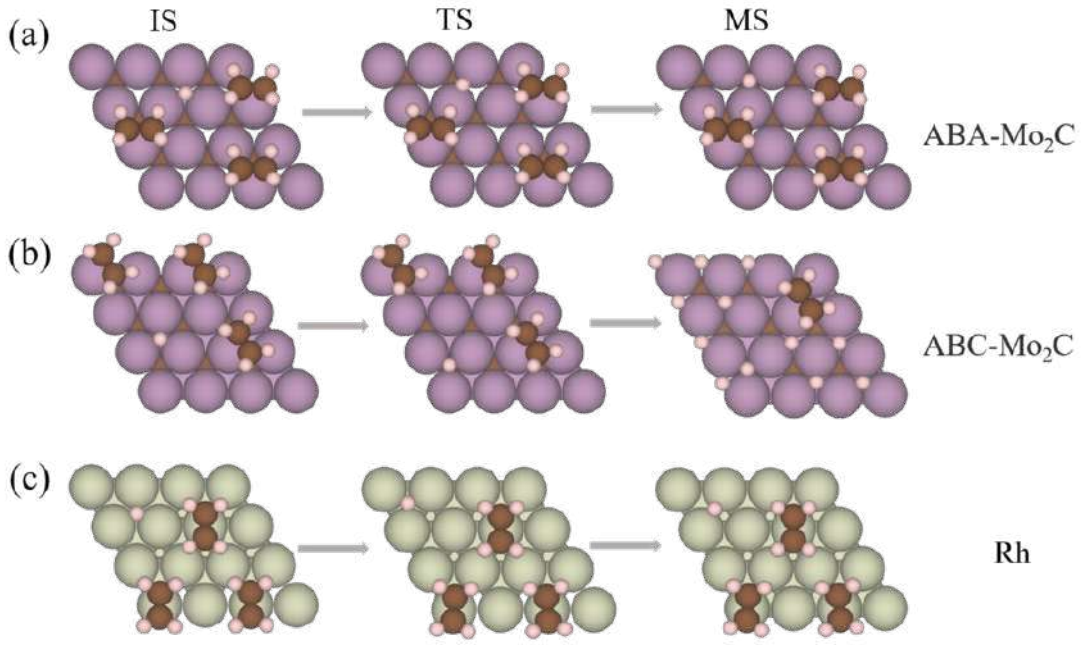

Figure S14. Top views of the IS, TS, and MS of H diffusion on (a) ABA-Mo_2C, (b) ABC-Mo_2C, and (c) Rh (111) surface models with ¾ ML of C_2H_4*. Notice that because of symmetry, the final diffusion from MS to FS is the same as from IS to MS.

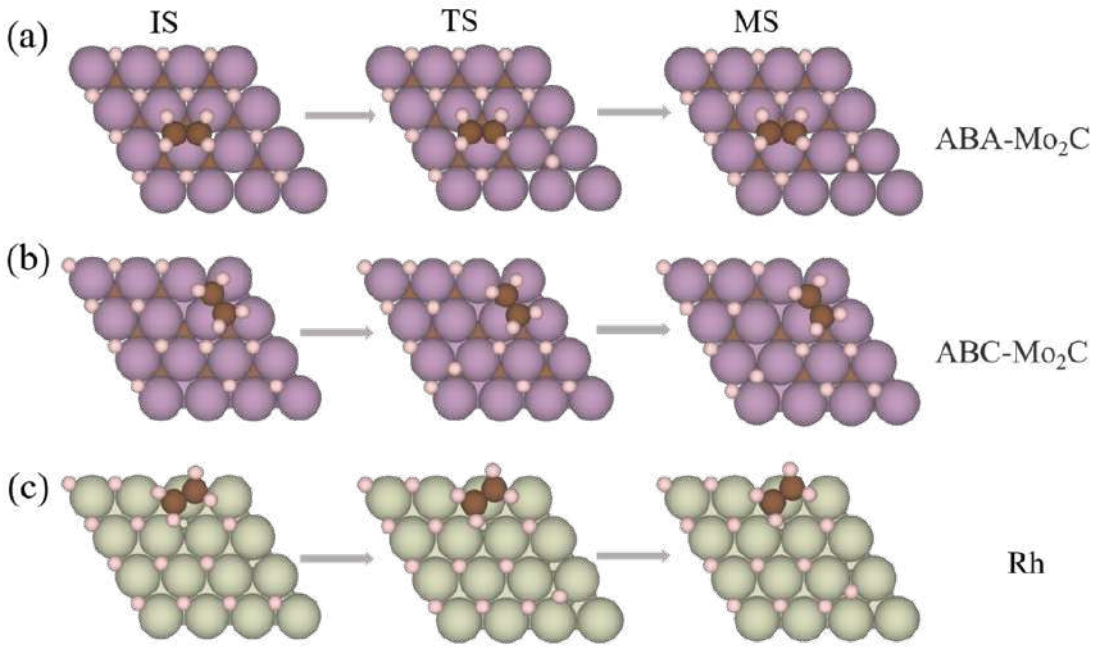

Figure S15. Top views of the IS, TS, and MS of H diffusion on (a) ABA-Mo_2C, (b) ABC-Mo_2C, and (c) Rh (111) surface models with ¾ ML of H*. Notice that because of symmetry, the final diffusion from MS to FS is the same as from IS to MS.

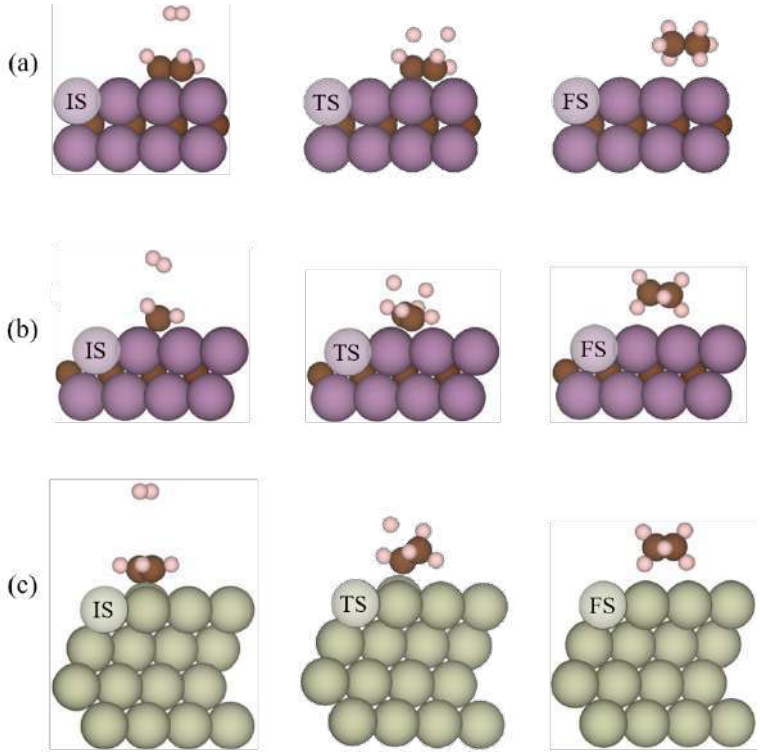

Figure S16. Side views of the IS, TS, and FS of Eley-Rideal mechanism on (a) ABA-Mo_2C, (b) ABC-Mo_2C, and (c) Rh (111) pristine surface mo

Table S11. Energy barriers, E_b, for H diffusion on ABA-Mo_2C, ABC-Mo_2C, and Rh surfaces, either on their pristine models, or having ¾ ML of H or C_2H_4 depicted in Figure 4. All values are given in eV.

	Clean	¾ ML H	¾ ML C_2H_4
ABA-Mo_2C	0.37	0.42	0.36
ABC-Mo_2C	0.28	0.42	0.27
Rh	0.10	0.16	0.11

Table S12. Conversion of propene, $X_{C_3H_6}$, and NMR signal enhancement, SE, for the CH_3-groups of propane obtained in the hydrogenation of propene with p-H_2 over Mo_2CT_{x-500} and Rh/TiO_2 catalysts at different temperatures (see the experimental section for details).

Catalyst	*T*, °C	Flow rate, mLs min^{-1}	X_{C3H6}, %	*SE*
Mo_2CT_{x-500}	165	26	100	–
		155	86	–
		240	75	–
	205	26	100	–
		156	82	–
		240	73	1.1
	235	26	100	–
		156	79	1.9
		240	62	2
	275	26	100	–
		156	60	–
		240	49	4
	325	26	97	–
		156	42	1.3
		240	32	5
	375	26	74	–
		240	9	10
Rh/TiO_2	43	26	43	–
		156	11	161
		240	5	337
	53	26	52	–
		156	12	169
		240	7	347
	60	26	61	–
		156	20	154
		240	11	331
	70	26	72	–
		156	23	154
		240	14	352
	85	26	94	–
		156	32	143
		240	22	316
	100	26	100	–
		156	38	145

		240	28	318
	125	26	100	–
		156	47	131
		240	36	297
	150	26	100	–
		156	53	127
		240	40	298

References

(1) Gilson, M. K.; Irikura, K. K. Symmetry Numbers for Rigid, Flexible, and Fluxional Molecules: Theory and Applications. *J. Phys. Chem. B* **2010**, *114* (49), 16304–16317.

(2) "Collision Theory." Chemistry LibreTexts, Libretexts, 22 May 2017.

(3) Kunkel, C.; Viñes, F.; Illas, F. Transition Metal Carbides as Novel Materials for CO_2 Capture, Storage, and Activation. *Energy Environ. Sci.* **2016**, *9* (1), 141–144.

(4) Truhlar, D. G.; Garrett, B. C.; Klippenstein, S. J. Current Status of Transition-State Theory. *J. Phys. Chem.* **1996**, *100* (31), 12771–12800.

(5) Guiducci, A. E.; Boyd, C. L.; Clot, E.; Mountford, P., Reactions of Cyclopentadienyl-Amidinate Titanium Imido Compounds with CO2: Cycloaddition-Extrusion *vs.* Cycloaddition-Insertion. *Dalton Trans.* **2009**, *30*, 5960–5979.

(6) Tukov, A. A.; Normand, A. T.; Nechaev, M. S., N-Heterocyclic Carbenes Bearing Two, One and No Nitrogen Atoms at the Ylidenecarbon: Insight from Theoretical Calculations. *Dalton Trans.* **2009**, *30*, 7015–7028.

(7) Kozuch, S.; Shaik, S., How to Conceptualize Catalytic Cycles? The Energetic Span Model. *Acc. Chem. Res.* **2011,** *44*, 101–110.

(8) Kozuch, S., A Refinement of Everyday Thinking: the Energetic Span Model for Kinetic Assessment of Catalytic Cycles. *Comput. Mol. Sci.* **2012,** *2*, 795–815.

Appendix E

Supporting Information for "Computationally Screening Non-Precious Single Atom Catalysts for Oxygen Reduction in Alkaline Media."

Computationally Screening Non-Precious Single Atom Catalysts for Oxygen Reduction in Alkaline Media

Tahereh Jangjooye Shaldehi,[1] Ling Meng,[2] Soosan Rowshanzamir,[1*] Mohammad Javad Parnian,[3] Kai Exner,[4] Francesc Viñes,[2] Francesc Illas[2*]

[1]*SHydrogen & Fuel Cell Research Laboratory, School of Chemical, Petroleum and Gas Engineering, Iran University of Science and Technology, Narmak, Tehran 16846-13114, Iran*

[2]*Departament de Ciència de Materials i Química Física & Institut de Química Teòrica i Computacional (IQTCUB), Universitat de Barcelona, c/ Martí i Franquès 1-11, 08028 Barcelona, Spain*

[3]*Department of Chemical and Petroleum Engineering, University of Calgary, 2500 University Dr. NW, Calgary, Alberta T2N 1N4, Canada*

[4]*University Duisburg-Essen, Faculty of Chemistry, Theoretical Inorganic Chemistry, Universitätsstraße 5, 45141 Essen, Germany; Cluster of Excellence RESOLV, Bochum, Germany; Center for Nanointegration (CENIDE) Duisburg-Essen, Duisburg, Germany.*

*Corresponding authors: Francesc Illasa (francesc.illas@ub.edu), Soosan Rowshanzamir (rowshanzamir@iust.ac.ir)

Table S1. Adsorption energy (E_{ads} in eV) of $*O_2$, *OOH, *O, and *OH on the SAC catalysts.

Catalysts	$*O_2$	*OOH	*O	*OH
Sc	-3.19	-4.00	-5.59	-5.48
Ti	-4.68	-6.35	-7.84	-5.62
V	-3.79	-6.20	-7.78	-4.98
Mn	-0.93	-1.75	-4.86	-3.09
Fe	-0.88	-1.89	-4.56	-3.03
Ni	-0.18	-0.52	-1.92	-1.59
Cu	-0.24	-0.62	-1.93	-1.75
Pt	-0.17	-0.28	-1.36	-1.21

Table S2. Calculated total energy (E), vibrational zero-point energy (E_{ZPE}), TS, and Gibbs free energy for *OOH (G_{*OOH}) in ORR on M@NC (M = Sc, Ti, V, Mn, Fe, Ni, Cu, and Pt) at U = 0 V.

Structure	E (eV)	E_{ZPE} (eV)	TS (eV)	G_{*OOH} (eV)
Sc	-464.84	1.07	0.28	-464.05
Ti	-467.35	1.07	0.31	-466.59
V	-467.79	1.09	0.27	-466.97
Mn	-463.93	1.04	0.29	-463.18
Fe	-462.94	1.07	0.36	-462.23
Ni	-459.32	1.06	0.42	-458.62
Cu	-456.38	1.04	0.41	-455.75
Pt	-458.93	1.06	0.33	-458.20

Table S3. Calculated total energy (*E*), vibrational zero-point energy (E_{ZPE}), *TS*, and Gibbs free energy for *O (G_{*O}) in ORR on M@NC (M = Sc, Ti, V, Mn, Fe, Ni, Cu, and Pt) at U = 0 V.

Structure	***E* (eV)**	**E_{ZPE} (eV)**	***TS* (eV)**	**G_{*O} (eV)**
Sc	-454.79	0.69	0.24	-454.34
Ti	-457.19	0.72	0.21	-456.68
V	-457.71	0.72	0.20	-457.19
Mn	-455.38	0.72	0.19	-454.85
Fe	-453.95	0.71	0.19	-453.43
Ni	-449.06	0.63	0.21	-448.64
Cu	-446.03	0.65	0.3	-445.68
Pt	-448.35	0.71	0.24	-447.88

Table S4. Calculated total energy (*E*), vibrational zero-point energy (E_{ZPE}), *TS*, and Gibbs free energy for *OH (G_{*OH}) in ORR on M@NC (M = Sc, Ti, V, Mn, Fe, Ni, Cu, and Pt) at U = 0 V.

Structure	***E* (eV)**	**E_{ZPE} (eV)**	**TS (eV)**	**G_{*OH} (eV)**
Sc	-460.66	0.96	0.28	-459.98
Ti	-460.95	0.93	0.26	-460.28
V	-460.90	0.95	0.26	-460.21
Mn	-459.60	0.95	0.21	-458.86
Fe	-458.41	1.00	0.23	-457.64
Ni	-454.71	0.97	0.26	-454.00
Cu	-451.84	0.94	0.31	-451.21
Pt	-454.19	0.97	0.32	-453.54

Figure S1. Total and PDOS diagrams of: a) Sc@NC, b) Ti@NC, c) V@NC, d) Mn@NC, e) Fe@NC, f) Ni@NC, g) Cu@NC, and h) Pt@NC SAC models. Energy levels are referred to the Fermi energy.

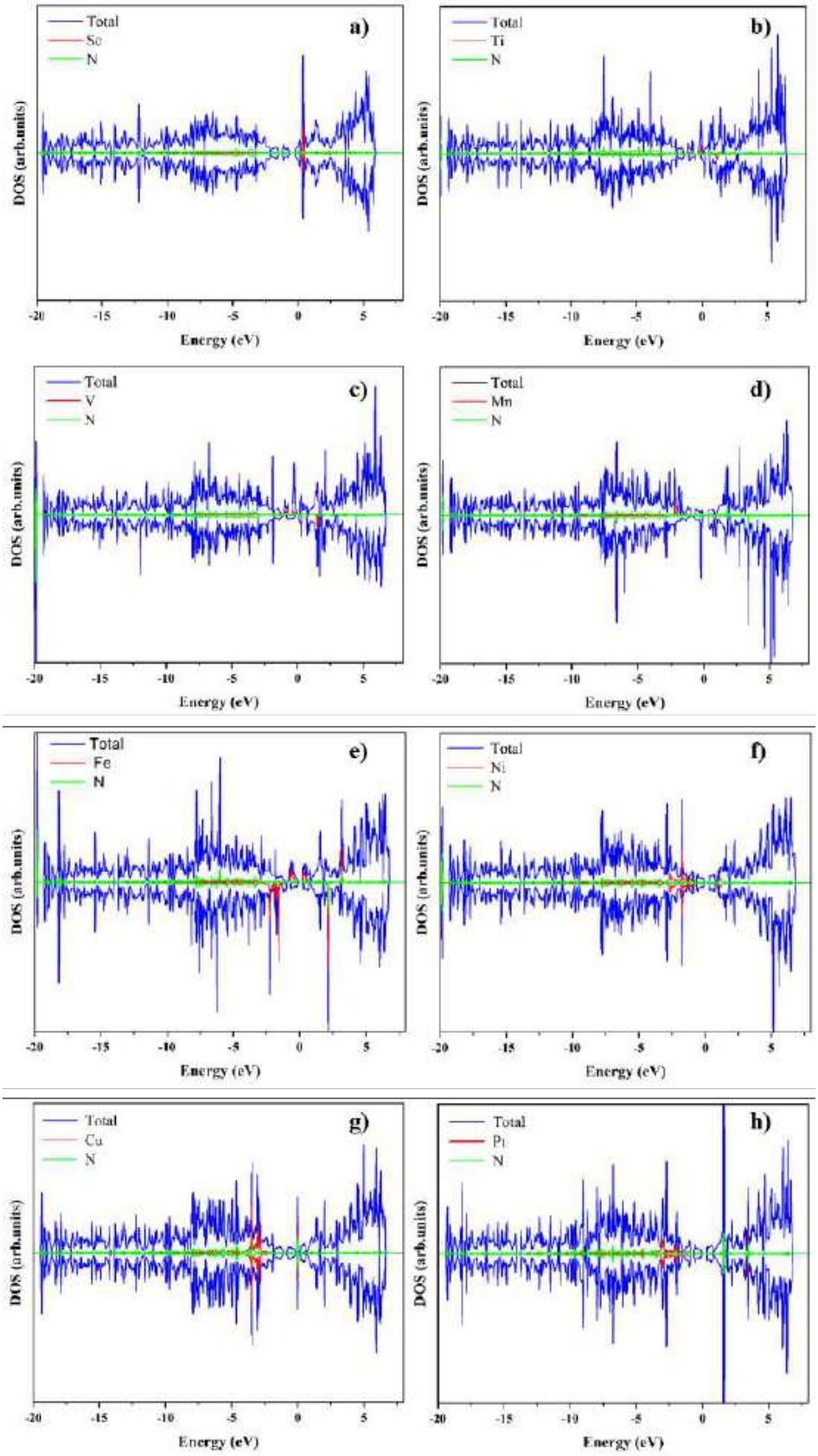

Figure S2. Gibbs free energy diagrams of ORR in alkaline media for: a) to h) Sc, Ti, V, Mn, Fe, Ni, Cu, and Pt SAC models considered at different electrode potentials and *pH* = 14.

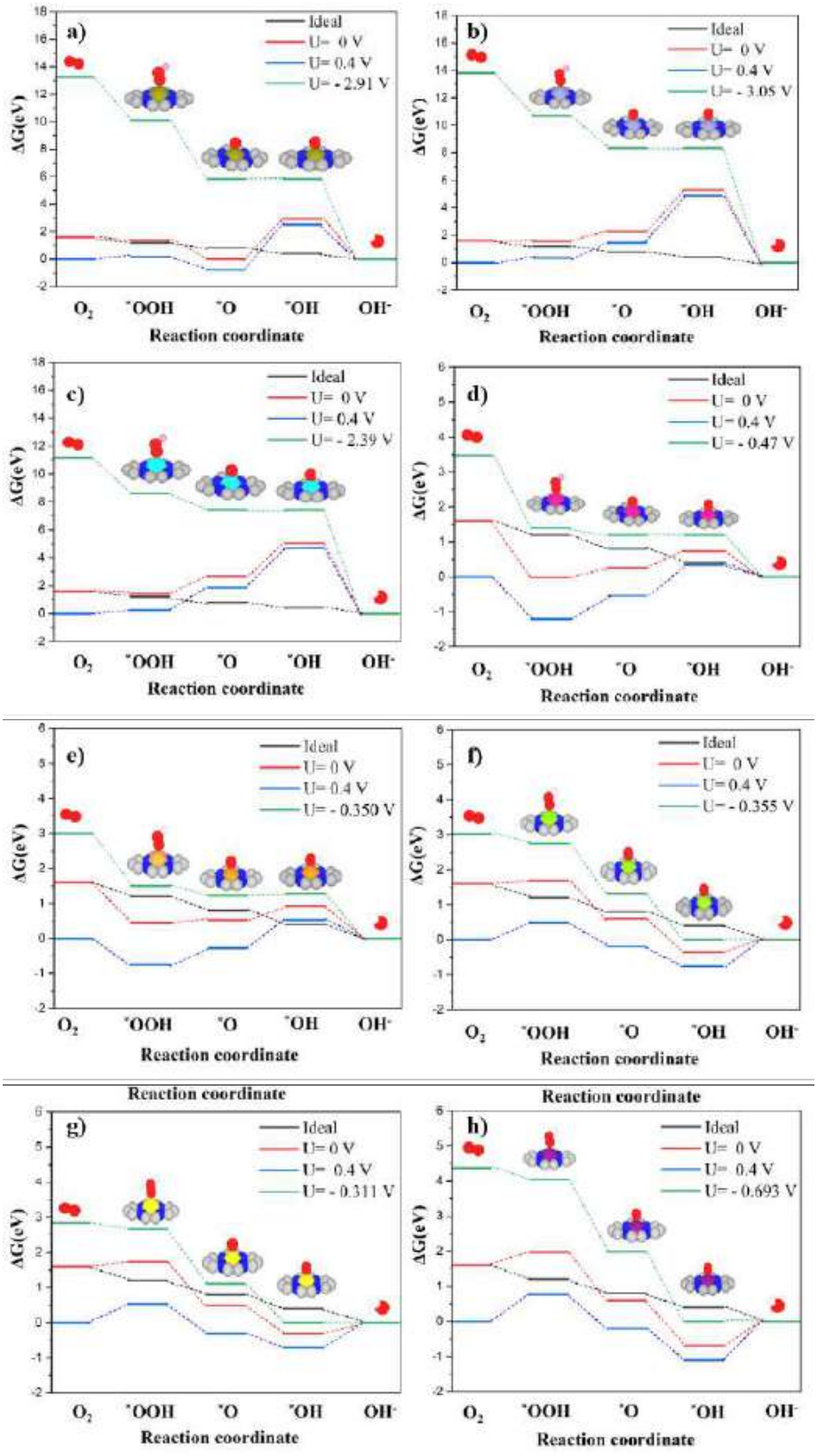

Appendix F

Supporting Information for “Importance of Broken Geometric Symmetry of Single-Atom Pt Sites for Efficient Electrocatalysis.”

Importance of Broken Geometric Symmetry of Single-Atom Pt Sites for Efficient Electrocatalysis

Junsic Cho[1,†], Taejung Lim[2,†], Haesol Kim[1,†], Ling Meng[3], Jinjong Kim[2], Jong Hoon Lee[4], Gwan Yeong Jung[5], Francesc Viñes[3], Francesc Illas[3], Kai S. Exner[6,*], Sang Hoon Joo[2,*] & Chang Hyuck Choi[1,*]

[1]Department of Chemistry, Pohang University of Science and Technology (POSTECH), Pohang 37673, Republic of Korea.

[2]Department of Chemistry, Ulsan National Institute of Science and Technology (UNIST), Ulsan 44919, Republic of Korea.

[3]Departament de Ciència de Materials i Química Física & Institut de Química Teòrica i Computacional (IQTCUB), Universitat de Barcelona, c/ Martí i Franquès 1-11, 08028 Barcelona, Spain.

[4]UNIST Central Research Facilities (UCRF), Ulsan National Institute of Science and Technology (UNIST), Ulsan 44919, Republic of Korea.

[5]School of Energy and Chemical Engineering, Ulsan National Institute of Science and Technology (UNIST), Ulsan 44919, Republic of Korea.

[6]Faculty of Chemistry, Theoretical Inorganic Chemistry, University of Duisburg-Essen, 45141 Essen, Germany; Cluster of Excellence RESOLV, 44801 Bochum, Germany; Center for Nanointegration Duisburg-Essen (CENIDE), 47057 Duisburg, Germany.

†These authors contributed equally to this work.

*Corresponding authors: (K.S.E) kai.exner@uni-due.de; (S.H.J) shjoo@unist.ac.kr; (C.H.C) chchoi@postech.ac.kr

Experimental details

Preparation of the Pt_1/CNT catalysts

Before synthesizing the catalysts, multiwalled carbon nanotubes (CNTs; MR99, Carbon Nano-material Technology Co., Ltd.) with an average diameter of 10 nm and an average length of 10 μm were heated and subsequently acid washed to remove metallic impurities[1,2]. In detail, CNTs (38.0 g) were calcined at 500 ℃ for 1 h in a box furnace at a heating rate of 7.9 ℃ min^{-1}. The heat-treated CNT powder was then acid washed at 80 ℃ for 12 h in 810 g of 6 M HNO_3 (diluted from 60% HNO_3, Samchun Chemicals) under vigorous stirring. After filtration and washing with excess deionized (DI) water, the powder was treated with 720 g of 6 M HCl (diluted from 36% HCl, Samchun Chemicals) as described above. The acid-treated CNTs were collected after drying overnight in an oven at 60 ℃.

Pt_1/CNT catalysts with various Pt contents (Pt_1(X)/CNT, where X = nominal wt.% of Pt) were synthesized by solid-state mixing of CNT and Pt-macrocycle precursor following by annealing[3]. The acid-treated CNT (500 mg) and Pt^{II} meso-tetraphenylporphine (PtTPP, 95%, Frontier Scientific) were ground in an agate mortar over 20 min until the color and texture became constant. The PtTPP contents in the precursor mixtures were 71.0, 21.6, and 2.1 mg for Pt_1(3)/CNT, Pt_1(1)/CNT, and Pt_1(0.15)/CNT, respectively. Subsequently, the powder mixture was pyrolyzed at 700 ℃ for 3 h under an N_2 flow (5N, 1 L min^{-1}) at a heating rate of 2.1 ℃ min^{-1}. N-doped CNT was synthesized by a similar method, but with 54.0 mg of TPP (1−3% Chlorin, Frontier Scientific), which is equivalent to 71.0 mg of PtTPP, was used as a precursor.

Two model catalysts with abundant oxygen (O-Pt_1(3)/CNT) or chlorine (Cl-Pt_1(3)/CNT) functionalities were prepared by post-treatment of Pt_1(3)/CNT. O-Pt_1(3)/CNT (150 mg) was prepared by ozone treatment at 25 ℃ for 1 h using an ozone generator (LAB-I, Ozonetech Inc.). Cl-Pt_1(3)/CNT was prepared by sequential H_2O_2 and SO_2Cl_2 treatments[4]. Pt_1(3)/CNT (75 mg) was mixed with a 12.7 wt.% H_2O_2 solution (1.5 L; diluted from 29–32% H_2O_2, Alfa Aesar) and the mixture was stirred at 70 ℃ for 2 h. The catalyst powder was collected by filtration and washed several times with DI water. Subsequently, H_2O_2-treated Pt_1(3)/CNT (70 mg) was dispersed in 4.2 mL of acetonitrile (99.8%, Sigma-Aldrich) and 280 mg of SO_2Cl_2 (97%, Sigma-Aldrich) was added. The mixture was stirred for 2 h at 75 ℃ and subsequently, heated and refluxed for 5 h at 75 ℃. Cl-Pt_1(3)/CNT was collected *via* filtration and washed several times with DI water.

Physical characterizations

High-angle annular dark-field scanning transmission electron microscopy (HAADF-STEM) images were obtained using a Titan^3 G2 60-300 microscope (FEI Company) equipped with a double-sided spherical aberration (Cs) corrector operated at an accelerating voltage of 200 kV. X-ray diffraction (XRD) patterns were obtained using a high-power X-ray diffractometer (D/MAX2500V/PC, Rigaku) equipped with Cu Kα radiation operated at 40 kV and 200 mA. The XRD patterns were measured in the 2θ range from 10° to 90° at a scan rate of 2° min^{-1}. XRD samples were prepared by pelletizing 50 mg of the catalyst in a sample holder (13 mm in width) under 8 tons of hydraulic pressure. X-ray photoelectron spectroscopy (XPS) measurements were performed using a K-Alpha spectrometer (Thermo Fisher Scientific) equipped with a monochromatic Al Kα X-ray source (1486.6 eV). XPS Pt 4f and N 1s spectra were analyzed using the XPSPeak41 software with a mixed Gaussian (70)–Lorentzian (30) function after applying Shirley-type background correction. The spin-orbit components of the XPS Pt 4f spectra were fixed at 3.34 eV. To quantify the Pt content in the catalysts, a microwave digestion system (Mars 6, CEM) was used to completely dissolve Pt in aqua regia (36% HCl:60% HNO_3 = 3:1, v/v) at 220 ℃ for 40 min (600 W, heating rate of 6.7 ℃ min^{-1}). Subsequently, the resulting solution was analyzed by inductively coupled plasma-optical emission spectroscopy (ICP-OES; 700-ES, Varian).

Pt L_3-edge X-ray absorption spectroscopy (XAS) spectra were collected at the 6D beamline of the Pohang Accelerator Laboratory (PAL). The XAS spectra of the samples were obtained in the transmission mode after pelletizing the catalysts in a sample holder (1 cm in width). Background removal and normalization of the absorption coefficient for X-ray absorption near edge structure (XANES) spectra and fitting for the Fourier transformed k^3-weighted extended X-ray absorption fine structure (EXAFS) spectra were performed using the Athena and Artemis software with 1.1 of Rbkg in a Hanning-type window[5]. Crystallographic data for the PtTPP molecule were used for multishell fitting with the first-shell of Pt–N and the second-shell of Pt···C[6,7]. The amplitude reduction factor (S_0^2) of Pt was fixed at 0.84 after calibration using a standard Pt foil. For the XANES white line (WL) fitting, the interpolation plot of Pt references in our previous report was used to estimate the average oxidation number from the WL area[8].

Electrochemical characterizations

Electrochemical measurements were conducted in a conventional three-electrode H-type cell using a potentiostat (VMP3, Bio-Logic Science Inc.). A homemade rotating disk electrode (RDE) with mirror-polished glassy carbon (5 mm diameter), Pt wire (CE-100, EC Frontier), and saturated Ag/AgCl (RE-T1A, EC Frontier) electrodes were used as the working, counter, and reference electrodes, respectively. The counter electrode was separated from the working and reference electrodes using a glass frit. To prevent unexpected contamination from the reference electrode[9], it was doubly separated from the electrolyte using a glass tube equipped with a glass frit. Ar-saturated 0.1 M $HClO_4$ solutions with and without 1 M NaCl (or 1 M NH_4Cl), which were prepared using DI water (≥18.2 Ω, Arium Mini, Sartorius), concentrated $HClO_4$ solution (70%, Sigma-Aldrich), NaCl (99%, Sigma-Aldrich), and NH_4Cl (99.5%, Sigma-Aldrich), were used as electrolytes. All potentials are given relative to the reversible hydrogen electrode (RHE) scale after calibration of the reference electrode with a Pt wire electrode in an H_2-saturated electrolyte before each electrochemical measurement.

A thin-film electrode was fabricated by drop-casting the catalyst ink (10 μL) onto an RDE. The catalyst loading was 100 μg cm^{-2}. The catalyst ink was prepared by dispersing 5 mg of the catalyst in a mixed solution of DI water (2122 μL), isopropyl alcohol (374 μL), and 5 wt.% Nafion solution (50 μL). Before measuring the chlorine evolution reaction (CER) activity, the working electrode was electrochemically activated by 50 cycles of cyclic voltammetry (CV) in the potential range of 0.05–1.2 V_{RHE} at a scan rate of 500 mV s^{-1} in an Ar-saturated 0.1 M $HClO_4$ electrolyte. CER polarization curves were obtained in the potential range of 1.0–1.6 V_{RHE} at a scan rate of 10 mV s^{-1} in Ar-saturated 0.1 M $HClO_4$ with 1 M NaCl. During the measurements, the working electrode was rotated at 1600 rpm using a rotor (RRDE-3A, ALS). Durability tests were performed using 500 CV cycles in the potential range of 1.0–1.6 V_{RHE} at a scan rate of 100 mV s^{-1}. In this study, the onset potential of the CER was defined as the potential at 1 mA cm^{-2} during CER polarization. All electrochemical results were shown after 85% *iR* compensation correction, which was conducted by electrochemical impedance spectroscopy (EIS) at a fixed potential of 0.9 V_{RHE} in the frequency range of 100 kHz–1 Hz with a potential amplitude of 10 mV.

The electrochemical Cl_2 formation was analyzed by chronoamperometry (CA) using a rotating ring-disk electrode (RRDE; 012613, ALS). The CER selectivity was measured for 120 s at an electrode rotation speed of 1600 rpm; this step was repeated five times

with an intermittent break of 1 min. The applied disk potential was adjusted to generate a current density of ≥10 mA cm^{-2}, but the applied Pt ring potential was fixed at 0.95 V_{RHE}[10]. Prior to the RRDE study, the background currents of the disk and ring electrodes were stabilized at 0.95 V_{RHE} with an electrode rotation of 1600 rpm. The net CER current (i_{CER}) at the disk electrode and CER selectivity were calculated using the following equations.

$$i_{CER} = \left|\frac{i_r}{N}\right| \quad \text{(Eqn. S1)},$$

$$Cl_2 \text{ selectivity } (\%) = 100 \cdot \frac{2 \cdot i_{CER}}{i_d + i_{CER}} = 100 \cdot \frac{2 \cdot \left|\frac{i_r}{N}\right|}{i_d + \left|\frac{i_r}{N}\right|} \quad \text{(Eqn. S2)},$$

where i_r, N, and i_d denote the background-corrected ring current, collection efficiency (0.35–0.37, calibrated using $K_3[Fe(CN)_6]$), and background-corrected disk current, respectively.

Online EFC/ICP-MS measurements

Online Pt dissolution was analyzed by inductively coupled plasma-mass spectrometry (ICP-MS; iCAP RQ, Thermo-Fisher Science) coupled with a homemade electrochemical flow cell (EFC). The EFC was composed of a U-shaped channel (1 mm diameter) and two openings (3 mm diameter). On one opening side, a mirror-polished 3 mm glassy carbon electrode (002012, ALS) made electrochemical contact with the electrolyte (**Supplementary Fig. 8**). On the other opening side, a 3 mm Teflon tube, which was sealed with a polytetrafluoroethylene (PTFE) membrane (WP-020-80, Sumitomo Electric Ind., Ltd.) at one end, was approached to the working electrode to extract any evolved gas products by vacuum. The counter electrode was a graphite rod separated from the electrolyte by a Nafion 115 membrane (DuPont). The reference electrode was a saturated Ag/AgCl electrode that was directly connected to the outlet of the EFC. The electrolyte was Ar-saturated 0.1 M $HClO_4$ with 1 M NH_4Cl, which continuously flowed to the EFC at a flow rate of 400 μL min^{-1} (Note: we avoided using 1 M NaCl due to significant damage on the sampler and skimmer corns of the ICP-MS instrument; **Supplementary Fig. 9**). Prior to introducing the electrolyte to the ICP-MS instrument, it was mixed with 0.5 M HNO_3 containing 5 ppb ^{187}Re as an internal standard at a mixing ratio of 1:1 using a Y-connector. Online Pt dissolution was estimated using the ratio of ^{195}Pt to ^{187}Re signals during the electrochemical treatments. The catalyst loading on the working electrode was 100 μg cm^{-2}. After stabilizing the online ICP-MS signals for 30 min at an open-circuit potential (OCP), the working electrode was electrochemically activated by 50 CV cycles at a scan rate of 500 mV s^{-1} in the potential range of 0.05–1.2 V_{RHE}. Subsequently, Pt

dissolution was monitored over 500 CV cycles at a scan rate of 100 mV s^{-1} in the potential range of 1.0–1.6 V_{RHE}.

DFT calculations

1. Computational details

Electronic structure calculations for periodically replicated appropriate models were performed using the Vienna *ab initio* simulation package (VASP 5.4.1) based on the framework of density functional theory (DFT)[11]. The exchange–correlation potential was treated as in the generalized gradient approximation (GGA) with form proposed by Perdew–Burke–Ernzerhof (PBE)[12]. The valence electron density was expanded on a plane wave basis set with an optimal kinetic energy cutoff of 415 eV, and the projected augmented wave (PAW) method[13], as implemented in VASP by Kresse and Joubert[14], was used to take into account the effect of core electrons on the valence electron density. To carry out the necessary numerical integrations in the reciprocal space, the Brillouin zone was sampled using a 4×4×1 **k**-point **Γ**-centered Monkhorst-Pack grid. A convergence criterion of 10^{-5} eV was used for the total energy, while the relaxation of atomic positions was stopped when forces acting on all relaxed atoms were smaller than 0.01 eV $Å^{-1}$. The calculation of vibrational frequencies for the optimized geometries were carried out by taking the elements of the Hessian matrix as finite differences of analytical gradients with intervals of 0.03 Å. A vacuum width of 25 Å was added to the *x*- and *y*-direction (along the plane direction defined by the employed models), whereas a vacuum width of 20 Å was added in the *z*-direction in all cases to avert artificial interactions between the periodically repeated models. An effective description of the dispersion interactions was included using the Grimme's DFT-D3 method[15]. The adsorption energy was calculated as follows:

$$E_{ads} = E_{i/sub} - (E_{sub} + E_i) \quad \text{(Eqn. S3)},$$

where E_{sub} is the energy of relaxed Pt–N_4 or Pt–N_3(V), E_i is the energy of the reference molecule, and $E_{i/sub}$ is the energy of the intermediate adsorbed on the active Pt sites of Pt–N_4 or Pt–N_3(V). Based on this definition, it follows the more negative the E_{ads} value, the more stable the adsorption structure.

The CER/OER performance was evaluated by calculating the free-energy changes (ΔG) for each elementary reaction step according to the following equation:

$$\Delta G = \Delta E + \Delta E_{ZPE} - T\Delta S \quad \text{(Eqn. S4)},$$

where ΔE corresponds to E_{ads} (*cf.* Eqn. S3), ΔE_{ZPE} is the change in zero-point energy for the step of interest, T is the temperature in Kelvin, and ΔS is the change in entropy. ΔE_{ZPE} was obtained directly from the calculated vibrational frequencies in the harmonic approximation whereas the $T\Delta S$ term requires evaluating the vibrational partition functions which are also related to the vibrational frequencies[16].

2. Surface Pourbaix diagrams

In this study, the free energies of the intermediate structures (*Cl, *OCl, *O, *OH, and *OOH) were considered for Pt–N_4 and Pt–N_3(V). To include the applied electrode potential, U, in the analysis of free-energy changes, the computational hydrogen electrode approach (CHE) was used[17]. This was achieved by considering the stoichiometric coefficients of the transferred electrons (e^-) and protons (H^+), denoted as $\nu(e^-)$ and $\nu(H^+)$, respectively, when compiling reaction equations for each adsorption process[18]. We derive the following formula:

$$\Delta G\,(\mathrm{pH}, U) = \Delta E_{tot} + \Delta E_{ZPE} - T\Delta S - \nu(H^+)\,0.059\ \mathrm{pH} - \nu(e^-) \cdot eU \qquad \text{(Eqn. S5).}$$

The value of 0.059 eV was derived from the term $k_B T \cdot \ln 10$ evaluated at room temperature, where k_B is Boltzmann's constant and U is the applied electrode potential on the standard hydrogen electrode (SHE) scale[19].

The most thermodynamically favorable structure was determined by the minimization of the ΔG values for each adsorbate among the set of considered surface structures. The resulting surface phase (Pourbaix) diagram is shown as a function of overpotential η, defined by $\eta = U - 1.36$ V. For the analysis, the pH was fixed at zero, because we aimed to comprehend trends for the anodic CER in an acidic medium[20]. Hence, we are not discussing pH effects for which the application of grand canonical schemes is called for[21].

3. Mechanistic studies: Assessment of electrocatalytic activity

Free-energy diagrams for the CER over Pt–N_4 and Pt–N_3(V) were constructed to evaluate the CER activity of these active sites. Based on the knowledge gained in previous studies[3,8,22], the CER was assumed to proceed *via* the Volmer–Heyrovsky mechanism[23,24]. Two different Volmer–Heyrovsky pathways with dissimilar intermediates (*i.e.*, *Cl or *OCl) were considered in our theoretical study[25].

(I) Pathway mediated by the *Cl intermediate:

$$\Delta G_1: \quad * + Cl^-\,(aq) \rightleftharpoons *Cl + e^- \qquad \text{(Eqn. S6),}$$

$$\Delta G_2: \quad *Cl + Cl^-\,(aq) \rightleftharpoons Cl_2\,(g) + e^- \qquad \text{(Eqn. S7).}$$

(II) Pathway mediated by the *OCl intermediate:

ΔG_3: $*O + Cl^- (aq) \rightleftharpoons *OCl + e^-$ (Eqn. S8),

ΔG_4: $*OCl + Cl^- (aq) \rightleftharpoons *O + Cl_2 (g) + e^-$ (Eqn. S9).

The free energy of chloride in solution, $G(Cl^-_{aq})$, is related to that of the Cl_2 gas molecule as follows:

$Cl^- (aq) \rightleftharpoons 1/2Cl_2 (g) + e^-$, $\Delta G = 0$ eV @ $U = 1.36$ V_{SHE} (Eqn. S10).

Consequently, the ΔG_j values for each elementary step are given by:

$\Delta G_1 = -\Delta G_2 = G(*Cl) - 1/2 \cdot G(Cl_2) - G(*)$ (Eqn. S11),

$\Delta G_3 = -\Delta G_4 = G(*OCl) - 1/2 \cdot G(Cl_2) - G(*O)$ (Eqn. S12),

where $G(*Cl)$, $G(*O)$, and $G(*OCl)$ are the total energies of the adsorbed intermediates and $G(*)$ is the total energy of Pt–N_4 and Pt–N_3(V) without adsorbed intermediates. Note that the relations $\Delta G_1 = -\Delta G_2$ and $\Delta G_3 = -\Delta G_4$ are fulfilled at the CER equilibrium potential, that is, $U = 1.36$ V_{SHE}.

The oxygen evolution reaction (OER), $2H_2O (aq) \rightarrow O_2 (g) + 4H^+ (aq) + 4e^-$, $U°_{OER} = 1.23$ V_{RHE}, was modelled by assuming the mononuclear mechanism[26]:

ΔG_5: $* + H_2O (l) \rightleftharpoons *OH + H^+ + e^-$ (Eqn. S13),

ΔG_6: $*OH \rightleftharpoons *O + H^+ + e^-$ (Eqn. S14),

ΔG_7: $*O + H_2O (l) \rightleftharpoons *OOH + H^+ + e^-$ (Eqn. S15)

ΔG_8: $*OOH \rightleftharpoons O_2 (g) + H^+ + e^-$ (Eqn. S16).

The free energy of a proton-electron pair, $G(H^+ + e^-)$, can be related to the H_2 gas molecule using the CHE approach as follows:

$H^+ + e^- \rightleftharpoons 1/2H_2 (g)$, $\Delta G = 0$ eV @ $U = 0$ V_{SHE} (Eqn. S17).

Therefore, the ΔG values for each elementary step are:

$\Delta G_5 = G(*OH) + 1/2 \cdot G(H_2) - G(H_2O) - G(*)$ (Eqn. S18),

$\Delta G_6 = G(*O) + 1/2 \cdot G(H_2) - G(*OH)$ (Eqn. S19),

$\Delta G_7 = G(*OOH) + 1/2 \cdot G(H_2) - G(H_2O) - G(*O)$ (Eqn. S20),

$\Delta G_8 = 4 \times 1.23$ eV $- (\Delta G_5 + \Delta G_6 + \Delta G_7)$ (Eqn. S21),

where $G(*OH)$, $G(*O)$, and $G(*OOH)$ are the total energies of the adsorbed intermediates and $G(*)$ is the total energy of Pt–N_4 and Pt–N_3(V) without adsorbed intermediates.

To quantify the electrocatalytic activity for the CER and OER, the recently introduced descriptor $G_{max}(U)$, which is an activity measure that goes beyond the conventional approach in terms of the thermodynamic overpotential only, was used[27,28]. This descriptor relies on a free-energy span model by extracting the largest free-energy difference between intermediate states at a given target electrode potential:

$G_{max}(U) = \max[G_{span\ \#k}(U), k = 1, \ldots, n]$ (Eqn. S22).

For further information on how to define the free-energy spans, $G_{\text{span \#}k}$ (U), for a two-electron (CER) or four-electron process (OER), we refer the reader to recent publications by the authors[29,30].

4. Selectivity assessment

The descriptor G_{max} (U) was extracted for both OER and CER at well-defined electrode potentials, U >1.36 V_{SHE}. The free-energy difference, G_{sel} (U), defined as

$$G_{\text{sel}}(U) = G_{\text{max}}(U)^{\text{OER}} - G_{\text{max}}(U)^{\text{CER}} \qquad \text{(Eqn. S23)},$$

is a measure of the CER selectivity[31]. This quantity was used to determine the CER selectivity in percentage using the following relation[25,31]:

$$\text{CER selectivity}(U) = \frac{exp\left(\frac{G_{\text{sel}}}{k_B.T}\right)}{exp\left(\frac{G_{\text{sel}}}{k_B.T}\right)+1} \qquad \text{(Eqn. S24)}.$$

5. Stability assessment

Considering that PtO_2 is the preferred state of Pt under CER conditions[32], the tendency of the active Pt^{II} sites toward oxidative demetallation to PtO_2 was analyzed for Pt–N_4 and Pt–N_3(V). More precisely, the free-energy change, ΔG_{stab}, for the equation [Pt] + $2H_2O$ → [ ] + PtO_2 + $4H^+$ + $4e^-$ was determined by DFT. Here, [ ] denotes the empty pocket of the Pt–N_4 and Pt–N_3(V) moieties. Based on the obtained ΔG_{stab} value, the equilibrium dissolution potential, U_{diss}, was calculated as follows:

$$U_{\text{diss}} = \frac{\Delta G_{\text{stab}}}{4} \qquad \text{(Eqn. S25)}.$$

The U_{diss} value indicates the electrode potential at which the oxidative demetallation of central Pt species to PtO_2 becomes thermodynamically favorable. Adequate stability of the Pt–N_4 and Pt–N_3(V) sites is provided if the U_{diss} value significantly exceeds the CER equilibrium potential (*i.e.*, 1.36 V_{SHE}).

Supplementary Note 1

Physical characterization of Pt_1(X)/CNTs

HAADF-STEM analysis was performed to identify the atomic distribution of the Pt species on Pt_1(X)/CNT. The results showed a uniform distribution of atomically dispersed Pt species without appreciable amounts of Pt clusters or nanoparticles (**Supplementary Fig. 1**). The Pt contents of Pt_1(3)/CNT, Pt_1(1)/CNT, and Pt_1(0.15)/CNT were 3, 1, and 0.15 wt.%, respectively, confirmed by ICP-OES. In the XRD spectrum, Pt_1(3)/CNT (and Pt_1(1)/CNT and Pt_1(0.15)/CNT) exhibited an almost identical XRD pattern to that of a Pt-free CNT-supporting substrate (**Supplementary Fig. 2**). More evidently, the k^3-weighted Pt L_3-edge EXAFS spectra revealed a strong scattering peak at approximately 2.0 Å (**Supplementary Fig. 3**), which corresponds to Pt–N bonding. Their fitting parameters further confirmed the first-shell Pt–N bonding and second-shell Pt–C bonding without any Pt–Pt bonding. The coordination number of the Pt–N bonding for Pt_1(3)/CNT was approximately four (**Supplementary Table 1**). Both the XANES and XPS spectra verified that the oxidation state of the Pt species on Pt_1(3)/CNT was Pt^{II} (**Supplementary Figs. 4 and 5**). Therefore, these physical characterization results revealed that Pt_1(3)/CNT was composed of abundant porphyrin-like Pt^{II}–N_4 moieties covalently embedded on the CNT support.

Supplementary Figures

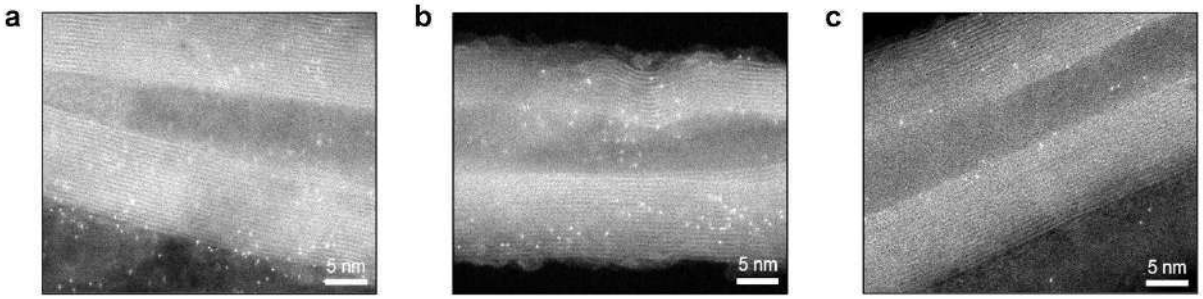

Supplementary Fig. 1: a–c, HAADF-STEM images of Pt_1(3)/CNT (**a**), Pt_1(1)/CNT (**b**), and Pt_1(0.15)/CNT (**c**).

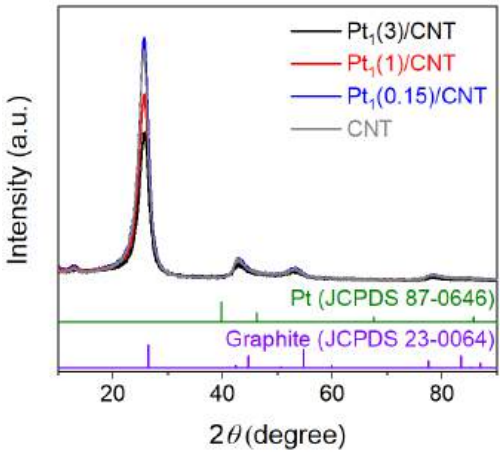

Supplementary Fig. 2: XRD patterns of the Pt_1(X)/CNT catalysts and CNT supporting substrate. For better comparison, XRD patterns of graphite (JCPDS 23-0064) and Pt (JCPDS 87-0646) are also shown.

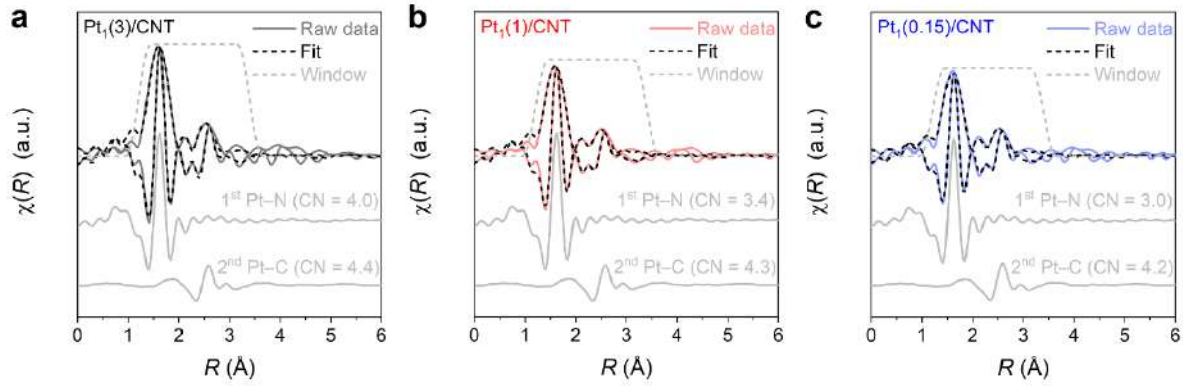

Supplementary Fig. 3: a–c, The k^3-weighted Pt L_3-edge EXAFS spectra and fitted curves of Pt_1(3)/CNT (**a**), Pt_1(1)/CNT (**b**), and Pt_1(0.15)/CNT (**c**). The detailed fitting parameters are provided in **Supplementary Table 1**.

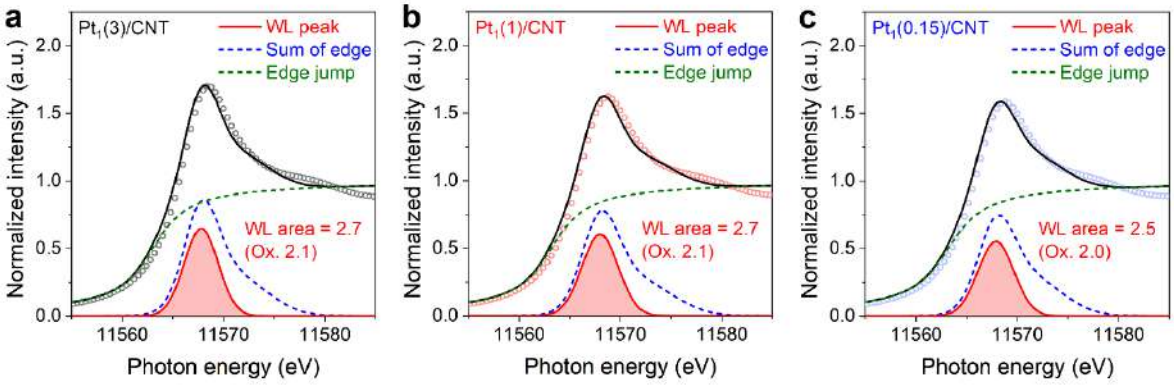

Supplementary Fig. 4: a–c, Pt L_3-edge XANES spectra of $Pt_1(3)/CNT$ (**a**), $Pt_1(1)/CNT$ (**b**), and $Pt_1(0.15)/CNT$ (**c**). The results show that average oxidation state of the catalysts is Pt^{II}. The XANES WL fitting was conducted using the interpolation equation of Pt references in our previous report[8].

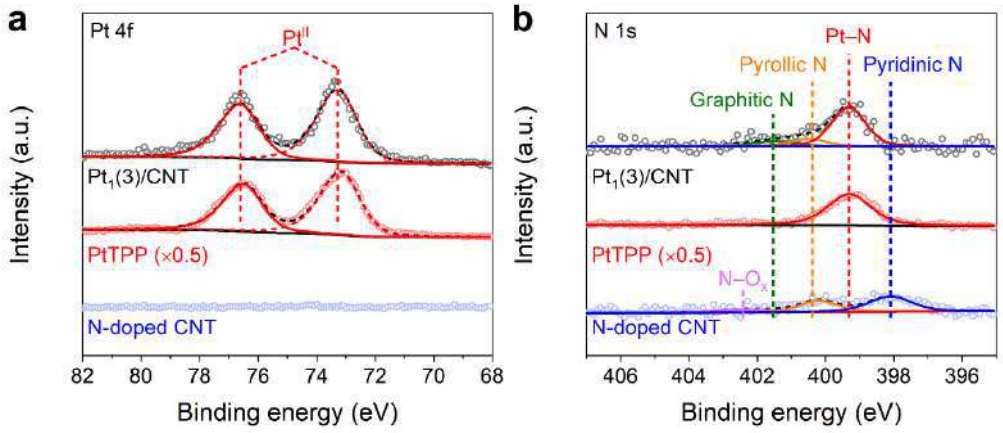

Supplementary Fig. 5: a, XPS Pt 4f and **b**, N 1s spectra of $Pt_1(3)/CNT$, PtTPP, and N-doped CNT. The XPS Pt $4f_{7/2}$ spectrum of $Pt_1(3)/CNT$ shows strong peaks at 73.2 and 76.6 eV, almost identical to those of PtTPP with a Pt^{II} center.

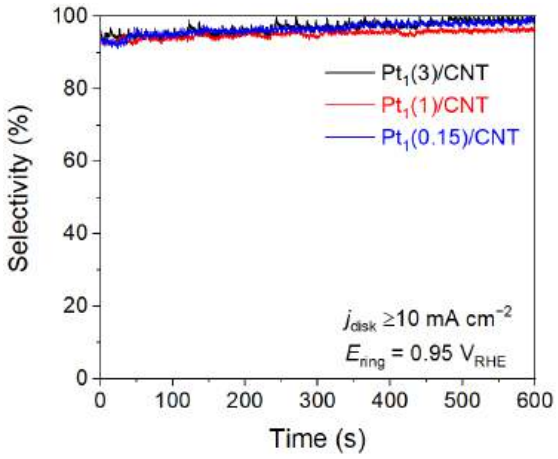

Supplementary Fig. 6: CER selectivity of $Pt_1(3)$/CNT, $Pt_1(1)$/CNT, and $Pt_1(0.15)$/CNT measured using an RRDE in Ar-saturated 0.1 M $HClO_4$ with 1 M NaCl. The CER selectivity of all the catalysts is almost 100%.

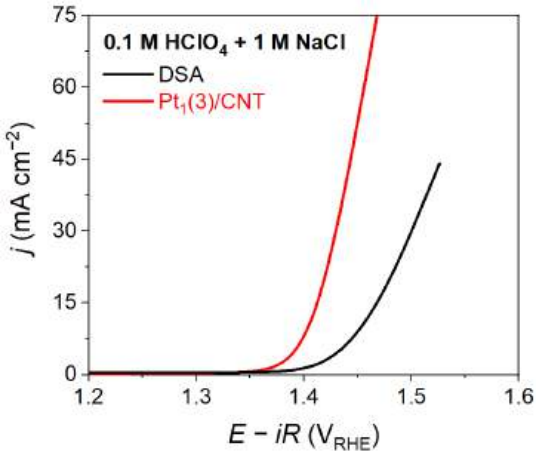

Supplementary Fig. 7: CER polarization curves of $Pt_1(3)$/CNT and Ru/Ir-based dimensionally stable anode (DSA; Ru/Ir atomic ratio = 0.5; provided by Siontech Inc.). The $Pt_1(3)$/CNT has a much higher CER activity than DSA.

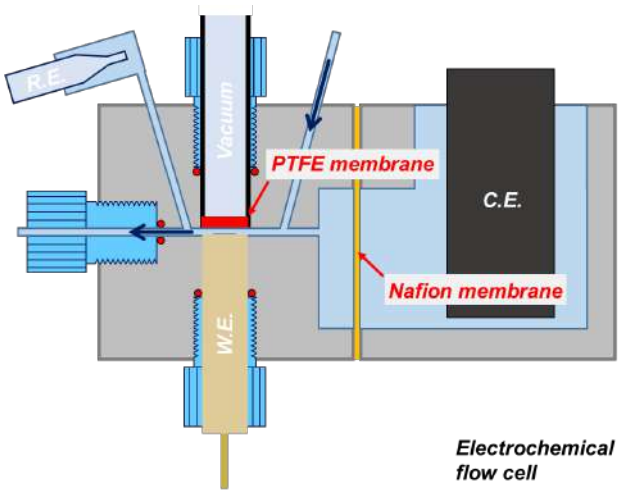

Supplementary Fig. 8: Schematic image of a homemade EFC connected to the ICP-MS. A PTFE membrane-sealed Teflon tube was installed into the EFC to remove the gaseous chlorine product by vacuum. The Nafion membrane was used to separate the counter electrode from the main body of the EFC.

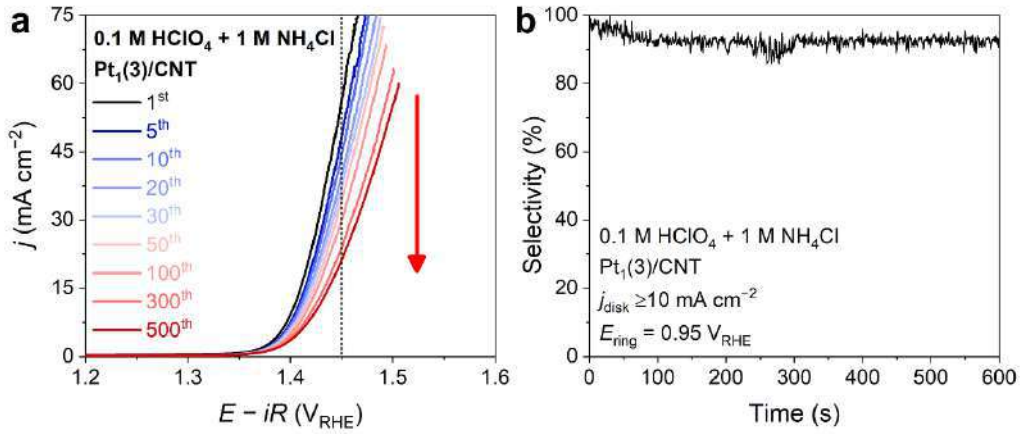

Supplementary Fig. 9: a, CER activity and durability measurements in Ar-saturated 0.1 M $HClO_4$ with 1 M NH_4Cl. **b**, CER selectivity of $Pt_1(3)/CNT$ measured using an RRDE in Ar-saturated 0.1 M $HClO_4$ with 1 M NH_4Cl. The CER activity and selectivity of $Pt_1(3)/CNT$ are comparable with those measured in Ar-saturated 0.1 M $HClO_4$ with 1 M NaCl, indicating no significant effects of the Cl^- precursors on the CER electrocatalysis on $Pt_1(3)/CNT$. Therefore, to prevent the harmful accumulation of NaCl on the sampler and skimmer corns of the ICP-MS instrument, NH_4Cl was used as a Cl^- precursor for the online EFC/ICP-MS studies.

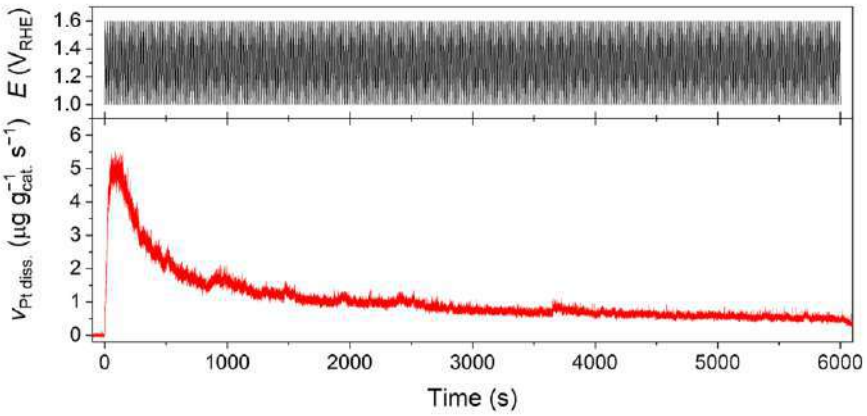

Supplementary Fig. 10: Real-time Pt dissolution of $Pt_1(3)$/CNT. The online EFC/ICP-MS signals measured during 500 CV cycles in the potential range of 1.0–1.6 V_{RHE} in Ar-saturated 0.1 M $HClO_4$ with 1 M NH_4Cl.

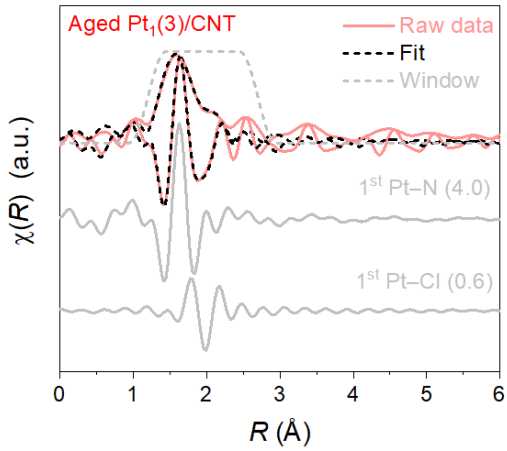

Supplementary Fig. 11: The k^3-weighted Pt L_3-edge EXAFS spectra and fitted curves of $Pt_1(3)$/CNT after 500 CVs in the potential range of 1.0–1.6 V_{RHE} in Ar-saturated 0.1 M $HClO_4$ with 1 M NaCl. The detailed fitting parameters are provided in **Supplementary Table 1**.

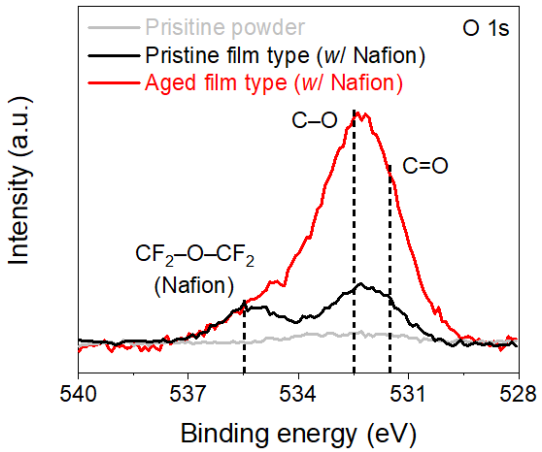

Supplementary Fig. 12: The XPS O 1s spectra of pristine $Pt_1(3)$/CNT powder sample, pristine $Pt_1(3)$/CNT film with Nafion binder, and aged $Pt_1(3)$/CNT film with Nafion binder after 500 CVs in the potential range of 1.0–1.6 V_{RHE} in Ar-saturated 0.1 M $HClO_4$ with 1 M NaCl. Fabrication of powder $Pt_1(3)$/CNT with the Nafion ionomer is a prerequisite for preparing the working electrode. Consequently, the XPS O 1s spectrum of the aged $Pt_1(3)$/CNT film results from convoluted signals of the newly generated oxygen functionalities and Nafion ionomer[33,34]. Thus, the XPS O 1s spectrum of the pristine $Pt_1(3)$/CNT film was subtracted from that of the aged $Pt_1(3)$/CNT film to deconvolute the XPS signals of the newly generated oxygen functionalities without the Nafion contribution (shown in **Fig. 2a** in the main article).

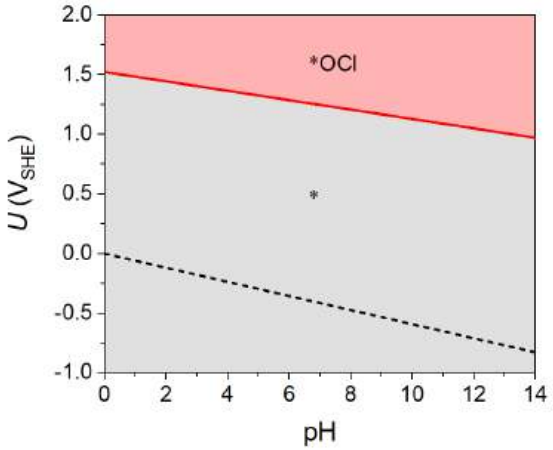

Supplementary Fig. 13: Surface Pourbaix diagram of the square planar Pt–N_4 model.

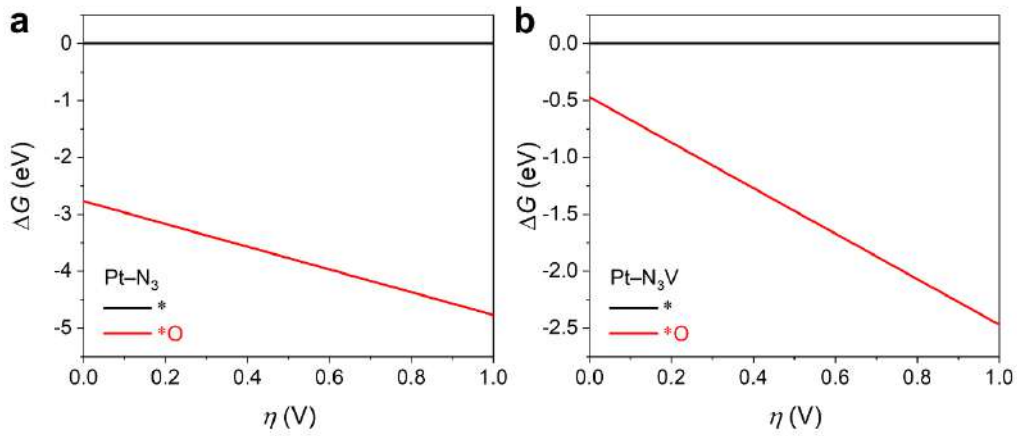

Supplementary Fig. 14: Pourbaix-like diagrams for the **a**, trigonal planar Pt–N_3 and **b**, T-shaped Pt–N_3V models.

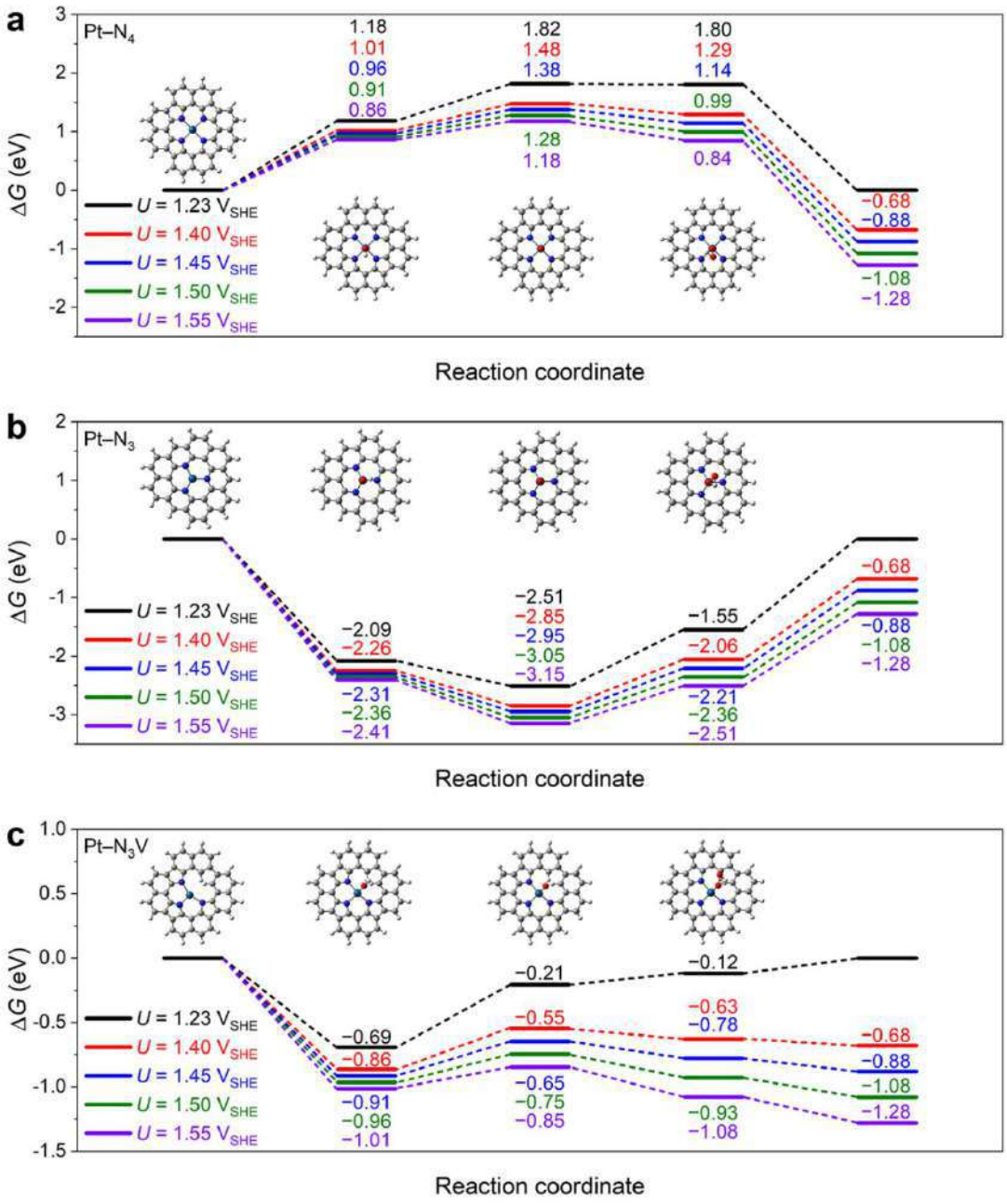

Supplementary Fig. 15: a–c, Free-energy diagrams of the OER, assuming the mononuclear mechanism *via* the *OH, *O, and *OOH adsorbates, for Pt–N_4 (**a**), Pt–N_3 (**b**), and Pt–N_3V (**c**).

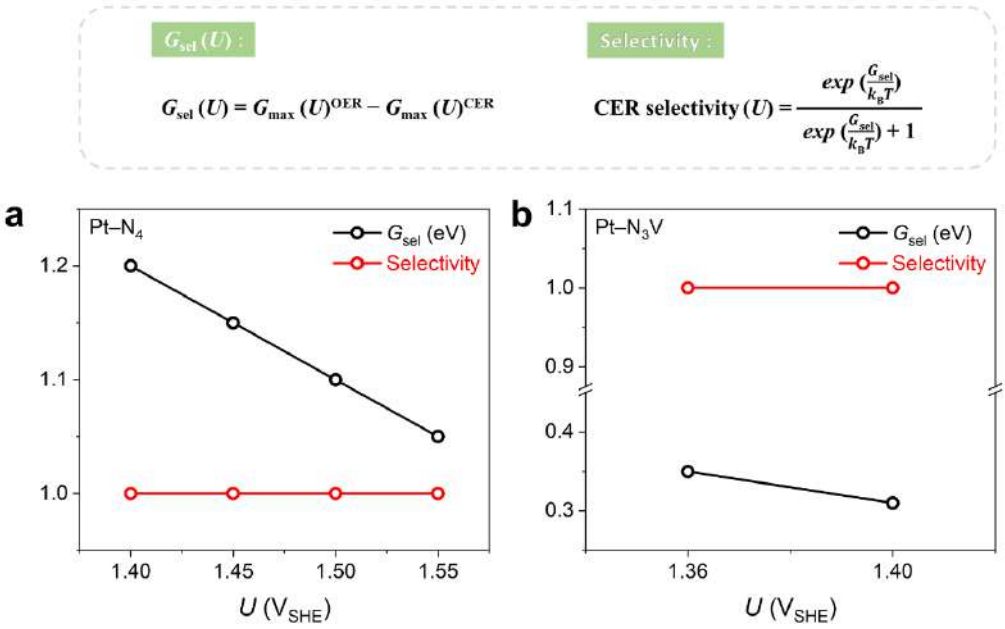

Supplementary Fig. 16: Selectivity analysis for the competing CER and OER processes over the **a**, Pt–N_4 and **b**, Pt–N_3V sites.

Supplementary Table 1: Summary of EXAFS fitting parameters of pristine $Pt_1(X)/CNT$, aged $Pt_1(3)/CNT$, and Pt foil.

Sample	***k* range**	**R range**	**Shell**	**CN**	***R* (Å)**	**σ^2 (10^{-3} Å^{-2})**	**ΔE_0 (eV)**	***R* factor (%)**
$Pt_1(0.15)/CNT$	2.7−11.2	1.2−3.4	Pt−N	3.0 (± 0.3)	2.01 (± 0.01)	3.56 (± 0.97)	16.43 (± 0.33)	1.2
			Pt···C	4.2 (± 1.3)	2.99 (± 0.02)	8.44 (± 4.01)		
$Pt_1(1)/CNT$			Pt−N	3.4 (± 0.4)	2.00 (± 0.01)	4.26 (± 1.00)	15.59 (± 0.91)	1.2
			Pt···C	4.3 (± 1.5)	2.97 (± 0.02)	9.38 (± 4.71)		
$Pt_1(3)/CNT$			Pt−N	4.0 (± 0.4)	2.01 (± 0.01)	3.58 (± 0.99)	15.89 (± 1.00)	1.3
			Pt···C	4.4 (± 1.6)	3.01 (± 0.00)	6.42 (± 4.11)		
Aged $Pt_1(3)/CNT$			Pt−N	4.0*	2.02 (± 0.02)	3.39 (± 0.98)	15.18 (± 2.42)	6.0
			Pt−Cl	0.6 (± 0.2)	2.33 (± 0.03)	1.00*		
Pt foil	2.1−13.5	1.7−3.8	Pt−Pt	12*	2.77 (± 0.02)	4.59 (± 0.27)	9.26 (± 0.50)	0.3

Pt–N indicates a single scattering path of the first-shell. Pt···C indicates a single scattering path of the second-shell (**Shell** column). The **CN** is the coordination number obtained from the amplitude reduction factor (S_0^2) of 0.84. ***R*** indicates bond distance. $\boldsymbol{\sigma^2}$ indicates the Debye-Waller factor. $\boldsymbol{\Delta E_0}$ indicates the energy shift. ***R* factor** was obtained from the best fit for the respective catalysts. (*Defined parameters to reduce correlations between variables)

Supplementary Table 2: Summary of G_{max} (U) for the CER and OER over Pt–N_4 and Pt–N_3(V) at pH = 0.

G_{max} (U) (eV)	Pt–N_4	Pt–N_3	Pt–N_3V
CER	0.32[a] (0.28[b])	0.21 (0.17)	0.05 (0.01)
OER	1.56 (1.48)	2.25 (2.17)	0.35 (0.31)

[a] U = 1.36 V_{SHE}

[b] U = 1.40 V_{SHE}

References

1 Sa, Y. J. *et al.* A General Approach to Preferential Formation of Active Fe–N_x Sites in Fe–N/C Electrocatalysts for Efficient Oxygen Reduction Reaction. *J. Am. Chem. Soc.* **138**, 15046-15056 (2016).

2 Woo, J. *et al.* Promoting Oxygen Reduction Reaction Activity of Fe–N/C Electrocatalysts by Silica-Coating-Mediated Synthesis for Anion-Exchange Membrane Fuel Cells. *Chem. Mater.* **30**, 6684-6701 (2018).

3 Lim, T. *et al.* Atomically Dispersed Pt–N_4 Sites as Efficient and Selective Electrocatalysts for the Chlorine Evolution Reaction. *Nat. Commun.* **11**, 412 (2020).

4 Wang, C., Zhou, J. & Chu, L. Chlorine-Functionalized Reduced Graphene Oxide for Methylene Blue Removal. *RSC Adv.* **5**, 52466-52472 (2015).

5 Ravel, B. & Newville, M. ATHENA, ARTEMIS, HEPHAESTUS: Data Analysis for X-ray Absorption Spectroscopy using IFEFFIT. *J. Synchrotron Radiat.* **12**, 537-541 (2005).

6 Hazell, A. Structure of (5,10,15,20-tetraphenyl-21*H*,23*H*-porphinato)platinum(II), $C_{44}H_{28}N_4Pt$. *Acta Cryst.* **40**, 751-753 (1984).

7 Chang, Y. H., Choi, K. H., Ford, W. T., Cho, S. J. & Ryoo, R. XANES and EXAFS Study of a Platinum Phthalocyanine. *J. Chem. Soc. Chem. Commun.*, 785-788 (1994).

8 Lim, T. *et al.* General Efficacy of Atomically Dispersed Pt Catalysts for the Chlorine Evolution Reaction: Potential-Dependent Switching of the Kinetics and Mechanism. *ACS Catal.* **11**, 12232-12246 (2021).

9 Ji, S. G., Kim, H., Choi, H., Lee, S. & Choi, C. H. Overestimation of Photoelectrochemical Hydrogen Evolution Reactivity Induced by Noble Metal Impurities Dissolved from Counter/Reference Electrodes. *ACS Catal.* **10**, 3381-3389 (2020).

10 Vos, J. G. & Koper, M. T. M. Measurement of Competition between Oxygen Evolution and Chlorine Evolution using Rotating Ring-disk Electrode Voltammetry. *J. Electroanal. Chem.* **819**, 260-268 (2018).

11 Li, N. *et al.* Double Transition Metal Carbides MXenes (D-MXenes) as Promising Electrocatalysts for Hydrogen Reduction Reaction: *Ab Initio* Calculations. *ACS Omega* **6**, 23676-23682 (2021).

12 Perdew, J. P. *et al.* Atoms, Molecules, Solids, and Surfaces: Applications of the Generalized Gradient Approximation for Exchange and Correlation. *Phys. Rev. B* **46**, 6671-6687 (1992).

13 Kresse, G. & Furthmüller, J. Efficient Iterative Schemes for *Ab Initio* Total-Energy Calculations using a Plane-Wave Basis Set. *Phys. Rev. B* **54**, 11169-11186 (1996).

14 Kresse, G. & Joubert, D. From Ultrasoft Pseudopotentials to the Projector Augmented-Wave Method. *Phys. Rev. B* **59**, 1758-1775 (1999).

15 Grimme, S. Semiempirical GGA-Type Density Functional Constructed with a Long-Range Dispersion Correction. *J. Comput. Chem.* **27**, 1787-1799 (2006).

16 López, M., Exner, K. S., Viñes, F. & Illas, F. Computational Pourbaix Diagrams for MXenes: A Key Ingredient toward Proper Theoretical Electrocatalytic Studies. *Adv. Theory Simul.*, 2200217 (2022).

17 Nørskov, J. K. *et al.* Origin of the Overpotential for Oxygen Reduction at a Fuel-Cell Cathode. *J. Phys. Chem. B* **108**, 17886-17892 (2004).

18 Exner, K. S., Anton, J., Jacob, T. & Over, H. Chlorine Evolution Reaction on RuO_2(110): *Ab Initio* Atomistic Thermodynamics Study - Pourbaix Diagrams. *Electrochim. Acta* **120**, 460-466 (2014).

19 Kibsgaard, J. *et al.* Designing an Improved Transition Metal Phosphide Catalyst for Hydrogen Evolution using Experimental and Theoretical Trends. *Energy Environ. Sci.* **8**, 3022-3029 (2015).

20 Exner, K. S., Anton, J., Jacob, T. & Over, H. Controlling Selectivity in the Chlorine Evolution Reaction over RuO_2-Based Catalysts. *Angew. Chem. Int. Ed.* **53**, 11032-11035 (2014).

21 Groß, A. Reversible vs Standard Hydrogen Electrode Scale in Interfacial Electrochemistry from a Theoretician's Atomistic Point of View. *J. Phys. Chem. C* **126**, 11439-11446 (2022).

22 Exner, K. S., Anton, J., Jacob, T. & Over, H. Full Kinetics from First Principles of the Chlorine Evolution Reaction over a RuO_2(110) Model Electrode. *Angew. Chem. Int. Ed.* **55**, 7501-7504 (2016).

23 Janssen, L. J. J., Starmans, L. M. C., Visser, J. G. & Barendrecht, E. Mechanism of the Chlorine Evolution on a Ruthenium Oxide/Titanium Oxide Electrode and on a Ruthenium Electrode. *Electrochim. Acta* **22**, 1093-1100 (1977).

24 Trasatti, S. *Electrodes of Conductive Metallic Oxides, Part B (Studies in Physical & Theoretical Chemistry)*. (Elsevier Science Ltd, Amsterdam-Oxford-New York, 1981).

25 Exner, K. S. Design Criteria for the Competing Chlorine and Oxygen Evolution Reactions: Avoid the OCl Adsorbate to Enhance Chlorine Selectivity. *Phys. Chem. Chem. Phys.* **22**, 22451-22458 (2020).

26 Man, I. C. *et al.* Universality in Oxygen Evolution Electrocatalysis on Oxide Surfaces. *ChemCatChem* **3**, 1159-1165 (2011).

27 Exner, K. S. A Universal Descriptor for the Screening of Electrode Materials for Multiple-Electron Processes: Beyond the Thermodynamic Overpotential. *ACS Catal.* **10**, 12607-12617 (2020).

28 Exner, K. S. Why Approximating Electrocatalytic Activity by a Single Free-Energy Change is Insufficient. *Electrochim. Acta* **375**, 137975 (2021).

29 Razzaq, S. & Exner, K. S. Method to Determine the Bifunctional Index for the Oxygen Electrocatalysis from Theory. *ChemElectroChem* **9**, e202101603 (2022).

30 Exner, K. S. Beyond the Thermodynamic Volcano Picture in the Nitrogen Reduction Reaction over Transition-Metal Oxides: Implications for Materials Screening. *Chin. J. Catal.* **43**, 2871-2880 (2022).

31 Exner, K. S. Controlling Stability and Selectivity in the Competing Chlorine and Oxygen Evolution Reaction over Transition Metal Oxide Electrodes. *ChemElectroChem* **6**, 3401-3409 (2019).

32 Goeke, R. S., Datye, A. K., Atanassov, P. & St-Pierre, J. Model Electrode Structures for Studies of Electrocatalyst Degradation. *ECS Trans.* **33**, 361 (2010).

33 Friedman, A. K., Shi, W., Losovyj, Y., Siedle, A., R. & Baker, L. A. Mapping Microscale Chemical Heterogeneity in Nafion Membranes with X-ray Photoelectron Spectroscopy. *J. Electrochem. Soc.* **165**, H733 (2018).

34 Moulder, J. F. & Chastain, J. *Handbook of X-ray Photoelectron Spectroscopy: A Reference Book of Standard Spectra for Identification and Interpretation of XPS Data*. (Physical Electronics Division, Perkin-Elmer Corporation, 1992).